

DECEMBER 2022

AJNR

VOLUME 43 • PP 1687–1833

AJNR

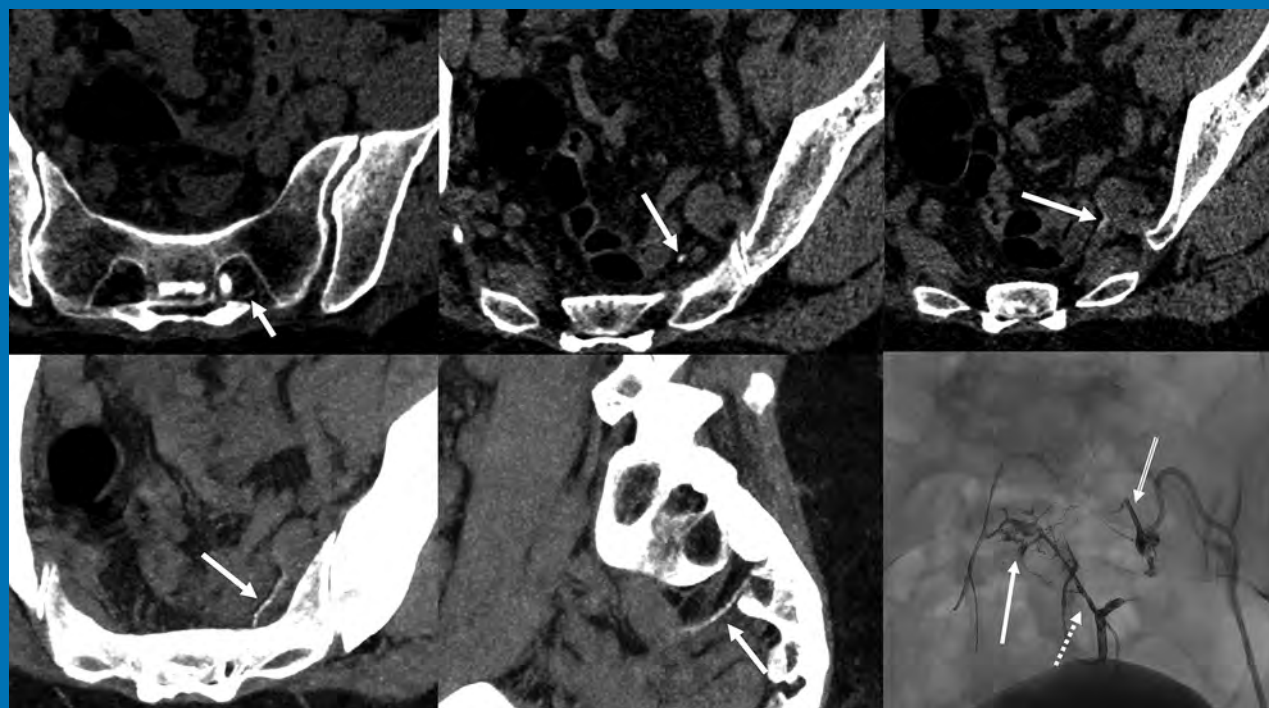
AMERICAN JOURNAL OF NEURORADIOLOGY

DECEMBER 2022
VOLUME 43
NUMBER 12
WWW.AJNR.ORG

THE JOURNAL OF DIAGNOSTIC AND
INTERVENTIONAL NEURORADIOLOGY

Automated detection of cerebral aneurysms
Association of dural AVFs and venous thrombosis
Predictors of endovascular procedural complications in stroke
Effects of COVID-19 on the human olfactory system

Official Journal ASNR • ASFNR • ASHNR • ASPNR • ASSR



FRED™ X™

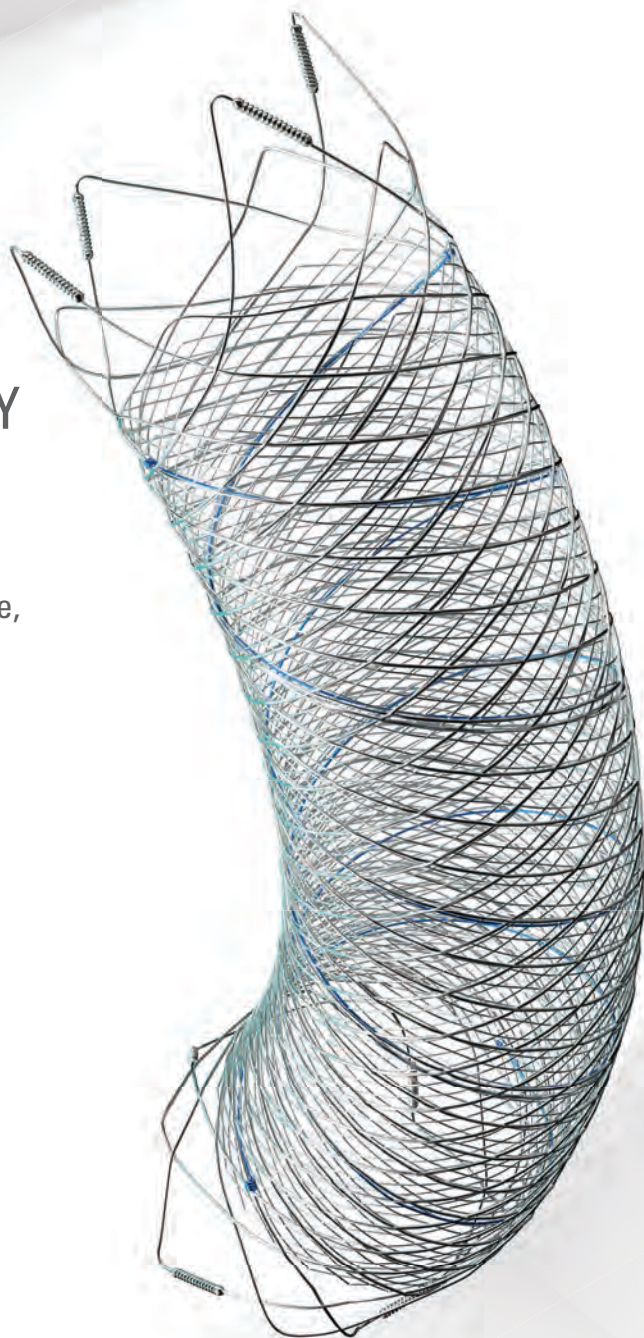
Flow Diverter Stent

THE NEXT ADVANCEMENT IN FLOW DIVERSION TECHNOLOGY

The FRED™ X Flow Diverter features the same precise placement and immediate opening of the FRED™ Device, now with X Technology. X Technology is a covalently bonded, nanoscale surface treatment, designed to:

- **REDUCE MATERIAL THROMBOGENICITY¹**
- **MAINTAIN NATURAL VESSEL HEALING RESPONSE^{2,3,4}**
- **IMPROVE DEVICE DELIVERABILITY AND RESHEATHING¹**

The only FDA PMA approved portfolio with a 0.021" delivery system for smaller device sizes, and no distal lead wire.



For more information, contact your local MicroVention sales representative or visit our website. www.microvention.com



^{*} Data is derived from in vivo and ex vitro testing and may not be representative of clinical performance.

¹ Data on file

² Tanaka M et al. Design of biocompatible and biodegradable polymers based on intermediate water concept. Polymer Journal. 2015;47:114-121.

³ Tanaka M et al. Blood compatible aspects of poly(2-methoxyethylacrylate) (PMEA) – relationship between protein adsorption and platelet adhesion on PMEA surface. Biomaterials. 2000;21:1471-1481.

⁴ Schiel L et al. X Coating™: A new biopassive polymer coating. Canadian Perfusion Canadienne. June 2001;11(2):9.

Indications for Use: The FRED X System is indicated for use in the internal carotid artery from the petrous segment to the terminus for the endovascular treatment of adult patients (22 years of age or older) with wide-necked (neck width 4 mm or dome-to-neck ratio < 2) saccular or fusiform intracranial aneurysms arising from a parent vessel with a diameter 2.0 mm and 5.0 mm.

Rx Only: Federal (United States) law restricts this device to sale by or on the order of a physician. For Healthcare professionals intended use only.

MICROVENTION, FRED and HEADWAY are registered trademarks of MicroVention, Inc. in the United States and other jurisdictions. Stylized X is a trademark of MicroVention, Inc. © 2022 MicroVention, Inc. MM1222 US 03/22

WEB™ 17

Aneurysm Embolization System

LOWER PROFILE



NEW SIZES



MORE ACCESS OPTIONS



INDICATIONS FOR USE:

The WEB Aneurysm Embolization System is intended for the endovascular embolization of ruptured and unruptured intracranial aneurysms and other neurovascular abnormalities such as arteriovenous fistulae (AVF). The WEB Aneurysm Embolization System is also intended for vascular occlusion of blood vessels within the neurovascular system to permanently obstruct blood flow to an aneurysm or other vascular malformation.

POTENTIAL COMPLICATIONS:

Potential complications include but are not limited to the following: hematoma at the site of entry, aneurysm rupture, emboli, vessel perforation, parent artery occlusion, hemorrhage, ischemia, vasospasm, clot formation, device migration or misplacement, premature or difficult device detachment, non-detachment, incomplete aneurysm filling, revascularization, post-embolization syndrome, and neurological deficits including stroke and death. For complete indications, potential complications, warnings, precautions, and instructions, see instructions for use (IFU provided with the device).

VIA 21, 27, 33 - The VIA Microcatheter is intended for the introduction of interventional devices (such as the WEB device/stents/flow diverters) and infusion of diagnostic agents (such as contrast media) into the neuro, peripheral, and coronary vasculature.

VIA 17, 17 Preshaped - The VIA Microcatheter is intended for the introduction of interventional devices (such as the WEB device/stents/flow diverters) and infusion of diagnostic agents (such as contrast media) into the neuro, peripheral, and coronary vasculature.

The VIA Microcatheter is contraindicated for use with liquid embolic materials, such as n-butyl 2-cyanoacrylate or ethylene vinyl alcohol & DMSO (dimethyl sulfoxide).

The device should only be used by physicians who have undergone training in all aspects of the WEB Aneurysm Embolization System procedure as prescribed by the manufacturer.

RX Only: Federal law restricts this device to sale by or on the order of a physician.

For healthcare professional intended use only.



MicroVenture Worldwide
Innovation Center

PH +1.714.247.8000

35 Enterprise
Aliso Viejo, CA 92656 USA
MicroVenture UK Limited
MicroVenture Europe, S.A.R.L.
MicroVenture Deutschland GmbH
Website

PH +44 (0) 191 258 6777
PH +33 (1) 39 21 77 46
PH +49 211 210 798-0
microvention.com



WEB™ and VIA™ are registered trademarks
of Sequent Medical, Inc. in the United States.

©2021 MicroVenture, Inc. MM1184 WW 11/2021

LIFE IS FULL OF COMPROMISES.
IT'S TIME TO TAKE A STAND.

NO COMPROMISE

HIGH RELAXIVITY, HIGH STABILITY:^{1,2}
I CHOOSE BOTH.

The individual who appears is for illustrative purposes. The person depicted is a model and not a real healthcare professional. Please see Brief Summary of Prescribing Information including Boxed Warning on adjacent page.

VUEWAY™ (gadopichlenol) solution for injection

Indications

VUEWAY injection is indicated in adults and children aged 2 years and older for use with magnetic resonance imaging (MRI) to detect and visualize lesions with abnormal vascularity in:

- the central nervous system (brain, spine and surrounding tissues),
- the body (head and neck, thorax, abdomen, pelvis, and musculoskeletal system).

IMPORTANT SAFETY INFORMATION

WARNING: NEPHROGENIC SYSTEMIC FIBROSIS (NSF)

Gadolinium-based contrast agents (GBCAs) increase the risk for NSF among patients with impaired elimination of the drugs. Avoid use of GBCAs in these patients unless the diagnostic information is essential and not available with non-contrast MRI or other modalities. NSF may result in fatal or debilitating fibrosis affecting the skin, muscle and internal organs.

- The risk for NSF appears highest among patients with:
 - Chronic, severe kidney disease (GFR < 30 mL/min/1.73 m²), or
 - Acute kidney injury.
- Screen patients for acute kidney injury and other conditions that may reduce renal function. For patients at risk for chronically reduced renal function (e.g. age > 60 years,

hypertension, diabetes), estimate the glomerular filtration rate (GFR) through laboratory testing.

- For patients at highest risk for NSF, do not exceed the recommended VUEWAY dose and allow a sufficient period of time for elimination of the drug from the body prior to any re-administration.

Contraindications

VUEWAY injection is contraindicated in patients with history of hypersensitivity reactions to VUEWAY.

Warnings


Risk of **nephrogenic systemic fibrosis** is increased in patients using GBCA agents that have impaired elimination of the drugs, with the highest risk in patients chronic, severe kidney disease as well as patients with acute kidney injury. Avoid use of GBCAs among these patients unless the diagnostic information is essential and not available with non-contrast MRI or other modalities.

Hypersensitivity reactions, including serious hypersensitivity reactions, could occur during use or shortly following VUEWAY administration. Assess all patients for any history of a reaction to contrast media, bronchial asthma and/or allergic disorders, administer VUEWAY only in situations where trained personnel and therapies are promptly available for the treatment of hypersensitivity reactions, and observe patients for signs and symptoms of hypersensitivity reactions after administration.



IN MRI

INTRODUCING


Vueway™
(gadopiclenol) injection
485.1 mg/mL

HALF THE GADOLINIUM DOSE COMPARED TO OTHER
MACROCYCLIC GBCAs IN APPROVED INDICATIONS.^{1,3-6}
FROM BRACCO, YOUR TRUSTED PARTNER IN MRI.



Gadolinium retention can be for months or years in several organs after administration. The highest concentrations (nanomoles per gram of tissue) have been identified in the bone, followed by other organs (brain, skin, kidney, liver and spleen). Minimize repetitive GBCA imaging studies, particularly closely spaced studies, when possible.

Acute kidney injury requiring dialysis has occurred with the use of GBCAs in patients with chronically reduced renal function. The risk of acute kidney injury may increase with increasing dose of the contrast agent.

Ensure catheter and venous patency before injecting as **extravasation** may occur, and cause tissue irritation.

VUEWAY may **impair the visualization of lesions** seen on non-contrast MRI. Therefore, caution should be exercised when Vueway MRI scans are interpreted without a companion non-contrast MRI scan.

The most common adverse reactions (incidence $\geq 0.5\%$) are injection site pain (0.7%), and headache (0.7%).

You are encouraged to report negative side effects of prescription drugs to the FDA. Visit www.fda.gov/medwatch or call 1-800-FDA-1088.

Please see BRIEF SUMMARY of Prescribing Information for VUEWAY, including BOXED WARNING on Nephrogenic Systemic Fibrosis.

Manufactured for Bracco Diagnostics Inc. by Liebel-Flarsheim Company LLC - Raleigh, NC, USA 27616.

VUEWAY is a trademark of Bracco Imaging S.p.A.

References: 1. Vueway™ (gadopiclenol) Injection Full Prescribing Information. Monroe Twp., NJ: Bracco Diagnostics Inc.; September 2022. 2. Robic C, Port M, Rousseaux O, et al. Physicochemical and Pharmacokinetic Profiles of Gadopiclenol: A New Macrocyyclic Gadolinium Chelate With High T1 Relaxivity. *Invest Radiol.* 2019 Aug;54: 475–484. 3. GADAVIST® (gadobutrol) Injection. Full Prescribing Information. Bayer HealthCare Pharmaceuticals Inc. Whippany, NJ; April 2022. 4. DOTAREM® (gadoterate meglumine) Injection. Full Prescribing Information. Guerbet LLC. Princeton, NJ; April 2022. 5. CLARISCAN™ (gadoterate meglumine) injection for intravenous use. Full Prescribing Information. GE Healthcare. Marlborough, MA; February 2020. 6. ProHance® (Gadoteridol) Injection. Full Prescribing Information and Patient Medication Guide. Monroe Twp., NJ: Bracco Diagnostics Inc.; December 2020.

Bracco Diagnostics Inc.
259 Prospect Plains Road, Building H
Monroe Township, NJ 08831 USA
Phone: 609-514-2200
Toll Free: 1-877-272-2269 (U.S. only)
Fax: 609-514-2446
© 2022 Bracco Diagnostics Inc.
All Rights Reserved. US-VW-2200012 10/22

VISIT
VUEWAY.COM
FOR MORE
INFORMATION



Vueway™

(gadopiclenol) injection, for intravenous use

BRIEF SUMMARY: Please see package insert of full prescribing information.

WARNING: NEPHROGENIC SYSTEMIC FIBROSIS (NSF)

Gadolinium-based contrast agents (GBCAs) increase the risk for NSF among patients with impaired elimination of the drugs. Avoid use of GBCAs in these patients unless the diagnostic information is essential and not available with non-contrast MRI or other modalities. NSF may result in fatal or debilitating fibrosis affecting the skin, muscle and internal organs.

- The risk for NSF appears highest among patients with:
 - Chronic, severe kidney disease (GFR < 30 mL/min/1.73 m²), or
 - Acute kidney injury.
- Screen patients for acute kidney injury and other conditions that may reduce renal function. For patients at risk for chronically reduced renal function (e.g. age > 60 years, hypertension, diabetes), estimate the glomerular filtration rate (GFR) through laboratory testing.
- For patients at highest risk for NSF, do not exceed the recommended Vueway dose and allow a sufficient period of time for elimination of the drug from the body prior to any re-administration [see Warnings and Precautions (5.1) in the full Prescribing Information].

INDICATIONS AND USAGE

Vueway™ (gadopiclenol) is a gadolinium-based contrast agent indicated in adult and pediatric patients aged 2 years and older for use with magnetic resonance imaging (MRI) to detect and visualize lesions with abnormal vascularity in:

- the central nervous system (brain, spine, and associated tissues),
- the body (head and neck, thorax, abdomen, pelvis, and musculoskeletal system).

CONTRAINDICATIONS

Vueway is contraindicated in patients with history of hypersensitivity reactions to gadopicholol.

WARNINGS AND PRECAUTIONS

Nephrogenic Systemic Fibrosis Gadolinium-based contrast agents (GBCAs) increase the risk for nephrogenic systemic fibrosis (NSF) among patients with impaired elimination of the drugs. Avoid use of GBCAs among these patients unless the diagnostic information is essential and not available with non-contrast MRI or other modalities. The GBCA-associated NSF risk appears highest for patients with chronic, severe kidney disease (GFR < 30 mL/min/1.73 m²) as well as patients with acute kidney injury. The risk appears lower for patients with chronic, moderate kidney disease (GFR 30-59 mL/min/1.73 m²) and little, if any, for patients with chronic, mild kidney disease (GFR 60-89 mL/min/1.73 m²). NSF may result in fatal or debilitating fibrosis affecting the skin, muscle, and internal organs. Report any diagnosis of NSF following Vueway administration to Bracco Diagnostics Inc. (1-800-257-5181) or FDA (1-800-FDA-1088 or www.fda.gov/medwatch).

Screen patients for acute kidney injury and other conditions that may reduce renal function. Features of acute kidney injury consist of rapid (over hours to days) and usually reversible decrease in kidney function, commonly in the setting of surgery, severe infection, injury or drug-induced kidney toxicity. Serum creatinine levels and estimated GFR may not reliably assess renal function in the setting of acute kidney injury. For patients at risk for chronically reduced renal function (e.g., age > 60 years, diabetes mellitus or chronic hypertension), estimate the GFR through laboratory testing.

Among the factors that may increase the risk for NSF are repeated or higher than recommended doses of a GBCA and the degree of renal impairment at the time of exposure. Record the specific GBCA and the dose administered to a patient. For patients at highest risk for NSF, do not exceed the recommended Vueway dose and allow a sufficient period of time for elimination of the drug prior to re-administration. For patients receiving hemodialysis, physicians may consider the prompt initiation of hemodialysis following the administration of a GBCA in order to enhance the contrast agent's elimination [see Use in Specific Populations (8.6) and Clinical Pharmacology (12.3) in the full Prescribing Information]. The usefulness of hemodialysis in the prevention of NSF is unknown.

Hypersensitivity Reactions With GBCAs, serious hypersensitivity reactions have occurred. In most cases, initial symptoms occurred within minutes of GBCA administration and resolved with prompt emergency treatment.

- Before Vueway administration, assess all patients for any history of a reaction to contrast media, bronchial asthma and/or allergic disorders. These patients may have an increased risk for a hypersensitivity reaction to Vueway.
- Vueway is contraindicated in patients with history of hypersensitivity reactions to Vueway [see Contraindications (4) in the full Prescribing Information].
- Administer Vueway only in situations where trained personnel and therapies are promptly available for the treatment of hypersensitivity reactions, including personnel trained in resuscitation.
- During and following Vueway administration, observe patients for signs and symptoms of hypersensitivity reactions.

Gadolinium Retention Gadolinium is retained for months or years in several organs. The highest concentrations (nanomoles per gram of tissue) have been identified in the bone, followed by other organs (e.g. brain, skin, kidney, liver, and spleen). The duration of retention also varies by tissue and is longest in bone. Linear GBCAs cause more retention than macrocyclic GBCAs. At equivalent doses, gadolinium retention varies among the linear agents with gadodiamide causing greater retention than other linear agents such as gadoxetate disodium, and gadobenate dimeglumine. Retention is lowest and similar

among the macrocyclic GBCAs such as gadoterate meglumine, gadobutrol, gadoteridol, and gadopicholol.

Consequences of gadolinium retention in the brain have not been established. Pathologic and clinical consequences of GBCA administration and retention in skin and other organs have been established in patients with impaired renal function [see Warnings and Precautions (5.1) in the full Prescribing Information]. There are rare reports of pathologic skin changes in patients with normal renal function. Adverse events involving multiple organ systems have been reported in patients with normal renal function without an established causal link to gadolinium.

While clinical consequences of gadolinium retention have not been established in patients with normal renal function, certain patients might be at higher risk. These include patients requiring multiple lifetime doses, pregnant and pediatric patients, and patients with inflammatory conditions. Consider the retention characteristics of the agent when choosing a GBCA for these patients. Minimize repetitive GBCA imaging studies, particularly closely spaced studies, when possible.

Acute Kidney Injury In patients with chronically reduced renal function, acute kidney injury requiring dialysis has occurred with the use of GBCAs. The risk of acute kidney injury may increase with increasing dose of the contrast agent. Do not exceed the recommended dose.

Extravasation and Injection Site Reactions Injection site reactions such as injection site pain have been reported in the clinical studies with Vueway [see Adverse Reactions (6.1) in the full Prescribing Information]. Extravasation during Vueway administration may result in tissue irritation [see Nonclinical Toxicology (13.2) in the full Prescribing Information]. Ensure catheter and venous patency before the injection of Vueway.

Interference with Visualization of Lesions Visible with Non-Contrast MRI As with any GBCA, Vueway may impair the visualization of lesions seen on non-contrast MRI. Therefore, caution should be exercised when Vueway MRI scans are interpreted without a companion non-contrast MRI scan.

ADVERSE REACTIONS

The following serious adverse reactions are discussed elsewhere in labeling:

- Nephrogenic Systemic Fibrosis [see Warnings and Precautions (5.1) in the full Prescribing Information]
- Hypersensitivity Reactions [see Contraindications (4) and Warnings and Precautions (5.2) in the full Prescribing Information]

Clinical Trials Experience Because clinical trials are conducted under widely varying conditions, adverse reaction rates observed in the clinical trials of a drug cannot be directly compared to rates in the clinical trials of another drug and may not reflect the rates observed in clinical practice.

The safety of Vueway was evaluated in 1,047 patients who received Vueway at doses ranging from 0.025 mmol/kg (one half the recommended dose) to 0.3 mmol/kg (six times the recommended dose). A total of 708 patients received the recommended dose of 0.05 mmol/kg. Among patients who received the recommended dose, the average age was 51 years (range 2 years to 88 years) and 56% were female. The ethnic distribution was 79% White, 10% Asian, 7% American Indian or Alaska native, 2% Black, and 2% patients of other or unspecified ethnic groups.

Overall, approximately 4.7% of subjects receiving the labeled dose reported one or more adverse reactions.

Table 1 lists adverse reactions that occurred in > 0.2% of patients who received 0.05 mmol/kg Vueway.

TABLE 1. ADVERSE REACTIONS REPORTED IN > 0.2% OF PATIENTS RECEIVING VUEWAY IN CLINICAL TRIALS	
Adverse Reaction	Vueway 0.05 mmol/kg (n=708) (%)
Injection site pain	0.7
Headache	0.7
Nausea	0.4
Injection site warmth	0.4
Injection site coldness	0.3
Dizziness	0.3
Local swelling	0.3

Adverse reactions that occurred with a frequency < 0.2% in patients who received 0.05 mmol/kg Vueway included: maculopapular rash, vomiting, worsened renal impairment, feeling hot, pyrexia, oral paresthesia, dysgeusia, diarrhea, pruritus, allergic dermatitis, erythema, injection site paresthesia, Cystatin C increase, and blood creatinine increase.

Adverse Reactions in Pediatric Patients

One study with a single dose of Vueway (0.05 mmol/kg) was conducted in 80 pediatric patients aged 2 years to 17 years, including 60 patients who underwent a central nervous system (CNS) MRI and 20 patients who underwent a body MRI. One adverse reaction (maculopapular rash of moderate severity) in one patient (1.3%) was reported in the CNS cohort.

USE IN SPECIFIC POPULATIONS

Pregnancy Risk Summary There are no available data on Vueway use in pregnant women to evaluate for a drug-associated risk of major birth defects, miscarriage or other adverse maternal or fetal outcomes. GBCAs cross the human placenta and result in fetal exposure and gadolinium retention. The available human data on GBCA exposure during pregnancy and adverse fetal outcomes are limited and inconclusive [see Data]. In animal reproduction studies, there were no adverse developmental effects observed in rats or rabbits with intravenous administration of Vueway during organogenesis [see Data]. Because of the potential risks of gadolinium to the fetus, use Vueway only if imaging is essential during pregnancy and cannot be delayed. The estimated background risk of major birth defects and miscarriage for the indicated population(s) are unknown. All pregnancies have a background risk of birth defect, loss, or other adverse outcomes. In the U.S. general population, the estimated background risk of major birth defects and miscarriage in clinically recognized pregnancies is 2% to 4% and 15% to 20% respectively. Data Human Data Contrast enhancement is visualized in the placenta and fetal tissues after maternal GBCA administration. Cohort studies and case reports on exposure to GBCAs during pregnancy have not reported a clear association between GBCAs and adverse effects in the exposed neonates. However, a retrospective cohort study comparing pregnant women who had a GBCA MRI to pregnant women who did not have an MRI reported a higher occurrence of stillbirths and neonatal deaths in the group receiving GBCA MRI. Limitations of this study include a lack of comparison with non-contrast MRI and lack of information about the maternal indication for MRI. Overall, these data preclude

a reliable evaluation of the potential risk of adverse fetal outcomes with the use of GBCAs in pregnancy.

Animal Data Gadolinium Retention: GBCAs administered to pregnant non-human primates (0.1 mmol/kg on gestational days 85 and 135) result in measurable gadolinium concentration in the offspring in bone, brain, skin, liver, kidney, and spleen for at least 7 months. GBCAs administered to pregnant mice (2 mmol/kg daily on gestational days 16 through 19) result in measurable gadolinium concentrations in the pups in bone, brain, kidney, liver, blood, muscle, and spleen at one-month postnatal age.

Reproductive Toxicology: Animal reproduction studies conducted with gadopicholol showed some signs of maternal toxicity in rats at 10 mmol/kg and rabbits at 5 mmol/kg (corresponding to 52 times and 57 times the recommended human dose, respectively). This maternal toxicity was characterized in both species by swelling, decreased activity, and lower gestation weight gain and food consumption.

No effect on embryo-fetal development was observed in rats at 10 mmol/kg (corresponding to 52 times the recommended human dose). In rabbits, a lower mean fetal body weight was observed at 5 mmol/kg (corresponding to 57 times the recommended human dose) and this was attributed as a consequence of the lower gestation weight gain.

Lactation Risk Summary There are no data on the presence of gadopicholol in human milk, the effects on the breastfed infant, or the effects on milk production. However, published lactation data on other GBCAs indicate that 0.01% to 0.04% of the maternal gadolinium dose is excreted in breast milk. Additionally, there is limited GBCA gastrointestinal absorption in the breast-fed infant. Gadopicholol is present in rat milk. When a drug is present in animal milk, it is likely that the drug will be present in human milk [see Data]. The developmental and health benefits of breastfeeding should be considered along with the mother's clinical need for Vueway and any potential adverse effects on the breastfed infant from Vueway or from the underlying maternal condition. Data In lactating rats receiving single intravenous injection of [¹⁵³Gd]-gadopiclenol, 0.3% and 0.2% of the total administered radioactivity was transferred to the pups via maternal milk at 6 hours and 24 hours after administration, respectively. Furthermore, in nursing rat pups, oral absorption of gadopicholol was 3.6%.

Pediatric Use The safety and effectiveness of Vueway for use with MRI to detect and visualize lesions with abnormal vascularity in the CNS (brain, spine, and associated tissues), and the body (head and neck, thorax, abdomen, pelvis, and musculoskeletal system) have been established in pediatric patients aged 2 years and older.

Use of Vueway in this age group is supported by evidence from adequate and well-controlled studies in adults with additional pharmacokinetic and safety data from an open-label, uncontrolled, multicenter, single dose study of Vueway (0.05 mmol/kg) in 80 pediatric patients aged 2 to 17 years. The 80 patients consisted of 60 patients who underwent a CNS MRI and 20 patients who underwent a body MRI [see Adverse Reactions (6.1) and Clinical Pharmacology (12.3) in the full Prescribing Information].

The safety and effectiveness of Vueway have not been established in pediatric patients younger than 2 years of age.

Geriatric Use Of the total number of Vueway-treated patients in clinical studies, 270 (26%) patients were 65 years of age and over, while 62 (6%) patients were 75 years of age and over. No overall differences in safety or efficacy were observed between these subjects and younger subjects.

This drug is known to be substantially excreted by the kidney, and the risk of adverse reactions to this drug may be greater in patients with impaired renal function. Because elderly patients are more likely to have decreased renal function, it may be useful to monitor renal function.

Renal Impairment In patients with renal impairment, the exposure of gadopicholol is increased compared to patients with normal renal function. This may increase the risk of adverse reactions such as nephrogenic systemic fibrosis (NSF). Avoid use of GBCAs among these patients unless the diagnostic information is essential and not available with non-contrast MRI or other modalities. No dose adjustment of Vueway is recommended for patients with renal impairment. Vueway can be removed from the body by hemodialysis [see Warnings and Precautions (5.1, 5.3, 5.4) and Clinical Pharmacology (12.3) in the full Prescribing Information].

OVERDOSAGE

Among subjects who received a single 0.3 mmol/kg intravenous dose of gadopicholol (6 times the recommended dose of Vueway), headache and nausea were the most frequently reported adverse reactions. Gadopicholol can be removed from the body by hemodialysis [see Clinical Pharmacology (12.3) in the full Prescribing Information].

PATIENT COUNSELING INFORMATION Advise the patient to read the FDA-approved patient labeling (Medication Guide).

Nephrogenic Systemic Fibrosis Inform the patient that Vueway may increase the risk for NSF among patients with impaired elimination of the drugs and that NSF may result in fatal or debilitating fibrosis affecting the skin, muscle and internal organs.

Instruct the patients to contact their physician if they develop signs or symptoms of NSF following Vueway administration, such as burning, itching, swelling, scaling, hardening and tightening of the skin; red or dark patches on the skin; stiffness in joints with trouble moving, bending or straightening the arms, hands, legs or feet; pain in the hip bones or ribs; or muscle weakness [see Warnings and Precautions (5.1) in the full Prescribing Information].

Gadolinium Retention Advise patients that gadolinium is retained for months or years in brain, bone, skin, and other organs following Vueway administration even in patients with normal renal function. The clinical consequences of retention are unknown. Retention depends on multiple factors and is greater following administration of linear GBCAs than following administration of macrocyclic GBCAs [see Warnings and Precautions (5.3) in the full Prescribing Information].

Injection Site Reactions Inform the patient that Vueway may cause reactions along the venous injection site, such as mild and transient burning or pain or feeling of warmth or coldness at the injection site [see Warnings and Precautions (5.5) in the full Prescribing Information].

Pregnancy Advise pregnant women of the potential risk of fetal exposure to Vueway [see Use in Specific Populations (8.1) in the full Prescribing Information].

Rx only

US Patent No. 10,973,934
 Manufactured for Bracco Diagnostics Inc. by Liebel-Flarsheim Company LLC
 - Raleigh, NC, USA 27616.
 Toll Free: 1-877-272-2269 (U.S. only)
 Revised November 2022

CALL FOR AJNR EDITORIAL FELLOWSHIP CANDIDATES

2023 Candidate Information and Requirements

ASNR and AJNR are pleased once again to join efforts with other imaging-related journals that have training programs on editorial aspects of publishing for trainees or junior staff (<5 years on staff), including Radiology (Olmsted fellowship), AJR (Figley and Rogers fellowships), JACR (Bruce J. Hillman fellowship), and Radiologia.

GOALS

- Increase interest in editorial and publication-related activities in younger individuals.
- Increase understanding and participation in the AJNR review process.
- Incorporate into AJNR's Editorial Board younger individuals who have previous experience in the review and publication process.
- Fill a specific need in neuroradiology not offered by other similar fellowships.
- Increase the relationship between "new" generation of neuroradiologists and more established individuals.
- Increase visibility of AJNR among younger neuroradiologists.

ACTIVITIES OF THE FELLOWSHIP

- Serve as Editorial Fellow for one year. This individual will be listed on the masthead as such.
- Review at least one manuscript per month for 12 months. Evaluate all review articles submitted to AJNR.
- Learn how electronic manuscript review systems work.
- Be involved in the final decision of selected manuscripts together with the Editor-in-Chief.
- Participate in all monthly Senior Editor telephone conference calls.
- Participate in 2 virtual meetings of the Editorial Board.
- Evaluate progress and adjust program to specific needs in annual meeting or telephone conference with the Editor-in-Chief.
- Embark on an editorial scientific or bibliometric project that will lead to the submission of an article to AJNR or another appropriate journal as determined by the Editor-in-Chief. This project will be presented by the Editorial Fellow at the ASNR annual meeting. The Foundation of the ASNR will provide \$2000 funding for this activity.
- Recruit trainees as reviewers as determined by the Editor-in-Chief.
- Serve as Guest Editor for an issue of AJNR's News Digest with a timely topic.

QUALIFICATIONS

- Be a fellow in neuroradiology from North America, including Canada (this may be extended to include other countries).
- Be a junior faculty neuroradiology member (< 5 years) in either an academic or private environment.
- Be an "in-training" or member of ASNR in any other category.

APPLICATION

- Include a short letter of intent with statement of goals and desired research project. CV must be included.
- Include a letter of recommendation from the Division Chief or fellowship program director. A statement of protected time to perform the functions outlined is desirable.
- Applications will be evaluated by AJNR's Senior Editors prior to the ASNR annual meeting. The name of the selected individual will be announced at the meeting.
- Applications should be received by March 1, 2023 and sent to Ms. Karen Halm, AJNR Managing Editor, electronically at khalm@asnr.org.

AJNR *go green*

***AJNR* urges American Society of Neuroradiology members to reduce their environmental footprint by voluntarily suspending their print subscription.**

The savings in paper, printing, transportation, and postage directly fund new electronic enhancements and expanded content.

The digital edition of *AJNR* presents the print version in its entirety, along with extra features including:

- Publication Preview
- Case Collection
- Podcasts
- The *AJNR* News Digest
- The *AJNR* Blog

It also reaches subscribers much faster than print. An electronic table of contents will be sent directly to your mailbox to notify you as soon as it publishes.

Readers can search, reference, and bookmark current and archived content 24 hours a day on www.ajnr.org.

ASNR members who wish to opt out of print can do so by using the *AJNR* Go Green link on the *AJNR* Website (<http://www.ajnr.org/content/subscriber-help-and-services>). Just type your name in the email form to stop print and spare our ecosystem.

In Planning for Brain Metastases Treatment, Imaging may be the Missing Link in Cost Containment¹

When faced with a patient presenting with metastatic brain cancer, determining whether to use up-front stereotactic radiosurgery (SRS) vs. first treating with whole brain radiotherapy (WBRT) is a significant clinical decision.

WBRT: The whole story on cognitive impairment

While whole brain radiotherapy (WBRT) has been the main treatment option for many years, experts agree that it often results in cognitive deterioration and a negative impact on quality of life. This mental decline has a devastating impact on patients and their families and adds ongoing costs for the healthcare systems managing these symptoms.

Using WBRT instead of SRS in some patients is estimated to decrease the total costs of brain metastasis management, though with increased toxicity.

SRS: Fewer side effects but greater risk of missed tumors

The cost of upfront SRS is the greatest contributor to cost of brain metastasis management.¹ SRS is often more expensive than WBRT. What's more, multiple applications of SRS can increase the cost of treatment greatly.

Stereotactic radiosurgery (SRS) has far fewer side effects, but upfront use of SRS is expensive and can carry the risk of missed tumors, requiring repeat procedures such as salvage SRS.¹

Number of lesions and lesion size are key factors to be considered when determining the treatment plan for these patients. It follows that increased diagnostic information and accuracy could be beneficial in directing the proper therapy and improving overall long-term patient outcomes and containing costs. Getting the diagnosis right the first time is crucial to ensure proper treatment begins quickly, and high cost/high stakes procedures such as SRS need precise surgical planning.

What does optimal visualization mean for outcomes and cost?

For surgical planning with SRS, radiologists need the best visualization achievable to accurately count the number and size of the lesions. These metrics are the key predictors of the need for SRS,¹ WBRT, or a combination of both.

By selecting the ideal contrast agent and equipment protocols, neuroradiologists can identify the proximate numbers of metastases for upfront treatment and reduced salvage treatment occurrences.

The role of radiology

As medical care for oncology patients continues to evolve, it will be increasingly important to assess the cost of various interventions given the often-limited life expectancy of cancer patients, the rising costs of cancer therapy, and the increasing prevalence of cancer in an aging population.

Through seeing all the tumors and tumor borders as clearly as technology allows, radiology can play a part in ensuring that proper treatment can begin quickly,

while containing costs through optimized patient care. Efforts to carefully manage treatment approaches require improvements in protocol design, contrast administration in imaging, and utilizing multimodal imaging approaches.

In this era of precision medicine, radiology departments' contribution to this improved standard of care will have significant short and long-term implications by reducing cost of care, providing a more proximate diagnosis, and ensuring optimal patient outcomes. ■



Getting the diagnosis right the first time is crucial to ensure proper treatment begins quickly.

Reference: 1. Shenker, R. F., McTyre, E. R., Taksler, D et al. Analysis of the drivers of cost of management when patients with brain metastases are treated with upfront radiosurgery. *Clin Neurol Neurosurg.* 2019 Jan;176:10-14.



For more information on MRI contrast agents, precision medicine, and reducing cost of care please visit bracco.com

© 2022 Bracco Diagnostics Inc.

I am a global citizen.

I am patient-centered care.

I am committed to health equity.

I am a teacher.

I am a life-long learner.

I am determined.

I am curious.

I am a collaborative team player.

I am a volunteer.

I am ASNR.

Don't miss out on the tools, resources and relationships you've come to rely on. Log in and renew your ASNR membership today! www.asnr.org

AJNR

AMERICAN JOURNAL OF NEURORADIOLOGY

DECEMBER 2022
VOLUME 43
NUMBER 12
WWW.AJNR.ORG

Publication Preview at www.ajnr.org features articles released in advance of print.
Visit www.ajnrblog.org to comment on AJNR content and chat with colleagues
and AJNR's News Digest at <http://ajnrndigest.org> to read the stories behind the
latest research in neuroimaging.

1687 **PERSPECTIVES** *M. Hauben*

REVIEW ARTICLE

- 1688 **Quantitative MRI in Multiple Sclerosis: From Theory to Application**
M. Tranfa, et al.

ADULT BRAIN

RADIOLOGY-PATHOLOGY CORRELATION
















- 1696 **Malignant Melanotic Nerve Sheath Tumor** *J.C. Benson, et al.*

SPINE

GENERAL CONTENTS


- 1700 **Automated Detection of Cerebral Aneurysms on TOF-MRA Using a Deep Learning Approach: An External Validation Study** *N.C. Lehnen, et al.* **ADULT BRAIN**
- 1706 **Effects of Arterial Stiffness on Cerebral WM Integrity in Older Adults: A Neurite Orientation Dispersion and Density Imaging and Magnetization Transfer Saturation Imaging Study** *J. Kikuta, et al.* **ADULT BRAIN FUNCTIONAL**
- 1713 **Improved Blood Suppression of Motion-Sensitized Driven Equilibrium in High-Resolution Whole-Brain Vessel Wall Imaging: Comparison of Contrast-Enhanced 3D T1-Weighted FSE with Motion-Sensitized Driven Equilibrium and Delay Alternating with Nutation for Tailored Excitation** *D.J. Kim, et al.* **ADULT BRAIN**
- 1719 **Intracranial Vessel Segmentation in 3D High-Resolution T1 Black-Blood MRI** *S. Elsheikh, et al.* **ADULT BRAIN**
- 1722 **Association between Dural AVFs and Cerebral Venous Thrombosis** *L. Kuiper, et al.* **ADULT BRAIN INTERVENTIONAL**
- 1730 **Mechanical Thrombectomy for the Treatment of Anterior Cerebral Artery Occlusion: A Systematic Review of the Literature** *N. Dabhi, et al.* **INTERVENTIONAL**
- 1736 **Thrombectomy Using the EmboTrap Clot-Retrieving Device for the Treatment of Acute Ischemic Stroke: A Glimpse of Clinical Evidence** *X. Bai, et al.* **INTERVENTIONAL**
- 1743 **Predictors of Endovascular Treatment Procedural Complications in Acute Ischemic Stroke: A Single-Center Cohort Study** *E. Maslías, et al.* **INTERVENTIONAL**
- 1749 **Material-Specific Roadmap Modes Can Improve the Visibility of Liquid Embolic Agents for Endovascular Embolization: A Systematic In Vitro Study** *N. Schmitt, et al.* **INTERVENTIONAL**

AJNR (Am J Neuroradiol ISSN 0195–6108) is a journal published monthly, owned and published by the American Society of Neuroradiology (ASNR), 820 Jorie Boulevard, Oak Brook, IL 60523. Annual dues for the ASNR include approximately 21% for a journal subscription. The journal is printed by Intellicor Communications, 330 Eden Road, Lancaster, PA 17601; Periodicals postage paid at Oak Brook, IL and additional mailing offices. Printed in the U.S.A. POSTMASTER: Please send address changes to American Journal of Neuroradiology, P.O. Box 3000, Denver, NJ 07834, U.S.A. Subscription rates: nonmember \$452 (\$530 foreign) print and online, \$320 online only; institutions \$520 (\$594 foreign) print and basic online, \$1029 (\$1103 foreign) print and extended online, \$380 online only (basic), \$825 online only (extended); single copies are \$35 each (\$40 foreign). Indexed by PubMed/MEDLINE, BIOSIS Previews, Current Contents (Clinical Medicine and Life Sciences), EMBASE, Google Scholar, HighWire Press, Q-Sensei, RefSeek, Science Citation Index, SCI Expanded, ReadCube, and Semantic Scholar. Copyright © American Society of Neuroradiology.

-  1756 Survey of the American Society of Neuroradiology Membership on the Use and Value of Extracranial Carotid Vessel Wall MRI *M. Mossa-Basha, et al.* **EXTRACRANIAL VASCULAR**
-   1762 MRI Detection of Carotid Intraplaque Hemorrhage and Postintervention Cognition *S. Culleton, et al.* **EXTRACRANIAL VASCULAR**
-   1770 Different Features of a Metabolic Connectivity Map and the Granger Causality Method in Revealing Directed Dopamine Pathways: A Study Based on Integrated PET/MR Imaging *L. Wang, et al.* **ADULT BRAIN FUNCTIONAL**
-   1777 Effects of COVID-19 on the Human Central Olfactory System: A Natural Pre-Post Experiment *E. Thunell, et al.* **HEAD & NECK**
-    1784 A Gamified Social Media-Based Head and Neck Radiology Education Initiative of the American Society of Head and Neck Radiology: Viewership and Engagement Trends at 3 Years *N.A. Koontz, et al.* **HEAD & NECK**
- 1792 High-Resolution T2-Weighted Imaging for Surveillance in Postoperative Vestibular Schwannoma: Equivalence with Contrast-Enhanced T1WI for Measurement and Surveillance of Residual Tumor *S.B. Strauss, et al.* **HEAD & NECK**
-  1797 Accelerated Nonenhanced 3D T1-MPRAGE Using Wave-Controlled Aliasing in Parallel Imaging for Infant Brain Imaging *S.Y. Yun, et al.* **PEDIATRICS**
-  1802 Imaging Findings in Children Presenting with CNS Nelarabine Toxicity *B.L. Serrallach, et al.* **PEDIATRICS**
-  1810 Expanding the Spectrum of Early Neuroradiologic Findings in β Propeller Protein–Associated Neurodegeneration *A. Papandreou, et al.* **PEDIATRICS**
- 1815 *Commentary*
Early Neuroimaging Markers in β Propeller Protein–Associated Neurodegeneration *L. Chiapparini, et al.*
-  1817 Synthetic MR Imaging–Based WM Signal Suppression Identifies Neonatal Brainstem Pathways In Vivo *V.U. Schmidbauer, et al.* **PEDIATRICS**
- 1824 Sacral CSF-Venous Fistulas and Potential Imaging Techniques *I.T. Mark, et al.* **SPINE**
-  1827 How Are We Handling Fluoroscopy-Guided Lumbar Puncture Requests? A Nationwide Survey of Practice Trends *T.J. Richards, et al.* **SPINE**

ONLINE FEATURES

WHITE PAPER

-  E46 ACR White Paper on Magnetoencephalography and Magnetic Source Imaging: A Report from the ACR Commission on Neuroradiology
J.A. Maldjian, et al.
- E54 A Brief History of Neuroradiology and the 60th Anniversary of the ASNR: “Through the Decades with ASNR” *M.H. Lev, et al.*

LETTERS

- E60 Regarding “Altered Blood Flow in the Ophthalmic and Internal Carotid Arteries in Patients with Age-Related Macular Degeneration Measured Using Noncontrast MR Angiography at 7T” *N. Ribarich, et al.*
- E62 *Reply* *M.L. Hibert, et al.*
- E64 Fair Performance of CT in Diagnosing Unilateral Vocal Fold Paralysis
F. Deng

BOOK REVIEWS *R.M. Quencer, Section Editor*

Please visit www.ajnrblog.org to read and comment on Book Reviews.



Left S2 CSF-venous fistula from Mark, et al, in this issue.



Indicates Editor's Choices selection



Indicates Fellows' Journal Club selection



Indicates open access to non-subscribers at www.ajnr.org



Indicates article with supplemental online data



Indicates article with supplemental online video



Evidence-Based Medicine Level 1



Evidence-Based Medicine Level 2

EDITOR-IN-CHIEF

Jeffrey S. Ross, MD

Professor of Radiology, Department of Radiology,
Mayo Clinic College of Medicine, Phoenix, AZ

SENIOR EDITORS

Harry J. Cloft, MD, PhD

Professor of Radiology and Neurosurgery,
Department of Radiology, Mayo Clinic College of
Medicine, Rochester, MN

Christopher G. Filippi, MD

Professor and Alice Ettinger-Jack R. Dreyfuss
Chair of Radiology,
Tufts University School of Medicine,
Radiologist-in-Chief
Tufts University Medical Center, Boston, MA

Thierry A.G.M. Huisman, MD, PD, FICIS, FACR

Radiologist-in-Chief and Chair of Radiology, Texas
Children's Hospital,
Professor of Radiology, Pediatrics, Neurosurgery,
and OBGYN, Baylor College of Medicine,
Houston, TX

Yvonne W. Lui, MD

Associate Professor of Radiology,
Chief of Neuroradiology,
New York University School of Medicine,
New York, NY

C.D. Phillips, MD, FACR

Professor of Radiology, Weill Cornell Medical
College, Director of Head and Neck Imaging,
New York-Presbyterian Hospital, New York, NY

Lubdhra M. Shah, MD, MS

Professor of Radiology and Director of Spine
Imaging, University of Utah Department of
Radiology and Imaging Sciences, Salt Lake City, UT

STATISTICAL SENIOR EDITOR

Bryan A. Comstock, MS

Senior Biostatistician,
Department of Biostatistics,
University of Washington, Seattle, WA

ARTIFICIAL INTELLIGENCE DEPUTY EDITOR

Peter D. Chang, MD

Assistant Professor-in-Residence,
Departments of Radiological Sciences,
Computer Sciences, and Pathology,
Director, Center for Artificial Intelligence in
Diagnostic Medicine (CAIDM),
University of California, Irvine, Irvine, CA

EDITORIAL BOARD

Ashley H. Aiken, *Atlanta, GA*

Matthew D. Alexander, *Salt Lake City, UT*

Lea M. Alhilali, *Phoenix, AZ*

Jason W. Allen, *Atlanta, GA*

Mohammed A. Almekhlafi, *Calgary, Alberta, Canada*

Niranjan Balu, *Seattle, WA*

Matthew J. Barkovich, *San Francisco, CA*

Joachim Berkefeld, *Frankfurt, Germany*

Karen Buch, *Boston, MA*

Judah Burns, *New York, NY*

Danielle Byrne, *Dublin, Ireland*

Federico Cagnazzo, *Montpellier, France*

Gloria C. Chiang, *New York, NY*

Daniel Chow, *Irvine, CA*

Kars C.J. Compagne, *Rotterdam, The Netherlands*

Yonghong Ding, *Rochester, MN*

Birgit Ertl-Wagner, *Toronto, Ontario, Canada*

Aaron Field, *Madison, WI*

Nils D. Forkert, *Calgary, Alberta, Canada*

Frank Gaillard, *Melbourne, Australia*

Joseph J. Gemmete, *Ann Arbor, Michigan*

Brent Griffith, *Detroit, MI*

Michael J. Hoch, *Philadelphia, PA*

Joseph M. Hoxworth, *Phoenix, AZ*

Raymond Y. Huang, *Boston, MA*

Susie Y. Huang, *Boston, MA*

Ferdinand K. Hui, *Honolulu, HI*

Christof Karmonik, *Houston, TX*

Gregor Kasprian, *Vienna, Austria*

Timothy J. Kaufmann, *Rochester, MN*

Hillary R. Kelly, *Boston, MA*

Toshibumi Kinoshita, *Akita, Japan*

Ioannis Koktzoglu, *Evanston, IL*

Stephen F. Kralik, *Houston, TX*

Luke Ledbetter, *Los Angeles, CA*

Franklin A. Marden, *Chicago, IL*

Markus A. Möhlenbruch, *Heidelberg, Germany*

Mahmud Mossa-Basha, *Morrisville, NC*

Renato Hoffmann Nunes, *Sao Paulo, Brazil*

Sam Payabvash, *New Haven, CT*

Johannes A.R. Pfaff, *Salzburg, Austria*

Eike I. Piechowiak, *Bern, Switzerland*

Laurent Pierot, *Reims, France*

Alexander R. Podgorsak, *Chicago, IL*

Eytan Raz, *New York, NY*

Jeff Rudie, *San Diego, CA*

Paul M. Ruggieri, *Cleveland, OH*

Fatih Seker, *Heidelberg, Germany*

Maksim Shapiro, *New York, NY*

Timothy Shepherd, *New York, NY*

Mark S. Shiroishi, *Los Angeles, CA*

Neetu Soni, *Rochester, NY*

Ashok Srinivasan, *Ann Arbor, MI*

Jason F. Talbott, *San Francisco, CA*

Anderanik Tomasian, *Los Angeles, CA*

Fabio Triulzi, *Milan, Italy*

Arastoo Vossough, *Philadelphia, PA*

Richard Watts, *New Haven, CT*

Elysa Widjaja, *Toronto, Ontario, Canada*

Ronald Wolf, *Philadelphia, Pennsylvania*

Shuang Xia, *Tianjin, China*

Leonard Yeo, *Singapore*

Woong Yoon, *Gwangju, South Korea*

David M. Yousem, *Evergreen, CO*

Carlos Zamora, *Chapel Hill, NC*

Chengcheng Zhu, *Seattle, WA*

EDITORIAL FELLOW

Alexandre Boutet, *Toronto, Ontario, Canada*

SPECIAL CONSULTANTS TO THE EDITOR

AJNR Blog Editor

Neil Lall, *Denver, CO*

Case of the Month Editor

Nicholas Stence, *Aurora, CO*

Case of the Week Editors

Matylda Machnowska, *Toronto, Ontario, Canada*

Anvita Pauranik, *Calgary, Alberta, Canada*

Vinil Shah, *San Francisco, CA*

Classic Case Editor

Sandy Cheng-Yu Chen, *Taipei, Taiwan*

Health Care and Socioeconomics Editor

Pina C. Sanelli, *New York, NY*

Physics Editor

Greg Zaharchuk, *Stanford, CA*

Podcast Editor

Kevin Hiatt, *Winston-Salem, NC*

Twitter Editor

Jacob Ormsby, *Albuquerque, NM*

Official Journal:

American Society of Neuroradiology

American Society of Functional Neuroradiology

American Society of Head and Neck Radiology

American Society of Pediatric Neuroradiology

American Society of Spine Radiology

Founding Editor
Juan M. Taveras

Editors Emeriti
Mauricio Castillo, Robert I. Grossman,
Michael S. Huckman, Robert M. Quencer

Managing Editor
Karen Halm
Assistant Managing Editor
Laura Wilhelm
Executive Director, ASNR
Mary Beth Hepp



Title: East 59th Street Stack. The East 59th Street stack marks 1 of the 6 Con Ed steam power substations in New York City. It is located, not surprisingly, next to the "59th Street Bridge" and billows huge white plumes in the winter. Also not surprisingly, all the substations are located along the major New York City waterways of the East and Hudson Rivers. The New York City steam system is the largest district heating network in the country. It feeds about 120 million tons of steam per year through 105 miles of pipes to around 1800 buildings in New York City, most in lower and mid-Manhattan, which have the highest concentration of taller buildings. The steam powers various processes, including heating, refrigeration, sterilization (eg, hospitals), and humidification (eg, art museums). Without district heating the Manhattan skyline would be very different with 1800 or more spewing chimney stacks and pots peppering the rooftops, not to mention the corresponding constraints on rooftop architectural innovation.

Manfred Hauben, MD, MPH, Pfizer Inc and NYU Langone Health, New York City

Quantitative MRI in Multiple Sclerosis: From Theory to Application

 M. Tranfa,  G. Pontillo,  M. Petracca,  A. Brunetti,  E. Tedeschi,  G. Palma, and  S. Cocozza



ABSTRACT

SUMMARY: Quantitative MR imaging techniques allow evaluating different aspects of brain microstructure, providing meaningful information about the pathophysiology of damage in CNS disorders. In the study of patients with MS, quantitative MR imaging techniques represent an invaluable tool for studying changes in myelin and iron content occurring in the context of inflammatory and neurodegenerative processes. In the first section of this review, we summarize the physics behind quantitative MR imaging, here defined as relaxometry and quantitative susceptibility mapping, and describe the neurobiological correlates of quantitative MR imaging findings. In the second section, we focus on quantitative MR imaging application in MS, reporting the main findings in both the gray and white matter compartments, separately addressing macroscopically damaged and normal-appearing parenchyma.

ABBREVIATIONS: bSSFP = balanced steady-state free precession; CL = cortical lesions; GRE = gradient recalled-echo; NAWM = normal-appearing white matter; PD = proton density; qMRI = quantitative MR imaging; QSM = quantitative susceptibility mapping; RF = radiofrequency

While conventional MR imaging plays an unquestionable role in the diagnosis and management of MS,^{1,2} it offers very limited information about the pathophysiology of tissue damage because conventional sequences are not able to detect subtle changes affecting WM and GM. Quantitative MR imaging (qMRI) bridges this gap, detecting brain microstructural alterations with high sensitivity and robustness to interscanner and interobserver variability, thus providing measures that can be compared among sites and longitudinal examinations. Furthermore, this technique has been successfully used to differentiate MS from other demyelinating diseases, such as neuromyelitis optica, which presents a different spectrum of relaxometry alterations³ and a peculiar spatial deep gray matter involvement,⁴ and also to characterize other conditions with different etiologies, from vascular disease to brain tumors.^{5,6} However, the applications of qMRI extend beyond the brain, being able to depict changes in liver iron concentration⁷ as well as the presence of fibrosis,⁸ and prostatic

calcifications,⁹ and to evaluate cortical bone mineral density¹⁰ or myocardial structural alterations.¹¹

Although the definition of qMRI is open to different interpretations, several advanced MR imaging techniques are usually grouped under this umbrella, including relaxometry, magnetic susceptibility, diffusion invariants, magnetization transfer, and, to some extent, perfusion parameters.¹² Each of these techniques offers different, sometimes complementary, insights into the complex tissue alterations occurring in MS.¹³ In this light, it is noteworthy to remember that, while demyelination represents the end result of a complex phenomenon of inflammation, ultimately leading to axonal and neuronal degeneration, change in iron homeostasis is a crucial step in the pathophysiology of damage in MS, linked to microglial activation and modifications in oligodendrocyte functionality.^{14,15} Relaxometry plays a unique role, given that most of the above-mentioned qMRI techniques offer valuable and sensitive tools in myelin assessment but they lack iron-detection sensitivity. Indeed, relaxometry assesses abnormalities of iron and myelin, elements that are at the crossroads of the inflammatory and neurodegenerative components in MS pathophysiology.¹²

In this review, we summarize the role and the application of qMRI techniques, here defined as relaxometry (estimating R1, R2, R2*, and, by extension, proton density [PD]) and quantitative susceptibility mapping (QSM), to the study of patients with MS.

In the first section, we briefly describe the physics behind qMRI, together with its neurobiological correlates. In the second

Received January 12, 2022; accepted after revision February 22.

From the Departments of Advanced Biomedical Sciences (M.T., G. Pontillo, A.B., E.T., S.C.), and Electrical Engineering and Information Technology (G. Pontillo), University of Naples "Federico II," Naples, Italy; Department of Human Neurosciences (M.P.), Sapienza University of Rome, Rome, Italy; and Institute of Nanotechnology (G. Palma), National Research Council, Lecce, Italy.

Please address correspondence to Giuseppe Pontillo, MD, Department of Advanced Biomedical Sciences, University "Federico II," Via Pansini, 5, 80131 Naples, Italy; e-mail: giuseppe.pontillo@unina.it; @NeuroN_Lab

 Indicates open access to non-subscribers at www.ajnr.org

<http://dx.doi.org/10.3174/ajnr.A7536>

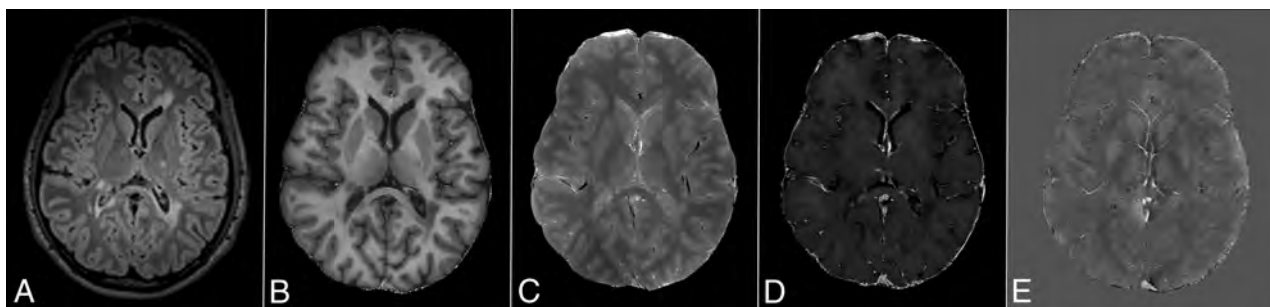


FIG 1. An example of quantitative MR imaging maps. Along with findings of a conventional FLAIR sequence (A) are examples of R1 (B), PD (C), R2* (D), and QSM (E) maps from a 22-year-old man with MS.

section, we summarize brain qMRI findings in MS for both the normal-appearing parenchyma and lesions in the GM and WM compartments.

qMRI Theory

Impact of Excitation Pulses and Significance of 3D Sequences.

The R1 and R2 relaxation rates, defined as the inverses of T1 and T2 relaxation times, measure the efficiency of the kinetics mechanisms restoring the thermal equilibrium of the longitudinal and transverse components of the spin isochromats. An isochromat represents the magnetic moment associated with a subset of nuclei (protons, for our purposes) whose cardinality is large enough to justify a classic description of its dynamics (in terms of the expectation value of the quantum magnetic moment operator) and whose spatial extent is small enough to assume a strictly uniform macroscopic magnetic field throughout the subset. The evolution of the isochromats in an MR imaging sequence (radiofrequency [RF] and gradient pulses) is strongly dependent on the flip angles they experience. This shows why accurate R1 and R2 mapping is only possible through 3D sequences, which, unlike 2D sequences, guarantee a roughly uniform RF excitation throughout each voxel.

Estimation of Quantitative Maps. In general, the viable protocols for R1 and R2 mapping in neuroimaging routine rely on the acquisition of multiple 3D spoiled gradient recalled echo (GRE, for R1) and balanced steady-state free precession (bSSFP, for the additional information required to estimate R2) sequences at variable flip angles.¹⁶ However, several aspects need to be considered to obtain accurate relaxation maps. First, nonideal slab profiles can be accounted for with a dedicated sequence for flip angle mapping¹⁷ or through an iterative approach based on the information content of the estimated relaxation maps.¹⁸ The bias from nonideal RF spoiling can be removed according to the specific phase increment implemented by each vendor.¹⁹ Finally, to factor out the effects of off-resonance phenomena impacting the bSSFP images in the form of banding artifacts, one needs to adopt a modified version of the original bSSFP approach,¹⁸ based on a synthetic contrast from multiple phase-cycled bSSFP.²⁰

The estimation of the free induction decay rate (R2*) is comparatively simpler because it depends only on the ratios of the signals at different TEs, with no RF pulses in between. It is usually obtained through a multi-GRE sequence with flip angles close to

the Ernst angle for SNR convenience and, therefore, can be estimated on the basis of the same protocol structure adopted for R1 mapping.²¹

Once R1 and R2* (which rule the signal equation of the spoiled GRE sequence) have been obtained, PD is ideally obtained without further acquisitions. Nevertheless, the spatial sensitivity of the receiver coil for the brain is substantially inhomogeneous; therefore, an additional low-resolution acquisition of one of the sequences with the body coil helps to mitigate the inhomogeneity bias.²²

Finally, the phase of the complex images acquired for R2* mapping permits QSM.²³ The raw phase is first unwrapped and then filtered to remove the background component that is not associated with the local magnetization induced in the parenchyma by the main magnetic field.²⁴ The filtered phase is finally processed to solve the inverse problem leading to the QSM.⁵ In this step, special care must be taken to avoid the occurrence of streaking artifacts that could impact the clinical value of the image by mimicking spurious anatomic structures (Fig 1).

Importance of Denoising Schemes. The mathematic problems associated with the qMRI protocols are typically ill-conditioned, thus leading to a detrimental noise propagation from the acquired images to the reconstructed maps. Therefore, besides the customary optimization of the acquisition protocol to maximize the SNR of the quantitative maps, a denoising step is warranted upstream of the qMRI pipeline. In this context, multispectral versions of the non-local means algorithms have been devised to account for the power distribution of noise in parallel imaging and to reconstruct the true signal from the raw statistical moments of the acquired images.^{25,26}

Pathophysiologic Correlates of qMRI. The pathophysiology of brain damage in MS is multifaceted, being characterized by a sequence of demyelination and partial remyelination events associated with neurodegeneration.²⁷

Microglia activation within normal-appearing WM (NAWM) is one of the earliest and most prominent features in MS pathophysiology.²⁸ Subsequently, a loss of integrity of the blood-brain barrier, driven by proinflammatory mediators produced by resident and endothelial cells, as well as indirect leukocyte-dependent damage,²⁷ leads to focal demyelination. As the disease progresses, oligodendrocyte depletion occurs,²⁹ as well as oligodendroglial iron release,³⁰ secondary to the high concentration of proinflammatory

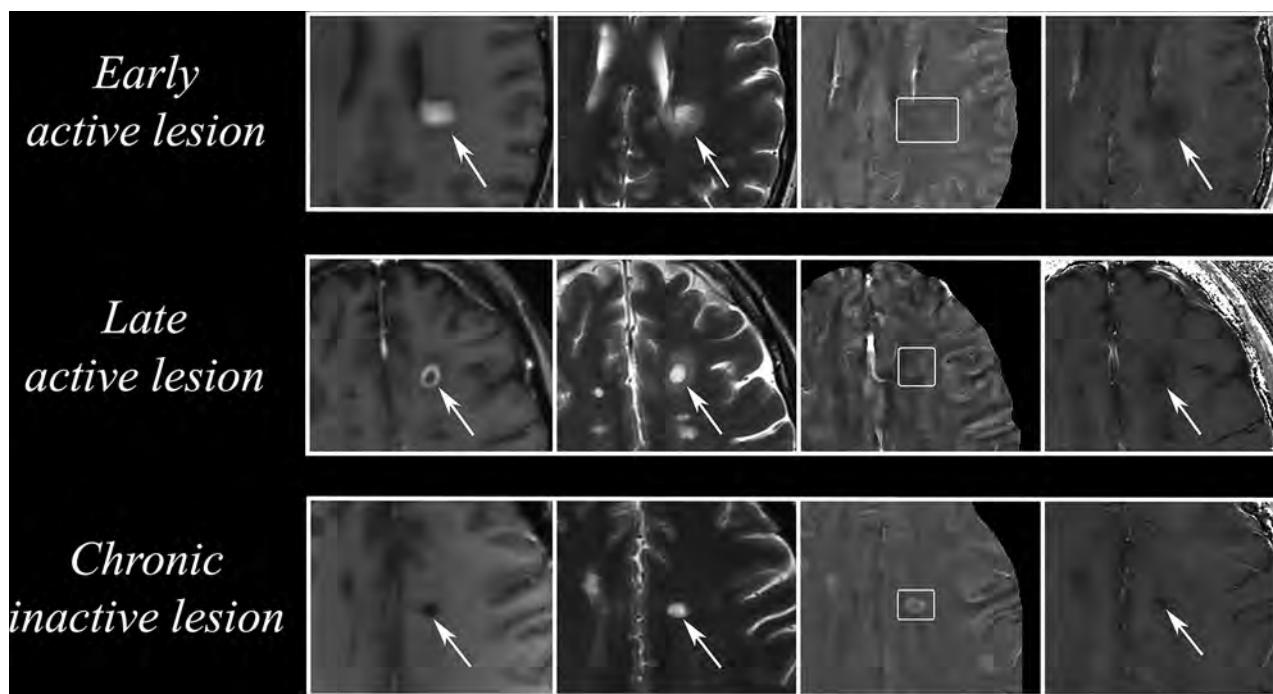


FIG 2. Conventional and quantitative MR imaging findings of WM lesions at different stages. In the *upper row*, conventional findings (postgadolinium T1-weighted and precontrast T2-weighted, *first and second images from left to right respectively*) of a typical pattern of nodular enhancement in an early active lesion (*arrows*) showing isointense signal in QSM (*third image, white box*) and mild hypointensity in R2* map (*fourth image*). In late active lesions (*middle row, arrows*), a peripheral pattern of enhancement is present, coupled with an area of increased signal at QSM and a slightly more pronounced hypointensity on R2* maps compared with the previous stage. As lesion staging further increases, the lesion eventually enters its chronic inactive stage (*lower row, arrows*), characterized by absent gadolinium enhancement, a QSM hyperintensity, and a hypointense R2* signal. Modified with permission from Zhang et al.⁴⁵

cytokines produced by the chronically activated microglia,¹⁴ with these mechanisms ultimately resulting in oxidative stress via Fenton chemistry and reduced regenerative capacity.³⁰

Because these different microstructural changes influence multiple MR imaging contrasts contemporarily, multiparameter qMRI represents the most apt approach to explore pathologic alterations occurring in the MS brain. The undeniable advantage of qMRI relies on the possibility of generating spatial maps in which each voxel corresponds to a numeric value reflecting the physical properties of the examined tissues, such as free water proportion (PD, R1, R2), myelination (R1, R2, R2*, QSM), or iron content (R2* and QSM).^{31,32}

While PD is an established measure of the brain free water pool,³³ with PD increase documented in the presence of vasogenic edema,³⁴ R1 and R2 vary as a function of free water and myelin concentration, with a higher degree of myelination causing relaxation time shortening.^{35,36}

With reference to iron, in normal brain tissue, it is mostly bound to ferritin in oligodendrocytes,³⁷ and its presence is required for the activity of enzymes involved in myelin production and preservation.¹⁵ Along with myelin, iron accounts for the larger part of the MR imaging contrast obtained through R2* and QSM.³⁸ However, whereas both iron and myelin determine an R2* increase, they play opposite roles in QSM. Given the paramagnetic properties of iron, an increase in its concentration is unequivocally coupled to an increase in susceptibility, while myelin, being a diamagnetic compound, influences susceptibility in the opposite direction.³⁸

WM Lesions

Focal WM lesions represent the most typical expression of tissue damage in MS.³⁹ According to their activity phase, WM lesions can be histologically subcategorized as early active, late active, chronic active (also described as slowly expanding or smoldering lesions), chronic inactive, and shadow plaques (remyelinated lesions).⁴⁰

In early active lesions, inflammatory activity blooms from venules, following blood-brain barrier disruption and immune cell infiltration, thus leading to progressive demyelination and axonal loss with a centrifugal spread.⁴¹ From an MR imaging perspective, these phenomena are mirrored by the pattern of enhancement after gadolinium administration. Indeed, at this stage, lesions usually enhance centrifugally, with a more pronounced nodular appearance.⁴² As inflammation proceeds, cellular infiltrates grow and, combined with myelin breaking down and edema, result in decreased R1 and R2 values, coupled to increased PD values within lesions⁴³ and transitional values in periplaque WM⁴⁴ in comparison with NAWM. These findings are associated with a similar edema-driven R2* decrease, with no QSM changes because the loss of diamagnetic myelin is not detectable at this stage (Fig 2).⁴⁵

In late active lesions, showing a peripheral or ringlike pattern of enhancement,⁴² myelin degradation and removal become progressively more substantial, therefore influencing lesion magnetic susceptibility as assessed by QSM.^{45,46} At this stage, R1, R2, and PD values show the same pattern of changes as the early active lesions in comparison with NAWM, while in R2*, a further signal decrease is present, coupled to a QSM increase, especially in the lesion

Table 1: Major qMRI findings in MS—WM compartment

Site	Pathologic Processes and qMRI Correlates
WM lesions	
Early active	Decreased R1, R2, and R2* values, along with increased PD, reflecting initial myelin degradation and edema ^{43,45}
Late active	Decreased R1 and R2 values, coupled with increased PD, with myelin debris removal that determines further R2* decrease and QSM increase ^{43,45,51}
Chronic active	Further R1 and R2 decrease, with PD increase, due to demyelination progression; ⁴³ increased R2* and QSM at the periphery of the lesions due to iron-laden microglia and macrophages ^{45,46}
Chronic inactive	Compared with chronic active, R2* decreases with high QSM values; across time, susceptibility values gradually become similar to those in NAWM ⁴⁶
NAWM	Decreased R1 and R2 values, with increased PD, compared with the WM of healthy controls, ^{50,51} reflecting edema and myelin loss secondary to inflammatory infiltration. During active phases of the disease, iron is released from oligodendrocytes and begins to accumulate in newly forming lesions, causing an R2* decrease ⁵⁰ and no relevant modification of QSM signal ⁵²

center, due to additional myelin debris removal⁴⁵ by anti-inflammatory M2 macrophages.¹⁴ Although iron begins concentrating in M1 macrophages and activated microglia at a later stage,¹⁴ its levels may acutely increase following rapid oligodendrocyte destruction, counterbalancing myelin loss in R2* and reinforcing QSM hyperintensity in some lesions (Fig 2).⁴⁷

When blood-brain barrier damage is resolved, MS lesions no longer show postgadolinium enhancement and are, therefore, categorized as chronic, further subdivided into active or inactive, depending on whether some degree of inflammatory activity persists.⁴⁰ In chronic lesions, the combination of demyelination, hypocellularity, and free water fraction increase leads to R1 and R2 decrease, while PD increases, compared with early and late active lesions.⁴³ Transition to chronicity is associated with a complex pattern of changes in iron content.³⁸ Indeed, while iron concentration may decrease due to myelin sheaths and oligodendrocyte depletion,^{29,37} some degree of iron accumulation occurs, in parallel, within iron-laden macrophages and microglia at lesions borders.^{14,32} In chronic active lesions, this inflammation-related iron accumulation at the rim of the lesions is emphasized, leading to increased R2* and QSM values.^{45,46} With time, lesions eventually become chronic inactive or shadow plaques,⁴⁰ with low R2* values but still high QSM signal, which only ultimately decreases in very late stages to resemble NAWM signal, due to iron depletion and partial remyelination (Fig 2).⁴⁶

NAWM

Despite appearing spared by lesions on conventional MR imaging sequences, NAWM is characterized by complex microstructural changes reflecting inflammation, demyelination, gliosis, and axonal loss.²⁸ The mechanisms underlying NAWM damage are mainly Wallerian degeneration of fibers transected by focal lesions and diffuse microglial activation.^{28,48} Axonal swelling and edema⁴⁹ have also been observed globally in NAWM and, together with alteration

in iron homeostasis, can be assessed through relaxation and magnetic susceptibility variations.^{24,38}

The NAWM usually shows lower R1 and R2 and higher PD values, compared with the WM of healthy controls.^{50,51} These changes seem to be mostly related to inflammatory infiltration, with edema and myelin loss.⁴⁹ A decrease in iron concentration has been observed in patients with MS in comparison with healthy controls using R2* maps.⁵⁰ This reduced relaxation rate might be driven by iron release from oligodendrocytes during chronic inflammation.^{14,29} Most interesting, the iron level in NAWM, estimated by QSM, is not stationary but fluctuates according to the presence of inflammatory activity.⁵² Indeed, during the active phases of the disease, when iron begins to accumulate in newly forming lesions, NAWM magnetic susceptibility values appear to be similar to

those observed in the WM of healthy controls,⁵² as also confirmed by ex vivo data.²⁹ On the contrary, mean QSM values of the NAWM seem to increase in the absence of gadolinium-enhancing lesions, suggesting that iron might play a role in tissue regeneration during periods of disease inactivity.¹⁵

Main qMRI findings in the WM compartment are reported in Table 1.

Deep Gray Matter

The major structures of the deep gray matter nuclei can be anatomically and functionally subdivided in the thalamus and basal ganglia, whose most relevant nuclei are the globus pallidus, putamen, and caudate nucleus. Given their relatively different histology, the thalamus and basal ganglia will be discussed separately.

Thalamus. Thalamic involvement in MS has been documented by both ex-⁵³⁻⁵⁵ and in vivo⁵³ studies. This region is not only a site of primary axonal damage, but given its high interconnectivity with other brain regions, it suffers from secondary degeneration caused by WM lesions involving thalamic projection fibers.^{53,54} Recently, a decrease in both thalamic iron content and concentration⁵⁶⁻⁶¹ has been documented in patients with MS in comparison with healthy controls, with the most evident changes detected within the pulvinar.^{59,61}

Previous studies, however, reported conflicting results,⁶²⁻⁶⁶ only partially ascribable to the physiologic nonlinear trajectory followed by thalamic iron concentration during the life span.⁶⁷ Such conflicting data should be interpreted considering the impact of atrophy on iron concentration.^{57,68} In particular, the concept of R2* mass (the sum of all the R2* values in a specific region)⁵⁷ was recently introduced as an index of iron content independent of atrophy. With this approach, the decrease in thalamic iron content has been confirmed,⁵⁷ highlighting the importance of distinguishing between (and reporting both) iron concentration and content (Fig 3).^{56,57,59,60}

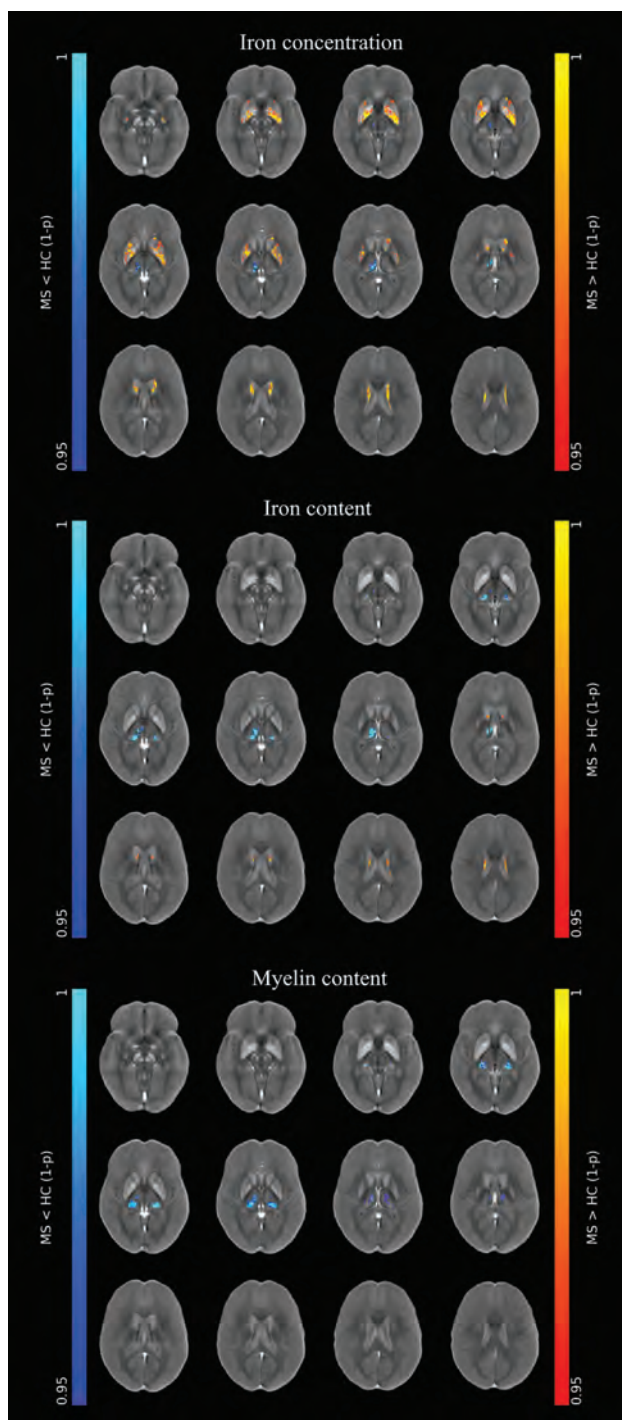


FIG 3. Pattern of iron concentration, iron content, and myelin content changes in deep gray matter nuclei in MS. Results of voxelwise analyses comparing patients with MS with healthy controls, showing the presence of an increased iron concentration at the level of the basal ganglia (red-yellow), coupled with a decrease in iron and myelin content mainly affecting the thalami and, in particular, the pulvinar nuclei (blue-light blue). Modified with permission from Pontillo et al.⁵⁹ HC indicates healthy control; 1-*p*, 1 minus *P* value.

Basal Ganglia. The basal ganglia are also the site of both demyelination⁶⁹ and neurodegeneration, with reduced neuronal density, axonal damage, and oligodendrocytes loss.^{44,55}

Similar to what we described for the thalamus, the progressive damage of the basal ganglia leads to atrophy.⁶⁹ Here, studies have more consistently reported an increase in $R2^*$ ^{58,64-66,70,71} or susceptibility^{61,64,66,70,72} in patients with MS compared with controls, suggesting a progressive iron accumulation, beyond the analogous physiologic process detectable in healthy individuals.⁷³

Nonetheless, these findings should also be interpreted in view of the effect of atrophy on tissue iron concentration.⁵⁷ Indeed, even with stable regional iron content, volume reduction leads to increased mean iron concentration.⁵⁷ In particular, a prominent decline in iron content with time in all basal ganglia has been demonstrated, coupled with an increased or stable iron concentration compared with controls at the level of putamen, caudate nucleus, and globus pallidus.^{60,72} In line with these results, some recent studies failed to identify any difference between patients with MS and controls in terms of iron content,⁵⁹ while others reported a decrease of this parameter in the putamen and caudate nucleus of patients with MS (Fig 3).^{56,57}

Cortical Lesions

From a relaxometry perspective, no studies have investigated $R1$ changes in cortical lesions (CL). However, beyond demyelination, CL are characterized by a decreased iron load, a feature that allows differentiating them from a normal-appearing cortex through the evaluation of $R2^*$ maps, as shown in postmortem samples.^{74,75} In particular, the progressive destruction of iron-rich myelin sheaths and oligodendrocytes⁷⁶ and the subsequent uptake of iron and myelin debris by activated macrophages and microglia lead to decreased $R2^*$ values in CL.⁷⁷ On the other hand, QSM has been used to analyze the heterogeneity of CL in different disease stages,⁷⁸ showing a mixed pattern of appearance. While QSM-hyperintense CL have been more frequently observed in patients with relapsing-remitting MS, QSM-hypointense CL are mostly identified in subjects with a secondary-progressive phenotype.⁷⁸ While the increased susceptibility might be due to iron release from oligodendrocytes, typical of the inflammatory phase of the disease, the reduced susceptibility might be linked to iron depletion in chronic lesions.²⁹

Normal-Appearing Cortex

Similar to the NAWM, the cortex, which does not show signal changes on conventional MR imaging, is subject, from a pathologic standpoint, to neuronal and axonal loss occurring regardless of demyelination.^{76,79} The assessment of relaxometry and QSM changes in normal-appearing cortex is confounded by the physiologic layer-specific iron content,⁸⁰ which represents the main source of cortical $R2^*$ ⁸¹ and susceptibility contrast.³⁶ Nevertheless, a decrease in both $R1$ and $R2^*$ values has been reported in MS in normal-appearing cortex, accounting for demyelination and iron depletion, respectively.⁵⁰ Consistent with the hypothesis of cortical demyelination triggered by chemokines produced by lymphocytic infiltrates in the meningeal compartment,⁸² a recent study has reported coherent cortical gradients of $R1$ and $R2^*$, oriented from the subpial layer to the WM interface.⁸³ In the same study, QSM showed a lack of sensitivity in distinguishing the different layers, probably due to the counteracting effects of diamagnetic myelin and paramagnetic iron modifications.⁸³

Table 2: Major qMRI findings in MS—GM compartment

Site	Pathologic Processes and qMRI Correlates
Deep gray matter Basal ganglia	Increased R2* ^{58,64–66,70,71} and QSM values ^{61,64,66,70,72} indicating increased iron concentrations, with atrophy that might play a role in causing these changes ^{57,68}
Thalamus	The more recent findings suggest the presence of reduced iron content and concentration, along with demyelination, as shown by decreased RI, R2*, and QSM values ^{56–61}
Cortical gray matter Cortical lesions	Reduced R2* signal due to demyelination and iron depletion; ^{74,75} cortical lesions are more heterogeneous on QSM, with decreased-to-increased values, depending on the level of inflammatory activity ⁷⁸
Normal-appearing cortex	Demyelination and iron depletion lead to reduced RI and R2* values, ⁵⁰ with a gradient indicating the WM interface ⁸³

The main qMRI findings of the GM compartment are reported in Table 2.

CONCLUSIONS

In this review, we offered a comprehensive overview of qMRI applications in MS, while also describing the theory behind map generation and the most likely histologic correlates of qMRI findings. The multiparameter nature of qMRI has already allowed researchers to gain additional, valuable insights about the multifaceted pathophysiology of brain damage in MS. Given the increasing accessibility to quantitative sequences on novel MR imaging scanners, in the near future, qMRI will also likely play a fundamental role in clinical practice as a sensitive tool to quantitatively assess brain damage in patients with MS, with relevant implications for prognostic stratification and treatment-response evaluation.

Disclosure forms provided by the authors are available with the full text and PDF of this article at www.ajnr.org.

REFERENCES

- Rovira À, Wattjes MP, Tintoré M, et al; MAGNIMS Study Group. Evidence-based guidelines: MAGNIMS consensus guidelines on the use of MRI in multiple sclerosis-clinical implementation in the diagnostic process. *Nat Rev Neurol* 2015;11:471–82 CrossRef Medline
- Wattjes MP, Ciccarelli O, Reich DS, et al; North American Imaging in Multiple Sclerosis Cooperative MRI Guidelines Working Group. MAGNIMS-CMSC-NAIMS consensus recommendations on the use of MRI in patients with multiple sclerosis. *Lancet Neurol* 2021;20:653–70 CrossRef Medline
- Hagiwara A, Otsuka Y, Andica C, et al. Differentiation between multiple sclerosis and neuromyelitis optica spectrum disorders by multiparametric quantitative MRI using convolutional neural network. *J Clin Neurosci* 2021;87:55–58 CrossRef Medline
- Pudlac A, Burgetova A, Dusek P, et al. Deep gray matter iron content in neuromyelitis optica and multiple sclerosis. *BioMed Res Int* 2020;2020:6492786 CrossRef Medline
- Deistung A, Schweser F, Reichenbach JR. Overview of quantitative susceptibility mapping. *NMR Biomed* 2017;30:e3569 CrossRef Medline
- Seiler A, Nöth U, Hok P, et al. Multiparametric quantitative MRI in neurological diseases. *Front Neurol* 2021;12:640239 CrossRef Medline
- Li J, Lin H, Liu T, et al. Quantitative susceptibility mapping (QSM) minimizes interference from cellular pathology in R2* estimation

of liver iron concentration. *J Magn Reson Imaging* 2018;48:1069–79 CrossRef Medline

- Banerjee R, Pavlides M, Tunnick EM, et al. Multiparametric magnetic resonance for the non-invasive diagnosis of liver disease. *J Hepatol* 2014;60:69–77 CrossRef Medline
- Straub S, Laun FB, Emmerich J, et al. Potential of quantitative susceptibility mapping for detection of prostatic calcifications. *J Magn Reson Imaging* 2017;45:889–98 CrossRef Medline
- Jerban S, Lu X, Jang H, et al. Significant correlations between human cortical bone mineral density and quantitative susceptibility mapping (QSM) obtained with 3D cones ultrashort echo time magnetic resonance imaging (UTE-MRI). *Magn Reson Imaging* 2019;62:104–10 CrossRef Medline
- Karur GR, Hanneman K. Cardiac MRI T1, T2, and T2* mapping in clinical practice. *Advances in Clinical Radiology* 2019;1:27–41 CrossRef
- Granziera C, Wuerfel J, Barkhof F, et al; MAGNIMS Study Group. Quantitative magnetic resonance imaging towards clinical application in multiple sclerosis. *Brain* 2021;144:1296–1311 CrossRef Medline
- Pontillo G, Cocozza S, Lanzillo R, et al. Determinants of deep gray matter atrophy in multiple sclerosis: a multimodal MRI study. *AJNR Am J Neuroradiol* 2019;40:99–106 CrossRef Medline
- Mehta V, Pei W, Yang G, et al. Iron is a sensitive biomarker for inflammation in multiple sclerosis lesions. *PLoS One* 2013;8:e57573 CrossRef Medline
- Möller HE, Bossoni L, Connor JR, et al. Iron, myelin, and the brain: neuroimaging meets neurobiology. *Trends Neurosci* 2019;42:384–401 CrossRef Medline
- Deoni SC, Rutt BK, Peters TM. Rapid combined T1 and T2 mapping using gradient recalled acquisition in the steady state. *Magn Reson Med* 2003;49:515–26 CrossRef Medline
- Yarnykh VL. Actual flip-angle imaging in the pulsed steady state: a method for rapid three-dimensional mapping of the transmitted radiofrequency field. *Magn Reson Med* 2007;57:192–200 CrossRef Medline
- Palma G, Tedeschi E, Borrelli P, et al. A novel multiparametric approach to 3D quantitative MRI of the brain. *PLoS One* 2015;10:e0134963 CrossRef Medline
- Baudrexel S, Nöth U, Schüre JR, et al. T1 mapping with the variable flip angle technique: a simple correction for insufficient spoiling of transverse magnetization. *Magn Reson Med* 2018;79:3082–92 CrossRef Medline
- Björk M, Ingle RR, Gudmundson E, et al. Parameter estimation approach to banding artifact reduction in balanced steady-state free precession. *Magn Reson Med* 2014;72:880–92 CrossRef Medline
- Monti S, Borrelli P, Tedeschi E, et al. RESUME: turning an SWI acquisition into a fast qMRI protocol. *PLoS One* 2017;12:e0189933 CrossRef Medline
- Monti S, Pontillo G, Russo C, et al. RESUME^N: a flexible class of multi-parameter qMRI protocols. *Phys Med* 2021;88:23–36 CrossRef Medline
- Li W, Wang N, Yu F, et al. A method for estimating and removing streaking artifacts in quantitative susceptibility mapping. *Neuroimage* 2015;108:111–22 CrossRef Medline
- Li W, Wu B, Liu C. Quantitative susceptibility mapping of human brain reflects spatial variation in tissue composition. *Neuroimage* 2011;55:1645–56 CrossRef Medline
- Aja-Fernández S, Pieciak T, Vegas-Sánchez-Ferrero G. Spatially variant noise estimation in MRI: a homomorphic approach. *Med Image Anal* 2015;20:184–97 CrossRef Medline

26. Borrelli P, Palma G, Tedeschi E, et al. **Improving signal-to-noise ratio in susceptibility weighted imaging: a novel multicomponent non-local approach.** *PLoS One* 2015;10:e0126835 CrossRef Medline
27. Filippi M, Bar-Or A, Piehl F, et al. **Multiple sclerosis.** *Nat Rev Dis Primers* 2018;4:43 CrossRef Medline
28. Allen IV, McQuaid S, Mirakhur M, et al. **Pathological abnormalities in the normal-appearing white matter in multiple sclerosis.** *Neurolo Sci* 2001;22:141–44 CrossRef Medline
29. Hametner S, Wimmer I, Haider L, et al. **Iron and neurodegeneration in the multiple sclerosis brain.** *Ann Neurol* 2013;74:848–61 CrossRef Medline
30. Stephenson E, Nathoo N, Mahjoub Y, et al. **Iron in multiple sclerosis: roles in neurodegeneration and repair.** *Nat Rev Neurol* 2014;10:459–68 CrossRef Medline
31. Weiskopf N, Edwards LJ, Helms G, et al. **Quantitative magnetic resonance imaging of brain anatomy and in vivo histology.** *Nat Rev Phys* 2021;3:570–88 CrossRef
32. Wisniewski C, Ramanan S, Olesik J, et al. **Quantitative susceptibility mapping (QSM) of white matter multiple sclerosis lesions: Interpreting positive susceptibility and the presence of iron.** *Magn Reson Med* 2015;74:564–70 CrossRef Medline
33. Tofts PS. PD: proton density of tissue water. In: Tofts PS. *Quantitative MRI of the Brain: Measuring Changes Caused by Disease.* Wiley Online Library; 2003:85–109
34. Eis M, Els T, Hoehn-Berlage M. **High resolution quantitative relaxation and diffusion MRI of three different experimental brain tumors in rat.** *Magn Reson Med* 1995;34:835–44 CrossRef Medline
35. Schmierer K, Wheeler-Kingshott CA, Tozer DJ, et al. **Quantitative magnetic resonance of postmortem multiple sclerosis brain before and after fixation.** *Magn Reson Med* 2008;59:268–77 CrossRef Medline
36. Stüber C, Morawski M, Schäfer A, et al. **Myelin and iron concentration in the human brain: a quantitative study of MRI contrast.** *Neuroimage* 2014;93 Pt 1:95–106 CrossRef Medline
37. Bagnato F, Hametner S, Yao B, et al. **Tracking iron in multiple sclerosis: a combined imaging and histopathological study at 7 Tesla.** *Brain* 2011;134:3602–15 CrossRef Medline
38. Hametner S, Endmayr V, Deistung A, et al. **The influence of brain iron and myelin on magnetic susceptibility and effective transverse relaxation: a biochemical and histological validation study.** *Neuroimage* 2018;179:117–33 CrossRef Medline
39. van der Valk P, De Groot CJ. **Staging of multiple sclerosis (MS) lesions: pathology of the time frame of MS.** *Neuropathol Appl Neurobiol* 2000;26:2–10 CrossRef Medline
40. Frischer JM, Weigand SD, Guo Y, et al. **Clinical and pathological insights into the dynamic nature of the white matter multiple sclerosis plaque.** *Ann Neurol* 2015;78:710–21 CrossRef Medline
41. Tallantyre EC, Brookes MJ, Dixon JE, et al. **Demonstrating the perivascular distribution of MS lesions in vivo with 7-Tesla MRI.** *Neurology* 2008;70:2076–78 CrossRef Medline
42. Gaitán MI, Shea CD, Evangelou IE, et al. **Evolution of the blood-brain barrier in newly forming multiple sclerosis lesions.** *Ann Neurol* 2011;70:22–29 CrossRef Medline
43. Blystad I, Håkansson I, Tisell A, et al. **Quantitative MRI for analysis of active multiple sclerosis lesions without gadolinium-based contrast agent.** *AJNR Am J Neuroradiol* 2016;37:94–100 CrossRef Medline
44. Hagihara A, Hori M, Yokoyama K, et al. **Utility of a multiparametric quantitative MRI model that assesses myelin and edema for evaluating plaques, periplaque white matter, and normal-appearing white matter in patients with multiple sclerosis: a feasibility study.** *AJNR Am J Neuroradiol* 2017;38:237–42 CrossRef Medline
45. Zhang Y, Gauthier SA, Gupta A, et al. **Quantitative susceptibility mapping and R2* measured changes during white matter lesion development in multiple sclerosis: myelin breakdown, myelin debris degradation and removal, and iron accumulation.** *AJNR Am J Neuroradiol* 2016;37:1629–35 CrossRef Medline
46. Chen W, Gauthier SA, Gupta A, et al. **Quantitative susceptibility mapping of multiple sclerosis lesions at various ages.** *Radiology* 2014;271:183–92 CrossRef Medline
47. Harrison DM, Li X, Liu H, et al. **Lesion heterogeneity on high-field susceptibility MRI is associated with multiple sclerosis severity.** *AJNR Am J Neuroradiol* 2016;37:1447–53 CrossRef Medline
48. Dzedzic T, Metz I, Dallenga T, et al. **Wallerian degeneration: a major component of early axonal pathology in multiple sclerosis.** *Brain Pathol* 2010;20:976–85 CrossRef Medline
49. Filippi M, Rocca MA, Barkhof F, et al; Attendees of the Correlation between Pathological MRI Findings in MS Workshop. **Association between pathological and MRI findings in multiple sclerosis.** *Lancet Neurol* 2012;11:349–60 CrossRef Medline
50. Lommers E, Simon J, Reuter G, et al. **Multiparameter MRI quantification of microstructural tissue alterations in multiple sclerosis.** *Neuroimage Clin* 2019;23:101879 CrossRef Medline
51. West J, Aalto A, Tisell A, et al. **Normal-appearing and diffusely abnormal white matter in patients with multiple sclerosis assessed with quantitative MR.** *PLoS One* 2014;9:e95161 CrossRef Medline
52. Chen W, Zhang Y, Mu K, et al. **Quantifying the susceptibility variation of normal-appearing white matter in multiple sclerosis by quantitative susceptibility mapping.** *AJR Am J Roentgenol* 2017;209:889–94 CrossRef Medline
53. Cifelli A, Arridge M, Jezzard P, et al. **Thalamic neurodegeneration in multiple sclerosis.** *Ann Neurol* 2002;52:650–53 CrossRef Medline
54. Mahajan KR, Nakamura K, Cohen JA, et al. **Intrinsic and extrinsic mechanisms of thalamic pathology in multiple sclerosis.** *Ann Neurol* 2020;88:81–92 CrossRef Medline
55. Vercellino M, Masera S, Lorenzatti M, et al. **Demyelination, inflammation, and neurodegeneration in multiple sclerosis deep gray matter.** *J Neuropathol Exp Neurol* 2009;68:489–502 CrossRef Medline
56. Elkady AM, Cobzas D, Sun H, et al. **Five year iron changes in relapsing-remitting multiple sclerosis deep gray matter compared to healthy controls.** *Mult Scler Relat Disord* 2019;33:107–15 CrossRef Medline
57. Hernández-Torres E, Wiggermann V, Machan L, et al. **Increased mean R2* in the deep gray matter of multiple sclerosis patients: have we been measuring atrophy?** *J Magn Reson Imaging* 2019;50:201–08 CrossRef Medline
58. Khalil M, Langkammer C, Pichler A, et al. **Dynamics of brain iron levels in multiple sclerosis: a longitudinal 3T MRI study.** *Neurology* 2015;84:2396–2402 CrossRef Medline
59. Pontillo G, Petracca M, Monti S, et al. **Unraveling deep gray matter atrophy and iron and myelin changes in multiple sclerosis.** *AJNR Am J Neuroradiol* 2021;42:1223–30 CrossRef Medline
60. Schweser F, Hagemeyer J, Dwyer MG, et al. **Decreasing brain iron in multiple sclerosis: the difference between concentration and content in iron MRI.** *Hum Brain Mapp* 2021;42:1463–74 CrossRef Medline
61. Zivadinov R, Tavazzi E, Bergsland N, et al. **Brain iron at quantitative MRI is associated with disability in multiple sclerosis.** *Radiology* 2018;289:487–96 CrossRef Medline
62. Cobzas D, Sun H, Walsh AJ, et al. **Subcortical gray matter segmentation and voxel-based analysis using transverse relaxation and quantitative susceptibility mapping with application to multiple sclerosis.** *J Magn Reson Imaging* 2015;42:1601–10 CrossRef Medline
63. Lebel RM, Eissa A, Seres P, et al. **Quantitative high-field imaging of sub-cortical gray matter in multiple sclerosis.** *Mult Scler* 2012;18:433–41 CrossRef Medline
64. Rudko DA, Solovey I, Gati JS, et al. **Multiple sclerosis: improved identification of disease-relevant changes in gray and white matter by using susceptibility-based MR imaging.** *Radiology* 2014;272:851–64 CrossRef Medline
65. Walsh AJ, Blevins G, Lebel RM, et al. **Longitudinal MR imaging of iron in multiple sclerosis: an imaging marker of disease.** *Radiology* 2014;270:186–96 CrossRef Medline
66. Fujiwara E, Kmech JA, Cobzas D, et al. **Cognitive implications of deep gray matter iron in multiple sclerosis.** *AJNR Am J Neuroradiol* 2017;38:942–48 CrossRef Medline
67. Hallgren B, Sourander P. **The effect of age on the non-haemin iron in the human brain.** *Neurochem* 1958;3:41–51 CrossRef Medline

68. Eshaghi A, Marinescu RV, Young AL, et al. **Progression of regional grey matter atrophy in multiple sclerosis.** *Brain* 2018;141:1665–77 CrossRef Medline
69. Haider L, Simeonidou C, Steinberger G, et al. **Multiple sclerosis deep grey matter: the relation between demyelination, neurodegeneration, inflammation and iron.** *J Neurol Neurosurg Psychiatry* 2014;85:1386–95 CrossRef Medline
70. Elkady AM, Cobzas D, Sun H, et al. **Progressive iron accumulation across multiple sclerosis phenotypes revealed by sparse classification of deep gray matter.** *J Magn Reson Imaging* 2017;46:1464–73 CrossRef Medline
71. Ropele S, Kilsdonk ID, Wattjes MP, et al. **Determinants of iron accumulation in deep grey matter of multiple sclerosis patients.** *Mult Scler* 2014;20:1692–98 CrossRef Medline
72. Hagemeier J, Zivadinov R, Dwyer MG, et al. **Changes of deep gray matter magnetic susceptibility over 2 years in multiple sclerosis and healthy control brain.** *Neuroimage Clin* 2018;18:1007–16 CrossRef Medline
73. Haacke EM, Cheng NY, House MJ, et al. **Imaging iron stores in the brain using magnetic resonance imaging.** *Magn Reson Imaging* 2005;23:1–25 CrossRef Medline
74. Jonkman LE, Fleysher L, Steenwijk MD, et al. **Ultra-high field MTR and qR2* differentiates subpial cortical lesions from normal-appearing gray matter in multiple sclerosis.** *Mult Scler* 2016;22:1306–14 CrossRef Medline
75. Yao B, Hametner S, van Gelderen P, et al. **7 Tesla magnetic resonance imaging to detect cortical pathology in multiple sclerosis.** *PLoS One* 2014;9:e108863 CrossRef Medline
76. Peterson JW, Bö L, Mörk S, et al. **Transected neurites, apoptotic neurons, and reduced inflammation in cortical multiple sclerosis lesions.** *Ann Neurol* 2001;50:389–400 CrossRef Medline
77. Fischer MT, Wimmer I, Höftberger R, et al. **Disease-specific molecular events in cortical multiple sclerosis lesions.** *Brain* 2013;136:1799–1815 CrossRef Medline
78. Castellaro M, Magliozzi R, Palombi A, et al. **Heterogeneity of cortical lesion susceptibility mapping in multiple sclerosis.** *AJNR Am J Neuroradiol* 2017;38:1087–95 CrossRef Medline
79. Magliozzi R, Howell OW, Reeves C, et al. **A Gradient of neuronal loss and meningeal inflammation in multiple sclerosis.** *Ann Neurol* 2010;68:477–93 CrossRef Medline
80. Fukunaga M, Li TQ, van Gelderen P, et al. **Layer-specific variation of iron content in cerebral cortex as a source of MRI contrast.** *Proc Natl Acad Sci U S A* 2010;107:3834–39 CrossRef Medline
81. Bagnato F, Hametner S, Boyd E, et al. **Untangling the R2* contrast in multiple sclerosis: a combined MRI-histology study at 7.0 Tesla.** *PLoS One* 2018;13:e0193839 CrossRef Medline
82. Magliozzi R, Reynolds R, Calabrese M. **MRI of cortical lesions and its use in studying their role in MS pathogenesis and disease course.** *Brain Pathol* 2018;28:735–42 CrossRef Medline
83. Lema Dopico A, Choi S, Hua J, et al. **Multi-layer analysis of quantitative 7 T magnetic resonance imaging in the cortex of multiple sclerosis patients reveals pathology associated with disability.** *Mult Scler* 2021;27:2040–51 CrossRef Medline

Malignant Melanotic Nerve Sheath Tumor

J.C. Benson, M.D. Marais, P.M. Flanigan, M. Bydon, C. Giannini, R.J. Spinner, and A.L. Folpe

ABSTRACT

SUMMARY: Malignant melanotic nerve sheath tumors are uncommon pigmented tumors of Schwann cell origin, most often found along the spinal nerves. Although well-described in the literature, the tumors are quite rare, making up <1% of nerve sheath tumors. Physicians are, therefore, often unfamiliar with both the appearance and the optimal treatment of such tumors. Morphologically, many imaging features overlap with schwannomas and neurofibromas. Nevertheless, the malignant melanotic nerve sheath tumors are crucial to identify. They can be extremely aggressive, and the management of these tumors is considerably different from their benign counterparts. In this radiology-pathology review, we will highlight the imaging appearance, histologic features, surgical resection, and subsequent therapeutic strategies in a patient with a lumbar malignant melanotic nerve sheath tumor.

ABBREVIATION: MMNST = malignant melanotic nerve sheath tumor

The patient is a 39-year-old woman with no notable medical history who presented with a 5-year history of progressive left, lower-extremity, radicular symptoms. Her symptoms began as intermittent pain in her left leg, which evolved into constant pain and dysesthesias. On physical examination, she demonstrated mild weakness of left toe extension and trace weakness of left ankle inversion/eversion. An initial lumbar spine MR imaging performed at an outside institution 4 years prior to presentation was interpreted as having normal findings. Follow-up imaging, performed 1 year before presentation, identified a mass along the L5 nerve root. In retrospect, this had been present on the first examination and had grown in the interim. The patient presented to our institution for further management.

Imaging

MR imaging of the lumbar spine demonstrated an elongated well-circumscribed mass centered in the left L5-S1 foramen with both intra- and extradural components. The mass extended centrally to the left lateral recess and peripherally into the extraforaminal space along the exiting nerve root. There was no remodeling of the adjacent bone. Intratumoral signal was homogeneously hyperintense on T1 and hypointense on T2 (Fig 1). Homogeneous enhancement

was observed on postcontrast images. Comparison with prior imaging demonstrated progressive growth of the tumor during the course of the prior MRIs, from 1.0 to 1.6 cm in maximum axial diameter during a 4-year period. Because of its imaging characteristics, the mass was thought most likely to represent a malignant melanotic nerve sheath tumor. A melanin-containing metastasis was also considered possible, though less likely given the patient's negative medical history. A benign hemorrhagic nerve sheath tumor was thought to be unlikely, given its homogeneous intraleSIONAL signal and consistent appearance across time.

Imaging findings of the brain and cervical and thoracic spine were normal, without evidence of leptomeningeal metastases.

Operative Report

Given the patient's steadily worsening radicular symptoms, mild weakness on examination, and the uncertain malignant potential of the mass, surgical treatment was recommended. The tumoral resection required an L5 laminectomy and a complete left L5-S1 facetectomy due to the extensive involvement of the mass along the nerve (from the nerve root axilla to the extraforaminal segment of the left L5 nerve, even extending underneath the sacral ala). Intraoperatively, after the above bony elements had been removed, the melanotic-appearing spinal nerve was identified along its course by careful dissection of overlying soft tissues. Neuromonitoring was used to enhance intraoperative understanding of regional anatomy. Despite appropriate firing of other nerves in the operative field, a firing response was not able to be elicited, suggesting the nerve was nonfunctional from a motor standpoint.

Received August 15, 2022; accepted after revision September 30.

From the Departments of Radiology (J.C.B., M.D.M.), Neurologic Surgery (P.M.F., M.B.), and Laboratory Medicine and Pathology (C.G., R.J.S., A.L.F.), Mayo Clinic, Rochester, Minnesota.

Please address correspondence to John C. Benson, MD, Department of Radiology, Mayo Clinic, 200 1st St SW, Rochester, MN 55902; e-mail: benson.john3@mayo.edu
<http://dx.doi.org/10.3174/ajnr.A7691>

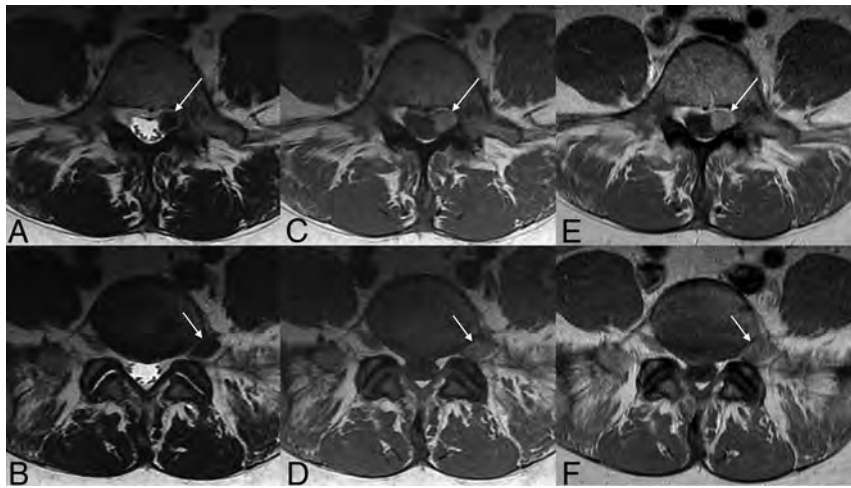


FIG 1 Axial T2 (A and B), T1 precontrast (C and D), and postgadolinium T1 (E and F) images of the lumbar spine. On each image, the tumor is seen transverse the left L5-S1 foramen along the exiting nerve root (arrows). The mass is distinctively hypointense to adjacent muscle on T2 and hyperintense to muscle on T1. Faint-but-convincing enhancement is noted on postcontrast images.

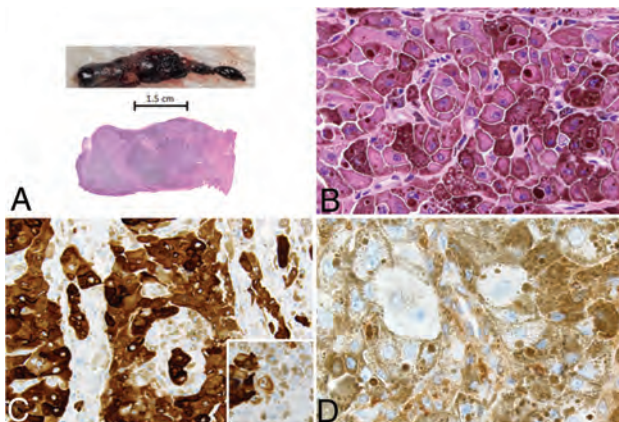


FIG 2 A, Gross photograph of a malignant melanotic schwannian tumor, presenting as a jet-black, roughly dumbbell-shaped mass involving the neural foramen. B, Microscopic view of malignant melanotic schwannoma, composed of moderately variable epithelioid cells with abundant intracytoplasmic melanin pigment and variably prominent nucleoli (H&E, original magnification $\times 200$). C, The tumor was strongly positive for Melan-A. D, Expression of the Carney complex–associated tumor-suppressor gene *PRKARIA* was entirely absent. Loss of *PRKARIA* expression is seen both in syndromic and nonsyndromic MMNSTs.

Under the microscope, the multilobular tumor was separated from the nerve using standard microsurgical dissection techniques. After identifying the most distal aspect of the tumor, a dissection plane was made between it and the nerve, proceeding in a distal-to-proximal direction. At its proximal extent, a small portion of intradural tumor extension was encountered and, consequently, CSF egress occurred from that site. The spinal fluid leak ultimately was repaired satisfactorily. A substantial majority of the mass was removed en bloc (Fig 2), and there was no trace of residual tumor seen grossly. The patient awoke at the neurologic baseline and had an uneventful postoperative course.

Pathology

Grossly, the tumor appeared as a jet-black, multinodular, fusiform expansion of the nerve root, measuring 4.5 cm in greatest dimension. Microscopically, the tumor cells were predominantly epithelioid in morphology, with abundant intracytoplasmic melanin pigment and variably-sized nuclei with prominent nucleoli; mitotic activity was $<1/50$ high-powered fields; and necrosis was absent (Fig 2). By immunohistochemistry, the neoplastic cells showed diffuse expression of S-100 protein and Melan-A with complete loss of *PRKARIA*, an immunophenotype diagnosis of malignant melanotic nerve sheath tumor (MMNST) in this clinical and morphologic context. Loss of *PRKARIA* expression is commonly seen in MMNST¹ and is not a feature of conventional malignant melanoma or melanoma arising

in a cellular blue nevus,² melanocytic tumors that share some morphologic and immunohistochemical features with MMNST. Although molecular genetic studies were not needed in the present case, MMNST also differed genetically from other malignant melanotic tumors, with MMNST having *PRKARIA* mutations; conventional melanomas showing mutations in *BRAF*, *NRAS* or *KRAS*; and melanoma arising in a blue nevus containing mutations in the *GNA* genes.

DISCUSSION

MMNSTs are pigmented tumors often located in the spine and paraspinal soft tissues.³ Formerly known as melanotic schwannomas, these tumors were reclassified in 2020 to reflect their aggressive clinical behavior.^{4,5} MMNSTs are rare, making up $<1\%$ of all nerve sheath tumors.⁶ The tumors tend to occur in the fourth decade of life without a sex predilection.⁷ Although MMNSTs can occur along cranial nerves, they tend to grow along the dorsal spinal nerve roots, and patients often present with indolent pain, weakness, or paresthesia along a corresponding dermatome.^{8,9} Tumors may also be discovered incidentally on spinal imaging. Although acute presentations have been described in MMNSTs, these reports are rare.^{10,11}

On imaging, spinal MMNSTs generally appear similar to the appearance presented in the current case: intradural, extramedullary tumors. In the spine, the tumors typically grow along spinal nerve roots, sometimes assuming a dumbbell configuration if they extend through a foramen. Tumors demonstrate enhancement on CT and are FDG-avid on PET.¹² Paramagnetic free radicals associated with the intratumoral melanin give the tumors a distinctive T1-hyperintense and T2-hypointense appearance. This feature is inconstant; 1 review found that only 65% of tumors demonstrated T1 hyperintensity, likely reflecting the variable concentrations of intratumoral melanin and cellular densities of tumors.¹³ Intratumoral T2 hyperintensity, too, is variable.⁸ In very rare cases, the tumors may arise from within

the spinal cord.^{14–16} No imaging features have been identified to serve as prognostic markers to predict the aggressiveness of the tumor.⁸

The major differential considerations for MMNSTs are those of other intradural, extramedullary tumors closely related to spinal nerves. The most likely entities would be benign schwannomas and neurofibromas, meningiomas, malignant peripheral nerve sheath tumors, or metastases. On CT, distinguishing these tumors may be impossible. The “dumbbell” morphology, for instance, is nonspecific; all of these tumors can take this shape if they contain both intradural and extradural components.¹⁷ On MR imaging, however, the intrinsic T1 hyperintensity associated with MMNSTs can be used to distinguish such tumors from their mimics. Schwannomas and neurofibromas tend to be hypointense on T1 and hyperintense on T2. Larger schwannomas, in particular, can be markedly T2 hyperintense and even demonstrate ringlike enhancement because they often undergo cystic degeneration.¹⁸ Nevertheless, T1 hyperintensity can also be seen in the setting of meningeal melanotic neoplasms and melanoma metastases, both of which could be included as differential considerations on imaging.¹⁹

The management of patients with MMNSTs can be complex. The tumors are capable of substantial malignant spread, with local recurrence found in more than one-third of patients, and metastatic disease, in 44% of cases.¹ Lungs are the most common site of metastases, though many other sites have been reported.^{20–22} Some tumors can lead to considerable leptomeningeal spread.²³ MMNSTs are known to recur or spread after 5 years, even without sinister histologic markers.⁹

Furthermore, the tumors are associated with the Carney complex, an autosomal dominant syndrome characterized by cardiac and extracardiac myxomas, spotty skin pigmentation, endocrine overactivity, and testicular tumors.²⁴ The precise association between MMNSTs and Carney complex has been a matter of debate. Carney²⁵ reported that one-half of patients with MMNSTs containing psammoma bodies (previously called “psammomatous melanotic schwannomas”) had Carney complex features. Others, most notably Torres-Mora et al,¹ found no clinicopathologic differences between psammomatous and nonpsammomatous melanotic tumors, and they have doubted that any distinction exists between these tumor subtypes and their associations with Carney complex.

Surgical resection is the mainstay of treatment, with gross total resection recommended.²⁶ Adjuvant therapy and management of metastatic or recidivist disease, however, are less well-defined, given the scarcity of MMNSTs. Some authors suggest adjuvant radiation therapy following resection that did not accomplish clear surgical margins, though the evidence for this remains mostly anecdotal in the literature.^{6,27,28} The patient presented in this case is expected to have a favorable postoperative course. His most recent imaging, performed 4 months after the operation, showed no evidence of residual or recurrent tumor. He will be assessed by radiation oncology to consider adjuvant treatment and will undergo surveillance imaging to rule out recidivist disease.

Case Summary

- Although rare, MMNSTs are crucial to identify on imaging because they are aggressive and prone to metastasizing

- On MRI, MMNSTs demonstrate characteristic T1 hyperintensity and T2 hypointensity related to intratumoral melanin
- Characteristic morphologic features and loss of *PRKARIA* expression help to distinguish MMNSTs from morphologic mimics, in particular metastatic melanoma and melanoma arising from a cellular blue nevus
- Surgical resection of the tumor should focus on safe and complete resection and should be en bloc when possible, given the variable metastatic and malignant potential of the tumor.

Disclosure forms provided by the authors are available with the full text and PDF of this article at www.ajnr.org.

REFERENCES

1. Torres-Mora J, Dry S, Li X, et al. **Malignant melanotic schwannian tumor: a clinicopathologic, immunohistochemical, and gene expression profiling study of 40 cases, with a proposal for the reclassification of “melanotic schwannoma.”** *Am J Surg Pathol* 2014;38:94–105 CrossRef
2. Shah K, Folpe AL, Miller M, et al. **Primary intra-abdominal melanoma arising in association with extracutaneous blue naevus: a report of two cases.** *Histopathology* 2021;78:281–89 CrossRef Medline
3. Meyer A, Billings SD. **What’s new in nerve sheath tumors.** *Virchows Arch* 2020;476:65–80 CrossRef Medline
4. Kallen ME, Hornick JL. **The 2020 WHO Classification: what’s new in soft tissue tumor pathology?** *Am J Surg Pathol* 2021;45:e1–23 CrossRef Medline
5. Sbaraglia M, Bellan E, Dei Tos AP. **The 2020 WHO Classification of Soft-Tissue Tumours: news and perspectives.** *Pathologica* 2021;113:70–84 CrossRef Medline
6. Sahay A, Epari S, Gupta P, et al. **Melanotic schwannoma, a deceptive misnomer for a tumor with relative aggressive behavior: a series of 7 cranial and spinal cases.** *Int J Surg Pathol* 2020;28:850–58 CrossRef Medline
7. Alexiev BA, Chou PM, Jennings LJ. **Pathology of melanotic schwannoma.** *Arch Pathol Lab Med* 2018;142:1517–23 CrossRef Medline
8. Khoo M, Pressney I, Hargunani R, et al. **Melanotic schwannoma: an 11-year case series.** *Skeletal Radiol* 2016;45:29–34 CrossRef Medline
9. Vallat-Decouvelaere AV, Wassef M, Lot G, et al. **Spinal melanotic schwannoma: a tumour with poor prognosis.** *Histopathology* 1999;35:558–66 CrossRef Medline
10. Zaninovich O, Ramey W, Eldersveld J, et al. **Malignant melanotic schwannian tumor presenting with spinal cord infarction due to occlusion of the artery of Adamkiewicz: case report and review of the literature.** *World Neurosurg* 2019;128:422–25 CrossRef Medline
11. Soyland DJ, Goehner DR, Hoerschgen KM, et al. **Hemorrhagic spinal melanotic schwannoma presenting as acute chest pain: a case report and literature review.** *Surg Neurol Int* 2021;12:164 CrossRef Medline
12. Liu E, Sun T, Liu C, et al. **Giant melanotic malignant peripheral nerve sheath tumor in the pelvis: contrast-enhanced CT and 18F-FDG PET/CT finding.** *Clin Nucl Med* 2019;44:895–97 CrossRef Medline
13. Solomou G, Dulanka Silva AH, Wong A, et al. **Extramedullary malignant melanotic schwannoma of the spine: case report and an up-to-date systematic review of the literature.** *Ann Med Surg (Lond)* 2020;59:217–23 CrossRef Medline
14. Hoover JM, Bledsoe JM, Giannini C, et al. **Intramedullary melanotic schwannoma.** *Rare Tumors* 2012;4:e3 CrossRef Medline
15. Hu L, Wang C. **Intramedullary melanotic schwannoma of the cervical spine: a case report and literature review.** *Mol Clin Oncol* 2018;8:567–70 CrossRef Medline
16. Santaguida C, Sabbagh AJ, Guiot MC, et al. **Aggressive intramedullary melanotic schwannoma: case report.** *Neurosurgery* 2004;55:1430 CrossRef Medline

17. Abul-Kasim K, Thurnher MM, McKeever P, et al. **Intradural spinal tumors: current classification and MRI features.** *Neuroradiology* 2008;50:301–14 CrossRef Medline
18. Koeller KK, Shih RY. **Intradural extramedullary spinal neoplasms: radiologic-pathologic correlation.** *Radiographics* 2019;39:468–90 CrossRef Medline
19. Rodriguez FJ, Folpe AL, Giannini C, et al. **Pathology of peripheral nerve sheath tumors: diagnostic overview and update on selected diagnostic problems.** *Acta Neuropathol* 2012;123:295–319 CrossRef Medline
20. Watson JC, Stratakis CA, Bryant-Greenwood PK, et al. **Neurosurgical implications of Carney complex.** *J Neurosurg* 2000;92:413–18 CrossRef Medline
21. Jackson C, Linos K, Liu X. **Malignant melanotic nerve sheath tumor in pleural effusion: deceitful cytology with significant repercussions.** *Diagn Cytopathol* 2022;50:E76–80 CrossRef Medline
22. Shen XZ, Wang W, Luo ZY. **18F-FDG PET/CT imaging for aggressive melanotic schwannoma of the L3 spinal root: a case report.** *Medicine (Baltimore)* 2021;100:e24803 CrossRef Medline
23. Shui C, Davey L, Scholsem M. **Leptomeningeal dissemination of a malignant melanotic nerve sheath tumor: a case report and review of the literature.** *Surg Neurol Int* 2022;13:59 CrossRef Medline
24. Grebenc ML, Rosado de Christenson ML, Burke AP, et al. **Primary cardiac and pericardial neoplasms: radiologic-pathologic correlation.** *Radiographics* 2000;20:1073–1103; quiz 1110–11, 12 CrossRef Medline
25. Carney JA. **Psammomatous melanotic schwannoma: a distinctive, heritable tumor with special associations, including cardiac myxoma and the Cushing syndrome.** *Am J Surg Pathol* 1990;14:206–22 CrossRef Medline
26. Zhang HY, Yang GH, Chen HJ, et al. **Clinicopathological, immunohistochemical, and ultrastructural study of 13 cases of melanotic schwannoma.** *Chin Med J (Engl)* 2005;118:1451–61 Medline
27. Hall JC, Chang SD, Wilson TJ, et al. **Post-operative stereotactic radiosurgery of malignant melanotic schwannoma.** *Cureus* 2022;14:e22849 CrossRef Medline
28. Spina A, Gagliardi F, Boari N, et al. **Intracranial melanotic schwannomas.** *J Neurol Surg A Cent Eur Neurosurg* 2015;76:399–406 CrossRef Medline

Automated Detection of Cerebral Aneurysms on TOF-MRA Using a Deep Learning Approach: An External Validation Study

N.C. Lehen, R. Haase, F.C. Schmeel, H. Vatter, F. Dorn, A. Radbruch, and D. Paech



ABSTRACT

BACKGROUND AND PURPOSE: Cerebral aneurysms yield the risk of rupture, severe disability and death. Thus, early detection of cerebral aneurysms is crucial to ensure timely treatment, if necessary. AI-based software tools are expected to enhance radiologists' performance in detecting pathologies like cerebral aneurysms in the future. Our aim was to evaluate the diagnostic performance of an artificial intelligence-based software designed to detect intracranial aneurysms on TOF-MRA.

MATERIALS AND METHODS: One hundred ninety-one MR imaging data sets were analyzed using the software mbrain for the presence of intracranial aneurysms on TOF-MRA obtained using two 3T MR imaging scanners or a 1.5T MR imaging scanner according to our clinical standard protocol. The results were compared with the reading of an experienced radiologist as a criterion standard to measure the sensitivity, specificity, positive and negative predictive values, and accuracy of the software. Additionally, detection rates depending on size, morphology, and location of the aneurysms were evaluated.

RESULTS: Fifty-four aneurysms were detected by the expert reader. The overall sensitivity of the software for the detection of cerebral aneurysms was 72.6%, the specificity was 87.2%, and the accuracy was 82.6%. The positive predictive value was 67.9%, and the negative predictive value was 88.5%. We observed a sensitivity of 100% for saccular aneurysms of >5 mm without signs of thrombosis and low detection rates for fusiform or thrombosed aneurysms of 33.3% and 16.7%, respectively. Of 8 aneurysms that were not included in the initial written reports but were detected by the expert reader, retrospectively, 4 were detected by the software.

CONCLUSIONS: Our data suggest that the software can assist radiologists in reporting TOF-MRA. The software was highly reliable in detecting saccular aneurysms, while for fusiform or thrombosed aneurysms, further improvements are needed. Further studies are necessary to investigate the impact of the software on detection rates, interrater reliability, and reading times.

ABBREVIATION: AI = artificial intelligence

The prevalence of intracranial aneurysms has been estimated to be up to 2% of the population. They account for up to 85% of nontraumatic SAHs, potentially leading to severe disability and death.¹ MR imaging and CT have been shown to be reliable tools for the detection of intracranial aneurysms with accuracies of up to 90%.² Due to the workload of radiologists increasing during the past years,³ innovative tools are needed to reduce the radiologist's

workload while maintaining or even improving the quality of patient care.

There have been early attempts to introduce conventional computer-aided diagnosis for the detection of intracranial aneurysms with sensitivities of 80% and 95%, respectively, but with the need to accept high rates of false-positive findings.⁴ Computer-aided diagnosis without the use of modern machine learning algorithms has also been shown to improve the diagnostic performance of radiologists in terms of the detection of cerebral aneurysms by TOF-MRA.^{5,6} More recently, research has shifted toward more advanced technologies using deep learning algorithms that showed promising results in the detection of intracranial aneurysms using both CTA⁷⁻⁹ and TOF-MRA.¹⁰⁻¹⁶ In addition, it has been shown that the use of deep learning software solutions could increase the reader's performance in terms of the detection of aneurysms by TOF-MRA.¹⁷

Mbrain (mediaire) is a CE-marked, commercially available software solution that has been designed to assist radiologists when reporting MR imaging of the brain. The authors of the current

Received May 3, 2022; accepted after revision October 5.

From the Departments of Neuroradiology (N.C.L., R.H., F.C.S., F.D., A.R., D.P.) and Neurosurgery (H.V.), University Hospital Bonn, Rheinische Friedrich-Wilhelms-Universität Bonn, Bonn, Germany.

Mediaire GmbH provided technical details on the algorithm, including the training and validation process. The company had no influence on the conceptualization of the study or data acquisition or data interpretation.

Please address correspondence to Nils C. Lehen, MD, Department of Neuroradiology, University Hospital Bonn, Venusberg-Campus 1, 53127 Bonn, Germany; e-mail: nils.lehen@ukbonn.de; @PaechDC

Indicates article with online supplemental data.

<http://dx.doi.org/10.3174/ajnr.A7695>

study had an early version of an add-on to mdbrain designed to automatically detect intracranial aneurysms on TOF-MRA images at their disposal and performed an independent, external validation of its diagnostic performance. We hypothesized that the software can assist reading radiologists in the detection of intracranial aneurysms. Therefore, we created a diverse study sample with a large variety of aneurysm sizes, locations, and morphologies acquired on different clinical MR imaging scanners at 3T and 1.5T to test the diagnostic performance and the generalizability of the software.

MATERIALS AND METHODS

Institutional review board approval was obtained for this retrospective study, and the need for written informed consent was waived.

The data set consisted of a total of 209 MR imaging studies with TOF-MRA obtained between March 2018 and January 2022. Most studies were consecutive cases from our PACS system, but the data set was enriched with cases with known aneurysms. Eighteen imaging studies were excluded due to poor image quality deemed nondiagnostic by the expert reader or due to major competing pathologies, mainly major cerebral hemorrhage suspected of creating false-positive results.

The MR imaging studies included were retrospectively reviewed by an experienced radiologist (with 6 years of experience in interpreting MR imaging of the brain) for the presence, localization, size, and configuration of intracranial aneurysms under full consideration of the patients' clinical records, previous or subsequent imaging studies including DSA, and the respective written reports. For aneurysm size, the largest diameter of the aneurysm was measured using multiplanar reconstructions. This expert reading served as the diagnostic reference standard.

The images were obtained using either 2 clinical 3T MR imaging scanners (Achieva, Philips Healthcare; Discovery, GE Healthcare) or a 1.5T MR imaging scanner (Achieva). The patients were placed in the supine position. The axial 3D TOF sequences were acquired according to the routine clinical protocol used at our institution (TR = 19.33–20.12 ms; TE = 3.68–3.80 ms; section thickness = 1 mm; increment = 0.5 mm). FOV and matrix size were chosen according to the patient's characteristics by the radiology technician. The studies were anonymized and processed by the artificial intelligence (AI)-based software solution mdbrain, Version 4. Along with a reconstructed TOF sequence highlighting the detected aneurysms in color with a bounding box, quantitative reports were sent to the PACS system. Those reports displayed representative images highlighting the largest aneurysm detected and quantitative measures of the size of each detected aneurysm (volume in microliters and diameter in millimeters). The sensitivity and specificity of the software could not be adjusted by the authors.

The underlying segmentation algorithm is based on a 3D convolutional neural network with a U-NET architecture.¹⁸ The model was trained on >100 brain MR imaging data sets of both healthy subjects and subjects with saccular cerebral aneurysms, obtained on a variety of Philips scanners, at 1T, 1.5T, and 3T, respectively. For each subject, the data consisted of a TOF-MRA scan as well as a corresponding binary mask of the unruptured aneurysms, as segmented by an expert radiologist. The training data set contained a total of 93 saccular aneurysms; 4 (4.3%)

showed signs of partial thrombosis. The aneurysms were localized as follows: anterior communicating artery, 17%; A2 segment of the anterior cerebral artery, 10%; C6 segment of the ICA, 20%; C7 segment of the ICA, 22%; M1 or M2 segment of the MCA, 20%; and basilar artery, 9%. No fusiform aneurysms were included in the training process. Before training, all data were resampled to a fixed spacing before the intensity was normalized per image for zero mean and unit variance. During training of the neural network (using stochastic gradient descent), the input was provided in batches of patches, in which it was ensured that some patches contained aneurysm voxels and others did not. Augmentation was performed on the fly during training on the input patches to increase the generalization ability of the neural network. Mdbrain was purchased by the Department of Neuroradiology, University Hospital Bonn, at reduced cost. The authors had full control of the data and the information submitted for publication.

Statistical analyses were performed with R statistical and computing software, Version 4.0.3 (<http://www.r-project.org/>) and R Studio, Version 1.2.5033 (<http://rstudio.org/download/desktop>) using the caret package.¹⁹ The diagnostic performance of the AI software was compared with the radiologist's findings using confusion matrices. We calculated the overall sensitivity, specificity, positive predictive value, negative predictive value, and accuracy as well as for specific subgroups, like different aneurysm sizes, aneurysm localization (including extradural versus intradural in the anterior circulation), saccular and fusiform aneurysms, and aneurysms that showed signs of thrombosis or inhomogeneous signal intensity. The Mann-Whitney *U* test was used to determine statistical significance. Aneurysms that were detected by the radiologist and also by the software were defined as true-positive; those that were detected by the software but not by the radiologist were defined as false-positive. When there were no aneurysms reported by the software or the radiologist, the case was defined as true-negative. Each aneurysm that was missed by the software but detected by the radiologist was counted as a false-negative.

RESULTS

Our study sample consisted of 191 subjects with 54 aneurysms in total. One hundred nine (57.1%) subjects were women, and 82 patients were men. The mean age was 58.2 years (median, 62 years; range, 18–95 years). One hundred thirty-seven (71.7%) patients were scanned at 3T, 54 patients were scanned 1.5T. Forty-seven patients (24.6%) had at least 1 aneurysm by TOF-MRA, and 11 patients (5.8%) had >1 aneurysm. Twenty-eight (48.3%) aneurysms detected by the radiologist were angiographically proved. One aneurysm had a history of rupture with SAH. Fifty-one (94.4%) were saccular aneurysms, while the remaining 3 were classified as fusiform aneurysms. Six (11.1%) aneurysms showed signs of partial thrombosis. The mean largest diameter of the detected aneurysms was 7.3 mm (median, 4.1 mm; range, 1.2–45.4 mm).

In a subgroup analysis, we also analyzed the diameters of saccular aneurysms without any sign of thrombosis, with a mean largest diameter of 4.3 mm (median, 3.9 mm; range, 1.3–10 mm). Thirty-nine (72.2%) aneurysms were located in the anterior circulation, while the remaining 15 were located in the posterior circulation. Forty-six (85.2%) of the 54 aneurysms were correctly reported in

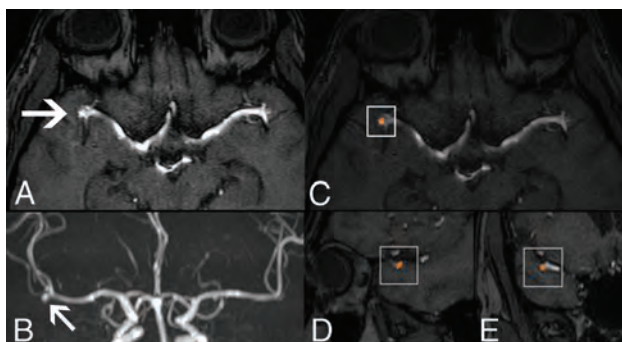


FIG 1. Right MCA aneurysm correctly detected by the software, cross-sectional (A) and MIP images (B). C–E, Axial, sagittal, and coronal view as reconstructed by the software, with the aneurysm highlighted in orange and with a surrounding white box.

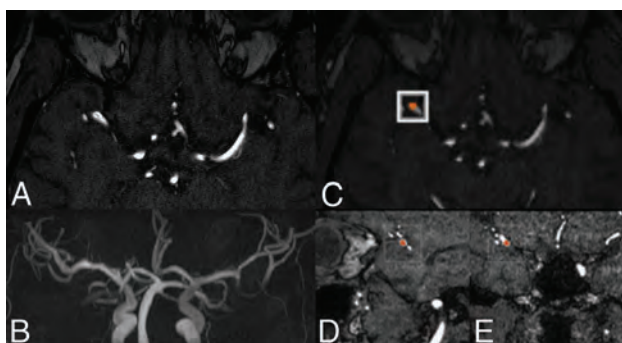


FIG 2. Right MCA bifurcation mistaken for an MCA aneurysm by the software. No aneurysm is shown by TOF-MRA, either by the cross-sectional image (A) or by MIP (B). C–E, Right MCA bifurcation highlighted in orange with a surrounding white box.

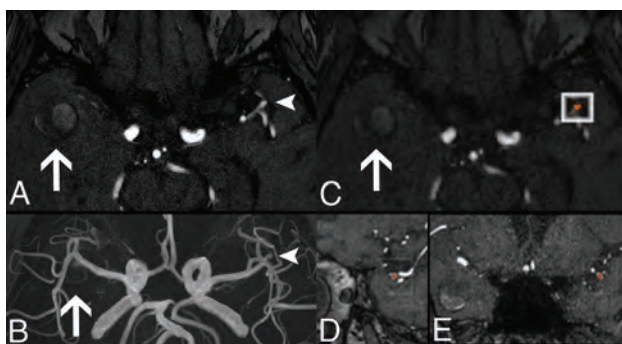


FIG 3. Large, thrombosed right MCA aneurysm (arrows) missed by the software and a small left MCA aneurysm (arrowheads) that was correctly detected by the software but missed in the initial read, probably due to satisfaction of search. A, Axial cross-sectional image of TOF-MRA. B, MIP image with the right MCA aneurysm barely visible and the left MCA aneurysm well visible. C–E, Axial, sagittal, and coronal reconstructions with the left MCA aneurysm being correctly highlighted in orange with a surrounding white box and the right MCA aneurysm not highlighted.

the initial written report, while the remaining 8 aneurysms were retrospectively found by the expert reader or were revealed by DSA and could be seen retrospectively on the initial MR imaging scan.

The cases finally included in our study could all be processed by the software. The overall diagnostic performance is summarized in the Online Supplemental Data. Examples of accurately and inaccurately reported findings are shown in Figs 1–3. The software detected a total of 56 aneurysms, of which 38 were true-positive findings; the remaining 18 were false-positive findings (0.1 false-positive/case). One hundred twenty-three studies were correctly classified as negative by the software, while 16 aneurysms found by the expert reader were missed by the software and declared false-negatives. The overall accuracy of the software was 82.6%, with a sensitivity of 70.4%, a specificity of 87.2%, a positive predictive value of 67.9%, and a negative predictive value of 88.5%. Three aneurysms were declared fusiform aneurysms by the expert reader, of which 2 (66.7%) were not detected by the software. In addition, 6 aneurysms showed signs of partial thrombosis, of which only 1 (16.7%) was correctly detected by the software, while the remaining 5 (83.3%) were not detected by the software. The remaining 11 aneurysms that were not detected by the software were saccular aneurysms with no signs of thrombosis. The mean largest diameter of the saccular aneurysms with no signs of thrombosis missed by the software was 2.2 mm (median, 2.3 mm; range, 1.3–4.3 mm).

There was a statistically significant difference between saccular aneurysms with no signs of thrombosis detected by the software and those that were not detected in terms of largest diameter ($P = .04$). Seven of the 11 aneurysms missed by the software were located at the C4 or C5 level of the ICA; the remaining aneurysms missed by the software were located at the anterior communicating artery ($n = 1$), posterior communicating artery ($n = 1$), basilar artery (basilar tip excluded, $n = 1$), and the superior cerebellar artery ($n = 1$). We observed that 50% of the aneurysms located at the ICA, levels C1–C4, were correctly diagnosed by the software. For supraophthalmic aneurysms in the anterior circulation, the sensitivity was 77.8%, with an accuracy of 85.7%. A detailed overview of the different localizations of the aneurysms and the detection rates of the algorithm is shown in the Table. For saccular aneurysms with diameters of ≥ 5 mm and no signs of thrombosis or inhomogeneous signal intensity, the sensitivity, specificity, and accuracy rose up to 100%, 87.2%, and 88.0%, respectively. Four of the 8 aneurysms initially missed in the original reports were correctly detected by the software.

DISCUSSION

This single-center study compared the diagnostic performance of an AI-based software trained on TOF-MRI studies to detect cerebral aneurysms with an expert radiologist's reading of 191 TOF-MRI studies.

Our goal was to test the software performance with a data set covering the variety seen in routine clinical care. In a patient cohort with a large range of ages, aneurysm sizes, configurations, and localizations examined with scanners of 2 different vendors at different field strengths, the software solution showed an overall accuracy of 82.6%, with a sensitivity and specificity of 70.4% and 87.2%, respectively. Our data suggest that the software can help the reading radiologist in detecting aneurysms when reporting TOF-MRI studies. Eight aneurysms found by the expert reader had not been reported in the initial, written reports. Four of these

Localizations of the aneurysms and the sensitivity of the software^a

Localization	No. (%)	Correctly Detected by CNN	%
Anterior circulation	39 (72.2%)	27	69.23%
C1–C4 (intraophthalmic)	12 (22.2%)	6	50.0%
Supraophthalmic	27 (50%)	21	77.8%
C5/6	7 (13.0%)	5	71.4%
ICA terminus	1 (1.9%)	1	100.0%
ACoMA	7 (13.0%)	6	85.7%
MCA	11 (20.4%)	8	72.7%
A1	1 (1.9%)	1	100.0%
Posterior circulation	15 (27.8%)	11	73.3%
Basilar tip	1 (1.9%)	1	100.0%
PCoMA	8 (14.8%)	7	87.5%
SCA	2 (3.7%)	1	50.0%
AICA	0 (0.0%)	0	NA
PICA	1 (1.9%)	1	100.0%
V4	1 (1.9%)	1	100.0%
Basilar artery	2 (3.7%)	0	0.0%

Note:—ACoMA indicates anterior communicating artery; PCoMA, posterior communicating artery; SCA, superior cerebellar artery; NA, not applicable; CNN, convolutional neural network.

^a The specificity of the algorithm was 87.2%. The term “basilar artery” indicates aneurysms of the basilar artery that do not arise from the basilar tip, the SCA, or the AICA. C5/6 includes ICA aneurysms that are located in the ICA segments C5 or C6. Aneurysms located at the ICA terminus or the origin of the PCoMA are listed separately.

aneurysms were correctly detected by the software and thus would not have been missed if the software had been used in the clinical practice.

Other investigators have already worked on software solutions to automatically detect aneurysms in TOF-MRI studies. Sichtermann et al¹³ achieved sensitivities as high as 90% with their convolutional neural network–based approach, but with 6.1 false-positives per case. When Sichtermann et al¹³ shifted toward more acceptable false-positive rates of 0.8 per case, the sensitivity decreased to 79%. Ueda et al¹¹ achieved sensitivities of 93% in their test data set, which was acquired at 4 different institutions, but they reported no specificity, only that their focus was not to miss aneurysms because their algorithm was intended to assist radiologists in not missing cerebral aneurysms. Stember et al¹² reported a sensitivity of 98.8% for the detection of cerebral aneurysms with only 1 of 86 aneurysms missed by their algorithm. However, they used only MIP images of TOF-MRA, while the aforementioned studies all used source images of 3D TOF-MRAs. In addition, they excluded aneurysms of <3 mm. Nakao et al¹⁰ reported a sensitivity of 94.2%, but with a high false-positive rate of 2.9 per case. At a sensitivity of 70%, they reported 0.26 false-positives per case. Like Stember et al, they used MIP images of TOF-MRAs for training, validation, and testing of their algorithm. Terasaki et al¹⁴ achieved a sensitivity of up to 89.1% with a rate of 4.2 false-positives per case. Chen et al¹⁵ reported a sensitivity of 82.1% with a false-positive rate of 0.86 per case. Claux et al¹⁶ reported a sensitivity of 78% with a rate of 0.5 false-positives per case.

While the sensitivities we report seem relatively lower compared with the aforementioned studies, there are some differences: First, we performed an external validation, a crucial step in the validation process of algorithms designed to assist radiologists in avoiding overfitting to the test data set and to prove the generalizability of the software solution.²⁰ Our data set was acquired on 3 different clinical scanners at an entirely different institution than the one where the data set was used to train, validate, and test the

software solution we report. In contrast, the aforementioned studies all reported the diagnostic performance of their algorithms on their test data sets that were acquired at the same institutions as the data sets used for training and validation, though Ueda et al¹¹ and Terasaki et al¹⁴ tried to avoid overfitting by using images from 4 different institutions. To the best of our knowledge, there have been no studies published on the diagnostic performance of other commercially available AI-tools addressing the automated detection of brain aneurysms by TOF-MRA that we could use to compare our results.

Second, we included not only MR imaging studies with aneurysms in our data set but also a high number of studies with negative findings showing no aneurysms, trying to get a more realistic collective to learn how far the algorithm

is able to reliably rule out the presence of aneurysms in studies that have been read as having normal findings by the expert reader. However, our data set still does not reflect reality because we enriched the collective with patients who had aneurysms, allowing us to further investigate different localizations, sizes, and configurations of the aneurysms detected. Third, the studies mentioned above reported high sensitivities but, in the case of Nakao et al¹⁰ and Sichtermann et al¹³, also a high rate of false-positive findings, with the sensitivities decreasing to 79% and 70%, respectively,^{10,13} when reducing the rate of false-positives, values that are comparable with our findings because we found a rate of only 0.1 false-positive finding per case. Because AI software solutions like mdbrain will likely not only be used on high-risk populations but will also be available for every examination acquired with no regard for the risk constellation, we regard a low rate of false-positive findings as highly important, mainly to reduce the risk of unnecessary follow-up examinations but also to actually reduce the workload of the radiologists using the software. Fourth, 2 of the studies used MIP images instead of source images of 3D TOF-MRA; thus, the comparability with our study is limited.

In a second step, we further evaluated different subgroups of aneurysms to further investigate the performance of the software. Most interesting, fusiform aneurysms were detected in only 1 of 3 cases, probably because the software has been trained only on saccular aneurysms and the current version is not recommended for use on fusiform aneurysms. Also, aneurysms that showed signs of thrombosis or inhomogeneous signal intensity by TOF-MRA were detected in only 1 of 6 cases, a phenomenon that has similarly been reported by Ueda et al.¹¹ We suspect that the low detection rate in this subgroup is due to the inhomogeneous signal within the aneurysms, making it more difficult for the algorithm to correctly segment the vessel and the aneurysm to their full extent. Also, the training data set contained only 4 cases of aneurysms with signs of partial thrombosis. Our findings may motivate further optimization of AI-based aneurysm detection for such cases.

While 5 aneurysms that were missed by the algorithm were either fusiform, thrombosed, or both, the remaining 11 aneurysms that were missed by the software were saccular aneurysms with regular signal intensity. Their mean diameter was 2.2 mm, compared with an overall mean diameter of 7.3 mm, with a statistically significant difference for aneurysm size in saccular aneurysms with no signs of thrombosis, so we may conclude that besides fusiform or thrombosed aneurysms, small aneurysms cannot be reliably excluded using the software. Here, one must also take into account that even an experienced reader can misinterpret infundibular artery origins or inhomogeneous flow signal as small aneurysms when no DSA data are available. In contrast, no saccular aneurysms with diameters of ≥ 5 mm with no signs of thrombosis were missed by the software, highlighting its potential use for clinically relevant findings that should not be missed.

As a third step, we investigated the diagnostic performance depending on the location of the aneurysms. Due to the low number of cases, we can only describe our findings: For infraophthalmic aneurysms in the anterior circulation, we found a sensitivity of only 50%. We hypothesize that the curvature of the vessel as well as the inhomogeneous signal intensity that can be observed in these regions account for this low detection rate. Also, there were no infraophthalmic ICA aneurysms included in the training data set, very likely leading to this comparably poor result. For supraophthalmic aneurysms in the anterior circulation, we found a higher sensitivity of 77.8% for this clinically more relevant subgroup because supraophthalmic aneurysms are at risk of causing SAH, while infraophthalmic aneurysms are not due to their extradural localization.²¹

Our study had some limitations. First, its retrospective nature, all MR imaging studies being acquired at the same institution, both the training data set and most of our MR imaging studies being acquired on MR imaging scanners of the same vendor, and our study sample being enriched with known aneurysms limit the possibility of evaluating the use of the algorithm in the setting of everyday clinical practice. However, it can serve as an external validation of the software solution because our data set was not acquired at the same institution as the data sets used for training, validation, and testing. Furthermore, our images were acquired on 3 different scanners by 2 different vendors, at field strengths of 3T and 1.5T, making them a heterogeneous study sample, representing the variety of examinations seen in our daily clinical routine. However, additional studies may be necessary to investigate how the software performs on images obtained on MR imaging scanners of different vendors.

Second, the number of cases is too small to draw final conclusions on differences depending on aneurysm locations; thus, our findings are of rather descriptive nature regarding location. Third, the software was not designed to replace the radiologist but to support radiologists in detecting aneurysms; our study investigated the diagnostic performance of the software alone against an experienced human reader. Sohn et al¹⁷ reported the improved diagnostic performance of a neurologist, a neurosurgeon, and a radiologist for the detection of cerebral aneurysms by TOF-MRA when supported by an AI software solution compared with their diagnostic performance without the support of the software. While we suspect that mbrain can have a similar effect on the

performance of readers, this was not systematically assessed in our study, and whether the software can assist radiologists in their daily work will be a matter of further investigation.

CONCLUSIONS

In our study, we assessed the potential of a commercially available and CE-marked software solution to automatically detect intracranial aneurysms on TOF-MRI data. Thus, our findings are important to radiologists using the software, to understand its capabilities but also its limitations. We demonstrated that the software has the potential to increase the detection rates for intracranial aneurysms while showing an acceptable rate of false-positive findings. There is need for further investigation to learn whether the software can assist radiologists in their daily routine to improve detection rates, interrater reliability, and reading times.

Disclosure forms provided by the authors are available with the full text and PDF of this article at www.ajnr.org.

REFERENCES

1. Brown RD, Broderick JP. **Unruptured intracranial aneurysms: epidemiology, natural history, management options, and familial screening.** *Lancet Neurol* 2014;13:393–404 CrossRef Medline
2. White PM, Wardlaw JM, Easton V. **Can noninvasive imaging accurately depict intracranial aneurysms? A systematic review.** *Radiology* 2000;217:361–70 CrossRef Medline
3. McDonald RJ, Schwartz KM, Eckel LJ, et al. **The effects of changes in utilization and technological advancements of cross-sectional imaging on radiologist workload.** *Acad Radiol* 2015;22:1191–98 CrossRef Medline
4. Yang X, Blezek DJ, Cheng LTE, et al. **Computer-aided detection of intracranial aneurysms in MR angiography.** *J Digit Imaging* 2011;24:86–95 CrossRef Medline
5. Hirai T, Korogi Y, Arimura H, et al. **Intracranial aneurysms at MR angiography: effect of computer-aided diagnosis on radiologists' detection performance.** *Radiology* 2005;237:605–10 CrossRef Medline
6. Štěpán-Buksakowska IL, Accurso JM, Diehn FE, et al. **Computer-aided diagnosis improves detection of small intracranial aneurysms on MRA in a clinical setting.** *AJNR Am J Neuroradiol* 2014;35:1897–902 CrossRef Medline
7. Yang J, Xie M, Hu C, et al. **Deep learning for detecting cerebral aneurysms with CT angiography.** *Radiology* 2021;298:155–63 CrossRef Medline
8. Park A, Chute C, Rajpurkar P, et al. **Deep learning-assisted diagnosis of cerebral aneurysms using the HeadXNet Model.** *JAMA Netw Open* 2019;2:e195600 CrossRef Medline
9. Shahzad R, Pennig L, Goertz L, et al. **Fully automated detection and segmentation of intracranial aneurysms in subarachnoid hemorrhage on CTA using deep learning.** *Sci Rep* 2020;10:21799 CrossRef Medline
10. Nakao T, Hanaoka S, Nomura Y, et al. **Deep neural network-based computer-assisted detection of cerebral aneurysms in MR angiography.** *J Magn Reson Imaging* 2018;47:948–53 CrossRef Medline
11. Ueda D, Yamamoto A, Nishimori M, et al. **Deep learning for MR angiography: automated detection of cerebral aneurysms.** *Radiology* 2019;290:187–94 CrossRef Medline
12. Stember JN, Chang P, Stember DM, et al. **Convolutional neural networks for the detection and measurement of cerebral aneurysms on magnetic resonance angiography.** *J Digit Imaging* 2019;32:808–15 CrossRef Medline
13. Sichtermann T, Faron A, Sijben R, et al. **Deep learning-based detection of intracranial aneurysms in 3D TOF-MRA.** *AJNR Am J Neuroradiol* 2019;40:25–32 CrossRef Medline

14. Terasaki Y, Yokota H, Tashiro K, et al. **Multidimensional deep learning reduces false-positives in the automated detection of cerebral aneurysms on time-of-flight magnetic resonance angiography: a multi-center study.** *Front Neurol* 2021;12:742126. CrossRef Medline
15. Chen G, Wei X, Lei H, et al. **Automated computer-assisted detection system for cerebral aneurysms in time-of-flight magnetic resonance angiography using fully convolutional network.** *Biomed Eng Online* 2020;19:38 CrossRef Medline
16. Claux F, Baudouin M, Bogey C, et al. **Dense, deep learning-based intracranial aneurysm detection on TOF MRI using two-stage regularized U-Net.** *J Neuroradiol* 2022 Mar 27. [Epub ahead of print] CrossRef Medline
17. Sohn B, Park KY, Choi J, et al. **Deep learning-based software improves clinicians' detection sensitivity of aneurysms on brain TOF-MRA.** *AJNR Am J Neuroradiol* 2021;42:1769–75 CrossRef Medline
18. Çiçek Ö, Abdulkadir A, Lienkamp SS, et al. **3D U-Net: Learning Dense Volumetric Segmentation from Sparse Annotation.** 2016. <https://arxiv.org/pdf/1606.06650>. Accessed April 4, 2022
19. Kuhn M. **Building predictive models in R using the caret package.** *Journal of Statistical Software* 2008;28:1–26 CrossRef
20. Park SH, Han K. **Methodologic guide for evaluating clinical performance and effect of artificial intelligence technology for medical diagnosis and prediction.** *Radiology* 2018;286:800–09 CrossRef Medline
21. Kupersmith MJ, Hurst R, Berenstein A, et al. **The benign course of cavernous carotid artery aneurysms.** *J Neurosurg* 1992;77:690–93 CrossRef Medline

Effects of Arterial Stiffness on Cerebral WM Integrity in Older Adults: A Neurite Orientation Dispersion and Density Imaging and Magnetization Transfer Saturation Imaging Study

J. Kikuta, K. Kamagata, M. Abe, C. Andica, Y. Saito, K. Takabayashi, W. Uchida, H. Naito, H. Tabata, A. Wada, Y. Tamura, R. Kawamori, H. Watada, and S. Aoki



ABSTRACT

BACKGROUND AND PURPOSE: Arterial stiffness is reported to be able to cause axonal demyelination or degeneration. The present study aimed to use advanced MR imaging techniques to examine the effect of arterial stiffness on the WM microstructure among older adults.

MATERIALS AND METHODS: Arterial stiffness was measured using the cardio-ankle vascular elasticity index (CAVI). The high-CAVI (mean CAVI ≥ 9 points) and the low-CAVI groups (mean CAVI < 9 points) were created. The neuronal fiber integrity of the WM was evaluated by neurite orientation dispersion and density imaging and magnetization transfer saturation imaging. Tract-Based Spatial Statistics and the tracts-of-interest analysis were performed. Specific WM regions (corpus callosum, internal capsule, anterior thalamic radiation, corona radiata, superior longitudinal fasciculus, forceps minor, and inferior fronto-occipital fasciculus) were selected in the tracts-of-interest analysis.

RESULTS: In Tract-Based Spatial Statistics, the high-CAVI group showed a significantly lower myelin volume fraction value in the broad WM and significantly higher radial diffusivity and isotropic volume fraction values in the corpus callosum, forceps minor, inferior fronto-occipital fasciculus, internal capsule, corona radiata, and anterior thalamic radiation than the low-CAVI group. In tracts-of-interest analysis using multivariate linear regression, significant associations were found between the mean CAVI and radial diffusivity in the anterior thalamic radiation and the corona radiata; isotropic volume fraction in the anterior thalamic radiation and the corona radiata; and myelin volume fraction in the superior longitudinal fasciculus ($P < .05$). Additionally, partial correlation coefficients were observed for the significant associations of executive function with radial diffusivity and myelin volume fraction ($P < .05$).

CONCLUSIONS: Arterial stiffness could be associated with demyelination rather than axonal degeneration.

ABBREVIATIONS: ATR = anterior thalamic radiation; CAVI = cardio-ankle vascular elasticity index; CC = corpus callosum; CR = corona radiata; FA = fractional anisotropy; FMI = forceps minor; IC = internal capsule; IFOF = inferior fronto-occipital fasciculus; ISOVF = isotropic volume fraction; NODDI = neurite orientation dispersion and density imaging; MT = magnetization transfer; MVF = myelin volume fraction; RD = radial diffusivity; SLF = superior longitudinal fasciculus; TBSS = Tract-Based Spatial Statistics; TMT = Trail-Making Test; TOI = tracts of interest

Arterial stiffness can be measured by several different methods. The pulse wave velocity has been measured by various methods

as an indirect index of arterial elasticity, but it is blood pressure-dependent.¹ Conversely, the cardio-ankle vascular elasticity index (CAVI) directly reflects vascular elasticity and is blood pressure-independent.² Reports regarding the association between CAVI-measured arterial stiffness and WM microstructure have still not been published, though some studies reported the association between pulse wave velocity-measured arterial stiffness and brain WM integrity.

Neurite orientation dispersion and density imaging (NODDI) is a new, advanced DWI technique that improves WM characterization using a multicompartiment model to describe different WM functions. By enabling the estimation of neurite structure, NODDI can provide more specific insight into the underlying WM microstructural changes.³ Thus, NODDI could be useful in assessing arterial stiffness-associated WM microstructure, though no study has tested

Received July 12, 2022; accepted after revision October 15.

From the Departments of Radiology (J.K., K.K., M.A., C.A., Y.S., K.T., W.U., A.W., S.A.), Metabolism and Endocrinology (H.N., Y.T., R.K., H.W.), and Sportology Center (H.T., Y.T., R.K., H.W.), Juntendo University Graduate School of Medicine, Tokyo, Japan; and Faculty of Health Data Science (C.A.), Juntendo University, Chiba, Japan.

J. Kikuta and K. Kamagata contributed equally to this work.

This work is supported by the Strategic Research Foundation at Private Universities (S1411006) and KAKENHI (18H03184, 18H02772, and 20K16737) from the Ministry of Education, Culture, Sports, Science and Technology of Japan.

Please address correspondence to Junko Kikuta, MD, PhD, Department of Radiology, Juntendo University Graduate School of Medicine, 2-1-1 Hongo, Bunkyo-ku, Tokyo 113-8421, Japan; e-mail: j.kikuta.hy@juntendo.ac.jp

Indicates open access to non-subscribers at www.ajnr.org

<http://dx.doi.org/10.3174/ajnr.A7709>

Table 1: Demographic characteristics of the participants^a

	All Participants (<i>n</i> = 110)	High-CAVI (<i>n</i> = 60)	Low-CAVI (<i>n</i> = 50)	High- vs Low-CAVI (<i>P</i> Value)
Sex (men/female)	66:44	37:23	29:21	.70
Age (yr)	72.65 (SD, 4.90)	72.72 (SD, 5.00)	72.58 (SD, 4.82)	.96
Mean CAVI	9.12 (SD, 0.84)	9.71 (SD, 0.57)	8.41 (SD, 0.46)	<.001
Antihypertensive therapy	71	43	28	.09
Education (yr)	14.31 (SD, 2.11)	14.30 (SD, 2.09)	14.32 (SD, 2.15)	.96
Body mass index	22.54 (SD, 2.84)	22.79 (SD, 2.54)	22.24 (SD, 3.16)	.31
Systolic blood pressure	137.47 (SD, 15.67)	139.60 (SD, 15.21)	134.92 (SD, 16.00)	.12
Diastolic blood pressure	86.05 (SD, 9.35)	86.52 (SD, 8.49)	85.48 (SD, 10.34)	.56
Heart rate	65.70 (SD, 23.73)	66.16 (SD, 33.88)	65.31 (SD, 9.85)	.85
Montreal Cognitive Assessment (Japanese version)	25.19 (SD, 2.87)	25.31 (SD, 2.95)	25.04 (SD, 2.66)	.61
Mini-Mental State Examination	27.93 (SD, 1.68)	28.07 (SD, 1.59)	27.76 (SD, 1.78)	.34
TMT A	42.51 (SD, 13.90)	43.32 (SD, 14.24)	41.54 (SD, 13.56)	.51
TMT B	115.82 (SD, 50.38)	116.78 (SD, 40.22)	114.66 (SD, 60.80)	.83
TMT B minus A	73.31 (SD, 44.11)	73.47 (SD, 36.01)	73.12 (SD, 52.60)	.97
Periventricular hyperintensity	1.14 (SD, 0.39)	1.17 (SD, 0.42)	1.10 (SD, 0.36)	.372
Deep and subcortical WM hyperintensity	1.25 (SD, 0.53)	1.31 (SD, 0.60)	1.18 (SD, 0.48)	.135

^a Data are means.

this hypothesis. Moreover, myelin-sensitive imaging using MR imaging can evaluate the WM microstructure from a different viewpoint from DWI.

Arterial stiffness is indicated to cause axonal demyelination or degeneration.^{4,5} Notably, Badji et al⁶ showed that carotid-femoral pulse wave velocity is significantly associated with both fractional anisotropy (FA) and radial diffusivity (RD) but not with the myelin volume fraction (MVF). The results suggested that arterial stiffness is associated with axonal degeneration rather than with demyelination. However, reports supporting such results are still limited. We hypothesized that the impact of arterial stiffness on the brain WM microstructure could be better understood by using the above-mentioned multimodal WM-sensitive MR imaging techniques. Hence, this study aimed to explore the associations between CAVI-measured arterial stiffness and WM-sensitive MR imaging measures of the brain in older adults.

MATERIALS AND METHODS

The institutional review board of Juntendo University Hospital in Japan approved this study in compliance with the World Medical Association's Code of Ethics (Declaration of Helsinki) for experiments involving humans.

Study Participants

The Bunkyo Health Study is a prospective cohort study of 1629 older individuals.⁷ Of these, 160 participants underwent both FLAIR imaging and DWI. Exclusion criteria included major psychiatric or neurologic disorders, heart failure, stroke, and/or a history of alcohol or drug abuse. Ultimately, 110 older participants were included for the analysis. Arteriosclerosis was estimated by CAVI determined by using an automatic waveform analyzer (Vascular Screening System VaSera VS1500; Fukuda Denshi).⁸ High CAVI (≥ 9.0) implies progression of carotid and coronary arteriosclerosis;⁹ thus, CAVI 9 was set as the cutoff value. The eligible participants were divided into the high-CAVI group (those with a mean [average of left and right values] CAVI of ≥ 9 points; 37 men and 23 women; mean age, 72.72 [SD, 5.00] years) and the

low-CAVI group (those with a mean CAVI of < 9 points; 29 men and 21 women; mean age, 72.58 [SD, 4.82] years). Table 1 shows the demographic characteristics. Deep and subcortical WM hyperintensity and periventricular hyperintensity were evaluated using the Fazekas scale,¹⁰ according to axial FLAIR imaging.

Image Acquisition

MR imaging data were acquired using a 3T MR imaging scanner (Magnetom Prisma; Siemens) with a 64-channel head coil. We acquired multishell DWI data using a spin-echo echo-planar imaging sequence, which included 2 b-values of 1000 and 2000 s/mm² along 64 isotropic diffusion gradients uniformly distributed on a sphere, with a simultaneous multisection echo-planar imaging sequence in the anterior-posterior phase-encoding direction with the following parameters: TR = 3300 ms; TE = 70 ms; FOV = 229 × 229 mm; matrix size = 130 × 130; section thickness = 1.8 mm; resolution = 1.8 × 1.8 mm; acquisition time = 7 minutes and 29 seconds. DWI acquisition was completed with a *b* = 0 image. Standard and antiphase-encoded blipping images were acquired without diffusion weighting to compensate for the distortion caused by the magnetic susceptibility associated with the echo-planar imaging acquisition. The predominant T1-weighted, proton density-weighted, and magnetization transfer (MT)-weighted images were obtained using a 3D multiecho high-speed low-angle shot sequence for calculating the MT saturation index.¹¹ The settings for the MT saturation sequences were as follows: for MT_{off} and MT_{on} scanning, TE = 2.53 ms, TR = 24 ms, flip angle = 5°; for T1WI, TE = 2.53 ms, TR = 10 ms, flip angle = 13°, with parallel imaging using generalized autocalibrating partially parallel acquisition with a factor of 2 in the phase-encoding direction, 7/8 partial Fourier acquisition in the partition direction, bandwidth = 260 Hz/pixel, matrix = 128 × 128, acquisition time = 6 minutes 25 seconds, section thickness = 1.8 mm, FOV = 224 × 224 mm.

Diffusion MR Imaging Processing

For eliminating artifacts, the eddy (<https://fsl.fmrib.ox.ac.uk/fsl/fslwiki/eddy/UsersGuide>) and topup (<https://fsl.fmrib.ox.ac.uk/>

Table 2: Summary of WM metrics

Diffusion MR Imaging	Parameter	Explanation
DTI	FA	Overall direction of water diffusion in brain tissue
	Mean diffusivity	The magnitude of isotropic diffusion in brain tissue
	Axial diffusivity	The coefficient of diffusion across the long axis of the ellipsoid
	RD	The coefficient of diffusion perpendicular to the long axis
NODDI	Intracellular volume fraction	Neurite density based on intracellular diffusion
	Orientation dispersion index	Dispersion of neurites in the intracellular compartment
	ISOVF	The measure of extracellular water diffusion

fsl/fslwiki/topup) toolboxes, which are part of the FSL (www.fmrib.ox.ac.uk/fsl), were used.¹² The resulting images were fitted to the NODDI model³ using the NODDI Matlab Toolbox 5 (http://www.nitrc.org/projects/noddi_toolbox). Table 2 summarizes the parameters of DTI and NODDI. The maps of the orientation dispersion index, isotropic volume fraction (ISOVF), and intracellular volume fraction were generated using the Accelerated Microstructure Imaging via Convex Optimization.¹³ Furthermore, the DTIFit tool (<https://open.win.ox.ac.uk/pages/fsl/fslpy/fsl.data.dtfits.html>) was used to generate tensor-derived maps according to the ordinary least-squares method¹⁴ using DWI data with b-values of 0 and 1000 s/mm².

Myelin-Sensitive Imaging Processing

MT saturation (MT_{sat}) data were analyzed using a Matlab script (<https://www.mathworks.com/help/matlab/ref/run.html>).¹⁵ First, the apparent longitudinal relaxation rate (R_{1app}) was calculated as the following equation:

$$R_{1app} = \frac{1}{2} \frac{S_{T1} \alpha_{T1} / TR_{T1} - S_{PD} \alpha_{PD} / TR_{PD}}{S_{PD} / \alpha_{PD} - S_{T1} / \alpha_{T1}}.$$

Here, S_{T1} and S_{PD} indicate the signal strength of T1- and proton-density (PD)-weighted imaging, respectively. TR_{T1} and TR_{PD} reflect the TRs of T1- and PD-weighted imaging, respectively. α_{T1} and α_{PD} show the excitation flip angles of T1- and PD-weighted imaging. Second, the apparent signal amplitude (A_{app}) was calculated as the following:

$$A_{app} = S_{PD} S_{T1} \frac{TR_{PD} \alpha_{T1} / \alpha_{PD} - TR_{T1} \alpha_{PD} / \alpha_{T1}}{S_{T1} TR_{T1} - S_{PD} TR_{PD}}.$$

Third, the apparent δ_{app} was calculated as the following equation:

$$\delta_{app} = (A_{app} \alpha_{MT} / S_{MT} - 1) R_{1app} TR_{MT} - \alpha_{MT} 2/2.$$

TR_{MT} , S_{MT} , and α_{MT} show the TR, signal intensity, and excitation flip angle of the MT-weighted imaging respectively. The following formula was applied to fix the small residual high-order dependency of MT_{sat} on the local radiofrequency (RF) transmit field:¹⁶

$$MT_{sat} = \frac{\delta_{app}(1 - 0.4)}{1 - 0.4 RF_{local}}.$$

RF_{local} was calculated using the dual-angle method.¹⁷ In addition, we added 2 B₁ maps with flip angles of 10° and 20°, respectively, obtained by echo-planar imaging in about 10 seconds. The first and second images were obtained after excitation with flip angles α and

2α proportional to $\sin\alpha$ and $\sin 2\alpha$, respectively. The ratio of the 2 acquisitions was calculated using the following formula:

$$\frac{\sin\alpha}{\sin 2\alpha} = \frac{1}{2\cos\alpha}.$$

From there, the local flip angle α was calculated.

Tract-Based Spatial Statistics Analysis

Voxelwise statistical analysis was performed using Tract-Based Spatial Statistics (TBSS; <http://fsl.fmrib.ox.ac.uk/fsl/fslwiki/TBSS>) implemented in FSL.¹⁸ The TBSS procedure was as follows: First, using FMRIB's Nonlinear Registration Tool (FNIRT; <http://fsl.fmrib.ox.ac.uk/fsl/fslwiki/FNIRT>), we aligned the FA maps of all participants into the Montreal Neurological Institute 152 standard space with $1 \times 1 \times 1$ mm³ voxel size. Second, we created and thinned a population-based mean FA image to establish the mean FA skeleton, which shows the centers of all tracts common to the group. The threshold of the mean FA skeleton was 0.2 to exclude the peripheral tracts and GM. Third, a binary mask of the FA skeletonized image was used as the mask image to make a voxel-by-voxel statistical comparison between the high- and low-CAVI groups of the 4D skeleton image file. This comparison was performed using FSL's Randomise tool (<http://fsl.fmrib.ox.ac.uk/fsl/fslwiki/Randomise/UserGuide>), and the number of permutations was set to 10,000. The data for other WM metrics was analyzed using the tbss_non_FA script (https://fsl.fmrib.ox.ac.uk/fsl/fslwiki/TBSS/UserGuide#Using_non-FA_Images_in_TBSS) to generate a 4D skeleton image file for each metric.

Tract-of-Interest Analysis

Tracts of interest (TOI) were analyzed using the ICBM DTI-81 Atlas (http://www.bmap.ucla.edu/portfolio/atlas/ICBM_DTI-81_Atlas/).¹⁹ According to the TBSS results (Figure) and previous studies showing arterial stiffness-associated WM regions, 6 major WM tracts, namely, the corpus callosum (CC), internal capsule (IC), corona radiata (CR), inferior fronto-occipital fasciculus (IFOF), forceps minor (FMi), and anterior thalamic radiation (ATR), were identified as TOI of RD and ISOVF. Additionally, 7 major WM tracts, namely, the CC, IC, CR, IFOF, FMi, ATR, and superior longitudinal fasciculus (SLF), were selected as TOI of the MVF. These WM regions are reportedly vulnerable to increased arterial stiffness.^{4,5,20,21} Then, the mean value (the average of left and right values) within each ROI was computed for each WM metric.

Statistical Analysis

All statistical data were analyzed using SPSS Statistics, Version 27 (IBM). Demographic and clinical data were analyzed using the

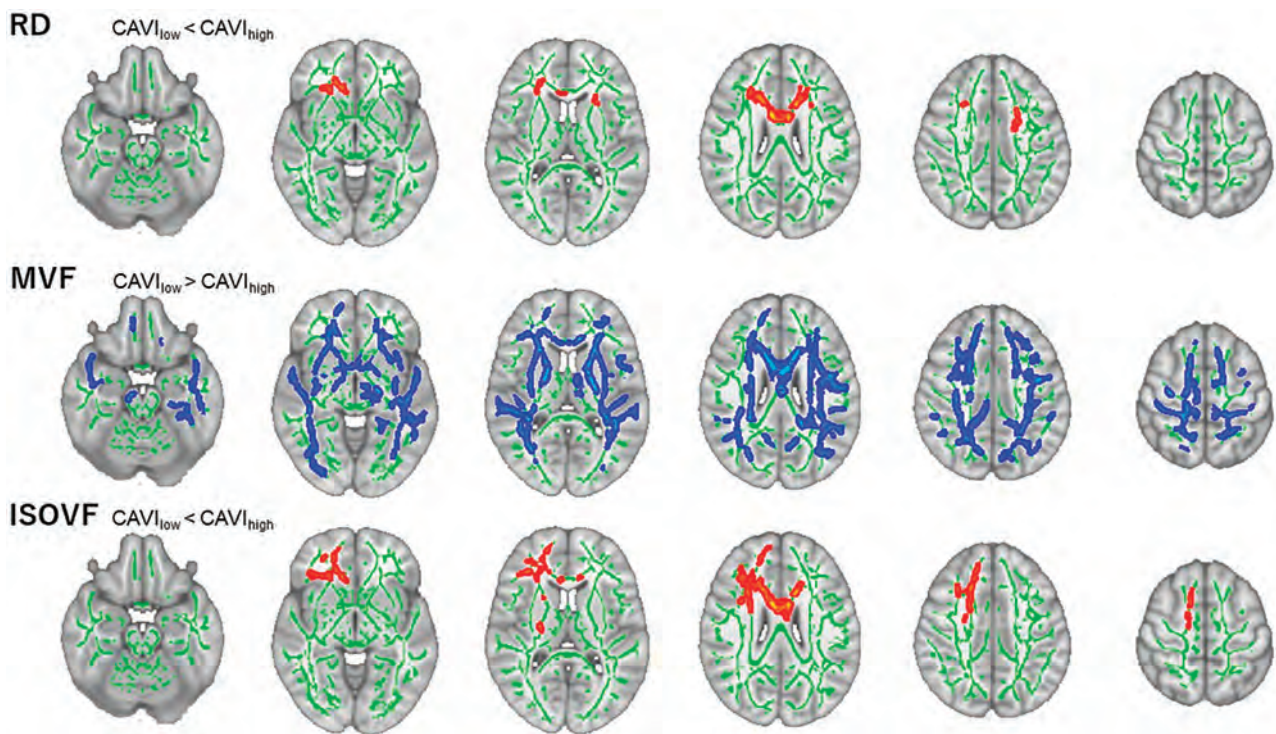


FIGURE. Comparison between the high- and low-CAVI groups. For TBSS, the low- and high-CAVI groups were compared (family-wise error-corrected $P < .05$, adjusting for age, sex, antihypertensive therapy use, intracranial volume, and systolic blood pressure). Red-yellow voxels demonstrate significantly higher RD and ISOVF values in the high-CAVI group than in the low-CAVI group. Blue-light blue voxels illustrate a significantly lower MVF value in the high-CAVI group than in the low-CAVI group.

χ^2 or Mann-Whitney U test. A P value (2-tailed) $< .05$ was considered statistically significant.

For TBSS, the high- and low-CAVI groups were compared using the Randomize tool (family-wise error-corrected $P < .05$, adjusting for age, sex, antihypertensive therapy use, systolic blood pressure, and intracranial volume).

In all participants, we applied univariate linear regression analyses for each WM metric as a dependent variable and the mean CAVI as an independent variable. Subsequently, multivariate linear regression analyses were conducted using backward linear regression to identify independent factors associated with the mean CAVI. The variable $P < .2$ in the univariate model was included in the back-removal procedure with P -removal = .1. Age, sex, antihypertensive therapy, systolic blood pressure, and intracranial volume were considered confounding covariates to separate from the strength of the relation between the mean CAVI and WM integrity.

Additionally, the partial correlation analyses between each WM metric and the cognitive performance scores were examined separately for all participants, the high-CAVI group, and the low-CAVI group, adjusting for age, sex, and education level. Multiple comparisons were corrected using the false discovery rate procedure for each WM metric and region.²² The false discovery rate-corrected $P < .05$ was considered significant.

RESULTS

Participant Characteristics

Table 1 shows all participant characteristics. The high-CAVI group showed a significantly higher mean CAVI than the low-

CAVI group. However, age, sex, education level, body mass index, heart rate, systolic blood pressure, diastolic blood pressure, and antihypertensive therapy history; the Mini-Mental State Examination; the Montreal Cognitive Assessment (Japanese version); Trail Making Test (TMT) A, TMT B, TMT B minus A; deep and subcortical WM hyperintensity; and periventricular hyperintensity were not significantly different between the 2 groups.

Whole-Brain Analysis

TBSS results identified a significantly lower MVF in the high-CAVI group than in the low-CAVI group in the broad WM area (family-wise error-corrected $P < .05$; Figure). RD was significantly higher in the high-CAVI group in specific WM areas such as the CC, FMi, bilateral IFOF, bilateral ATR, bilateral CR, and left IC compared with the low-CAVI group. The ISOVF was significantly higher in the high-CAVI group than in the low-CAVI group in the CC, FMi, right IC, right CR, right ATR, and right IFOF. Most interesting, RD and ISOVF changes were relatively overlapped, mainly observed in the anterior area. Whereas FA, mean diffusivity, axial diffusivity, the orientation dispersion index, and intracellular volume fraction did not significantly differ between 2 groups.

Tract-Specific Analysis

The univariate linear regression analysis revealed the significant associations of the mean CAVI with RD in the FMi; ISOVF in the CC, CR, and FMi; and MVF in the CR, IC, FMi, IFOF, ATR, and SLF (false discovery rate-corrected $P < .05$; Table 3). In the multivariate linear regression analyses adjusted for age, sex,

Table 3: Univariate and multivariate linear regression analyses adjusted for age, sex, antihypertensive therapy, systolic blood pressure, and intracranial volume for the association of mean CAVI with WM metrics in specific regions

	Univariate Linear Regression		Multivariate Linear Regression	
	P	β	P	β
RD				
ATR	.121	0.149	.015	1.549
CC	.075	0.171		
CR	.079	0.168	.004	−0.737
FMI	.01	0.245	.061	0.296
IC	.279	0.104		
IFOF	.163	0.134		
ISOVF				
ATR	.16	0.135	.014	−1.531
CC	.036	0.2		
CR	.031	0.206	.005	0.596
FMI	.037	0.2		
IC	.271	0.106		
IFOF	.123	0.148		
MVF				
ATR	.005	−0.265		
CC	.174	−0.13		
CR	.015	−0.231		
FMI	.028	−0.21		
IC	.009	−0.249		
IFOF	.019	−0.224		
SLF	.015	−0.231	.036	−0.218

Table 4: Partial correlation coefficients between WM metrics and TMT B, adjusted for age, sex, and education^a

	All Participants		High-CAVI Group		Low-CAVI Group	
	Corrected P Value	r	Corrected P Value	r	Corrected P Value	r
RD						
ATR	.818	0.023	.898	−0.017	.545	0.090
CC	.121	0.160	.658	0.078	.291	0.174
CR	.046	0.220	.658	0.080	.107	0.307
FMI	.016	0.288	.650	0.135	.013	0.436
IC	.046	0.221	.650	0.152	.276	0.197
IFOF	.050	0.206	.650	0.121	.246	0.228
ISOVF						
ATR	.866	−0.016	.983	−0.008	.865	0.025
CC	.669	0.094	.983	0.003	.437	0.183
CR	.464	0.139	.983	0.055	.272	0.250
FMI	.464	0.147	.983	0.044	.256	0.297
IC	.822	0.059	.983	0.058	.865	0.047
IFOF	.861	−0.035	.983	−0.108	.788	0.095
MVF						
ATR	.042	−0.200	.549	−0.116	.054	−0.283
CC	.042	−0.200	.659	−0.060	.051	−0.324
CR	.022	−0.275	.549	−0.145	.027	−0.414
FMI	.026	−0.235	.614	−0.086	.051	−0.306
IC	.033	−0.219	.549	−0.134	.054	−0.283
ISOVF	.022	−0.250	.549	−0.121	.051	−0.331
SLF	.022	−0.250	.549	−0.205	.051	−0.312

^a False discovery rate–corrected P value < .05.

antihypertensive therapy, systolic blood pressure, and intracranial volume, the mean CAVI was significantly associated with RD and ISOVF in the ATR and CR, and the MVF in the SLF (false discovery rate–corrected $P < .05$; Table 3).

In all participants, the partial correlation analyses demonstrated significant associations of TMT B with RD in the CR, FMI, and IC, or MVF in all tested WM regions (false discovery rate–corrected $P < .05$; Table 4). In the low-CAVI group, TMT B was significantly associated with RD in the FMI and MVF in the CR (false discovery rate–corrected $P < .05$; Table 4). Furthermore, the partial correlation coefficients for the significant associations of TMT B minus A with RD in the CR, IC, and FMI and with MVF in the ATR, CR, and FMI were noted in all participants (false discovery rate–corrected $P < .05$; Table 5). Meanwhile, the low-CAVI group had partial correlation coefficients for the significant associations of TMT B minus A with MVF in the CC, CR, FMI, IC, IFOF, and SLF (false discovery rate–corrected $P < .05$; Table 5). However, the partial correlation coefficients showed no significant associations among the Mini-Mental State Examination, the Montreal Cognitive Assessment (Japanese version), and TMT A and WM metrics.

DISCUSSION

The present study evaluated the WM microstructural changes in older adults with arterial stiffness. The major findings are as follows: First, whole-brain voxelwise results identified a significantly lower MVF in the high-CAVI group than in the low-CAVI group in the broad WM regions. TBSS results also showed significantly higher RD and ISOVF in the high-CAVI group than in the low-CAVI group in the CC, FMI, IFOF, IC, CR, and ATR. Second, the multivariate linear analysis noted significant associations of the mean CAVI with RD and ISOVF in the ATR and CR; and with MVF in the SLF. Finally, we found partial correlation coefficients for the significant associations between the executive function scores and RD and MVF in specific WM areas.

Whole-brain voxelwise results revealed that the high-CAVI group had a significantly lower MVF value than the low-CAVI group in the broad WM area. Low MVF values indicate the loss of the myelin sheath insulating the nerves, implying WM demyelination.²³ In this study, the high-CAVI group also had higher RD and ISOVF values than the low-CAVI

Table 5: Partial correlation coefficients between WM metrics and TMT B minus A, adjusted for age, sex, and education^a

	All Participants		High-CAVI Group		Low-CAVI Group	
	Corrected P Value	r	Corrected P Value	r	Corrected P Value	r
RD						
ATR	.286	0.104	.280	0.172	.846	0.029
CC	.060	0.199	.270	0.191	.508	0.127
CR	.019	0.262	.270	0.200	.162	0.283
FMI	.006	0.315	.270	0.265	.143	0.329
IC	.046	0.219	.270	0.203	.508	0.120
IFOF	.136	0.154	.419	0.109	.508	0.164
ISOVF						
ATR	.506	0.065	.333	0.187	.774	−0.053
CC	.233	0.153	.344	0.156	.774	0.099
CR	.201	0.178	.333	0.178	.774	0.156
FMI	.120	0.225	.333	0.230	.774	0.176
IC	.395	0.095	.333	0.176	.774	−0.043
IFOF	.386	−0.110	.526	−0.102	.774	−0.051
MVF						
ATR	.038	−0.232	.817	−0.207	.082	−0.256
CC	.088	−0.166	.855	0.025	.017	−0.390
CR	.038	−0.265	.817	−0.114	.008	−0.460
FMI	.038	−0.232	.817	−0.074	.019	−0.363
IC	.057	−0.192	.817	−0.083	.037	−0.314
IFOF	.051	−0.211	.847	−0.048	.017	−0.388
SLF	.057	−0.191	0.817	−0.088	.019	−0.358

^a False discovery rate—corrected P value < .05.

group. High ISOVF values associated with high CAVI suggest increased extracellular water diffusion and have been shown to be related to increased inflammatory activation or blood-brain barrier permeability.²⁴ Moreover, elevated RD is also associated with demyelination.²⁵ From these results, the WM in the high-CAVI group could involve demyelination more than in the low-CAVI group. Furthermore, there were no significant differences in the degree of WM hyperintensities between the high- and low-CAVI groups in this study. Considering that TBSS showed significant differences in RD, ISOVF, and MVF between the two groups, our results suggest that WM microstructural changes precede WM hyperintensities and brain atrophy. In support of our findings, prior studies have indicated that DTI metrics capture ultrastructural changes in WM before the onset of WM hyperintensities and brain atrophy.^{26,27} Therefore, it is thought that there was no correlation between the degree of WM hyperintensities and WM metrics.

In the multivariate linear analyses, the mean CAVI was significantly associated with RD in the ATR, CR, and FMI; ISOVF in the ATR and CR; and MVF in the SLF. These findings could reflect arteriosclerosis relating to demyelination. In previous studies, the WM microstructure has been reported to be vulnerable to circulatory alterations and correlates with arterial stiffness.^{4-6,20} Notably, Badji et al⁶ showed that carotid-femoral pulse wave velocity was significantly associated with both FA and RD but not with MVF.¹⁷ The present study indicated the significant associations between the mean CAVI and not only DTI and NODDI metrics but also MVF, possibly reflecting the progression of arteriosclerosis exacerbating demyelination. The conflicting results regarding MVF between this study and that of Badji et al might be caused by differences in the characteristics of the target cohort. For instance, in our study, the average value of the body mass index (22.54 [SD, 2.84] kg/m²) in all

participants was lower than that in the study of Badji et al (26.1 [SD, 4.23] kg/m²). However, the average value of systolic blood pressure (137.47 [SD, 15.67] mm Hg) in our study was higher than that in the study of Badji et al (125.66 [SD, 11.65] mm Hg). Suzuki et al²⁴ showed that pathologic processes related to hypertension are associated with image differences, suggesting changes in WM axons. In addition, WM integrity is particularly vulnerable to obesity.²⁸ A higher body mass index is associated with lower FA in the FMI and CC.²⁹ Therefore, except for the degree of arterial stiffness, the difference in participants' physical characteristics may influence WM integrity. However, exact matching of these clinical findings is difficult. Additionally, our participants were all Japanese, whereas the participants of Badji et al were all Canadian; thus, racial differences may affect WM integrity.³⁰

The present study also showed the existence of the partial correlation coefficients for the significant associations between the executive function and WM metrics. In all participants and the low-CAVI group, the MVF in several WM areas was negatively associated with the executive function. These findings suggest that executive dysfunction may be associated with demyelination. However, in the high-CAVI group of the study, there was no significant connection between WM metrics and TMT scores, which are measures of executive function. Furthermore, although there was no difference in the TMT scores between the high- and low-CAVI groups, we found significant differences in WM metrics between two groups. The findings imply that WM microstructural changes may have already occurred before the impairment of executive function.

This study has some limitations. First, it is based on data obtained from Japanese individuals living in the city; hence, bias in genetic factors and environmental factors, such as eating habits, may occur. Second, it was conducted in a single facility. Thus, multicenter and epidemiologic studies are needed to examine further these investigations.

CONCLUSIONS

Arterial stiffness could be strongly associated with demyelination rather than axonal degeneration.

Disclosure forms provided by the authors are available with the full text and PDF of this article at www.ajnr.org.

REFERENCES

1. Lim J, Pearman M, Park W, et al. Interrelationships among various measures of central artery stiffness. *Am J Hypertens* 2016;29:1024–28 CrossRef Medline

2. Matsushita K, Ding N, Kim ED, et al. **Cardio-ankle vascular index and cardiovascular disease: systematic review and meta-analysis of prospective and cross-sectional studies.** *J Clin Hypertens (Greenwich)* 2019;21:16–24 CrossRef Medline
3. Zhang H, Schneider T, Wheeler-Kingshott CA, et al. **NODDI: practical in vivo neurite orientation dispersion and density imaging of the human brain.** *NeuroImage* 2012;61:1000–16 CrossRef Medline
4. Maillard P, Mitchell GF, Himali JJ, et al. **Aortic stiffness, increased white matter free water, and altered microstructural integrity: a continuum of injury.** *Stroke* 2017;48:1567–73 CrossRef Medline
5. Tarumi T, de Jong DL, Zhu DC, et al. **Central artery stiffness, baroreflex sensitivity, and brain white matter neuronal fiber integrity in older adults.** *Neuroimage* 2015;110:162–70 CrossRef Medline
6. Badji A, Noriega de la Colina A, Karakuzu A, et al. **Arterial stiffness and white matter integrity in the elderly: a diffusion tensor and magnetization transfer imaging study.** *Neuroimage* 2019;186:577–85 CrossRef Medline
7. Someya Y, Tamura Y, Kaga H, et al. **Skeletal muscle function and need for long-term care of urban elderly people in Japan (the Bunkyo Health Study): a prospective cohort study.** *BMJ Open* 2019;9:e031584 CrossRef Medline
8. Shirai K, Utino J, Otsuka K, et al. **A novel blood pressure-independent arterial wall stiffness parameter: cardio-ankle vascular index (CAVI).** *J Atheroscler Thromb* 2006;13:101–07 CrossRef Medline
9. Izuhara M, Shioji K, Kadota S, et al. **Relationship of cardio-ankle vascular index (CAVI) to carotid and coronary arteriosclerosis.** *Circ J* 2008;72:1762–67 CrossRef Medline
10. Fazekas F, Chawluk JB, Alavi A, et al. **MR signal abnormalities at 1.5 T in Alzheimer's dementia and normal aging.** *AJR Am J Roentgenol* 1987;149:351–56 CrossRef Medline
11. Kamagata K, Zalesky A, Yokoyama K, et al. **MR g-ratio-weighted connectome analysis in patients with multiple sclerosis.** *Sci Rep* 2019;9:13522 CrossRef Medline
12. Yamada H, Abe O, Shizukuishi T, et al. **Efficacy of distortion correction on diffusion imaging: comparison of FSL Eddy and Eddy_Correct using 30 and 60 directions diffusion encoding.** *PLoS One* 2014;9:e112411 CrossRef Medline
13. Daducci A, Canales-Rodríguez EJ, Zhang H, et al. **Accelerated Microstructure Imaging via Convex Optimization (AMICO) from diffusion MRI data.** *Neuroimage* 2015;105:32–44 CrossRef Medline
14. Basser PJ, Mattiello J, LeBihan D. **Estimation of the effective self-diffusion tensor from the NMR spin echo.** *J Magn Reson B* 1994;103:247–54 CrossRef Medline
15. Helms G, Dathe H, Kallenberg K, et al. **High-resolution maps of magnetization transfer with inherent correction for RF inhomogeneity and T1 relaxation obtained from 3D FLASH MRI.** *Magn Reson Med* 2008;60:1396–407 CrossRef Medline
16. Weiskopf N, Suckling J, Williams G, et al. **Quantitative multi-parameter mapping of R1, PD*, MT, and R2* at 3T: a multi-center validation.** *Front Neurosci* 2013;7:95 CrossRef Medline
17. Morrell GR, Schabel MC. **An analysis of the accuracy of magnetic resonance flip angle measurement methods.** *Phys Med Biol* 2010;55:6157–74 CrossRef Medline
18. Smith SM, Jenkinson M, Johansen-Berg H, et al. **Tract-Based Spatial Statistics: voxelwise analysis of multi-subject diffusion data.** *Neuroimage* 2006;31:1487–505 CrossRef Medline
19. Mori S, Oishi K, Jiang H, et al. **Stereotaxic white matter atlas based on diffusion tensor imaging in an ICBM template.** *Neuroimage* 2008;40:570–82 CrossRef Medline
20. Maillard P, Mitchell GF, Himali JJ, et al. **Effects of arterial stiffness on brain integrity in young adults from the Framingham heart study.** *Stroke* 2016;47:1030–36 CrossRef Medline
21. Tamura Y, Shimoji K, Ishikawa J, et al. **Subclinical atherosclerosis, vascular risk factors, and white matter alterations in diffusion tensor imaging findings of older adults with cardiometabolic diseases.** *Front Aging Neurosci* 2021;13:712385 CrossRef Medline
22. Benjamini Y, Hochberg Y. **Controlling the false discovery rate: a practical and powerful approach to multiple testing.** *Journal of the Royal Statistical Society: Series B (Methodological)* 1995;57:289–300
23. Duval T, Stikov N, Cohen-Adad J. **Modeling white matter microstructure.** *Funct Neurol* 2016;31:217–28 CrossRef Medline
24. Suzuki H, Gao H, Bai W, et al. **Abnormal brain white matter microstructure is associated with both pre-hypertension and hypertension.** *PLoS One* 2017;12:e0187600 CrossRef Medline
25. Song SK, Yoshino J, Le TQ, et al. **Demyelination increases radial diffusivity in corpus callosum of mouse brain.** *Neuroimage* 2005;26:132–40 CrossRef Medline
26. Andica C, Kamagata K, Hatano T, et al. **Free-water imaging in white and gray matter in Parkinson's disease.** *Cells* 2019;8:839 CrossRef Medline
27. Maillard P, Carmichael O, Harvey D, et al. **FLAIR and diffusion MRI signals are independent predictors of white matter hyperintensities.** *AJNR Am J Neuroradiol* 2013;34:54–61 CrossRef Medline
28. Bettcher BM, Walsh CM, Watson C, et al. **Body mass and white matter integrity: the influence of vascular and inflammatory markers.** *PLoS One* 2013;8:e77741 CrossRef Medline
29. Kullmann S, Schweizer F, Veit R, et al. **Compromised white matter integrity in obesity.** *Obes Rev* 2015;16:273–81 CrossRef Medline
30. Liu G, Allen B, Lopez O, et al. **Racial differences in gray matter integrity by diffusion tensor in black and white octogenarians.** *Curr Alzheimer Res* 2015;12:648–54 CrossRef Medline

Improved Blood Suppression of Motion-Sensitized Driven Equilibrium in High-Resolution Whole-Brain Vessel Wall Imaging: Comparison of Contrast-Enhanced 3D T1-Weighted FSE with Motion-Sensitized Driven Equilibrium and Delay Alternating with Nutation for Tailored Excitation

D.J. Kim, H.-J. Lee, J. Baik, M.J. Hwang, M. Miyoshi, and Y. Kang



ABSTRACT

BACKGROUND AND PURPOSE: High-resolution vessel wall MR imaging is prone to slow-flow artifacts, particularly when gadolinium shortens the T1 relaxation time of blood. This study aimed to determine the optimal preparation pulses for contrast-enhanced high-resolution vessel wall MR imaging.

MATERIALS AND METHODS: Fifty patients who underwent both motion-sensitized driven equilibrium and delay alternating with nutation for tailored excitation (DANTE) preparation pulses with contrast-enhanced 3D-T1-FSE were retrospectively included. Qualitative analysis was performed using a 4-grade visual scoring system for black-blood performance in the small-sized intracranial vessels, overall image quality, severity of artifacts, and the degree of blood suppression in all cortical veins as well as transverse sinuses. Quantitative analysis of the M1 segment of the MCA was also performed.

RESULTS: The qualitative analysis revealed that motion-sensitized driven equilibrium demonstrated a significantly higher black-blood score than DANTE in contrast-enhanced 3D-T1-FSE of the A3 segment (3.90 versus 3.58, $P < .001$); M3 (3.72 versus 3.26, $P = .004$); P2 to P3 (3.86 versus 3.64, $P = .017$); the internal cerebral vein (3.72 versus 2.32, $P < .001$); and overall cortical veins (3.30 versus 2.74, $P < .001$); and transverse sinuses (2.82 versus 2.38, $P < .001$). SNR_{lumen} , contrast-to-noise ratio_{wall-lumen}, and SNR_{wall} in the M1 vessel were not significantly different between the 2 preparation pulses (all, $P > .05$).

CONCLUSIONS: Motion-sensitized driven equilibrium demonstrated improved blood suppression on contrast-enhanced 3D-T1-FSE in the small intracranial arteries and veins compared with DANTE. Motion-sensitized driven equilibrium is a useful preparation pulse for high-resolution vessel wall MR imaging to decrease venous contamination and suppress slow-flow artifacts when using contrast enhancement.

ABBREVIATIONS: BB = black-blood; CE = contrast-enhanced; CNR = contrast-to-noise ratio; DANTE = delay alternating with nutation for tailored excitation; HR-VWI = high-resolution vessel wall MR imaging; ICV = internal cerebral vein; MSDE = motion-sensitized driven equilibrium

High-resolution vessel wall MR imaging (HR-VWI) is a crucial technique used to diagnose various pathologic conditions that involve the vessel walls.¹⁻⁵ HR-VWI differs from conventional methods such as CTA, MRA, and DSA in that HR-VWI directly delineates the vessel walls rather than indirectly illustrating them

by projecting the luminal cavity.^{6,7} Thus, HR-VWI enables further characterization of minute changes in the vessel wall.^{2,5,8-10}

In HR-VWI, suppression of signals from the intraluminal blood and extraluminal CSF is required to precisely portray the vessel wall.^{2,11,12} The 3D-T1-FSE sequence is widely used for HR-VWI due to its inherent black-blood (BB) effect attained by intravoxel dephasing induced by gradient moments and stimulated echoes.^{12,13} However, there are technical challenges associated with HR-VWI, including slow-flow artifacts induced by intraluminal blood with slow-flow velocity, which may mimic vessel wall lesions, particularly when using contrast enhancement in which gadolinium shortens the T1 relaxation times of blood. These technical challenges are difficult to overcome if only the inherent BB effect of 3D-T1-FSE is used.⁵

Received May 12, 2022; accepted after revision September 15.

From the Department of Radiology (D.J.K., H.-J.L., J.B., Y.K.), Haeundae Paik Hospital, Inje University College of Medicine, Busan, South Korea; Department of Radiology (J.B.), Good Gang-An Hospital, Busan, South Korea; GE Healthcare Korea (M.J.H.), Seoul, South Korea; and GE Healthcare Japan (M.M.), Tokyo, Japan.

Please address correspondence to Yeonah Kang, MD, Department of Radiology, Haeundae Paik Hospital, Inje University College of Medicine, Busan, South Korea; e-mail: bsb2312@gmail.com

Indicates open access to non-subscribers at www.ajnr.org

Indicates article with online supplemental data.

<http://dx.doi.org/10.3174/ajnr.A7678>

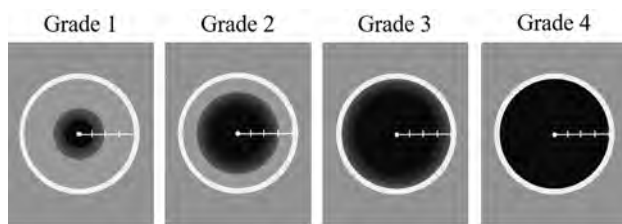


FIG 1. Schematic illustration of vessels with different visual grade scores for BB performance: 1) less than one-half of the target lumen dimension visible with black signal intensity; 2) one-half to three-quarters of the target lumen dimension visible with black signal intensity; 3) more than three-quarters of the target lumen dimension visible with black signal intensity (with unsuppressed flow near the wall); and 4) completely suppressed flow (with the entire target lumen dimension visible with black signal intensity).

Management of these technical pitfalls is necessary because the contrast-enhanced (CE) sequence gives essential clinical information on vasculopathy. The plaque enhancement can be used as a measure of the vulnerability of atherosclerotic plaques.^{4,5,9} Abnormal vessel wall enhancement indicates inflammatory activity, and the degree of enhancement may be reduced after steroid therapy.^{4,5,9} However, incomplete blood flow suppression may mimic atherosclerotic plaque enhancement or vessel wall enhancement.⁵ Hence, additional preparation pulses for HR-VWI such as motion-sensitized driven equilibrium (MSDE) and delay alternating with nutation for tailored excitation (DANTE) have been developed to minimize the degradation of the BB effect and are currently used in various clinical scenarios.^{11,14-19}

To date, effort has been made to find an optimal method for increasing the BB effect in HR-VWI.^{3,13,14,17} Recently, an increased number of studies reported that DANTE has advantages in intracranial application in terms of the provision of effective CSF suppression over MSDE, which has signal drop owing to inherent T2 decay.²⁰⁻²² However, regarding CE situations, we speculated that because MSDE has the characteristics of T2 preparation pulses with a motion-sensitized gradient, fast T1 recovery of the contrast agent may not influence the flow suppression of MSDE. Nevertheless, comparisons between MSDE and DANTE in HR-VWI using CE 3D-T1-FSE have not yet been reported. Therefore, we compared the BB effect of MSDE and DANTE in CE 3D-T1-FSE, particularly in small vessels with slow intraluminal blood flow.

MATERIALS AND METHODS

Patient Selection

The institutional review board of Inje University of Haeundae Paik Hospital approved this study, and the requirement for informed consent was waived due to its retrospective nature. Seventy-one consecutive patients who underwent HR-VWI between January and July 2020 were retrospectively enrolled. Patients who underwent CE 3D-T1-FSE with only 1 BB technique ($n = 19$) or those with poor image quality due to severe motion artifacts ($n = 2$) were excluded. Finally, 50 patients (mean age, 65.6 years; range, 33–87 years) were included in the study.

MR Imaging Protocol

All MR images were acquired using a single 3T MR imaging unit (Signa Architect; GE Healthcare) with a 48-channel head coil.

Examinations were performed 5 minutes after intravenous administration of gadobutrol (Gadovist; Bayer Schering Pharma) at a dose of 0.1 mmol/kg of body weight.⁵ We used identical imaging parameters (TR, 800 ms; echo-train length, 48; bandwidth, 416 Hz/pixel; matrix, 300×300 pixels; FOV, 180×180 mm²; voxel size, $0.6 \times 0.6 \times 0.6$ mm³; 11.7-cm coverage on the coronal plane; compressed sensing factor, 1.2; Autocalibrating reconstruction for Cartesian imaging (ARC) acceleration, phase $\times 2$ and section $\times 1$; acquisition time, 5 minutes 8 seconds with fat saturation) for all the patients. The TE was set to the minimum value; consequently, the TEs were 28 and 17 ms for the MSDE and DANTE scans, respectively. Images of CE 3D-T1-FSE with MSDE (composite-type MSDE; velocity-suppressed target, 3.0 cm/s) and those with the DANTE (flip angle, 13°; Gxyz = 18 mT/m; echo space, 1500 μ s; total duration of the DANTE pulse, 142 ms) were acquired in a randomized order. Among the 50 patients finally included, 26 had images of CE 3D-T1-FSE with DANTE acquired before MSDE, while 24 had images of CE 3D-T1-FSE with MSDE acquired before DANTE.

Image Analysis

Qualitative and quantitative analyses of the BB effects of MSDE and DANTE were performed by 2 radiologists (Y.K. and H.-J.L. with 8 and 13 years' experience in neuroradiology, respectively), blinded to patient clinical information. Qualitative analysis was performed in the M1 segment of the MCA and 4 parts of the small intracranial vessels: the A3 segment of the anterior cerebral artery (A3), M3 segment of middle cerebral artery (M3), from P2 to P3 segment of posterior cerebral artery (P2 to P3), and internal cerebral vein (ICV). For the qualitative analysis, a 4-grade visual scoring system was used and defined as follows: 1) less than one-half of the target lumen dimension visible with black signal intensity; 2) one-half to three-quarters of the target lumen dimension visible with black signal intensity; 3) more than three-quarters of the target lumen dimension visible with black signal intensity (with unsuppressed flow near the wall); and 4) completely suppressed flow (with the entire target lumen dimension visible with black signal intensity). Figure 1 shows the schematic illustration of vessels with different visual grade scores for BB performances. For quantitative analysis, the SNR and contrast-to-noise ratio (CNR) were measured in the same area of the M1 segment of the MCA and calculated according to an equation used in a previous work by Xie et al:¹⁶ $SNR_x = 0.695 \times S_x / \sigma$, $CNR_{x \rightarrow y} = 0.695 \times (S_x - S_y) / \sigma$; S_x represents the signal intensity of x anatomy, and the noise level (σ) was defined as the signal SD within an ROI drawn in the adjacent air space of the image uncontaminated by artifacts. The SNR_{wall} , SNR_{lumen} , SNR_{csf} , $CNR_{wall-lumen}$, and $CNR_{wall-csf}$ were calculated. The sizes of each drawn ROI of the vessel wall and the vessel lumen during quantitative analysis were also recorded. The Online Supplemental Data show an example of SNR measurement with a displayed ROI. All analyses were repeated by another radiologist (J.B., with 7 years' experience in neuroradiology) for the evaluation of interobserver reliability for the BB effect.

Grading of overall image quality, severity of artifacts, and the degree of blood suppression in all cortical veins and both sides of the transverse sinuses was rated in each individual CE 3D-T1-FSE with DANTE or MSDE by 2 reviewers in a blinded manner, and consensus was reached. Each rater evaluated the overall image quality using a 4-grade scoring system as follows: 1) nondiagnostic

Table 1: Visual scoring evaluation of the BB effect in the small-sized intracranial arteries, ICV, and the M1 segment of the MCA

Locations	3D-T1-FSE with MSDE	3D-T1-FSE with DANTE	P Value
A3	3.90	3.58	<.001
M3	3.72	3.26	.004
P2 to P3	3.86	3.64	.017
ICV	3.72	2.32	.001
M1	3.66	3.60	.497

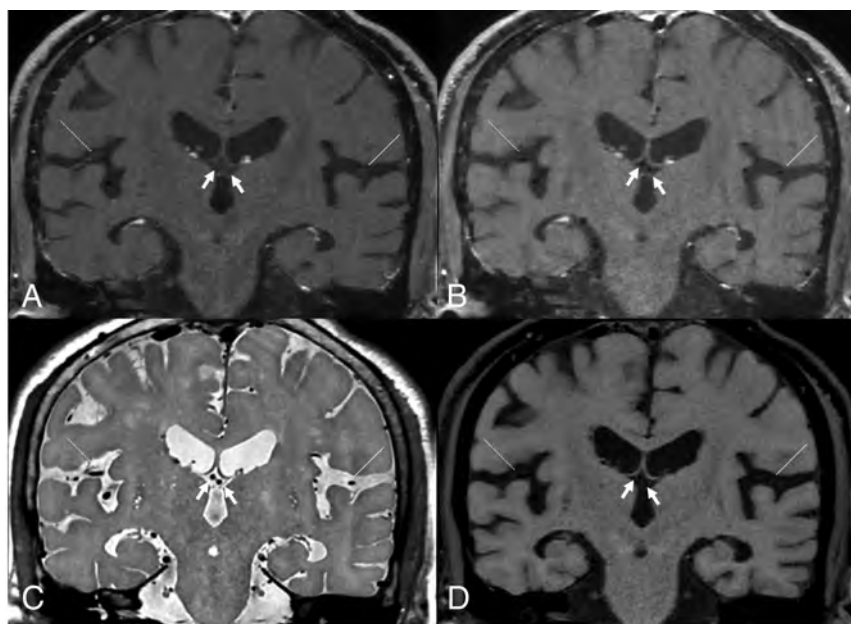


FIG 2. A 78-year-old man who underwent HR-VWI. CE 3D-T1-FSE with DANTE (A), CE 3D-T1-FSE with MSDE (B), a proton-density-weighted sequence (C), and a T1-weighted sequence (D). There are nonsuppressed peripheral flows at the ICV (arrows), cortical vein (dotted line), and left M3 (solid line) on CE 3D-T1-FSE with DANTE (A). However, CE 3D-T1-FSE with MSDE (B) shows complete blood suppression at the aforementioned structures.

image quality; 2) moderately diminished image quality, affecting general diagnosis; 3) minimally diminished image quality, not affecting general diagnosis; and 4) optimal image quality. The severity of artifacts was evaluated using the following 4-grade scoring system: 1) presence of any artifact that inhibits diagnosis of the targeted vessel anatomy; 2) existence of artifacts that affect the targeted vessel anatomy, but still interpretable; 3) existence of artifacts that do not affect the diagnosis of the targeted vessel anatomy; and 4) no artifacts at all. The overall cortical vein suppression score was evaluated using the following 4-grade scoring system: 1) severe nonsuppressed cortical veins that mimic pathology; 2) moderate nonsuppressed cortical veins that do not mimic pathology; 3) mild nonsuppressed cortical veins that do not interfere with interpretation; and 4) complete blood suppression in the cortical veins. The degree of blood suppression on both sides of the transverse sinuses was evaluated using the following 4-grade scoring system: 1) severe nonsuppressed transverse sinuses that mimic pathology; 2) moderate nonsuppressed transverse sinuses with central nonsuppressed blood signals; 3) mild nonsuppressed transverse sinuses with only peripheral nonsuppressed blood signals; and 4) complete blood suppression in the transverse sinuses.

Statistical Analysis

All statistical analyses were performed using R software for Windows (Version 3.3.3; <http://www.r-project.org/>). The normality test for each variable was performed using the Kolmogorov-Smirnov test. Either a paired *t* test or Wilcoxon signed-rank test was performed for comparison. The weighted κ and intraclass correlation coefficients were used to evaluate the interobserver agreement. Statistical significance was set at $P < .05$. The strength of the interobserver agreement was categorized as follows: κ values and intraclass correlation coefficients < 0.20 , poor agreement; 0.21 – 0.40 , fair agreement; 0.41 – 0.60 , moderate agreement; 0.61 – 0.80 , good agreement; and 0.81 – 1.00 , excellent agreement.²³

RESULTS

Qualitative Analysis

CE 3D-T1-FSE with MSDE had a significantly higher visual score than 3D-T1-FSE with DANTE in the small-sized vessels: A3 (3.90 versus 3.58, $P < .001$); M3 (3.72 versus 3.26, $P = .004$); P2 to P3 (3.86 versus 3.64, $P = .017$); and the ICV (3.72 versus 2.32, $P < .001$) (Table 1). In the M1, the qualitative analysis of CE 3D-T1-FSE with MSDE and with DANTE showed no significant difference between the two (3.66 versus 3.60, $P = .497$). Figures 2 and 3 and the

Online Supplemental Data illustrate representative cases in which the BB effect of CE 3D-T1-FSE with MSDE surpassed that with DANTE. Subgroup analysis results of the BB effect according to the scan order are provided in the Online Supplemental Data.

Quantitative Analysis

There were no significant differences in SNR_{lumen} , $CNR_{wall-lumen}$, and SNR_{wall} between CE 3D-T1-FSE with MSDE and with DANTE in the M1 (all, $P > .05$) (Table 2). However, $CNR_{wall-csf}$ was higher on 3D-T1-FSE with DANTE than with MSDE (1.785 versus 1.047; $P = .013$). The mean sizes of the drawn ROI of the vessel wall and the vessel lumen were approximately 0.0037 cm^2 and 0.0437 cm^2 , respectively.

Interobserver Reliability

The interobserver reliability evaluation indicated good agreement in both qualitative (0.78; 95% CI, 0.69–0.86) and quantitative (0.71; 95% CI, 0.63–0.77) analyses (Online Supplemental Data).

Image-Quality Assessment

CE 3D-T1-FSE with DANTE was rated slightly higher than with MSDE for overall image quality (3.54 versus 3.42, $P =$

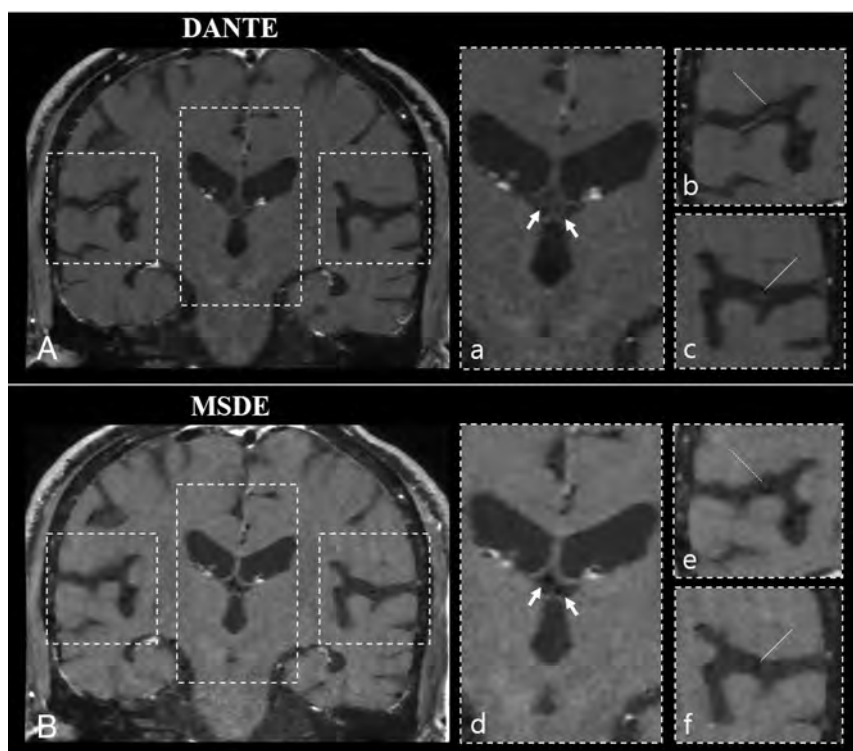


FIG 3. The detailed view of CE 3D-T1-FSE with DANTE (A) and with MSDE (B). The peripherally unsuppressed flow of the ICV (a, arrows), cortical vein in the right temporal sulci (b, dotted line), and the left M3 (c, solid line) on the CE 3D-T1-FSE with DANTE. However, superior blood suppression of the same point in each vessel was noted on CE 3D-T1-FSE with MSDE (d, arrows; e, dotted line; f, solid line).

Table 2: Comparison of SNR and CNR in the M1 segment of the MCA

Locations	3D-T1-FSE with MSDE	3D-T1-FSE with DANTE	P Value
SNR _{wall}	15.556	16.426	.099
SNR _{lumen}	7.880	8.356	.089
SNR _{csf}	16.950	16.728	.674
CNR _{wall-lumen}	10.082	9.408	.183
CNR _{wall-csf}	1.047	1.785	.013

Table 3: Comparison of image quality between 3D-T1-FSE with MSDE and DANTE

	3D-T1-FSE with MSDE	3D-T1-FSE with DANTE	P Value
Overall image quality	3.42	3.54	.013
Artifacts	3	3	NA
Blood suppression in cortical veins	3.30	2.74	<.001
Blood suppression in transverse sinuses	2.82	2.38	<.001

Note:—NA indicates not available.

.013). On the other hand, CE 3D-T1-FSE with MSDE had better blood-suppression ratings than with DANTE for the cortical veins (3.30 versus 2.74, $P < .001$) and transverse sinuses (2.82 versus 2.38, $P < .001$) (Table 3). The severity of artifacts in CE 3D-T1-FSE with MSDE and in CE 3D-T1-FSE with DANTE was rated 3 in all patients, indicating identical results.

DISCUSSION

In this study, we compared the BB effect of CE 3D-T1-FSE with MSDE and with DANTE. In the qualitative analysis, CE 3D-T1-FSE with MSDE had a significantly greater BB effect than CE 3D-T1-FSE with DANTE in the small intracranial arteries and even in the cerebral veins, cortical veins, internal cerebral veins, and transverse sinus. Both qualitative and quantitative analyses of the BB effect in the M1 of the MCA did not show significant differences between CE 3D-T1-FSE with MSDE and with DANTE. Thus, CE 3D-T1-FSE with MSDE may improve lesion conspicuity for pathologic enhancement of the vessel wall and intraluminal enhancing lesions in small vessels by decreasing venous contamination and suppressing signals from slow-flowing blood.

DANTE suppresses signals from both the blood and CSF using an alternative arrangement of low flip angle nonselective radiofrequency pulses with gradient pulses, causing static spin systems to fall into steady states.^{2,12,16} Signal suppression of the blood and CSF results from the failure of flowing spins to establish this steady state due to the spoiling effect.^{2,16} Previous studies that compared HR-VWI with or without DANTE reported that DANTE demonstrated an improved BB effect.^{3,16} Several previous studies comparing the BB effects of DANTE with those of MSDE reported the superiority of DANTE over MSDE;^{3,14,15,24,25} however, these were based on evaluations of the carotid artery,^{14,24} a phantom model of an aneurysm,³ or vessels of the neck or lower extremities.²⁵

Our study evaluated small-sized intracranial vessels using contrast enhancement because the CE sequence gives essential clinical information on vasculopathy. An adequate BB effect is crucial in avoiding incomplete blood flow suppression, which may mimic atherosclerotic plaque enhancement or vessel wall enhancement.

In contrast to previous phantom results,³ we found that DANTE demonstrated a lesser BB effect in the small intracranial vessels than MSDE. Cornelissen et al³ indicated that the use of preparation pulses when conducting HR-VWI improved the BB effect in an aneurysmal phantom, especially when using 3D-T1-turbo spin-echo (TSE) with DANTE compared with 3D-T1-TSE with MSDE. However, blood-

signal suppression is a delicate task that is affected not only by preparation pulses but also by the complex interactions of certain imaging parameters, such as voxel size, TR, TE, receiver bandwidth, and flow rate.^{26,27} Pravdivtseva et al²⁷ demonstrated the complicated relationships among flow rate, spatial resolution, and preparation pulses regarding blood-signal suppression in 3D-T1-TSE. In a scenario with a slow blood flow rate, a larger voxel size was efficient in suppressing the blood signals, more from the dominant intravoxel dephasing effect than the flow effect of the blood from the imaging section. However, when we used MSDE, the BB effect was similar between voxel sizes of 0.5 and 0.9 mm.^{3,27} Because the highest clinically feasible resolution is recommended in HR-VWI to minimize the partial volume effect,⁹ using preparation pulses with a high-spatial-resolution setting may help achieve a greater BB effect in a scenario with slow blood flow.

MSDE consists of block-shaped radiofrequency pulses with 90°–180°–90° flip angles and motion-sensitizing gradients, which dephase all moving blood spins before imaging, thus, suppressing signals from the blood.^{17,18} Previous studies have discussed the efficacy of MSDE in suppressing signals from the blood and CSF, with results indicating MSDE as an effective tool to delineate vessel walls.^{11,18,28,29} Because there is a substantial intraluminal signal increase after gadolinium injection, Lindenholz et al⁵ emphasized careful interpretation of slow-flow artifacts mostly induced by venous flow near the artery, which may cause misinterpretation of arterial wall enhancement. In our study, the visual scores of the BB effect, in the cortical veins as well as the ICV, were noticeably higher in CE 3D-T1-FSE with MSDE than in CE 3D-T1-FSE with DANTE (3.30 versus 2.74, $P < .001$; 3.72 versus 2.32, $P < .001$). We speculated that the basic difference in the composition of the 2 preparation pulse diagrams may account for our result, which is the CE situation.

DANTE is a low flip angle gradient-recalled acquisition in steady state sequence, which has T1-weighted contrast. Turbulence flow breaks the steady state, and its signal is suppressed. However, if the flow is slow or laminar, signal suppression becomes less. When the contrast agent is used, the blood-signal suppression effect may become less because of fast T1 recovery. On the other hand, the MSDE preparation consists of a 90° excitation pulse, two 180° refocusing pulses with each pulse sandwiched by bipolar motion-sensitizing gradients, and a –90° flip back pulse;²⁹ in other words, it has the characteristics of a spin-echo sequence with a motion-sensitized gradient like the diffusion-weighted spin-echo sequence. The fast T1 recovery of the contrast agent may have a low impact on the flow suppression of MSDE because MSDE has spin-echo-based T2-weighted contrast. Moreover, the gradient size is much larger than that of DANTE, and the large motion-sensitized gradient can suppress slow laminar flow.

In the qualitative analysis, although the overall image quality of MSDE was notable, CE 3D-T1-FSE with DANTE received a significantly higher score than CE 3D-T1-FSE with MSDE (3.54 versus 3.42, $P = .013$). Li et al¹⁴ speculated that compared with DANTE, MSDE reduces SNR due to T2 decay; however, our quantitative analysis revealed no significant differences in the SNR_{wall} and SNR_{csf} between CE 3D-T1-FSE with DANTE and with MSDE. There is a concern that the vessel wall SNR would be

decreased when using preparation pulses for 3D-T1-FSE.²⁰ Cho et al¹³ reported that preparation pulses may not be a requisite for MR imaging sequences with a long echo-train length and an appropriate TR (below 1160 ms; which enhances the differentiation of vessel walls from CSF and brain simultaneously clinically feasible acquisition time) in vessel wall imaging. However, we believe that preparation pulses, especially those of MSDE, need to be applied in the CE 3D-T1-FSE sequence because the intracranial blood flow is often slow, stagnant, or turbulent; thus, artifacts may pose problems in the interpretation of possible vessel wall pathologies,^{5,30} particularly when gadolinium shortens the T1 relaxation times of blood.

This study had several limitations. First, this was a retrospective study that included patients who underwent HR-VWI at a single center during a short time period. Therefore, we included only a limited number of patients. However, we used precisely controlled MR imaging settings for all patients with a randomized order of image acquisition to minimize potential bias, which could be magnified in a limited sample size. Nevertheless, the optimal sample size requires further validation. Second, we did not conduct quantitative analysis in the smaller vessels, A3, M3, P2 to P3, and the ICV, unlike in the M1 segment of the MCA. Due to the excessively thin walls of these vessels, the signal intensity acquired by measuring the ROI was easily altered by partial volume artifacts. As a substitute, we performed a qualitative analysis of the small-sized vessels using a 4-grade visual scoring system. Third, although image analysis of the lesion-free portion of the vessels was performed, the patients included in our study were those who satisfied the clinical indications of the HR-VWI examination, rather than healthy volunteers. In actual clinical settings, most individuals examined with HR-VWI are patients with pathologies. Hence, our cohort study might serve as a representative sample. Future studies including both healthy volunteers and patients with pathologies may clarify the optimal preparation pulse that could be widely used for HR-VWI.

CONCLUSIONS

MSDE demonstrated a preferable BB effect compared with DANTE on CE 3D-T1-FSE in the small intracranial arteries and even in the cerebral veins. Therefore, we suggest that CE 3D-T1-FSE with MSDE is a useful sequence for decreasing venous contamination and suppressing slow-flow artifacts, possibly leading to increased lesion conspicuity for pathologic enhancement of the vessel walls and intraluminal enhancing lesions.

Disclosure forms provided by the authors are available with the full text and PDF of this article at www.ajnr.org.

REFERENCES

- Alexander MD, Yuan C, Rutman A, et al. **High-resolution intracranial vessel wall imaging: imaging beyond the lumen.** *J Neurol Neurosurg Psychiatry* 2016;87:589–97 CrossRef Medline
- Arenillas JF, Dieleman N, Bos D. **Intracranial arterial wall imaging: techniques, clinical applicability, and future perspectives.** *Int J Stroke* 2019;14:564–73 CrossRef Medline
- Cornelissen BM, Leemans EL, Coolen BF, et al. **Insufficient slow-flow suppression mimicking aneurysm wall enhancement in magnetic**

- resonance vessel wall imaging: a phantom study. *Neurosurg Focus* 2019;47:E19 CrossRef Medline
4. Dieleman N, van der Kolk AG, Zwanenburg JJ, et al. **Imaging intracranial vessel wall pathology with magnetic resonance imaging: current prospects and future directions.** *Circulation* 2014;130:192–201 CrossRef Medline
5. Lindenholz A, van der Kolk AG, Zwanenburg JJ, et al. **The use and pitfalls of intracranial vessel wall imaging: how we do it.** *Radiology* 2018;286:12–28 CrossRef Medline
6. Lee NJ, Chung MS, Jung SC, et al. **Comparison of high-resolution MR imaging and digital subtraction angiography for the characterization and diagnosis of intracranial artery disease.** *AJNR Am J Neuroradiol* 2016;37:2245–50 CrossRef Medline
7. Park JE, Jung SC, Lee SH, et al. **Comparison of 3D magnetic resonance imaging and digital subtraction angiography for intracranial artery stenosis.** *Eur Radiol* 2017;27:4737–46 CrossRef Medline
8. Chaganti J, Woodford H, Tomlinson S, et al. **Black blood imaging of intracranial vessel walls.** *Pract Neurol* 2020 Dec 23 [Epub ahead of print] CrossRef Medline
9. Mandell DM, Mossa-Basha M, Qiao Y, et al; Vessel Wall Imaging Study Group of the American Society of Neuroradiology. **Intracranial Vessel Wall MRI: Principles and Expert Consensus Recommendations of the American Society of Neuroradiology.** *AJNR Am J Neuroradiol* 2017;38:218–29 CrossRef Medline
10. Pacheco FT, Cruz Junior L, Padilha IG, et al. **Current uses of intracranial vessel wall imaging for clinical practice: a high-resolution MR technique recently available.** *Arq Neuropsiquiatr* 2020;78:642–50 CrossRef Medline
11. Wang J, Yarnykh VL, Yuan C. **Enhanced image quality in black-blood MRI using the improved motion-sensitized driven-equilibrium (iMSDE) sequence.** *J Magn Reson Imaging* 2010;31:1256–63 CrossRef Medline
12. Zhang L, Zhang N, Wu J, et al. **High resolution simultaneous imaging of intracranial and extracranial arterial wall with improved cerebrospinal fluid suppression.** *Magn Reson Imaging* 2017;44:65–71 CrossRef Medline
13. Cho SJ, Jung SC, Suh CH, et al. **High-resolution magnetic resonance imaging of intracranial vessel walls: comparison of 3D T1-weighted turbo spin echo with or without DANTE or iMSDE.** *PLoS One* 2019;14:e0220603 CrossRef Medline
14. Li L, Chai JT, Biasioli L, et al. **Black-blood multicontrast imaging of carotid arteries with DANTE-prepared 2D and 3D MR imaging.** *Radiology* 2014;273:560–69 CrossRef Medline
15. Matsuda T, Kimura H, Kabasawa H, et al. **Three-dimensional arterial spin labeling imaging with a DANTE preparation pulse.** *Magn Reson Imaging* 2018;49:131–37 CrossRef Medline
16. Xie Y, Yang Q, Xie G, et al. **Improved black-blood imaging using DANTE-SPACE for simultaneous carotid and intracranial vessel wall evaluation.** *Magn Reson Med* 2016;75:2286–94 CrossRef Medline
17. Obara M, Kuroda K, Wang J, et al. **Comparison between two types of improved motion-sensitized driven-equilibrium (iMSDE) for intracranial black-blood imaging at 3.0 Tesla.** *J Magn Reson Imaging* 2014;40:824–31 CrossRef Medline
18. Wang J, Yarnykh VL, Hatsukami T, et al. **Improved suppression of plaque-mimicking artifacts in black-blood carotid atherosclerosis imaging using a multislice motion-sensitized driven-equilibrium (MSDE) turbo spin-echo (TSE) sequence.** *Magn Reson Med* 2007;58:973–81 CrossRef Medline
19. Yoneyama M, Nakamura M, Takahara T, et al. **Improvement of T1 contrast in whole-brain black-blood imaging using motion-sensitized driven-equilibrium prepared 3D turbo spin echo (3D MSDE-TSE).** *Magn Reson Med Sci* 2014;13:61–65 CrossRef Medline
20. Cogswell PM, Siero JC, Lants SK, et al. **Variable impact of CSF flow suppression on quantitative 3.0T intracranial vessel wall measurements.** *J Magn Reson Imaging* 2018;48:1120–28 CrossRef Medline
21. Coolen BF, Schoormans J, Gilbert G, et al. **Double delay alternating with nutation for tailored excitation facilitates banding-free isotropic high-resolution intracranial vessel wall imaging.** *NMR Biomed* 2021;34:e4567 CrossRef Medline
22. Sannanjanja B, Zhu C, Colip CG, et al. **Image-quality assessment of 3D intracranial vessel wall MRI using DANTE or DANTE-CAIPI for blood suppression and imaging acceleration.** *AJNR Am J Neuroradiol* 2022;43:837–43 CrossRef Medline
23. Kang HJ, Lee JM, Joo I, et al. **Assessment of malignant potential in intraductal papillary mucinous neoplasms of the pancreas: comparison between multidetector CT and MR imaging with MR cholangiopancreatography.** *Radiology* 2016;279:128–39 CrossRef Medline
24. Papoutsis K, Li L, Near J, et al. **A purpose-built neck coil for black-blood DANTE-prepared carotid artery imaging at 7T.** *Magn Reson Imaging* 2017;40:53–61 CrossRef Medline
25. Su S, Ren Y, Shi C, et al. **Black-blood T2* mapping with delay alternating with nutation for tailored excitation.** *Magn Reson Imaging* 2017;40:91–97 CrossRef Medline
26. Alexander AL, Buswell HR, Sun Y, et al. **Intracranial black-blood MR angiography with high-resolution 3D fast spin echo.** *Magn Reson Med* 1998;40:298–310 CrossRef Medline
27. Pravdivtseva MS, Gaidzik F, Berg P, et al. **Pseudo-enhancement in intracranial aneurysms on black-blood MRI: effects of flow rate, spatial resolution, and additional flow suppression.** *J Magn Reson Imaging* 2021;54:888–901 CrossRef Medline
28. Kanoto M, Toyoguchi Y, Hosoya T, et al. **Visualization of the trochlear nerve in the cistern with use of high-resolution turbo spin-echo multisection motion-sensitized driven equilibrium.** *AJNR Am J Neuroradiol* 2013;34:1434–37 CrossRef Medline
29. Nagao E, Yoshiura T, Hiwatashi A, et al. **3D turbo spin-echo sequence with motion-sensitized driven-equilibrium preparation for detection of brain metastases on 3T MR imaging.** *AJNR Am J Neuroradiol* 2011;32:664–70 CrossRef Medline
30. Kalsoum E, Chabernaude Negrier A, Tuilier T, et al. **Blood flow mimicking aneurysmal wall enhancement: a diagnostic pitfall of vessel wall MRI using the postcontrast 3D turbo spin-echo MR imaging sequence.** *AJNR Am J Neuroradiol* 2018;39:1065–67 CrossRef Medline

Intracranial Vessel Segmentation in 3D High-Resolution T1 Black-Blood MRI

S. Elsheikh, H. Urbach, and M. Reiser



ABSTRACT

SUMMARY: We demonstrate the feasibility of intracranial vascular segmentation based on the hypointense signal in non-contrast-enhanced black-blood MR imaging using convolutional neural networks. We selected 37 cases. Qualitatively, we observed no degradation due to stent artifacts, a comparable recognition of an aneurysm recurrence with TOF-MRA, and consistent success in the differentiation of intracranial arteries and veins. False-positive and false-negative results were observed. Quantitatively, our model achieved a promising Dice similarity coefficient of 0.72.

ABBREVIATIONS: BBMRI = black-blood compressed-sensing MRI; CNN = convolutional neural networks; DSC = Dice similarity coefficient

Automated segmentation techniques of the cerebral vasculature are an area of interest, with numerous previous publications.¹ Currently, convolutional neural networks (CNN) are the criterion standard for medical image segmentation.² Publications applying CNN segmentation of the cerebral vessels were largely based on TOF-MRA.³

Recently, a black-blood compressed-sensing MRI (BBMRI) sequence was introduced. It allows isotropic voxels of 0.5 mm³, suppression of signal within the vessels, and covering a large volume. These advantages are useful in diverse clinical applications.⁴ We aimed to test the feasibility of intracranial vascular segmentation based on the hypointense signal in BBMRI using CNN.

Technical Report

After obtaining institutional review board approval, we retrospectively searched our PACS for examinations including BBMRI. We selected 37 (training, 26; testing, 11 randomly assigned [repeat examinations of the same patients were manually assigned to the training data set]) cases. The imaging indication was post-coiling examination in 34 cases, vasculitis in 2 cases, and dissection in 1 case.

All images were scanned on a 3T MR imaging (Magnetom Prisma; Siemens).⁴ The image matrix was 384 × 384 × 256; voxel size, 0.55 × 0.55 × 0.6 mm³.

We limited the volume of interest to cover the proximal course of the intracranial vessels and to extend beyond the circle of Willis (Online Supplemental Data). A binary mask was manually created in the Montreal Neurological Institute space (Online Supplemental Data) and then transformed to the individual patient space; this was used to define the cropped volume. Ground truth annotation was performed by a neuroradiologist (S.E.) with 15 years of experience in neurovascular imaging.

We used a hierarchic, multiscale, 3D CNN motivated by Yu et al.⁵ Four scales of nested patches with a matrix size of 32³ voxels were used. Scale sizes ranged from 105.6 × 105.6 × 76.8 mm³ to 17.6 × 17.6 × 19.2 mm³. The 2 intermediate scales were exponentially interpolated. The scales were randomly selected but with a 50% probability that the scale center lay within the target label. In each scale, a UNET-type architecture similar to that in Ronneberger et al.² was used. The feature dimensions were 8, 16, 16, 32, 64. Max pooling in the encoding layers and transposed convolutions in the decoding layers were used. The input to the network was the BBMRI contrast normalized by the global signal mean. The output channels of each scale were forwarded as the input to the next scale (Online Supplemental Data). We trained the network using the Adam optimizer,⁶ with a rate of 0.001 and binary cross-entropy. The network application used a random patching scheme, in which in each layer, only the highest probability (50%) daughter patches were further processed (<https://bitbucket.org/reiser/patchwork/>).

For evaluation of our test results, we measured the overlap and spatial distance metrics^{7,8} using the Deepmind library (<https://github.com/deepmind/surface-distance>).

Received January 21, 2022; accepted after revision October 5.

From the Departments of Neuroradiology (S.E., H.U.) and Medical Physics, Functional Neurosurgery, and Stereotaxy (M.R.), Faculty of Medicine, Medical Center—University of Freiburg, Freiburg, Germany.

Please address correspondence to Samer Elsheikh, MD, Department of Neuroradiology, Breisacherstr 64, 79106 Freiburg im Breisgau, Germany; e-mail: samer.elsheikh@uniklinik-freiburg.de; @samerelsheikh

Indicates article with online supplemental data.

<http://dx.doi.org/10.3174/ajnr.A7700>

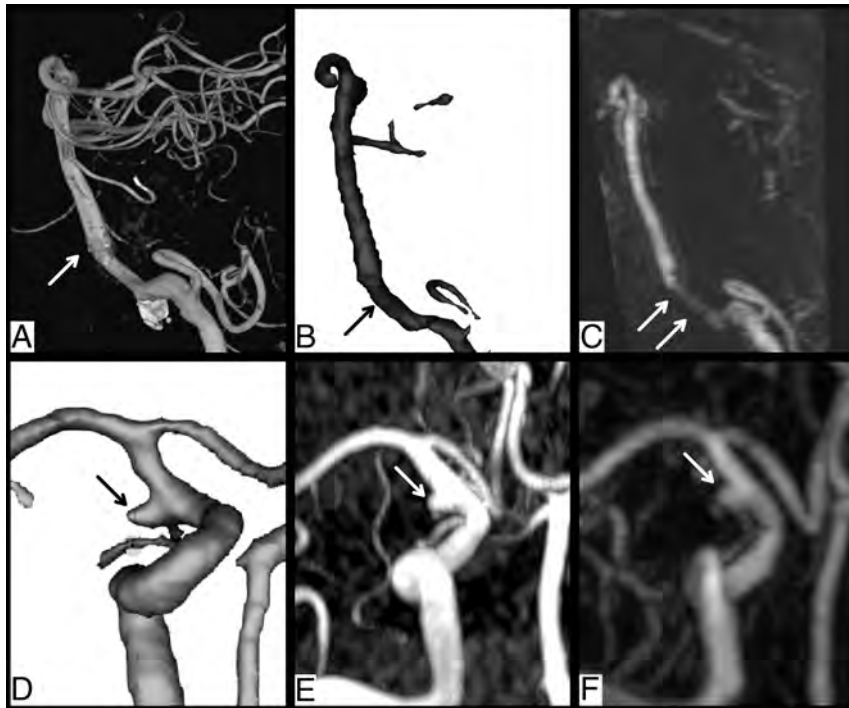


FIG 1. Sample images of advantageous findings. Identification of the vessel lumen following stent placement during treatment of a ruptured, dissecting aneurysm of the right vertebral artery in a test subject. A, 3D-rendering of rotational DSA in a lateral oblique projection following stent-assisted coiling (arrow, distal stent markers). B, Volume-rendering of the BBMRI model prediction (arrow, vessel lumen within the stent). C, Contrast-enhanced MRA shows partial signal degradation within the stent (arrows). D–F, Correct identification of a small recurrence (arrows) 6 months following coiling of a ruptured right posterior communicating artery aneurysm in a test subject. Volume-rendering in a coronal, oblique view of the BBMRI model prediction (D), of the TOF-MRA (E), and of the contrast medium-enhanced MRA (F).



FIG 2. Anterior-posterior 3D-rendering of the intracranial vessel tree. A, BBMRI model prediction. B, TOF-MRA. C, Contrast-enhanced MRA.

Illustrative Findings in Testing Data Set

Segmentation of the vessel lumen following stent-assisted coiling of a ruptured dissecting aneurysm of the right vertebral artery was possible. The corresponding contrast-enhanced MRA showed signal degradation in the corresponding segment (Fig 1A–C). In another example, a small recurrence following coiling of a ruptured right posterior communicating artery aneurysm was successfully segmented. The segmentation was comparable with that in the TOF-MRA and the contrast-enhanced MRA (Fig 1D–F; overview, Fig 2). We observed a consistent true-positive and true-negative segmentation of intracranial arterial and venous structures in the volume of interest (Online Supplemental Data).

False-negative results were encountered in small-diameter vessels and in the distal vertebral arteries. They were rarely

encountered in larger-diameter vessels. False-positive results were seen in areas showing low signal intensity in close proximity to the vessels, eg, metal artifacts following aneurysm clipping and in nearby bony structures (Online Supplemental Data).

Our model achieved Dice similarity coefficients (DSCs) of 0.77 and 0.72 in the training and testing data sets, respectively. The average evaluation metrics and corresponding plot are available in the Online Supplemental Data.

DISCUSSION

In this preliminary work, we demonstrate the feasibility of automated segmentation of the cerebral vasculature based on the negative contrast of the vessels in the non-contrast-enhanced BBMRI sequence. To our knowledge, this has not been previously attempted.

Qualitatively, vascular evaluation in the BBMRI is feasible. Differentiation between arterial and venous structures as well as recognition of morphologic changes (eg, aneurysm recurrence) were possible. Signal degradation following intracranial stent placement was not encountered (Fig 1 and Online Supplemental Data). The segmentation of smaller vessels and the distal vertebral arteries as well as the differentiation between vessels and nearby structures of low signal intensity (bony structures and aneurysm clips) were less accurate (Online Supplemental Data).

Quantitatively, our model achieved promising DSCs of 0.77 and of 0.72 in the training and testing data sets, respectively, indicating negligible overfitting. Our results are comparable with those of other TOF-based published works

using CNN or thresholding techniques (DSC, 0.73–0.78). A more complex segmentation pipeline achieved a better DSC, reaching 0.93.^{3,9,10}

A morphologic, flow-independent visualization of the cerebral vessels in the BBMRI has potential advantages. It avoids the flow-related artifacts and the stent-related signal degradation in TOF-MRA.^{11,12} The large FOV and the high resolution⁴ could allow segmentation of a large volume of interest. Furthermore, no application of contrast medium is required. Future prospects include further optimization of the machine learning parameters using a larger and more diverse data set, expanding the volume of interest, and testing performance in various intracranial pathologies.

CONCLUSIONS

CNN segmentation of the arteries of the circle of Willis and its branches in non-contrast-enhanced BBMRI with accuracy comparable with that of TOF-based segmentation techniques is feasible and promising.

Disclosure forms provided by the authors are available with the full text and PDF of this article at www.ajnr.org.

REFERENCES

1. Lesage D, Angelini ED, Bloch I, et al. **A review of 3D vessel lumen segmentation techniques: models, features and extraction schemes.** *Med Image Anal* 2009;13:819–45 CrossRef Medline
2. Ronneberger O, Fischer P, Brox T. **U-net: Convolutional networks for biomedical image segmentation.** In: Navab N, Hornegger J, Wells WM, et al, eds. *Medical Image Computing and Computer-Assisted Intervention—MICCAI 2015*. Springer; 2015:234–41
3. Cardoso MJ, Arbel T, Lee SL, et al, eds. *Intravascular Imaging and Computer Assisted Stenting, and Large-Scale Annotation of Biomedical Data and Expert Label Synthesis*. Springer; 2017 CrossRef
4. Guggenberger K, Krafft AJ, Ludwig U, et al. **High-resolution compressed-sensing T1 black-blood MRI.** *Clin Neuroradiol* 2021;31:207–16 CrossRef Medline
5. Xu Y, Gong M, Fu H, et al. **Multi-scale masked 3-D U-Net for brain tumor segmentation.** In: Xu Y, Gong M, Fu H, et al. *Brainlesion: Glioma, Multiple Sclerosis, Stroke and Traumatic Brain Injuries*. Springer; 2019:222–33 CrossRef
6. Kingma DP, Ba J. **Adam: A Method for Stochastic Optimization.** In: *Proceedings of the 3rd International Conference for Learning Representations*, San Diego, California. May 7–9, 2015
7. Taha AA, Hanbury A. **Metrics for evaluating 3D medical image segmentation: analysis, selection, and tool.** *BMC Med Imaging* 2015;15:29 CrossRef
8. Yeghiazaryan V, Voiculescu I. **Family of boundary overlap metrics for the evaluation of medical image segmentation.** *J Med Imaging (Bellingham)* 2018;5:015006 CrossRef Medline
9. Chen L, Xie Y, Sun J, et al. **3D intracranial artery segmentation using a convolutional autoencoder.** In: *Proceedings of the 2017 IEEE International Conference on Bioinformatics and Biomedicine (BIBM)*, Kansas City, Kansas. November 13–16, 2017 CrossRef
10. Zhang B, Liu S, Zhou S, et al. **Cerebrovascular segmentation from TOF-MRA using model- and data-driven method via sparse labels.** *Neurocomputing* 2020;380:162–79 CrossRef
11. Özsarlak Ö, Van Goethem JW, Maes M, et al. **MR angiography of the intracranial vessels: technical aspects and clinical applications.** *Neuroradiology* 2004;46:955–72 CrossRef Medline
12. Marciano D, Soize S, Metaxas G, et al. **Follow-up of intracranial aneurysms treated with stent-assisted coiling: comparison of contrast-enhanced MRA, time-of-flight MRA, and digital subtraction angiography.** *J Neuroradiol* 2017;44:44–51 CrossRef Medline

Association between Dural AVFs and Cerebral Venous Thrombosis

 L. Kuiper,  M. Sánchez van Kammen, B.A. Coert,  D. Verbaan, B.J. Emmer,  J.M. Coutinho, and  R. van den Berg



ABSTRACT

BACKGROUND AND PURPOSE: Recent reports suggest an association between dural AVFs and cerebral venous thrombosis. We aimed to investigate the specific temporal and anatomic association between the 2 conditions.

MATERIALS AND METHODS: A consecutive cohort of adult patients with dural AVFs was seen at Amsterdam University Medical Centers (2007–2020). An experienced neuroradiologist re-evaluated the presence and imaging characteristics of dural AVFs and cerebral venous thrombosis on all available imaging. The temporal (previous/concurrent/subsequent) and anatomic (same/adjacent/unrelated venous sinus or vein) association between dural AVFs and cerebral venous thrombosis was determined.

RESULTS: Among 178 patients with dural AVFs, the mean age was 58.3 (SD, 13.2) years and 85 (48%) were women. Of 55 patients (31%) with cerebral venous thrombosis, 34 (62%) were women. Four patients (7%) had cerebral venous thrombosis before the development of a dural AVF, 33 (60%) had cerebral venous thrombosis at the time of dural AVF diagnosis (concurrent), and 18 (33%) developed cerebral venous thrombosis during follow-up after conservative treatment. The incidence rate of cerebral venous thrombosis after a dural AVF was 79 per 1000 person-years (95% CI, 50–124). In 45 (82%) patients with dural AVFs and cerebral venous thrombosis, the thrombosis was located in the same venous sinus as the dural AVF, whereas in 8 (15%) patients, thrombosis occurred in a venous sinus adjacent to the dural AVF.

CONCLUSIONS: One-third of patients with a dural AVF in this study were diagnosed with cerebral venous thrombosis. In almost two-thirds of patients, cerebral venous thrombosis was diagnosed prior to or concurrent with the dural AVF. In 97% of patients, there was an anatomic association between the dural AVF and cerebral venous thrombosis. These data support the hypothesis of a bidirectional association between the 2 diseases.

ABBREVIATIONS: CVT = cerebral venous thrombosis; dAVF = dural AVF; IQR = interquartile range

Dural AVFs (dAVFs) account for only 10%–15% of intracranial vascular malformations,¹ with an estimated incidence rate of 0.15–0.29 cases per 100,000 person-years.^{2,3} In dAVFs, multiple arteriovenous shunts exist between the meningeal arteries and the intracranial venous system. The most common locations of dAVFs are the sigmoid, transverse, and cavernous sinuses. They may cause relatively benign symptoms such as tinnitus, headache, and dizziness, but in the presence of retrograde

flow to the cortical venous system, dAVFs can also cause venous hypertension and/or intracranial hemorrhage, leading to a variety of neurologic symptoms.⁴

Cerebral venous thrombosis (CVT) is a rare neurologic condition with an incidence rate of approximately 1.32 per 100,000 person-years (95% CI, 1.06–1.61).⁵ CVT is most frequently seen in adults younger than 50 years of age, and women are affected 3 times more often than men.^{6,7} Although the clinical presentation is variable, common symptoms include headache, seizures, focal neurologic deficits, and decreased consciousness.⁸

It is believed that CVT and dAVF have a bidirectional association: CVT can initiate the development of a dAVF, but a dAVF can also cause CVT.^{1,9} It has been suggested from animal model studies that venous hypertension, through increased levels of vascular endothelial growth factor, plays a key role in the development of dAVFs.^{10,11} Recent clinical studies and case reports have investigated the association between dAVF and CVT.^{12–14} In a cohort study of 69 patients with dAVF, 27 (39%) patients were

Received March 28, 2022; accepted after revision July 19.

From the Departments of Neurology (L.K., M.S.v.K., J.M.C.), Neurosurgery (B.A.C., D.V.), and Radiology and Nuclear Medicine (B.J.E., R.v.d.B.), Amsterdam University Medical Center, Amsterdam, the Netherlands.

L. Kuiper and M.S. van Kammen contributed equally to this work.

Please address correspondence to Ren  van den Berg, PhD, MSc, Department of Radiology and Nuclear Medicine, Amsterdam University Medical Center, Location AMC, Meibergdreef 9, 1105 AZ Amsterdam, the Netherlands; e-mail: r.vdberg@amsterdamumc.nl

 Indicates article with online supplemental data.

<http://dx.doi.org/10.3174/ajnr.A7652>



FIG 1. A 44-year-old woman presenting with pulsatile tinnitus due to a Cognard type I dAVF. Selective injection of the external carotid artery (A) shows supply from the middle meningeal artery to the dAVF. The sigmoid sinus shows irregularities due to postthrombotic changes with reopened vascular channels. The venous drainage of the brain (B) is unrestricted through the contralateral side.

diagnosed with CVT. Among patients with dAVF and CVT in this study, most of the dural sinuses affected by the CVT were directly connected to the dAVFs, indicating a possible spatial association between the 2 diseases.¹⁵ The temporal association between dAVF and CVT was not reported in this study. In contrast, another cohort study systematically screened 112 patients 6 months after acute CVT using MRA. The authors did not find any new dAVFs and, therefore, concluded that routine screening for dAVF 6 months after CVT is not recommended.¹⁶

The aim of this study was to assess the proportion of patients with dAVFs who had previous or concurrent CVT and to determine the incidence of a new CVT during follow-up in a large, consecutive cohort of patients with dAVF, regardless of treatment strategy. Additionally, we studied the anatomic association between CVT and dAVF in patients with both diagnoses.

MATERIALS AND METHODS

Data will be shared with academic researchers on reasonable request to the corresponding author.

Study Population and Study Design

We conducted a retrospective cohort study on all consecutive adult patients with a radiologically confirmed diagnosis of dAVF seen at the Amsterdam University Medical Centers (location AMC) between January 2007 and October 2020. Patients younger than 18 years of age with direct carotid-cavernous fistulas in whom baseline vascular imaging at the time of CVT or dAVF diagnosis was not available were excluded.

Ethics Approval

For this observational study, the Ethical Committee of the Amsterdam University Medical Centers waived the necessity for formal approval. In accordance with the General Data Protection

Regulation, all eligible patients received an information letter about the study with the option of refusing the use of their pseudonymized care data.

Data Collection

Data on demographics, clinical signs and symptoms at the time of dAVF diagnosis, CVT risk factors, and functional outcome were obtained from the electronic medical records. Functional outcome at the last follow-up visit was retrospectively assessed using the mRS.¹⁷

An experienced interventional neuroradiologist (R.v.d.B.) re-evaluated all available brain imaging including CTA, MRA, and DSA until the last follow-up for the hemorrhage, CVT, dAVF location, Cognard classification,¹⁸ date of dAVF diagnosis, and type of dAVF treatment. With respect to dAVF diagnosis and classification and CVT diagnosis, the findings after re-evaluation were compared with the original radiology report. Treatment of the dAVF was categorized into conservative treatment, endovascular treatment (transarterial or transvenous), neurosurgical treatment, stereotactic radiosurgery, or a combination of therapies. If a patient had multiple dAVFs, each dAVF was assessed separately. In addition, all available neuroimaging was re-evaluated for the presence of previous, concurrent, or subsequent CVT, regardless of the presence of symptoms suspicious for CVT. CVT was defined as acute or subacute when a filling defect was visible in the venous sinus, cortical or superior ophthalmic vein, or as chronic when the appearance of the sinus on vascular imaging showed no flow or was irregular with residual defects in the lumen of the venous sinus or the presence of vascular channels (Fig 1).¹⁹

Evaluation of Temporal and Anatomic Relation

For patients who were diagnosed with CVT, the location of the thrombosis and the temporal and anatomic association between

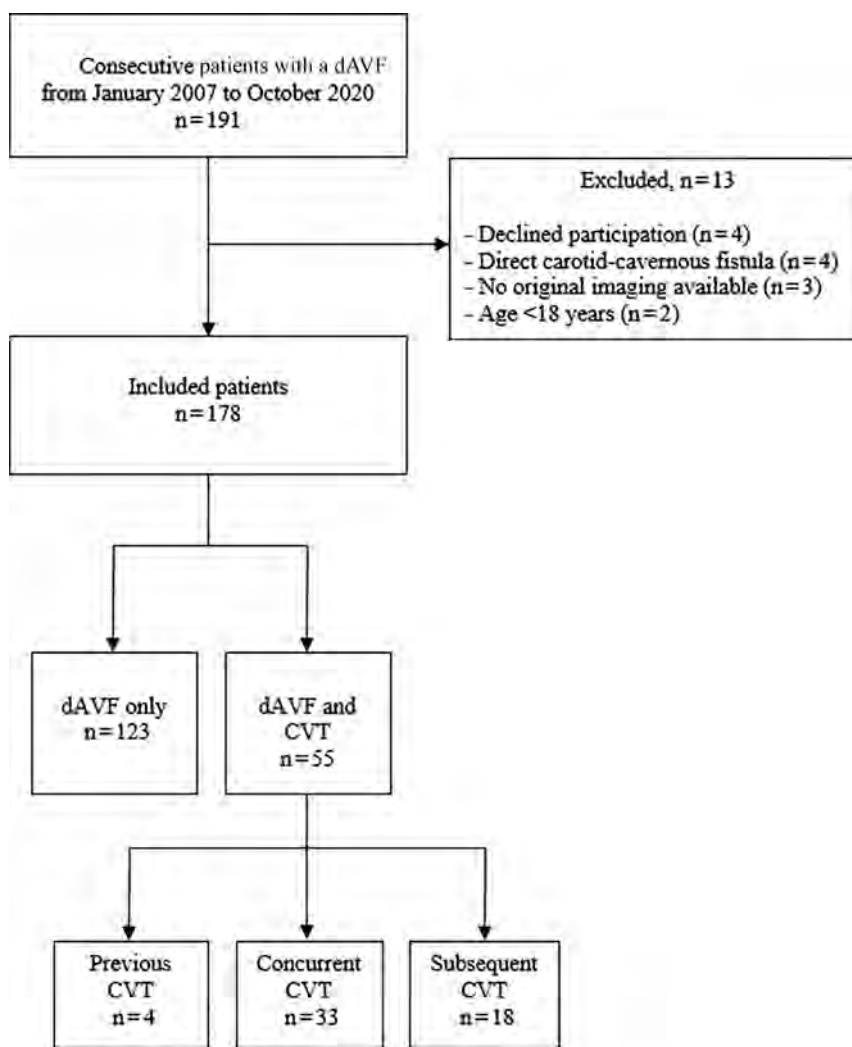


FIG 2. Flow chart showing patient cohort.

CVT and dAVF were assessed. The time of the CVT diagnosis relative to the dAVF diagnosis was classified into 1 of 3 main categories: 1) imaging-proved CVT diagnosis before the dAVF diagnosis, 2) CVT diagnosis concurrent with the dAVF diagnosis without prior imaging to assess the sequence of events, and 3) CVT diagnosis after the dAVF diagnosis. The third category was further subdivided into following dAVF treatment and following conservative management of the dAVF.

The spatial anatomic association between the CVT and the dAVF was categorized as having a probable, possible, or unlikely association. These associations are defined as follows: 1) probable, if the dAVF and CVT were located in the same venous sinus or vein, 2) possible, if CVT occurred directly up- or downstream in the adjacent venous sinus or vein in spatial association with the dAVF, or 3) unlikely, if there was no anatomic association. If thrombosis was present in multiple sinuses or veins or if multiple dAVFs were present, an anatomic association was considered probable or possible if at least one of the thrombosed sinuses or veins met the applicable criteria.

Statistical Analysis

Categorical data are shown as frequencies and proportions, and non-normally distributed continuous data (defined as the Shapiro-Wilk statistic of <0.9), as medians with interquartile ranges (IQRs). The Fisher exact test was used to compare categorical variables for patients with dAVFs with and without CVT. A P value of $<.05$ was considered statistically significant. We calculated the incidence rate (with 95% CI) of CVT after a dAVF diagnosis per 1000 person-years. For this calculation, we included only patients with dAVFs who did not have a previous diagnosis of CVT or a concurrent CVT at the time of the dAVF diagnosis.

RESULTS

Patient Selection

Of 191 eligible patients, a total of 178 patients were included in the study. Four patients declined participation, and 2 patients were excluded because they were younger than 18 years of age at the time of the dAVF diagnosis. Four patients were excluded because they had a direct carotid-cavernous fistula, and 3 referred patients were excluded because the initial cross-sectional imaging at the time of the dAVF diagnosis was not available for re-evaluation (Fig 2).

Table 1 provides an overview of the baseline patient characteristics at the time of the dAVF diagnosis. There was a female predominance in the dAVF

and CVT group compared with the dAVF-only group (62% versus 42%, $P = .010$). The mean age was similar in both groups.

Imaging Findings

Of the 178 included patients, 55 patients (31%) showed signs of CVT. In 11 of these 55 patients (20%), the diagnosis of CVT was made after re-evaluation of the imaging. In all 11 patients, CVT-related abnormalities were only visible on DSA.

In 33 (60%) patients with dAVF and CVT, signs of recent or past CVT (with or without partial recanalization) were visible as concurrent findings when the diagnosis of dAVF was made on imaging. Subacute or acute CVT was seen in 4 patients; all CVTs were localized to the superior ophthalmic vein in cavernous sinus dAVF locations. In addition, 29 patients showed signs of chronic thrombosis, in which the sinus was either completely occluded or partially occluded with reopened vascular channels. Only 4 patients (7%) had a confirmed history of CVT before the dAVF diagnosis (Fig 3). Finally, CVT developed secondary to the dAVF in an additional 18 patients (33%) during a median follow-up of

Table 1: Baseline characteristics at time of dAVF diagnosis

	All Patients (n = 178)	dAVF and CVT (n = 55)	dAVF Only (n = 123)
Clinical features			
Women (n/N) (%)	85/178 (48)	34/55 (62)	51/123 (42)
Median age (IQR) (yr)	59.0 (49–67)	58.5 (49–68)	60.0 (49–67)
Asymptomatic	8/178 (4)	0/55	8/123 (7)
Tinnitus	90/176 (51)	30/54 (56)	60/122 (49)
Headache	87/177 (49)	27/55 (49)	60/122 (49)
Ocular symptoms	60/177 (34)	19/55 (35)	41/121 (34)
Focal neurologic deficit	42/177 (24)	14/55 (13)	28/122 (23)
Dizziness	28/176 (16)	7/55 (13)	21/121 (17)
Gait disturbances	16/176 (9)	2/55 (4)	14/121 (12)
Seizures	10/176 (6)	7/55 (13)	3/121 (3)
Cranial nerve deficit	14/177 (8)	2/55 (4)	12/122 (10)
Hearing loss	9/176 (5)	3/54 (6)	6/122 (5)
Thrombotic risk factors (n/N) (%)			
Traumatic head injury	29/176 (16)	10/54 (19)	19/122 (16)
Head or neck infection	13/177 (7)	2/54 (4)	11/123 (9)
Active cancer (treatment <6 months or distant metastases)	5/174 (3)	1/53 (2)	4/121 (3)
Previous thromboembolism	6/99 (6)	2/29 (7)	4/70 (6)
OAC use (at time of diagnosis) ^a	4/81 (5)	3/31 (10)	1/50 (2)
Hormone replacement therapy (at time of diagnosis) ^a	4/81 (5)	1/31 (3)	3/50 (6)
Pregnancy or postpartum (<12 weeks) ^a	2/83 (2)	1/33 (3)	1/50 (2)
Obesity (BMI >30 kg/m ²)	19/123 (15)	5/41 (12)	14/82 (17)
Immobility (≥4 days)	1/173 (1)	0/52	1/121 (1)

Note:—OAC indicates oral contraceptive; BMI, body mass index.

^aProportions of female patients.

9 months (IQR = 5–24 months). In 11 of 18 patients, CVT occurred after dAVF treatment in the affected sinus or vein. In the other 7 patients (13%), spontaneous occlusion of the dAVF was seen during conservative management. Of these 7 dAVFs, 6 were located at the cavernous sinus region with drainage into the superior ophthalmic vein. Of the treated patients with development of thrombosis, 3 patients (3%) presented with a headache. None of these treated patients with de novo thrombosis had a history of CVT. The incidence rate of CVT after dAVF diagnosis was 79 per 1000 person-years (95% CI, 50–124).

Patients with CVT more often presented with seizures at the time of dAVF diagnosis (13% versus 3%, $P = .014$). There was no difference in the presence of thrombotic risk factors between the 2 groups. No significant difference in the hemorrhage rate was seen between the dAVF-only group compared with dAVF and CVT groups (18/123 patients versus 4/55 patients, $P = .084$).

No changes in the diagnosis or grading of the dAVF were recorded between the original report and findings after re-evaluation. A total of 17 (10%) patients presented with multiple dAVFs (Online Supplemental Data). The most common dAVF locations in the dAVF and CVT group were the lateral sinus (64%) and the cavernous sinus (22%, Online Supplemental Data). In the dAVF-only group, the dAVF was most frequently located in the cortical veins (30%) and the lateral sinus (22%).

Cognard classifications and treatment of the dAVFs are outlined in Table 2. Overall, 178 patients had a total of 201 dAVFs, including 86 (48%) benign (Cognard I and IIa) and 115 (65%) aggressive (Cognard IIb and more) dAVFs. The most frequent dAVF location was the sigmoid and transverse (lateral) sinuses. Among the 59 patients with CVT, a total 73 dAVFs were seen, 37 (51%) classified as Cognard I/IIa, and 11 (15%), as Cognard >III.

Among the 119 patients with dAVF-only (no CVT), a total of 128 dAVF were seen, 49 (38%) classified as Cognard I/IIa and 64 (50%) as Cognard >III. Four of 40 patients (10%) with a Cognard IIb or IIa–b classification presented with a hemorrhage; all had CVT. Three of 4 patients had a parenchymal hematoma; all 3 had concurrent CVT. The other patient presented with an SAH due to a ruptured ectatic venous pouch (Cognard IV) and developed progressive thrombosis of the draining vein after treatment. Eighteen of 75 patients (24%) with a Cognard III or more classification presented with a hemorrhage; only 1 of these 18 patients had concurrent CVT. In both groups, endovascular embolization was the most frequent treatment, followed by conservative treatment. Spontaneous occlusion of the dAVF occurred in 23 of 61 (38%) conservatively treated patients. In 7 of these patients, thrombosis of the anatomically linked draining vein or sinus was seen. A higher rate of spontaneous dAVF thrombosis was found among patients with a dAVF in the cavernous sinus (40%) compared with a dAVF in all other locations (9%).

Among the 55 patients with a dAVF and CVT, thrombosis was most frequently seen in the sigmoid (51%) and transverse sinuses (47%; Online Supplemental Data). Most patients with multiple CVT locations had thrombosis in both the sigmoid and transverse sinuses. Table 3 outlines the anatomic and temporal association between dAVF and CVT. Thrombosis in the venous system after treatment (Table 3) was seen after complete occlusion in 4 of 11 patients and after partial occlusion in 7 patients. In 45 (82%) patients, CVT occurred in the same venous sinus as the dAVF (probable anatomic relation). In only 2 (4%) patients was no anatomic association found. The Online Supplemental Data show the clinical presentation in patients who developed CVT during follow-up (after intervention or conservative treatment of

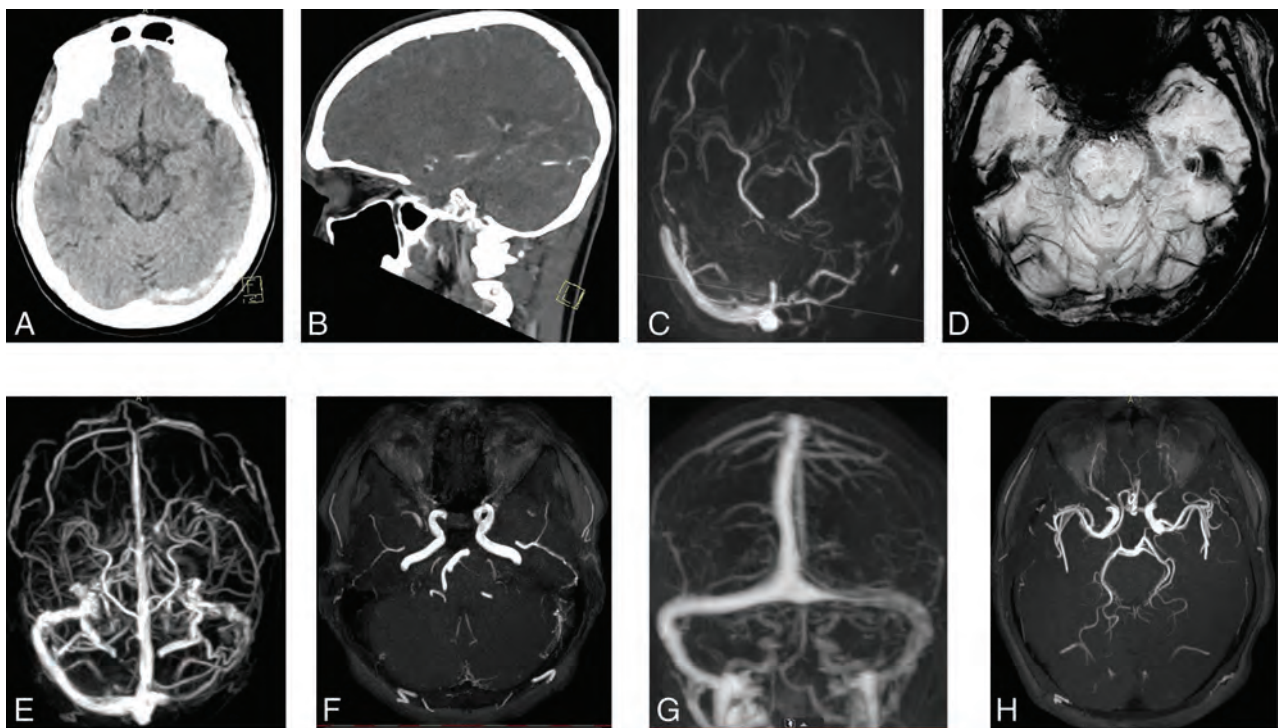


FIG 3. A 19-year-old man with a history of alpha-thalassemia type 2, a carrier of sickle cell disease and ulcerative colitis, underwent imaging because of relapsing headaches. Noncontrast CT shows hyperdensity in the left transverse sinus (A). Sinus thrombosis is confirmed on CT venography (B). One week later, phase-contrast MR venography shows absent flow in the left transverse and sigmoid sinuses without signs of arterIALIZATION of the sinuses (C). Persistent thrombosis of the sinus is depicted on SWI (D). Six months later, the patient presented with a pulsatile tinnitus; repeat MR imaging shows partial reopening of the sigmoid sinus (E) but also reveals a dAVF at the left sigmoid sinus (F). One year later, dynamic contrast-enhanced MRA (G) shows restoration of sinus flow and spontaneous obliteration of the dAVF (H).

the dAVF). Five of 11 patients (46%) who developed CVT following dAVF treatment were asymptomatic. Headache and ocular symptoms were the most common presenting symptoms of subsequent CVT in conservatively treated patients, the latter mostly related to cavernous sinus locations.

Clinical Outcome

The median time from dAVF diagnosis until the last available follow-up was 9 months in both the dAVF and CVT (IQR = 5–24 months) and dAVF-only (IQR = 5–23 months) groups. None of the included patients had died at last follow-up, and most patients (44 [80%] versus 91 [74%] in the dAVF and CVT and dAVF-only groups, respectively) were functionally independent (mRS 0–2). Figure 4 outlines the mRS scores at last follow-up for patients with a dAVF with and without CVT with benign and aggressive dAVFs, respectively. Functional independence (mRS 0–2) was seen in 89% of the patients with a benign dAVF, compared with 69% of the patients with an aggressive dAVF. Of 22 patients with an aggressive dAVF presenting with a hemorrhage, 14 (64%) had a favorable outcome and 8 had an unfavorable outcome.

DISCUSSION

In this cohort study of 178 consecutive patients with dAVFs, approximately 1 in 3 patients had a previous, concurrent, or subsequent diagnosis of CVT. We found both an anatomic and temporal association between dAVF and CVT. In most patients, CVT

was located in the same sinus as the dAVF, and in more than half of patients, CVT and dAVF were diagnosed concurrently.

Several studies have proposed potential mechanisms to explain the association between dAVF and CVT. First, CVT may cause a dAVF due to the angiogenetic activity induced by decreased cerebral perfusion secondary to venous hypertension or by enlarging pre-existing arteriovenous shunts due to elevated venous pressure.^{9,10} This mechanism has been demonstrated in several animal model studies.^{10,11,20,21} It can be postulated that the extent of the thrombosis determines the behavior of the dAVF: A more severe thrombosis increases the risk of corticovenous reflux when sinus outflow is no longer available. On the other hand, a dAVF may also precede CVT, especially when the dAVF shows spontaneous occlusion. This sequence of events was confirmed in this study in conservatively managed patients. The proposed mechanism is that venous hypertension and venous stasis caused by dAVFs may cause secondary thrombosis.¹ A second possible mechanism is that during the development of a dAVF, the sinus wall thickens, possibly causing stenosis and eventually inducing CVT.²²

Previous studies have found venous thrombotic risk factors to be associated with dAVF development.^{23–26} This finding is inconsistent with our finding that there were no major differences in the occurrence of risk factors for the development of thrombosis in the dAVF-only group compared with the dAVF and CVT group. Our findings are limited because we did not routinely test for inherited or acquired thrombophilia such as Factor V Leiden or elevated homocysteine levels, but these are well-known risk factors.²³

Table 2: dAVF characteristics

	All Patients (n = 178)	dAVF and CVT (n = 55) ^a	dAVF Only (n = 123) ^b
Cognard dAVF classification (n/N) (%)			
Benign			
I	58/178 (33)	23/55 (42)	35/123 (28)
Ila	28/178 (16)	12/55 (22)	16/123 (13)
Aggressive			
Ilb	25/178 (14)	16/55 (29)	9/123 (7)
Ila+b	15/178 (8)	8/55 (15)	7/123 (6)
III	33/178 (19)	6/55 (11)	27/123 (22)
IV	40/178 (22)	4/55 (7)	36/123 (29)
V	2/178 (1)	0/55	2/123 (2)
dAVF treatment type (n/N) (%)			
Conservative	61/178 (34)	42/55 (39)	38/123 (31)
Endovascular only	113/178 (63)	36/55 (65)	77/123 (63)
Surgical resection only	8/178 (4)	2/55 (4)	6/123 (5)
Endovascular + surgical resection	14/178 (8)	5/55 (9)	9/123 (7)
Endovascular + surgical resection + stereotactic radiation therapy	2/178 (1)	2/55 (4)	0/123

^a Eight patients had 2 dAVFs, 1 patient had 3 dAVFs, and 1 patient had 5 dAVFs.

^b Six patients had 2 dAVFs, and 1 patient had 4 dAVFs.

Table 3: CVT characteristics among patients with dAVF and CVT diagnoses

	dAVF and CVT (n = 55)
Anatomic association of dAVF and CVT (n/N) (%)	
Probable ^a	45/55 (82)
Possible ^b	8/55 (15)
Unlikely ^c	2/55 (4)
Time correlation of dAVF and CVT (n/N) (%)	
Previous CVT	4/55 (7)
Concurrent CVT	33/55 (60)
Subsequent CVT	18/55 (33)
Following dAVF treatment	11/55 (20)
Following conservative dAVF treatment	7/55 (13)

^a dAVF and CVT located at the same venous sinus.

^b CVT located up- or downstream of the dAVF, but not in the same venous sinus.

^c No anatomic association.

In our study, 21% of all patients with dAVFs had previous or concurrent CVT. The incidence rate of CVT during follow-up was 7900 per 100,000 person-years (95% CI, 5000–12,400) in our study versus 1.32 per 100,000 person-years (95% CI, 1.06–1.61) in the general population.⁵ With a low incidence of dAVF in the population of 0.15–0.29 cases per 100,000 person-years,^{2,3} besides management of the dAVF, patient care should also focus on CVT risk factors. Thus, the association between dAVF and CVT is more pronounced in patients primarily presenting with a dAVF than in patients presenting initially with CVT. The finding that CVT both precedes and is seen during follow-up of dAVF supports the hypothesis of a bidirectional association between the 2 diseases, and clinicians should be vigilant for CVT among patients with dAVFs. This advice is especially important when the dAVF-affected sinus is occluded for treatment purposes because future contralateral sinus thrombosis can then be a clinically devastating event. Moreover, our data show that the diagnosis of CVT is easily missed on CT and/or MR imaging. Especially in this population at risk for CVT, it is important to look for changes in the venous system on DSA that might indicate previous thrombosis. A clinical clue to CVT in patients with a dAVF is when they present with or have a history of seizures.²⁷

Our finding that CVT was most often located in the same or adjacent venous sinus as the dAVF is in line with a previous cohort study of 69 patients with dAVFs.¹⁵ The proportion of patients with dAVFs who had CVT was also similar in our cohort compared with previous cohort studies.^{15,28} In contrast, the proportion of patients with CVT who had a previous or concurrent dAVF is reported to be only around 1.6%–2.4%.^{14,29} On the contrary, from another prospective study, no patients with CVT developed a dAVF during follow-up when screened after 6 months.¹⁶

We propose that the temporal association between dAVF and CVT might at least be partially location-dependent with a preference for the sigmoid and transverse sinuses and also the cavernous sinus. Progressive occlusion of a dAVF with thrombosis of the venous outlet was more often seen in patients with dAVFs in the cavernous sinus region compared with dAVFs in other locations in our study. This finding might be related to the anatomic disposition of the superior ophthalmic vein, which serves as a major drainage route in most of these dAVFs and has to pass the orbital septum. Because of narrowing of the vein at the orbital septal junction, it can be hypothesized that the focal venous outflow restriction promotes the thrombotic process.

At the last follow-up assessment, most patients in our study had an mRS score of 0–2. In a previous study of 40 patients with dAVFs (including 13 patients with carotid-cavernous fistulas), an mRS score of 0–2 was found in 91% of patients after a mean follow-up of 6.2 years (range, 0.7–14.8 years, with 20% lost to follow-up).³⁰ Although the reason for this difference in functional outcome between our study and the previous study is not entirely clear, our results seem to indicate the important burden of residual symptoms among patients with dAVFs. Further research to better identify

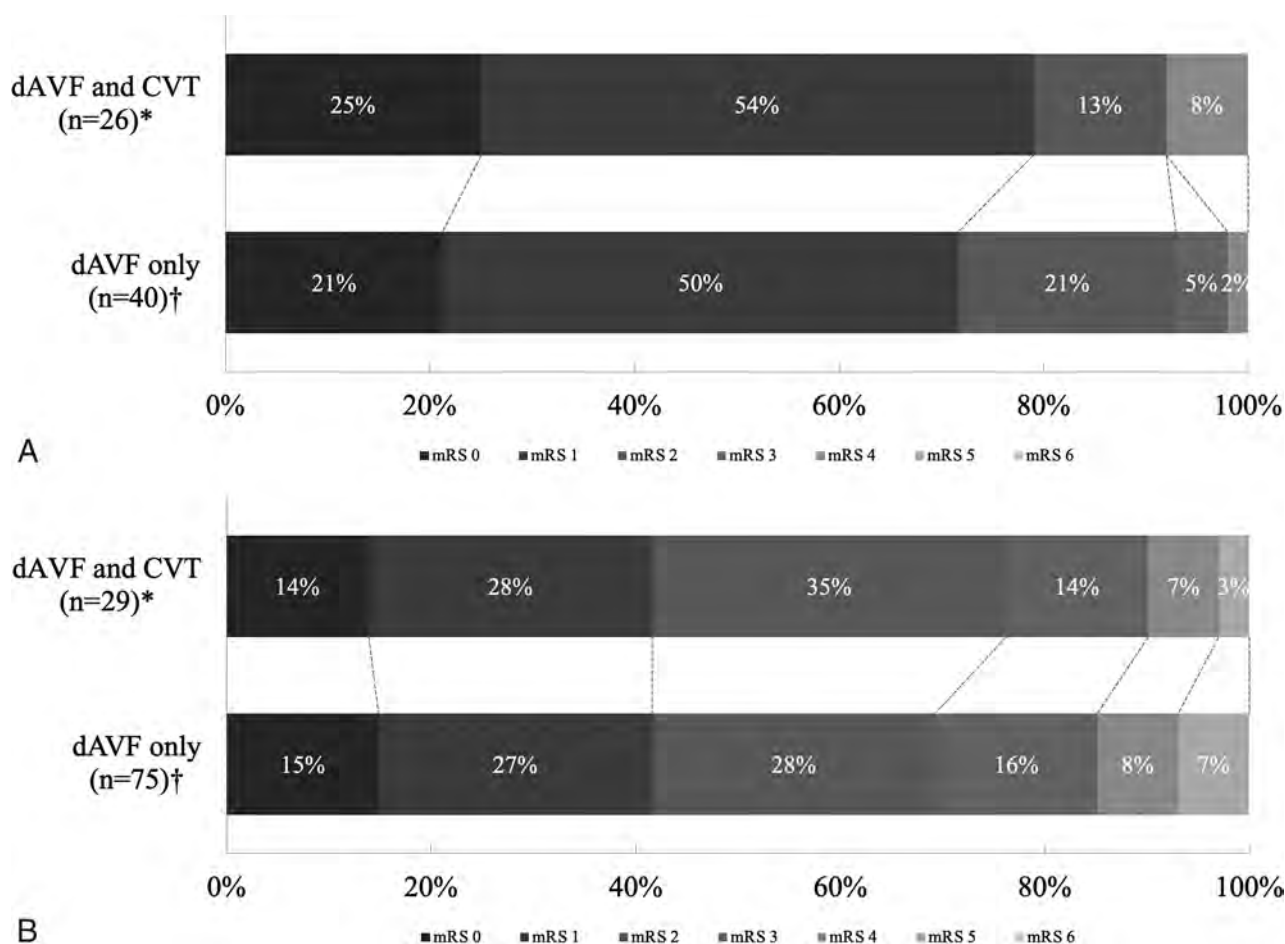


FIG 4. A, Last available mRS score in patients with benign dAVFs. Asterisk indicates median follow-up time 16 months (IQR 7–29). There were no patients with mRS 3, 5, or 6. Dagger indicates median follow-up time 9 months (IQR 2–21). There were no patients with mRS 5 or 6. B, Last available score mRS in patients with aggressive dAVFs. Asterisk indicates median follow-up time 8 months (IQR 5–20). There were no patients with mRS 6. Dagger indicates median follow-up time 10 months (IQR 7–27). There were no patients with mRS 6.

optimal treatment strategies for individual patients with dAVF is thus warranted.

To our knowledge, this is the first study to investigate both the anatomic and temporal association between dAVF and CVT in a large cohort of consecutive patients with dAVFs. In all patients, brain imaging was re-evaluated by an experienced interventional neuroradiologist for this study to increase the reliability and validity of image interpretation. Several limitations warrant comment, however. First, due to the retrospective study design, data on several CVT risk factors (such as oral contraceptive use) were missing in a considerable proportion of patients. Second, patients with a benign dAVF and relatively benign symptoms (eg, tinnitus) who did not require treatment were usually discharged from follow-up. This limited follow-up time for some patients may have both biased our estimate of the incidence rate of CVT during follow-up and limited our functional-outcome assessment. Third, most patients with dAVFs underwent routine follow-up imaging, which increased the chance of incidentally finding asymptomatic CVT. This is supported by our finding that nearly half (44%) of the patients who developed CVT during follow-up had asymptomatic CVT.

CONCLUSIONS

CVT occurred in 31% of patients with dAVFs either initially or during follow-up. In 82% of cases, there was an anatomic relation between the dAVF and CVT. These data support the hypothesis of a bidirectional association between the 2 diseases.

Disclosure forms provided by the authors are available with the full text and PDF of this article at www.ajnr.org.

REFERENCES

- Wilson M, Enevoldson P, Menezes B. Intracranial dural arterio-venous fistula. *Pract Neurol* 2008;8:362–69 CrossRef Medline
- Al-Shahi R, Bhattacharya JJ, Currie DG, et al. Scottish Intracranial Vascular Malformation Study (SIVMS): evaluation of methods, ICD-10 coding, and potential sources of bias in a prospective, population-based cohort. *Stroke* 2003;34:1156–62 CrossRef
- Kuwayama N. Epidemiologic survey of dural arteriovenous fistulas in Japan: clinical frequency and present status of treatment. *Acta Neurochir Suppl* 2016;123:185–88 CrossRef Medline
- Padiilha IG, Pacheco FT, Araujo AI, et al. Tips and tricks in the diagnosis of intracranial dural arteriovenous fistulas: a pictorial review. *J Neuroradiol* 2020;47:369–81 CrossRef Medline

5. Coutinho JM, Zuurbier SM, Aramideh M, et al. **The incidence of cerebral venous thrombosis: a cross-sectional study.** *Stroke* 2012;43:3375–77 CrossRef Medline
6. Bushnell C, Saposnik G. **Evaluation and management of cerebral venous thrombosis.** *Continuum (Minneapolis Minn)* 2014;20:335–51 CrossRef Medline
7. Zuurbier SM, Middeldorp S, Stam J, et al. **Sex differences in cerebral venous thrombosis: a systematic analysis of a shift over time.** *Int J Stroke* 2016;11:164–70 CrossRef Medline
8. Boussier MG, Ferro JM. **Cerebral venous thrombosis: an update.** *Lancet Neurol* 2007;6:162–70 CrossRef Medline
9. Gandhi D, Chen J, Pearl M, et al. **Intracranial dural arteriovenous fistulas: classification, imaging findings, and treatment.** *AJNR Am J Neuroradiol* 2012;33:1007–13 CrossRef Medline
10. Kojima T, Miyachi S, Sahara Y, et al. **The relationship between venous hypertension and expression of vascular endothelial growth factor: hemodynamic and immunohistochemical examinations in a rat venous hypertension model.** *Surg Neurol* 2007;68:277–84; discussion 84 CrossRef Medline
11. Wang SS, Li CH, Zhang XJ, et al. **Investigation of the mechanism of dural arteriovenous fistula formation induced by high intracranial venous pressure in a rabbit model.** *BMC Neurosci* 2014;15:101 CrossRef Medline
12. Johansen M, Southerland A, Worrall B. **Analysis of concurrent cerebral venous thrombosis and dural arteriovenous fistula (P1.008).** *Neurology* 2015;84(14 Suppl):P1.008
13. Kang MK, Cho YD, Kang HS, et al. **Development of a dural arteriovenous fistula subsequent to cerebral venous thrombosis by venous hypertension.** *eNeurologicalSci* 2019;14:24–27 CrossRef Medline
14. Lindgren E, Rentzos A, Hiltunen S, et al; International CVT Consortium. **Dural arteriovenous fistulas in cerebral venous thrombosis: data from the International Cerebral Venous Thrombosis Consortium.** *Eur J Neurol* 2022;29:761–70 CrossRef
15. Tsai LK, Jeng JS, Liu HM, et al. **Intracranial dural arteriovenous fistulas with or without cerebral sinus thrombosis: analysis of 69 patients.** *J Neurol Neurosurg Psychiatry* 2004;75:1639–41 CrossRef Medline
16. Ferro JM, Coutinho JM, Jansen O, et al; RE-SPECT CVT Study Group. **Dural arteriovenous fistulae after cerebral venous thrombosis.** *Stroke* 2020;51:3344–47 CrossRef Medline
17. van Swieten JC, Koudstaal PJ, Visser MC, et al. **Interobserver agreement for the assessment of handicap in stroke patients.** *Stroke* 1988;19:604–07 CrossRef Medline
18. Cognard C, Gobin YP, Pierot L, et al. **Cerebral dural arteriovenous fistulas: clinical and angiographic correlation with a revised classification of venous drainage.** *Radiology* 1995;194:671–80 CrossRef Medline
19. Canedo-Antelo M, Baleato-González S, Mosqueira AJ, et al. **Radiologic clues to cerebral venous thrombosis.** *Radiographics* 2019;39:1611–28 CrossRef Medline
20. Chen L, Mao Y, Zhou LF. **Local chronic hypoperfusion secondary to sinus high pressure seems to be mainly responsible for the formation of intracranial dural arteriovenous fistula.** *Neurosurgery* 2009;64:973–83; discussion 983 CrossRef Medline
21. Lawton MT, Jacobowitz R, Spetzler RF. **Redefined role of angiogenesis in the pathogenesis of dural arteriovenous malformations.** *J Neurosurg* 1997;87:267–74 CrossRef Medline
22. Hamada Y, Goto K, Inoue T, et al. **Histopathological aspects of dural arteriovenous fistulas in the transverse-sigmoid sinus region in nine patients.** *Neurosurgery* 1997;40:452–56; discussion 56–58 CrossRef Medline
23. Aiello G, Rinaldo L, Marshall AL, et al. **Incidence of hereditary thrombophilia in patients with cranial dural arteriovenous fistulae.** *J Clin Neurosci* 2020;73:136–39 CrossRef Medline
24. Gerlach R, Boehm-Weigert M, Berkefeld J, et al. **Thrombophilic risk factors in patients with cranial and spinal dural arteriovenous fistulae.** *Neurosurgery* 2008;63:693–99; discussion 698–99 CrossRef
25. Gerlach R, Yahya H, Rohde S, et al. **Increased incidence of thrombophilic abnormalities in patients with cranial dural arteriovenous fistulae.** *Neurol Res* 2003;25:745–48 CrossRef Medline
26. Liang H, Xu C, Xu J. **Cerebral venous sinus thrombosis and dural arteriovenous fistula associated with protein S deficiency: a case series study.** *BMC Neurol* 2022;22:164 CrossRef Medline
27. Sanchez van Kammen M, Lindgren E, Silvius SM, et al. **Late seizures in cerebral venous thrombosis.** *Neurology* 2020;95:e1716–23 CrossRef
28. Yeh SJ, Tsai LK, Liu HM, et al. **Ischemic stroke in patients with intracranial dural arteriovenous fistulas.** *J Formos Med Assoc* 2011;110:299–305 CrossRef Medline
29. Ferro JM, Canhao P, Stam J, et al; ISCVT Investigators. **Prognosis of cerebral vein and dural sinus thrombosis: results of the International Study on Cerebral Vein and Dural Sinus Thrombosis (ISCVT).** *Stroke* 2004;35:664–70 CrossRef Medline
30. Corbelli I, De Maria F, Eusebi P, et al. **Dural arteriovenous fistulas and headache features: an observational study.** *J Headache Pain* 2020;21:6 CrossRef

Mechanical Thrombectomy for the Treatment of Anterior Cerebral Artery Occlusion: A Systematic Review of the Literature

 N. Dabhi,  P. Mastorakos,  J. Sokolowski,  R.T. Kellogg, and  M.S. Park



ABSTRACT

BACKGROUND: The overall safety and efficacy of mechanical thrombectomy for anterior cerebral artery strokes remain unclear.

PURPOSE: Our aim was to summarize procedural and clinical outcomes in patients who underwent mechanical thrombectomy for treatment of anterior cerebral artery ischemic stroke.

DATA SOURCES: A systematic literature review was performed using PubMed, Ovid MEDLINE, and the Web of Science from inception until March 4, 2022.

STUDY SELECTION: We identified 9 studies with a total of 168 patients with mechanical thrombectomy–treated anterior cerebral artery occlusions.

DATA ANALYSIS: Recanalization, procedural data, and clinical outcome at last follow-up were collected and summarized. Categorical variables were reported as proportions. The χ^2 test of independence or the Kruskal-Wallis test was performed to assess the relationship between selected variables and the anterior cerebral artery embolus type (ie, primary isolated anterior cerebral artery, primary combined anterior cerebral artery, and secondary anterior cerebral artery occlusion) or the mechanical thrombectomy technique.

DATA SYNTHESIS: For mechanical thrombectomy–treated anterior cerebral artery occlusions, recanalization modified TIC1 2b/3 was achieved in 80%, postprocedural complications occurred in 17% of patients, and the 90-day mortality rate was 19%. The rate of symptomatic intracranial hemorrhage varied depending on the anterior cerebral artery embolus type ($\chi^2 = 8.45$, $P = .01$).

LIMITATIONS: This analysis did not consider factors such as small-study effects that affect reliability and limit interpretation.

CONCLUSIONS: Mechanical thrombectomy for the treatment of anterior cerebral artery occlusions is safe and efficacious, offering a favorable rate of recanalization and procedural complications. Mechanical thrombectomy–treated anterior cerebral artery occlusions appear to have lower rates of short-term good functional outcomes and an increased risk of symptomatic intracerebral hemorrhage compared with mechanical thrombectomy–treated MCA/ICA occlusions. Single and multicenter studies are needed to further examine the safety and efficacy of mechanical thrombectomy–treated anterior cerebral artery occlusions.

ABBREVIATIONS: ACA = anterior cerebral artery; ICH = intracerebral hemorrhage; MT = mechanical thrombectomy; mTIC1 = modified TIC1

Strokes of the anterior cerebral artery (ACA) and its branches account for up to 4.4% of ischemic strokes.¹ Although patients presenting with acute occlusion of the ACA can have varied presentations, in up to 90% of patients, motor deficits typically


involving the lower extremity contralateral to infarct location are present.^{1,2} ACA strokes have been associated with disability after discharge due to the resultant motor, cognitive, and behavioral impairments.^{1,3} In-hospital mortality from isolated ACA territory infarct has been reported to be 8%.^{1,2} Additionally, emboli in the ACA territory may occur secondary to endovascular treatment involving other territories, leading to increased risk of hemorrhagic complications and mortality, despite successful reperfusion.^{1,2}

While mechanical thrombectomy (MT) has been established as safe and highly effective in the treatment of thromboembolic occlusion of the MCA, ICA, and basilar artery, the safety and efficiency of MT for the treatment of acute ACA occlusions have not

Received August 9, 2022; accepted after revision September 27.

From the Department of Neurosurgery, University of Virginia Health System, Charlottesville, Virginia.

Please address correspondence to Panagiotis Mastorakos, MD, PhD, Box 800212, Department of Neurosurgery, University of Virginia Health System, Charlottesville, VA 22908; e-mail: Panagiotis.mastorakos@gmail.com

 Indicates article with online supplemental data.

<http://dx.doi.org/10.3174/ajnr.A7690>

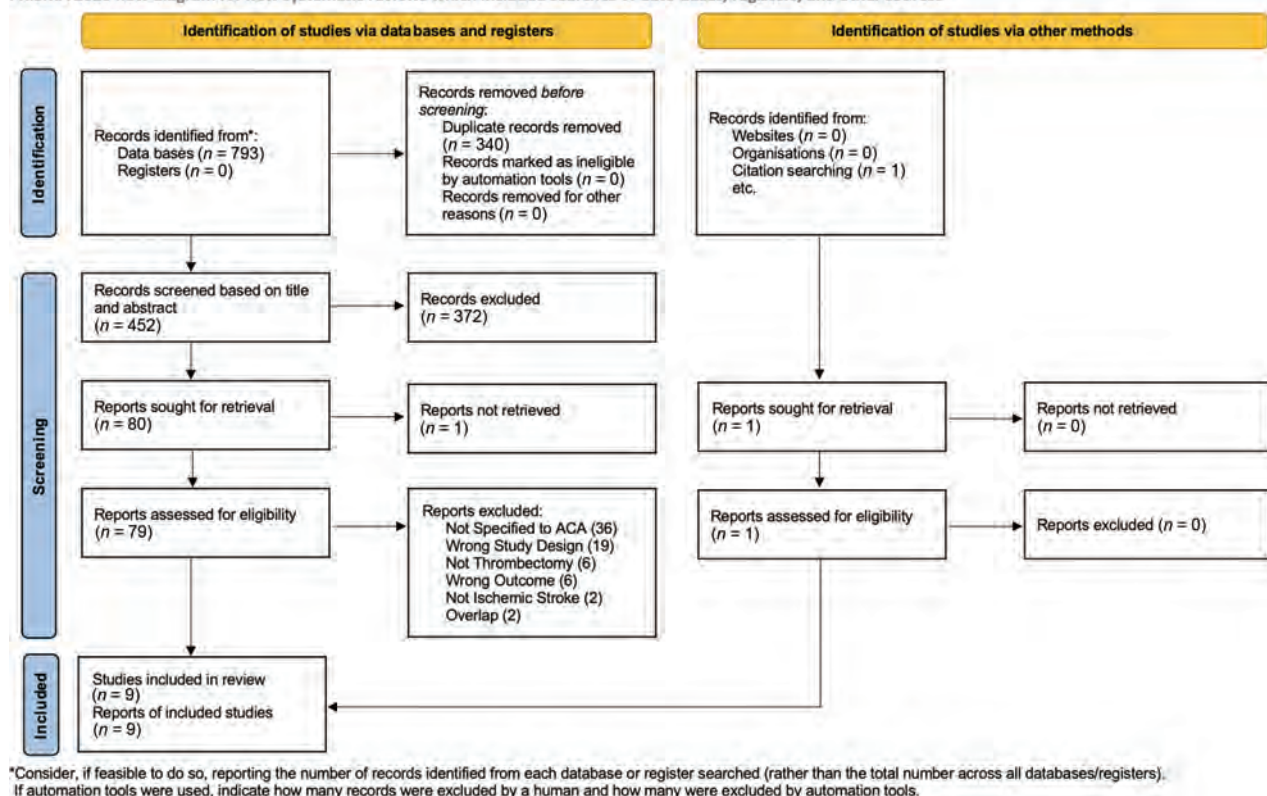


FIGURE. Flow chart showing the study-selection process.

been clearly delineated to date.⁴ Recent single and multicenter studies have provided additional data to examine the complication profile and outcomes related to MT for ACA occlusion.⁵⁻¹³ This systematic review aimed to summarize procedural and clinical outcomes in patients who underwent MT for the treatment of ACA occlusion.

MATERIALS AND METHODS

Electronic Literature Search

A systematic review of the literature was performed and presented in accordance with the Preferred Reporting Items for Systematic Reviews and Meta-Analyses (PRISMA) guidelines. A PRISMA checklist is provided (Online Supplemental Data). The electronic databases PubMed, Web of Science, and Ovid MEDLINE were searched from inception to March 4, 2022. A keyword search using the Boolean operators OR & AND with terms including “anterior cerebral artery” and “thrombectomy” was conducted (Online Supplemental Data). Duplicates of search results from different databases were identified and removed. A PRISMA 2020 flow diagram is presented in the Figure. The protocol used for this review is provided in the Online Supplemental Data. This protocol was not prospectively registered.

Literature Review

Inclusion and exclusion criteria were determined a priori. Studies that included patients with primary or secondary acute ACA occlusions treated with aspiration or stent-retriever-mediated

MT with data related to clinical outcomes were considered. We excluded the following studies: 1) those that were in the form of abstracts, case reports, and editorials; 2) did not include clinical or procedural outcomes related to MT for acute ACA occlusion; or 3) had no English version. Articles that grouped acute ACA occlusions with other territory occlusions in their analysis (ie, did not detail individual characteristics or outcome data of patients with ACA strokes) were also not considered.

All articles were initially screened on the basis of their titles and abstracts. Two authors evaluated full-text articles independently and selected those that fit the inclusion criteria. Reference lists of the selected articles were reviewed to identify articles potentially missed by the electronic literature search.

Data Extraction

One author extracted data from each selected study, which was then verified by an additional author for accuracy. We collected the following baseline data from each included study: age, sex, NIHSS score at admission, ASPECTS, clinical presentation of stroke, stroke etiology (ie, atherosclerotic, cardiogenic), and ACA stroke location (ie, A1–A5). Proximal callosomarginal artery occlusions were grouped with the A4 segment, and distal downstream occlusions of the ACA branches were grouped with A5.

Primary isolated ACA stroke was defined as an acute, isolated ACA occlusion that did not occur due to thrombectomy or thrombolytic therapy. Primary combined ACA occlusion was

defined as an ACA occlusion in conjunction with other vessels of the anterior circulation, not resulting from thrombectomy or thrombolytic therapy. Secondary ACA stroke included occlusions of the ACA territory that occurred as a result of the thrombectomy procedure or thrombolytic therapy.

Procedural data collected included the number of patients having undergone thrombolytic therapy, the type of MT technique (ie, stent retriever, aspiration), incidents of procedural failure, time from symptom onset to recanalization, procedural time, number of passes, the modified TICI (mTICI) score, and postprocedural complications. The mTICI score referred to the recanalization score for ACA occlusion. Postprocedural complications were defined as complications that occurred after and could be attributable to the procedure, with or without clinical sequelae. These complications would include hemorrhage and formation of a new embolus. Procedural failure was defined as an inability of device deployment, specifically concerning stent retrievers, due to placement of a guidewire or microcatheter (see the Online Supplemental Data for full definitions). Clinical outcome data collected included the number of patients with intracerebral hemorrhage (ICH), average clinical follow-up time, number of patients available for clinical follow-up, mortality rates (3 months and overall), and the mRS score (3 months and overall).

Primary outcomes were the rate of successful recanalization (mTICI 2b/3) and the rate of good clinical outcome (mRS 0–2) at last clinical follow-up. Secondary outcome measures included rates of postprocedural complications and mortality. The data were further substratified on the basis of primary isolated, primary combined, and secondary ACA occlusion (Online Supplemental Data) and on the type of MT technique (ie, stent, aspiration, hybrid) (Online Supplemental Data). Patients were included in each grouping only if mTICI, intraprocedural complications, ICH, mortality, procedural time, or the mRS score was provided.

Data Synthesis and Quality Assessment

For each included article, continuous variables such as age, ASPECTS, time to recanalization, procedural time, and number of passes were reported as medians with ranges or means (SDs). The crude estimate for each continuous variable was computed as the mean (ie, times) or median (ie, for age, ASPECTS) of all included studies. Categorical variables, such as stroke location (ie, A1–A5), MT technique (ie, stent retriever, aspiration), and postprocedural complications, were reported as proportions for each article. The crude estimate for each variable was the total proportion of all included studies. The χ^2 test of independence was performed to assess the relationship between selected variables (ie, mTICI, postprocedural complications, ICH, mortality, mRS) and ACA embolus type or MT technique (Online Supplemental Data). The Kruskal-Wallis test was used to determine significant differences in ASPECTS and NIHSS scores among ACA occlusion types and MT technique (Online Supplemental Data). Statistical analysis was performed using R statistical and computing software, Version 4.2.1 (<http://www.r-project.org/>). The quality of each study was assessed using the Newcastle-Ottawa Scale (Online Supplemental Data).

RESULTS

A total of 9 studies were included in this review.^{5–13} The Figure demonstrates the PRISMA flow chart for the selection of studies. The relevant studies differed as far as their scope, which included outcomes of MT for ACA occlusion, outcomes of MT for distal ACA occlusion, comparison of MT and thrombolysis outcomes for ACA occlusion, ACA embolism during MCA thrombectomy, and distal endovascular thrombectomy. Studies varied in the complete clinical, procedural, and outcome data they presented and the degree of statistical analysis. This variation, in addition to the small sample sizes, provides the risk for selection and information bias. The Newcastle-Ottawa Assessment Scale score ranged from 3 to 6 with a median of 6 (Online Supplemental Data).

Patient and ACA Territory Ischemic Stroke Characteristics

Baseline patient and stroke characteristics, procedural details and complications, and clinical outcomes of each individual study are summarized in the Online Supplemental Data. The Online Supplemental Data detail patient demographics and baseline stroke characteristics. Among the 9 studies, there were 168 patients with acute ACA occlusion treated with MT. The median patient age was 74 years (range, 64–80 years) and 47% (77/163) were women. Regarding occlusion type, 43% (72/168), 24% (40/168), and 33% (56/168) had primary isolated ACA occlusion, primary combined ACA occlusion, and secondary ACA occlusion, respectively. Stroke etiology was atherosclerotic in 23% (20/87), cardiogenic in 41% (36/87), and other in 36% (31/87). The location of occlusion along the ACA included the A1 in 13% (18/134), A2 in 43% (57/134), A3 in 22% (29/134), A4 in 21% (28/134), and A5 in 1% (2/134).

The median NIHSS score at admission of all patients was 17.5 (range, 10–24). The median ASPECTS was 8 (range, 7–8.5). Among 18 patients with data regarding clinical presentation, 78% (14/18) and 94% (17/18) presented with speech disturbance and hemiparesis, respectively. Among primary isolated, primary combined, and secondary ACA occlusions, the median NIHSS scores at admission were 18 (range, 10–21), 23 (range, 18–28), and 19 (range, 14–24), respectively ($\chi^2 = 1.13$, $P = .57$) (Online Supplemental Data). The median ASPECTS was ten, 8.5 (range, 8–9), and 8 for primary isolated, primary combined, and secondary ACA occlusion, respectively ($\chi^2 = 2.25$, $P = .33$) (Online Supplemental Data).

Thrombectomy Procedural Characteristics

The Online Supplemental Data summarize procedural characteristics during MT. Thrombolytic therapy was performed in 41% (62/151) of patients. Stent-retriever MT was performed in 65% (85/131) of patients, aspiration was performed in 23% (30/131) of patients, and stent retriever with aspiration was performed in 12% (16/131) of patients.

Procedural failure occurred in 3% (5/168) of patients. The mean time from onset to recanalization was 219 (SD, 50) minutes, and the mean procedural time was 58 (SD, 13) minutes. The median number of passes was 1. mTICI 2b/3 was achieved in 80% (134/168) of all patients included in the study. Among patients with primary isolated ACA occlusion, 74% (37/50) achieved mTICI 2b/3, while 88% (14/16) of primary combined ACA occlusion and 89% (8/9) of secondary ACA occlusion had this result

($\chi^2 = 1.95$, $P = .38$) (Online Supplemental Data). Among ACA occlusions treated with stent retrievers or aspiration alone, mTICI 2b/3 was reached in 82% (42/51) and 94% (17/18), respectively (Online Supplemental Data). When a stent retriever with aspiration was used, mTICI 2b/3 was achieved in 100% (12/12) ($\chi^2 = 3.78$, $P = .15$) (Online Supplemental Data).

Complications and Clinical Follow-up Outcomes

The Online Supplemental Data describe postprocedural complications and clinical follow-up data. Postprocedural complications occurred in 17% (29/168) of patients, with a symptomatic postprocedural complication rate of 11% (19/168). Symptomatic complications included ICH (8.3% [14/168]), cerebral edema (2% [4/168]), and ACA dissection (0.5% [1/168]) (Online Supplemental Data). Symptomatic postprocedural complications occurred in 2% (1/49), 25% (3/12), and 20% (1/5) of patients with primary isolated ACA occlusion, primary combined ACA occlusion, and secondary ACA occlusion, respectively ($\chi^2 = 8.45$, $P = .01$) (Online Supplemental Data). Symptomatic postprocedural complications occurred in 7% (3/44), 56% (9/16), and 25% (3/12) of patients in whom a stent retriever, aspiration, or combination MT technique was used ($\chi^2 = 17.5$, $P < .01$) (Online Supplemental Data). ICH occurred in 13% (22/168) of patients, symptomatic ICH occurred in 8.3% (14/168), SAH occurred in 6% (10/168), and symptomatic SAH occurred in 1.2% (2/168) (Online Supplemental Data). Symptomatic ICH was located in the MCA territory (2.4% [4/168]), ACA territory (0.6% [1/168]), and unspecified location (5.3% [9/168]) (Online Supplemental Data). Among patients with primary isolated ACA occlusion, primary combined ACA occlusion, and secondary ACA occlusion, symptomatic ICH occurred in 2% (1/49), 25% (3/12), and 20% (1/5), respectively ($\chi^2 = 8.45$, $P = .01$) (Online Supplemental Data).

The mean clinical follow-up time was 3 (SD, 0) months. At the 3-month follow-up, 32% (48/148) and 68% (100/148) of all patients had good and poor clinical outcomes, respectively. Overall, 31% (51/163) of patients had a good outcome, and 69% (112/163) had a poor outcome. When we further substratified the results, good clinical outcome was achieved in 48% (24/50), 25% (4/16), and 0% (0/4) of patients with primary isolated ACA occlusion, primary combined ACA occlusion, and secondary ACA occlusion, respectively ($\chi^2 = 5.5$, $P = .06$) (Online Supplemental Data). Additionally, poor clinical outcome occurred in 52% (26/50), 75% (12/16), and 100% (4/4) of patients with primary isolated ACA occlusion, primary combined ACA occlusion, and secondary ACA occlusion, respectively ($\chi^2 = 5.5$, $P = .06$) (Online Supplemental Data). The mortality rate at 3 months was 19% (22/118), and the overall mortality rate was 22% (30/138). Among patients with primary isolated ACA occlusion, primary combined ACA occlusion, and secondary ACA occlusion with specified outcomes, the mortality rates were 47% (8/17), 13% (2/16), and 44% (4/9), respectively ($\chi^2 = 5.07$, $P = .08$) (Online Supplemental Data).

DISCUSSION

An increasing number of ACA occlusions are targeted for endovascular treatment. However, the safety and efficiency of MT for the treatment of acute ACA occlusions have not been clearly

defined.⁴ Here, we identified the literature outlining the outcome data related to ACA occlusions treated with MT. In our review, recanalization was achieved in 80% of patients and postprocedural complications occurred in 17% of patients. At the last clinical follow-up of 3 months, the mortality rate was 19% and the rate of good functional outcome was 32%.

Rigorous clinical trial data support MT in patients with intracranial and extracranial occlusions of the ICA, including tandem or isolated occlusions of the M1 and M2 segments of the MCA.^{4,14,15} Highly Effective Reperfusion evaluated in Multiple Endovascular Stroke (HERMES), a meta-analysis using individual patient data from 5 of these randomized controlled trials (MR CLEAN, ESCAPE, REVASCAT, SWIFT PRIME, and EXTEND IA), found that patients with ICA and proximal MCA occlusions who underwent thrombectomy had similar rates of symptomatic ICH (4.4%) and 90-day mortality (15.3%), with higher rates of functional independence at 90 days (46%) compared with controls (26.5%).¹⁶ MT in patients with ACA occlusions may also share similar benefits, specifically improving morbidity outcomes poststroke.^{17,18} However, because the natural history of these strokes is overall more favorable compared with ICA or MCA occlusions, the risks of MT may outweigh the potential benefits.¹⁸ The risk of vessel perforation and vasospasm in MT-treated ACA occlusions may be increased, given the distal location, smaller diameter, and thinner walls of the ACA.¹⁷⁻¹⁹ In our review, the overall recanalization rate for MT-treated primary and secondary ACA occlusions was found to be 80% (94% for aspiration, 82% for stent retriever), similar to that of large-vessel occlusions (81.9% for aspiration, 88%–91% for stent retriever).^{4,20} Procedural time for primary and secondary ACA occlusions treated with MT (58 minutes) was similar to that of MT-treated thrombectomies of the MCA (54–70 minutes).^{4,17,21} Our data demonstrate that recanalization rates and procedural times in thrombectomy-treated ACA and MCA/ICA strokes are comparable.

Symptomatic complications for MT-treated ACA strokes were ICH (8.3%) and cerebral edema (0.6%). Although the overall rate of symptomatic procedural complications in MT-treated primary and secondary ACA occlusions (11%) is comparable with that of MT-treated MCA/ICA occlusions (range, 7%–16%), in our review, the rate of symptomatic ICH for ACA occlusions treated with MT was found to be greater (8.3%, compared with 4.4% for MT-treated MCA/ICA occlusions).¹⁶ This finding may be attributed to more distal and smaller vessel targets that may be injured during ACA MT.^{7,17} However, among the few studies that reported the location of ICH, the most common location was the MCA territory (2.4% [4/168]). The postprocedural complication rate differed significantly, depending on the type of ACA occlusion. Specifically, primary isolated ACA occlusions were found to be associated with fewer postprocedural complications compared with primary combined and secondary ACA occlusions ($\chi^2 = 8.45$, $P = .01$). The rate of symptomatic ICH also was significantly different among these 3 occlusion types, with primary isolated ACA occlusions associated with the lowest ICH incidence ($\chi^2 = 8.45$, $P = .01$). The symptomatic complication rate for MT-treated ACA occlusions also differed on the basis of the MT technique used, with stent-retriever and hybrid techniques being associated with fewer complications ($\chi^2 = 17.5$,

$P < .01$), though in MT-treated MCA/ICA occlusions, the safety profiles of stent and aspiration techniques were similar.^{4,22}

The 90-day mortality rate for MT-treated ACA occlusions (19% [22/118]) was also found to be comparable with that for MT-treated ICA/MCA occlusions in the HERMES meta-analysis (15.3%).^{7,16} However, relatively fewer patients in our review achieved a good 90-day outcome (32% [48/148]) compared with those with MT-treated ICA/MCA strokes (46% in HERMES).¹⁶ We found that patients with primary, isolated ACA occlusions had a relatively greater rate of good outcomes at 90 days (48% [24/50]) compared with those with primary combined (25% [4/16]) or secondary (0% [0/4]) ACA occlusions, though the differences were not statistically significant. Moreover, the rate of good functional outcome at 90 days may be lower in patients with MT-treated ACA strokes compared with the numbers reported for non-MT-treated ACA strokes.¹⁻³ Specifically, patients with non-MT-treated primary isolated ACA occlusions have achieved a 90-day rate of good functional outcome of 85% compared with 48% for MT-treated primary isolated ACA occlusions found in our review.²³ In controlled trials comparing MT- and non-MT-treated ICA/MCA occlusions, there were significant differences in good functional outcome that favored MT treatment of selected strokes (46% in MT-treated, 26.5% in controls).¹⁶ While there have been no controlled studies to directly compare MT- and non-MT-treated ACA strokes on the basis of initial severity, our findings warrant further investigation to determine the ideal characteristics of ACA occlusions and the patient population that would benefit from MT regarding mortality and morbidity.

Our systematic review of the literature suggests that MT can be used to treat primary or secondary ACA occlusions with recanalization rates, procedural complications, and 90-day mortality comparable with those of MT-treated MCA/ICA occlusions. However, ACA thrombectomy is associated with higher rates of ICH compared with those reported for ICA/MCA thrombectomy, and outcomes of primary ACA occlusion following thrombectomy do not appear to differ from the reported natural history of primary ACA occlusion. Of note, the outcomes are dependent on the type of ACA occlusion (primary, primary combined, or secondary) and type of MT technique used (stent, aspiration, hybrid). Currently, the safety and efficacy of MT in medium-sized cerebral vessels, including the ACA, are being evaluated in the DISTAL multicenter, randomized clinical trial that ends in 2026.²⁴ Until the initial results are known, it is important to understand that the initial baseline functional status of the patient as well as degree of severity of ACA stroke are complex factors to consider when deciding to use MT for the treatment of ACA occlusion.

Limitations

We acknowledge several limitations of this review. The relevant studies identified differed as far as their scope and varied in the complete clinical, procedural, and outcome data they presented. Many studies did not report the location, type, or severity of ICH, which may overestimate ACA thrombectomy complications and provide a barrier for decision-making. While many articles screened for full-text review included MT-treated ACA occlusions in their data, they did not specify individual results for this group and could not be included in the analysis. Individual

patient data and further subgroup analysis were not possible. As a result, we were unable to completely stratify complications and outcomes on the basis of baseline functional outcomes (ie, baseline mRS score), MT technique used, the use of concurrent thrombolytic therapy, and the type of ACA occlusion (ie, primary, secondary).

We could not directly compare the outcomes of MT-treated ACA occlusions with those of either non-MT-treated ACA occlusions or MT-treated ICA/MCA occlusions because no study to date has produced a comparison. Several studies had small sample sizes, increasing the risk of selection and information bias. The included studies varied as to the degree of statistical analysis because only 2 studies performed a complete multivariable analysis, leading to an increased risk of confounding bias for the remaining studies.

To minimize bias associated with data collection, 2 authors were involved in data extraction; one author (N.D.) conducted the data extraction and rated the certainty of evidence, while the second (P.M.) checked the accuracy of the data. Both authors contributed to data analysis.

CONCLUSIONS

MT for the treatment of ACA occlusions offers a favorable overall safety and efficacy profile associated with rates of recanalization, procedural complications, and mortality comparable with that of MT in larger vessels. However, the rate of short-term good functional outcome appears to be decreased, while the rate of symptomatic ICH seems to be increased compared with MT-treated MCA/ICA occlusions, necessitating the establishment of criteria to determine the appropriate ACA occlusions amenable by MT treatment. More single and multicenter studies are needed to further examine the safety and efficacy of MT in ACA occlusions. Increased operator experience and more direct comparisons with alternative approaches are necessary to establish the optimal treatment for ACA occlusions.

Disclosure forms provided by the authors are available with the full text and PDF of this article at www.ajnr.org.

REFERENCES

1. Cho H, Kim T, Kim YD, et al. **A clinical study of 288 patients with anterior cerebral artery infarction.** *J Neurol* 2022;269:2999–3005 CrossRef Medline
2. Arboix A, García-Eroles L, Sellarés N, et al. **Infarction in the territory of the anterior cerebral artery: clinical study of 51 patients.** *BMC Neurol* 2009;9:30 CrossRef Medline
3. Kang SY, Kim JS. **Anterior cerebral artery infarction: stroke mechanism and clinical-imaging study in 100 patients.** *Neurology* 2008;70:2386–93 CrossRef Medline
4. Mordasini P, Schroth G, Gralla J. **Mechanical recanalization in acute stroke treatment.** *Perspectives in Medicine* 2012;1:54–58 CrossRef
5. Miszczuk M, Kleine JF, Riegler C, et al. **Mechanical thrombectomy of acute occlusions of individual distal anterior cerebral artery branches.** *J Clin Neurosci* 2022;98:137–41 CrossRef Medline
6. Filioglo A, Simaan N, Honig A, et al. **Outcomes after reperfusion therapies in patients with ACA stroke: a multicenter cohort study from the EVATRISP collaboration.** *J Neurol Sci* 2022;432:120081 CrossRef Medline
7. Nogueira RG, Mohammed MH, Haussen DC, et al. **Endovascular therapy in the distal neurovascular territory: results of a large**

- prospective registry. *J Neurointerv Surg* 2021;13:979–84 CrossRef Medline
8. Kim H, Jin SC, Lee H. **Clinical and radiological outcomes of mechanical thrombectomy in simultaneous anterior cerebral artery and middle cerebral artery occlusion.** *J Cerebrovasc Endovasc Neurosurg* 2022;24:137–43 CrossRef Medline
 9. Hudson JS, Gross BA. **Anterior cerebral artery thrombectomy: a case series and technical description.** *Interdisciplinary Neurosurgery* 2021;26:101331 CrossRef
 10. Uno J, Kameda K, Otsuji R, et al. **Mechanical thrombectomy for acute anterior cerebral artery occlusion.** *World Neurosurg* 2018;120:e957–61 CrossRef Medline
 11. Chung GH, Kwak HS, Park JS, et al. **Manual aspiration thrombectomy with a Penumbra catheter for acute anterior cerebral artery occlusion.** *Interv Neuroradiol* 2017;23:416–21 CrossRef Medline
 12. Pfaff J, Herweh C, Pham M, et al. **Mechanical thrombectomy of distal occlusions in the anterior cerebral artery: recanalization rates, periprocedural complications, and clinical outcome.** *AJNR Am J Neuroradiol* 2016;37:673–78 CrossRef Medline
 13. Kurre W, Vorlaender K, Aguilar-Pérez M, et al. **Frequency and relevance of anterior cerebral artery embolism caused by mechanical thrombectomy of middle cerebral artery occlusion.** *AJNR Am J Neuroradiol* 2013;34:1606–11 CrossRef Medline
 14. Albers GW, Marks MP, Kemp S, et al. **Thrombectomy for stroke at 6 to 16 hours with selection by perfusion imaging.** *N Engl J Med* 2018;378:708–18 CrossRef Medline
 15. Nogueira RG, Jadhav AP, Haussen DC, et al. **Thrombectomy 6 to 24 hours after stroke with a mismatch between deficit and infarct.** *N Engl J Med* 2018;378:11–21 CrossRef Medline
 16. Goyal M, Menon BK, van Zwam WH, et al; HERMES collaborators. **Endovascular thrombectomy after large-vessel ischaemic stroke: a meta-analysis of individual patient data from five randomised trials.** *Lancet* 2016;387:1723–31 CrossRef Medline
 17. Haruyama H, Uno J, Takahara K, et al. **Mechanical thrombectomy of primary distal anterior cerebral artery occlusion: a case report.** *Case Rep Neurol* 2019;11:265–70 CrossRef Medline
 18. Mokin M, Ansari SA, McTaggart RA, et al; Society of NeuroInterventional Surgery. **Indications for thrombectomy in acute ischemic stroke from emergent large vessel occlusion (ELVO): report of the SNIS Standards and Guidelines Committee.** *J Neurointerv Surg* 2019;11:215–20 CrossRef Medline
 19. Pilgram-Pastor SM, Piechowiak EI, Dobrocky T, et al. **Stroke thrombectomy complication management.** *J Neurointerv Surg* 2021;13:912–17 CrossRef Medline
 20. Salsano G, Pracucci G, Mavilio N, et al. **Complications of mechanical thrombectomy for acute ischemic stroke: Incidence, risk factors, and clinical relevance in the Italian Registry of Endovascular Treatment in Acute Stroke.** *Int J Stroke* 2021;16:818–27 CrossRef Medline
 21. Guzzardi G, del Sette B, Stanca C, et al. **Mechanical Thrombectomy by a Direct Aspiration First Pass Technique (ADAPT) in ischemic stroke: results of monocentric study based on multimodal CT patient selection.** *Stroke Res Treat* 2018;2018:6192483 CrossRef Medline
 22. Tsang CO, Cheung IH, Lau KK, et al. **Outcomes of stent retriever versus aspiration-first thrombectomy in ischemic stroke: a systematic review and meta-analysis.** *AJNR Am J Neuroradiol* 2018;39:2070–76 CrossRef Medline
 23. Park H, Jeong YS, Lee SH, et al. **Clinical prognosis of isolated anterior cerebral artery territory infarction: a retrospective study.** *BMC Neurol* 2021;21:171 CrossRef Medline
 24. Campbell BC, Nguyen TN. **Advances in stroke: treatments-interventional.** *Stroke* 2022;53:264–67 CrossRef Medline
 25. Page MJ, McKenzie JE, Bossuyt PM, et al. **The PRISMA 2020 statement: an updated guideline for reported systematic reviews.** *BMJ* 2021;372:n71 CrossRef Medline

Thrombectomy Using the EmboTrap Clot-Retrieving Device for the Treatment of Acute Ischemic Stroke: A Glimpse of Clinical Evidence

X. Bai, Z. Fu, Z. Sun, R. Xu, X. Guo, Q. Tian, A.A. Dmytriw, H. Zhao, W. Wang, X. Wang, A.B. Patel, B. Yang, and L. Jiao



ABSTRACT

BACKGROUND: The EmboTrap Recanalization Device is a novel stent retriever for thrombectomy in the setting of acute ischemic stroke due to large-vessel occlusion.

PURPOSE: Our aim was to summarize the safety and efficacy of the EmboTrap Recanalization Device in acute ischemic stroke—large-vessel occlusion through a systematic review and meta-analysis.

DATA SOURCES: Medline, EMBASE, the Cochrane Library, Web of Science, and Google Scholar were searched up to April 2022.

STUDY SELECTION: Nine observational studies using the EmboTrap Recanalization Device were selected.

DATA ANALYSIS: We adapted effect size with 95% CIs for dichotomous data. *P* value <.05 was statistically significant.

DATA SYNTHESIS: The estimated rate of successful recanalization (modified TICI 2b–3) was 90% (95% CI, 86%–95%; $I^2 = 82.4\%$); 90-day favorable outcome (mRS 0–2), 53% (95% CI, 42%–63%; $I^2 = 88.6\%$); modified first-pass effect, 43% (95% CI, 35%–51%; $I^2 = 63.7\%$); and first-pass effect, 36% (95% CI, 29%–46%; $I^2 = 10.7\%$). The rate of any intracerebral hemorrhage was 19% (95% CI, 16%–22%; $I^2 = 0.0\%$); symptomatic intracerebral hemorrhage, 5% (95% CI, 1%–8%; $I^2 = 84.6\%$); and 90-day mortality, 14% (95% CI, 9%–19%; $I^2 = 79.3\%$). Subgroup analysis showed higher rates of complete recanalization for EmboTrap II than for the EmboTrap System.

LIMITATIONS: The included studies are single-arm without direct comparison with other stent retrievers. Some of the studies recruited had a small sample size and were limited by the retrospective study design. In addition, the uncertain heterogeneity among studies was high.

CONCLUSIONS: The EmboTrap Recanalization Device is safe and efficient in treating acute ischemic stroke due to large-vessel occlusion.

ABBREVIATIONS: AIS = acute ischemic stroke; FPE = first-pass effect; ICH = intracerebral hemorrhage; LVO = large-vessel occlusion; mFPE = modified first-pass effect; MT = mechanical thrombectomy; mTICI = modified TICI; sICH = symptomatic intracerebral hemorrhage

Acute ischemic stroke (AIS) is a major cause of morbidity and mortality, and effective reperfusion of the affected tissue is

the most important defining factor for favorable outcomes.¹ Several trials have demonstrated the clinical benefit and superior reperfusion efficacy of mechanical thrombectomy (MT) using stent-retriever thrombectomy devices after AIS.^{2–4} Current guidelines recommended MT as the first-line therapy for AIS due to large-vessel occlusion (LVO).^{1,2,5} Currently, there are several types of stent-retriever thrombectomy devices studied that were used in clinical trials and nonclinical studies. Although the overall function of MT devices is similar, many aspects, such as distinct mechanisms of action, differing 3D structures, and the interaction between the stent retriever and vessel wall, may lead to different results and clinical consequences.^{6–8}

The EmboTrap Revascularization Device is an innovative stent retriever used to retrieve clots and restore blood flow.^{8–12} It offers a 2-layer structure designed with articulating petals and a distal

Received June 21, 2022; accepted after revision October 11.

From the Departments of Neurosurgery (X.B., Z.F., Z.S., R.X., H.Z., B.Y., L.J.), Library (W.W., X.W., A.B.P.), and Interventional Neuroradiology (L.J.), Xuanwu Hospital, Capital Medical University, Xicheng District, Beijing, China; China International Neuroscience Institute (X.B., Z.F., Z.S., R.X., H.Z., B.Y., L.J.), Beijing, China; Department of Neurology (X.G.), Loma Linda University Health, Loma Linda, California; Beijing Key Laboratory of Clinical Epidemiology (Q.T.), School of Public Health, Capital Medical University, Beijing, China; and Neuroendovascular Program (A.A.D.), Massachusetts General Hospital, Harvard Medical School, Boston, Massachusetts.

Xuesong Bai, Zhaolin Fu, and Ziyi Sun contributed equally and are co-first authors.

Please address correspondence to Liqun Jiao, MD, PhD, Department of Neurosurgery, Xuanwu Hospital, Capital Medical University, Beijing, China, No. 45 Changchun St, Xicheng District, Beijing, China 100053; e-mail: liqunjiao@sina.cn



Indicates article with online supplemental data.

<http://dx.doi.org/10.3174/ajnr.A7708>

capture zone for successful trapping, retention, and removal of diverse clot types to restore blood flow in AIS-LVO. The inner layer is a closed-cell stent, which aims to restore blood flow immediately. The external layer units include open inlet ports for catching clots during device retraction and articulating petals that promote clot entrapment and retention. High rates of substantial perfusion and functional independence have been demonstrated in patients with AIS-LVO from the single-arm trial, Analysis of Revascularization in Ischemic Stroke With EmboTrap (ARISE II).⁸ Thereafter, several studies tried to explore the safety and efficacy of the EmboTrap device in treating AIS-LVO based real-world data.^{11,12} In this study, we performed a systematic review and meta-analysis to evaluate the clinical benefit of the EmboTrap Revascularization Device.

MATERIALS AND METHODS

This study was conducted according to the statement of Preferred Reporting Items for Systematic Reviews and Meta-Analyses¹³ and Assessing the Methodological Quality of Systematic Reviews¹⁴ guidelines. The project has been registered in PROSPERO (https://www.crd.york.ac.uk/prospero/display_record.php?ID=CRD42022327897).

Search Strategy

Five databases, MEDLINE, EMBASE, the Cochrane Library, Web of Science, and Google Scholar were searched up to April 2022 by 2 independent reviewers for relevant studies. Publicly available clinical trials registers, for example, ClinicalTrials.gov, were also searched. All relevant publications since these databases were created were included in this analysis. The search strategy is provided in the Online Supplemental Data.

Study Eligibility

The criteria for the study design were specified according to The Population, Intervention, Comparison, Outcome model.

Patient-Selection Criteria. Inclusion criteria were adult patients (18 years of age or older) with AIS due to LVO, including anterior or posterior circulation occlusions, who underwent MT using the EmboTrap device. Arterial occlusion was confirmed by either CTA, MRA, or DSA. The patients had complete recanalization (defined as a modified TICI [mTICI] score of 2c–3) or successful recanalization (defined as an mTICI score of 2b–3) after MT, which was determined by postinterventional DSA. The scores of mTICI 2c–3 were combined into the complete recanalization group because patients who achieved mTICI 2c–3 scores are known to have similar clinical outcomes.¹⁵

Exclusion criteria were patients with baseline prestroke mRS scores of ≥ 3 ; patients with intracerebral hemorrhage (ICH), significant cerebellar mass effect, and acute hydrocephalus on CT or MR imaging before the thrombectomy procedure; or patients with studies that did not report the above outcomes or in which the exact number of complications was not available.

Intervention. MT was performed in patients with AS due to LVO with the EmboTrap Revascularization Device.

Outcomes. At least one of the following items was reported.

Primary Efficacy Outcomes

- 1) Favorable outcome defined as mRS of 0–2 or equal to the prestroke score at 3 months
- 2) Successful recanalization (mTICI 2b–3) determined by post-interventional DSA.

Secondary Efficacy Outcomes

- 1) Modified first-pass effect (mFPE) defined as achieving a successful recanalization (mTICI 2b–3) with a single thrombectomy device pass without rescue therapy¹⁶
- 2) The first-pass effect (FPE) defined as achieving a complete recanalization (mTICI 2c–3) with a single thrombectomy device pass without rescue therapy¹⁶
- 3) Complete recanalization (mTICI 2c–3) determined by postinterventional DSA
- 4) Rescue rate defined as using additional recanalization devices besides the EmboTrap, including intra-arterial thrombolysis, other thrombectomy devices, and pump aspiration.

Safety Outcomes. Safety outcomes were the following:

- 1) Mortality at 90-day follow-up
- 2) ICH
- 3) Symptomatic intracerebral hemorrhage (sICH) defined as intracerebral hemorrhage on imaging with a minimum increase of 4 points on the NIHSS within 24 hours postintervention by the second European Australasian Acute Stroke Study classification (ECASS II)¹⁷
- 4) Procedural complications, such as dissection or vessel perforation.

Studies. We included randomized controlled trials and observational studies including cohort studies, case-control studies, and case series with the minimum number ≥ 20 cases. The inclusion of observational studies allowed sufficient data for outcome assessment and minimization of type II errors arising from low statistical power.¹⁸ Studies not reporting the above outcomes or from which data for complications could not be extracted were excluded.

Selection of Studies and Data Extraction

Two reviewers independently searched the main databases for eligible studies. In the initial stage of screening, titles, keywords, and abstracts were reviewed, and irrelevant studies were excluded. Subsequently, full articles of all the remaining studies were obtained and carefully checked to assess eligibility, and reasons for inclusion or exclusion of studies were documented in detail. Conflicts in study selection between the 2 reviewers were resolved by a third reviewer.

Extraction of data from included studies was also performed by 2 independent reviewers following a standardized data-extraction form. The extracted information of included studies was as follows: 1) characteristics of the study, such as publication time, country, number of patients; 2) characteristics of the included patients, such as age, sex, medical history, site of occlusion by angiography, admission NIHSS score, and baseline ASPECTS; and 3) aforementioned outcomes such as any ICH, sICH, procedural complications, and favorable outcome. The resolution of

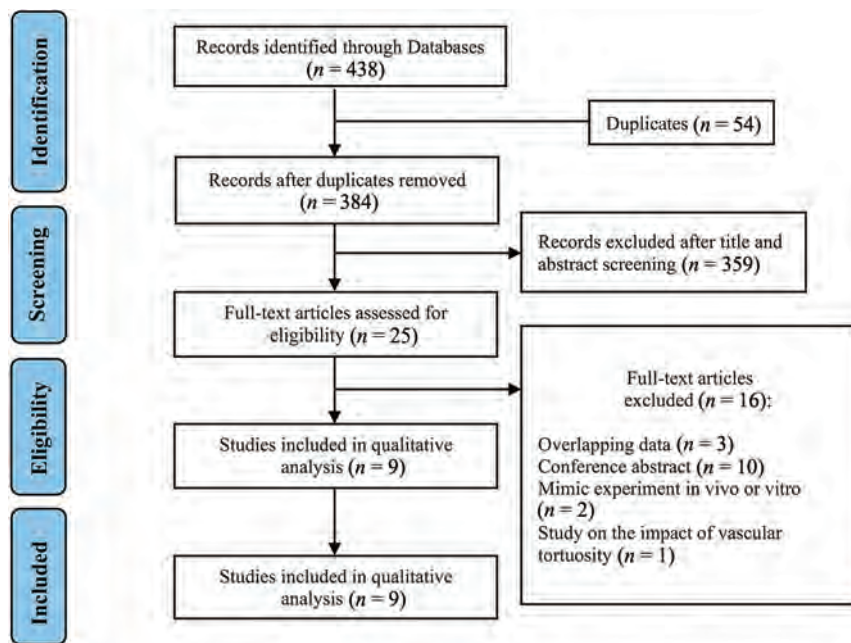


FIG 1. Flow diagram of literature for meta-analysis.

disagreement regarding data extraction was achieved through the assistance of a third reviewer. For missing or ambiguous data in the included studies, clarification of data through direct contact with the corresponding authors by e-mail was attempted.

Assessment of Risk Bias and Heterogeneity

Two reviewers independently assessed the risk of bias for each included study. The Cochrane Collaboration criteria were applied in the process of the selection of randomized controlled trials. The Methodological Index for Non-Randomized Studies scale was used for nonrandomized and single-arm studies. The heterogeneity of pooled outcomes was evaluated by the I^2 statistic. When the I^2 statistic was $>50\%$, it represented substantial heterogeneity; if the I^2 statistic was $<50\%$, it represented mild or moderate heterogeneity; and the DerSimonian and Laird method for random effects estimation was used for pooling outcomes. The Mantel-Haenszel method for fixed-effects estimation was used if heterogeneity was mild or moderate. For substantial heterogeneity of outcomes, we conducted sensitivity analysis to explore the potential source of heterogeneity.

Measures of Treatment Effect

A meta-analysis on a specific result was performed only when there were at least 2 suitable studies for analysis. If there were insufficient suitable studies for meta-analysis, results were described with narrative statistics. We adapted effect size with 95% CIs for dichotomous data and the mean differences with 95% CIs for continuous data. A P value $< .05$ was statistically significant. In addition to the meta-analyses of primary and secondary outcomes of the EmboTrap device, we also made a subgroup analysis of the EmboTrap II Recanalization Device. The STATA statistical software (Version 15.0; Stata Corp) was used for data analysis and heterogeneity assessment. The 2 independent-samples t tests by

SPSS software (Version 24.0; IBM) were used for the comparison of the EmboTrap System (the first generation of EmboTrap Recanalization Device) and EmboTrap II devices. Publication bias was assessed by visualization of funnel plots provided that the number of included studies was >10 .

RESULTS

Study Selection and Study Characteristics

We found 438 references, abstracts, and related clinical trials from the 5 main electronic databases and clinical trials registers in the first step. Among the results, 25 full-text articles were retrieved after initial checks, and 9 studies were finally eligible for inclusion in the qualitative and quantitative analyses. The process of study selection and reasons for exclusion are summarized in Fig 1, and the Online Supplemental Data show the characteristics of included

studies and patients. A total of 1230 patients were eligible for inclusion criteria.^{8-12,19-22} Among the pooled studies, 6 studies and 1070 individuals used the EmboTrap II device only, and the remaining 3 studies and 160 individuals used the EmboTrap System only. The inclusion and exclusion criteria of patients in included studies are summarized in the Online Supplemental Data. The inclusion criteria consisted of the time window and baseline neurologic and imaging evaluations. The number of patients in each included study ranged from 29 to 318, and the proportion of men was 49.4% (588/1190). The site of occlusion as determined by angiography was mostly located in anterior circulation, involving the ICA and M1 segment of the MCA.

Meta-analysis of Primary and Secondary Outcomes of the EmboTrap Device

According to our analysis, the rate of favorable outcome of the 90-day mRS 0–2 was 53% (95% CI, 42%–63%; $I^2 = 88.6\%$) (Fig 2). The estimated rate of successful recanalization of mTICI 2b–3 was 90% (95% CI, 86%–95%; $I^2 = 82.4\%$) (Fig 3). The rate of mFPE (mTICI score $\geq 2b$ with a single device pass without rescue) was 43% (95% CI, 35%–51%; $I^2 = 63.7\%$) (Fig 4). The above results and the outcomes of FPE (mTICI score $\geq 2c$ with a single device pass without rescue), complete recanalization (mTICI 2c–3), rescue rate, 90-day mortality, ICH, sICH, and procedure-related complications are summarized in the Table. The forest plots are presented in the Online Supplemental Data.

Subgroup Analyses of the EmboTrap System and EmboTrap II Devices

We also conducted subgroup analyses of outcomes in 1070 patients treated with the EmboTrap II Recanalization Device and 160 patients treated with the EmboTrap System (Online Supplemental Data). The 2 independent-samples t tests between the EmboTrap

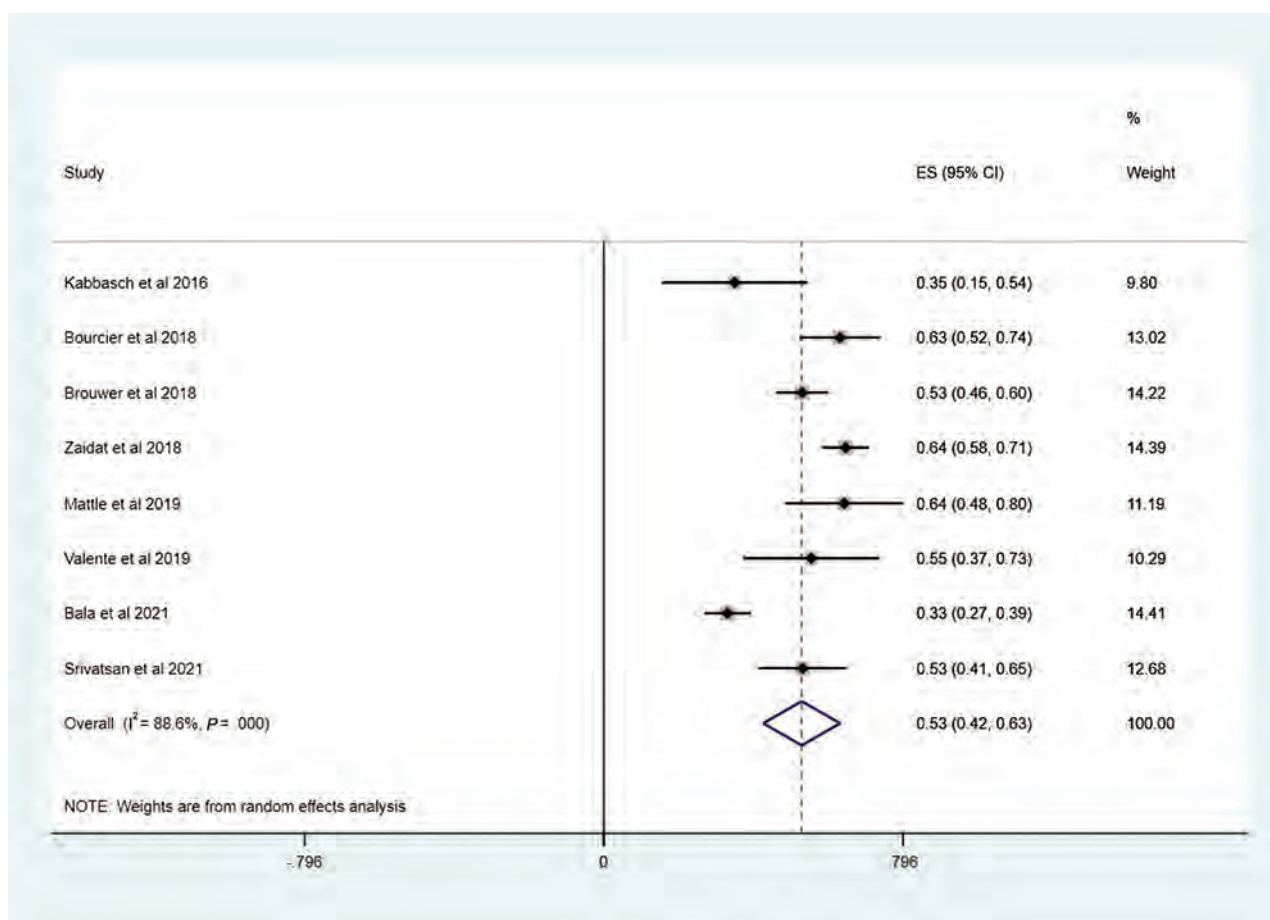


FIG 2. Forest plots of meta-analyses of favorable outcome at 90 days. ES indicates effect size.

System and EmboTrap II Recanalization Devices showed a significantly higher rate of complete recanalization of EmboTrap II than of EmboTrap System (0.60 versus 0.48, $P = .043$), while other results did not show a significant difference between the 2 devices. The results of EmboTrap II and the EmboTrap System are shown in the Online Supplemental Data. The subgroup analysis outcome of FPE for EmboTrap II was not listed because it pooled the same studies as the above results. Subgroup analysis of FPE, mFPE, and 90-day mortality for the EmboTrap System was not performed due to limited data.

Risk of Bias

The Methodological Index for Non-Randomized Studies criteria were used to assess the bias risk of nonrandomized and single-arm studies, with most included studies being at low risk for bias (Online Supplemental Data). Sensitivity analyses were conducted to explore potential heterogeneity, and the results did not suggest any possible source of high heterogeneity, which may be due to the intrinsic nature of single-arm studies. Because only 8 studies were pooled, funnel plots were not used.

DISCUSSION

This is the first systematic review and meta-analysis to explore the safety and efficacy of the EmboTrap Revascularization Device

in patients with AIS and LVO. The results of our analysis were similar to those in previous reports from the ARISE II study.⁸

Several trials have demonstrated the clinical benefit and superior reperfusion efficacy of MT using stent-retriever thrombectomy devices over standard medical therapy in treating AIS-LVO.⁴⁻¹⁰ In the guidelines from American Heart Association/American Stroke Association, MT using stent retrievers has been recommended.⁵ The EmboTrap Thrombectomy Device was originally designed for more effectively trapping, retaining, and removing clots through its unique design of dual-layer and a distal capture zone. A novel stent retriever with a unique 2-layer nitinol structure and an inner 1.25-mm closed cell stent, this device theoretically creates a flow channel through the occlusion. The outer structure leaflets are designed to maintain apposition with the vessel wall to retain the captured clot during retraction, particularly through tortuous vessels. In addition, the distal-closed structure aims at reducing the risk of distal embolization. Thus, in this study, the pooled data suggesting a high successful recanalization rate (90%) and acceptable safety outcomes (ICH, 19%; sICH, 5%; and procedural-related complications, 6%) of the EmboTrap Revascularization Device support its use in the real-world setting.

Most of the recruited studies were single-arm without direct comparison with other types of stent retrievers, and 87% of pooled patients underwent EmboTrap II thrombectomy, suggesting that

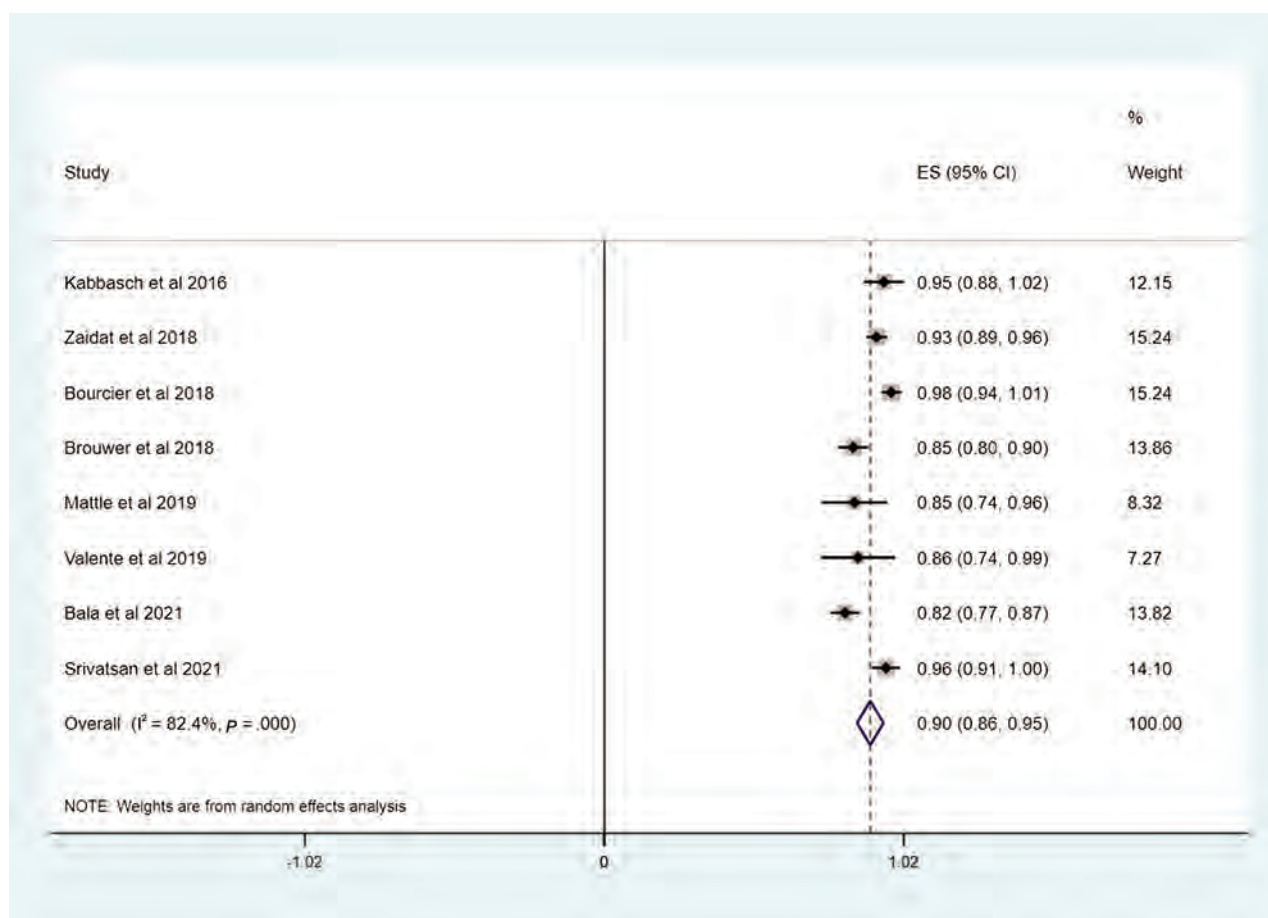


FIG 3. Forest plots of meta-analyses of successful recanalization. ES indicates effect size.

the data are more generalizable with that device. The second generation of stent retrievers, principally Solitaire (Medtronic) and Trevo (Stryker), have been widely adopted with their high efficacy in achieving reperfusion rates and clinical outcomes in AIS-LVO compared with medical therapy in early clinical trials.^{7,23,24} Compared with pooled results from randomized controlled trials using Solitaire and Trevo stents (ie, Highly Effective Reperfusion evaluated in Multiple Endovascular Stroke [HERMES]),²⁵ the EmboTrap device appears to have a greater chance of achieving successful recanalization (88% versus 71%) without increasing the safety events (sICH, 5% versus 4.4%). The procedural-related complication risk was also acceptable (6% in both the total population and subgroup analysis of EmboTrap II). Additionally, in the ARISE I study, the authors compared their EmboTrap arm with a meta-analysis of 8 randomized controlled trials, which yielded similar revascularization rates and good clinical outcomes.²⁰ Thus, further trials with direct comparison between the EmboTrap device and other devices may be warranted to better clarify the superiority of the EmboTrap device.

FPE (mTICI score $\geq 2c$ with a single device pass without rescue) is a new metric to evaluate the efficacy of thrombectomy devices.¹⁶ Previous meta-analyses reported better clinical outcomes of FPE or mFPE (mTICI score $\geq 2b$ with a single device pass without rescue) compared with a multiple-pass effect in patients with AIS

and LVO.²⁶ In our study, the rate of mFPE in EmboTrap II subgroup analysis was 43%, which was higher than that in other stent retrievers reported.²⁷ The higher rate of mFPE of EmboTrap II may be due to several reasons: As a new generation device, it has a new structure with a double proximal marker, which could hypothetically facilitate correct positioning and optimal device capture. The addition of 2 more structural units may further improve its capturing capability.¹² The unique design of an inner blood channel theoretically ensures temporary-but-rapid reperfusion of ischemic brain tissue. This may be validated by the higher favorable outcome of EmboTrap II observed in this study than of Solitaire and Trevo in the study of HERMES collaborators (51% versus 46%).²⁵

This study has certain limitations. Some of the studies recruited had a relatively small sample size and were limited by the retrospective study design. In addition, the heterogeneity among studies was high. Most studies were single-arm without direct comparison with other stent retrievers. We included studies that did not control the use of balloon-guide catheters, occlusion location, and onset-to-puncture time, among numerous other variables that may function as variables in outcomes and likely contribute to the high degree of interstudy heterogeneity. Furthermore, patients with occlusion of both the anterior or posterior circulation were recruited, potentially leading to the heterogeneity of the study population. Because the

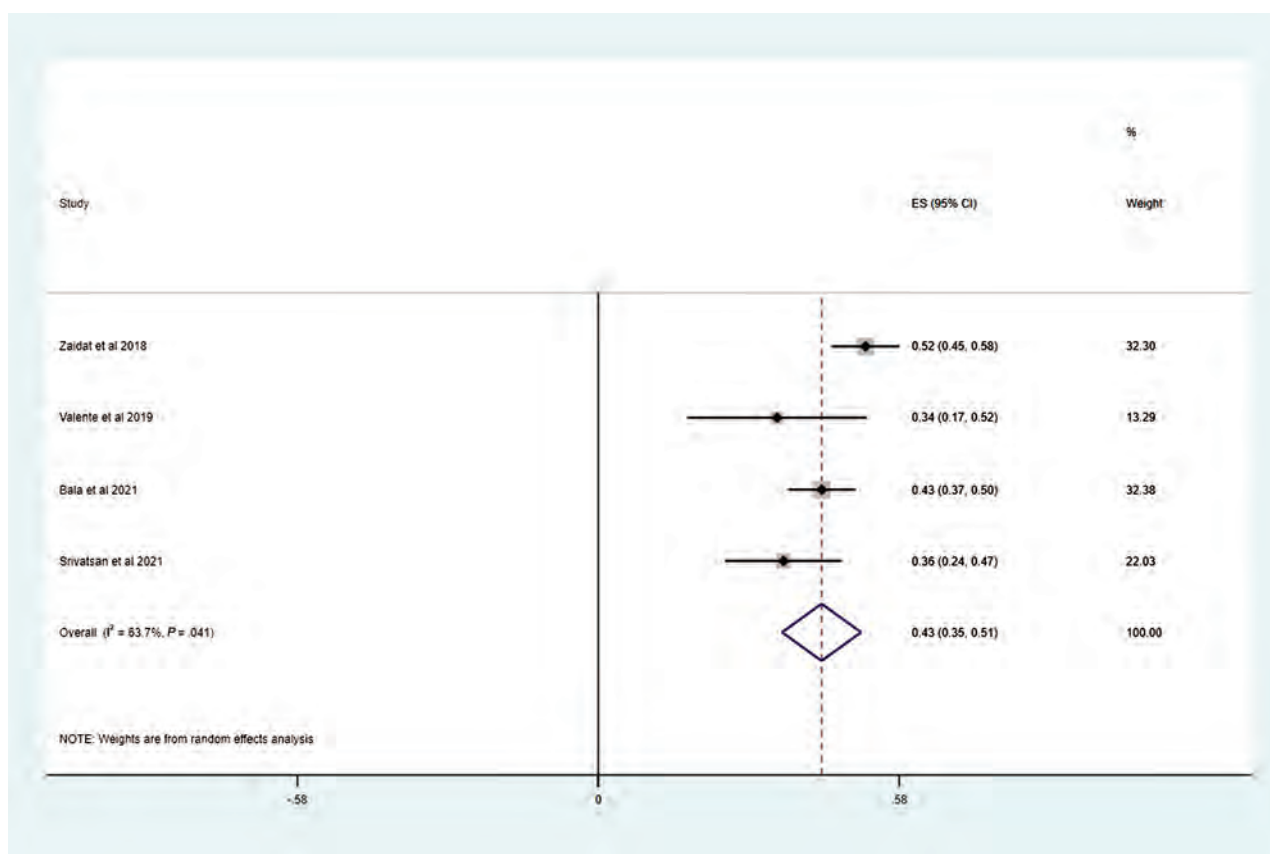


FIG 4. Forest plots of meta-analyses of mFPE. ES indicates effect size.

The primary and secondary outcomes of the EmboTrap Recanalization Device

Outcomes	ES (95% CI)	I ²	P Value ^a
Favorable outcome at 90 days	0.53 (0.42–0.63)	88.6%	<.001
Rate of successful recanalization	0.90 (0.86–0.95)	82.4%	<.001
Rate of complete recanalization	0.55 (0.46–0.64)	77.1%	.004
mFPE (mTICI score $\geq 2b$)	0.43 (0.35–0.51)	63.7%	.041
FPE (mTICI score 2c–3)	0.36 (0.30–0.42)	10.7%	.326
Rescue rate	0.14 (0.08–0.21)	88.4%	<.001
90-day mortality	0.14 (0.09–0.19)	79.3%	<.001
Any ICH	0.19 (0.16–0.22)	0.0%	.510
Symptomatic ICH	0.05 (0.01–0.08)	84.6%	<.001
Procedure-related complications	0.06 (0.05–0.08)	0.0%	.529

Note:— I^2 indicates the variation attributable to heterogeneity; ES, effect size.

^a P value indicates the significance of heterogeneity.

recruited studies were conducted in European countries and the United States, racial generalizability could be limited. Also, trials with direct comparison between EmboTrap and other devices may be required to further validate the results of this systematic review and meta-analysis.

CONCLUSIONS

For patients with AIS due to LVO, MT with the EmboTrap Recanalization Device is at least as safe and effective as the current generation of stent retrievers. This new device may also be associated with a higher FPE without an associated increase in safety events.

Disclosure forms provided by the authors are available with the full text and PDF of this article at www.ajnr.org.

REFERENCES

- Campbell BCV, De Silva DA, Macleod MR, et al. **Ischaemic stroke.** *Nat Rev Dis Primers* 2019;5:70 CrossRef Medline
- Campbell BCV, Donnan GA, Lees KR, et al. **Endovascular stent thrombectomy: the new standard of care for large vessel ischaemic stroke.** *Lancet Neurol* 2015;14:846–54 CrossRef Medline
- Goyal M, Menon BK, van Zwam WH, et al; HERMES Collaborators. **Endovascular thrombectomy after large-vessel ischaemic stroke: a meta-analysis of individual patient data from five randomised trials.** *Lancet* 2016;387:1723–31 CrossRef Medline
- Lambrinos A, Schaink AK, Dhalla I, et al. **Mechanical thrombectomy in acute ischemic stroke: a systematic review.** *Can J Neurol Sci* 2016;43:455–60 CrossRef Medline
- Tsao CW, Aday AW, Almarzooq ZI, et al. **Heart Disease and Stroke Statistics-2022 Update: a Report From the American Heart Association.** *Circulation* 2022;145:e153–639 CrossRef Medline
- Goyal M, Demchuk AM, Menon BK, et al; ESCAPE Trial Investigators. **Randomized assessment of rapid endovascular treatment of ischemic stroke.** *N Engl J Med* 2015;372:1019–30 CrossRef Medline
- Jovin TG, Chamorro A, Cobo E, et al; REVASCAT Trial Investigators. **Thrombectomy within 8 hours after symptom onset in ischemic stroke.** *N Engl J Med* 2015;372:2296–306 CrossRef Medline

8. Zaidat OO, Bozorgchami H, Ribo M, et al. **Primary results of the multicenter ARISE II study (Analysis of Revascularization in Ischemic Stroke With EmboTrap).** *Stroke* 2018;49:1107–15 CrossRef Medline
9. Brinjikji W, Ikeme S, Kottenmeier E, et al. **Real-world outcomes associated with the use of the EmboTrap revascularization device for ischemic stroke in the United States.** *J Neurointerv Surg* 2022;14:1068–72 CrossRef Medline
10. Brouwer PA, Yeo LL, Holmberg A, et al. **Thrombectomy using the EmboTrap device: core laboratory-assessed results in 201 consecutive patients in a real-world setting.** *J Neurointerv Surg* 2018;10:964–68 CrossRef Medline
11. Kabbasch C, Mpotsaris A, Liebig T, et al. **First-in-man procedural experience with the novel EmboTrap® revascularization device for the treatment of ischemic stroke: a European multicenter series.** *Clin Neuroradiol* 2016;26:221–28 CrossRef Medline
12. Valente I, Nappini S, Renieri L, et al. **Initial experience with the novel EmboTrap II clot-retrieving device for the treatment of ischaemic stroke.** *Interv Neuroradiol* 2019;25:271–76 CrossRef Medline
13. Page MJ, McKenzie JE, Bossuyt PM, et al. **The PRISMA 2020 statement: an updated guideline for reporting systematic reviews.** *Int J Surg* 2021;88:105906 CrossRef Medline
14. Shea BJ, Reeves BC, Wells G, et al. **AMSTAR 2: a critical appraisal tool for systematic reviews that include randomised or non-randomised studies of healthcare interventions, or both.** *BMJ* 2017;358:j4008 CrossRef Medline
15. Dargazanli C, Fahed R, Blanc R, et al; ASTER Trial Investigators. **Modified Thrombolysis in Cerebral Infarction 2C/Thrombolysis in Cerebral Infarction 3 reperfusion should be the aim of mechanical thrombectomy: insights from the ASTER Trial (Contact Aspiration Versus Stent Retriever for Successful Revascularization).** *Stroke* 2018;49:1189–96 CrossRef Medline
16. Zaidat OO, Castonguay AC, Linfante I, et al. **First-pass effect: a new measure for stroke thrombectomy devices.** *Stroke* 2018;49:660–66 CrossRef Medline
17. Krishnan R, Mays W, Elijevich L. **Complications of mechanical thrombectomy in acute ischemic stroke.** *Neurology* 2021;97:S115–25 CrossRef Medline
18. Feng Y, Li L, Bai X, et al. **Risk factors for new ischaemic cerebral lesions after carotid artery stenting: protocol for a systematic review and meta-analysis.** *BMJ Open* 2019;9:e030025 CrossRef Medline
19. Srivatsan A, Srinivasan VM, Starke RM, et al. **Early postmarket results with EmboTrap II stent retriever for mechanical thrombectomy: a multicenter experience.** *AJNR Am J Neuroradiol* 2021;42:904–09 CrossRef Medline
20. Mattle HP, Scarrott C, Claffey M, et al; ARISE I Study Group. **Analysis of revascularisation in ischaemic stroke with EmboTrap (ARISE I study) and meta-analysis of thrombectomy.** *Interv Neuroradiol* 2019;25:261–70 CrossRef Medline
21. Bourcier R, Abed D, Piotin M, et al. **Multicenter initial experience with the EmboTrap device in acute anterior ischemic stroke.** *J Neuroradiol* 2018;45:230–35 CrossRef Medline
22. Bala F, Ferrigno M, Personnic T, et al. **Thrombectomy using the EmboTrap II device in late treatment patients in the real-world setting.** *World Neurosurg* 2021;151:e387–94 CrossRef Medline
23. Berkhemer OA, Fransen PS, Beumer D, et al; MR CLEAN Investigators. **A randomized trial of intra-arterial treatment for acute ischemic stroke.** *N Engl J Med* 2015;372:11–20 CrossRef Medline
24. Saver JL, Goyal M, Bonafe A, et al SWIFT PRIME Investigators. **Stent-retriever thrombectomy after intravenous t-PA vs. t-PA alone in stroke.** *N Engl J Med* 2015;372:2285–95 CrossRef Medline
25. Goyal M, Menon BK, van Zwam WH, et al. **Endovascular thrombectomy after large-vessel ischaemic stroke: a meta-analysis of individual patient data from five randomised trials.** *Lancet* 2016;387:1723–31 CrossRef Medline
26. Bai X, Zhang X, Yang W, et al. **Influence of first-pass effect on recanalization outcomes in the era of mechanical thrombectomy: a systemic review and meta-analysis.** *Neuroradiology* 2021;63:795–807 CrossRef Medline
27. Zhou T, Li T, Zhu L, et al. **Comparing the efficacy and safety of the Skyflow device with those of the Solitaire FR stent in patients with acute ischemic stroke: a prospective, multicenter, randomized, non-inferiority clinical trial.** *J Neurointerv Surg* 2022;14:1130–34 CrossRef Medline

Predictors of Endovascular Treatment Procedural Complications in Acute Ischemic Stroke: A Single-Center Cohort Study

E. Maslias, F. Puccinelli, S. Nannoni, S.D. Hajdu, B. Bartolini, F. Ricciardi, V. Dunet, P. Maeder, D. Strambo, G. Saliou, and P. Michel



ABSTRACT

BACKGROUND AND PURPOSE: Procedural complications occur in 4%–29% of endovascular treatments in acute ischemic stroke. However, little is known about their predictors and clinical impact in the real world. We aimed to investigate the frequency and clinical impact of procedural complications of endovascular treatment and identify associated risk factors.

MATERIALS AND METHODS: From 2015–2019, we retrospectively reviewed all patients with acute ischemic stroke receiving endovascular treatment within 24 hours included in the Acute STroke Registry and Analysis of Lausanne. We identified patients having an endovascular treatment procedural complication (local access complication, arterial perforation, dissection or vasospasm, and embolization in a previously nonischemic territory) and performed logistic regression analyses to identify associated predictors. We also correlated procedural complications with long-term clinical outcome.

RESULTS: Of the 684 consecutive patients receiving endovascular treatment, 113 (16.5%) had at least 1 procedural complication. The most powerful predictors were groin puncture off-hours (OR = 2.24), treatment of 2 arterial sites (OR = 2.71), and active smoking (OR = 1.93). Patients with a complication had a significantly less favorable short-term clinical outcome (Δ -NIHSS score of -2.2 versus -4.33 , P -value adjusted $< .001$), but a similar long-term clinical outcome (mRS at 3 months = 3 versus 2, P -value adjusted = .272).

CONCLUSIONS: Procedural complications are quite common in endovascular treatment and lead to a less favorable short-term but similar long-term outcome. Their association with treatment off-hours and at 2 arterial sites requires particular attention in these situations to optimize the overall benefit of endovascular treatment.

ABBREVIATIONS: AIS = acute ischemic stroke; EVT = endovascular treatment

Endovascular treatment (EVT) with stent retrievers or the direct aspiration first-pass technique is considered the criterion standard procedure for eligible patients with acute ischemic stroke (AIS) with proximal intracranial large-vessel occlusion.^{1–3} Even though complication rates of 4%–29% have been reported,^{4–10} they do not eliminate its global beneficial effect.

Received April 5, 2022; accepted after revision October 12.

From the Stroke Centre (E.M., S.N., D.S., P. Michel), Neurology Service, Department of Clinical Neurosciences, and Department of Diagnostic and Interventional Radiology (F.P., S.D.H., B.B., V.D., P. Maeder, G.S.), Neuroradiology Unit, Lausanne University Hospital and University of Lausanne, Lausanne, Switzerland; and Department of Statistical Science (F.R.), University College London, London, UK.

S. Nannoni and V. Dunet received a grant from the Swiss National Science Foundation; D. Strambo received grants from the Swiss Heart Foundation and the University of Lausanne; and P. Maeder received grants from the Swiss National Science Foundation and the Swiss Heart Foundation.

Please address correspondence to Errikos Maslias, MD, Neurology Service, Lausanne University Hospital, Rue du Bugnon, 46, 1011 Lausanne, Switzerland; e-mail: Errikos.Maslias@chuv.ch

Indicates open access to non-subscribers at www.ajnr.org

Indicates article with online supplemental data.

<http://dx.doi.org/10.3174/ajnr.A7705>

Procedural complications during EVT include local-access complications (ie, hemorrhage or arterial lesion at the access site) and cerebrovascular complications (ie, arterial dissection, embolization in a previously nonischemic territory, arterial perforation, or vasospasm). The occurrence of procedural complications carries the risk of additional diagnostic and therapeutic procedures, longer hospital stays, and increased illness, mortality, and costs.

Awareness of the frequency and clinical impact of EVT procedural complications and of the independently associated risk factors could guide stroke teams in patient selection and complication's prevention during the procedure. In addition, the presence of such risk factors should intensify intraprocedural monitoring, which may permit a more proactive management of complications. Although the timing of AIS and EVT cannot be chosen by patients or the medical system, recent reports described longer door-to-reperfusion delays at night and on weekends¹¹ and poorer outcomes in patients treated in the afternoon.¹²

Given the paucity of clinical data,¹³ we aimed to investigate the frequency and clinical impact of the overall EVT procedural

complications and identify associated risk factors in a consecutive real-world AIS population in the modern EVT era.

MATERIALS AND METHODS

Study Design and Cohort Selection

We retrospectively reviewed all patients with AIS receiving EVT from January 2015 to December 2019 in the prospectively constructed Acute STroke Registry and Analysis of Lausanne (ASTRAL), which collects all adults with AIS admitted to the stroke unit and/or intensive care unit of Lausanne University Hospital (CHUV).¹⁴

For this analysis, we selected all patients receiving EVT within 24 hours, with or without preceding IV thrombolysis, including patients for whom the target occlusion was not reached for technical reasons or in whom the target occlusion on DSA was already re-canalized at the time of the EVT attempt. We excluded patients receiving rescue endovascular procedures, ie, EVT after secondary worsening and/or >24 hours after stroke onset.

Acute Neuroimaging, EVT Eligibility, and Procedure

Acute brain imaging on admission was based mainly on CT until April 2018 using a 64-detector row CT scanner and mainly on MR imaging from May 2018 with 3T MR imaging scanners. We obtained at least 1 arterial study of the cervical and cerebral arteries before EVT, mostly CTA, alternatively MRA, followed by DSA with the intention to perform EVT. A senior vascular neurologist and senior neuroradiologist assessed all noninvasive neuroimaging, and an interventional neuroradiologist, all DSAs to identify procedure-related cerebrovascular complications in a nonblinded manner. A tandem lesion was defined as the simultaneous presence of an arterial occlusion or stenosis ($\geq 70\%$ extracranially, $\geq 50\%$ intracranially) in both the extra- and intracranial circulation in the same vascular axis.

Since October 2014, we have offered EVT in our center within 6 hours for a disabling deficit and an ASPECTS of ≥ 5 , similar to the Multicenter Randomized Clinical trial of Endovascular treatment for Acute Ischemic stroke in the Netherlands (MR CLEAN)⁷ and initial European criteria.² Since May 2017, patients were treated up to 8 hours using the same criteria.¹⁵ After 8 hours, treatment was given following the modified Clinical Mismatch in the Triage of Wake Up and Late Presenting Strokes Undergoing Neurointervention with Trevo (DAWN) criteria, ie, in the presence of an NIHSS score of ≥ 10 and an ASPECTS of ≥ 7 or, if the stroke was disabling, an NIHSS score of 1–10 and an ASPECTS of ≥ 8 .^{4,16} Since January 2018, late treatment was alternatively based on any NIHSS, a core <70 mL and a mismatch ratio [(penumbra + core)/core] of > 1.8 , according to the Endovascular Therapy Following Imaging Evaluation for Acute Ischemic Stroke 3 (DEFUSE-3) criteria, in accordance with the updated Swiss,¹⁷ European,¹ and American recommendations.³

We treated basilar artery occlusions until April 2017 with EVT up to 6 hours in the absence of extensive brainstem infarct on imaging. From May 2017, the treatment window was extended to 8 hours if the posterior circulation ASPECTS was ≥ 7 , and to 24 hours if no transverse irreversible brainstem ischemia was present on MR imaging or if the posterior circulation ASPECTS was ≥ 8 on plain CT.

We performed femoral access under sonographic guidance. The type of sedation was recorded (local versus general anesthesia), with the latter being the preferred method in our center. We routinely add 2 mg of nimodipine in the flushing line of the guiding catheter to prevent vasospasm during the intervention. The degree of recanalization at the end of the procedure was recorded according to the modified TICI grading scale.¹⁸

During working hours, there is a board-certified neurologist on-site and available any time, whereas during off-hours, there is a neurology resident-in-training on site who is supervised by phone by a board-certified neurologist. During working hours, there are always 3–4 board-certified interventional neuroradiologists in-house; during off-hours, the on-call board-certified interventional neuroradiologist arrives within 20 minutes at the hospital when called for an EVT. Finally, there are 2 interventional technicians available in-house during working hours, and only 1 after hours. Emergency department staffing by the physician residents and nurses is identical at all times, but during working hours, there are twice as many board-certified internists present.

EVT Procedural Complications

We defined procedural complications related to EVT in accordance with the current literature.^{19,20}

Access Complications

- 1) Hemorrhage in the arterial puncture area: any important external bleeding or internal hematoma (ie, femoral, retroperitoneal)
- 2) Arterial access damage: symptomatic or radiologic pseudoaneurysm, arterial dissection, occlusion or embolization in a peripheral territory, and floating thrombus at the punctured artery.

Procedural Cerebrovascular Complications

- 1) Embolization in the nonischemic cerebral territory: any embolization in a previously not occluded artery (with the exclusion of clot fragmentation and embolization in a distal segment of the already affected artery)
- 2) Iatrogenic dissections of cervical or intracranial arteries or vasospasms requiring therapeutic interventions by intra-arterial vasodilator drugs
- 3) Intracranial arterial perforation or postprocedural SAH: contrast extravasation observed during the procedure or SAH in the territory of the treated artery on any control neuroimaging within 24 hours.

We did not consider the occurrence of parenchymatous hemorrhage and cerebral edema as procedural complications because their proportion was not increased in large, randomized, controlled trials of EVT^{21,22} and most of these occur in the postprocedural phase. Therefore, they were not included in the current analysis.

Post-EVT monitoring in our stroke unit is described in the Online Supplemental Data.

Primary End Points

As primary outcomes, we evaluated the frequency and predictors of EVT procedure-related complications.

Table 1: Frequency of EVT procedural complications

EVT Procedural Complications	Frequency (No.) (%)
Significant at access site < 7 days	13 (1.9%)
External bleeding	6 (46.2%)
Internal hematoma	7 (53.8%)
Any local arterial damage at access site <7 days	9 (1.3%)
Cerebral arterial complications, ie, dissection (<i>n</i> = 27) and treated vasospasm (<i>n</i> = 1)	28 (4.1%)
Embolization in previously normal territory	21 (3.1%)
Arterial intracranial perforation during EVT (observed acutely, SAH on subacute imaging)	42 (6.1%)
Total EVT procedure complications	113 (16.5%)

Table 2: Multivariate analysis of significant factors associated with EVT procedural complications

Predictors of EVT Procedural Complications	OR	95% CI	P Value
Two sites treated	2.71	1.49–4.86	<.001
Groin puncture off-hours	2.24	1.37–3.69	<.001
Smoking	1.93	1.10–3.33	.02

Secondary End Points

In patients with procedural complications, we assessed the short-term outcome using the 24-hour Δ -NIHSS, defined as the difference between the NIHSS score at 24 hours and the NIHSS score at admission. We decided to analyze the NIHSS as an ordinal variable, to increase the power of the study to identify independent associations with dependent variables. The Δ -NIHSS was preferred over early neurologic deterioration, which lacks a uniform definition in the literature.

In these patients, we used the mRS for evaluation of the long-term outcome at 3 months.

For patients with-versus-without complications, we compared the length of hospitalization, the disposition after acute hospitalization, early ischemic stroke or TIA recurrence up to 7 days, and mortality at 7 days and 3 and 12 months using univariate analysis.

Statistical Analysis and Ethics Considerations

Differences between patients with and without EVT procedural complications were explored using appropriate statistical testing such as the Mann-Whitney *U*, χ^2 , or Fisher Exact tests.

To identify factors independently associated with the occurrence of any procedural complication, we used logistic regression models. We initially performed unadjusted univariate analyses, fitting models with the complications/no complications indicator as the only explanatory variable. Variables that were significant in the univariate approach (using a threshold *P* value of .20) were then used for the multivariate analysis, in which a stepwise variable-selection method based on the Akaike information criterion was performed to obtain the final multivariate logit model. The following variables were entered into the final model: active smoking, hypertension, diabetes mellitus, groin puncture during regular working hours (8:00 AM–5:59 PM) versus off-hours (6:00 PM–7:59 AM), and 2 arterial sites treated.

For short-term outcome (24-hour Δ -NIHSS), a multivariate linear model was used and well-known factors associated with clinical outcome such as covariates, ie, age, admission NIHSS,

admission level of consciousness, pre-stroke modified Rankin Scale (mRS) score, acute ASPECTS (CT or DWI-MR imaging), pretreatment with intravenous thrombolysis, acute blood glucose, and stroke mechanism (grouped into cardioembolic, atheromatous, and other categories).

For the 3-month outcome (mRS as an ordinal variable, 0–6), a multivariate ordinal logistic model was used. Factors included in this outcome analysis were age, admission NIHSS, admission level of consciousness, prestroke mRS score, acute ASPECTS (CT or DWI), proximal-versus-distal site of large-vessel occlusion, and peripheral artery disease.

A *P* value < .05 was considered significant for all analyses.

ASTRAL follows the institutional regulations on clinical and research registries. Before analysis, the data were anonymized following the principles of the Swiss Human Research Ordinance from 2013 (HRO, Art.25). Given that only anonymized data were used, there was no need for local ethics committee approval or patient consent according to the Swiss Federal Act on Research involving Human Beings from 2011 (HRA, Art.3) and the applicable data protection legislation. Patients were informed in writing about the potential scientific use of their routinely collected data in anonymized form and their right to refuse scientific use of personal data for research purposes; any such refusal was honored before data extraction.

The anonymized data of this study are available from the authors on reasonable request.

For reporting, we used the Strengthening the Reporting of Observational Studies in Epidemiology checklist.²³

RESULTS

During the study period, 684 consecutive patients with EVT were included, with a median age of 72 years. The median NIHSS score was 14, and women were nonsignificantly underrepresented (47.3%). In total, 113 (16.5%) patients experienced an EVT procedure-related complication. The baseline characteristics of these patients are summarized in the Online Supplemental Data, and the frequency of EVT procedural complications, in Table 1.

Predictors for Procedural Complications during EVT

In the univariate analysis (Table 1), patients with a procedural complication during EVT had higher admission NIHSS scores and more cerebrovascular risk factors such as smoking; and more often had a tandem lesion, thus 2 arterial sites were treated. The number of device passages in the recanalization attempt of the occluded artery seemed to also be associated with EVT procedural complications in the univariate analysis.

In the multivariate analysis, we identified 3 independent associations of EVT with any procedural complication: groin puncture off-hours, treatment of 2 arterial sites, and active smoking (Table 2).

Table 3: Adjusted primary outcomes for patients with AIS with versus patients without EVT procedural complications

Clinical Outcome	AIS with Procedural Complications (n = 113)	AIS without Procedural Complications (n = 571)	Adjusted OR or β Coefficient (95% CI)	Adjusted P Value
Short-term clinical consequences (24-hour Δ -NIHSS)	-2.21 (10.06)	-4.33 (7.89)	2.73 (1.09–4.37)	<.001 ^a
Long-term functional outcome at 3 months (mRS) (median) (IQR)	3 (2–5)	2 (1–4)	1.32 (0.81–2.16)	.272

^aSignificant.

Secondary Outcomes

Patients with procedural complications had a significantly less favorable short-term clinical outcome in the adjusted analysis than patients without a procedural complication (24-hour Δ -NIHSS of -2.2 versus -4.33, $P < .001$). However, this difference did not persist when evaluating the adjusted long-term clinical outcome (mRS at 3 months = 3 versus 2, P -value adjusted = .272) (Table 3).

Concerning secondary outcomes, the unadjusted analysis between patients with or without a procedural complication (early stroke recurrence within 7 days of stroke onset, duration of hospitalization, discharge orientation, mortality at 7 days and 3 and 12 months and mRS score at 12 months) found no statistically significant differences (Online Supplemental Data).

DISCUSSION

Of 684 consecutive patients receiving EVT in the modern thrombectomy era in our hospital, 16.5% had a procedural complication. The most powerful predictors were EVT performed off-hours, treatment of 2 arterial sites, and a history of smoking. While short-term clinical outcome was significantly worse in patients with a procedural complication, it did not affect long-term outcome.

Our frequency of 16.5% for EVT procedural complications is in line with the literature, reporting a wide range of complications in randomized controlled trials (4%–29%). Lack of a uniform definition hampers comparability, however. In our study, we used a more liberal definition for some complications, in particular by considering any postprocedural SAH on neuroimaging as a complication. However, in some cases, the SAH may not be related to the procedural perforation but to arterial lacerating when pulling back the endovascular device or thrombolysis-facilitated rupture of an ischemic superficial artery.

Groin puncture off-hours was strongly associated with procedural complications. This could potentially be explained by the operator's fatigue due to sleep deprivation leading to impairment of motor, cognitive, and attention skills. Another explanation could be less staff, which is particularly prevalent after hours. Hajdu et al¹² demonstrated that EVT for AIS performed in the morning hours leads to a more favorable outcome at 3 months than EVT at the end of the workday, highlighting the potential influence of stroke unit staff fatigue. Another important factor could perhaps be that during off-hours, less experienced emergency and neurology physicians perform the pre-EVT management of patients with stroke.

Another powerful predictor of occurrence of EVT procedural complications was the treatment of 2 arterial sites. Such treatment

may be challenging, requiring particular neurointerventional skills. It also demands a higher number of EVT device passages, increasing the risk of dissection or perforation of the cervicocerebral arteries as well as the risk of embolization in a previously nonischemic territory. This variable seems to be more powerful in predicting complications than the number of device passes, which was associated with procedural complications in our univariate but not multivariate analysis.

Among patient characteristics, we identified active smoking as contributing to a higher procedural complication risk. Smoking has been demonstrated to increase the total calcification index of the carotid arteries and arterial stiffness and endothelial dysfunction and is associated with poorer control of other cerebrovascular risk factors, again potentially contributing to such arterial problems.²⁴

Most interesting, age, diabetes mellitus, stroke mechanism (Trial of Org 10172 in Acute Stroke Treatment [TOAST]),²⁵ and the type of anesthesia were not significantly associated with an increased occurrence of procedural complications. A higher stroke severity (admission NIHSS score) was associated with complications in the univariate but not multivariate analysis.

The fact that the 24-hour neurologic status was worse in patients with procedural complications highlights the need for close monitoring and proactive management of the complications. This initial disadvantage of problematic EVT did not translate into a statistical difference of the functional status at 3 months in the adjusted analysis. Similarly, other large series of patients with EVT, which did not analyze the rate of complications, showed no association of the time of treatment with clinical outcome.^{26,27} This reassuring observation is a further argument in favor of the relative safety of EVT.

Additional important findings of our study were the absence of statistically significant differences in the length of hospitalization, posthospital disposition, early ischemic event recurrence, and early or late mortality rates between patients with and without EVT procedure-related complications.

The main clinical implication of our study is the identification of predictors of EVT procedural complications. Given that the treating physicians cannot influence the 3 identified variables, they can at least inform patients and their next of kin of the additional risk. Furthermore, the interventional neuroradiologist may use special care or techniques in the recognized patients to avoid procedural complications to maximize the benefit of EVT. Third, awareness of these complication predictors may allow a closer monitoring during and after the EVT procedure for their early detection and treatment.

The main strength of our study is the enrollment of consecutive real-world patients, which makes our results more generalizable.

Furthermore, prespecified and liberal definitions of EVT complications by noninterventional neurologists decrease the risk of underreporting. Third, we considered only procedures from the modern EVT era (2015–2019) using mainly stent retrievers and the direct aspiration first-pass technique, which are the currently preferred revascularization methods.

The main limitations are, first, the retrospective, observational, nonrandomized, and single-center character of our study. Second, our results need to be confirmed in other populations because ASTRAL contains a predominantly elderly, white population. Third, the definitions of some of the procedural complications are debatable, given the lack of complete consensus.¹⁹ Similarly, the causal association of a “complication” and the EVT is not always certain, for example in the case of SAH, which can also occur spontaneously or due to IV thrombolysis. Finally, we did not include postprocedural parenchymal hemorrhage and cerebral edema in this analysis because we do not consider these procedure-related.^{10,22}

CONCLUSIONS

Procedural complications are quite common in endovascular treatment and lead to a less favorable short-term but similar long-term outcome. The most powerful predictors of procedural complications are EVT performed off-hours, treatment of two arterial sites, and a history of smoking. These situations require particular attention in order to optimize the overall benefit of endovascular treatment.










Disclosure forms provided by the authors are available with the full text and PDF of this article at www.ajnr.org.

REFERENCES

- Turc G, Bhogal P, Fischer U, et al. **European Stroke Organisation (ESO)-European Society for Minimally Invasive Neurological Therapy (ESMINT) Guidelines on Mechanical Thrombectomy in Acute Ischaemic Stroke Endorsed by Stroke Alliance for Europe (SAFE).** *Eur Stroke J* 2019;4:6–12 CrossRef Medline
- Fiehler J, Cognard C, Gallitelli M, et al. **European Recommendations on Organisation of Interventional Care in Acute Stroke (EROICAS).** *Int J Stroke* 2016;11:701–16 CrossRef Medline
- Powers WJ, Rabinstein AA, Ackerson T, et al; American Heart Association Stroke Council. **2018 Guidelines for the Early Management of Patients With Acute Ischemic Stroke: A Guideline for Healthcare Professionals From the American Heart Association/American Stroke Association.** *Stroke* 2018;49:e46–110 CrossRef Medline
- Nogueira RG, Jadhav AP, Haussen DC, et al; DAWN Trial Investigators. **Thrombectomy 6 to 24 hours after stroke with a mismatch between deficit and infarct.** *N Engl J Med* 2018;378:11–21 CrossRef Medline
- Albers GW, Marks MP, Kemp S, et al; DEFUSE 3 Investigators. **Thrombectomy for stroke at 6 to 16 hours with selection by perfusion imaging.** *N Engl J Med* 2018;378:708–18 CrossRef Medline
- Goyal M, Demchuk AM, Menon BK, et al; ESCAPE Trial Investigators. **Randomized assessment of rapid endovascular treatment of ischemic stroke.** *N Engl J Med* 2015;372:1019–30 CrossRef Medline
- Berkhemer OA, Fransen PS, Beumer D, et al; MR CLEAN Investigators. **A randomized trial of intraarterial treatment for acute ischemic stroke.** *N Engl J Med* 2015;372:11–20 CrossRef Medline
- Jovin TG, Chamorro A, Cobo E, et al; REVASCAT Trial Investigators. **Thrombectomy within 8 hours after symptom onset in ischemic stroke.** *N Engl J Med* 2015;372:2296–306 CrossRef Medline
- Balami JS, White PM, McMeekin PJ, et al. **Complications of endovascular treatment for acute ischemic stroke: prevention and management.** *Int J Stroke* 2018;13:348–61 CrossRef Medline
- Goyal M, Menon BK, van Zwam WH, et al; HERMES Collaborators. **Endovascular thrombectomy after large-vessel ischaemic stroke: a meta-analysis of individual patient data from five randomised trials.** *Lancet* 2016;387:1723–31 CrossRef Medline
- Mpotsaris A, Kowoll A, Weber W, et al. **Endovascular stroke therapy at nighttime and on weekends: as fast and effective as during normal business hours?** *J Vasc Interv Neurol* 2015;8:39–45 Medline
- Hajdu SD, Kaesmacher J, Michel P, et al. **Association of time of day when endovascular therapy for stroke starts and functional outcome.** *Neurology* 2021;96:e1124–36 CrossRef Medline
- Salsano G, Pracucci G, Mavilio N, et al. **Complications of mechanical thrombectomy for acute ischemic stroke: incidence, risk factors, and clinical relevance in the Italian Registry of Endovascular Treatment in acute stroke.** *Int J Stroke* 2021;16:818–27 CrossRef Medline
- Michel P, Odier C, Rutgers M, et al. **The Acute STroke Registry and Analysis of Lausanne (ASTRAL): design and baseline analysis of an ischemic stroke registry including acute multimodal imaging.** *Stroke* 2010;41:2491–98 CrossRef Medline
- Saver JL, Goyal M, van der Lugt A, et al; HERMES Collaborators. **Time to treatment with endovascular thrombectomy and outcomes from ischemic stroke: a meta-analysis.** *JAMA* 2016;316:1279–88 CrossRef Medline
- Nannoni S, Ricciardi F, Strambo D, et al. **Reproducing DAWN results in real life based on clinical-ASPECTS mismatch: an explanatory analysis [poster].** In: *Proceedings of the European Stroke Organisation Conference*, Milan, Italy. May 21–23, 2019
- Michel P, Diepers M, Mordasini P, et al; Swiss Stroke Society. **Acute revascularization in ischemic stroke: updated Swiss guidelines.** *Clinical and Translational Neuroscience* 2021;5:2514183X2199922 CrossRef
- Wintermark M, Albers GW, Broderick JP, et al; Stroke Imaging Research (STIR) and Virtual International Stroke Trials Archive (VISTA)-Imaging Investigators. **Acute Stroke Imaging Research Roadmap II.** *Stroke* 2013;44:2628–39 CrossRef Medline
- Sacks D, Baxter B, Campbell BC, et al. **Multisociety Consensus Quality Improvement Revised Consensus Statement for Endovascular Therapy of Acute Ischemic Stroke: From the American Association of Neurological Surgeons (AANS), American Society of Neuroradiology (ASNR), Cardiovascular and Interventional Radiology Society of Europe (CIRSE), Canadian Interventional Radiology Association (CIRA), Congress of Neurological Surgeons (CNS), European Society of Minimally Invasive Neurological Therapy (ESMINT), European Society of Neuroradiology (ESNR), European Stroke Organization (ESO), Society for Cardiovascular Angiography and Interventions (SCAI), Society of Interventional Radiology (SIR), Society of NeuroInterventional Surgery (SNIS), and World Stroke Organization (WSO).** *J Vasc Interv Radiol* 2018;29:441–53 CrossRef Medline
- Maslias E, Nannoni S, Ricciardi F, et al. **Procedural complications during early versus late endovascular treatment in acute stroke: frequency and clinical impact.** *Stroke* 2021;52:1079–82 CrossRef Medline
- Hao Y, Zhang Z, Zhang H, et al. **Risk of intracranial hemorrhage after endovascular treatment for acute ischemic stroke: systematic review and meta-analysis.** *Interv Neurol* 2017;6:57–64 CrossRef Medline
- Kimberly WT, Dutra BG, Boers AM, et al; MR CLEAN Investigators. **Association of reperfusion with brain edema in patients with acute ischemic stroke: a secondary analysis of the MR CLEAN trial.** *JAMA Neurol* 2018;75:453–61 CrossRef Medline
- von Elm E, Altman DG, Egger M, et al; STROBE Initiative. **Strengthening the Reporting of Observational Studies in Epidemiology (STROBE) statement: guidelines for reporting observational studies.** *J Clin Epidemiol* 2008;61:344–49 CrossRef Medline

24. Gać P, Jaźwiec P, Mazur G, et al. **Exposure to cigarette smoke and the carotid arteries calcification index in patients with essential hypertension.** *Cardiovasc Toxicol* 2017;17:335–43 CrossRef Medline
25. Chung JW, Park SH, Kim N, et al. **Trial of ORG 10172 in Acute Stroke Treatment (TOAST) classification and vascular territory of ischemic stroke lesions diagnosed by diffusion-weighted imaging.** *J Am Heart Assoc* 2014;11:e001119 CrossRef Medline
26. Tschoe C, Kittel C, Brown P, et al. **Impact of off-hour endovascular therapy on outcomes for acute ischemic stroke: insights from STAR.** *J Neurointerv Surg* 2021;13:693–96 CrossRef Medline
27. Grandhi R, Ravindra VM, Ney JP, et al. **Investigating the “weekend effect” on outcomes of patients undergoing endovascular mechanical thrombectomy for ischemic stroke.** *J Stroke Cerebrovasc Dis* 2021;30:106013 CrossRef Medline

Material-Specific Roadmap Modes Can Improve the Visibility of Liquid Embolic Agents for Endovascular Embolization: A Systematic In Vitro Study

 N. Schmitt,  L. Wucherpfennig,  S. Hohenstatt,  K. Karimian-Jazi,  M.O. Breckwoldt,  H.-U. Kauczor,  M. Bendszus,  M.A. Möhlenbruch, and  D.F. Vollherbst

ABSTRACT

BACKGROUND AND PURPOSE: Endovascular embolization using liquid embolic agents is a safe and effective treatment option for AVMs and fistulas. Because reliable visibility of these liquid embolic agents is essential for intraprocedural visual control to prevent complications, novel angiographic systems are equipped with material-specific roadmap modes. The aim of this study was the systematic in vitro comparison of conventional and material-specific roadmap modes regarding the visibility of the most used liquid embolic agents.

MATERIALS AND METHODS: A recently introduced in vitro model, resembling cerebral vessels, was embolized with Onyx 18, Squid 18, PHIL 25%, and *n*-BCA mixed with iodized oil ($n = 4$ for each liquid embolic agent), as well as with contrast medium and saline, both serving as a reference. Imaging was performed in conventional and material-specific roadmap modes. The visibility of the liquid embolic agents in both modes was compared quantitatively and qualitatively.

RESULTS: Significant differences between conventional and material-specific roadmap modes regarding the visibility of the liquid embolic agents were observed for all study groups. All liquid embolic agents were better visible in the material-specific roadmap modes compared with the conventional mode in qualitative and quantitative analyses (eg, Onyx in conventional-versus-material-specific modes along the 1.0-mm sector: mean contrast-to-noise ratio, 5.69 [SD, 0.85] versus 47.18 [SD, 5.72]; $P < .001$, respectively).

CONCLUSIONS: In this in vitro study, we demonstrated a better visibility of all investigated liquid embolic agents by using material-specific roadmap modes compared with the conventional roadmap technique. Especially in complex anatomic situations, these novel roadmap modes could improve the visual control and thus the safety and efficacy of embolization procedures in clinical practice.

ABBREVIATIONS: CNR = contrast-to-noise ratio; DU = density units; LEA = liquid embolic agent

Endovascular embolization using liquid embolic agents (LEAs) is an effective treatment mode for therapy of cerebral and spinal vascular disorders, such as AVMs or dural AVFs.^{1–6} In recent years, the range of available LEAs, each with different properties, has increased steadily. Onyx (Medtronic), Squid (Balt), and the precipitating hydrophobic injectable liquid (PHIL; MicroVention) represent the most commonly used copolymer-based, nonadhesive LEAs on the market. The embolic agents Onyx and Squid consist of ethylene-vinyl alcohol copolymer, dimethyl-sulfoxide,

and radiopaque tantalum powder, while PHIL consists of 2 specific copolymers (poly[lactide-co-glycolide] and polyhydroxyethylmethacrylate) and covalently bound triiodophenol for intrinsic radiopacity. Regarding both ethylene-vinyl alcohol copolymer-based LEAs, Squid features a smaller (“micronized”) grain size of the admixed tantalum powder, aiming for a more homogeneous radiopacity and thus better visibility during longer injection procedures.

Before the introduction of these nonadhesive embolic agents, liquid embolization was primarily performed with cyanoacrylates. With their most frequently used active component being *n*-BCA, cyanoacrylates are still applied frequently, for example, for the therapy of lesions that cannot be reached with dimethyl-sulfoxide-compatible catheters or for embolization of high-flow shunts in AVMs or dural AVFs. *n*-BCA and its derivatives are normally mixed with iodized oil (ratio 1:1; Lipiodol Ultra Fluid; Guerbet) to enable sufficient visibility.⁷ During embolization procedures, a reliable visibility of the embolic material is essential for

Received August 18, 2022; accepted after revision October 12.

From the Departments of Neuroradiology (N.S., S.H., K.K.-J., M.O.B., M.B., M.A.M., D.F.V.) and Diagnostic and Interventional Radiology (L.W., H.-U.K.), Heidelberg University Hospital, Heidelberg, Germany.

N. Schmitt and L. Wucherpfennig contributed equally to this work.

Please address correspondence to Dominik F. Vollherbst, MD, Department of Neuroradiology, Heidelberg University Hospital, INF 400, 69120 Heidelberg, Germany; e-mail: Dominik.Vollherbst@med.uni-heidelberg.de

<http://dx.doi.org/10.3174/ajnr.A7706>

visual control and to prevent possible complications, for example embolization of AVM-related draining veins or inadvertent embolization of vessels supplying healthy brain tissue. Therefore, the novel angiographic system Artis icono (Siemens Healthineers) is equipped with material-specific roadmap modes aimed at improving the visualization of LEAs. As described recently, the technical principle of these modes is based on a contrast-to-noise ratio (CNR)-driven exposure control, which adjusts the imaging setting of the angiography suite automatically and thereby optimizes image quality, while reducing the radiation dose at the same time.^{8,9}

To date, there is only 1 experimental study available investigating and comparing the visibility of different LEAs, while the potential of material-specific roadmap modes has not been investigated so far.¹⁰ The aim of the present study was the systematic in vitro comparison of conventional and material-specific roadmap techniques regarding the visibility of the most used LEAs.

MATERIALS AND METHODS

Sample Preparation

A recently introduced in vitro model was used for the present study, consisting of connected sectors with different diameters, ranging from 2.0 to 0.5 mm, and manufactured using a 3D printer, consisting of the biocompatible synthetic material VisiJet.¹⁰ Each in vitro model ($n = 4$ per LEA, contrast medium, and saline) was embolized by a manual pulsatile LEA injection using a standard embolization microcatheter (SONIC 1.2F, 35-mm detachable tip length; Balt) as well as 1-mL, dimethyl-sulfoxide-compatible syringes. Moreover, during the embolization procedure, there was a continuous flush of saline (NaCl 0.9%) with a flow of 60 mL per hour. All LEAs were prepared in accordance with the manufacturer's instructions and as recommended for clinical use. Embolization of the in vitro models was performed for the following LEAs: Onyx 18, Squid 18, PHIL 25%, *n*-BCA mixed with iodized oil as well as contrast medium (iopamidol, Imeron 300; Bracco) and NaCl 0.9%.

An exemplary image of an in vitro model embolized with Onyx is provided in Fig 1.

Imaging

Roadmap imaging was performed using the Artis icono angiography suite (Siemens Healthineers). A pulsed imaging mode with a pulse rate of 7.5 p/s was used, and images were acquired with standard settings according to clinical routine in a conventional (for all investigated LEAs, contrast medium, and saline) as well as a material-specific roadmap mode (tantalum-specific mode for Onyx and Squid; iodine-specific mode for PHIL and *n*-BCA mixed with iodized oil and contrast medium). The FOV of the receptor was 25 cm. Further acquisition settings, such as the tube parameters, collimations settings, and source-image distance, were adjusted automatically by the image-quality system OPTIQ (Siemens Healthineers).

Quantitative Analysis

Quantitative image analysis comparing the visibility of LEAs in a conventional and material-specific roadmap mode was performed on a PACS workstation. Five similar rectangular ROIs with a length of 4 mm and widths similar to the diameter of the cylindric cavity (2.0, 1.5, 1.5, and 0.5 mm, respectively) were drawn manually

along each sector of the in vitro models. Because the sector of the smallest cavity (0.5 mm) features a length of 30 mm, the ROIs were drawn along its proximal part. For each ROI, the mean density units (DU) were calculated. Simultaneously, 5 square ROIs (side length: 4 mm) were drawn in proximity on a similar level on the noncavity part of each in vitro model. For the ROIs on the noncavity part, the mean background DU and their corresponding SDs were calculated. Each ROI drawing was performed in consensus with a neuroradiology resident and a neuroradiology attending physician (6 and 9 years' experience in diagnostic imaging) and was for the conventional as well as the material-specific roadmap images. Afterward, the CNR was calculated for each level of the in vitro models using the following formula:¹¹

$$CNR = \frac{|\text{Mean DU}_{LEA} - \text{Mean DU}_{background}|}{SD_{background}}$$

Qualitative Image Analysis

Qualitative image analysis of the conventional and material-specific roadmap images was performed by 2 different readers (both with 6 years' experience in diagnostic imaging) on a PACS workstation. A second read was performed after 12 weeks to improve the quality of the qualitative analysis. Both readers were blinded to the type of roadmap mode as well as to the type of LEA, contrast medium, and saline. All window settings were left as predetermined by the angiography suite with a window width of 4095 DU and a level of 2047 DU, while a manual adjustment of the window settings was not allowed. The visibility of each LEA, contrast medium, and saline along each sector (diameters of 2.0, 1.5, 1.0, and 0.5 mm, respectively) was graded by a 5-point scale: 1) no visibility, 2) poor visibility, 3) acceptable visibility, 4) good visibility, and 5) excellent visibility. The grading was performed for both the conventional and material-specific roadmap modes, except saline for which images were only acquired and analyzed in conventional mode.

Statistics

GraphPad Prism (Version 9.3.1; GraphPad Software) was used for statistical analysis. The interreader and intrareader agreement were assessed with the Cohen κ coefficient. The κ values were interpreted as follows: ≤ 0.20 , poor agreement; 0.21–0.40, fair agreement; 0.41–0.60, moderate agreement; 0.61–0.80, good agreement; and 0.81–1.00, very good agreement.^{12,13} To evaluate statistical differences between the conventional and the material-specific roadmap modes regarding the visibility of the different LEAs, we performed the Mann-Whitney U test. There was no statistical testing for the control groups (contrast medium and saline) because they only served as a reference. The results of the quantitative analysis are presented as mean CNR (SD), and of the qualitative analysis as the mean score. The level of statistical significance was defined as $P < .05$.

RESULTS

Illustrations of the roadmap images in conventional and material-specific modes are demonstrated in Fig 1. The results of the quantitative and qualitative image analyses are summarized in Fig 2.

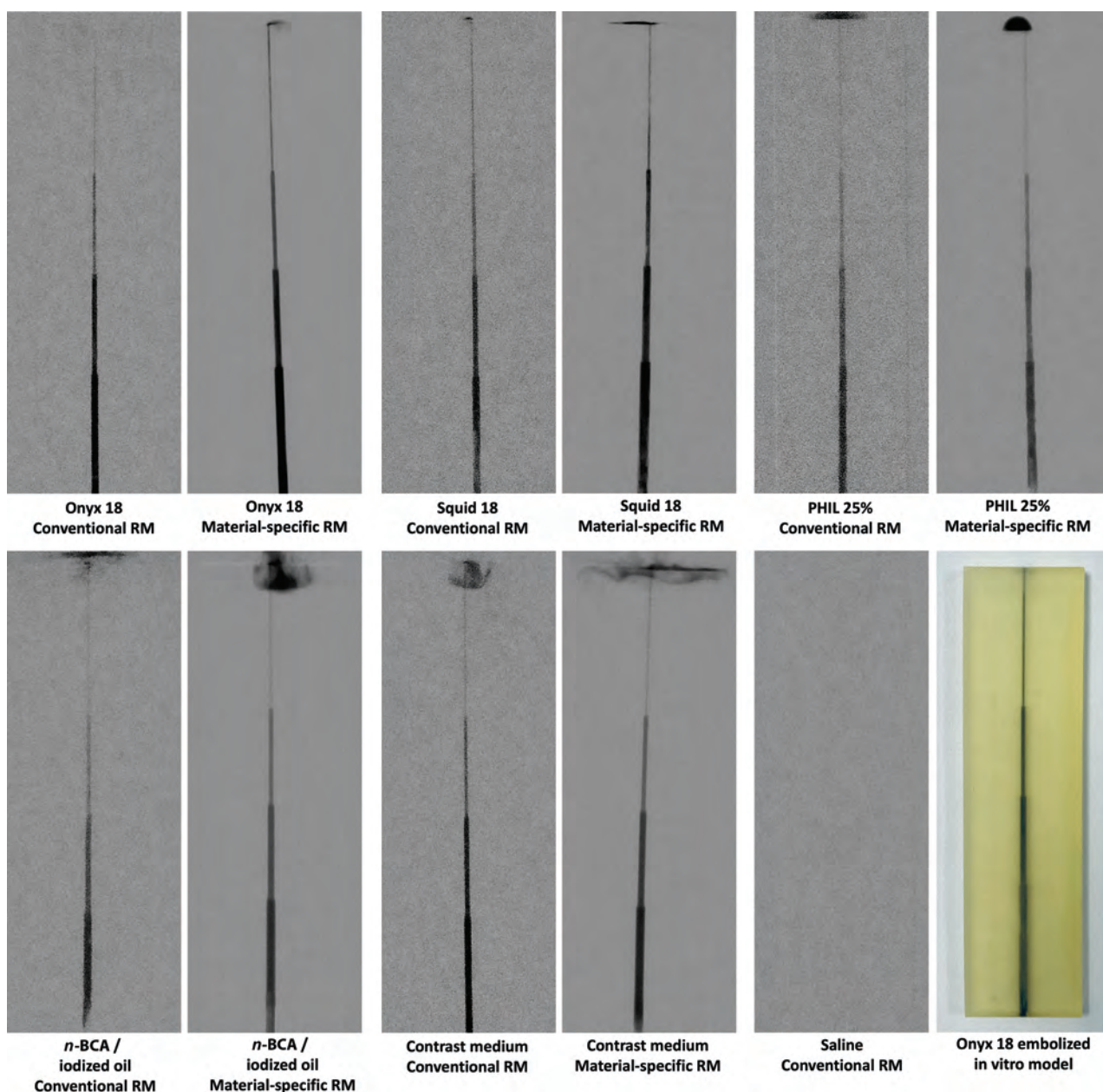


FIG 1. Representative images of the in vitro models embolized with different LEAs as well as contrast medium and saline, both serving as a reference. The images in the conventional and material-specific roadmap techniques are illustrated next to each other (left: conventional roadmap mode; right: material-specific roadmap mode) for each investigated LEA. The window width was set at 4095 DU, and the window level at 2047 DU. An exemplary image of an Onyx-embolized in vitro model is provided in the lower row as well. Please note the radiopaque embolic material at the upper end of most embolized models, which is of artificial character and had no influence on the present results. RM indicates roadmap mode.

Along all sectors of the in vitro model (2.0, 1.5, 1.0, and 0.5 mm), quantitative results demonstrated a significant difference ($P < .001$, respectively) among the CNRs of the investigated LEAs and thus a better visibility in the material-specific roadmap mode compared with the conventional roadmap mode (for example, Onyx 18 in conventional-versus-material-specific roadmap mode along all investigated diameters [mean CNR], 2.0 mm: 11.53 [SD, 0.57] versus 77.09 [SD, 3.23]; 1.5 mm: 10.17 [SD, 0.44] versus 66.06 [SD, 5.97]; 1.0 mm: 5.69 [SD, 0.85] versus 47.18 [SD, 5.72]; and 0.5 mm: 2.36 [SD, 0.83] versus 30.27 [SD, 6.78]; $P < .001$, respectively). Detailed information on the CNR values of the

investigated LEAs as well as the control groups (contrast medium and saline) are provided in Table 1.

The interreader reliability ($\kappa = 0.821$; range, 0.774–0.868) as well as the intrareader reliability ($\kappa = 0.862$; range, 0.820–0.904) both demonstrated very good agreement for the qualitative analysis of the roadmap images by both readers.

Compared with the quantitative results, the qualitative scores demonstrated similar findings. There was a higher score and thus better visibility of all investigated LEAs along each sector of the in vitro model ($P < .02$, respectively; for example, PHIL 25% in conventional-versus-material-specific roadmap mode [mean score],

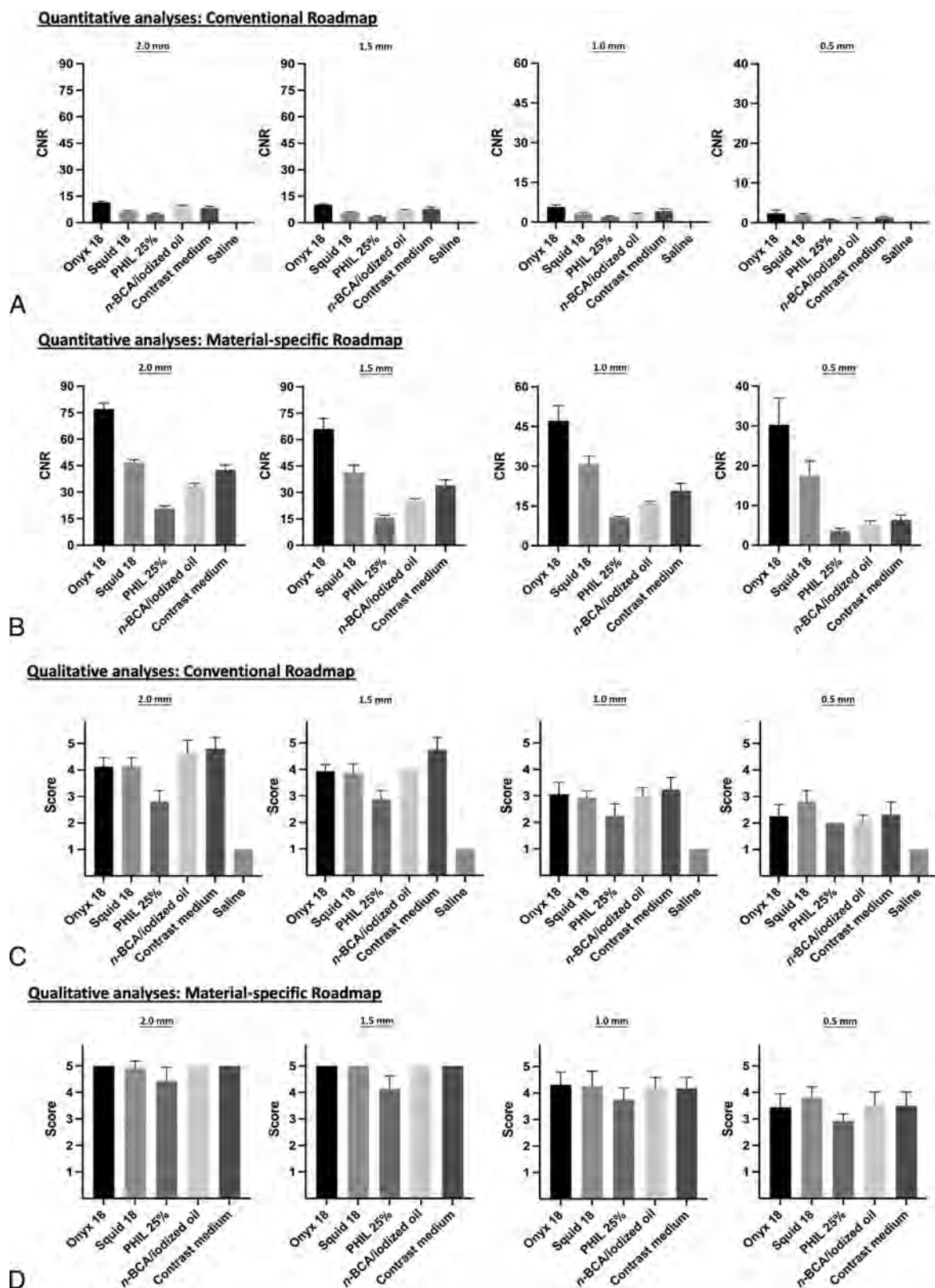


FIG 2. Results of the quantitative (A and B) and qualitative (C and D) analyses of the conventional and the material-specific roadmap images regarding the visibility of the different LEAs, contrast medium and saline, both serving as a reference. Material-specific roadmap images demonstrate an improved visibility of the different LEAs compared with the conventional roadmap technique along all sectors of the in vitro model (2.0, 1.5, 1.0, and 0.5 mm; $P < .05$, respectively). Roadmap images of saline were acquired only in conventional roadmap mode because there is no material-specific mode available.

Table 1: Summary of the results of the quantitative analysis^a

LEA	Conventional Roadmap	Material-Specific Roadmap	P Value
2.0 mm			
Onyx 18	11.53 (SD, 0.57)	77.09 (SD, 3.23)	$P < .001$
Squid 18	6.43 (SD, 0.40)	46.97 (SD, 1.42)	$P < .001$
PHIL 25%	4.91 (SD, 0.47)	20.69 (SD, 1.51)	$P < .001$
n-BCA/iodized oil	9.50 (SD, 0.42)	33.46 (SD, 1.66)	$P < .001$
Contrast medium	8.39 (SD, 0.96)	42.72 (SD, 2.76)	NA
Saline	0.08 (SD, 0.06)	NA	
1.5 mm			
Onyx 18	10.17 (SD, 0.44)	66.06 (SD, 5.97)	$P < .001$
Squid 18	5.77 (SD, 0.50)	41.52 (SD, 4.00)	$P < .001$
PHIL 25%	3.41 (SD, 0.52)	15.54 (SD, 1.63)	$P < .001$
n-BCA/iodized oil	6.96 (SD, 0.46)	25.44 (SD, 1.06)	$P < .001$
Contrast medium	7.75 (SD, 1.17)	34.01 (SD, 3.21)	NA
Saline	0.06 (SD, 0.03)	NA	
1.0 mm			
Onyx 18	5.69 (SD, 0.85)	47.18 (SD, 5.72)	$P < .001$
Squid 18	3.20 (SD, 0.53)	30.92 (SD, 3.00)	$P < .001$
PHIL 25%	1.97 (SD, 0.39)	10.47 (SD, 0.62)	$P < .001$
n-BCA/iodized oil	2.86 (SD, 0.52)	15.77 (SD, 0.94)	$P < .001$
Contrast medium	4.12 (SD, 0.89)	20.88 (SD, 2.64)	NA
Saline	0.10 (SD, 0.07)	NA	
0.5 mm			
Onyx 18	2.36 (SD, 0.83)	30.27 (SD, 6.78)	$P < .001$
Squid 18	1.91 (SD, 0.42)	17.40 (SD, 3.89)	$P < .001$
PHIL 25%	0.733 (SD, 0.19)	3.61 (SD, 0.67)	$P < .001$
n-BCA/iodized oil	0.97 (SD, 0.28)	5.16 (SD, 1.01)	$P < .001$
Contrast medium	1.34 (SD, 0.28)	6.35 (SD, 1.27)	NA
Saline	0.14 (SD, 0.06)	NA	

Note:—NA indicates that no *P* value is available because the contrast medium and saline only served as a reference with no material-specific roadmap mode available for saline.

^a Results are mean CNR.

Table 2: Summary of the results of the qualitative analysis^a

LEA	Conventional Roadmap	Material-Specific Roadmap	P Value
2.0 mm			
Onyx 18	4.13 (SD, 0.34)	5.00 (SD, 0.00)	$P < .001$
Squid 18	4.13 (SD, 0.34)	4.94 (SD, 0.25)	$P < .001$
PHIL 25%	2.81 (SD, 0.40)	4.44 (SD, 0.51)	$P < .001$
n-BCA/iodized oil	4.63 (SD, 0.50)	5.00 (SD, 0.00)	$P = .018$
Contrast medium	4.81 (SD, 0.40)	5.00 (SD, 0.00)	NA
Saline	1.00 (SD, 0.00)	NA	
1.5 mm			
Onyx 18	3.94 (SD, 0.25)	5.00 (SD, 0.00)	$P < .001$
Squid 18	3.88 (SD, 0.34)	5.00 (SD, 0.00)	$P < .001$
PHIL 25%	2.88 (SD, 0.34)	4.13 (SD, 0.50)	$P < .001$
n-BCA/iodized oil	4.00 (SD, 0.00)	5.00 (SD, 0.00)	$P < .001$
Contrast medium	4.75 (SD, 0.45)	5.00 (SD, 0.00)	NA
Saline	1.00 (SD, 0.00)	NA	
1.0 mm			
Onyx 18	3.06 (SD, 0.44)	4.31 (SD, 0.48)	$P < .001$
Squid 18	2.94 (SD, 0.25)	4.25 (SD, 0.58)	$P < .001$
PHIL 25%	2.25 (SD, 0.45)	3.75 (SD, 0.45)	$P < .001$
n-BCA/iodized oil	3.06 (SD, 0.25)	4.14 (SD, 0.34)	$P < .001$
Contrast medium	3.25 (SD, 0.45)	4.19 (SD, 0.40)	NA
Saline	1.00 (SD, 0.00)	NA	
0.5 mm			
Onyx 18	2.25 (SD, 0.45)	3.44 (SD, 0.51)	$P < .001$
Squid 18	2.81 (SD, 0.40)	3.81 (SD, 0.40)	$P < .001$
PHIL 25%	2.00 (SD, 0.00)	2.94 (SD, 0.25)	$P < .001$
n-BCA/iodized oil	2.06 (SD, 0.25)	3.94 (SD, 0.25)	$P < .001$
Contrast medium	2.31 (SD, 0.48)	3.50 (SD, 0.52)	NA
Saline	1.00 (SD, 0.00)	NA	

Note:—NA indicates that no *P* value is available because the contrast medium and saline only served as a reference with no material-specific roadmap mode available for saline.

^a Results are mean score.

2.0 mm: 2.81 [SD, 0.40] versus 4.44 [SD, 0.51]; 1.5 mm: 2.88 [SD, 0.34] versus 4.13 [SD, 0.50]; 1.0 mm: 2.25 [SD, 0.45] versus 3.75 [SD, 0.45]; and 0.5 mm: 2.00 [SD, 0.00] versus 2.94 [SD, 0.25]). Further details on the qualitative scores are provided in Table 2.

The automatically adjusted imaging parameters of the angiography suite were set as 40 kV(peak) for conventional as well as tantalum-specific roadmap modes, respectively, and 48 kV(p) for the iodine-specific roadmap mode. The automatically set tube current varied between 51 and 58 mA for the conventional and between 117 and 123 mA for the material-specific roadmap modes (tantalum-specific mode: range, 117–123 mA; iodine-specific mode: range, 118–123 mA).

DISCUSSION

In this in vitro study investigating the most commonly used LEAs for endovascular embolization, material-specific roadmap modes improved the visibility of these agents, both in quantitative and qualitative analyses.

During endovascular embolization procedures, adequate visibility of the embolic agent being used is of great importance. For example, unseen inadvertent embolization of healthy blood vessels can lead to ischemic stroke, and premature embolization of the draining veins of a cerebral AVM has the risk of periprocedural hemorrhage.¹⁴ Especially in complex anatomic situations, potentially aggravated by overlying embolic agents or bony structures and when embolizing very small vessels, the visibility can be impeded despite modern angiography systems. Each LEA that is used in clinical practice uses an admixed or an intrinsic material that causes radiopacity and thus enables the visibility of the embolic agent.⁷ To our knowledge, the Artis icono angiography suite is the only commercially available system that is equipped with material-specific roadmap modes to provide an improved visualization of the embolic material during embolization procedures. The potential of these novel roadmap modes has not been the focus of research until now. Therefore, the present study aimed to compare these material-specific road-

map modes with a conventional roadmap technique regarding the visibility of the most used LEAs. The results of our in vitro study demonstrated an improved visibility of the investigated embolic agents Onyx 18, Squid 18, PHIL 25%, and *n*-BCA mixed with iodized oil (ratio 1:1) in the material-specific roadmap modes (tantalum-specific mode for Onyx and Squid and iodine-specific mode for PHIL and *n*-BCA mixed with iodized oil) compared with the conventional roadmap mode ($P < .02$, respectively).

Today, there is only 1 study available investigating the angiographic visibility of LEAs.¹⁰ Schmitt et al¹⁰ compared the visibility of Onyx 18, Squid 18, Squid 12, PHIL 25%, PHIL LV, and *n*-BCA mixed with iodized oil (ratio 1:1) quantitatively and qualitatively in fluoroscopy. Using the same angiography suite and comparable imaging settings as in the present study, the authors described a better in vitro visibility of the tantalum-based LEAs Onyx and Squid as well as *n*-BCA mixed with iodized oil (ratio 1:1) compared with both triiodophenol-based formulations of PHIL. As a possible reason for their findings, they described the higher atomic number of tantalum (atomic number 73) compared with iodine (atomic number 53). The present study focused on the 4 clinically more frequently used LEAs, Onyx 18, Squid 18, PHIL 25%, and *n*-BCA mixed with iodized oil (ratio 1:1), 2 each containing tantalum and iodine as their radiopaque component. The direct comparison of different LEAs regarding their visibility was not the focus of the present research because this topic was described recently and the roadmap technique is based on postprocessing of fluoroscopy. As mentioned before, both material-specific roadmap modes of the Artis icono angiography suite demonstrated an enhanced visibility of the embolic agents compared with the conventional roadmap technique in both analyses. As a possible reason for the present results, we found the individual imaging settings that were adjusted automatically by the image-quality system OPTIQ of the Artis icono angiography suite. In this context, the kV (peak) for the conventional as well as the tantalum-specific roadmap mode was 40 kV(p), respectively, and 48 kV(p) for the iodine-specific roadmap mode. Furthermore, the tube current varied between 51 and 58 mA for the conventional and between 117 and 123 mA for the material-specific roadmap modes (tantalum-specific mode: range, 117–123 mA; iodine-specific mode: range, 118–123 mA) in our in vitro study.

Compared with the conventional roadmap technique, the increased tube voltage and tube current of the material-specific roadmap modes generate an increased quality and quantity of x-radiation. These automatically adjusted settings in combination with the automated, CNR-based adaption of the copper filter of the angiography suite may result in a hardening of the x-ray beam and thus optimize the visibility of the high atomic LEAs in the material-specific roadmap modes compared with the conventional roadmap technique. Two preclinical studies by Dehairs et al⁸ and Werncke et al⁹ further described the potential of a substantial dose reduction with this innovation, which is especially relevant for prolonged embolization procedures, embolization in younger patients, or the inclusion of the eye lens in the FOV. However, the present study focused on the in vitro comparison of material-specific and conventional roadmap modes regarding the visibility of the most used LEAs. Moreover, an additional measurement of the radiation dose was not possible because further test images in different positions of the in vitro model as well

as fluoroscopic images were acquired throughout this study, impeding an adequate comparability among the study groups. The impact of material-specific and conventional roadmap modes on the radiation dose is of great importance and needs to be investigated in a clinical setting in future studies.

This study has several limitations. In general, the transferability of in vitro roadmap imaging to clinical roadmap imaging is limited. Especially, the imaging settings of the angiography suite, which were set automatically, might differ substantially in clinical routine due to the distinct density of the human skull and soft tissues. Moreover, the properties of the LEAs relate closely to the physical properties of blood, such as the concentration of electrolytes, the pH value, or the body temperature; thus, a different visibility of the embolic agents might be possible. Only 4 samples per LEA as well as 1 mixture of *n*-BCA mixed with iodized oil (ratio 1:1) were investigated, mainly explained by the high expenses of the LEAs and the in vitro models used.

CONCLUSIONS

In this in vitro study, the potential of material-specific roadmap modes of the Artis icono angiography suite was compared with the conventional roadmap technique regarding the visibility of LEAs for embolization of vascular malformations. Quantitative and qualitative analyses showed a better visibility of all investigated LEAs (Onyx 18, Squid 18, PHIL 25%, and *n*-BCA mixed with iodized oil [ratio 1:1]) in the material-specific roadmap modes. Especially in complex anatomic situations, these novel roadmap modes could improve the visual control and thus the safety and efficacy of embolization procedures in clinical practice.

Disclosure forms provided by the authors are available with the full text and PDF of this article at www.ajnr.org.

REFERENCES

1. Gross BA, Du R. **Diagnosis and treatment of vascular malformations of the brain.** *Curr Treat Options Neurol* 2014;16:279 CrossRef Medline
2. Friedlander RM. **Clinical practice: arteriovenous malformations of the brain.** *N Engl J Med* 2007;356:2704–12 CrossRef Medline
3. Chen CJ, Ding D, Derdeyn CP, et al. **Brain arteriovenous malformations: a review of natural history, pathobiology, and interventions.** *Neurology* 2020;95:917–27 CrossRef Medline
4. Wu EM, El Ahmadieh TY, McDougall CM, et al. **Embolization of brain arteriovenous malformations with intent to cure: a systematic review.** *J Neurosurg* 2019;132:388–99 CrossRef Medline
5. Gross BA, Albuquerque FC, Moon K, et al. **Evolution of treatment and a detailed analysis of occlusion, recurrence, and clinical outcomes in an endovascular library of 260 dural arteriovenous fistulas.** *J Neurosurg* 2017;126:1884–93 CrossRef Medline
6. Patsalides A, Knopman J, Santillan A, et al. **Endovascular treatment of spinal arteriovenous lesions: beyond the dural fistula.** *AJNR Am J Neuroradiol* 2011;32:798–808 CrossRef Medline
7. Vollherbst DF, Chapot R, Bendszus M, et al. **Glue, Onyx, Squid or PHIL? Liquid embolic agents for the embolization of cerebral arteriovenous malformations and dural arteriovenous fistulas.** *Clin Neuroradiol* 2022;32:25–38 CrossRef
8. Dehairs M, Bosmans H, Marshall NW. **Implementation of a spatio-temporal figure of merit for new automatic dose rate control regimes in dynamic x-ray imaging.** *Phys Med Biol* 2019;64:045001 CrossRef Medline
9. Werncke T, Kemling M, Tashenov S, et al. **Impact of a contrast-to-noise ratio driven and material specific exposure control on image**

- quality and radiation exposure in angiography. *Phys Med Biol* 2021;66:065020 CrossRef Medline
10. Schmitt N, Wucherpfennig L, Hohenstatt S, et al. **Visibility of liquid embolic agents in fluoroscopy: a systematic in vitro study.** *J Neurointerv Surg* 2022;4:018958 CrossRef Medline
11. Goode AR, Snyder C, Snyder A, et al. **Signal and contrast to noise ratio evaluation of fluoroscopic loops for interventional fluoroscope quality control.** *J Appl Clin Med Phys* 2019;20:172–80 CrossRef Medline
12. Altman DG. *Practical Statistics for Medical Research*. CRC Press; 1990
13. Cohen J. **A coefficient of agreement for nominal scales.** *Educ Psychol Meas* 1960;20:37–46 CrossRef
14. Derdeyn CP, Zipfel GJ, Albuquerque FC, et al; American Heart Association Stroke Council. **Management of Brain Arteriovenous Malformations: A Scientific Statement for Healthcare Professionals From the American Heart Association/American Stroke Association.** *Stroke* 2017;48:e200–24 CrossRef Medline

Survey of the American Society of Neuroradiology Membership on the Use and Value of Extracranial Carotid Vessel Wall MRI

 M. Mossa-Basha,  C. Yuan,  B.A. Wasserman,  D.J. Mikulis,  T.S. Hatsukami,  N. Balu,  A. Gupta,  C. Zhu,  L. Saba,  D. Li,  J.K. DeMarco,  V.T. Lehman,  Y. Qiao,  H.R. Jager,  M. Wintermark,  W. Brinjikji,  C.P. Hess, and  D.A. Saloner



ABSTRACT

BACKGROUND AND PURPOSE: Extracranial vessel wall MRI (EC-VWI) contributes to vasculopathy characterization. This survey study investigated EC-VWI adoption by American Society of Neuroradiology (ASNR) members and indications and barriers to implementation.

MATERIALS AND METHODS: The ASNR Vessel Wall Imaging Study Group survey on EC-VWI use, frequency, applications, MR imaging systems and field strength used, protocol development approaches, vendor engagement, reasons for not using EC-VWI, ordering provider interest, and impact on clinical care was distributed to the ASNR membership between April 2, 2019, to August 30, 2019.

RESULTS: There were 532 responses; 79 were excluded due to minimal, incomplete response and 42 due to redundant institutional responses, leaving 411 responses. Twenty-six percent indicated that their institution performed EC-VWI, with 66.3% performing it ≤ 1 –2 times per month, most frequently on 3T MR imaging, with most using combined 3D and 2D protocols. Protocols most commonly included pre- and postcontrast T1-weighted imaging, TOF-MRA, and contrast-enhanced MRA. Inflammatory vasculopathy (63.3%), plaque vulnerability assessments (61.1%), intraplaque hemorrhage (61.1%), and dissection-detection/characterization (51.1%) were the most frequent applications. For those not performing EC-VWI, the reasons were a lack of ordering provider interest (63.9%), lack of radiologist time/interest (47.5%) or technical support (41.4%) for protocol development, and limited interpretation experience (44.9%) and knowledge of clinical applications (43.7%). Reasons given by 46.9% were that no providers approached radiology with interest in EC-VWI. If barriers were overcome, 51.1% of those not performing EC-VWI indicated they would perform it, and 40.6% were unsure; 48.6% did not think that EC-VWI had impacted patient management at their institution.

CONCLUSIONS: Only 26% of neuroradiology groups performed EC-VWI, most commonly due to limited clinician interest. Improved provider and radiologist education, protocols, processing techniques, technical support, and validation trials could increase adoption.

ABBREVIATIONS: EC-VWI = extracranial vessel wall MRI; IP = internet protocol; ASNR = American Society of Neuroradiology

Ischemic stroke is one of the leading causes of morbidity and mortality worldwide,¹ and extracranial carotid atherosclerotic disease is a major contributor.² Extracranial carotid vessel wall MRI

(EC-VWI) has improved the understanding of plaque pathophysiology during the past 35 years and has the potential to change the focus of plaque analysis from luminal stenosis to plaque composition for clinical decision-making.³ The American Society of Neuroradiology (ASNR) Vessel Wall Imaging Study Group was developed to disseminate vessel wall imaging techniques, to educate the general neuroradiology community on their implementation and interpretation, and to influence vendors to improve vessel wall imaging techniques.³ While EC-VWI has been adopted at many institutions to assess extracranial vascular disease, primarily atherosclerosis,

Received June 22, 2022; accepted after revision October 10.

From the Department of Radiology (M.M.-B.), University of North Carolina, Chapel Hill, North Carolina; Departments of Radiology (M.M.-B., N.B., C.Z.) and Surgery (T.S.H.), University of Washington, Seattle, Washington; Department of Radiology (C.Y.), University of Utah, Salt Lake City, Utah; Department of Radiology (B.A.W.), University of Maryland, Baltimore, Maryland; Department of Radiology (B.A.W., Y.Q.), Johns Hopkins University, Baltimore, Maryland; Joint Department of Medical Imaging (D.J.M.), The University Health Network and the University of Toronto, Toronto, Ontario, Canada; Department of Radiology (A.G.), Weill Cornell Medicine, New York, New York; Department of Radiology (L.S.), University of Cagliari, Cagliari, Sardinia, Italy; Biomedical Imaging Research Institute (D.L.), Cedars-Sinai Medical Center, Los Angeles, California; Department of Radiology (J.K.D.), Walter Reed National Military Medical Center, Bethesda, Maryland and Uniformed Services University of the Health Sciences, Bethesda, Maryland; Department of Radiology (V.T.L., W.B.), Mayo Clinic, Rochester, Minnesota; Neuroradiological Academic Unit (H.R.J.), Department of Brain Repair and Rehabilitation, University College London, Queen Square Institute of Neurology, London, UK; Department of Neuroradiology (M.W.), MD Anderson Cancer Institute, Houston, Texas; and Department of Radiology and Biomedical Imaging (C.P.H., D.A.S.), University of California, San Francisco, San Francisco, California.

The views expressed in this article are those of the author and do not reflect the official policy of the Department of Army/Navy/Air Force, Department of Defense, or U.S. Government.

Please address correspondence to Mahmud Mossa-Basha, MD, 101 Manning Dr, Chapel Hill, NC 27514; e-mail: mmossab@med.unc.edu; @mossabas

 Indicates article with online supplemental data.

<http://dx.doi.org/10.3174/ajnr.A7720>

arterial dissections, and inflammatory vasculopathies, barriers may still exist for its implementation for others, including technology, knowledge or expertise limitations, or vendor relations or workflow challenges. The ASNR membership represents the primary group of clinicians likely to benefit from the advances in EC-VWI in their clinical practice. Hence, the current survey study aimed to poll the ASNR membership on whether their institutions were performing EC-VWI, and if not, what barriers exist to its implementation and use. For institutions performing EC-VWI, we aimed to evaluate applications of the technique, which sequences were being used, how the techniques were developed, levels of clinician interest, and vendor collaboration for the development of the technique. To our knowledge, this is the first survey of the ASNR membership on EC-VWI use.

MATERIALS AND METHODS

This study is the extracranial portion of a survey administered, for which the intracranial portion had previously been published.⁴ The survey was discussed at ASNR Vessel Wall Imaging Study Group meetings and developed through input by multiple Study Group members. Through an iterative review process, the final survey was developed on the SurveyMonkey (<https://www.surveymonkey.com/>) platform. The survey was built with logic, and if a respondent indicated that he or she did not perform EC-VWI, the individual skipped to the last 4 questions of the EC-VWI portion of the survey, focused on barriers to EC-VWI performance and interest of the ordering provider (the questions in the survey are provided in the Online Supplement Data). Respondents who indicated that their institution did perform EC-VWI were expected to answer each EC-VWI question in the survey. After University of Washington institutional review board review, the survey received institutional review board exemption. The anonymous survey was first sent to the ASNR Vessel Wall Imaging Study Group and was opened to the group from March 30, 2018, through April 17, 2018, for revisions and approval. After approval from the ASNR Executive Committee, the survey was then sent to the ASNR membership on April 2, 2019. A second reminder was sent to the membership on August 14, 2019. Responses were gathered between April 2, 2019, and August 30, 2019, after which the survey was closed. Individuals could respond to the survey only once.

After the collection of survey responses, response quality was assessed, with exclusion of surveys in which the respondent spent <20 seconds on the survey and responded to ≤ 1 question. Internet Protocol (IP) addresses of the respondents were reviewed to determine the institution of origin for the response. For institutions with multiple responses, partially completed responses were excluded. If there was >1 complete response for an institution, the study investigators reviewed the institutional responses to assess accuracy on the basis of their knowledge of protocol and clinical performance based on publications, presentations, and/or personal knowledge of the specific institution at the time of the survey to determine the single institutional response to include. If this issue was yet unresolved, discussion with EC-VWI leaders at the particular institution was performed for clarification on their approach at the time of the survey, and the survey response that most closely approximated this was kept. IP addresses without institutional associations were not excluded. IP addresses were

also used to determine the region from which the response came. Responses were grouped into continent, country, and, for US responses, region of the country, divided on the basis of US Census definitions.⁵ For question 31 regarding obstacles to performing EC-VWI, responses were tabulated individually but also grouped into educational responses and technical responses. Any response that included no clinician interest, limited personal knowledge of applications/value, limited expertise of interpretation, no benefit for the patient population, or lack of evidence supporting the benefit were placed in the education category. Any response that included no radiologist time/interest for protocol development, no vendor/technical support for protocol development, long scan times limiting clinical feasibility, or lack of standardized protocols were placed in the technical category.

RESULTS

Respondents

The survey was distributed to 5552 ASNR members through 2 e-mails from the ASNR separated by 3 weeks, and 1854 individuals opened the e-mails. A total of 46 respondents were from the ASNR Vessel Wall Imaging Study Group, and 486 respondents were from the ASNR membership, for a total of 532 responses. The response rate was 9.6%. Respondents, on average, spent 11 minutes on the survey, and there was an 86% completion rate. We subsequently excluded survey responses for which <20 seconds was spent on the survey and the respondent answered 1 or no questions ($n = 79$), leaving 453 complete responses. Redundant institutional responses were then removed ($n = 42$), leaving 411 included responses.

Of the included responses, 81.3% were from North America, 7.5% from Europe, 5.8% from Asia, 3.6% from South America, 1.0% from Australia, and 0.7% from Africa. For countries, the United States had the most included responses, with 314, followed by Canada ($n = 16$), Brazil ($n = 12$), and South Korea ($n = 5$). For the 314 US responses, 30.3% were from the South; 24.5%, from the Midwest; 24.5%, from the East; and 20.7%, from the West. Of the 114 responses with institutional IP addresses, 52.6% were academic, 38.6% private practice, 5.3% federal, and 3.5% hybrid institutions.

EC-VWI Utilization

Most reported VWI performance either 1 to 2 times per month (29%) or once every couple of months (24%), though responses ranged from only a handful of times ever performed (13%) to at least twice per week (17%) (Fig 1). EC-VWI was most frequently performed as an add-on ordered by ordering providers (60.2%, 53/88), stand-alone ordered by providers (46.6%, 41/88), or an add-on from radiologists (46.6%, 41/88) (Fig 2). In the free text option, 3 respondents indicated that the technique was performed only for research.

Respondents indicated that EC-VWI was most frequently performed for evaluation of large-artery vasculitis (63.3%, 57/90), atherosclerotic intraplaque hemorrhage assessment (61.1%, 55/90), plaque-vulnerability assessment (61.1%, 55/90), and dissection characterization/detection (51.1%, 46/90) (Fig 3).

Of respondents from the United States, 21.7% (68/314) indicated that their institution performed EC-VWI. Among Eastern US respondents, 25% (19/76) indicated that their groups performed EC-VWI, compared with 25% (24/96) of Southern, 23.1% (15/65) of Western, and 13% (10/77) of Midwestern respondents.

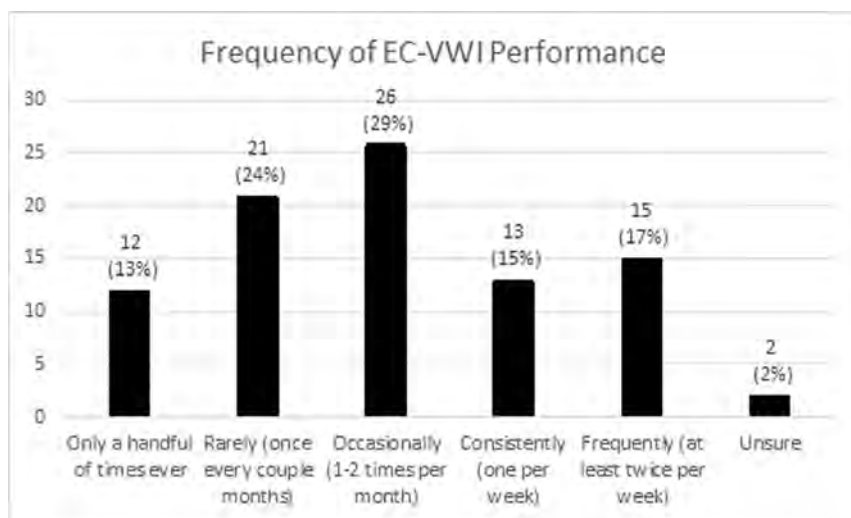


FIG 1. Question: If your institution performs carotid vessel wall MR imaging, on average how often? There were 89 respondents with 89 responses.

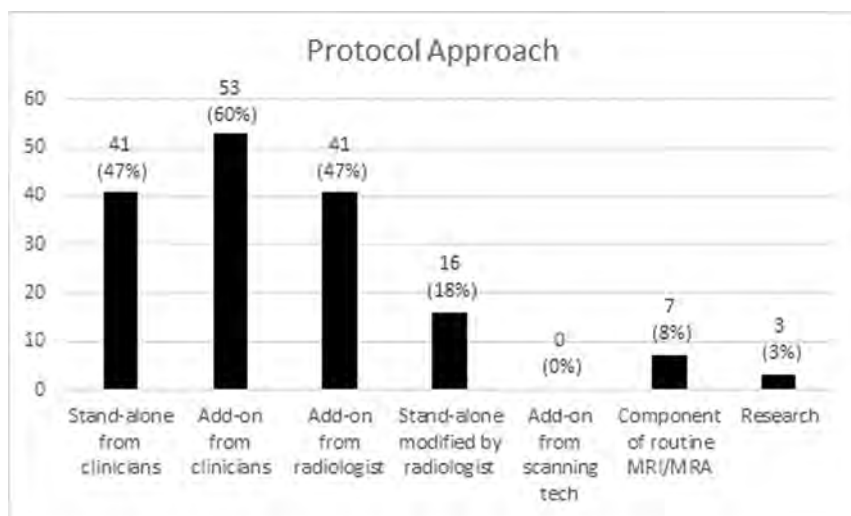


FIG 2. Question: Is carotid vessel wall MR imaging clinically being performed as (answer all that apply)? There were 88 respondents with 161 responses.

For those respondents from outside the United States, 50% of South American (8/16), 48.4% (15/31) of European, 43.8% (7/16) of Canadian, and 33.3% of Asian (8/24) and African (1/3) respondents indicated performance of EC-VWI. No Australian (0/4), Mexican (0/1), or Jamaican (0/2) respondents indicated EC-VWI use at their respective institutions.

In terms of practice type, 21.7% (10/46) of respondents from private radiology practices, 36.7% (22/60) of respondents from academic institutions, 50% (2/4) of respondents from federal institutions, and 25% (1/4) from hybrid institutions indicated that they performed EC-VWI. This was from 114 responses for which institutional information was available.

Vendor Environment

One hundred twelve total responses indicated that institutions performed EC-VWI on 3T MR imaging systems, while 50 responses

indicated that it was performed on 1.5T systems. EC-VWI was most frequently performed on 3T Siemens MR imaging systems (58%, 53/92), followed by 3T GE Healthcare systems (33%, 30/92) and 3T Philips Healthcare systems (30%, 28/92). Please refer to the Online Supplemental Data for full details. Sixty percent indicated that they performed EC-VWI only on 3T field strength, 34% indicated use of both 3T and 1.5T field strengths, while 5% only used 1.5T.

Forty-six percent indicated that their institution had a research agreement with their MR imaging vendors, 39% indicated they did not, while 16% were unsure. For those with a vendor research agreement, 45% sought vendor support for protocol development, 39% did not, while 16% were unsure. For those that were able to develop a protocol with vendor support, 54% did so with Siemens; 40%, with Philips Healthcare; and 33%, with GE Healthcare (Online Supplemental Data). Thirty-three percent indicated initial difficulties, 30% indicated limited vendor contribution, 26% were still looking for a solution, and 20% had an excellent experience (Online Supplemental Data). For those who responded that they did not seek vendor support for protocol development, 31% indicated limited vendor contribution, while 10% were still looking for a solution. Conversely, for those who indicated limited vendor contribution, 47% did not seek a contribution from the vendor, while 21% did and 32% were unsure.

EC-VWI Protocol

Of respondents, 24.7% indicated that they performed 2D imaging only; 24.7% indicated the use of only 3D imaging, while 50.6% performed a combined 2D and 3D protocol. On the basis of guidance from the literature, expert lectures, and/or the ASNR Vessel Wall Imaging Study Group, 63.1% pursued their imaging approach; 38.1% factored technical limitations of MR imaging equipment into their protocol development; 26.2% considered time constraints; and 3.5% indicated in the free text response that the protocol design was based on personal experience. In addition, 68.6% indicated that the protocol was developed in-house, 33.7% received the protocol from the vendor, 16.3% received their protocol from another institution, and 11.6% were unsure (Online Supplemental Data).

Institutions most frequently used T1-weighted pre- (88.2%) and postcontrast (83.5%), T2-weighted (49.4%), and 3D gradient recalled-echo (including MPRAGE and echo-spoiled gradient echo) (44.7%) sequences. For MRA techniques, TOF-MRA

(61.2%) and contrast-enhanced (57.6%) techniques were typically used (Online Supplemental Data).

Obstacles to EC-VWI Use

Three-hundred four respondents (74%) indicated that their institution did not perform EC-VWI. Among those respondents, 63.9% indicated that the reason for not performing EC-VWI was a lack of clinician/ordering-provider interest; 47.5%, due to lack of time/interest by the radiologist to provide input on protocol development; 44.9%, due to limited expertise of interpretation; 43.7%, from limited personal knowledge of applications and

value; and 41.4%, due to limited vendor and technical support for protocol development (see Fig 4 for full details). Of the 63.9% not performing EC-VWI, 17.4% did not provide an explanation for Question 31; 21% provided 1 reason; 13.5%, 2 reasons; 15.5%, 3 reasons; 12.8%, 4 reasons; 10.5%, 5 reasons; 5.3%, 6 reasons; and 2% provided 7 and 8 reasons for not performing EC-VWI, respectively. Educational obstacles were given for 72.04% of responses, while 37.5% of responses included technical challenges. Please see the Online Supplemental Data for distribution and patterns of individual responses.

For those not performing EC-VWI, 51.1% indicated that their institution would perform these scans if technical and expertise obstacles were overcome, 8.3% indicated they would not, and 40.6% were unsure.

Provider Interest in EC-VWI

The ordering providers most frequently approaching radiology departments in regard to EC-VWI were stroke neurology (37.2%), followed by neurosurgery (12.5%) and vascular surgery (11.3%). Of respondents, 46.9% indicated that no clinical services had approached radiology, and 13.1% were unsure (Online Supplemental Data).

EC-VWI Impact on Patient Management

Of respondents, 23.7% indicated that they thought EC-VWI had impacted

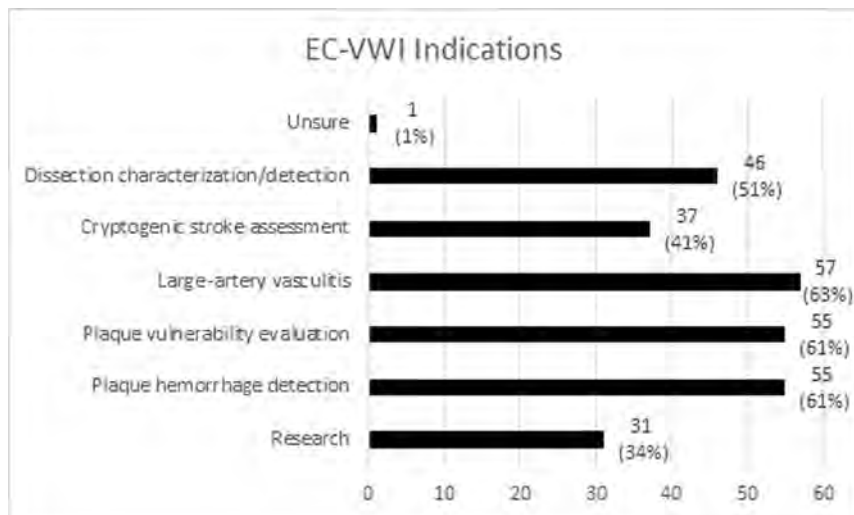


FIG 3. Question: For what primary purpose does your institution perform carotid vessel wall imaging (Choose all that apply)? There were 90 respondents with 282 responses.

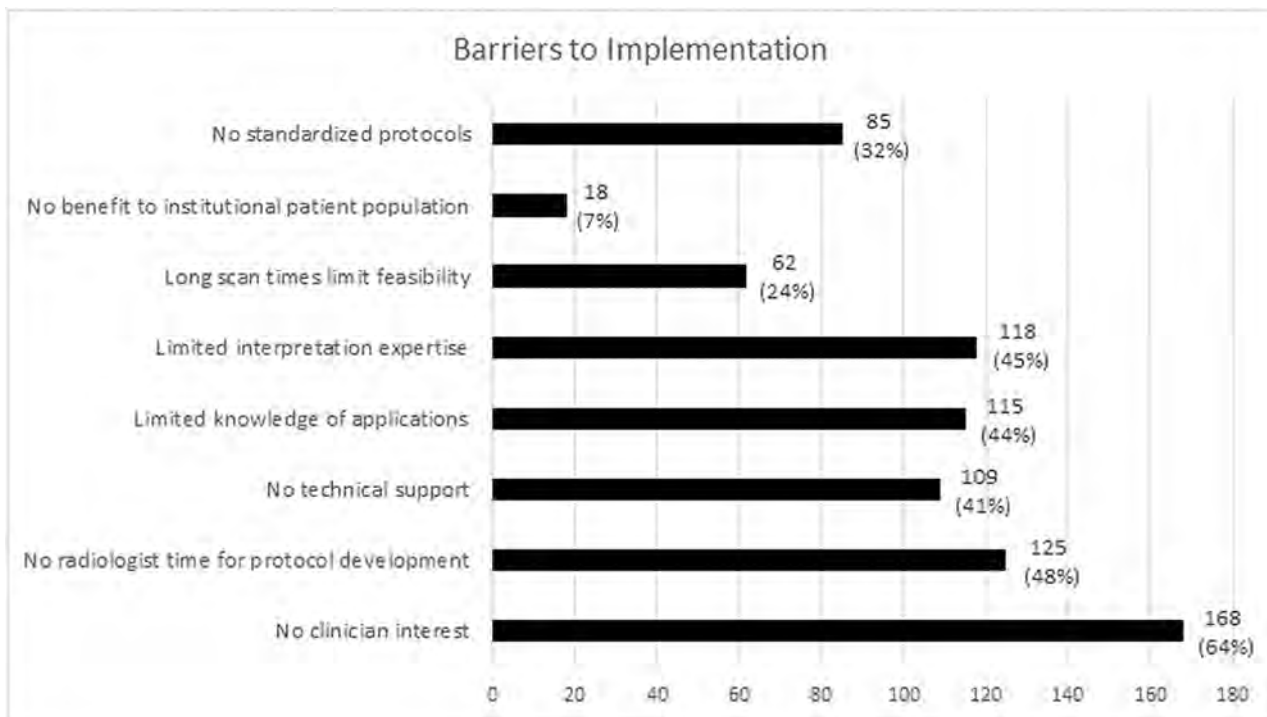


FIG 4. Question: If your institution is not performing carotid vessel wall imaging (respond to this question only if you are not using carotid VWI), what barriers does your institution face for implementation (choose all that apply)? There were 263 respondents with 800 responses.

patient management, 48.6% did not think EC-VWI influenced patient management, and 27.7% were unsure. Of those performing EC-VWI, 8.4% responded that they believed the technique had not impacted patient clinical management, 12.1% were unsure, and 79.5% believed that the technique had an impact on patient management.

DISCUSSION

This detailed survey of EC-VWI use among ASNR members yielded several important findings in regard to performance, indications, and barriers to implementation across many practices. Overall, only about one-quarter of practices offer EC-VWI, and one-third of those perform it on a frequent basis. The utilization rate may even be overinflated compared with general practice, considering a disproportionate response rate from the ASNR VWI Study Group and academic centers. Considering that the most frequent clinical application use indicated by respondents was inflammatory vasculopathy assessment, its adoption for the most studied and most common vascular disease process, carotid plaque risk assessment, is likely even lower than indicated. There was substantial variability of use among different regions of the United States and among countries, ranging from little-to-no reported use to use in about half of practices in some areas such as South American and European institutions. EC-VWI was more commonly performed in academic institutions than in private practices. There were many barriers to implementation: Chiefly, the primary barrier was a lack of clinician interest, but several technical or radiologist-related factors such as lack of interest, time, or expertise were also prevalent. These results reveal opportunities to substantially enhance implementation across practice types and geographic regions and ultimately optimize patient care.

EC-VWI is an established technique technically and scientifically, with substantial imaging-histologic correlation from carotid endarterectomy specimens—that is, important features of carotid plaque including intraplaque hemorrhage, lipid-rich necrotic core, fibrous cap disruption, positive remodeling, and neovascularity can be accurately assessed.^{3,6} There are data indicating the utility of EC-VWI for atherosclerotic stroke-risk stratification,^{3,6} identification of the source of cryptogenic stroke,⁷⁻⁹ and prediction of future stroke events,^{10,11} in addition to assessment of less common entities, including blunt cerebrovascular injury^{12,13} and inflammatory vasculopathy.^{14,15}

We found that despite these data, widespread adoption is lacking. Identification of the major reasons in the current study may help pinpoint strategies for improved implementation. Several issues of radiologists could be addressed by additional education about the utility of EC-VWI, which could spark interest and increased education related to interpretive skills. Specifically, this education could be accomplished in many forms, including formal Continuing Medical Education courses, practical how-to review articles, and one-on-one peer-to-peer mentorship. ASNR and the ASNR Vessel Wall Imaging Study Group would be well-positioned to take leading roles in this effort. Additional focus on the technical and interpretive aspects in neuroradiology fellowship programs could also assist dissemination across practices.

Although we cannot determine the reasons for lack of interest among some clinicians with certainty, enhanced education of

clinicians about the value of EC-VWI through increased presence in clinical journals and national meetings may be beneficial because some clinicians are unaware of, or unconvinced by, the current literature. The perception that EC-VWI does not change management in many patients may partially reflect clinician knowledge and/or philosophy. Randomized controlled surgical trials using EC-VWI for patient selection could provide additional support for the technique.

We found that about half of the practices surveyed that do not currently use EC-VWI would be interested in offering and performing this examination if barriers were reduced, presenting a substantial opportunity that can be accomplished via several methods. In addition to the educational and collaborative opportunities listed above, these include development of easy-to-use and readily accessible EC-VWI protocols by both vendors and radiologists, improved classification schemes, and improved processing. This survey also detailed the typical pulse sequences, field strengths used, and protocolling practices (clinician order versus radiologist add-on), which may be important considerations to facilitate wider adoption. Another potential technical obstacle that was not addressed in this survey is the use of specialized carotid coils for EC-VWI, which many groups may not have or may not be willing to acquire. Development of EC-VWI protocols that can be implemented with standard neurovascular coils would help lower this technical barrier and potentially increase adoption.

Development of commercially available image-processing techniques could also help lower the barrier to EC-VWI adoption. Automated techniques that could align imaging to standard projections,¹⁶ segment pathologic lesions, quantify vulnerable features,¹⁷ and stratify risk on the basis of these features would ease the interpretation burden on radiologists. In addition, lesion detection and stenosis quantification tools¹⁸ could also help augment workflow efficiency. Software tools could also help improve standardized interpretation and reporting approaches, providing improved quality and consistency of reporting and creating better value to ordering clinical services for patient management. These measures could lead to increased adoption, reliance, and acceptance of EC-VWI by radiology departments and ordering providers alike.

A previous multinational survey with 223 multidisciplinary respondents, including radiologists, neurologists, vascular surgeons, and technologists, focused on multitechnique imaging and management of carotid atherosclerotic disease and found that only 8% of respondents indicated that MR imaging was the first-line of imaging for symptomatic carotid atherosclerotic disease, and it was only 4% in asymptomatic carotid atherosclerosis.¹⁹ The use of MR imaging in our survey was higher, possibly due to the varied applications targeted beyond carotid atherosclerosis and possibly due to the cohort because our survey included more responses from the United States (76% versus 13%, respectively). The current survey focused more on EC-VWI applications, protocols, field strengths, and barriers to performance, while the previous survey focused more on first-line imaging and treatment.

The current survey has several limitations. First, it was a voluntary survey of a national society with a relatively low response rate, which could contribute to selection bias toward those more

motivated to respond to the survey due to interest or performance of EC-VWI. This bias is exemplified by the disproportionate response rate from the ASNR VWI Study Group, who are all ASNR members. Radiologists who are not current members of the ASNR or were not members at the time of survey administration would not have had an opportunity to respond to the survey. There was variability in total responses regionally, especially internationally, also limiting geographic comparisons of responses. These issues would lead to a limited sampling of the total neuroradiologist population. Second, this survey was performed in 2019, presenting the potential for changes in practice; however, EC-VWI is a relatively mature technique, and considering the intervening COVID pandemic, practice patterns and adoption likely have not changed appreciably. Third, the survey was anonymous because we did not request names or institutions of respondents. While we used IP addresses of responses to mitigate redundant institutional responses, this feature was not available for all responses, and it is possible that >1 response could have come from some institutions. Third, the survey asked about only MR imaging techniques; however, CTA and sonography can be used for plaque characterization, vasculitis, and dissection evaluation, each with their specific applications. This survey does not comprehensively assess other imaging modalities for cervical vascular imaging. A previous study, however, indicated that in clinical practice, radiologists rarely report on plaque characteristics on CTA neck studies, only stenosis measurements.²⁰

CONCLUSIONS

EC-VWI is an imaging technique that is used by approximately one-quarter of institutions as indicated by this survey of the ASNR membership, and for those performing the technique, two-thirds used it infrequently. When used, it is performed for a variety of indications. The most frequent reason for institutions not performing this technique was a lack of interest by clinicians, though technical support and radiologist-related reasons were also prevalent. More than half who were not performing EC-VWI indicated that if barriers were overcome, their institution would perform it, and another 40% were unsure. Improved technical support, processing techniques, user-friendly protocols, and education for ordering clinicians and radiologists as well as prospective randomized controlled trials validating the importance of the technique may enhance widespread adoption.

Disclosure forms provided by the authors are available with the full text and PDF of this article at www.ajnr.org.

REFERENCES

- Lozano R, Naghavi M, Foreman K, et al. **Global and regional mortality from 235 causes of death for 20 age groups in 1990 and 2010: a systematic analysis for the Global Burden of Disease Study 2010.** *Lancet* 2012;380:2095–128 CrossRef Medline
- Seeger JM, Barratt E, Lawson GA, et al. **The relationship between carotid plaque composition, plaque morphology, and neurologic symptoms.** *J Surg Res* 1995;58:330–36 CrossRef Medline
- Saba L, Yuan C, Hatsukami TS, et al; Vessel Wall Imaging Study Group of the American Society of Neuroradiology. **Carotid artery wall imaging: perspective and guidelines from the ASNR Vessel Wall Imaging Study Group and Expert Consensus Recommendations of the American Society of Neuroradiology.** *AJNR Am J Neuroradiol* 2018;39:E9–31 CrossRef Medline
- Mossa-Basha M, Zhu C, Yuan C, et al. **Survey of the American Society of Neuroradiology membership on the use and value of intracranial vessel wall MRI.** *AJNR Am J Neuroradiol* 2022;43:951–57 CrossRef Medline
- US Census Bureau. https://www2.census.gov/geo/pdfs/maps-data/maps/reference/us_regdiv.pdf. Accessed November 10, 2022
- Saba L, Brinjikji W, Spence JD, et al. **Roadmap consensus on carotid artery plaque imaging and impact on therapy strategies and guidelines: an international, multispecialty, expert review and position statement.** *AJNR Am J Neuroradiol* 2021;42:1566–75 CrossRef Medline
- Freilinger TM, Schindler A, Schmidt C, et al. **Prevalence of nonstenosing, complicated atherosclerotic plaques in cryptogenic stroke.** *JACC Cardiovasc Imaging* 2012;5:397–405 CrossRef Medline
- Kopczak A, Schindler A, Bayer-Karpinska A, et al. **Complicated carotid artery plaques as a cause of cryptogenic stroke.** *J Am Coll Cardiol* 2020;76:2212–22 CrossRef Medline
- Mark IT, Nasr DM, Huston J, et al. **Embolic stroke of undetermined source and carotid intraplaque hemorrhage on MRI: a systemic review and meta-analysis.** *Clin Neuroradiol* 2021;31:307–13 CrossRef Medline
- Brunner G, Virani SS, Sun W, et al. **Associations between carotid artery plaque burden, plaque characteristics, and cardiovascular events: the ARIC Carotid Magnetic Resonance Imaging Study.** *JAMA Cardiol* 2021;6:79–86 CrossRef Medline
- Kopczak A, Schindler A, Sepp D, et al. **Complicated carotid artery plaques and risk of recurrent ischemic stroke or TIA.** *J Am Coll Cardiol* 2022;79:2189–99 CrossRef Medline
- Vranic JE, Huynh TJ, Fata P, et al. **The ability of magnetic resonance black blood vessel wall imaging to evaluate blunt cerebrovascular injury following acute trauma.** *J Neuroradiol* 2020;47:210–15 CrossRef Medline
- Wu L, Christensen D, Call L, et al. **Natural history of blunt cerebrovascular injury: experience over a 10-year period at a level I trauma center.** *Radiology* 2020;297:428–35 CrossRef Medline
- Barra L, Kanji T, Malette J, et al. **Imaging modalities for the diagnosis and disease activity assessment of Takayasu's arteritis: a systematic review and meta-analysis.** *Autoimmun Rev* 2018;17:175–87 CrossRef Medline
- Spira D, Xenitidis T, Henes J, et al. **MRI parametric monitoring of biological therapies in primary large vessel vasculitides: a pilot study.** *Br J Radiol* 2016;89:20150892 CrossRef Medline
- Guo Y, Canton G, Chen L, et al. **Multi-planar, multi-contrast and multi-time point analysis tool (MOCHA) for intracranial vessel wall characterization.** *J Magn Reson Imaging* 2022;56:944–55 CrossRef Medline
- Ziegler M, Good E, Engvall J, et al. **Towards automated quantification of vessel wall composition using MRI.** *J Magn Reson Imaging* 2020;52:710–19 CrossRef Medline
- Suinesiaputra A, de Koning PJ, Zudilova-Seinstra E, et al. **Automated quantification of carotid artery stenosis on contrast-enhanced MRA data using a deformable vascular tube model.** *Int J Cardiovasc Imaging* 2012;28:1513–24 CrossRef Medline
- Saba L, Mossa-Basha M, Abbott A, et al. **Multinational survey of current practice from imaging to treatment of atherosclerotic carotid stenosis.** *Cerebrovasc Dis* 2021;50:108–20 CrossRef Medline
- Baradaran H, Foster T, Harrie P, et al. **Carotid artery plaque characteristics: current reporting practices on CT angiography.** *Neuroradiology* 2021;63:1013–18 CrossRef Medline

MRI Detection of Carotid Intraplaque Hemorrhage and Postintervention Cognition

 S. Culleton,  H. Baradaran,  S.-E. Kim,  G. Stoddard,  J. Roberts,  G. Treiman,  D. Parker,  K. Duff, and  J.S. McNally



ABSTRACT

BACKGROUND AND PURPOSE: Cognitive improvement has been reported after carotid revascularization and attributed to treating stenosis and correcting hypoperfusion. This study investigated the effect of carotid intraplaque hemorrhage on postintervention cognition.

MATERIALS AND METHODS: In this institutional review board–approved single-center study, consecutive patients scheduled for carotid surgery were recruited for preoperative carotid MR imaging (MPRAGE) and pre- and postintervention cognitive testing using the Repeatable Battery for the Assessment of Neuropsychological Status. Pre- and postintervention scores were compared using *t* tests and multivariable linear regression.

RESULTS: Twenty-three participants were included, with endarterectomy performed in 20 (87%) and angioplasty/stent placement, in 3 (13%). Overall, statistically significant improvements occurred in the pre- versus postintervention mean Total Scale score (92.1 [SD, 15.5] versus 96.1 [SD, 15.8], *P* = .04), immediate memory index (89.4 [SD, 18.2] versus 97.7 [SD, 14.9], *P* < .001), and verbal index (96.1 [SD, 14.1] versus 103.0 [SD, 12.0], *P* = .002). Intraplaque hemorrhage (+) participants (*n* = 11) had no significant improvement in any category, and the attention index significantly decreased (99.4 [SD, 18.0] versus 93.5 [SD, 19.4], *P* = .045). Intraplaque hemorrhage (−) participants (*n* = 12) significantly improved in the Total Scale score (86.4 [SD, 11.8] versus 95.5 [SD, 12.4], *P* = .004), immediate memory index (82.3 [SD, 14.6] versus 96.2 [SD, 14.1], *P* = .002), delayed memory index (94.3 [SD, 14.9] versus 102.4 [SD, 8.0], *P* = .03), and verbal index (94.3 [SD, 13.2] versus 101.5 [SD, 10.7], *P* = .009). Postintervention minus preintervention scores for intraplaque hemorrhage (+) versus (−) groups showed statistically significant differences in the Total Scale score (−0.4 [SD, 6.8] versus 8.0 [SD, 8.5], *P* = .02), attention index (−5.9 [SD, 8.5] versus 4.3 [SD, 11.9], *P* = .03), and immediate memory index (4.2 [SD, 6.7] versus 12.2 [SD, 10.2], *P* = .04).

CONCLUSIONS: Cognitive improvement was observed after carotid intervention, and this was attributable to intraplaque hemorrhage (−) plaque. MR imaging detection of intraplaque hemorrhage status may be an important determinant of cognitive change after intervention.

ABBREVIATIONS: ACA = anterior cerebral artery; BMI = body mass index; IPH = intraplaque hemorrhage; PCA = posterior cerebral artery; RBANS = Repeatable Battery for the Assessment of Neuropsychological Status

An association between dementia, carotid stenosis, and cognitive improvement following the restoration of blood flow was

proposed in the early 1950s.^{1,2} Subsequently, carotid atherosclerosis was identified as a risk factor for dementia,³ and revascularization was linked to improved cognition.^{4–6} Consequently, impaired hemodynamics secondary to flow-limiting stenosis was proposed as the primary mechanism for the association between carotid atherosclerosis and cognitive impairment.² This hypothesis was supported by an association between cerebral hypoperfusion, accelerated cognitive decline, and an increased risk of dementia.⁷

Contrary to this, however, computational models suggested that very high-grade carotid stenosis (up to 86%) was required to reduce the cerebral perfusion pressure.⁸ In addition, the Framingham Study showed that lesser degrees of stenosis down to 50% were still associated with poor executive function.⁹ Furthermore, a study of asymptomatic severe carotid stenosis

Received May 11, 2022; accepted after revision October 1.

From the Department of Radiology (S.C., H.B., S.-E.K., J.R., D.P., J.S.M.), Utah Center for Advanced Imaging Research, Division of Epidemiology (G.S.), Department of Internal Medicine, Department of Surgery (G.T.), and Center for Alzheimer's Care, Imaging and Research (K.D.), University of Utah, Salt Lake City, Utah.

This work was supported by the American Heart Association Scientist Development Grant 17SDG33460420 (J.S. McNally) and the National Institutes of Health R01 HL127582 (J.S. McNally).

Please address correspondence to Sinéad Culleton, MB, BCh, BAO, FRCR, FFR (RCSI), University of Utah, Department of Radiology, 30 North 1900 East, 1A071, Salt Lake City, UT 84132-2140; e-mail: Sinead.culleton@gmail.com



Indicates open access to non-subscribers at www.ajnr.org



Indicates article with online supplemental data.

<http://dx.doi.org/10.3174/ajnr.A7701>

found that downstream perfusion was predominantly unaltered.¹⁰ Together, these findings suggest that an alternative etiology underpins the association between carotid atherosclerosis and cognitive decline.

Vulnerable plaque is a manifestation of advanced carotid atherosclerosis, which may play a role in cognitive decline independent of stenosis. A major determinant of vulnerable plaque is intraplaque hemorrhage (IPH), which confers an increased risk of thromboembolic stroke.^{11–13} IPH was identified as a predictor of carotid-source stroke independent of stenosis.¹⁴ Vulnerable plaque with IPH may lead to increased cerebral microemboli, which are associated with a hastened progression of dementia.¹⁵ IPH is not only a marker of thromboembolic activity,¹⁶ but it may also influence downstream cerebral hemodynamics.^{17,18} Removal of vulnerable plaque has the potential to stabilize cognitive decline.¹⁹

Carotid atherosclerosis-associated cognitive decline could be multifactorial. Plaque composition may contribute in addition to the severity of the stenosis or downstream hypoperfusion. Prior to this study, the effect of IPH status on cognitive improvement after carotid surgery was unknown. This study aimed to assess the association between IPH(+) or (–) plaque and cognition following carotid revascularization. This study hypothesized that IPH status would play a role in cognitive benefit seen after carotid intervention and that removal of IPH(+) plaque would confer the greatest benefit.

MATERIALS AND METHODS

Study Design and Population

Local institutional review board (University of Utah) approval was granted for this prospective study, and informed consent was obtained. Study procedures including data acquisition and storage were compliant with the Health Insurance Portability and Accountability Act. The study protocol (ID 17SDG33460420/NCT03068442) can be viewed at <https://clinicaltrials.gov>.

Subjects were prospectively recruited from the neurovascular consultation and outpatient services at 2 institutions (University of Utah Medical Center and VA Salt Lake City Health Care System) between January 2017 and February 2020. Consecutive subjects with carotid disease necessitating intervention, either symptomatic with ≥ 1 carotid plaque with $\geq 50\%$ stenosis or asymptomatic with $\geq 70\%$ stenosis as per the Society for Vascular Surgery guidelines²⁰ were included. The exclusion criteria were the following: 1) contraindication to CTA or MR imaging (unsuitable pacemaker, contrast allergy, ocular foreign body, estimated glomerular filtration rate of < 30 mL/min), 2) stage IV malignancy, and 3) known dementia (vascular dementia or any other cause, including Alzheimer disease). Additionally, subjects with known cardioembolic stroke factors (eg, mechanical valve, atrial fibrillation) were excluded to eliminate any confounding effects from these stroke etiologies. Finally, subjects with carotid occlusion were excluded because chronicity is often indeterminate and preocclusion lumen features could not be assessed. Before enrollment, all participants underwent a standard-of-care preintervention carotid CTA. After recruitment, subjects underwent a research carotid MR imaging and cognitive testing pre- and postintervention.

Clinical Characteristics

Relevant demographic and clinical characteristics were recorded following chart review. Cerebrovascular risk factors included age, sex, body mass index (BMI), smoking status, diabetes, renal insufficiency, hypertension, and hyperlipidemia. Diagnoses were assigned using standard clinical definitions. Renal insufficiency was an estimated glomerular filtration rate of < 45 mL/min. Hypertension was diagnosed if the average of ≥ 2 diastolic blood pressure measurements on at least 2 subsequent visits was ≥ 90 mm Hg or the average of multiple systolic blood pressure readings on ≥ 2 subsequent visits was ≥ 140 mm Hg. Hyperlipidemia was assigned when low-density lipoprotein was > 100 mg/dL. Male or female sex was self-reported. Cerebrovascular medications including antiplatelets, anticoagulants, statins, and antihypertensives were recorded.

Imaging and Postprocessing Protocols

Carotid MR Imaging. Carotid MR imaging studies were performed with a 3T magnet (Magnetom Prisma; Siemens) using the vendor's head and neck coil in conjunction with a dedicated 7-channel custom neck coil.²¹ The protocol included a TOF (axial acquisition: TR/TE = 20/3.4 ms, FOV = 240×240 mm², matrix = $320 \times 320 \times 100$, voxel = $0.77 \times 0.77 \times 0.77$ mm³); a 3D T1-weighted MPRAGE obtained 20 mm below to 20 mm above the carotid bifurcation, 1.0-mm section thickness (coronal acquisition: TR/TE/TI = 6.39/2.37/370 ms, flip angle = 15°, FOV = $180 \times 180 \times 92$ mm³, matrix = $320 \times 320 \times 120$, voxel = $0.77 \times 0.77 \times 0.77$ mm³); and a 3D T1 sampling perfection with application-optimized contrasts using different flip angle evolution (SPACE; Siemens) sequence (coronal acquisition: TR/TE = 800/22 ms, delay alternating with nutation for tailored excitation [DANTE] preparation = 150 ms, FOV = $180 \times 180 \times 77$, matrix = $320 \times 320 \times 100$, voxel = $0.77 \times 0.77 \times 0.77$ mm³).

DSC Brain Imaging. DSC was performed with an axial acquisition (TR/TE = 2070/52 ms, voxel = $2.0 \times 2.0 \times 2.0$ mm³, 5.0-mm section thickness, 100 time points/15 sections and with 1 mmol/mL^{–1} of Gadobutrol [Gadavist; Bayer Schering Pharma]). DSC was preceded by an initial contrast predose to minimize errors in CBV estimates. Data were transferred to an external workstation and processed by a neuroradiologist blinded to additional imaging and clinical information using FDA-approved software (Olea Sphere, Version 3.0-SP5; Olea Medical) and automated arterial input function selection.

Imaging Analysis

Perfusion Analysis. For each cerebral hemisphere, ROIs were outlined for the anterior cerebral artery (ACA), MCA, and posterior cerebral artery (PCA) territories using arterial territory maps for reference.²² ROI analysis was conducted at 3 different levels of the brain separated by 2 axial slices, and the average measurement of these was used. Relative CBF, CBV, and MTT were assessed for the ACA, MCA and PCA territories for the ipsilateral (side of intervention) and contralateral vascular territories. Total CBF, CBV, and MTT perfusion was the sum of all the territories (ACA, MCA, and PCA) for the ipsilateral and contralateral hemispheres. Ratios were computed for the ACA, MCA, and PCA CBF, CBV, and MTT as a ratio of ipsilateral-to-contralateral territories.

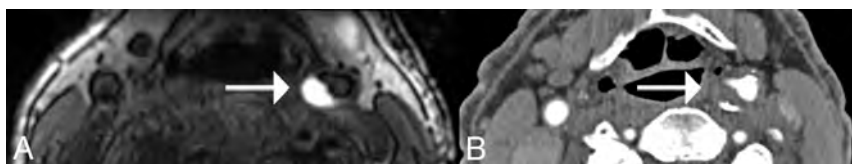


FIGURE Carotid IPH in a 77-year-old male participant. An axial MPRAGE (A) shows IPH(+) eccentric plaque at the left carotid bulb (arrow). The avid hyperintense signal on this heavily T1-weighted sequence is due to methemoglobin in the blood products. Axial CTA (B) shows the corresponding CTA appearance of this plaque. The predominantly noncalcified plaque (arrow) narrowed the vessel lumen by 62%.

Finally, the Total ratios were the total sum of all 3 hemispheric vascular territories expressed as a ratio of ipsilateral-to-contralateral hemispheres.

Carotid Plaque Features. A neuroradiologist blinded to all details evaluated each MPRAGE sequence for IPH. An IPH(+) status was assigned using a ≥ 2 -fold signal threshold over the adjacent sternocleidomastoid muscle, shown to have high interrater reliability and histologic correlation as previously described (Figure).²³ Lumen measurements were the consensus of a blinded neuroradiologist and a senior neuroradiology fellow. ICA stenosis was quantified on the preintervention CTA using the NASCET criteria $[(a - b)/a] \times 100\%$, where *a* is the ICA diameter distal to the stenosis and *b* is the diameter at the level of maximal stenosis.²⁴ Maximum plaque thickness was measured on precontrast 3D T1 SPACE perpendicular to the axis of the lumen.

Ischemic Stroke Evaluation

Ischemic stroke was defined according to the American Heart Association definition of CNS infarction as brain or retinal cell death attributable to ischemia based on imaging evidence of cerebral or retinal ischemia in the carotid distribution or clinical symptoms persisting for ≥ 24 hours, with other etiologies excluded.²⁵ Preceding intervention, ischemic stroke status was determined by neurologic examination supplemented with brain DWI concurrently performed during each research carotid MR imaging. DWI was reviewed by a blinded neuroradiologist for recent infarcts. DWI trace (hyperintense) and ADC (hypointense) were the imaging determinants of recent infarction.^{26,27}

WM Disease Rating

WM disease was assessed on T2-weighted FLAIR sequences from MR imaging brain studies using the Age-Related White Matter Changes rating scale.²⁸ Ratings were performed independently by a neuroradiologist blinded to cognitive and plaque results. WM changes were defined as hyperintense lesions of ≥ 5 mm on T2 or FLAIR, and lacunes were well-defined areas of > 2 mm.²⁸ The basal ganglia, and frontal, parieto-occipital, and temporal WM were rated on a 4-point scale and presented as a total score.²⁸

Repeatable Battery for the Assessment of Neuropsychological Status Cognitive Testing

The Repeatable Battery for the Assessment of Neuropsychological Status (RBANS) is a brief cognitive battery of 12 subtests, yielding 5 index scores: immediate memory index (list learning, story memory), visuospatial/constructional index (figure copy, line

orientation), language index (picture naming, semantic fluency), attention index (digit span, coding), delayed memory index (list recall, list recognition, story recall, figure recall), and a Total Scale score (all subtests).²⁹ Subtests were administered and scored according to the RBANS test manual, except for figure copy and figure recall subtests, which were scored with a modified set of scoring criteria.^{30, 31}

Data are presented as raw scores for the subtests, and the index and Total Scale scores are age-corrected standard scores (mean = 100 [SD, 15]) based on normative data in the test manual. Two additional indexes, visual and verbal indexes, were generated.³² Subtest scores were converted to age- and education-corrected scaled scores (mean = 10 [SD, 3]) using Table 2 from Duff et al.³² These age- and education-corrected scaled scores were used to generate the verbal index (list learning, story memory, list recall, list recognition, story recall) and visual index (figure copy, line orientation, coding, and figure recall).³⁰

RBANS has been previously described for subjects undergoing carotid endarterectomy^{33,34} and was administered preintervention and at least 1-month postintervention. The effects of hospitalization, anesthesia, and surgery should have been resolved by approximately 30 days postoperatively.³⁵ A research assistant administered alternate RBANS forms at visits to reduce practice effects. Across all scores (eg, raw, scaled, standard scores), higher scores indicate better cognitive performance. Baseline cognitive impairment was defined as a RBANS-1 score of ≤ 80 (> 1.3 SDs below the mean). RBANS interpretation was overseen by a neuropsychologist blinded to all patient information.

Reliable Change Assessment. Within neuropsychology, reliable change methods attempt to determine clinically meaningful cognitive change. These neuropsychology methods try to distinguish whether changes across 2 RBANS test sessions are the result of normal variations in the patient's performance and testing methods or are indeed consequential cognitive changes.³⁶ Factors that can affect cognitive testing results such as differential practice effects, systematic biases, and measurement error are taken into account.³⁶ Using regression-based prediction algorithms, predicted scores can be made for each patient's RBANS indexes and subtest scores.³⁶ Predicted postrevascularization scores, RBANS-2_{PD}, were generated with the prediction algorithms (derived from a sample of 129 cognitively intact older adults, mean age = 75.6 [SD, 7.5] years).³⁶ These scores (RBANS-2_{PD}) represent the expected RBANS scores at follow-up for each patient. Predicted RBANS-2_{PD} scores were subsequently compared with the actual observed scores of the study, RBANS-2_{OB}, by subtracting the predicted from the observed scores (RBANS-2_{OB} minus RBANS-2_{PD}).

Statistical Analysis

Continuous variables were expressed as mean (SD), and categorical variables, as frequencies. Two-sided *t* tests and χ^2 tests or Fisher exact tests were used to compare IPH groups. Univariable linear regression tested the association between the outcome variable

Table 1: Clinical characteristics^a

Parameter	Group (n = 23)	IPH(+) (n = 11)	IPH(-) (n = 12)	P
Participant characteristics				
Male	21 (91.3)	11 (100.0)	10 (83.3)	.48
Age (yr)	66.2 (SD, 8.0)	71.2 (SD, 7.6)	61.5 (SD, 5.2)	.002
BMI (kg/m ²)	31.7 (SD, 7.3)	33.4 (SD, 7.0)	30.1 (SD, 7.5)	.30
Right-handed	20 (87.0)	9 (81.8)	11 (91.7)	.59
Comorbidities				
Hyperlipidemia	18 (78.3)	10 (90.9)	8 (66.7)	.32
Hypertension	14 (60.9)	6 (54.6)	8 (66.7)	.68
Current smoker	4 (17.4)	0 (0.0)	4 (33.3)	.09
Prior smoker	14 (60.9)	8 (72.7)	6 (50.0)	.40
Renal insufficiency	1 (4.4)	1 (9.1)	0 (0.0)	.48
Diabetes	11 (47.8)	6 (54.6)	5 (41.7)	.54
Ischemic stroke and WM disease				
Ischemic stroke	7 (30.4)	3 (27.3)	4 (33.3)	1.00
Postintervention stroke	0 (0.0)	0 (0.0)	0 (0.0)	—
WM disease rating ^b	1.6 (SD, 1.2)	1.9 (SD, 1.4)	1.4 (SD, 1.0)	.36
Medications				
Statin	19 (82.6)	9 (81.8)	10 (83.3)	1.00
Antihypertensive	13 (56.5)	6 (54.6)	7 (58.3)	1.00
Antiplatelet	15 (65.2)	7 (63.6)	8 (66.7)	1.00
Anticoagulation	3 (13.4)	3 (27.3)	0 (0.0)	.09

Note: — indicates not assessed.

^a Data are mean (SD) or No (%).

^b Assessed for 19/23.

Table 2: Plaque, perfusion, and RBANS test characteristics^a

Parameter	Group (n = 23)	IPH(+) (n = 11)	IPH(-) (n = 12)	P
Ipsilateral plaque				
IPH	11 (47.8)	11 (100.0)	0 (0.0)	—
Ulceration	12 (52.2)	8 (72.7)	4 (33.3)	.06
Max plaque thickness (mm)	5.4 (SD, 1.6)	6 (SD, 1.9)	4.8 (SD, 1.1)	.08
NASCET (%)	68.0 (SD, 18.9)	65.1 (SD, 23.8)	70.7 (SD, 13.5)	.49
Intraluminal thrombus	3 (13.0)	1 (9.1)	2 (16.7)	1.00
Contralateral plaque				
Contra-IPH	6 (26.1)	3 (27.3)	3 (25.0)	1.00
Contra-ulceration	12 (52.2)	6 (54.6)	6 (50.0)	.83
Contra-max plaque thickness (mm)	4.2 (SD, 1.7)	4.4 (SD, 1.9)	4.1 (SD, 1.4)	.69
Contra-NASCET (%)	34.3 (SD, 30.3)	32.7 (SD, 31.4)	35.2 (SD, 31.4)	.85
Contra-intraluminal thrombus	0 (0.0)	0 (0.0)	0 (0.0)	—
Carotid intervention				
Carotid endarterectomy	20 (87.0)	10 (90.9)	10 (83.3)	.59
Right-sided intervention	14 (60.9)	7 (63.6)	4 (36.4)	1.00
Duration (min) ^b	133.1 (SD, 33.6)	132.2 (SD, 33.3)	134.1 (SD, 36.0)	.90
Perfusion				
Total CBF	34.2 (SD, 7.7)	31.5 (SD, 8.5)	36.7 (SD, 6.4)	.11
Total CBV	4.8 (SD, 0.9)	4.9 (SD, 1.1)	4.8 (SD, 0.8)	.92
Total MTT	8.3 (SD, 1.7)	9.0 (SD, 2.0)	7.6 (SD, 1.2)	.049
RBANS				
Education (yr)	15.2 (SD, 2.7)	14.8 (SD, 2.0)	15.5 (SD, 3.2)	.55
RBANS-1, \leq 80 baseline	6 (26.1)	1 (9.1)	5 (41.7)	.16
RBANS-1, preintervention (days)	28.5 (SD, 23.5)	33 (SD, 18.8)	24.3 (SD, 27.2)	.39
Intervention to RBANS-2 (days)	212.0 (SD, 255.3)	223.1 (SD, 249.5)	201.9 (SD, 250.0)	.84
RBANS-1 time to RBANS-2 (days)	266.6 (SD, 258.1)	243.9 (SD, 259.4)	287.3 (SD, 266.7)	.70

Note: — indicates not assessed; max, maximum.

^a Data are mean (SD) or No (%).

^b Assessed for 20/23.

(RBANS scores) and each covariate. Potential confounding variables were those covariates with $P < .20$ in univariable regression, and these were subsequently assessed using multivariable linear regression. For each multivariable linear regression model, the outcome of interest was Δ RBANS (RBANS-2 minus RBANS-1), and IPH was the primary predictor variable. Each covariate was eliminated using backwards elimination until all remaining variables met a $P < .10$ threshold. Consideration was given to the number of covariates to avoid overfitting the models. Analyses were performed using STATA software (Version 17.1; StataCorp).

RESULTS

Participant, Plaque, and Perfusion Characteristics

Whole Group. Twenty-three participants (mean age, 66.2 [SD, 8.0] years; 21 men [91.3%]) were recruited and included in the analyses. The mean percentage diameter stenosis on the side of the intervention was 68.0% (SD, 18.9%). Most participants, 16 (69.6%), were asymptomatic preceding the intervention. Eleven (47.8%) were IPH(+). The right ICA was the predominant carotid artery intervened on for 14 (60.9%) participants. All subjects were initially planned for endarterectomy, and the final decision on the method of intervention was endarterectomy in 20 (87%) and angioplasty/stent placement in 3 (13%). Procedures were performed by senior vascular surgeons with a mean of 20.3 (SD, 33.6) years of experience and lasted, on average, a mean of 133.1 (SD, 3.6) minutes. RBANS-1 test scores showed that 6 (26.1%) participants were cognitively impaired at baseline. Clinical characteristics are summarized in Table 1, and carotid plaque, perfusion, and cognition are shown in Table 2.

IPH(+) and IPH(-) Groups. Two parameters were significantly different between the IPH(+) and (-) groups: age and MTT Total. Participants with IPH(+) were older at a mean age of 71.2 (SD, 7.6) years compared with 61.5 (SD, 5.2) years ($P = .002$). The MTT Total

Table 3: Mean baseline and postintervention RBANS scores

RBANS	RBANS-1	RBANS-2	Δ RBANS	P
Total Scale score	92.1 (SD, 15.5)	96.1 (SD, 15.8)	4.0 (SD, 8.7)	.04
Attention index	91.9 (SD, 15.5)	91.3 (SD, 16.4)	−0.6 (SD, 11.4)	.82
Digit span	10.3 (SD, 2.4)	9.8 (SD, 2.9)	−0.5 (SD, 2.3)	.37
Coding	34.4 (SD, 8.4)	36.3 (SD, 9.1)	2.1 (SD, 6.0)	.13
Immediate memory index	89.4 (SD, 18.2)	97.7 (SD, 14.9)	8.3 (SD, 9.4)	<.001
List learning	22.8 (SD, 5.3)	26.3 (SD, 5.4)	3.5 (SD, 3.6)	<.001
Story memory	15.8 (SD, 4.5)	14.0 (SD, 3.1)	1.3 (SD, 3.3)	.08
Delayed memory index	96.2 (SD, 16.6)	99.6 (SD, 16.3)	3.4 (SD, 11.2)	.16
List recall	4.6 (SD, 2.5)	5.5 (SD, 2.7)	0.90 (SD, 2.5)	.08
List recognition	19.1 (SD, 1.4)	18.9 (SD, 2.2)	−0.2 (SD, 1.4)	.56
Story recall	7.8 (SD, 2.9)	9.0 (SD, 2.3)	1.2 (SD, 2.6)	.048
Figure recall	12.0 (SD, 4.5)	12.9 (SD, 4.4)	0.9 (SD, 3.5)	.23
Visuospatial/constructional index	97.5 (SD, 18.0)	96.9 (SD, 18.8)	−0.6 (SD, 15.4)	.85
Figure copy	17.0 (SD, 2.8)	16.9 (SD, 2.2)	−0.1 (SD, 2.6)	.81
Line orientation	16.9 (SD, 3.4)	16.5 (SD, 3.4)	−0.4 (SD, 2.4)	.44
Language index	95.9 (SD, 10.1)	97.7 (SD, 9.8)	1.9 (SD, 8.0)	.27
Picture naming	10.0 (SD, 0.0)	9.9 (SD, 0.3)	−0.1 (SD, 0.3)	.16
Semantic fluency	17.5 (SD, 4.9)	18.6 (SD, 4.7)	1.1 (SD, 4.4)	.25
Verbal index ^a	96.1 (SD, 14.1)	103.0 (SD, 12.0)	6.9 (SD, 9.2)	.002
Visual index ^b	93.5 (SD, 17.0)	95.6 (SD, 14.7)	2.1 (SD, 11.9)	.42

Note:— Δ RBANS indicates RBANS-2 minus RBANS-1 scores.

^a Verbal index subtests are list learning, story memory, list recall, list recognition, and story recall.

^b Visual index subtests are figure copy, line orientation, coding, and figure recall.

was significantly more delayed in the presence of IPH (mean = 9.0 [SD, 2.0] versus 7.6 [SD, 1.2], $P = .049$). WM disease ratings, ischemic stroke evaluation, and baseline cognition were not statistically significant between the 2 groups. Additionally, all remaining clinical, plaque, perfusion, procedural, and cognitive parameters (Tables 1 and 2) were not significantly different between the IPH groups at baseline.

Baseline and Postintervention Cognitive Assessment

Whole-Group Analysis. RBANS domains were compared before (RBANS-1) and after (RBANS-2) the carotid intervention (Table 3). RBANS-1 was performed preintervention at a mean of 28.5 (SD, 23.5) days (range, 1–90 days) and postintervention RBANS-2 at 266.6 (SD, 258.1) days (range, 53–838 days). Whole-group analysis revealed a statistically significant improvement from baseline in 3 domains: mean Total Scale score (RBANS-1, 92.1 [SD, 15.5] versus RBANS-2, 96.1 [SD, 15.8], $P = .04$); immediate memory index (RBANS-1, 89.4 [SD, 18.2] versus RBANS-2, 97.7 [SD, 14.9], $P < .001$), and verbal index (RBANS-1, 96.1 [SD, 14.1] versus RBANS-2, 103.0 [SD, 12.0], $P = .002$). The remaining indexes were not significantly changed after the intervention.

IPH Status and Postintervention Cognition

Analysis by IPH Status. RBANS-1 and RBANS-2 mean scores were compared between IPH(+) ($n = 11$) and IPH(−) ($n = 12$) groups (Online Supplemental Data). The range during which the RBANS-2 testing occurred was not significantly different between the IPH(+) and (−) groups. The IPH(+) group had no significant improvement in postintervention scores. One index, the attention index, significantly decreased from baseline (RBANS-1, 99.4 [SD, 18.0] versus RBANS-2, 93.5 [SD, 19.4], $P = .045$). Postintervention, the IPH(−) group significantly improved in 4 scores: Total Scale score (RBANS-1, 86.4 [SD, 11.8] versus RBANS-2, 95.5 [SD, 12.4], $P = .004$), immediate memory index (RBANS-1, 82.3 [SD, 14.6] versus RBANS-2, 96.2 [SD, 14.1], $P =$

.002), delayed memory index (RBANS-1, 94.3 [SD, 14.9] versus RBANS-2, 102.4 [SD, 8.0], $P = .03$), and verbal index (RBANS-1, 94.3 [SD, 13.2] versus RBANS-2, 101.5 [SD, 107.4], $P = .009$). Subtracted mean scores (RBANS-2 minus RBANS-1) for each domain were designated Δ RBANS. IPH(+) and (−) groups had statistically significant differences in the Δ RBANS Total Scale score: IPH(+), −0.4 (SD, 6.8) versus IPH(−), 8.0 (SD, 8.5), $P = .02$; attention index, IPH(+), −5.9 (SD, 8.5) versus IPH(−), 4.3 (SD, 11.9), $P = .03$; and immediate memory index IPH(+), 4.2 (SD, 6.7) versus IPH(−), 12.2 (SD, 10.2), $P = .04$.

Multivariable Analysis of Postintervention Cognitive Outcomes

Multivariable regression models were fitted to the 3 cognitive outcomes with significantly different Δ RBANS scores between subjects with IPH(+) and (−): Δ RBANS Total Scale score, attention index, and immediate memory index. The Δ RBANS Total Scale score final model consisted of IPH(+) plaque ($\beta = -6.17$; 95% CI, −12.49–0.15; $P = .06$) and hyperlipidemia ($\beta = -9.05$; 95% CI, −16.70 to −1.40; $P = .02$). The Δ RBANS attention index final model included only IPH(+) plaque ($\beta = -10.24$; 95% CI, −19.29 to −1.20; $P = .03$). The final model for Δ RBANS immediate memory index included IPH(+) plaque ($\beta = -8.17$; 95% CI, −15.10 to −1.24; $P = .02$), BMI ($\beta = 0.49$; 95% CI, 0.02–0.97; $P = .04$), and the MTT Total ratio ($\beta = -48.51$; 95% CI, −100.70–3.69; $P = .07$). All univariable and multivariable regression analyses are shown in Online Supplemental Data.

Reliable Change Assessment

Predicted RBANS-2 scores (RBANS-2_{PD}) were generated (Online Supplemental Data). Observed RBANS-2 scores (RBANS-2_{OB}) were subtracted from the predicted (RBANS-2_{PD}) for the whole group, Group_{OB-PD}, and according to IPH status, IPH(+)_{OB-PD} and IPH(−)_{OB-PD}. For the group, the attention index group_{OB-PD} (mean, −6.3 [SD, 11.2], $P = .01$), immediate memory index

group_{OB-PD} (mean, -5.0 [SD, 8.1], $P = .007$), and language index group_{OB-PD} (mean, -3.7 [SD, 6.7], $P = .02$) significantly deviated from predicted scores. IPH(+) status showed a significantly lower-than-expected attention index IPH(+)_{OB-PD} (mean, -8.9 [SD, 10.5], $P = .02$) and immediate memory index IPH(+)_{OB-PD} (mean, -5.3 [SD, 6.8], $P = .026$). The IPH(−) group's language index significantly deviated from predicted, IPH(−)_{OB-PD} (mean, -5.2 [SD, 6.1], $P = .01$).

DISCUSSION

This study examined the changes in cognition after carotid plaque removal and the impact of IPH status on postintervention scores. The effects of stenosis, perfusion, and additional potential confounders were also evaluated. Whole-group analysis showed improvement in three domains: the overall Total Scale score, immediate memory index, and verbal index following intervention. Subgroup evaluation indicated that preintervention IPH status impacted postintervention cognition. An IPH(−) status conferred the most cognitive benefit with a significantly improved Total Scale score, immediate memory index, delayed memory index, and verbal index. For IPH(+) participants, there was no statistically significant improvement in any of the scores, and the attention index declined.

The whole group's improved cognitive performance is in keeping with prior studies that also showed an association between carotid revascularization and improved cognition.^{2,33,34,37} Takaiwa et al^{33,34} demonstrated an improved RBANS Total Scale score and immediate memory index 3 months postcarotid endarterectomy, which was sustained after 1 year. Takaiwa et al additionally reported an improved attention index.^{33,34} In the present study, attention index performance differed according to IPH status. The IPH(−) group's attention index increased, though not significantly. Conversely, the IPH(+) group's score significantly decreased. This finding suggests that IPH could differentially affect some cognitive domains more than others.

The present study evaluated 2 additional indexes that may help to lateralize pathology. The verbal and visual indexes should be most representative of the left and right cerebral hemispheric function, respectively.^{32,38} Revascularization was most beneficial for the verbal index, which increased for the whole group, again attributable to those with IPH(−) plaque; however, the visual index remained unchanged. Improved verbal scores would be expected more with a left-sided intervention.^{32,38,39} In the current study, however, this finding was not explained by the side of revascularization. One possibility is that carotid disease may affect functional brain connectivity beyond the ipsilateral vascular territory.⁴⁰

Prior studies that examined postintervention cognitive effects had not considered plaque composition.^{2,33,34,37} At the outset, this study hypothesized that intervention on IPH(+) plaque should have the greatest cognitive benefit, given its underlying thromboembolic activity,¹⁶ risk of stroke, and TIA.¹¹⁻¹³ Instead, the converse occurred, and intervention on IPH(−) plaque ameliorated 4 cognitive outcomes (Total Scale score, attention index, immediate index, and verbal index). One explanation for the less-than-expected IPH(+) group's performance is microembolization during the intervention.⁴¹ An association between vulnerable plaque and postintervention ischemic events has been previously shown.⁴²⁻⁴⁵

During carotid endarterectomy, IPH increased the embolization risk, specifically during the dissection phase.⁴³ After stent placement, a higher risk of ipsilateral ischemic events was found and correlated with IPH volume.^{44,45} In the current study, no participant had a clinically evident postprocedural ischemic stroke; however, periprocedural monitoring for silent emboli or postprocedural MR imaging for covert infarction was not performed. Cognitive improvement with IPH(−) plaque could be attributable to plaque composition. Ulceration and intraluminal thrombus, both features of plaque instability, were not statistically different between the IPH groups. However, other plaque constituents or morphologic features including calcification or a lipid-rich necrotic core may be implicated in the amelioration of some IPH(−) cognitive domains.

Confounding was addressed during statistical analysis. Three confounders were identified; 2 (hyperlipidemia and MTT Total ratio) adversely affected cognition, while 1 (BMI) had a positive association. Of the cardiovascular risk factors, only hyperlipidemia was negatively associated with the Total Scale score. High cholesterol is a known risk factor for cognitive impairment.^{46,47} Secondly, the MTT Total ratio negatively impacted the immediate memory index and was statistically longer for the IPH(+) participants. MTT measures the average time of red blood cells in the capillary circulation and can indicate impaired perfusion. In addition to steno-occlusive disease, perfusion could be influenced by plaque components including IPH volume.¹⁷ BMI was positively associated with the attention index. At an older age, a high BMI could have a protective effect against the progression of dementia.⁴⁸⁻⁵⁰ A survivorship bias effect is one plausible explanation for this obesity-dementia paradox.⁵¹

In a further attempt to gauge the benefit of IPH removal, the reliable change methodology was used. Baseline scores were used to estimate expected follow-up cognition on the basis of predictions derived for healthy age- and education-matched community dwellers.³⁶ This was performed to indicate whether a change in a score was statistically different from what was expected at follow-up. At baseline, participants' scores were predominantly in the RBANS average range, with a small number cognitively impaired; however, the number with cognitive impairment was not statistically different between the groups. After the intervention, the IPH(+) group had a lower-than-predicted attention index and immediate memory index. For IPH(−) participants, the language index was lower than predicted. Findings suggest that despite intervention, some cognitive abilities were unrecoverable for both groups, and the IPH(+) group was most affected. This outcome could be related to the long-standing impact on neuroplasticity from recurrent microembolization.

This study has some limitations. The sample size was small, though this limitation was comparable with that in similar studies of postintervention carotid disease and cognition.^{33,34} Despite no enrollment restrictions on demographics, the group were all white and predominantly male, which is a known population at risk of carotid disease.⁵² Accordingly, ethnicity and sex influences were unattainable. The effect of periprocedural microembolization was not examined, and routine postprocedural MR imaging screening was not conducted. Emboli monitoring or postintervention MR imaging could further address the hypotheses of an

embolic-driven mechanism of cognitive impairment. Baseline cognition was not compared with a randomized control group; however, the predicted score calculations enabled comparison with a group of community-dwelling older adults.³⁶

CONCLUSIONS

Despite these limitations, this study was a critical initial step toward elucidating the effect of carotid IPH on cognition after revascularization. While the management of carotid bifurcation stenosis has been extensively investigated with recommendations for management,²⁰ guidelines regarding the role of cognition in decision-making or stratifying patients have yet to be established. Additionally, an extended follow-up period would evaluate the long-term stability of postintervention cognition changes. Future studies are warranted to further understand the association between plaque composition and cognition.

Disclosure forms provided by the authors are available with the full text and PDF of this article at www.ajnr.org.

REFERENCES

1. Fisher M. **Senile dementia: a new explanation of its causation.** *Can Med Assoc J* 1951;65:1–7 Medline
2. Lal BK, Dux MC, Sikdar S, et al. **Asymptomatic carotid stenosis is associated with cognitive impairment.** *J Vasc Surg* 2017;66:1083–92 CrossRef Medline
3. van Oijen M, de Jong FJ, Witteman JC, et al. **Atherosclerosis and risk for dementia.** *Ann Neurol* 2007;61:403–10 CrossRef Medline
4. Turowicz A, Czupiga A, Malinowski M, et al. **Carotid revascularization improves cognition in patients with asymptomatic carotid artery stenosis and cognitive decline. Greater improvement in younger patients with more disordered neuropsychological performance.** *J Stroke Cerebrovasc Dis* 2021;30:105608 CrossRef Medline
5. Ortega G, Alvarez B, Quintana M, et al. **Asymptomatic carotid stenosis and cognitive improvement using transcervical stenting with protective flow reversal technique.** *Eur J Vasc Endovasc Surg* 2014;47:585–92 CrossRef Medline
6. Germano da Paz O, Guillaumon AT, Lopes TM, et al. **Carotid stenting versus endarterectomy cognitive outcomes.** *Ann Vasc Surg* 2014;28:893–900 CrossRef Medline
7. Wolters FJ, Zonneveld HI, Hofman A, et al; Heart-Brain Connection Collaborative Research Group. **Cerebral perfusion and the risk of dementia.** *Circulation* 2017;136:719–28 CrossRef Medline
8. Long Q, Luppi L, König CS, et al. **Study of the collateral capacity of the circle of Willis of patients with severe carotid artery stenosis by 3D computational modeling.** *J Biomech* 2008;41:2735–42 CrossRef Medline
9. Romero JR, Beiser A, Seshadri S, et al. **Carotid artery atherosclerosis, MRI indices of brain ischemia, aging, and cognitive impairment: the Framingham study.** *Stroke* 2009;40:1590–96 CrossRef Medline
10. Fürst H, Hartl WH, Janssen I. **Patterns of cerebrovascular reactivity in patients with unilateral asymptomatic carotid artery stenosis.** *Stroke* 1994;25:1193–1200 CrossRef Medline
11. Gupta A, Baradaran H, Schweitzer AD, et al. **Carotid plaque MRI and stroke risk: a systematic review and meta-analysis.** *Stroke* 2013;44:3071–77 CrossRef Medline
12. Schindler A, Schinner R, Altat N, et al. **Prediction of stroke risk by detection of hemorrhage in carotid plaques: meta-analysis of individual patient data.** *JACC Cardiovasc Imaging* 2020;13:395–406 CrossRef Medline
13. Hosseini AA, Kandiyil N, Macsweeney ST, et al. **Carotid plaque hemorrhage on magnetic resonance imaging strongly predicts recurrent ischemia and stroke.** *Ann Neurol* 2013;73:774–84 CrossRef Medline
14. McNally JS, McLaughlin MS, Hinckley PJ, et al. **Intraluminal thrombus, intraplaque hemorrhage, plaque thickness, and current smoking optimally predict carotid stroke.** *Stroke* 2015;46:84–90 CrossRef Medline
15. Purandare N, Voshaar RC, Morris J, et al. **Asymptomatic spontaneous cerebral emboli predict cognitive and functional decline in dementia.** *Biol Psychiatry* 2007;62:339–44 CrossRef Medline
16. Altat N, Goode SD, Beech A, et al. **Plaque hemorrhage is a marker of thromboembolic activity in patients with symptomatic carotid disease.** *Radiology* 2011;258:538–45 CrossRef Medline
17. Hashimoto N, Hama S, Yamane K, et al. **Carotid arterial intraplaque hemorrhage and calcification influences cerebral hemodynamics.** *Neurosurg Rev* 2013;36:421–27 CrossRef Medline
18. Huo R, Xu H, Yang D, et al. **Associations between carotid plaque characteristics and improvement of cerebral blood perfusion in patients with moderate to severe carotid stenosis undergoing carotid endarterectomy.** *J Magn Reson Imaging* 2021;53:613–25 CrossRef Medline
19. Dempsey RJ, Jackson DC, Wilbrand SM, et al. **The preservation of cognition 1 year after carotid endarterectomy in patients with prior cognitive decline.** *Neurosurgery* 2018;82:322–28 CrossRef Medline
20. AbuRahma AF, Avgerinos ED, Chang RW, et al. **Society for Vascular Surgery clinical practice guidelines for management of extracranial cerebrovascular disease.** *J Vasc Surg* 2022;75:4s–22s CrossRef Medline
21. Beck MJ, Parker DL, Bolster BD Jr, et al. **Interchangeable neck shape-specific coils for a clinically realizable anterior neck phased array system.** *Magn Reson Med* 2017;78:2460–68 CrossRef Medline
22. Kim DE, Park JH, Schellingerhout D, et al. **Mapping the supratentorial cerebral arterial territories using 1160 large artery infarcts.** *JAMA Neurol* 2019;76:72–80 CrossRef Medline
23. McNally JS, Yoon HC, Kim SE, et al. **Carotid MRI detection of intraplaque hemorrhage at 3T and 1.5T.** *J Neuroimaging* 2015;25:390–96 CrossRef Medline
24. Fox AJ. **How to measure carotid stenosis.** *Radiology* 1993;186:316–18 CrossRef Medline
25. Sacco RL, Kasner SE, Broderick JP, et al; Council on Nutrition, Physical Activity and Metabolism. **An updated definition of stroke for the 21st century: a statement for healthcare professionals from the American Heart Association/American Stroke Association.** *Stroke* 2013;44:2064–89 CrossRef Medline
26. Lansberg MG, Thijs VN, O'Brien MW, et al. **Evolution of apparent diffusion coefficient, diffusion-weighted, and T2-weighted signal intensity of acute stroke.** *AJNR Am J Neuroradiol* 2001;22:637–44 Medline
27. Warach S, Gaa J, Siewert B, et al. **Acute human stroke studied by whole brain echo planar diffusion-weighted magnetic resonance imaging.** *Ann Neurol* 1995;37:231–41 CrossRef Medline
28. Wahlund LO, Barkhof F, Fazekas F, et al; European Task Force on Age-Related White Matter Changes. **A new rating scale for age-related white matter changes applicable to MRI and CT.** *Stroke* 2001;32:1318–22 CrossRef Medline
29. Randolph C, Tierney MC, Mohr E, et al. **The Repeatable Battery for the Assessment of Neuropsychological Status (RBANS): preliminary clinical validity.** *J Clin Exp Neuropsychol* 1998;20:310–19 CrossRef Medline
30. Duff K, Patton D, Schoenberg MR, et al. **Age- and education-corrected independent normative data for the RBANS in a community dwelling elderly sample.** *Clin Neuropsychol* 2003;17:351–66 CrossRef Medline
31. Duff K, Leber WR, Patton DE, et al. **Modified scoring criteria for the RBANS figures.** *Appl Neuropsychol* 2007;14:73–83 CrossRef Medline
32. Duff K, Langbehn DR, Schoenberg MR, et al. **Normative data on and psychometric properties of Verbal and Visual Indexes of the RBANS in older adults.** *Clin Neuropsychol* 2009;23:39–50 CrossRef Medline
33. Takaiwa A, Kuwayama N, Akioka N, et al. **Effect of carotid endarterectomy on cognitive function in patients with asymptomatic carotid**

- artery stenosis. *Acta Neurochir (Wien)* 2013;155:627–33 CrossRef Medline
34. Takaiwa A, Hayashi N, Kuwayama N, et al. **Changes in cognitive function during the 1-year period following endarterectomy and stenting of patients with high-grade carotid artery stenosis.** *Acta Neurochir (Wien)* 2009;151:1593–1600 CrossRef Medline
 35. Evered L, Silbert B, Knopman DS, et al; Nomenclature Consensus Working Group. **Recommendations for the nomenclature of cognitive change associated with anaesthesia and surgery—2018.** *Anesthesiology* 2018;129:872–79 CrossRef Medline
 36. Hammers DB, Suhrie KR, Porter SM, et al. **Generalizability of reliable change equations for the RBANS over one year in community-dwelling older adults.** *J Clin Exp Neuropsychol* 2020;42:394–405 CrossRef Medline
 37. Watanabe J, Ogata T, Higashi T, et al. **Cognitive change 1 year after CEA or CAS compared with medication.** *J Stroke Cerebrovasc Dis* 2017;26:1297–1305 CrossRef Medline
 38. Wilde MC. **The validity of the repeatable battery of neuropsychological status in acute stroke.** *Clin Neuropsychol* 2006;20:702–15 CrossRef Medline
 39. Ishihara H, Oka F, Shirao S, et al. **Cognitive outcome differences on the side of carotid artery stenting.** *J Vasc Surg* 2013;57:125–30 CrossRef Medline
 40. He S, Liu Z, Xu Z, et al. **Brain functional network in chronic asymptomatic carotid artery stenosis and occlusion: changes and compensation.** *Neural Plast* 2020;2020:9345602 CrossRef Medline
 41. Krámská L, Kovář M, Hrešková L, et al. **Neuropsychological performance after carotid endarterectomy.** *J Integr Neurosci* 2022;21:36 CrossRef Medline
 42. Verhoeven BA, de Vries JP, Pasterkamp G, et al. **Carotid atherosclerotic plaque characteristics are associated with microembolization during carotid endarterectomy and procedural outcome.** *Stroke* 2005;36:1735–40 CrossRef Medline
 43. Altaf N, Beech A, Goode SD, et al. **Carotid intraplaque hemorrhage detected by magnetic resonance imaging predicts embolization during carotid endarterectomy.** *J Vasc Surg* 2007;46:31–36 CrossRef Medline
 44. Zhao G, Tang X, Tang H, et al. **Recent intraplaque hemorrhage is associated with a higher risk of ipsilateral cerebral embolism during carotid artery stenting.** *World Neurosurg* 2020;137:e298–307 CrossRef Medline
 45. Ji A, Lv P, Dai Y, et al. **Associations between carotid intraplaque hemorrhage and new ipsilateral ischemic lesions after carotid artery stenting: a quantitative study with conventional multi-contrast MRI.** *Int J Cardiovasc Imaging* 2019;35:1047–54 CrossRef Medline
 46. van Vliet P. **Cholesterol and late-life cognitive decline.** *J Alzheimers Dis* 2012;30(Suppl 2):S147–12 CrossRef Medline
 47. Svensson T, Sawada N, Mimura M, et al. **The association between midlife serum high-density lipoprotein and mild cognitive impairment and dementia after 19 years of follow-up.** *Transl Psychiatry* 2019;9:26 CrossRef Medline
 48. Besser LM, Gill DP, Monsell SE, et al. **Body mass index, weight change, and clinical progression in mild cognitive impairment and Alzheimer disease.** *Alzheimer Dis Assoc Disord* 2014;28:36–43 CrossRef Medline
 49. Dahl AK, Löppönen M, Isoaho R, et al. **Overweight and obesity in old age are not associated with greater dementia risk.** *J Am Geriatr Soc* 2008;56:2261–66 CrossRef Medline
 50. Moser VA, Pike CJ. **Obesity and sex interact in the regulation of Alzheimer's disease.** *Neurosci Biobehav Rev* 2016;67:102–18 CrossRef Medline
 51. Michaud TL, Siahpush M, Farazi PA, et al. **The association between body mass index, and cognitive, functional, and behavioral declines for incident dementia.** *J Alzheimers Dis* 2018;66:1507–17 CrossRef Medline
 52. Dossabhoy S, Arya S. **Epidemiology of atherosclerotic carotid artery disease.** *Semin Vasc Surg* 2021;34:3–9 CrossRef Medline

Different Features of a Metabolic Connectivity Map and the Granger Causality Method in Revealing Directed Dopamine Pathways: A Study Based on Integrated PET/MR Imaging

L. Wang, L. Wei, L. Jin, Y. Li, Y. Wei, W. He, L. Shi, Q. Sun, W. Li, Q. Li, Y. Li, Y. Wu, Y. Wang, and M. Yuan



ABSTRACT

BACKGROUND AND PURPOSE: Exploring the directionality of neural information in the brain is important for understanding brain mechanisms and neurodegeneration development. Granger causality analysis and the metabolic connectivity map can be used to investigate directional transmission of information between brain regions, but their differences in depicting functional effective connectivity are not clear.

MATERIALS AND METHODS: Using the Monash rs-PET/MR imaging data set, we conducted Granger causality and metabolic connectivity map analyses of the dopamine reward circuit in the brain. The dopamine reward circuit is a well-known system consisting primarily of the bilateral orbital frontal cortex, caudate, nucleus accumbens, thalamus, and substantia nigra. We validated these circuit pathways using Granger causality and the metabolic connectivity map for identifying effective connectivities against a priori knowledge by testing the significance of directed pathways ($P < .05$, false discovery rate–corrected).

RESULTS: We found 3 types of effective connectivities in the dopamine reward circuit: long-range, neighborhood, and symmetric. Granger causality analysis revealed long-range connections in the orbital frontal cortex–caudate and orbital frontal cortex–nucleus accumbens regions. Metabolic connectivity map analysis revealed neighborhood connections in the nucleus accumbens–caudate, substantia nigra–thalamus, and thalamus–caudate regions. Metabolic connectivity map analysis also found symmetric connections in each of the bilateral nucleus accumbens, caudate, thalamus, and orbital frontal cortex–caudate regions. Different patterns in directional networks of the dopamine reward circuit were revealed by Granger causality and metabolic connectivity map analyses.

CONCLUSIONS: Granger causality analysis primarily identified bidirectional cortico–nucleus connections, while the metabolic connectivity map primarily identified direct connections among neighborhood and symmetric regions. The results of this study indicated that investigations of effective connectivities should use an appropriate analysis method depending on the purpose of the study.

ABBREVIATIONS: BOLD = blood oxygen level–dependent; BG = basal ganglia; CAU = caudate; DA = dopamine; EC = effective connectivity; FC = functional connectivity; FDR = false discovery rate; GC = Granger causality; GCI = Granger causality index; MCM = metabolic connectivity map; NAc = nucleus accumbens; OFC = orbital frontal cortex; SN = substantia nigra; THA = thalamus

The human brain has been recognized as a continuously communicating dynamic network.¹ Intrinsic activities in structures

as small as neurons can be analyzed with functional connectivity (FC) to identify functional brain networks. However, the directionality of the interactions within the brain networks built from these correlations cannot be determined. Effective connectivity (EC) provides the directional or causal relationships among brain region transmissions and can be used to explore these communications.² Understanding the directionality of brain networks provides insight into the diagnosis and treatment of neurologic or mental diseases, such as Alzheimer disease,³ schizophrenia,⁴ and addiction.⁵

Granger causality (GC) analysis is a statistical method that adopts a linear vector autoregressive model of stochastic time-series data. GC was proposed for use in economics, but its use in fMRI studies of brain disorders has revealed the directionality of transmissions among brain regions.^{5–8}

In studying the metabolic directionality among brain regions, Riedel et al⁹ proposed an approach called the metabolic connectivity

Received May 9, 2022; accepted after revision October 1.

From the Departments of Nuclear Medicine (L. Wang, L. Wei, L.J., YunBo Li, Y. Wei, W.H., L.S., M.Y.) and Radiology (W.L., Q.L.), Tangdu Hospital of Air Force Military Medical University, Xi'an, China; Department of Radiology (Q.S., Y. Wang), the First Affiliated Hospital of Xi'an Jiaotong University, Xi'an, China; Department of Radiology (YongBin Li), the First Hospital of Xi'an, Xi'an, China; and Siemens Healthineers Ltd (Y. Wu), Beijing, China.

Lei Wang, Longxiao Wei and Yarong Wang contributed equally to this work.

This work was supported by grants from the National Natural Science Foundation of China (82071497 to Y. Wang).

Please address correspondence to Menghui Yuan, MD, Department of Nuclear Medicine, Tangdu Hospital of Air Force Military Medical University, 569 Xinsi Rd, Baqiao District, Xi'an, China; e-mail: 13519196610@139.com

Indicates open access to non-subscribers at www.ajnr.org

Indicates article with online supplemental data.

<http://dx.doi.org/10.3174/ajnr.A7707>

map (MCM). The MCM is based on collecting energy consumption data in neuronal communications while simultaneously collecting PET and fMRI data. Most energy metabolism is dedicated to signaling and is consumed postsynaptically, in other words, at the target neurons.⁹⁻¹³ Riedl et al scaled this to the system level with the assumption that an increase in local metabolism reflects an increase in afferent EC from source regions. They further hypothesized that the spatial correlations between metabolic activity and FC represent this EC spatial profile. In other words, the MCM reflects the correlation between the pattern of improved glutamate consumption and the pattern of improved blood oxygen level-dependent (BOLD) signals in the target region. The MCM has been used to identify altered EC within the default mode network for Alzheimer disease,³ reveal the stable bidirectional connection among early/higher visual regions of healthy cohorts,⁹ and study the cognition task-induced reconfiguration of whole-brain networks.¹⁴

BOLD signals measure indirect neuronal activities and are influenced by intermediate physiologic responses, including the cerebral metabolism rate of glucose/oxygen and the CBF/CBV. [¹⁸F] FDG-PET signals measure glucose metabolism in the brain, which is also influenced by the CBF/CBV. When PET and fMRI data are collected simultaneously, both the levels of glucose metabolism and BOLD signals are influenced by the simultaneous CBF and share a common basis in central neurophysiology. Human brain metabolic connectivity derived from [¹⁸F] FDG-PET is comparable with that derived from resting-state fMRI analyses.^{15,16} While these studies confirmed the comparability of nondirectional metabolism connectivity and BOLD connectivity, little was revealed about the relationship between glucose metabolic EC and fMRI EC. This issue has not been studied due to the lack of simultaneously acquired and aligned fMRI and PET data.

The novel advantages of integrated PET/MR imaging provide a new insight into understanding the dopamine (DA) reward circuit. The DA reward circuit consists of 3 pathways: the nigrostriatal pathway, along which the substantia nigra (SN) sends a dopaminergic projection to the dorsal striatum; the mesolimbic pathway, where the ventral tegmental area (VTA) sends a similar type of dopaminergic projection to the nucleus accumbens (NAc); and the mesocortical pathway, where dopaminergic projections are sent from the SN/VTA through the thalamus (THA) and the prefrontal cortex.^{17,18} There are rich bidirectional projection pathways among these brain regions¹⁹⁻²¹ involved in the DA reward circuit. We chose brain areas involved in the DA reward system to validate the sensitivity and consistency of MCM and GC analyses and to identify the directed pathways among brain regions by ROI analysis.

MATERIALS AND METHODS

Data Sets

The data for this study were obtained from the Monash rsPET-MR data set²²⁻²⁵ in the OpenNeuro database (<https://doi.org/10.18112/openneuro.ds002898.v1.1.1>). It is a simultaneous fMRI-functional PET data set acquired from young, healthy individuals at rest. Participants ($n = 27$, 21 women) were all right-handed, 18–23 years in age (mean age, 19 years), with 13–18 years of education (mean, 14 years) and no history of diabetes, diagnosed Axis-I mental illness, or cardiovascular illness.²² Participants

underwent a 95-minute simultaneous MR imaging–PET scan in a 3T Biograph molecular MR imaging scanner (syngo VB20P; Siemens) as described previously.^{22,24} Briefly, [¹⁸F] FDG (average dose, 233 MBq) was infused over the course of the scan.²² During the first 30 minutes of the FDG infusion, T1 3D MPRAGE was acquired (Acquisition Time [TA] = 7 minutes 0.6 seconds, TR = 1640 ms, TE = 2.34 ms, flip angle = 8°, FOV = 256 × 256 mm², voxel size = 1 × 1 × 1 mm³, 176 slices, sagittal acquisition). For the remainder of the scan, 6 consecutive 10-minute blocks of T2*-weighted echo-planar images were acquired (TR = 2.45 seconds, TE = 30 ms, FOV = 190 mm², 3 × 3 × 3 mm³ voxels, 44 slices, ascending axial acquisition).

Image Preprocessing

The first 10-minute block of BOLD data, the corresponding 10-minute FDG-PET data, and the T1 3D MPRAGE data were used for structural segmentation and registration. Volumes from the PET data were reconstructed every 16 seconds, and the corresponding 10-minute data volume indexes were 129–165 for each participant. PET volumes were extracted and averaged to acquire static FDG-PET images.

The CONN toolbox (Version 20.b; <https://web.conn-toolbox.org/>)²⁶ was used for BOLD data preprocessing. It is a functional connectivity toolbox based on the Statistical Parameter Mapping 12 toolbox (SPM; <http://www.fil.ion.ucl.ac.uk/spm>). The default preprocessing pipeline for volume-based analyses (“direct normalization to Montreal Neurological Institute space” pipeline in CONN) was used, including the following steps: 1) realignment and unwarping; 2) section-timing correction for interslice differences in acquisition time; 3) Artifact Detection Tools–based outlier detection (https://www.nitrc.org/projects/artifact_detect) to identify outlier scans for scrubbing; 4) segmentation of functional and anatomic images to gray and white matter and CSF tissue classes using SPM-unified segmentation and normalization procedures; and 5) normalization to 2-mm (functional) or 1-mm (anatomic) isotropic voxel size in Montreal Neurological Institute space. The functional images were smoothed using spatial convolution with a Gaussian kernel of 4 mm at full width at half maximum values. After preprocessing, functional data were further denoised, removing potential confounding effects in the BOLD signal, such as noise components from WM and CSF areas,²⁷ estimated subject-motion parameters, scrubbing, and session effects.²⁸ Temporal frequencies <0.008 Hz or >0.09 Hz were removed from the BOLD signal to focus on slow-frequency fluctuations while minimizing the influence of physiologic, head-motion, and other noise sources.²⁹

ROI Definition and FC Analysis

FSL³⁰ (<http://www.fmrib.ox.ac.uk/fsl>) built-in atlases were used to generate 10 ROIs in the DA reward system.^{31,32} Eight bilateral ROIs were extracted from the Harvard-Oxford probability atlas with a threshold set to 50% probability, then binarized into masks. The 8 bilateral ROIs were the thalamus (THA, left: 1139, right: 1129 voxels), (NAc, left: 70, right: 56 voxels), caudate (CAU, left: 444, right: 457 voxels), and orbital frontal cortex (OFC, left: 905, right: 790 voxels). The Talairach Daemon atlas (included with FSL) was used to generate bilateral SN (left: 37, right: 43 voxels) ROI masks directly. Before ROI generation, the

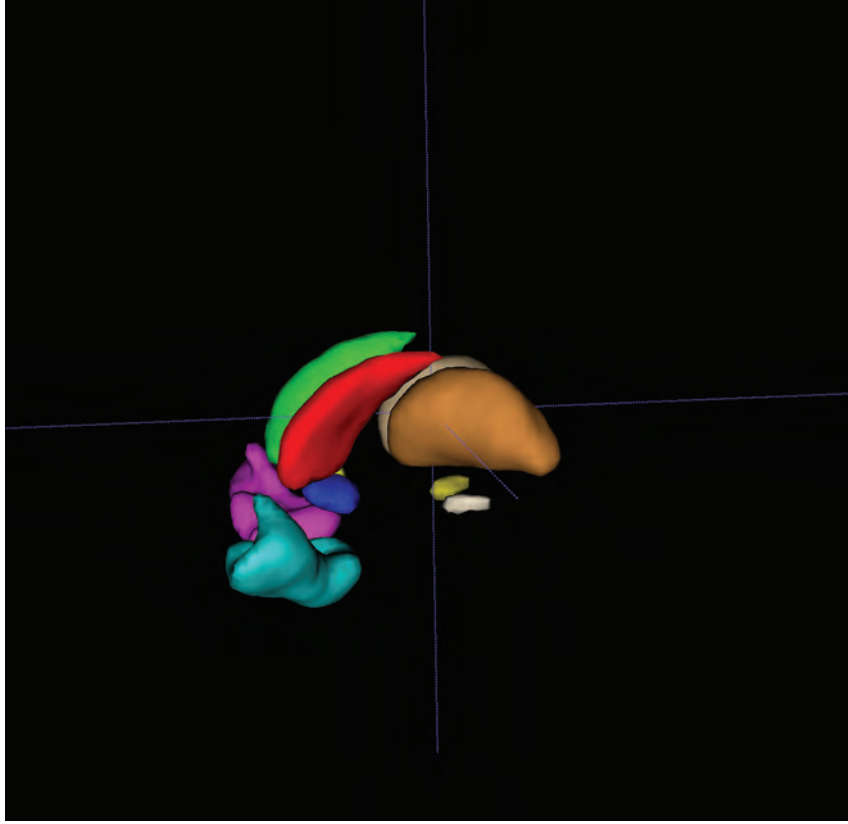


FIG 1. 3D display of 10 generated ROIs, rendered using ITK-SNAP 3.8.0 (www.itksnap.org).

atlas was registered and resampled to the same Montreal Neurological Institute 2-mm template in CONN, verifying that ROIs, preprocessed fMRI, and FDG-PET data were in the same space (Fig 1).

For each participant, we calculated the ROI and the voxelwise functional connectivity of every ROI, forming 1 FC matrix and 10 FC maps per participant. The element values in the FC matrices and voxel values in the FC maps were further transformed to z-values using the Fisher r-to-z transformation equation, ensuring that the distribution of z-values would be approximately normal.

Granger Causality Analysis

The Granger causality index (GCI) of each ROI pair was calculated along each group-wise statistically significant FC pathway. This GCI was calculated using an autoregressive model:

$$1) \quad Y_t = \sum_{k=1}^p b_k Y_{(t-k)} + cZ_t + \varepsilon_t.$$

The joint regressive representation was determined by

$$2) \quad Y_t = \sum_{k=1}^p a_k X_{(t-k)} + \sum_{k=1}^p b_k Y_{(t-k)} + cZ_t + \mu_t,$$

$$3) \quad F_{x \rightarrow y} = \ln \frac{\text{var}(\varepsilon_t)}{\text{var}(\mu_t)},$$

where $Y_{(t-k)}$ and $X_{(t-k)}$ are the preprocessed ROI signals, ε_t and μ_t are the residuals of autoregression and joint regression,

respectively, and p is the lag in the autoregression model. $F_{x \rightarrow y}$ is the GCI value defined as the GC effect from ROI_X to ROI_Y so that each ROI pair has 2 GCI values representing the GC effects in 2 directions. The lag in the vector autoregression model was determined to be 2.⁵

For the distribution of the GCI, we randomly switched ROI signals among participants' preprocessed BOLD data and calculated the GCI values of each ROI pair. We repeated this procedure 100,000 times. This process generated a simulated GCI null distribution for real data sets.

MCM Analysis

Static FDG-PET images were preprocessed using FSL (including registration and normalization to 2-mm voxel standard space) with the same Montreal Neurological Institute template to ensure the accuracy of the cross-technique registration. Standard uptake value ratio maps were converted by dividing the mean value of the reference region. The cerebellum GM was chosen as the reference region.^{33,34} The normalized standard uptake value ratio maps and BOLD

data of each participant were used to calculate the MCM values.⁹ The MCM value of seed ROI X to target ROI Y was calculated according to Riedl et al⁹ as follows:

$$4) \quad MCM_{X \rightarrow Y} = \text{Correlation}(FC_{Y|X}, FDG_Y),$$

where FDG_Y is the voxelwise profile in ROI_Y , representing the neuronal activity in ROI_Y ; $FC_{Y|X}$ is the voxelwise FC in ROI_Y , while ROI_X is the seed ROI representing the correlation between each voxel time-series in ROI_Y and the cluster time-series of ROI_X . The spatial correlation between FDG and FC voxelwise profiles is the MCM value, which represents the metabolic EC from ROI_X (seed) to ROI_Y (target).

On the basis of a cellular model of neuroenergetics, a positive $MCM_{X \rightarrow Y}$ value identifies the signaling input along the FC pathway from ROI_X to ROI_Y .

Statistical Analysis

After the calculation of all the required values of the brain DA reward network connections, a 1-sample t test was used to acquire group-wise statistics including the t value and P value for FC and the MCM, separately. Because GC distribution was not normal, the nonparametric 1-sample Wilcoxon signed-rank test was used to determine group-wise significant connections. Also because of the skewed distribution of the GCI, if the GCI value of 1 directional connection was significantly higher than the median value of the GCI null distribution, this directional connection was considered

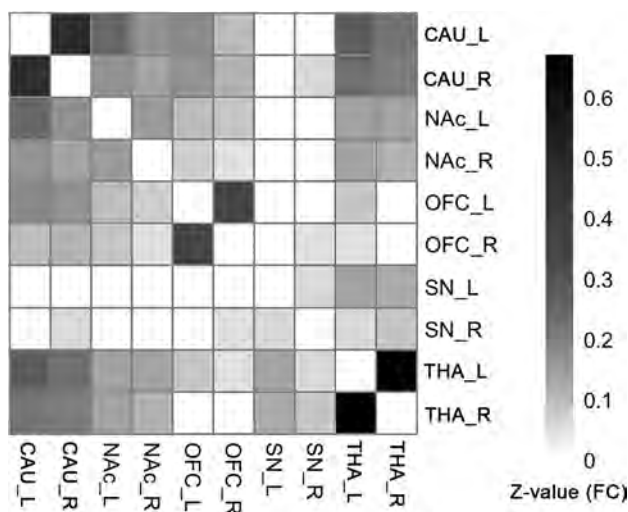


FIG 2. The group-level FC matrix shows that the bilateral CAU, NAc, OFC, and THA ROIs are significantly connected to each other. The SN is significantly connected to the THA. Color represents the z-transformed FC strength between ROI pairs. White means statistically not significant (1-sample *t* test, $P < .05$, FDR-corrected). Note that if a connection was not significant, its representing FC was set to zero, to focus on the significant connections.

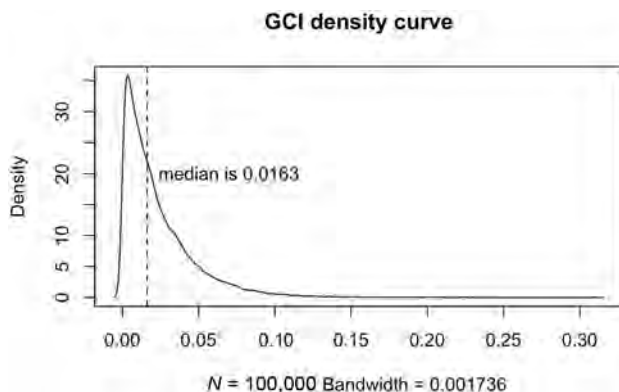


FIG 3. The GCI density curve. This curve comes from permutation-based technology to simulate the real-data GCI distribution with 100,000 times permutation. The distribution is a skewed curve, with 0.0163 as the median value, which is more appropriate than the mean value for the 1-sample test in this situation.

significant. The method to identify the group-wise significance of GC pathway was slightly different from FC and the MCM, which were considered following a normal distribution.

All the *P* values were corrected for multiple comparison using the false discovery rate (FDR) method to control the false-positive rate, and the significance level was set to corrected $P < .05$. The statistical analysis was performed using R software (Version 4.0.3; <https://www.r-project.org/>).

RESULTS

FC Analysis

FCs existed between most of the ROI pairs. The FC pathways connecting bilateral CAU, bilateral NAc, bilateral OFC, bilateral THA, and bilateral SN were significant for all ROIs. The FC pathways

between the left SN and bilateral CAU, bilateral NAc, bilateral OFC; the FC between the right SN and left CAU, bilateral NAc, left OFC; and between the right THA and bilateral OFC were not significant. All other FC pathways were significant except in the above-mentioned pathways (Fig 2, 1-sample *t* test, $P < .05$, FDR-corrected). The detailed statistical results of the 45 different FC pathways for the 10 ROIs can be found in the Online Supplemental Data.

GC Analysis

The distribution of the GCI after 100,000 simulations is shown in Fig 3. The GCI density curve was skewed with a median value at 0.0163. The μ parameter in the Wilcoxon signed-rank test thus was set to 0.0163. If the GCI was significantly higher than μ , the corresponding GC connection was considered significant.

After multiple comparison correction, significant GC connections were as follows: a bidirectional connection between the left NAc and the right OFC and 8 significant unidirectional connections, respectively, from the right THA to the left CAU, from the left CAU to the right CAU, from the left CAU to the left OFC, from the left NAc to the left CAU, from the right OFC to the left CAU, from the left OFC to the right CAU, from the right NAc to the left OFC, and from the left OFC to the right OFC (Fig 4, 1-sample Wilcoxon signed-rank test, $P < .05$, FDR-corrected). The detailed data can be found in the Online Supplemental Data.

MCM Analysis

The significant MCM connection of the significant group-wise FC pathways were as follows: 3 bidirectional connections, respectively, between the bilateral THA, between the left CAU and the left NAc, and between the right CAU and the right NAc, and 7 unidirectional connections, respectively, from the left SN to the right THA, from the right OFC to the right CAU, from the left OFC to the bilateral CAU, from the right NAc to the bilateral CAU, and from the left CAU to the right CAU (Fig 5, 1-sample *t* test, $P < .05$, FDR-corrected). The detailed data can be found in the Online Supplemental Data.

DISCUSSION

The GC and MCM methods were used to show differences in identifying directional connectivities of the DA brain reward system based on the Monash rsPET-MR data set. Our findings demonstrated that in the DA reward system, GC identified more cortico-nucleus bidirected connections and the MCM identified more directed connections among neighboring and symmetric regions. Each of the 2 methods has its own features, and researchers should carefully choose them before starting an analysis.

Both the GC and MCM identified modulation pathways in DA systems, but with different patterns. There are 3 major circuits in the DA reward system in the human brain: the basal ganglia (BG)-thalamocortical loop, the BG-thalamic loop, and the BG-habenulo-mesencephalic loop.^{18,31,35}

GC revealed that the THA→CAU pathway belonged to the BG-thalamic loop and the OFC→NAc and CAU pathways belonged to the BG-thalamocortical loop. MCM revealed that the SN-to-THA pathway belonged to the BG-thalamic loop and the OFC→CAU pathways and the rich connections between CAU and NAc belonged to the BG-thalamocortical loop. These results

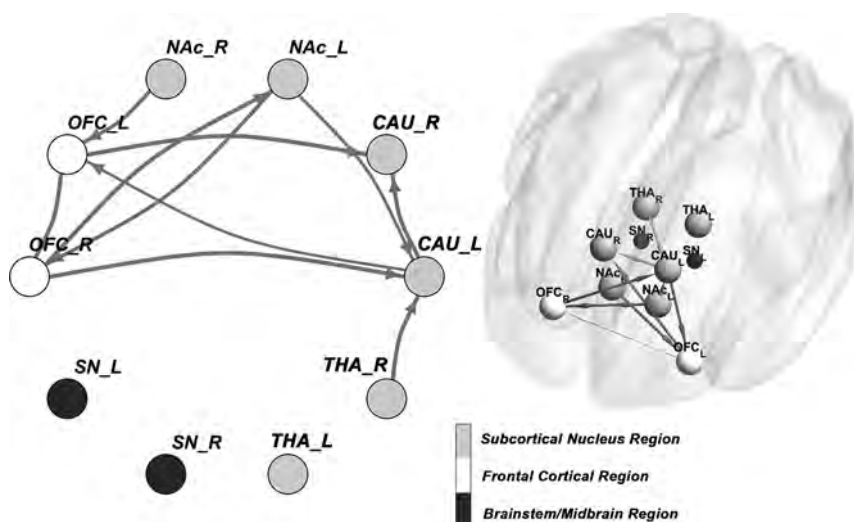


FIG 4. The group-wise directional network identified by GC. Arrows represent the direction of the pathways. The line thickness represents the relative strength of the GCI of that pathway. A bidirectional connection was identified between the right OFC and the left NAc (1-sample Wilcoxon signed-rank test, $P < .05$, FDR-corrected). L/R indicates left/right.

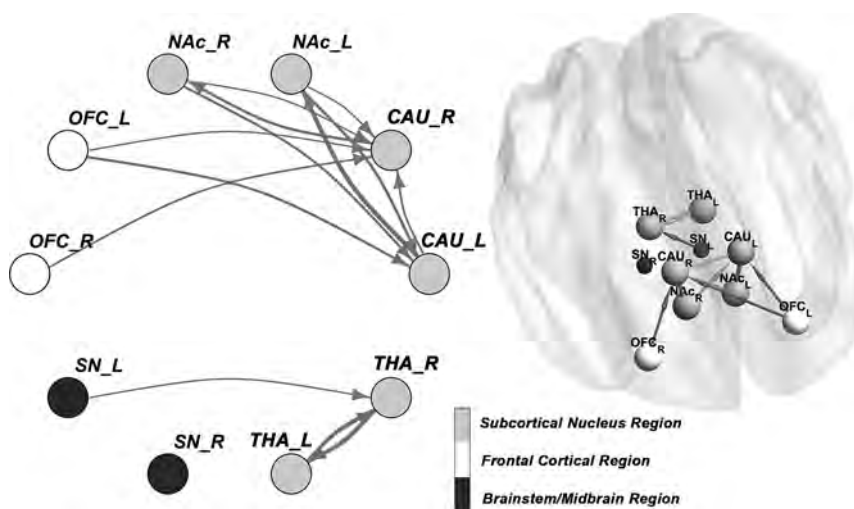


FIG 5. The group-wise directional pathways identified by the MCM method. Arrows represent the direction of the pathways. The line thickness represents the relative strength of the MCM. There are more bidirectional interactions between the NAc and CAU, and the unidirectional pathway from the OFC to the CAU reveals the regulation in the frontostriatal DA pathway (1-sample t test, $P < .05$, FDR-corrected). L/R indicates left/right.

are consistent with results from prior studies.^{18,31} The GC and MCM analytic approaches demonstrated the reliability of the 2 methods in revealing DA reward pathways. Neither GC or MCM analyses revealed the SN→limbic striatum pathway, implying that the sensitivities of the methods need to be improved. There were striatum→cortical pathways found by GC but not MCM, possibly caused by our omission of the existence of the THA mediation effect in our analysis.¹ This result indicates that in the absence of a proper model, the GC analysis does not always identify specific pathways, while the MCM is not influenced.

GC analysis identified long-range connections (cortico-nucleus). The bidirectional connections between the striatum and the OFC

were identified by GC, consistent with the mesocortical pathway in the reward circuits.³⁵ The MCM did well in identifying directed connections among neighboring brain areas (nucleus-nucleus) and among symmetric brain areas. These connections imply frequent communications between the dorsal and ventral striatum and the close communications between the bilateral subcortical brain areas in the resting-state brain.

The possible reason for the differences between GC and MCM may come from the different approaches of the 2 methods. The algorithm of the GC is based on a future temporal predictability from a knowledge of past activity.³⁶ GC analytic results should be interpreted as predictions between time-series.² If time-series X and Z have a high positive correlation, a high FC would result in a lower GC between X and Z because GC includes lags in its predictions between time-series and not correlations. For example, if X and Z are the same, there is no GC effect at all. In our results, the FC between the bilateral THA received the highest value, but there was no significant GC pathway between the bilateral THA. However, a high FC effect does not affect the ability of the MCM to identify this pathway because the algorithm of the MCM uses a voxelwise spatial pattern similarity between FDG and FC to generate the ROI-wise causality effect.^{3,9} The neighboring and symmetric brain regions often have higher FCs than long-distance brain regions. This inference is suggested by both observed phenomenologic and algorithmic differences.

Both the GC and MCM methods reported poor results for the subcortical areas. The MCM identified the important projections from the SN to the THA and the interaction pathways between the bilateral THA. Our results showed that the SN and THA were isolated from the cortical areas and the striatum. However, it is known that the SN and THA have interactions with cortical areas and the striatum. The failure of the approaches to identify these interactions may be due to several factors: First, GC analysis does not work well in the midbrain/brainstem areas due to signal loss and image distortion of BOLD signals.³⁷ GC analysis relies heavily on BOLD signal quality. High-resolution PET provided more benefit to MCM than GC. Second, the accuracy of the SN ROI template is limited because the SN is located in the midbrain and is more likely to have poor

registration results than the cortex area using regular normalization procedures.³⁷ Third, the correction method might be too stringent in 1-sample statistics compared with other studies that focused only on group differences in EC. For example, most of our GC studies calculated the between-group GC differences rather than within-group patterns, so we could test whether the group differences were significantly not equal to zero. When we focused on within-group patterns of GC, we had to choose a more stringent value to test. This strategy may have caused fewer identified results. The MCM, on the other hand, was less affected than GC when performing within-group analyses, resulting in a greater number of identified subcortical areas than were identified by GC.

Considering the above methodological issues, MCM generally outperforms than GC in revealing reasonable directed connection in subcortical nucleus and cerebellum network. Thus, it is recommended that when the study aim at diseases involves mostly the subcortical areas (e.g. cerebellum and subcortical nucleus), both FDG-PET and simultaneous BOLD data should be acquired and do MCM analysis.

This study has some limitations. First, the DA reward circuits involved ROIs that were arbitrarily selected and may have provided less comprehensive results. Second, the Monash rs-PET/MR data set acquired fMRI data using a TR = 2.45-second parameter, which may have limited the ability to identify DA pathways for GC. Third, the scan protocol of the Riedl et al⁹ study acquired 10-minute BOLD sequences immediately following the FDG injection, while the PET data used in our MCM analysis was collected 30 minutes after the FDG injection. In our study, the PET data represented the cumulated regional energy demands before the fMRI acquisition window, while the fMRI data reflected the neuronal dynamics during the acquisition phase. We assumed that the resting-state brain would have similar activities across sessions and that the FC would not change substantially, ensuring MCM stability. The stability of the MCM during the resting state in different sessions was not clear. Fourth, possible improvements to the original GC method,^{1,6,38} which may be more reliable, were not included in this study. Last, the present study comprised a small number of healthy participants ($n = 27$) only and was performed in a unique center; further studies could confirm the results with a larger sample size from multiple centers and validate the features in this study using patient data.

CONCLUSIONS

Our results showed that GC and MCM revealed different patterns in directional networks in the DA reward circuit. Our study demonstrated that both GC and the MCM could correctly identify some of the directed pathways among the DA reward circuits. GC identified long-range bidirectional connections, and the MCM identified directed connections among neighboring and symmetric regions. Poor connections in subcortical areas were identified by both methods, but MCM benefited from compensation of the high-resolution PET data. These results imply that future research on ECs requires an appropriate selection of methods according to the different objectives of the research.

ACKNOWLEDGMENT

The authors are grateful to S.D. Jamadar for sharing the OpenNeuro data set and to professor Riedl Valentin's enthusiastic help with MCM methodology.

Disclosure forms provided by the authors are available with the full text and PDF of this article at www.ajnr.org.

REFERENCES

1. Wang X, Wang R, Li F, et al. **Large-scale Granger causal brain network based on resting-state fMRI data.** *Neuroscience* 2020;425:169–80 CrossRef Medline
2. Cekic S, Grandjean D, Renaud O. **Time, frequency, and time-varying Granger-causality measures in neuroscience.** *Stat Med* 2018;37:1910–31 CrossRef Medline
3. Scherr M, Utz L, Tahmasian M, et al. **Effective connectivity in the default mode network is distinctively disrupted in Alzheimer's disease: a simultaneous resting-state FDG-PET/fMRI study.** *Hum Brain Mapp* 2021;42:4134–43 CrossRef Medline
4. Gao J, Zhang D, Wang L, et al. **Altered effective connectivity in schizophrenic patients with auditory verbal hallucinations: a resting-state fMRI study with Granger causality analysis.** *Front Psychiatry* 2020;11:575 CrossRef Medline
5. Zhang Y, Li Q, Wen X, et al. **Granger causality reveals a dominant role of memory circuit in chronic opioid dependence.** *Addict Biol* 2017;22:1068–80 CrossRef Medline
6. Seth AK, Barrett AB, Barnett L. **Granger causality analysis in neuroscience and neuroimaging.** *J Neurosci* 2015;35:3293–97 CrossRef Medline
7. Huang X, Zhang D, Wang P, et al. **Altered amygdala effective connectivity in migraine without aura: evidence from resting-state fMRI with Granger causality analysis.** *J Headache Pain* 2021;22:25 CrossRef Medline
8. Li H, Hu X, Gao Y, et al. **Neural primacy of the dorsolateral prefrontal cortex in patients with obsessive-compulsive disorder.** *Neuroimage Clin* 2020;28:102432 CrossRef Medline
9. Riedl V, Utz L, Castrillón G, et al. **Metabolic connectivity mapping reveals effective connectivity in the resting human brain.** *Proc Natl Acad Sci U S A* 2016;113:428–33 CrossRef Medline
10. Attwell D, Laughlin SB. **An energy budget for signaling in the grey matter of the brain.** *J Cereb Blood Flow Metab* 2001;21:1133–45 CrossRef Medline
11. Attwell D, Iadecola C. **The neural basis of functional brain imaging signals.** *Trends Neurosci* 2002;25:621–25 CrossRef Medline
12. Harris JJ, Jolivet R, Attwell D. **Synaptic energy use and supply.** *Neuron* 2012;75:762–77 CrossRef Medline
13. Vergara RC, Jaramillo-Riveri S, Luarte A, et al. **The energy homeostasis principle: neuronal energy regulation drives local network dynamics generating behavior.** *Front Comput Neurosci* 2019;13:49 CrossRef Medline
14. Hahn A, Breakspear M, Rischka L, et al. **Reconfiguration of functional brain networks and metabolic cost converge during task performance.** *ELife* 2020;9:e52443 CrossRef
15. Di X, Biswal BB, Alzheimer's Disease Neuroimaging Initiative. **Metabolic brain covariant networks as revealed by FDG-PET with reference to resting-state fMRI networks.** *Brain Connect* 2012;2:275–83 CrossRef Medline
16. Sala A, Caminiti SP, Presotto L, et al. **Altered brain metabolic connectivity at multiscale level in early Parkinson's disease.** *Sci Rep* 2017;7:4256 CrossRef Medline
17. Arias-Carrión O, Stamelou M, Murillo-Rodríguez E, et al. **Dopaminergic reward system: a short integrative review.** *Int Arch Med* 2010;3:24–26 CrossRef Medline

18. Ikemoto S, Yang C, Tan A. **Basal ganglia circuit loops, dopamine and motivation: a review and enquiry.** *Behav Brain Res* 2015;290:17–31 CrossRef Medline
19. Calabresi P, Picconi B, Tozzi A, et al. **Direct and indirect pathways of basal ganglia: a critical reappraisal.** *Nat Neurosci* 2014;17:1022–30 CrossRef Medline
20. Haber SN. **Corticostriatal circuitry.** *Dialogues Clin Neurosci* 2016;18:7–21 CrossRef Medline
21. Frank GK, DeGuzman MC, Shott ME, et al. **Association of brain reward learning response with harm avoidance, weight gain, and hypothalamic effective connectivity in adolescent anorexia nervosa.** *JAMA Psychiatry* 2018;75:1071–80 CrossRef Medline
22. Jamadar SD, Ward PG, Close TG, et al. **Simultaneous BOLD-fMRI and constant infusion FDG-PET data of the resting human brain.** *Sci Data* 2020;7:363 CrossRef Medline
23. Jamadar SD, Ward PG, Carey A, et al. **Radiotracer administration for high temporal resolution positron emission tomography of the human brain: application to FDG-fPET.** *J Vis Exp* 2019;22:(152) CrossRef Medline
24. Jamadar SD, Ward PG, Liang EX, et al. **Metabolic and hemodynamic resting-state connectivity of the human brain: a high-temporal resolution simultaneous BOLD-fMRI and FDG-fPET multimodality study.** *Cerebral Cortex* 2021;31:2855–67 CrossRef Medline
25. Jamadar SD, Ward PG, Li S, et al. **Simultaneous task-based BOLD-fMRI and [18-F] FDG functional PET for measurement of neuronal metabolism in the human visual cortex.** *Neuroimage* 2019;189:258–66 CrossRef Medline
26. Whitfield-Gabrieli S, Nieto-Castanon A. **Conn: a functional connectivity toolbox for correlated and anticorrelated brain networks.** *Brain Connect* 2012;2:125–41 CrossRef Medline
27. Behzadi Y, Restom K, Liao J, et al. **A component-based noise correction method (CompCor) for BOLD and perfusion based fMRI.** *Neuroimage* 2007;37:90–101 CrossRef Medline
28. Power JD, Mitra A, Laumann TO, et al. **Methods to detect, characterize, and remove motion artifact in resting state fMRI.** *Neuroimage* 2014;84:320–41 CrossRef Medline
29. Hallquist MN, Hwang K, Luna B. **The nuisance of nuisance regression: spectral misspecification in a common approach to resting-state fMRI preprocessing reintroduces noise and obscures functional connectivity.** *Neuroimage* 2013;82:208–25 CrossRef Medline
30. Jenkinson M, Beckmann CF, Behrens TE, et al. **FSL.** *Neuroimage* 2012;62:782–90 CrossRef Medline
31. Ikemoto S. **Brain reward circuitry beyond the mesolimbic dopamine system: a neurobiological theory.** *Neurosci Biobehav Rev* 2010;35:129–50 CrossRef Medline
32. Volkow ND, Wise RA, Baler R. **The dopamine motive system: implications for drug and food addiction.** *Nat Rev Neurosci* 2017;18:741–52 CrossRef Medline
33. Shin J, Tsui W, Li Y, et al. **Resting-state glucose metabolism level is associated with the regional pattern of amyloid pathology in Alzheimer's disease.** *Int J Alzheimers Dis* 2011;2011:759780 CrossRef Medline
34. Wang J, Shan Y, Dai J, et al. **Altered coupling between resting-state glucose metabolism and functional activity in epilepsy.** *Ann Clin Transl Neurol* 2020;7:1831–42 CrossRef Medline
35. Volkow ND, Michaelides M, Baler R. **The neuroscience of drug reward and addiction.** *Physiol Rev* 2019;99:2115–40 CrossRef Medline
36. Chen H, Uddin LQ, Zhang Y, et al. **Atypical effective connectivity of thalamo-cortical circuits in autism spectrum disorder: impaired thalamo-cortical connectivity in ASD.** *Autism Res* 2016;9:1183–90 CrossRef Medline
37. de la Cruz F, Wagner G, Schumann A, et al. **Interrelations between dopamine and serotonin producing sites and regions of the default mode network.** *Hum Brain Mapp* 2021;42:811–23 CrossRef Medline
38. Luo Q, Lu W, Cheng W, et al. **Spatio-temporal Granger causality: a new framework.** *Neuroimage* 2013;79:241–63 CrossRef Medline

Effects of COVID-19 on the Human Central Olfactory System: A Natural Pre-Post Experiment

 E. Thunell,  M.G. Peter,  V. Lenoir,  P. Andersson,  B.N. Landis,  M. Becker, and  J.N. Lundström



ABSTRACT

BACKGROUND AND PURPOSE: Reduced olfactory function is the symptom with the highest prevalence in coronavirus disease 2019 (COVID-19) with nearly 70% of infected individuals experiencing partial or total loss of their sense of smell at some point during the disease. The exact cause is not known, but beyond peripheral damage, studies have demonstrated insults to both the olfactory bulb and central olfactory brain areas. However, these studies often lack both baseline pre-COVID-19 assessments and control groups, and the effects could, therefore, simply reflect pre-existing risk factors.

MATERIALS AND METHODS: Shortly before the COVID-19 outbreak, we completed an olfactory-focused study, which included structural MR brain images and a full clinical olfactory test. Opportunistically, we invited participants back 1 year later, including 9 participants who had experienced mild-to-moderate COVID-19 (C19+) and 12 who had not (C19−), creating a natural pre-post experiment with a control group.

RESULTS: Despite C19+ participants reporting subjective olfactory dysfunction, few showed signs of objectively altered function. Critically, all except 1 individual in the C19+ group had reduced olfactory bulb volume (average reduction, 14.3%), but this did not amount to a significant statistical difference compared with the control group (2.3%) using inference statistics. We found no morphologic differences in olfactory brain areas but stronger functional connectivity between olfactory brain areas in the C19+ group at the postmeasure.

CONCLUSIONS: Our data suggest that COVID-19 might cause long-term reduction in olfactory bulb volume and altered functional connectivity but with no discernible morphologic differences in cerebral olfactory regions.

ABBREVIATIONS: C19+ = positive for COVID-19; C19− = negative for COVID-19; COVID-19 = coronavirus disease 2019; OB = olfactory bulb; SARS-CoV-2 = Severe Acute Respiratory Syndrome coronavirus 2

Olfactory dysfunction is a key symptom of coronavirus disease 2019 (COVID-19).¹ The reported prevalence of complete olfactory loss (anosmia) is about 50%, with an additional 10%–20% reporting less severe olfactory dysfunction at some

point during the disease.^{2,3} Thus, a reported reduced sense of smell is the symptom with the highest odds ratio in nonhospitalized cases.^{4,5} Despite the clear clinical link between olfactory dysfunction and COVID-19, our understanding of the mediating mechanisms is limited.


Much like the Severe Acute Respiratory Syndrome coronavirus 1 and influenza viruses,⁶ Severe Acute Respiratory Syndrome coronavirus 2 (SARS-CoV-2) can invade the central nervous system through the olfactory mucosa via a retrograde route.⁷ SARS-CoV-2 nucleoproteins and associated inflammation have been detected in infected animal models along the entire olfactory route from the olfactory sensory neurons to the olfactory bulb (OB).⁷ In humans, there is indirect and mixed evidence of SARS-CoV-2 as a neurotropic virus. Studies have demonstrated postmortem brain pathologies after COVID-19 but without clear evidence of SARS-CoV-2 RNA presence.⁸ There is further conflicting or weak evidence of neuroinvasion within the olfactory system in humans with a dominance of case studies or assessment of severe cases. A postmortem

Received May 14, 2022; accepted after revision October 11.

From the Department of Clinical Neuroscience (E.T., M.G.P., J.N.L.), Karolinska Institutet, Stockholm, Sweden; Diagnostic Department (V.L., M.B.), Division of Radiology, and Department of Otorhinolaryngology (B.N.L.), Rhinology-Olfactology Unit, Geneva University Hospital, Geneva, Switzerland; Stockholm University Brain Imaging Center (P.A., J.N.L.), Stockholm University, Stockholm, Sweden; and Monell Chemical Senses Center (J.N.L.), Philadelphia, Pennsylvania.

Funding was provided by grants awarded to J.N. Lundström from the Knut and Alice Wallenberg Foundation (KAW 2018.0152), the Swedish Research Council (2021-06527), and a donation from Stiftelsen Bygg-Göta för Vetenskaplig forskning. Data acquisition was supported by a grant to the Stockholm University Brain Imaging Center (SU FV-5.1.2-1035-15).

Please address correspondence to Johan Lundström, PhD, Department of Clinical Neuroscience, Karolinska Institutet, Nobels väg 9, 17177 Stockholm, Sweden; e-mail: johan.lundstrom@ki.se; @Odorjohan

 Indicates open access to non-subscribers at www.ajnr.org

<http://dx.doi.org/10.3174/ajnr.A7713>

case study found low levels of virus RNA in the OB,⁹ and several neuroimaging studies have demonstrated anosmia-related edemas and abnormalities evident on CT or MR images of the OB post-COVID-19 infection.^{10–14} On the other hand, the absence of a significant difference in OB volume between a COVID-19–related anosmia group and a general postviral anosmia group has been reported,¹⁵ and a postmortem tissue examination from patients with severe COVID-19 indeed found virus in the olfactory nerve but only in the leptomeninges layer of the OB,¹⁶ leaving no consensus as to whether COVID-19 is a neurotropic virus.

Full psychometric assessment of olfactory function and measures of morphology of the central olfactory system are needed to understand the central mechanisms of COVID-19-related olfactory dysfunction in humans, preferably from the same individual both before and after infection and with the inclusion of a relevant control group for comparison. Nevertheless, inducing COVID-19 for experiments is ethically questionable. However, in the months leading up to the first COVID-19 outbreak in Stockholm (late 2019 to early 2020), we acquired full-scale psychometric olfactory assessments and structural MR images from a group of healthy individuals as a control group in a study assessing the neural effects of olfactory dysfunction. One year into the pandemic and before the general vaccination program was initiated in Sweden, we recruited participants who had COVID-19 since the first study and participants who had not. In this natural experiment with pre- and postmeasures in both COVID-19-affected individuals and a comparable control group, we aimed to determine whether COVID-19 alters olfactory function and the morphology of cerebral areas associated with olfactory processing: the olfactory bulb, anterior and posterior piriform cortex, and central areas of the orbitofrontal cortex. Second, we aimed to assess potential links between morphologic changes and changes in olfactory functions due to COVID-19. In addition, we measured functional connectivity between olfactory areas in both groups in the poststudy. Critically, we preregistered our hypotheses and analyses before assessing the data. A previous version of this article exists as a preprint.¹⁷ Results and main conclusions are similar between this and the preprint versions, but textual differences exist.

MATERIALS AND METHODS

All methods and analyses are according to our preregistration (<https://aspredicted.org/wr4d9.pdf>) unless otherwise explicitly stated.

Participants

All participants were recruited from a previous study, referred to here as the “prestudy” ($n = 52$) that took place September 2019 to February 2020. A total of 40 individuals (77%) responded to our request to participate in the poststudy, of which we classified 9 (6 women) as having been infected with COVID-19 (C19+) with mild-to-moderate symptoms. Eight of these reported having tested positive for either ongoing infection ($n = 4$) and/or antibodies ($n = 5$), and 1 reported being diagnosed by a medical doctor without being tested (this happened before testing without hospital admittance was available in Sweden). We also recruited 12 control participants (5 women) classified as not having contracted COVID-19 (C19–) on the basis of the absence of symptoms during the pandemic as well as antibody tests negative for

COVID-19 ($n = 10$). One individual in the negative for COVID-19 (C19–) group tested positive for ongoing infection a few weeks after the poststudy. Once recovered, she participated in the poststudy once more; this time as a C19+ participant, thereby contributing to both the C19– and C19+ groups. The C19+ participants were, on average, 38 (SD, 8) years of age (range 30–51 years), and the C19– participants were, on average, 33 (SD, 7) years of age (range, 26–49 years) at the prestudy. The poststudy took place between 3 weeks and 12 months after infection for the C19+ group (mean, 7 [SD, 4] months). In the prestudy, all participants reported having normal or corrected-to-normal vision, hearing, and olfactory function.

All procedures were approved by the Swedish Ethical Review Authority, and all participants provided written informed consent before participating in both the pre- and the poststudy.

Psychometric Odor Assessment

Individual olfactory performance was assessed after the MR imaging data acquisition in both the pre- and poststudy. We measured the odor-detection threshold, olfactory quality discrimination, and cued olfactory identification (sum score, threshold-discrimination-identification) using the validated Sniffin’ Sticks smell tests (Burghart).

Neuroimaging Acquisition and Processing

MR Imaging Data Acquisition. For both sessions, the same 3T Magnetom Prisma MR imaging (Siemens) scanner with a 20-channel head coil was used. We acquired structural images in both studies using identical protocols with a 3D MPRAGE T1-weighted sequence (208 slices, TR = 2300 ms, TE = 2.89 ms, flip angle = 9°, voxel size = $1 \times 1 \times 1$ mm, FOV = 256×256 voxels). To assess potential effects of COVID-19 on olfactory functional connectivity, the poststudy included a 12-minute functional resting-state scan using an echo-planar imaging sequence (56 slices, TR = 1700 ms, TE = 30 ms, flip angle = 70°, voxel size = $2.2 \times 2.2 \times 2.2$ mm, FOV = 94×94 voxels). For 1 participant in the C19+ group, all neuroimaging data were excluded from analysis due to excessive motion artifacts, making delineation of the olfactory bulbs problematic.

Volumetric Measures. OB volume was assessed manually for each structural image and hemisphere (Fig 1). Data from both sessions for each participant were assigned to 1 of 2 experienced neuroradiologist raters (coauthors V.L. and M.B.) who were naïve to whether participants belonged to the C19+ or C19– groups. For the full cerebral cortex, voxel-based morphometry analysis was performed using the longitudinal pipeline in the Computational Anatomy Toolbox, Version 12.8 for SPM12 (<http://www.fil.ion.ucl.ac.uk/spm/software/spm12>). Our preregistered analysis plan was based on a cross-sectional publication,¹⁸ whereas the current study has a longitudinal nature. Consequently, we used the longitudinal pipeline in the CAT12 toolbox,¹⁹ which entails additional intrasubject processing steps and the use of Geodesic Shooting²⁰ instead of the Diffeomorphic Anatomical Registration Through Exponentiated Lie Algebra Toolbox (DARTEL, part of SPM) for spatial registration.

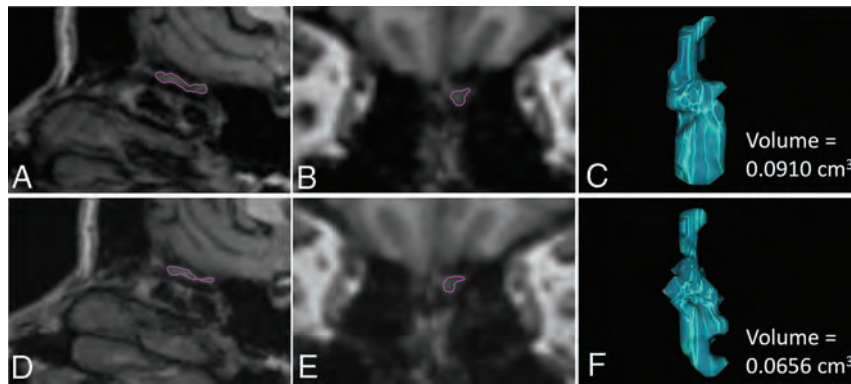


FIG 1. Illustration of the volumetric measurements of the left OB in a C19+ participant, in whom a decrease in OB volumes was observed 11 months after infection compared with the premeasure. The *upper panel* shows sagittal (A) and coronal (B) reconstructions of the high-resolution 3D T1WI sequence from the premeasure MR imaging with the left OB delineated in purple and the resulting computed OB volume (C). The corresponding data are shown for the postmeasure in the *lower panel* (D–F).

Connectivity Measures. Data preprocessing and denoising of functional images was performed using SPM12 and the CONN functional connectivity toolbox, Version 20.b (<https://web.conn-toolbox.org/resources/documentation>) following the steps outlined in Peter et al.²¹ No group differences in motion were demonstrated on the basis of Welch *t* tests of mean framewise displacement (C19+: 0.2 mm; C19–: 0.18 mm; $t(16.4) = 1.25$, $P = .31$) or the number of volumes with a framewise displacement >0.5 mm (C19+: 6.1; C19–: 4.9; $t(13.7) = 0.39$, $P = .7$).

Creation of ROIs. Three ROIs were included to assess potential COVID-19-related alterations in cortical structure and functional connectivity in areas associated with olfactory processing: the anterior piriform cortex, posterior piriform cortex, and orbitofrontal cortex, all based on a published olfactory activation likelihood analysis²² and restricted to core processing areas.²³ Auditory and visual ROIs corresponding to the functions of the olfactory ROIs were included as control regions for the functional connectivity analysis: the primary auditory cortex, higher order auditory cortex, primary visual cortex, and the lateral occipital complex; all defined in Porada et al.²³

Statistical Analyses

Change scores were calculated as (post) – (pre) for each individual for the measures that were acquired in both sessions.

Olfactory Function. The hypothesis of reduced olfactory function (more negative change score) in the C19+ group compared with the C19–group was assessed with a 1-sided Welch *t* test, $\alpha = .05$, for all tests unless otherwise stated, on the olfactory threshold-discrimination-identification change scores.

Volumetric Measures. We computed the average OB volume across the left and right hemispheres. Our hypothesis of reduced OB volume in the C19+ compared with the C19– group was assessed using a 1-sided Welch *t* test on the change scores. In addition, we performed a nonpreregistered binomial test to assess

whether the number of participants with an increased or decreased OB volume differed between groups. In this test, each participant was classified as having an either increased or decreased OB volume (positive or negative change score, respectively), and the number of participants in each category in each group was then compared with the expected null distribution.

GM volume in the preregistered olfactory ROIs (anterior piriform cortex and posterior piriform cortex) as well as in an additional olfactory ROI (orbitofrontal cortex) was extracted and then averaged over the hemispheres. Our hypothesis of reduced GM volume in the C19+ group compared with the C19– group was tested using 1-sided Welch *t* tests on the change scores. We also per-

formed an exploratory whole-brain-group comparison of voxelwise tests of the interaction between the factors group (C19+/C19–) and time (pre/post), with a threshold of $P < .001$ and a minimum cluster size of 10 voxels.

Connectivity Measures. Blood oxygen level–dependent time-series were extracted from all ROIs, and functional connectivity between the regions was calculated on the basis of a pair-wise Pearson correlation within the 3 sensory systems separately. The correlation values were Fisher *z*-transformed for statistical comparisons between the 2 groups, performed using 2-sided Welch *t* tests.

Data Availability

Data not provided in the article because of space limitations may be shared (anonymized) at the request of any qualified investigator for purposes of replicating procedures and results.

RESULTS

We first assessed the objective change in olfactory function due to COVID-19 by comparing the change in threshold and threshold-discrimination-identification scores of the C19+ and C19– groups. We hypothesized that the C19+ group would demonstrate a larger reduction in olfactory performance than the control group. However, there was no significant difference between the groups in either threshold ($t(12.1) = 0.97$, $P = .82$) or threshold-discrimination-identification ($t(9.4) = 0.60$, $P = .72$; 1-sided Welch's *t* tests). Contrary to this lack of an apparent objective difference between the C19+ and C19– groups in olfactory function, 4 of the 9 participants in the C19+ group did experience subjective olfactory dysfunction at the time of the poststudy, including 1 case of parosmia and 1 case of potential phantosmia (Table). The self-estimated overall olfactory function, compared with the function around the time of the prestudy, ranged from 50% to 100% (mean, 87.5%, SD, 17.9%) in the C19+ group, whereas for the C19– group, 100% of participants rated themselves as experiencing no difference in olfactory performance.

Self-reported acute and persisting chemosensory-related symptoms for all C19+ participants and demographic information. Rows indicate participants

Age at Poststudy (yr)	Sex	Months since Infection at Poststudy	Acute Symptoms	Remaining Symptoms	Estimated Sense of Smell Compared with Premeasure (%)
31	Female	10	Anosmia, ageusia	—	100
35	Female	3	Anosmia	—	100
39	Male	7.5	—	—	100
51	Female	12	Anosmia, ageusia	Weaker sense of smell. Some things smell stronger; some weaker (eg, coffee); some completely different (eg, sweat smells like raw onion), more bitterness	70
50	Female	9.5	Numbness in the mouth	—	100
32	Male	3	Anosmia, ageusia	Worsened sense of smell and taste, especially tip of the tongue	80
46	Female	0.75	Anosmia	Poor taste and constant stale taste. Selective anosmia (eg, coffee, shampoo, wine, 3 test odors)	50
30	Male	3	Anosmia	Slightly affected sense of smell	87.5
32	Female	11	—	—	100

Note:— indicates none.

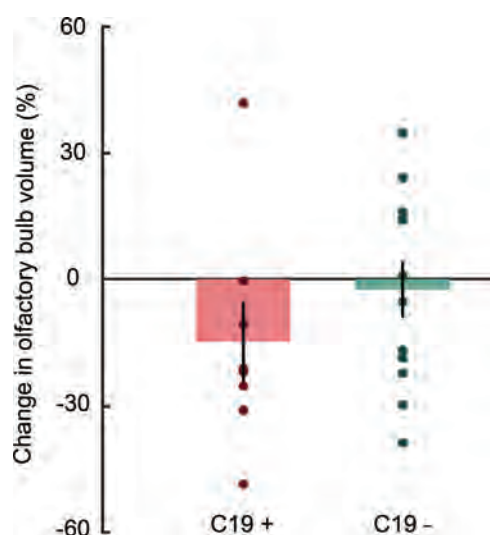


FIG 2. Mean (bars) and individual (dots) OB volume change from the pre- to the poststudy for the C19+ and C19- groups. Error bars denote ± 1 standard error of the mean.

Next, we determined whether COVID-19 might lead to a long-term reduction in OB volume. On average, the OB volume in the C19+ group was reduced by 14.6% (SD, 26.8%) in the post-COVID measure compared with the pre-COVID measure. In the C19- group, the corresponding number was a 2.3% (SD, 23.2%) volume reduction (Fig 2). Our preregistered 1-sided Welch *t* test on the change scores showed that this difference between groups was nonsignificant according to our α criterion, $t(15.2) = 1.3$, $P = .1$, Hedges' $g = .58$. However, in the C19+ group, 87.5% of participants (7 of 8) demonstrated a reduction in OB volume (mean for these participants, 22.7% [SD, 15.2%]). When assessing the likelihood that the observed reduction in OB volume in the C19+ occurred due to chance (binomial test), we

found that the probability that ≥ 7 C19+ participants would demonstrate a reduction was $P = .035$, $z = 1.76$.

Although we did not systematically interview participants about parosmia and phantosmia symptoms nor did we test them for such, we made an inventory of their spontaneous reports of acute remaining symptoms, which were both of a chemosensory and general nature. The details of the self-reported acute and remaining chemosensory symptoms and demographics for each participant are shown in the Table. The participant who contributed to both the C19- and C19+ groups had a relatively unchanged OB volume when participating in the C19- group (0.8% increase) but showed a 31% volume reduction shortly after COVID-19 infection. Her persistent olfactory problems included a constant strange stale taste in the mouth, a potential sign of phantosmia, as well as selective anosmia for 3 of the sample odors in the discrimination task; something that she did not recall experiencing at the premeasure. She also reported experiencing selective anosmia in her everyday life. The C19+ participant who showed an increase in OB volume (outlier in Fig 2) also reported persistent chemosensory problems, including signs of parosmia. These were the only 2 participants who reported signs of parosmia or phantosmia. One participant reported sensing more bitterness, and another reported poor taste, especially on the tip of the tongue, both of which might be signs of actual gustation problems.

Next, we assessed whether COVID-19 leads to loss of GM volume in central olfactory areas by determining whether the GM volume change score was different in the C19+ group compared with the C19- group. We did not find any statistically significant differences in the 3 ROIs (all, $P_s > .27$; Fig 3). Finally, in an exploratory analysis, we assessed whether there were signs of volumetric changes to any nonhypothesized brain areas by performing a whole-brain contrast between C19+ and C19- groups. No voxels survived the set statistical threshold.

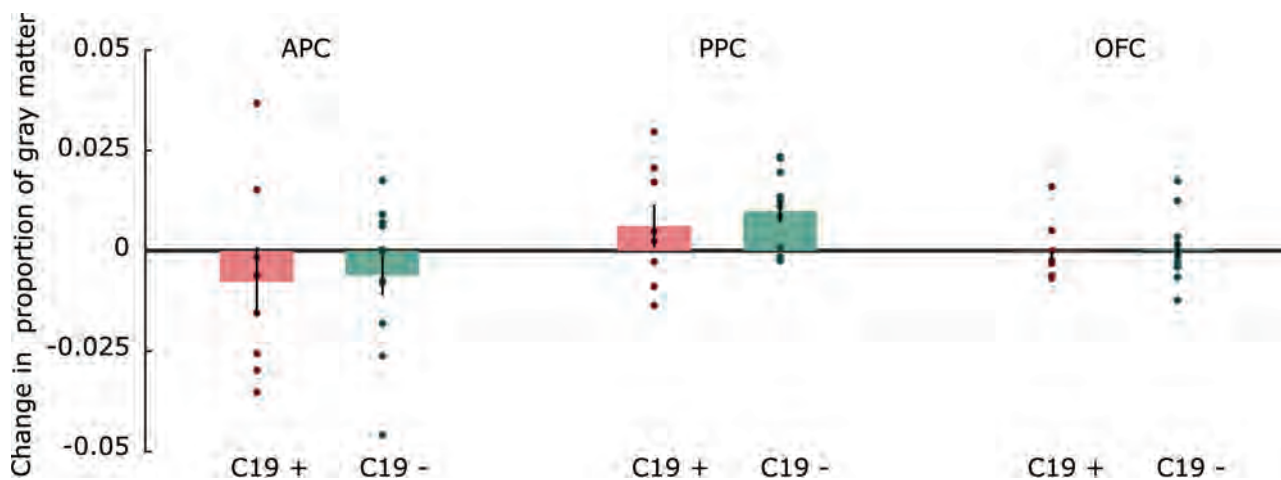


FIG 3. Mean (bars) and individual (dots) pre- to postchange scores for GM volume within the C19+ and C19- groups, separately for each ROI. Error bars denote ± 1 standard error of the mean. APC indicates anterior piriform cortex; PPC, posterior piriform cortex; OFC, orbitofrontal cortex.

Finally, we assessed whether COVID-19 could be linked to alterations in resting-state functional connectivity between core olfactory regions. The C19+ group demonstrated an increase in functional connectivity between the orbitofrontal cortex and the anterior piriform cortex, $t(14.6) = 3.92$, $P < .005$, Hedges' $g = 1.73$, as well as the orbitofrontal cortex and the posterior piriform cortex, $t(12.1) = 3.07$, $P < .01$, Hedges' $g = 1.42$ compared with the C19- group. However, we found no significant group differences between the closely located anterior and posterior piriform cortex, $t(13.6) = 0.15$, $P = .89$, Hedges' $g = .07$. Likewise, we found no significant group differences between auditory and visual control regions (all, P s $> .17$).

DISCUSSION

In the present study, we used a unique group of participants that allowed us to assess COVID-19-dependent effects on the morphology of the human OB and cerebral olfactory areas using a within-subject design with a comparable control group. In line with our preregistered hypothesis, we observed a consistent decrease of OB volume in 7 of 8 measured individuals within the C19+ group with an average of about a 14% decrease in volume at an average of 7 months after their infection by SARS-CoV-2. In the control group, 6 had an increase, and 6 had a decrease with time, with an average decrease of about 2% in OB volume. Although this was not a statistically significant difference between groups, according to the preregistered inference analyses, it is interesting to note that a binominal test indicates a medium effect size that is unlikely to occur due to chance, even when including the deviating participant with a large increase in OB volume. Thus, it can be speculated whether the lack of clear significant effects according to our preregistered analyses plan is mainly due to the small sample size, regulated by the unique and restricted population and the outlier participant.

Although multiple past studies have demonstrated that OB volume is modulated by changes in olfactory performance,²⁴ the mechanism allowing this plasticity is not known. Studies in animal models have demonstrated that neurogenesis can occur in

the OB,²⁵ but studies in human cadavers have not supported this phenomenon. A more straightforward mechanism that might explain the link between the fast changes in OB volume that olfactory training is known to induce is potential changes in the OB vascularization. Recent data suggest that nearly all individuals infected by SARS-CoV-2 experience endothelial cell death, which causes microvascular damage to tissue along the olfactory pathway.^{9,26} Given the flexibility of the OB vascularization and close link to the amount of olfactory input,²⁷ olfactory training might help alleviate OB morphologic loss due to COVID-19. However, we cannot dissociate between direct effects from SARS-CoV-2 and effects from a potential reduction in sensory input. Nevertheless, although several participants in the C19+ group reported subjective changes in olfactory functions, we did not find any statistically significant changes in objective olfactory performance.

We speculate that the participants' self-reported olfactory problems might be parosmia-related, which is not well captured by the threshold-discrimination-identification test. For example, the ability to identify and discriminate odors is not necessarily affected by a change in their perceived nature and valence. Many individuals with parosmia will readily identify an odor, for example coffee, but will report that they no longer appreciate the odor and that coffee now smells more like smoke. We did not specifically interview participants about parosmia symptoms nor test for such, but 1 participant spontaneously shared that some odors had changed character (eg, sweat smelling like raw onions). Another participant even reported a constant strange stale taste in the mouth, a potential sign of phantosmia or phantogeusia. Another possibility is that our C19+ participants had specific anosmia (not coinciding with the 16 identification test odors). For example, 1 C19+ participant was surprised that he or she did not detect some of the odors in the discrimination task and did not recall having experienced this in the prestudy. Because this selective anosmia occurred only for, at most, 1 odor in each set for this participant, it did not impede the participant from performing the task. In fact, the discrimination task may even become easier when one of the odors in a set is odorless to the participant because they will, for example, easily detect the odd one out as

being the only one that is odorless. Last, participants might have taste alterations that are easily confused with olfactory alterations, something that we did not assess in our study. One participant did report sensing more bitterness, and another reported poor taste, especially on the tip of the tongue, both of which might be signs of dysgeusia.

We found no evidence that a COVID-19 infection causes long-term insult to cerebral areas of the olfactory system, but we did demonstrate a significant increase of functional connectivity between the orbitofrontal cortex and both the anterior and posterior piriform cortex. These outcomes were not expected according to our hypothesis. However, absence of clear COVID-19-related morphologic changes to the piriform cortex, often referred to as the primary olfactory cortex, was also demonstrated in a recent study on the UK-biobank material in which pre- and post-COVID-19 infection data were included.²⁸ In contrast, the UK-Biobank study found COVID-19-related reduction in GM within the orbitofrontal cortex, whereas we found no differences. The 2 studies differed in sample size, scanning parameters, and location of our olfactory-related ROIs. Nonetheless, our lack of significant results supports the emerging consensus that COVID-19 does not cause long-term morphologic alterations to the olfactory cortex of such magnitude that it can be clearly demonstrated, on average, 7 months after the infection. Although we did not expect an increased connectivity between the orbitofrontal cortex and the piriform cortex, our data clearly indicated that the C19+ group had a significantly higher functional connectivity between these 2 areas compared with the C19– group at the postmeasure. The piriform cortex is the largest cortical recipient of afferent OB fibers, whereas the orbitofrontal cortex (higher order multimodal sensory cortex) encodes information regarding olfactory stimuli (secondary olfactory functional area).

A recent study by Esposito et al²⁹ evaluating olfactory loss and connectivity of the olfactory cortex after COVID-19 found that structural and functional connectivity metrics were significantly increased in participants with a previous COVID-19 infection compared with noninfected participants. As pointed out by these authors, limitations of their study included a small sample size as well as no data on pre-COVID olfactory performance. In addition, the authors did not perform resting-state fMRI assessment of the auditory or visual cortex (control regions) but focused only on the olfactory cortex. Although the authors could not exclude that the observed differences between the 2 groups (previously infected versus noninfected participants) might already have existed before the pandemic, they hypothesized that the observed increased functional connectivity of the olfactory cortex may be the result of a compensatory CNS response. Our study suggests that the observed increased connectivity between the piriform and orbitofrontal cortices may indeed reflect a mechanism of CNS neuroplasticity, in particular because we found no significant group difference in connectivity in the 2 control regions, the auditory and visual cortices.

The only C19+ patient who presented with a dramatic increase in OB volume reported parosmia symptoms. The increase in OB volume observed in this participant is probably caused by persistent localized edema and inflammation following infection. While transient bilateral edema of the OB has been described on MR images in C19+ patients during the

acute phase of infection,¹³ a subset of patients presented with persistent olfactory deficits with or without perceptual distortions after COVID-19 infection.³⁰ MR imaging, clinical, histopathologic, and molecular data suggest that in this subset of patients, localized inflammation of the olfactory pathways is responsible for the persistent olfactory deficits.³⁰

The present study is in many ways unique in that we assessed the effects of COVID-19 infection within subjects, with a matching control group and using a study designed for assessing the potential neural effects of olfactory dysfunction. Without baseline pre-COVID-19 assessment or a control group, effects could be population-wide or reflect pre-existing COVID-19 risk factors. Nevertheless, our study is limited by the restricted sample size and does not have the same predicted power as a randomized control study. However, our baseline measures of the individual's state before infection and, critically, the inclusion of individuals with only mild-to-moderate COVID-19 symptoms are a strength over studies assessing clinical cases with more severe symptoms in which the incidence of olfactory dysfunction is known to be much lower.³¹ Our cohort could potentially provide further unique data in the future by allowing assessment of tentative altered OB volume and connectivity in individuals experiencing either spontaneous or olfactory training-induced recovery.

Evidence from both animal and human data have demonstrated that a range of DNA and RNA viruses are first detected in the OB during neurotropic infections of the CNS.⁶ In line with this notion are recent data suggesting that though wide-spread disease-associated microglia signatures are found in COVID-19-infected patients' cortices, there are no molecular traces of SARS-CoV-2 in the cortex beyond the OB,³² a finding supported by the discovery of SARS-CoV-2 in the olfactory bulb but not beyond in an animal model.⁷ These findings are further in line with past data suggesting that OB interneurons are not affected by neurotropic coronaviruses³³ and that the OB might provide virologic control by clearing viruses rapidly after infection.³⁴ Our results of tentative long-term morphologic effects in the OB, but not the olfactory cortex, therefore support the notion that the OB is functioning as an immunosensory effector organ during neurotropic viral infections.⁶ Although our goal was not to assess the immediate clinical relevance and therapeutic significance of neuroimaging findings, our study may contribute to our understanding of the olfactory system. Critically, the understanding that OB volume is likely affected by COVID-19 further promotes the notion that clinicians should recommend olfactory training to patients with COVID-19 with lingering olfactory disturbances, given that olfactory training is known to affect OB volume.²⁴

CONCLUSIONS

We found tentative evidence that COVID-19 reduces the volume of the OB with an average of 14% but does not affect GM volume of the main cerebral olfactory areas. Although 87.5% of our participants demonstrated a reduced OB volume after COVID-19 and binomial testing suggests that the result is not due to chance, our findings did not reach formal statistical significance.

Disclosure forms provided by the authors are available with the full text and PDF of this article at www.ajnr.org.

REFERENCES

- Gerkin RC, Ohla K, Veldhuizen MG, et al. **Recent smell loss is the best predictor of COVID-19 among individuals with recent respiratory symptoms.** *Chem Senses* 2021;46:bjaa081 CrossRef Medline
- Hannum ME, Ramirez VA, Lipson SJ, et al. **Objective sensory testing methods reveal a higher prevalence of olfactory loss in COVID-19-positive patients compared to subjective methods: a systematic review and meta-analysis.** *Chem Senses* 2020;45:865–74 Medline
- Iravani B, Arshamian A, Ravia A, et al. **Relationship between odor intensity estimates and COVID-19 prevalence prediction in a Swedish population.** *Chem Senses* 2020 May 22. [Epub ahead of print] CrossRef Medline
- Menni C, Valdes AM, Freidin MB, et al. **Real-time tracking of self-reported symptoms to predict potential COVID-19.** *Nat Med* 2020;26:1037–40 CrossRef Medline
- Rudberg A-S, Havervall S, Månberg A, et al. **SARS-CoV-2 exposure, symptoms and seroprevalence in healthcare workers in Sweden.** *Nat Commun* 2020;11:5064 CrossRef Medline
- Durrant DM, Ghosh S, Klein RS. **The olfactory bulb: an immunosensory effector organ during neurotropic viral infections.** *ACS Chem Neurosci* 2016;7:464–69 CrossRef Medline
- de Melo GD, Lazarini F, Levallois S, et al. **COVID-19-related anosmia is associated with viral persistence and inflammation in human olfactory epithelium and brain infection in hamsters.** *Sci Transl Med* 2021;13:13596 CrossRef Medline
- Mukerji SS, Solomon IH. **What can we learn from brain autopsies in COVID-19?** *Neurosci Lett* 2021;742:135528 CrossRef Medline
- Meinhardt J, Radke J, Dittmayer C, et al. **Olfactory transmucosal SARS-CoV-2 invasion as a port of central nervous system entry in individuals with COVID-19.** *Nat Neurosci* 2021;24:168–75 CrossRef Medline
- Aragão MFVV, Leal MC, Cartaxo Filho OQ, et al. **Anosmia in COVID-19 associated with injury to the olfactory bulbs evident on MRI.** *AJNR Am J Neuroradiol* 2020;41:1703–06 CrossRef Medline
- Galougahi MK, Ghorbani J, Bakhshayeshkaram M, et al. **Olfactory bulb magnetic resonance imaging in SARS-CoV-2-induced anosmia: the first report.** *Acad Radiol* 2020;27:892–93 CrossRef Medline
- Kandemirli SG, Altundag A, Yildirim D, et al. **Olfactory bulb MRI and paranasal sinus CT findings in persistent COVID-19 anosmia.** *Acad Radiol* 2021;28:28–35 CrossRef Medline
- Laurendon T, Radulesco T, Mugnier J, et al. **Bilateral transient olfactory bulb edema during COVID-19-related anosmia.** *Neurology* 2020;95:224–25 CrossRef Medline
- Strauss SB, Lantos JE, Heier LA, et al. **Olfactory bulb signal abnormality in patients with COVID-19 who present with neurologic symptoms.** *AJNR Am J Neuroradiol* 2020;41:1882–87 CrossRef Medline
- Altundag A, Yildirim D, Tekcan Sanli DE, et al. **Olfactory cleft measurements and COVID-19-related anosmia.** *Otolaryngol Head Neck Surg* 2021;164:1337–44 CrossRef Medline
- Khan M, Yoo SJ, Clijsters M, et al. **Visualizing in deceased COVID-19 patients how SARS-CoV-2 attacks the respiratory and olfactory mucosae but spares the olfactory bulb.** *Cell* 2021;184:5932–5949.e15 CrossRef Medline
- Thunell E, Peter MG, Lenoir V, et al. **Effects of COVID-19 on the human central olfactory system: a natural pre-post experiment.** *medRxiv* 2021 <https://www.medrxiv.org/content/10.1101/2021.12.27.21268455v1> Accessed September 1, 2022
- Peter MG, Mårtensson G, Postma EM, et al. **Morphological changes in secondary, but not primary, sensory cortex in individuals with life-long olfactory sensory deprivation.** *Neuroimage* 2020;218:117005 CrossRef Medline
- Gaser C, Dahnke R, Kurth K, Luders E; Alzheimer's Disease Neuroimaging Initiative. **A computational anatomy toolbox for the analysis of structural MRI data.** *bioRxiv* 2020 <https://www.biorxiv.org/content/10.1101/2022.06.11.495736v1>
- Ashburner J, Friston KJ. **Diffomorphic registration using geodesic shooting and Gauss-Newton optimisation.** *Neuroimage* 2011;55:954–67 CrossRef Medline
- Peter MG, Fransson P, Mårtensson G, et al. **Normal olfactory functional connectivity despite lifelong absence of olfactory experiences.** *Cereb Cortex* 2021;31:159–68 CrossRef Medline
- Seubert J, Freiherr J, Djordjevic J, et al. **Statistical localization of human olfactory cortex.** *Neuroimage* 2013;66:333–42 CrossRef Medline
- Porada DK, Regenbogen C, Seubert J, et al. **Multisensory enhancement of odor object processing in primary olfactory cortex.** *Neuroscience* 2019;418:254–65 CrossRef Medline
- Negoias S, Pietsch K, Hummel T. **Changes in olfactory bulb volume following lateralized olfactory training.** *Brain Imaging Behav* 2017;11:998–1005 CrossRef Medline
- Bergmann O, Liebl J, Bernard S, et al. **The age of olfactory bulb neurons in humans.** *Neuron* 2012;74:634–39 CrossRef Medline
- Wenzel J, Lampe J, Müller-Fielitz H, et al. **The SARS-CoV-2 main protease M^{pro} causes microvascular brain pathology by cleaving NEMO in brain endothelial cells.** *Nat Neurosci* 2021;24:1522–33 CrossRef Medline
- Korol DL, Brunjes PC. **Unilateral naris closure and vascular development in the rat olfactory bulb.** *Neuroscience* 1992;463:631–41 CrossRef Medline
- Douaud G, Lee S, Alfaro-Almagro F, et al. **SARS-CoV-2 is associated with changes in brain structure in UK Biobank.** *Nature* 2022;604:697–707 CrossRef Medline
- Esposito F, Cirillo M, De Micco R, et al. **Olfactory loss and brain connectivity after COVID-19.** *Hum Brain Mapp* 2022;43:1548–60 CrossRef Medline
- Xydakis MS, Albers MW, Holbrook EH, et al. **Post-viral effects of COVID-19 in the olfactory system and their implications.** *Lancet Neurol* 2021;20:753–61 CrossRef Medline
- von Bartheld CS, Hagen MM, Butowt R. **Prevalence of chemosensory dysfunction in COVID-19 patients: a systematic review and meta-analysis reveals significant ethnic differences.** *ACS Chem Neurosci* 2020;11:2944–61 CrossRef Medline
- Yang AC, Kern F, Losada PM, et al. **Dysregulation of brain and choroid plexus cell types in severe COVID-19.** *Nature* 2021;595:565–71 CrossRef Medline
- Wheeler DL, Athmer J, Meyerholz DK, et al. **Murine olfactory bulb interneurons survive infection with a neurotropic coronavirus.** *J Virol* 2017;91:e01099–17 CrossRef Medline
- Kalinke U, Bechmann I, Detje CN. **Host strategies against virus entry via the olfactory system.** *Virulence* 2011;24:367–70 CrossRef Medline

A Gamified Social Media–Based Head and Neck Radiology Education Initiative of the American Society of Head and Neck Radiology: Viewership and Engagement Trends at 3 Years

 N.A. Koontz,  C.M. Tomblinson,  D.R. Shatzkes,  C.M. Glastonbury,  C.D. Phillips,  K. Dean,  S. Strauss,  M. Agarwal,  C.D. Robson, and  R.H. Wiggins



ABSTRACT

BACKGROUND AND PURPOSE: Social media has made inroads in medical education. We report the creation and 3-year (2018–2021) longitudinal assessment of the American Society of Head and Neck Radiology Case of the Week (#ASHNRCOTW), assessing viewership, engagement, and impact of the coronavirus disease 2019 (COVID-19) pandemic on this Twitter-based education initiative.

MATERIALS AND METHODS: Unknown cases were tweeted from the American Society of Head and Neck Radiology account weekly. Tweet impressions (number of times seen), engagements (number of interactions), and new followers were tabulated. A social media marketing platform identified worldwide distribution of Twitter followers. Summary and *t* test statistics were performed.

RESULTS: #ASHNRCOTW was highly visible with 2,082,280 impressions and 203,137 engagements. There were significantly greater mean case impressions (9917 versus 6346), mean case engagements (1305 versus 474), case engagement rates (13.06% versus 7.76%), mean answer impressions (8760 versus 5556), mean answer engagements (908 versus 436), answer engagement rates (10.38% versus 7.87%), mean total (case + answer) impressions (18,677 versus 11,912), mean total engagements (2214 versus 910), and total engagement rates (11.79% versus 7.69%) for cases published after the pandemic started (all *P* values < .001). There was a significant increase in monthly new followers after starting #ASHNRCOTW (mean, 134 versus 6; *P* < .001) and significantly increased monthly new followers after the pandemic started compared with prepandemic (mean, 178 versus 101; *P* = .003). The American Society of Head and Neck Radiology has 7564 Twitter followers throughout 130 countries (66% outside the United States).

CONCLUSIONS: Social media affords substantial visibility, engagement, and global outreach for radiology education. #ASHNRCOTW viewership and engagement increased significantly during the COVID-19 pandemic.

ABBREVIATIONS: ASHNR = American Society of Head and Neck Radiology; #ASHNRCOTW = ASHNR Case of the Week hashtag; @ASHNRSociety = ASHNR Twitter account handle; ER = engagement rate; GIF = Graphics Interchange Format; COVID-19 = coronavirus disease 2019


Social media is pervasive in modern life with 72% of Americans reporting using social media in 2021, up from 65% in 2015 and just 7% in 2005.^{1,2} Using such platforms as Twitter, Facebook, YouTube, Instagram, TikTok, and LinkedIn, social media offers a widely available, easily accessible, highly portable, and free networking infrastructure that can be accessed via mobile smartphones and tablets, in addition to traditional

online computer access. Particularly in a time of social distancing related to the coronavirus disease 2019 (COVID-19) pandemic, social media has many attributes that make it an attractive instrument for radiology education, including the ability to rapidly disseminate image-rich content in a free open-access model, low (or no) overhead costs, ease of cross-institutional and multidisciplinary collaboration, lack of geographic boundaries, pre-existing networks of engaged users, and a general lack of hierarchical and social barriers that might otherwise inhibit interactions.^{3,4}

Received August 20, 2022; accepted after revision September 21.

From the Department of Radiology and Imaging Sciences (N.A.K.), Indiana University School of Medicine, Indianapolis, Indiana; Department of Radiology and Radiological Sciences (C.M.T.), Vanderbilt University Medical Center, Nashville, Tennessee; Department of Radiology (D.R.S.), Lenox Hill Hospital, New York, New York; Department of Radiology and Biomedical Imaging (C.M.G.), University of California San Francisco, San Francisco, California; Department of Radiology (C.D.P., K.D., S.S.), Weill Cornell Medicine, New York, New York; Department of Radiology (M.A.), Medical College of Wisconsin, Milwaukee, Wisconsin; Department of Radiology and Harvard Medical School (C.D.R.), Boston Children's Hospital, Boston, Massachusetts; and Department of Radiology and Imaging Sciences (R.H.W.), University of Utah School of Medicine, Salt Lake City, Utah.

Please address correspondence to Nicholas A. Koontz, MD, Indiana University School of Medicine, 550 N University Blvd, Room 0663, Indianapolis, IN 46202; e-mail: nakoontz@iu.edu; @nakoontz

 Indicates open access to non-subscribers at www.ajnr.org

 Indicates article with online supplemental data.

<http://dx.doi.org/10.3174/ajnr.A7711>

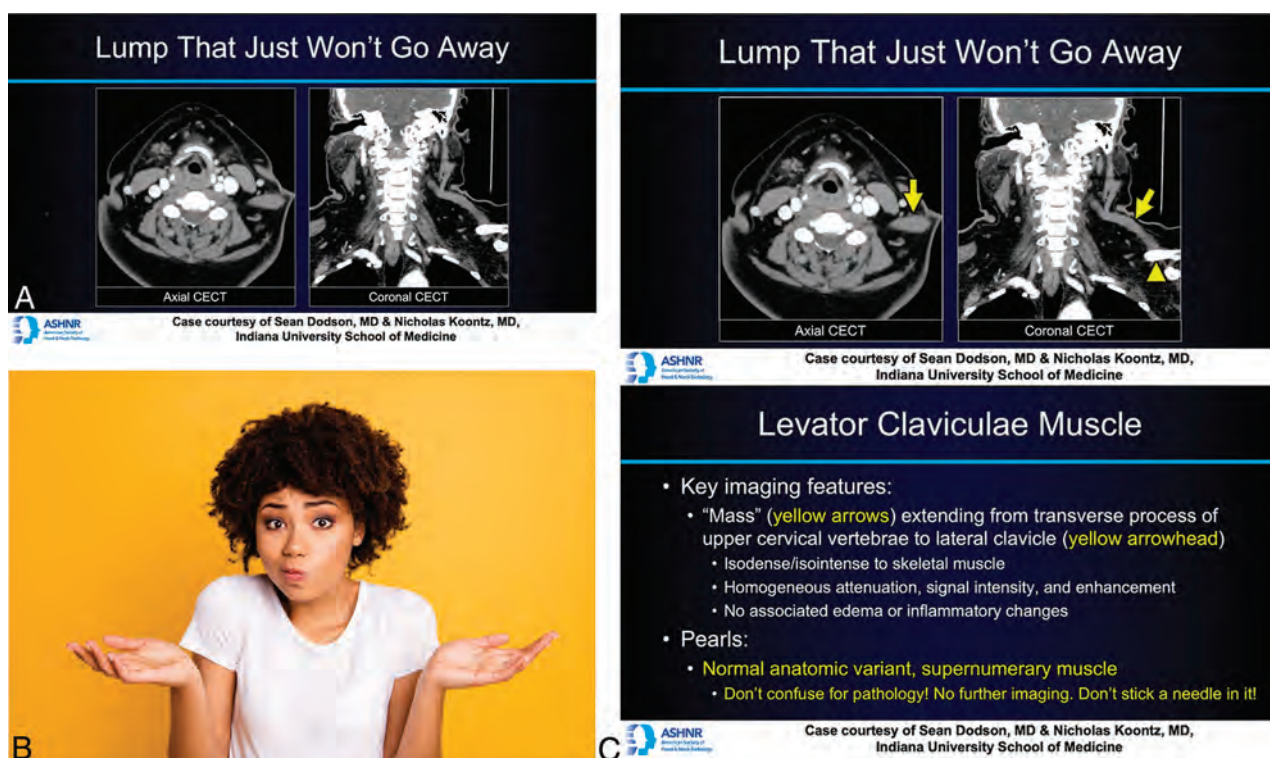


FIG 1. Representative #ASHNRCOTW. Each Wednesday, a new unknown case is tweeted by the @ASHNRSociety Twitter account, including a brief clinical history and 2–3 representative images (A). Participants are allowed a 24-hour response period, during which they reply to the original tweet by submitting an appropriate, thematically relevant, animated GIF image (B). Thus, users participate in the edutainment without spoiling the answer for other participants. Moreover, GIFs allow learners to form a “guidepost” memory affiliated with the case content with the intent to improve learning and increase future clinical accuracy performance as a radiologist. In this case of an accessory levator claviculae muscle, a learner submitted an animated GIF of a woman shrugging her shoulders to hint at the correct response. After the 24-hour response period, the case answer is tweeted by the ASHNR, including annotated images and a summary slide with key points (C).

Several prior publications have described the potential roles of social media for radiology education, detailing the experiences of individual and departmental accounts.^{4–14} Others have detailed the value of social media by radiology departments for engaging faculty members,^{4,15} by national medical societies for increasing engagement of members during national meetings,^{16–22} and for increasing readership and engagement of medical journals.^{23–27} During the past 4 years, multiple neuroradiology societies have implemented social media–based educational outreach initiatives, the earliest being the American Society of Head and Neck Radiology (ASHNR), which launched a weekly case-based education initiative in 2018 using Twitter as the primary vehicle for content dissemination. These social media–based, free open-access medical education initiatives serve the purposes of carrying out societal education missions, increasing global outreach, engaging members, advertising the society, and increasing society membership. However, no published studies have evaluated the implementation and outcomes of social media–based education initiatives by radiology societies.

We report the development, implementation, and longitudinal assessment of the ASHNR Case of the Week (#ASHNRCOTW) education initiative, detailing the viewership and engagement trends of this new social media–based educational offering during its first 3 years of existence (2018–2021), as well as comparing viewership and engagement trends before and during the COVID-19 pandemic.

MATERIALS AND METHODS

This investigation was compliant with Health Insurance Portability and Accountability Act standards. All protected health information regarding this educational initiative and study was carefully monitored by the principal investigator, and topical or time-sensitive case material was intentionally excluded to maintain compliance and safeguard protected health information.

#ASHNRCOTW Overview

On March 21, 2018, the ASHNR launched a new radiology education initiative using social media and gamified learning as the vehicles for delivering image-rich, case-based head and neck imaging content to participants. This new education offering was proposed by members of the ASHNR Website Committee and ad hoc Social Media Committee, approved by a vote of the Executive Committee, and remains an ongoing educational offering overseen by the subsequently formalized ASHNR Website and Social Media Committee. The educational content is disseminated via Twitter from the official ASHNR account (@ASHNRSociety) and uses a standard 3-step format: 1) tweeting an unknown case with salient history, 2) a 24-hour response period during which participants can submit responses, and 3) tweeting the case answer and summary content the following day (Fig 1). Participants are registered Twitter users who engage the content by replying directly to the tweet.

Content Design

Case material is compiled and vetted by the chair of the ASHNR Website and Social Media Committee, an attending neuroradiologist and a subspecialty head and neck imager with >7 years' post-fellowship experience, who additionally creates and solicits case content using a standard PowerPoint (Microsoft) template. This standard template is used for maintaining a consistent appearance, style, and organizational branding for the #ASHNRCOTW. Case content is provided by volunteer ASHNR members, all of whom are attending neuroradiologists with head and neck imaging subspecialty expertise. To facilitate the development of content, encourage society membership, promote engagement among trainees, and foster mentor-mentee relationships, volunteer faculty are encouraged to partner with and mentor residents and fellows with case-content generation.

Content Dissemination

Each Wednesday at noon Eastern Daylight Time (EDT), an unknown case is tweeted via the official Twitter account of the ASHNR using TweetDeck (<https://tweetdeck.twitter.com/>), a social media dashboard application that allows clients to schedule tweets in advance. Core content of each case includes a brief clinical history; a collage of 2–3 salient images labeled with plane, technique, and, when indicated, sequence modifiers (Fig 1A); a designation of the case contributors and their home institution; and instructions to answer the case by replying to the tweet with a thematically relevant and appropriate animated Graphics Interchange Format (GIF) image. A standard hashtag (#ASHNRCOTW) is used for referencing and archiving the content in perpetuity on Twitter, making the case database searchable by any online user. Several society members who are active on Twitter are tagged using their respective Twitter handles to encourage case discussion and to amplify viewership by retweeting the case of the week, the number of which varies each week to conform to the 280-character limit for tweets.

The purpose of using an animated GIF response (Fig 1B) is 3-fold: 1) It allows users to participate in the learning instrument without “giving away” the specific answer to other users, 2) it acts as an engaging vehicle to gamify the educational content (so-called “edutainment”) resulting in increased online discussion, and 3) it allows learners to develop a unique “guidepost” memory affiliated with the case content with the intent to improve learning and increase future clinical accuracy performance as a radiologist. To ensure that submitted GIFs are appropriate and professional, the chair and other members of the ASHNR Website and Social Media Committee monitor responses closely. If submitted GIFs are deemed inappropriate or offensive or if a learner submits the answer in text form (giving away the answer), his or her tweet is hidden using the “hide reply” functionality in Twitter. Repeat offenses or unprofessional conduct results in users being blocked by the @ASHNRSociety Twitter account.

Twitter followers are allowed 24 hours to publicly submit responses to the unknown case by replying to the original tweet, at which point the follow-up case answer is then tweeted by the official ASHNR Twitter account via a scheduled tweet from the TweetDeck application. This follow-up includes the answer to the unknown case, an annotated version of the original 2- to

3-image collage with arrows denoting salient findings, a summary slide containing key facts and imaging pearls regarding the diagnosis, and a designation of the contributors and their home institution (Fig 1C). The answer tweet is tagged with the #ASHNRCOTW hashtag to facilitate searchability, and multiple society members are again tagged using their respective Twitter handles up to the 280-character limit for tweets.

Case and answer pairs are tweeted weekly on Wednesday and Thursday at noon Eastern Daylight Time, respectively, except for certain holiday weeks each year. This schedule allows the material to be available for review during “routine business hours” across the continental United States, irrespective of a learner's time zone.

Data Collection

For the primary aim of this study, we used the analytics functionality of Twitter to tabulate impressions (defined as “times people saw a tweet on Twitter”) and engagements (defined as “times people interacted with a tweet,” for example retweeting content, “liking” a tweet, clicking on media to enlarge pictures, following the @ASHNRSociety, or clicking a hashtag embedded in the tweet) for both the case and the answer tweets during the first 3 years of the #ASHNRCOTW postings (from March 21, 2018, through March 17, 2021). With these data, we extrapolated an engagement rate (ER) defined as $\frac{\text{Number of Engagements}}{\text{Number of Impressions}}$. As a secondary outcome, we used Twitter analytics to tabulate the number of new monthly followers of the official ASHNR Twitter account. Last, to quantify the extent of international scope, we used a third-party social media marketing platform (Tweepsmap; <https://tweepsmap.com/>) to determine the geographic distribution of followers. All data are current through January 19, 2022.

Statistical Analysis

Statistical analysis was performed using Excel (Microsoft), including summary statistics, *F*-test of the equality of variances, (Student) *t* test, and (Welch) *t* test of unequal variances when appropriate. *P* values < .05 are considered statistically significant.

RESULTS

Twitter Viewership and Engagement

One hundred forty-three unique #ASHNRCOTW cases were created and disseminated during the first 3 years of this initiative. Content spanned the breadth of the head and neck imaging domain, including pediatric/congenital, infectious/inflammatory, oncology, trauma, temporal bone, sinonasal, skull base, orbits, glands, dental, vascular, suprahyoid and infrahyoid neck, upper aerodigestive tract, visceral space, sellar/parasellar, and cervical spine/musculoskeletal cases. A complete list of diagnoses can be found in the Online Supplemental Data. During the first 3 years, 26 neuroradiology/head and neck imaging faculty from 21 different institutions contributed case material for the #ASHNRCOTW initiative, mentoring 38 trainees in a total of 70 of the cases.

During its first 3 years, the #ASHNRCOTW cases demonstrated high visibility on Twitter with case tweets garnering a total of 1,107,464 impressions (mean, 7745 [SD = 2857]; range, 2310–17,159) (Fig 2). In addition to being seen >1.1 million times, interaction with the #ASHNRCOTW case tweets was high with 114,351 case tweet engagements (mean, 800 [SD, 520]; range,

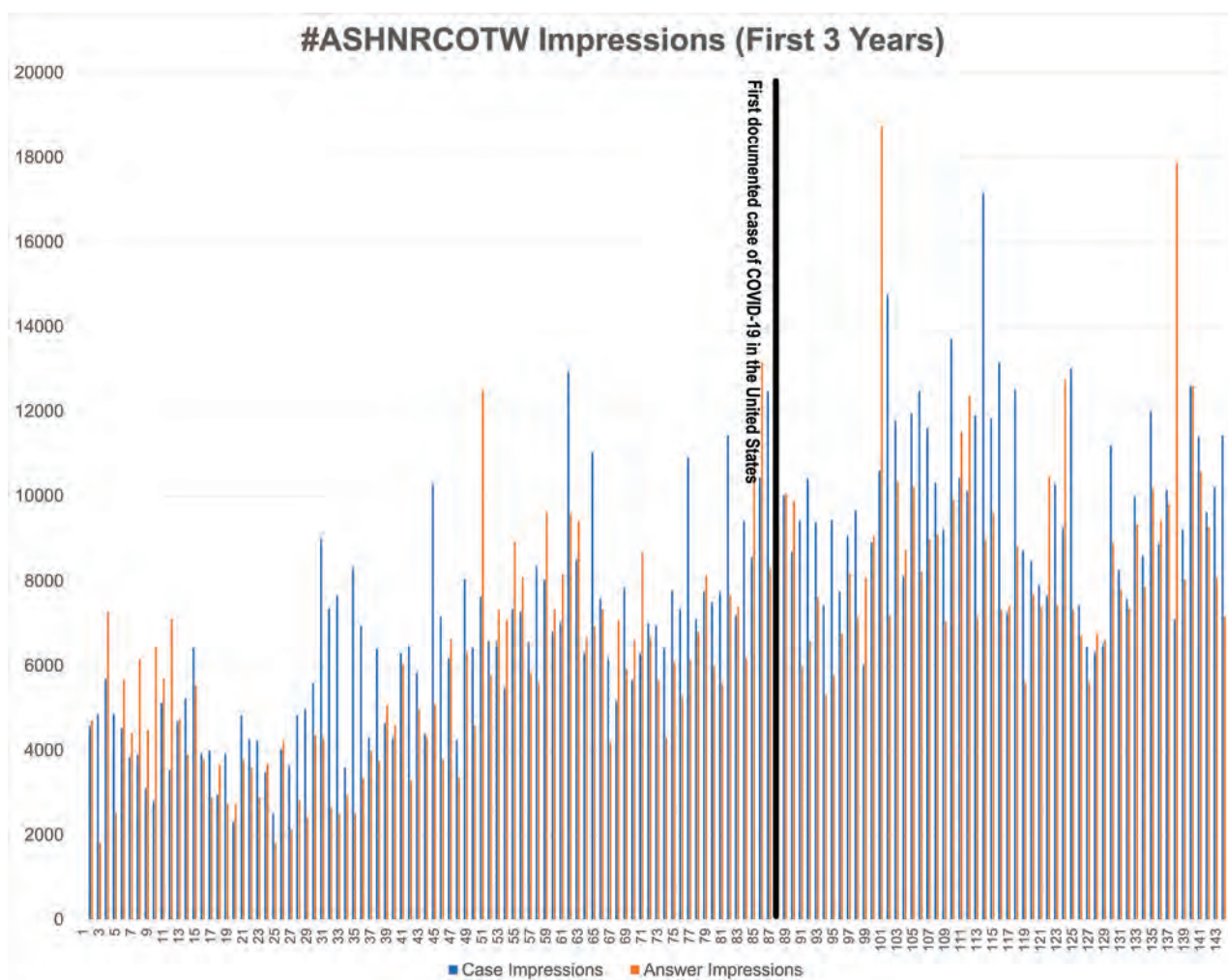


FIG 2. #ASHNRCOTW tweet impressions during the first 3 years. Case impressions (number of times seen) are recorded in blue, and answer impressions are recorded in orange. Note growth of the Twitter viewership during the first 3 years, which was significantly greater after the onset of the COVID-19 pandemic compared with prepandemic ($P < .001$).

200–2576) and a mean engagement rate of 9.8% (SD, 0.035; range, 4%–21.5%), indicating that approximately 10% of people who saw the case on Twitter interacted with it (Fig 3). During the same time interval, the #ASHNRCOTW answer tweets were slightly less visible on Twitter, garnering a total of 974,816 impressions (mean, 6817 [SD, 2879]; range, 1808–18,727) (Fig 2). Answer tweets also demonstrated fewer interactions with a total of 88,786 engagements (mean, 621 [SD, 336]; range, 105–1945), yielding a mean engagement rate of 8.9% (SD, 0.019; range, 4.4%–15.3%) (Fig 3).

When one considers case and answer tweets together, the #ASHNRCOTW was highly visible during the first 3 years with 2,082,280 total impressions (mean, 14,561 [SD, 5131]; range, 4318–29,329). In addition to being seen nearly 2.1 million times, interaction with #ASHNRCOTW was high with 203,137 total engagements (mean, 1421 [SD, 797]; range, 366–3866) and a mean engagement rate of 9.3% (SD, 0.026; range, 5%–17.4%).

Using the date of the first reported case of COVID-19 in the United States (January 20, 2020)²⁸ as a separation point, 87 cases were designated in the pre-COVID era and 56 cases were designated in the post-COVID era. There were significantly greater mean case impressions (9917 versus 6346), mean case engagements

(1305 versus 474), case engagement rates (13.06% versus 7.76%), mean answer impressions (8760 versus 5556), mean answer engagements (908 versus 436), answer engagement rates (10.38% versus 7.87%), mean total (case + answer) impressions (18,677 versus 11,912), mean total (case + answer) engagements (2214 versus 910), and total (case + answer) engagement rates (11.79% versus 7.69%) for #ASHNRCOTW tweets posted after the start of the COVID-19 pandemic in the United States compared with those posted before the start of the COVID-19 pandemic (all P values $< .001$) (Online Supplemental Data).

Twitter Followers

Before the #ASHNRCOTW education initiative (July 2016 to February 2018), the ASHNR official Twitter account amassed a total of 130 new Twitter followers during 20 months, amounting to a mean of 6.5 (SD, 9.04) new followers per month (range, 0–37). Following the start of the #ASHNRCOTW (March 2018 to March 2021), ASHNR accumulated 4811 new followers during 36 months, yielding a mean of 134.6 (SD, 64.1) new followers per month (range, 48–374). This increase in mean monthly new Twitter followers was statistically significant ($P < .001$). In a subset analysis of

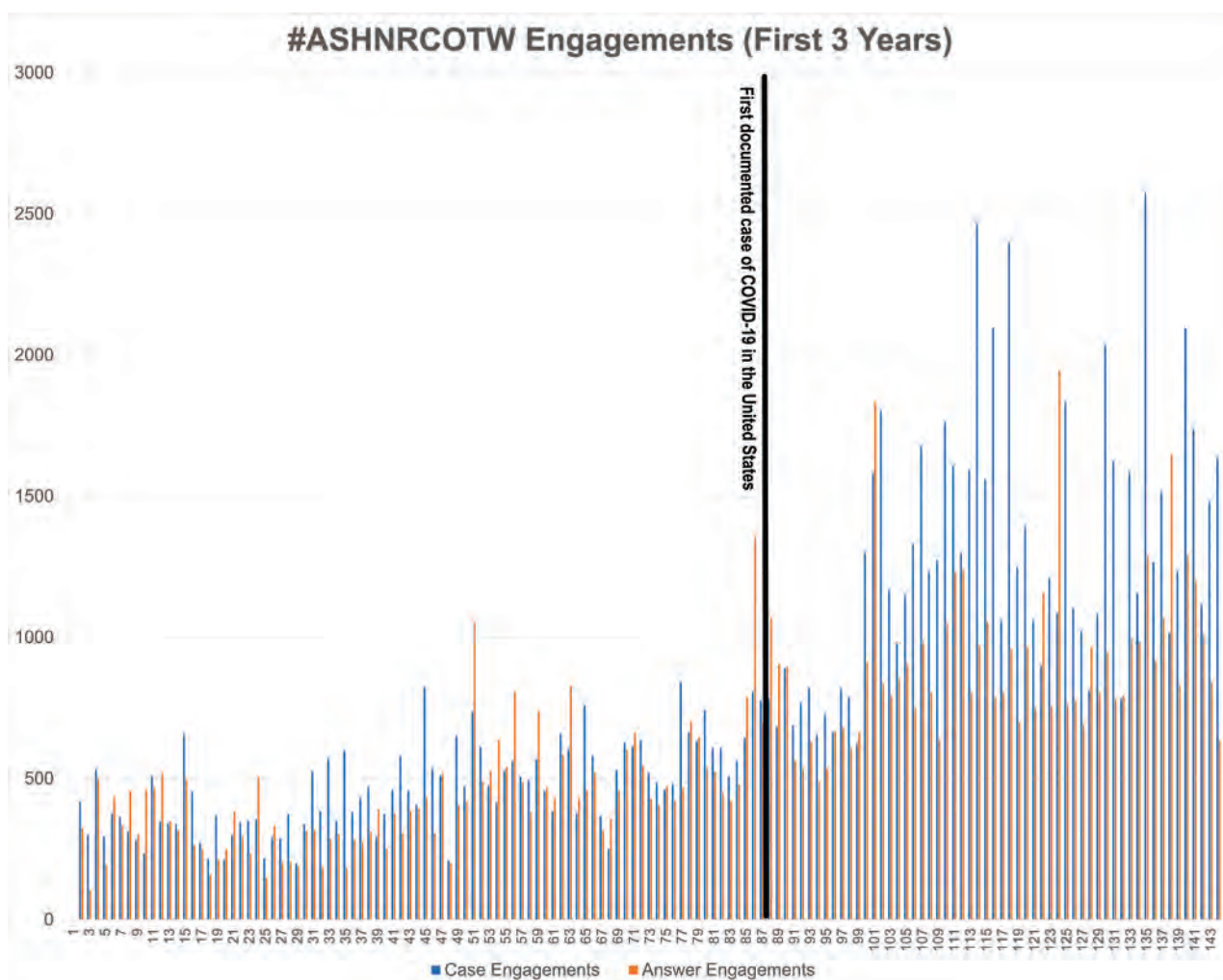


FIG 3. #ASHNRCOTW tweet engagements during the first 3 years. Case engagements (number of times interacted with) are recorded in blue and answer engagements are recorded in orange. There was also growth of the Twitter engagement over the first 3 years, which was significantly greater after the onset of the COVID-19 pandemic compared with prepandemic ($P < .001$).

monthly mean new Twitter followers after the implementation of the #ASHNRCOTW, there was a statistically significant increase in mean monthly new Twitter followers after the start of the COVID-19 pandemic (mean, 178 [SD, 77.9]; range, 90–374) compared with before the COVID-19 pandemic (mean, 101 [SD, 25.4]; range, 48–176) ($P = .003$).

International Scope

At the time of this research, the official Twitter account of the ASHNR (@ASHNRSociety) has 7564 followers throughout 130 countries worldwide. The largest cohort of followers originates from the United States ($n = 2584$, 34.16%), followed by India ($n = 897$, 11.86%), the United Kingdom ($n = 436$, 5.77%), Saudi Arabia ($n = 344$, 4.55%), Brazil ($n = 201$, 2.66%), Mexico ($n = 199$, 2.63%), Spain ($n = 194$, 2.57%), Canada ($n = 180$, 2.38%), Egypt ($n = 164$, 2.17%), Turkey ($n = 154$, 2.03%), and Australia ($n = 116$, 1.54%).

DISCUSSION

We report the design, implementation, and 3-year longitudinal assessment of a new social media-based educational initiative

sponsored by the ASHNR. This new initiative is used by radiology learners of all levels of training (medical students, interns, residents, fellows, and practicing radiologists), as well as nonradiologist physicians (eg, otolaryngologists) and nonphysician health care providers (eg, dentists) worldwide. We found Twitter to be a highly visible and engaging tool for radiology education, as evidenced by the >2 million views and >200,000 interactions during the first 3 years of the #ASHNRCOTW initiative (Figs 2 and 3). We also found Twitter to be particularly well-suited for the delivery of education/edutainment content during the COVID-19 pandemic, as evidenced by the statistically significant increase in all viewership and engagement metrics during the pandemic compared with prepandemic levels (Online Supplemental Data). During this era of social distancing and lack of in-person societal meetings, social media provided a forum for society members to continue to interact and network, benefitting from an international form of asynchronous interactive transmedia storytelling to continue educational efforts alongside virtual conferences and online webinars. We also observed a statistically significant increase in mean new monthly followers of the @ASHNRSociety Twitter

account during the pandemic compared with prepandemic levels, as well as a 5718% increase in total followers when comparing post-#ASHNRCOTW (7564 followers) to pre-#ASHNRCOTW (130 followers) levels. This growth in @ASHNRSociety Twitter followers outpaced the general growth of overall Twitter users during the same time period, which increased 41% from 122 million users in the second quarter of 2018 to 206 million users in the second quarter of 2021.²⁹ Most important, we note the potential for global radiology education outreach with this platform, as evidenced by the 7564 Twitter followers of ASHNR distributed throughout 130 countries, 66% of whom reside outside the United States.

Before the implementation of the #ASHNRCOTW, the @ASHNRSociety Twitter account was primarily used to advertise the annual meeting and provide occasional member updates regarding society news. Thus, viewership and visibility were limited, and content was directed primarily at existing society members. By establishing an ad hoc social media committee (and, subsequently, merging it with the pre-existing website committee), the ASHNR empowered a group of society members to design, implement, and oversee what has grown into a long-running, highly visible, and engaging educational initiative. This translates into an established outward-facing advertisement of the society's educational offerings that is powered by the volunteer effort of engaged society members, incurs essentially no financial cost to the society, and uses an educational delivery vehicle that has previously been shown to appeal greatly to younger generations of learners.⁴ This initiative has also increased the society's outreach and mentoring efforts, connecting head and neck radiologists internationally with a platform to interact and educate with novel edutainment technology.

The concept of using social media as a platform for medical education is not a new one, dating back to the first published medical literature description of a microbiology blog in 2010.³⁰ Multiple authors have previously detailed potential strengths and applications of using social media as a tool for radiology education, but these are largely limited to editorials and perspectives with few data-driven or outcomes-based investigations of this novel education tool. In a 2021 study from radiologists at Johns Hopkins, the authors found Twitter to be a useful tool for disseminating radiology education with scroll-through videos offering the highest level per tweet impressions and case images offering the highest level of per tweet engagements in their study.⁸ In a 2018 study from radiologists at Indiana University School of Medicine, the authors detailed a departmental social media-based radiology education initiative, documenting a linear growth trend of increased per-case Twitter impressions and engagements during its first year of implementation.¹³ In comparison, our study shows a growth trend in both Twitter impressions and engagements over a longer study duration (3 years), including a statistically significant increase in Twitter viewership and participation during the COVID-19 pandemic compared with prepandemic cases. The reasons for the increase in #ASHNRCOTW participation during the pandemic are not resolved by this study but may relate to the transient decrease in imaging volumes, leading to more available time for education or an increased desire for professional interaction during this time of social distancing and isolation. Similar to the results of the Indiana University study,¹³ we also found that the unknown #ASHNRCOTW case tweets had greater mean engagements than

the answer tweets. This difference in overall interaction with the answer tweets is likely due to the gamified learning fostered by this educational initiative.

A key element of the #ASHNRCOTW education initiative was the explicit use of gamification, in this case, soliciting participants to submit answers to the unknown cases in the form of GIF images, to increase engagement and improve learning. Gamification refers to the integration of game elements into a nongaming environment, a concept that has increasingly been applied to medical education during the past decade with the goal of improving learning outcomes.³¹ A growing body of literature suggests that gamification is a valuable tool for medical education, contributing to increased learner engagement, increased use of education resources, increased learner satisfaction, and improved learning outcomes.³¹⁻³⁵ Gamified learning strategies have made inroads in radiology education, including such tools as in-lecture audience response systems, resident or fellow leaderboards, game fiction scenarios and role-playing, and positive reinforcement with performance rewards for trainees.³⁶⁻³⁹

We intentionally gamified the #ASHNRCOTW initiative to rely on audience submission of GIF images as the primary means of participation. The benefits of using GIF images are 3-fold: 1) Participants can drop hints at the correct answer without spoiling it for other participants, 2) participants weave a storylike tapestry of memorable GIF images that combine narrative and flashbulb episodic memory with factual medical information (semantic memory) to augment learning, and 3) GIF images offer a light-hearted and often comical vehicle for approaching learning, which adds to the enjoyment of participation. This unique interactive edutainment allows participants to make connections they might not otherwise contemplate between the unknown cases and their answers using GIF images, fostering interactivity and potentially increasing the knowledge retention and understanding of complex head and neck anatomy and pathology. This asynchronous interactivity allows our educational effort to expand internationally and continuously throughout the year, expanding our audience from traditional academic radiology in-person annual conferences alone.

This study does have a few important limitations. First, we used Twitter analytics data to assess #ASHNRCOTW viewership and engagement but did not explicitly assess learning. Thus, we can demonstrate significant increases in viewership, engagement, and account followers after the establishment of the #ASHNRCOTW, but we cannot be certain that participants improved their head and neck radiology knowledge base or retention. Second, Twitter viewership data may be exaggerated due to the presence of social robots ("bots"), which are automated programs that generate or share content on social media with the intent of influencing users. Bots are estimated to account for 9%–15% of active Twitter accounts,⁴⁰ creating uncertainty in the exact number of human eyes our cases reached. The influence of bots on the niche Twitter demographic of head and neck imagers is likely small and probably has a limited effect on #ASHNRCOTW viewership. Third, we did not directly survey participants about their perceptions of this educational initiative. Thus, we cannot be certain whether participants found #ASHNRCOTW to be useful for their learning needs, though the high engagement rate (9.3%) suggests that they found it valuable.

For reference, Twitter engagement rates of >1% are considered strong.⁴¹ Last, we observed a significant increase in #ASHNRCOTW Twitter viewership, engagement, and account followers corresponding with the COVID-19 pandemic. We cannot be certain whether these increases represent durable trends or a transient effect of pandemic era learning, which would require long-term studies of post-pandemic viewership trends.

CONCLUSIONS

Social media affords substantial visibility, engagement, and global outreach for radiology education. Despite logistic and social challenges posed by COVID-19, the ASHNR engaged learners during the pandemic with its Case of the Week edutainment initiative on Twitter, which significantly increased viewership and learner engagement during the pandemic. As we evolve into our post-pandemic “new normal,” social media-based education initiatives and similar transmedia storytelling efforts may be beneficial for interactive teaching, learning, and education beyond the traditional annual conferences of academic medical societies.

ACKNOWLEDGMENTS

We wish to acknowledge the following individuals, who have contributed case content to the ASHNR Case of the Week to date: Joseph Aulino, MD, Amanda Baker, MD, Ian Bezahler, MD, Patrick Budny, MD, Paul Bunch, MD, Charlotte Chung, MD, PhD, David Collins, MD, Rebecca Cornelius, MD, Allison Crone, MD, Kelly Dahlstrom, MD, Hisham Dahmouh, MBBCh, Miriam DeFilipp, MD, Nerina DiSomma, MD, Sean Dodson, MD, Adriene Eastaway, MD, Nancy Fischbein, MD, Ben Freeze, MD, Elliott Friedman, MD, Elizabeth George, MD, Larry Ginsberg, MD, Benjamin Gray, MD, Michael Groswald, MD, Nathan Gruenhagen, MD, Kelsey Guerreso, MD, Zhe Guan, MD, Jeffrey Huang, MD, Pui-Nn Ho, MD, Kevin Hsu, MD, Charles Jacobs, MD, Roger Jordan, MD, Andrew Klein, MD, Cody Larson, MD, Luke Ledbetter, MD, Remy Lobo, MD, Evan Lustbader, MD, John Mahon, MD, Matthieu Mayer, MD, Morgan McLuckey, MD, Ben Morrissey, MD, Kristine Mosier, DMD, PhD, Gul Moonis, MD, Suresh Mukherji, MD, Mohsin Mukhtar, MD, Srikala Narayanan, MD, Ethan Neufeld, MD, Jimmy Nguyen, MD, Myles Nightingale, MD, William O'Brien, DO, Hilary Orłowski, MD, Igor Passioura, MD, Matthew Parsons, MD, Shreya Patel, MD, Priya Rajagopalan, MBBS, Syed Faraz Rizvi, MD, David Rockwell, MD, Michelle Roytman, MD, Rachel Seltman, MD, Ted Seltman, MD, Ilson Sepúlveda, DMD, Umber Shafique, MD, Vishal Sinha, MD, John Sowinski, MD, David Smullen, MD, Khaled Al Tawil, MD, and Rachel Wise, MD. We also wish to acknowledge the ASHNR, who funded color prints and open access status of this article.

Disclosure forms provided by the authors are available with the full text and PDF of this article at www.ajnr.org.

REFERENCES

- Auxier B, Anderson M. **Social media use in 2021.** Pew Research Center; <https://www.pewresearch.org/internet/2021/04/07/social-media-use-in-2021>. Accessed May 24, 2022
- Perrin A. **Social media usage: 2005–2015.** <https://www.pewresearch.org/internet/2015/10/08/social-networking-usage-2005-2015/>. Accessed May 24, 2022
- Prager R, Pratte MT, Unni RR, et al. **Content analysis and characterization of medical tweets during the early Covid-19 pandemic.** *Cureus* 2021;13:e13594 CrossRef Medline
- Koontz NA, Kamer AP, Dodson SC, et al. **Social media utilization at an academic radiology practice.** *Acad Radiol* 2018;25:111–17 CrossRef Medline
- Shea Johnstone LA, Towbin AJ. **The use of social media in radiology education.** *Acad Radiol* 2022;29:84–86 CrossRef Medline
- Kauffman L, Weisberg EM, Fishman EK. **Not only for career networking: can LinkedIn be used for radiology education?** *Curr Probl Diagn Radiol* 2022;51:166–70 CrossRef Medline
- Yu C, Sharma N. **Growth and utilization of radiology Instagram accounts: insight and template from an online radiologist educator.** *Acad Radiol* 2022;29:609–18 CrossRef Medline
- Kauffman L, Weisberg EM, Zember WF, et al. **#RadEd: how and why to use Twitter for online radiology education.** *Curr Probl Diagn Radiol* 2021;50:369–73 CrossRef Medline
- Kauffman L, Weisberg EM, Eng J, et al. **YouTube and radiology: the viability, pitfalls, and untapped potential of the premier social media video platform for image-based education.** *Acad Radiol* 2022;29 (Suppl 5):S1–S8 CrossRef Medline
- Staziaki PV, Santo ID, Skobodzinski AA, et al. **How to use YouTube for radiology education.** *Curr Probl Diagn Radiol* 2021;50:461–68 CrossRef Medline
- Gadde JA, Peterson RB, Koontz NA. **“Failing up” on social media: finding opportunities in moments of #Fail.** *J Am Coll Radiol* 2021;18:531–33 CrossRef Medline
- Shafer S, Johnson MB, Thomas RB, et al. **Instagram as a vehicle for education: what radiology educators need to know.** *Acad Radiol* 2018;25:819–22 CrossRef Medline
- Koontz NA, Hill DV, Dodson SC, et al. **Electronic and social media-based radiology learning initiative: development, implementation, viewership trends, and assessment at 1 year.** *Acad Radiol* 2018;25:687–98 CrossRef Medline
- Nickerson JP. **Social media and radiology education: are we #ready?** *Acad Radiol* 2019;26:986–88 CrossRef Medline
- Prabhu V, Rosenkrantz AB. **Enriched audience engagement through Twitter: should more academic radiology departments seize the opportunity?** *J Am Coll Radiol* 2015;12:756–59 CrossRef Medline
- Shetty M, Aggarwal NR, Parwani P, et al. **Social media to enhance engagement and science dissemination during in-person and virtual medical conferences: the SCMR 2020 and 2021 experiences—a report of the SCMR Social Media Task Force.** *J Cardiovasc Magn Reson* 2022;24:15 CrossRef Medline
- Bunch PM, Wortman JR, Andriole KP. **Social media and scientific meetings: education exhibit “likes” at the Radiological Society of North America Annual Meeting.** *Acad Radiol* 2016;23:382–88 CrossRef Medline
- Bhargava P. **Using Twitter to amplify your presence during radiology meetings.** *Curr Probl Diagn Radiol* 2017;46:261–62 CrossRef Medline
- Beste NC, Davis X, Kloeckner R, et al. **Comprehensive analysis of Twitter usage during a major medical conference held virtually versus in-person.** *Insights Imaging* 2022;13:8 CrossRef Medline
- Suh D, Yoon W, Lavingia KS, et al. **Analysis of Twitter activity and engagement from annual meetings of the Society for Vascular Surgery and the Society of Interventional Radiology.** *Ann Vasc Surg* 2021;76:481–87 CrossRef Medline
- D’Anna G, Pyatigorskaya N, Appelman A, et al. **Exploring new landmarks: analysis of Twitter usage during the 41st ESNR Annual Meeting.** *Neuroradiology* 2019;61:621–26 CrossRef Medline
- Hawkins CM, Duszak R, Rawson JV. **Social media in radiology: early trends in Twitter microblogging at radiology’s largest international meeting.** *J Am Coll Radiol* 2014;11:387–90 CrossRef Medline

23. Tomblinson CM, Jaswal S, Bunch PM. **Social media and digital innovation: an expanding frontier for journal engagement.** *Radiographics* 2021;41:E103–04 CrossRef Medline
24. Patel V, Li CH, Acharya J, et al. **Changes in social media impact of the radiological literature during the COVID-19 pandemic.** *Acad Radiol* 2021;28:151–57 CrossRef Medline
25. Wadhwa V, Latimer E, Chatterjee K, et al. **Maximizing the tweet engagement rate in academia: analysis of the AJNR Twitter feed.** *AJNR Am J Neuroradiol* 2017;38:1866–68 CrossRef Medline
26. Hawkins CM, Hillman BJ, Carlos RC, et al. **The impact of social media on readership of a peer-reviewed medical journal.** *J Am Coll Radiol* 2014;11:1038–43 CrossRef Medline
27. Tomblinson CM, Wadhwa V, Latimer E, et al. **Publicly available metrics underestimate AJNR Twitter impact and follower engagement.** *AJNR Am J Neuroradiol* 2019;40:1994–97 CrossRef Medline
28. Omer SB, Malani P, Del Rio C. **The COVID-19 pandemic in the US: a clinical update.** *JAMA* 2020;323:1767–68 CrossRef Medline
29. Dixon S. **Number of monetizable daily active Twitter users (mDAU) worldwide from 1st quarter 2017 to 1st quarter 2022.** Statista; <https://www.statista.com/statistics/970920/monetizable-daily-active-twitter-users-worldwide>. Accessed June 14, 2022
30. Racaniello VR. **Social media and microbiology education.** *PLoS Pathog* 2010;6:e1001095 CrossRef Medline
31. van Gaalen AE, Brouwer J, Schonrock-Adema J, et al. **Gamification of health professions education: a systematic review.** *Adv Health Sci Educ Theory Pract* 2021;26:683–711 CrossRef Medline
32. McCoy L, Lewis JH, Dalton D. **Gamification and multimedia for medical education: a landscape review.** *J Am Osteopath Assoc* 2016;116:22–34 CrossRef Medline
33. Nevin CR, Westfall AO, Rodriguez JM, et al. **Gamification as a tool for enhancing graduate medical education.** *Postgrad Med J* 2014;90:685–93 CrossRef Medline
34. Gentry SV, Gauthier A, L'Estrade Ehrstrom B, et al. **Serious gaming and gamification education in health professions: systematic review.** *J Med Internet Res* 2019;21:e12994 CrossRef Medline
35. Winkel DJ, Brantner P, Lutz J, et al. **Gamification of electronic learning in radiology education to improve diagnostic confidence and reduce error rates.** *AJR Am J Roentgenol* 2020;214:618–23 CrossRef Medline
36. Awan OA, Shaikh F, Kalbfleisch B, et al. **RSNA Diagnosis Live: a novel web-based audience response tool to promote evidence-based learning.** *Radiographics* 2017;37:1111–18 CrossRef Medline
37. Wu X, Peterson RB, Gadde JA, et al. **Winter is here: a case study in updating the neuroradiology didactic curriculum through a gamification of thrones solution.** *J Am Coll Radiol* 2020;17:1485–90 CrossRef Medline
38. Chen PH, Roth H, Galperin-Aizenberg M, et al. **Improving abnormality detection on chest radiography using game-like reinforcement mechanics.** *Acad Radiol* 2017;24:1428–35 CrossRef Medline
39. Awan O, Dako F, Akhter T, et al. **Utilizing audience response to foster evidence-based learning in a pilot study: does it really work?** *Cureus* 2018;10:e3799 CrossRef Medline
40. Varol O, Ferrara E, Davis CA, et al. **Online human-Bot interactions: detection, estimation, and characterization.** In: *Proceedings of the International AAAI Conference on Web and Social Media* 2017, Montreal, Canada. May 16–18, 2017
41. Adobe Express. **Your Guide to Social Media Engagement Rates.** Adobe Inc.; <http://www.adobe.com/express/learn/blog/what-is-a-good-social-media-engagement-rate>. Accessed May 24, 2022

High-Resolution T2-Weighted Imaging for Surveillance in Postoperative Vestibular Schwannoma: Equivalence with Contrast-Enhanced T1WI for Measurement and Surveillance of Residual Tumor

S.B. Strauss, S. Stern, J.E. Lantos, E. Lin, J. Shin, P. Yao, S.H. Selesnick, and C.D. Phillips

ABSTRACT

BACKGROUND AND PURPOSE: Patients with surgically resected vestibular schwannoma will undergo multiple postoperative surveillance examinations, typically including postcontrast sequences. The purpose of this study was to compare high-resolution T2WI with gadolinium T1WI in the postoperative assessment of vestibular schwannoma.

MATERIALS AND METHODS: This was a retrospective study of patients with a history of resected vestibular schwannoma at a single institution. High-resolution T2WI and gadolinium T1WI were independently evaluated for residual disease. In addition, 3D and 2D measurements were performed in the group of patients with residual tumor. Statistical analysis was performed to evaluate the agreement between sequences on the binary assessment (presence/absence of tumor on initial postoperative examination) and to evaluate the equivalence of measurements for the 2 sequences on 3D and 2D quantitative assessment in individuals with residual disease.

RESULTS: One hundred forty-eight patients with retrosigmoid-approach resection of vestibular schwannomas were included in the final analysis. There was moderate-to-substantial agreement between the 2 sequences for the evaluation of the presence versus absence of tumor (Cohen κ coefficient = 0.78; 95% CI, 0.68–0.88). The 2 sequences were significantly equivalent for 2D and 3D quantitative assessments (short-axis P value = .021; long-axis P value = .015; 3D P value = .039).

CONCLUSIONS: In this retrospective study, we demonstrate moderate-to-substantial agreement in the categoric assessment for the presence versus absence of tumor and equivalence between the 2 sequences for both 2D and volumetric tumor measurements as performed in the subset of patients with measurable residual. On the basis of these results, high-resolution T2WI alone may be sufficient for early postoperative imaging surveillance in this patient population.

ABBREVIATIONS: Gd-T1WI = gadolinium T1-weighted imaging; HR-T2WI = high-resolution T2-weighted MRI; SSFP = steady-state free precession

Vestibular schwannoma is a benign neoplasm (World Health Organization I) arising from Schwann cells enveloping the eighth cranial nerve, usually in the internal auditory canal and cerebellopontine angle, and is the most common benign neoplasm at these locations. The average rate of growth for vestibular schwannoma is 1.2 mm/year,¹ but a subset may progress more rapidly. Management recommendations include observation, stereotactic

radiosurgery, and complete, subtotal, or near-total microsurgical resection.^{2,3} In the postoperative setting, imaging surveillance is necessary for at least 10 years postprocedure,⁴ because reported recurrence/residual rates range from 0.17% to 7.7%, depending, in large part, on the completeness of the initial resection.⁵ Moreover, as subtotal resection strategies have been increasingly applied for the purpose of facial nerve and hearing preservation,³ long-term imaging surveillance has become more integral. In practice, the criterion standard for imaging surveillance remains serial, postoperative, gadolinium T1WI (Gd-T1WI) of the internal auditory canal.⁴ However, there are concerns within the medical and lay literature regarding the use of gadolinium-based contrast, particularly linear and nonionic agents, due to both gadolinium accumulation in brain tissue and the development of nephrogenic systemic fibrosis,^{6–8} particularly in a population undergoing multiple surveillance examinations. Moreover, an abbreviated, noncontrast examination is a more cost-effective approach for posttreatment surveillance.⁹

Received May 9, 2022; accepted after revision September 26.

From the Departments of Radiology (S.B.S., J.E.L., E.L.J.S., C.D.P.) and Otolaryngology-Head and Neck Surgery (S.H.S.), New York Presbyterian/Weill Cornell Medical Center, New York, New York; Department of Otolaryngology, Head and Neck Surgery, (S.S.), Hadassah Medical Center, Hebrew University, Jerusalem, Israel; Weill Cornell Medical College (P.Y.), New York, New York; and Department of Neurological Surgery (S.H.S.), Memorial Sloan Kettering Cancer Center, New York, New York.

Sara Strauss and Sagit Stern contributed equally to this article as co-first authors.

Please address correspondence to C. Douglas Phillips, MD, New York Presbyterian/Weill Cornell Medical Center, 525 East 68th St, New York, NY 10065; e-mail: cdp2001@med.cornell.edu; @CDP_Rad

<http://dx.doi.org/10.3174/ajnr.A7685>

The current recommendations of the American College of Radiology for screening in patients with asymmetric sensorineural hearing loss include both MR imaging of the head and internal auditory canal without and with IV contrast and MR imaging of the head and internal auditory canal without IV contrast, with the latter being an acceptable route when there is a contraindication to contrast administration. There are no existing American College of Radiology recommendations regarding imaging surveillance in the postoperative setting in patients with vestibular schwannoma; however, contrast-enhanced sequences are typically included.^{10,11} Prior studies have demonstrated the accuracy¹²⁻¹⁴ and cost effectiveness^{9,15,16} of T2WI steady-state free precession (SSFP) alone, without contrast-enhanced T1WI, for vestibular schwannoma screening in patients presenting with asymmetric sensorineural hearing loss. Studies have also shown noncontrast T2WI to be accurate in the detection of interval growth in patients with known, surgically-naïve vestibular schwannoma.^{17,18} To our knowledge, no studies exist examining the use of noncontrast T2WI for postoperative surveillance.

Steady-state sequences (eg, CISS, driven equilibrium radiofrequency reset pulse [DRIVE], and FIESTA-C) confers high spatial resolution using both T2 and T1 contrast, allowing excellent distinction between CSF and adjacent soft tissue, thereby optimizing tumor conspicuity above standard T2-weighted sequences. The purpose of this study was to compare high-resolution T2-weighted MR imaging (HR-T2WI) with Gd-T1WI in the postoperative assessment of vestibular schwannoma. We hypothesized that HR-T2WI will be equivalent to contrast-enhanced T1WI in the postoperative surveillance of vestibular schwannoma. This equivalence might ultimately present a cost- and time-effective option to a population undergoing long-term imaging surveillance.

MATERIALS AND METHODS

Patient Selection

This was a Weill Cornell Medicine institutional review board-approved, Health Insurance Portability and Accountability Act-compliant retrospective study of patients with a history of vestibular schwannoma who had undergone surgical resection and postoperative surveillance imaging. Adult patients 18 years of age and older with a history of vestibular schwannoma treated with surgical management between September 1, 2007, and April 17, 2018, with an examination performed within 1 year after surgery were eligible for inclusion in the study. Subjects were excluded if postoperative imaging was not available on the PACS (ie, performed at an outside institution and not uploaded to the hospital's systems), if examinations were nondiagnostic due to motion degradation or other technical factors, or if either SSFP and postcontrast T1WI was not performed. Basic demographic information (age and sex at birth) was documented.

Imaging Acquisition and Postprocessing

For each subject, Gd-T1WI and HR-T2WI were performed. Gd-T1WI studies were performed on GE Healthcare (1.5T, 3T) and Siemens (1.5T, 3T) scanners (TR = 354–973 ms, TE = 7.5–22.02 ms, percentage of phase FOV = 75%–100%, number of excitations = 0.5–3, matrix = 256 × 168–320 × 256). HR-T2WI studies were performed on GE Healthcare (GE LX Excited HDxt 1.5T,

Signa Architect 3T) and Siemens (Aera 1.5T, Skyra 3T, Biograph MMR 3T) scanners (TR = 5.08–9570 ms, TE = 1.7–269 ms, percentage of phase FOV = 75%–100%, number of excitations = 0.6–7, matrix = 256 × 128–512 × 312). N4 bias field correction was applied to images to remove low-frequency intensity and nonuniformity. High-resolution T2-weighted images were compared with and, when applicable, resampled to match the contrast-enhanced T1-weighted image voxel size, to mitigate section-selection bias. Gd-T1WI and resampled HR-T2WI were segmented using a combination of manual contouring and signal-intensity thresholding.

Imaging Assessment

Two coauthors (J.E.L. and E.L.), both Certificate of Added Qualification–certified neuroradiologists with 10 years of imaging experience, reviewed Gd-T1WI and HR-T2WI sequences from 1-year postoperative examinations and classified subjects according to the presence or absence of residual tumor (dichotomous) on each of the 2 sequences during separate sessions, blinded to the original radiology report. In addition, 3D and 2D (short- and long-axis) measurements were performed on the group of patients determined to have residual tumor on the basis of the 1-year radiology report. A team of 4 technologists were trained in identification and segmentation of tumor volume by 3 of the authors (J.S., S.B.S., C.D.P.) for HR-T2WI and Gd-T1WI separately using the Segment Editor Module in 3D Slicer (<http://www.slicer.org>). After the initial segmentation, tumor volumes were reviewed by 2 coauthors (S.B.S., S.S.) for accuracy (correct tumor identification and appropriate exclusion of postoperative changes) and edited as necessary. Long- and short-axis measurements were performed by 2 neuroradiologists (J.E.L. and E.L.) on HR-T2WI and Gd-T1WI separately using 3D Slicer; the maximal long-axis axial measurement was identified and measured, and the short-axis measurement, designated as perpendicular to the long-axis, was thereby defined.

Statistical Analysis

Statistical analysis was performed in R Version 4.0.2 (<http://www.r-project.org/>) and NCSS 2020, (Version 20.0.7; <https://www.ncss.com/download/ncss/updates/ncss-2020/>). The Cohen κ coefficient for agreement between sequences was calculated for binary assessment (presence versus absence of tumor on the first postoperative examination). The Wilcoxon signed-rank test for equivalence was performed as a test for equivalence between Gd-T1WI and HR-T2WI for the 2D data, given that the data were not normally distributed, with an equivalence margin of 1.5 mm for short-axis measurements and 4.5 for long-axis measurements. Paired tests for equivalence (TOST; <https://gist.github.com/josef-pkt/3900314>) were performed to test for equivalence between Gd-T1WI and HR-T2WI for the volumetric measurements, given that these were normally distributed, with an equivalence margin of 20 mm³. A paired-sample *t* test was performed to determine the significance of the difference in change with time based on HR-T2WI and Gd-T1WI using both 3D and 2D measurements.

RESULTS

Patient Characteristics

One hundred eighty-four patients were initially identified on the basis of chart review, of whom 36 were excluded due to the

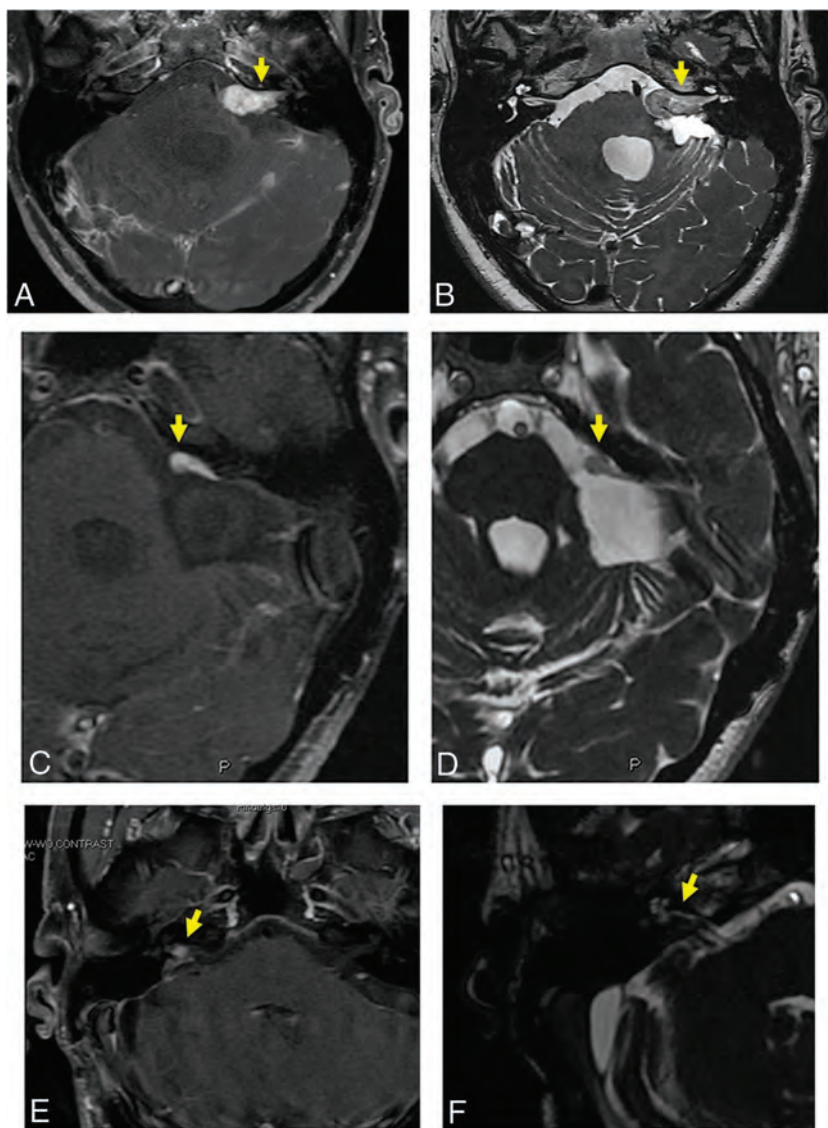


FIGURE. A and B, A 66-year-old-man with a history of retrosigmoid-approach resection of a left vestibular schwannoma. Axial Gd-T1WI (A) and HR-T2WI (B) demonstrate postprocedural changes, including encephalomalacia and gliosis in the left brachium pontis and lateral cerebellar hemisphere. A large-volume tumor is detectable on both the Gd-T1WI and HR-T2WI, as indicated by the yellow arrow. C and D, A 51-year-old woman with a history of retrosigmoid-approach resection of a left vestibular schwannoma. Axial Gd-T1WI (C) and HR-T2WI (D) demonstrate residual disease within the left cerebellopontine angle cistern, detectable on both Gd-T1WI and HR-T2WI, as indicated by the yellow arrow. E and F, A 60-year-old man with a history of retrosigmoid-approach resection of a right vestibular schwannoma. Axial Gd-T1WI (E) and HR-T2WI (F) demonstrate residual disease in the right internal auditory canal, as indicated by the yellow arrow.

aforementioned study criteria. One hundred forty-eight patients consisting of 75 men and 73 women with mean age of 48.9 years (range, 13–78 years) were included in the study. The average time interval between tumor resection and postoperative examination was 595 days (range, 51–2254 days). None of the included patients had a diagnosis of type 2 neurofibromatosis, and all subjects underwent surgical resection via a retrosigmoid approach.

Binary Assessment

At 1 year after the operation, 93 patients were classified as having residual tumor on the basis of HR-T2WI alone, and 90 patients

were classified as having residual tumor on the basis of Gd-T1WI alone. The Cohen κ coefficient for agreement (presence versus absence of tumor) between the 2 sequences was 0.78 (95% CI, 0.68–0.88), indicating moderate-to-substantial agreement. The Figure shows examples of patients with prior vestibular schwannoma resection and representative Gd-T1WI and HR-T2WI demonstrating residual/recurrent disease.

2D Assessment

Long- and short-axis measurements were performed in 81 subjects with residual tumor on the basis of the radiology report from the early postoperative examination performed at 1 year postsurgery. Measurements were performed for the Gd-T1WI and HR-T2WI, separately. The mean short-axis measurement was 7.3 mm (range, 1.3–24.5 mm) on HR-T2WI and 7.3 mm (range, 1.2–24.3 mm) on Gd-T1WI. The mean long-axis measurement was 13.0 mm (range, 2.3–34.8 mm) on SSFP and 13.3 mm (range, 2.2–35.9) on postcontrast T1WI. The Wilcoxon signed-rank test for equivalence using TOST showed that the short-axis measurements for the 2 sequences were significantly equivalent ($P = .021$) and the long-axis measurements for the 2 sequences were significantly equivalent ($P = .015$).

Volumetric Assessment

Volumetric calculation was performed in the 81 subjects with residual tumor on the early postoperative examination performed at 1 year postsurgery. Tumor was segmented using the Segmentation Editor Module in 3D Slicer 4.10.2, and tumor volumes (cubic millimeters) were extracted. The mean tumor volume was 1096.7 mm³ (range, 19.7–11,502.1 mm³) on HR-T2WI and 1106.0 mm³ (range, 24.1–11,578.5 mm³) on Gd-T1WI. The paired t test for equivalence using TOST showed that the 2 sequences were significantly equivalent ($P = .039$).

Change with Time

Of the 81 subjects with residual tumor on the early postoperative examination performed at 1 year postsurgery, residual disease was measured on a single subsequent follow-up examination in 39 subjects. The mean time interval between the 2 postoperative examinations was 865.6 days (range, 75–2720 days). The mean tumor growth with time was 265.7 mm³ (3D: range, 0–1802.16 mm³),

1.3 mm (long-axis: range, 0.1–5.8 mm), and 1.1 mm (short-axis: range, 0–6 mm) on HR-T2WI and 247.6 mm³ (3D: range, 0–1897.45 mm³), 1.3 mm (long-axis: range, 0–7.3 mm), and 1.2 mm (short-axis: range, 0–4.4 mm) on Gd-T1WI, measured in this group of patients. The paired-sample *t* test demonstrated no significant difference between HR-T2WI and Gd-T1WI in measured change with time for the 3D ($P = .264$), short-axis ($P = .521$), and long-axis ($P = .362$) measurements.

DISCUSSION

Imaging evaluation of the postoperative vestibular schwannoma is more complex as compared to untreated vestibular schwannoma, as postsurgical changes such as scar tissue formation and anatomic distortion can make evaluation for residual or recurrent disease more difficult. This study demonstrates that HR-T2WI is equivalent to Gd-T1WI in the evaluation of residual vestibular schwannoma in patients with prior tumor resection. We demonstrate moderate-to-substantial agreement in the categorical assessment for the presence versus absence of tumor and equivalence between the 2 sequences for both 2D and volumetric tumor measurements. On the basis of these results, HR-T2WI alone may be sufficient for early imaging surveillance in this patient population.

These findings are consistent with those of previous studies in patients with surgically-naïve vestibular schwannoma. For instance, Buch et al¹⁹ found no significant difference in the measurement of vestibular schwannoma performed on Gd-T1WI and HR-T2WI. In a meta-analysis including 10 studies, Kim et al¹⁸ found that T2WI was as accurate as Gd-T1WI in tumor and showed high inter- and intrarater agreement for HR-T2WI measurements. The current study demonstrates similar findings in a large sample of postoperative vestibular schwannomas.

We chose to study both 3D assessment in addition to 2D assessment. Volumetric analysis has been shown to detect changes in tumor size earlier than linear assessment alone and is more sensitive to the detection of growth in the craniocaudal dimension, growth of multilobulated tumor, and growth difficult to detect because of differences in the scan angle between examinations.²⁰ We found both measurement approaches to be statistically equivalent between the HR-T2WI and Gd-T1WI examinations. Future studies exploring automated approaches to 3D segmentation on the basis of HR-T2WI might further improve the efficiency of examination performance and interpretation.

There are several limitations to this study. First, the patient sample was derived from a single institution and neurotology practice; therefore, a more diverse sample would be required to increase generalizability. All subjects in this study underwent resection via a retrosigmoid approach; thus, it is conceivable that HR-T2WI alone might be less effective in subjects with resection via middle cranial fossa (with a potentially larger cerebellopontine angle residual) or translabyrinthine (in which the postoperative examination is further complicated by placement of fat graft material) approaches. Additionally, we did not specifically explore potential factors such as cystic vestibular schwannoma, the presence of hemosiderin deposition, or a purely intrameatal remnant in the successful detection of residual on the noncontrast HR-T2WI examination.

In this study, evaluation for the presence versus absence of residual tumor was performed by highly experienced neuroradiologists, and external validation by less-experienced readers might yield worse results. Finally, the average time interval between the operation and the initial postoperative imaging examination was 1.6 years; however, imaging surveillance typically continues until at least 10 years postsurgery. Thus, additional longitudinal imaging demonstrating equivalence between HR-T2WI and Gd-T1WI is warranted to support the abbreviated noncontrast examination at longer-interval follow-up.

CONCLUSIONS

In this retrospective study, we demonstrate HR-T2WI to be equivalent to Gd-T1WI in the evaluation of residual vestibular schwannoma in patients with prior tumor resection. These findings suggest that HR-T2WI alone may be sufficient for early imaging surveillance in this patient population, thereby reducing examination time and obviating need for multiple contrast doses with time.

Disclosure forms provided by the authors are available with the full text and PDF of this article at www.ajnr.org.

REFERENCES

1. Yoshimoto Y. **Systematic review of the natural history of vestibular schwannoma.** *J Neurosurg* 2005;103:59–63 CrossRef Medline
2. Chen Z, Prasad SC, Di Lella F, et al. **The behavior of residual tumors and facial nerve outcomes after incomplete excision of vestibular schwannomas.** *J Neurosurg* 2014;120:1278–87 CrossRef Medline
3. Tang S, Griffin AS, Waksal JA, et al. **Surveillance after resection of vestibular schwannoma: measurement techniques and predictors of growth.** *Otol Neurotol* 2014;35:1271–76 CrossRef Medline
4. Miller ME, Lin H, Mastrodimos B, et al. **Long-term MRI surveillance after microsurgery for vestibular schwannoma.** *Laryngoscope* 2017;127:2132–38 CrossRef Medline
5. Ahmad RARL, Sivalingam S, Topsakal V, et al. **Rate of recurrent vestibular schwannoma after total removal via different surgical approaches.** *Ann Otol Rhinol Laryngol* 2012;121:156–61 CrossRef Medline
6. Mathur M, Jones JR, Weinreb JC. **Gadolinium deposition and nephrogenic systemic fibrosis: a radiologist's primer.** *Radiographics* 2020;40:153–62 CrossRef Medline
7. Robert P, Fingerhut S, Factor C, et al. **One-year retention of gadolinium in the brain: comparison of gadodiamide and gadoterate meglumine in a rodent model.** *Radiology* 2018;288:424–33 CrossRef Medline
8. Radbruch A, Weberling LD, Kieslich PJ, et al. **Gadolinium retention in the dentate nucleus and globus pallidus is dependent on the class of contrast agent.** *Radiology* 2015;275:783–91 CrossRef Medline
9. Crowson MG, Rocke DJ, Hoang JK, et al. **Cost-effectiveness analysis of a non-contrast screening MRI protocol for vestibular schwannoma in patients with asymmetric sensorineural hearing loss.** *Neuroradiology* 2017;59:727–36 CrossRef Medline
10. Dunn IF, Bi WL, Mukundan S, et al. **Congress of Neurological Surgeons systematic review and evidence-based guidelines on the role of imaging in the diagnosis and management of patients with vestibular schwannomas.** *Neurosurgery* 2018;82:E32–34 CrossRef Medline
11. Dang L, Tu NC-Y, Chan EY. **Current imaging tools for vestibular schwannoma.** *Curr Opin Otolaryngol Head Neck Surg* 2020;28:302–07 CrossRef Medline
12. Schmalbrock P, Chakeres DW, Monroe JW, et al. **Assessment of internal auditory canal tumors: a comparison of contrast-enhanced T1-**

- weighted and steady-state T2-weighted gradient-echo MR imaging.** *AJNR Am J Neuroradiol* 1999;20:1207–13 Medline
13. Annesley-Williams D, Laitt R, Jenkins J, et al. **Magnetic resonance imaging in the investigation of sensorineural hearing loss: is contrast enhancement still necessary?** *J Laryngol Otol* 2001;115:14–21 CrossRef Medline
 14. Fukui MB, Weissman JL, Curtin HD, et al. **T2-weighted MR characteristics of internal auditory canal masses.** *AJNR Am J Neuroradiol* 1996;17:1211–18 Medline
 15. Shelton C, Harnsberger HR, Allen R, et al. **Fast spin echo magnetic resonance imaging: clinical application in screening for acoustic neuroma.** *Otolaryngol Head Neck Surg* 1996;114:71–76 CrossRef Medline
 16. Verret D, Adelson RT, Defatta RJ. **Asymmetric sensorineural hearing loss evaluation with T2 FSE-MRI in a public hospital.** *Acta Otolaryngol* 2006;126:705–07 CrossRef Medline
 17. Currie S, Saunders D, Macmullen-Price J, et al. **Should we be moving to a national standardized non-gadolinium MR imaging protocol for the surveillance of vestibular schwannomas?** *Br J Radiol* 2019;92:20180833 CrossRef Medline
 18. Kim DH, Lee S, Hwang SH. **Non-contrast magnetic resonance imaging for diagnosis and monitoring of vestibular schwannomas: a systematic review and meta-analysis.** *Otol Neurotol* 2019;40:1126–33 CrossRef Medline
 19. Buch K, Juliano A, Stankovic KM, et al. **Noncontrast vestibular schwannoma surveillance imaging including an MR cisternographic sequence: is there a need for postcontrast imaging?** *J Neurosurg* 2018;131:549–54 CrossRef Medline
 20. Lees KA, Tombers NM, Link MJ, et al. **Natural history of sporadic vestibular schwannoma: a volumetric study of tumor growth.** *Otolaryngol Head Neck Surg* 2018;159:535–42 CrossRef Medline

Accelerated Nonenhanced 3D T1-MPRAGE Using Wave-Controlled Aliasing in Parallel Imaging for Infant Brain Imaging

S.Y. Yun and Y.J. Heo



ABSTRACT

BACKGROUND AND PURPOSE: MPRAGE is the most commonly used sequence for high-resolution 3D T1-weighted imaging in pediatric patients. However, its longer scan time is a major drawback because pediatric patients are prone to motion and frequently require sedation. This study compared nonenhanced accelerated MPRAGE using wave-controlled aliasing in parallel imaging (wave-TI-MPRAGE) with standard MPRAGE in infants.

MATERIALS AND METHODS: We retrospectively evaluated 68 infants (mean age, 1.78 [SD, 1.70] months) who underwent nonenhanced standard and wave-TI-MPRAGE. Two neuroradiologists independently assessed each image for image quality, artifacts, myelination degree, and anatomic delineation using the 4-point Likert scale. For diagnostic performance, both observers determined whether nonenhancing lesions were present in the brain parenchyma in 2 types of nonenhanced MPRAGE sequences.

RESULTS: Wave-TI-MPRAGE showed a significantly lower mean score and lower interobserver agreement for overall image quality and anatomic delineation than standard MPRAGE ($P < .001$ for each). However, there were no significant differences between the 2 types of MPRAGE sequences for motion artifacts ($P = .90$ for observer 1, $P = .14$ for observer 2) and degree of myelination ($P = .16$ for observer 1, $P = .32$ for observer 2). Among the nonenhancing pathologic lesions observed on standard MPRAGE by both observers, only 2 were missed on wave-TI-MPRAGE, and they were very tiny, faint, nonhemorrhagic WM injuries.

CONCLUSIONS: Although wave-TI-MPRAGE showed lower overall image quality than standard MPRAGE, the diagnostic performance for nonenhancing parenchymal lesions was comparable. Wave-TI-MPRAGE could be an alternative for diagnosing intracranial lesions in infants, with marked scan time reduction.

ABBREVIATIONS: wave-TI-MPRAGE = MPRAGE using wave-controlled aliasing in parallel imaging; wave-CAIPI = wave-controlled aliasing in parallel imaging

The MPRAGE sequence is a widely used sequence for acquisition of 3D data sets of the pediatric brain because it provides high contrast between gray and white matter along with excellent spatial resolution.¹ However, it requires a long scan time due to the large amount of k -space encoding and added T1 required to achieve the prepared T1-weighted contrast. It is susceptible to motion artifacts because the conventional Cartesian sampling and long scan time increase the possibility of patient movement and anxiety. Scan-time reduction is particularly important for pediatric brain imaging

because it can reduce the need for sedation before performing MR imaging as well as decrease the chance of motion artifacts.²

Recently, various kinds of accelerated MR imaging techniques³⁻⁷ have been applied to adult brain imaging for achieving scan-time reduction; however, only a few have been applied to pediatric brain imaging.^{2,8,9} Synthetic MR imaging enables the reconstruction of multiple synthetic sequences by simultaneous quantification of T1/T2 relaxation times and proton density for achieving whole-brain coverage from a single scan. No significant difference was found between synthetic and conventional images in the evaluation of image quality and artifacts in neonatal brain imaging.¹⁰ Wave-controlled aliasing in parallel imaging (wave-CAIPI; Siemens) is a kind of advanced parallel imaging technique that combines a corkscrew gradient trajectory with CAIPI shifts in the ky and kz directions to ensure efficient encoding of k -space along with an even spread of the voxel aliasing in all dimensions. It has been applied to various MR images and has been proved to have relatively preserved image quality and scan-time reduction compared with standard MR imaging.^{7,8,11,12}

Received June 16, 2022; accepted after revision September 19.

From the Department of Radiology, Inje University Busan Paik Hospital, Busan, South Korea.

This work was supported by 2022 Inje University Busan Paik Hospital research grant.

Please address correspondence to Young Jin Heo, MD, Department of Radiology, Inje University Busan Paik Hospital, Bokji-ro 75, Busanjin-Gu, Busan 47392, South Korea; e-mail: youngjin726@hanmail.net

Indicates article with online supplemental data.

<http://dx.doi.org/10.3174/ajnr.A7680>

Image parameters of standard MPAGE and wave-T1-MPAGE

	Standard MPAGE	Wave-T1-MPAGE
FOV (mm ²)	180 × 180	180 × 80
Voxel size (mm ³)	0.8 × 0.8 × 0.9	0.8 × 0.8 × 0.9
TR (ms)	2400	2200
TE (ms)	2.96	3.05
Flip angle	9°	9°
Bandwidth (Hz)	260	260
T1 (ms)	1200	1090
Number of excitations	1	1
Parallel imaging method	GRAPPA ^a	CAIPIRINHA ^b
Acceleration factor (phase)	2	2
Acceleration factor (section)	—	2
Scan time	4 min 55 sec	2 min 14 sec

Note:—indicates none.

^a Generalized autocalibrating partially parallel acquisition.

^b Controlled aliasing in parallel imaging results in higher acceleration.

There are only a few studies on the application of wave-CAIPI to MPAGE in pediatric patients.^{11,13} However, to our knowledge, no study has evaluated the clinical feasibility of nonenhanced MPAGE using wave-CAIPI (wave-T1-MPAGE) in infants. Because infants have a different condition during MR imaging and different brain tissue contrast compared with adults, application of pediatric neuroimaging (especially for the neonatal brain) can be more difficult than in adults. Thus, the purpose of our study was to compare the overall diagnostic image quality of standard MPAGE and wave-T1-MPAGE in infants.

MATERIALS AND METHODS

Patients

This study was approved by the institutional review board of our hospital and informed consent was not required for reviewing the images and records due to the retrospective nature of the study. We retrospectively reviewed the database and identified consecutive pediatric patients who underwent brain MR imaging between July 2021 and April 2022. The inclusion criteria of this study were consecutive patients who underwent standard- and wave-T1-MPAGE in the same imaging session and were younger than 1 year of age. A total of 68 infants (29 boys, 39 girls; 1.78 [SD, 1.70] months of age; range, 0–9 months) were included in this study. The reasons for brain MR imaging were prematurity (57/68, 83.8%), microcephaly (4/68, 5.89%), seizure (2/68, 2.94%), fatal asphyxia (2/68, 2.94%), nystagmus (2/68, 2.94%), and prenatal ventriculomegaly (1/68, 1.47%). All patients were sedated with an oral sedative (chloral hydrate; Pocral syrup 10% mL).

Image Acquisition

All studies were performed using a 3T MR imaging scanner (Magnetom Skyra; Siemens) with a 20-channel head coil. Detailed scan parameters of standard MPAGE and wave-T1-MPAGE are described in the Table. In addition to the standard- and wave-T1-MPAGE, a standard MR imaging sequence was obtained with axial FLAIR, T2-weighted, gradient-echo images. The order of the sequences was the following: wave-T1-MPAGE followed

by standard MPAGE in 65 patients and standard MPAGE followed by wave-T1-MPAGE in 3 patients.

Image Analysis

Two neuroradiologists, one with 8 years of experience and the other with 2 years of experience in neuroimaging, independently reviewed all the standard MPAGE and wave-T1-MPAGE images using the PACS. They were blinded to the clinical information to minimize bias. Each MPAGE sequence was reviewed at 2 different time points with at least a 4-week interval to avoid recall bias. The image quality was graded according to the following criteria: 1) overall image quality, 2) motion artifacts, 3) degree of myelination, 4) differentiation of GM-WM at the level of the lateral ventricles, 5) demarcation of the basal ganglia, and 6) demarcation of the cerebral sulci. Overall image quality was graded using the 4-point Likert scale: 1, inadequate (not acceptable for diagnostic use); 2, sufficient (acceptable for diagnostic use but with minor issues); 3, good (acceptable for diagnostic use); and 4, excellent (acceptable for diagnostic use). Motion artifacts were also graded using a 4-point grading system: 1, severe artifacts (not acceptable for diagnostic use); 2, moderate artifacts (sufficient for diagnostic use but with minor issues); 3, mild artifacts (acceptable for diagnostic use because minor artifacts do not adversely affect diagnostic use); and 4, images do not contain visible artifacts (acceptable for diagnostic use). The degree of myelination¹⁴ was assessed by the signal intensity of myelination and graded using a 4-point grading system in comparison with the adjacent GM: 1, low signal; 2, isosignal; 3, slightly high signal; and 4, prominent high signal intensity. Each criterion for structural demarcation was graded using the 4-point Likert scale: 1, not visible; 2, detectable (subtle differentiation from the neighboring structures); 3, easily delineated (easily differentiated from the neighboring structures); and 4, excellent delineation.

To evaluate the diagnostic performance, we determined whether nonenhancing pathologic lesions were present in the brain parenchyma in both MPAGE sequences.

Statistical Analysis

The image-quality assessments of nonenhanced standard MPAGE and wave-T1-MPAGE were assigned numeric values. We summarized the readers' ratings for each MPAGE sequence and described it as mean (SD). The Wilcoxon signed-rank test was used to compare the mean values of the readers' grading, and the McNemar test for evaluating the presence of pathologic lesions. Interobserver agreement between the 2 readers was calculated by weighted κ statistics; 0–0.20, 0.21–0.40, 0.41–0.60, 0.61–0.80, and 0.81–1.00 were regarded as slight, fair, moderate, substantial, and almost in perfect agreement, respectively, based on the Landis and Koch method.¹⁴ All statistical analyses were performed using statistical software packages (SPSS, Version 26.0, IBM; MedCalc, Version 19.8, MedCalc Software), and P value < .05 was considered statistically significant.

RESULTS

Although the overall image quality of nonenhanced wave-T1-MPAGE was significantly lower than that of standard

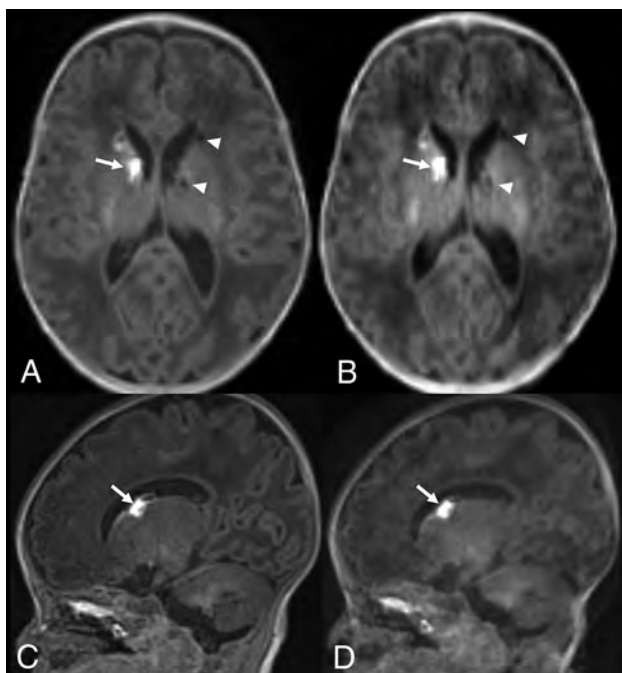


FIG 1. Term-equivalent-age MR imaging of a premature infant (29 weeks' gestation). Nonenhanced standard MPAGE images (A and C) show hyperintense germinal matrix hemorrhage (arrows) in the right caudothalamic groove and cystic changes of germinal matrix hemorrhage (arrowheads) in the left caudothalamic groove. Although wave-T1-MPRAGE images (B and D) demonstrate lower image quality than standard MPAGE, both caudothalamic lesions are well-delineated in nonenhanced wave-T1-MPRAGE images.

MPAGE for both observers ($P < .001$ for each observer) (Online Supplemental Data), Wave-T1-MPRAGE showed sufficient-to-excellent image quality with a score of >2 , except in 1 patient who had poor image quality due to severe motion artifacts and was scored 1 by observer 1. Nonenhanced wave-T1-MPRAGE also demonstrated significantly poor differentiation of GM-WM as well as demarcation of the basal ganglia and cerebral sulci compared with standard MPAGE for both observers (all, $P < .001$ for all parameters and for both observers). Interobserver agreement of nonenhanced wave-T1-MPRAGE was significantly lower than that of standard MPAGE (0.516 versus 0.735 for differentiation of GM-WM; 0.445 versus 0.538 for demarcation of the basal ganglia; and 0.425 versus 0.734 for demarcation of the cerebral sulci). However, motion artifacts and the degree of myelination were not significantly different between the 2 sequences for both observers (all, $P > .05$ for all parameters and for each observer). Furthermore, the degree of myelination had almost perfect agreement between nonenhanced standard MPAGE and wave-T1-MPRAGE for both observers (0.885 for observer one, 0.916 for observer 2) ($P < .001$ for each observer).

Of the 68 patients, 19 patients (27.9%) showed nonenhancing lesions on standard MPAGE images, including germinal matrix hemorrhage (6/19, 31.6%), hemorrhagic and nonhemorrhagic WM injuries (5/19, 26.3%), various types of hemorrhage (2/19, 10.5%), germinal matrix hemorrhage with intraventricular hemorrhage (1/19, 5.26%), periventricular leukomalacia (1/19, 5.26%),

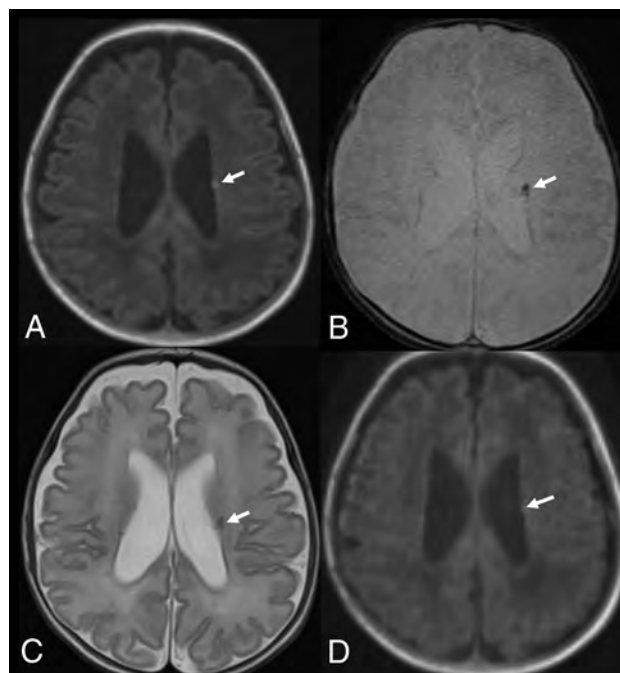


FIG 2. Term-equivalent-age MR imaging of a premature infant (31 weeks' gestation). Nonenhanced standard MPAGE (A) shows decreased cerebral WM volume and a focal T1-hyperintense lesion (arrow) at the left corona radiata. The focal corona radiata lesion (arrows) demonstrates hypointensity on gradient recalled-echo (B) and T2-weighted (C) images. Although the wave-MPRAGE image (D) shows lower image quality than standard MPAGE, the focal T1-hyperintense lesion (arrow) at the left corona radiata is also visible in the wave-MPRAGE image.

congenital anomaly (corpus callosum agenesis) (1/19, 5.26%), congenital cyst (1/19, 5.26%), parenchymal atrophy (1/19, 5.26%), and intraventricular hemorrhage (1/19, 5.26%) (Figs 1 and 2). Each observer missed 1 nonenhancing lesion on nonenhanced wave-T1-MPRAGE, and the 2 lesions were tiny, nonenhancing hyperintensities in the cerebral WM (Fig 3). Visualization of pathologic, nonenhancing lesions was not significantly different between wave-T1-MPRAGE and standard MPAGE ($P = 1.000$ for each observer).

DISCUSSION

In the current study, we performed the clinical evaluation of nonenhanced wave-T1-MPRAGE by assessing the overall diagnostic image quality in infants. Several studies have evaluated the clinical feasibility of wave-T1-MPRAGE;^{5,11,13} however, only a few studies^{11,13} have evaluated the clinical feasibility of wave-T1-MPRAGE in pediatric patients. To our knowledge, there has been no study on the application of nonenhanced wave-T1-MPRAGE images only for infant brain imaging. T1 and T2 properties are known to show significant changes during the first few months after birth, with a marked decrease in the brain-water content.¹⁵ In the present study, wave-T1-MPRAGE had inferior image quality and poorer anatomic demarcation than standard MPAGE. However, there were no significant differences between wave-T1-MPRAGE and standard MPAGE for motion artifacts, degree of myelination, and

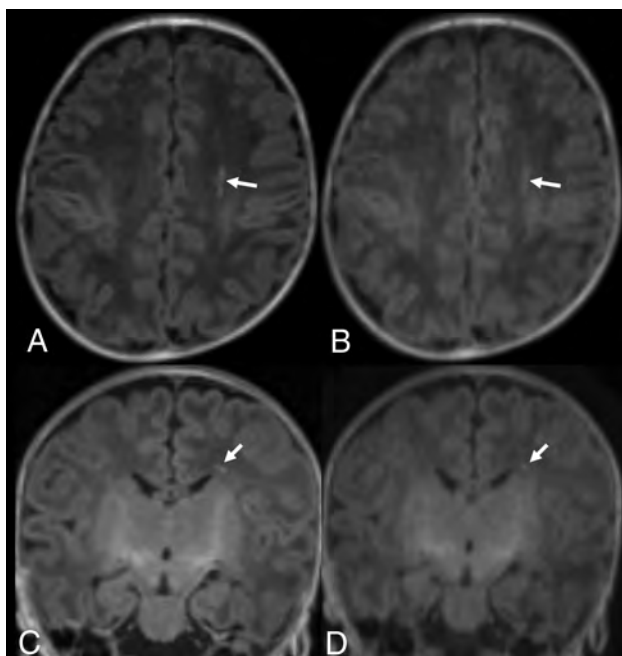


FIG 3. Term-equivalent-age MR imaging of a premature infant (33 weeks' gestation). Nonenhanced standard MPRAGE images (A and C) show a focal hyperintense lesion (arrows) in the left periventricular WM. Although the wave-T1-MPRAGE images (B and D) also show the focal, hyperintense lesion (arrows) in the left periventricular WM, it is less prominently visualized than in the standard MPRAGE; thus, 1 observer missed the lesion.

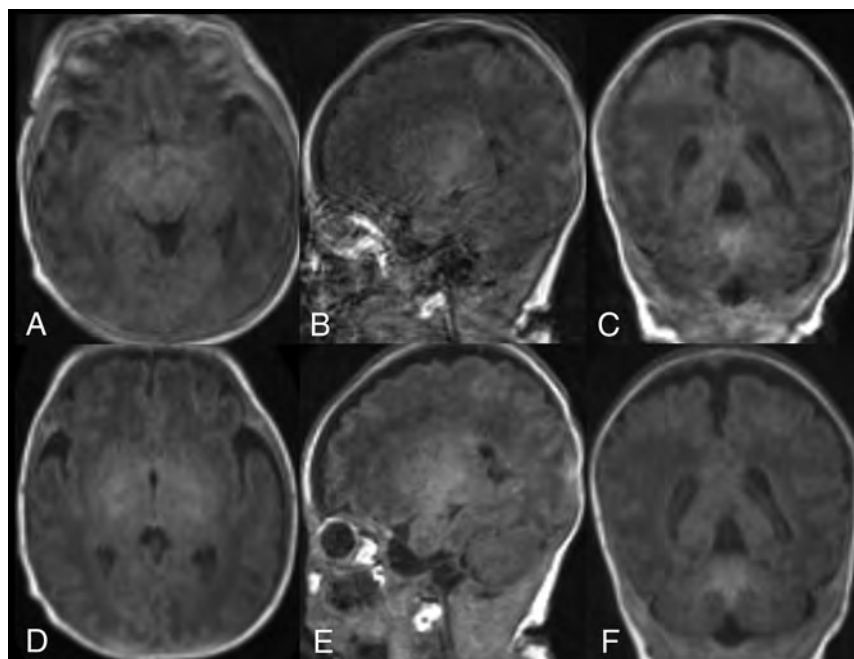


FIG 4. Brain MR imaging of a premature infant (29 weeks' gestation) 1 month after birth. Nonenhanced standard MPRAGE images (A–C) show severe motion artifacts, which are not acceptable for diagnostic use, while wave-T1-MPRAGE (D–F) shows mild motion artifacts, which are acceptable for diagnostic use.

visualization of nonenhancing pathologic lesions. Furthermore, the use of wave-CAIPI reduced the acquisition time by 45% compared with standard MPRAGE (2 minutes 14 seconds versus 4 minutes 55 seconds).

Previous studies^{11,13} that applied wave-CAIPI to MPRAGE in pediatric brain imaging protocol also showed a marked reduction in the total scan time. Tabari et al¹¹ used an even higher acceleration factor than that used in our study (acceleration factor: 6 or 9 versus 4) and reported that wave-T1-MPRAGE had more image noise and was less preferable for the evaluation of anatomic structures compared with standard MPRAGE. However, there were no cases in which enhancing or nonenhancing pathologic lesions were not visualized on wave-T1-MPRAGE. Their results were consistent with those of our study showing lower image quality and poor anatomic demarcation with wave-T1-MPRAGE; however, the visualization of nonenhancing pathologic lesions was not significantly different between wave-T1-MPRAGE and standard MPRAGE.

Unlike our study, Yim et al¹³ reported that there was no significant difference between wave-T1-MPRAGE and standard MPRAGE for the differentiation of GM-WM and demarcation of the basal ganglia and cerebral sulci. Although they applied wave-T1-MPRAGE to pediatric patients, the mean age of their study subjects was much older than that of the infants in our study (71.9 [SD, 60.8] months versus 1.78 [SD, 1.70] months); thus, this factor might account for the different study results. However, the overall image quality of wave-T1-MPRAGE was also significantly lower than that of standard MPRAGE, similar to our study. Furthermore, they showed excellent agreement between wave-T1-MPRAGE and standard MPRAGE for the detection of enhancing and nonenhancing lesions.

Lower image quality of wave-T1-MPRAGE than standard MPRAGE might be associated with more noise in wave-CAIPI images. Previous studies^{8,12,13} have reported that the wave-CAIPI images showed lower SNR in the central coil area than in the peripheral area, and decreasing SNR was associated with an increase in the acceleration factor. Future technical developments in post-processing for denoising and image regularization could minimize the noise amplification and wave-specific blurring artifacts.

In our study, motion artifacts were not significantly different between wave-T1-MPRAGE and standard MPRAGE. However, 2 cases showed severe motion artifacts, which are not acceptable for diagnostic use on standard MPRAGE, while wave-T1-MPRAGE showed mild artifacts, which are acceptable for diagnostic use (Fig 4). Tabari et al¹¹ also demonstrated 1 case with more severe motion artifacts on standard MPRAGE compared with wave-T1-MPRAGE. These

cases show the potential for a faster scan to improve the image quality in motion-prone pediatric patients. According to previous technical studies,^{16,17} wave-CAIPI reduces the overall motion artifacts because it permits each average to be acquired within a

shorter timeframe. Further studies are needed to validate the potential for a faster scan to improve the image quality.

This study has several limitations. First, it has an inevitable selection bias due to its retrospective nature. Future multicenter studies evaluating the clinical feasibility of nonenhanced wave-T1-MPRAGE in a larger number of infants are required for validating our results. Second, we could not randomize the order of wave-T1-MPRAGE and standard MPRAGE because of the retrospective design of the study. Thus, the motion artifacts of wave-T1-MPRAGE might be underestimated in this study. Future studies with a randomized order of image acquisition are needed to validate the results. Third, we could not perform quantitative analyses for the image quality. Because we performed wave-T1-MPRAGE in infants younger than 1 year of age, we could not perform quantitative analyses such as calculating the contrast-to-noise ratio and contrast ratio between the gray-white matter in the 2 types of T1-MPRAGE sequences. Furthermore, we could not perform brain tissue segmentation using commercial software. We tried to measure it automatically using NeuroQuant software (CorTechs Labs), but it was not successful. Because myelination is incomplete and the FOV is relatively small in the infant period and infants are vulnerable to movement, brain tissue segmentation is more difficult compared with that in older pediatric patients.^{18,19}

CONCLUSIONS

Although nonenhanced wave-T1-MPRAGE showed lower overall image quality and anatomic demarcation than standard MPRAGE, the diagnostic performance for the presence of nonenhancing parenchymal lesions was comparable with that of standard MPRAGE. Therefore, nonenhanced wave-T1-MPRAGE could be an alternative method for diagnosing intracranial lesions in infants, with the advantage of marked reduction in the scan time.

Disclosure forms provided by the authors are available with the full text and PDF of this article at www.ajnr.org.

REFERENCES

1. Mugler JP 3rd, Brookeman JR. **Rapid three-dimensional T1-weighted MR imaging with the MP-RAGE sequence.** *J Magn Reson Imaging* 1991;1:561–67 CrossRef Medline
2. Kozak BM, Jaimes C, Kirsch J, et al. **MRI techniques to decrease imaging times in children.** *Radiographics* 2020;40:485–502 CrossRef Medline
3. Ryu K, Baek H, Skare S, et al. **Clinical feasibility of ultrafast contrast-enhanced T1-weighted 3D-EPI for evaluating intracranial enhancing lesions in oncology patients: comparison with standard 3D MPRAGE sequence.** *AJNR Am J Neuroradiol* 2022;43:195–201 CrossRef Medline
4. Vranic JE, Cross NM, Wang Y, et al. **Compressed sensing-sensitivity encoding (CS-SENSE) accelerated brain imaging: reduced scan**

- time without reduced image quality.** *AJNR Am J Neuroradiol* 2019;40:92–98 CrossRef Medline
5. Longo M, Conklin J, Cauley S, et al. **Evaluation of ultrafast wave-CAIPI MPRAGE for visual grading and automated measurement of brain tissue volume.** *AJNR Am J Neuroradiol* 2020;41:1388–96 CrossRef Medline
6. Patel SH, Batchala PP, Schallert K, et al. **3D fast low-angle shot (FLASH) technique for 3T contrast-enhanced brain MRI in the inpatient and emergency setting: comparison with 3D magnetization-prepared rapid gradient echo (MPRAGE) technique.** *Neuroradiology* 2021;63:897–904 CrossRef Medline
7. Baek H, Heo Y, Kim D, et al. **Usefulness of wave-CAIPI for postcontrast 3D T1-SPACE in the evaluation of brain metastases.** *AJNR Am J Neuroradiol* 2022;43:857–63 CrossRef Medline
8. Conklin J, Tabari A, Longo MG, et al. **Evaluation of highly accelerated wave-controlled aliasing in parallel imaging (Wave-CAIPI) susceptibility-weighted imaging in the non-sedated pediatric setting: a pilot study.** *Pediatr Radiol* 2022;52:1115–24 CrossRef Medline
9. Kim HG, Oh SW, Han D, et al. **Accelerated 3D T2-weighted SPACE using compressed sensing for paediatric brain imaging.** *Neuroradiology* 2022 Aug 3. [Epub ahead of print] CrossRef Medline
10. Vanderhasselt T, Naeyaert M, Watté N, et al. **Synthetic MRI of pre-term infants at term-equivalent age: evaluation of diagnostic image quality and automated brain volume segmentation.** *AJNR Am J Neuroradiol* 2020;41:882–88 CrossRef Medline
11. Tabari A, Conklin J, Figueiro Longo MG, et al. **Comparison of ultrafast wave-controlled aliasing in parallel imaging (CAIPI) magnetization-prepared rapid acquisition gradient echo (MP-RAGE) and standard MP-RAGE in non-sedated children: initial clinical experience.** *Pediatr Radiol* 2021;51:2009–17 CrossRef Medline
12. Polak D, Cauley S, Huang SY, et al. **Highly-accelerated volumetric brain examination using optimized wave-CAIPI encoding.** *J Magn Reson Imaging* 2019;50:961–74 CrossRef Medline
13. Yim Y, Chung MS, Kim SY, et al. **Wave-controlled aliasing in parallel imaging magnetization-prepared gradient echo (wave-CAIPI MPRAGE) accelerates speed for pediatric brain MRI with comparable diagnostic performance.** *Sci Rep* 2021;11:13296 CrossRef Medline
14. Aida N, Niwa T, Fujii Y, et al. **Quiet T1-weighted pointwise encoding time reduction with radial acquisition for assessing myelination in the pediatric brain.** *AJNR Am J Neuroradiol* 2016;37:1528–34 CrossRef Medline
15. Dobbing J, Sands J. **Quantitative growth and development of human brain.** *Arch Dis Child* 1973;48:757–67 CrossRef Medline
16. Bilgic B, Gagoski BA, Cauley SF, et al. **Wave-CAIPI for highly accelerated 3D imaging.** *Magn Reson Med* 2015;73:2152–62 CrossRef Medline
17. Polak D, Setsompop K, Cauley SF, et al. **Wave-CAIPI for highly accelerated MP-RAGE imaging.** *Magn Reson Med* 2018;79:401–06 CrossRef Medline
18. Lee SM, Choi YH, Cheon J-E, et al. **Image quality at synthetic brain magnetic resonance imaging in children.** *Pediatr Radiol* 2017;47:1638–47 CrossRef Medline
19. Ha JY, Baek HJ, Ryu KH, et al. **One-minute ultrafast brain MRI with full basic sequences: can it be a promising way forward for pediatric neuroimaging?** *AJR Am J Roentgenol* 2020;215:198–205 CrossRef Medline

Imaging Findings in Children Presenting with CNS Nelarabine Toxicity

 B.L. Serrallach,  E.S. Schafer,  S.K. Kralik,  B.H. Tran,  T.A.G.M. Huisman,  J.N. Wright,  L.A. Morgan, and  N.K. Desai



ABSTRACT

SUMMARY: Nelarabine is a nucleoside analog critical for the treatment of patients with T-cell acute lymphoblastic leukemia/lymphoma. However, clinical peripheral and central neurologic adverse events associated with nelarabine administration have been reported. Neuroimaging of brain neurotoxicity has only been described in very few reports in pediatric patients so far. Six children with diagnosed T-cell acute lymphoblastic leukemia who clinically experienced possible, probable, or definite nelarabine-induced toxicity and underwent spine and/or brain MR imaging were reviewed. Neuroimaging findings showed a mixture of patterns including features of acute toxic leukoencephalopathy (seen in 6 cases), posterior reversible encephalopathy syndrome (2 cases), involvement of deep gray structures (1 case) and brainstem (2 cases), cranial and spinal neuropathy (2 cases each), and myelopathy (2 cases). Even though neuroimaging findings are nonspecific, the goal of this article was to alert the pediatric neuroradiologists, radiologists, and clinicians about the possibility of nelarabine-induced neurotoxicity and its broad neuroimaging spectrum.

ABBREVIATIONS: aBFM = augmented Berlin-Frankfurt-Münster; AE = adverse event; ATL = acute toxic leukoencephalopathy; PA = post (after) nelarabine administration; PRES = posterior reversible encephalopathy syndrome; T-ALL = T-cell acute lymphoblastic leukemia; TI+C = contrast-enhanced T1WI

Nelarabine is a nucleoside analog and was approved by the US Food and Drug Administration for the treatment of patients with relapsed or refractory T-cell acute lymphoblastic leukemia (T-ALL) and T-cell lymphoblastic lymphoma in October 2005¹ and is now considered a gold standard therapeutic treatment option for de novo pediatric T-ALL.² Clinical peripheral and central neurologic adverse events (AEs) associated with nelarabine administration have been described in both the pediatric and adult populations.³⁻⁶ The exact mechanism of nelarabine-associated neurotoxicity is still unclear and presumably multifactorial.⁷ There is only sparse literature addressing neuroimaging findings in nelarabine-induced neurotoxicity in children and adults.⁸⁻¹⁶ To the best of our knowledge, only 9 case reports dealt with neuroimaging findings in nelarabine-associated neurotoxicity,⁸⁻¹⁶ with all 9 reports depicting myelotoxicity, and so far, only 2

articles additionally showed intracranial toxicity in pediatric patients.^{11,13}

Affected patients developed clinical signs and symptoms such as extremity weakness, reduction or loss of sensation, pain, ataxia, abnormal reflexes, and bladder or bowel dysfunction.⁸⁻¹⁷ Devastating and occasionally permanent CNS encephalopathy, often preceded by somnolence, while rare, has also been reported.³ However, neither imaging findings nor biomarkers of toxicity have been comprehensively described. On neuroimaging, an involvement of mainly the dorsal column of the spinal cord^{8-10,12,14,16} and cross-sectionally extending myelopathy or involvement of the lateral column of the myelon have been reported.^{8,13} Imaging findings in nelarabine-associated intracranial toxicity have only been rarely described.^{11,13} Hence, the goal of this article was to describe the neuroimaging spectrum of nelarabine-induced neurotoxicity in a pediatric case series to make the pediatric neuroradiologists, radiologists and clinicians aware of the existence of nelarabine-induced neurotoxicity.

Case Series

Following institutional review board approval, a retrospective study was performed on the pediatric neuroradiology database and electronic health records of 2 quaternary care children's hospitals (January 1, 2010, to September 30, 2021). Informed consent was waived for this purely retrospective study. Inclusion criteria were the following: 1) pediatric cases (< 18 years) with diagnosed

Received July 29, 2022; accepted after revision September 29.

From the Edward B. Singleton Department of Radiology (B.L.S., S.K.K., B.H.T., T.A.G.M.H., N.K.D.) and Department of Pediatrics (E.S.S.), Section of Hematology-Oncology, Texas Children's Hospital and Baylor College of Medicine, Houston, Texas; and Departments of Radiology (J.N.W.) and Neurology (L.A.M.), Division of Child Neurology, Seattle Children's Hospital, Seattle, Washington.

B.L. Serrallach was supported by the Edward B. Singleton endowment.

The authors declare no potential conflicts of interest with respect to the research, authorship, and/or publication of this article.

Please address correspondence to Bettina L. Serrallach, MD, Edward B. Singleton Department of Radiology, Texas Children's Hospital and Baylor College of Medicine, 6701 Fannin St, Suite 470, Houston, TX 77030; e-mail: bettinaserallach@icloud.com

<https://dx.doi.org/10.3174/ajnr.A7692>

T-ALL, 2) who received nelarabine, 3) experienced a neurotoxic event possibly, probably, or definitely nelarabine-related, and 4) had a spinal and/or brain MR imaging performed within 30 days of the clinical symptoms due to suspected nelarabine-induced toxicity. A board-certified pediatric oncologist (E.S.S.) and a board-certified pediatric neurologist (L.A.M.) reviewed the electronic health records and graded and assigned attribution to neurotoxic events on the basis of the current gold standard of AE reporting in the field of oncology:¹⁸ the National Cancer Institute Guidelines for Investigators: Adverse Events Reporting Requirements.¹⁹ Briefly, AEs were identified and graded (1, mild; 2, moderate; 3, severe; 4, life-threatening; 5, death) for severity using the Common Terminology Criteria for Adverse Events guide.²⁰ Then attribution was assigned by the responsible physician using his or her best judgment based on factors including the subject's baseline health status, disease history, comorbidities, and knowledge about the safety profile of the intervention (both personal and in reference to the interventions comprehensive AE and potential risks list¹⁹) in question.²¹

Defined AE categories were the following: "unrelated" (AE is clearly not related to the intervention), "unlikely" (AE is doubtfully intervention-related), "possible" (AE may be intervention-related), "probable" (AE is likely intervention-related), and "definite" (AE is clearly intervention-related).¹⁹ AEs listed as "possibly, probably, or definitely" related to the investigational agent or intervention are considered to have a suspected reasonable causal relationship to the investigational agent/intervention.¹⁹ The MR imaging studies were evaluated by 2 experienced board-certified pediatric neuroradiologists with >10 years and 10 years of experience, respectively (N.K.D. and J.N.W.). Each neuroradiologist performed the review independently at the respective institution. The reviewers, who were not blinded to the patient's medical history, performed a descriptive review of the imaging data. In total 6 patients (6 boys; mean age, 9.67 years; age range, 6–14 years) were included.

Patient 1 was an 8-year-old boy with de novo T-ALL in induction failure who received a 5-day pulse of nelarabine before augmented Berlin-Frankfurt-Münster (aBFM)²² high-risk consolidation.⁵ In the evening post (after) nelarabine administration (PA), he developed an advancing depressed level of consciousness (grade 4, definitely nelarabine-related) during 48 hours, which began with somnolence and progressed to overt hallucinations, confusion, agitation without focus, and finally frank psychosis for which he was intubated and sedated. Initial brain MR imaging, 3 days PA demonstrated mild cerebral volume loss but was otherwise normal. Seizures and dystonia then became evident. Follow-up MR imaging, 12 days PA, demonstrated small patchy areas of T2-weighted/FLAIR hyperintensities in the cortical and subcortical regions of the bilateral posterior temporal and occipital lobes without corresponding diffusion restriction, paralleling posterior reversible encephalopathy syndrome (PRES). There was interval development of T2-weighted hyperintensities within the splenium of the corpus callosum, caudate head, and dorsal thalami, with progressive mild supratentorial volume loss and abnormal T2-weighted/FLAIR signal in the right pons with restricted diffusion.

Initial spine MR imaging showed mild enhancement of the cauda equina nerve roots and paraspinal soft-tissue edema. During this time, the patient became encephalopathic with

progression to coma with minimal brainstem reflexes in addition to axonal neuropathy. Brain MR imaging after 30 days demonstrated interval development of multifocal T2-weighted prolongation in the subcortical WM now involving the bilateral frontal and parietal lobes and, to a lesser extent, the posterior centrum semiovale and periaxial WM, with improvement of cortical edema in the occipital and parietal lobes. Additional T2 hyperintensity was noted within the pons bilaterally and in the medulla oblongata, without a definitive matching diffusion restriction. Slight enhancement of cranial nerve II (cisternal portion) and avid enhancement of cranial nerves III and V were now apparent.

Forty-nine days PA there was progression with confluent non-enhancing T2-weighted/FLAIR hyperintensity throughout the entire supratentorial, subcortical, periventricular, and deep WM, corpus callosum, bilateral caudate head, dorsal thalami, anterior putamen, insula, pons, and medulla oblongata. Figure 1 summarizes the evolution of the MR imaging findings. Enhancement of cranial nerves II, III, and V remained present (Fig 2). Spinal MR imaging showed new abnormal T2 hyperintensity throughout the spinal cord, most prominent in the dorsal aspects (Fig 3), and equivocal enhancement of the nerve roots within the cauda equina as well as paraspinal soft-tissue edema. The CSF examination was negative for leukemic involvement. The symptoms secondary to the nelarabine-induced toxicity only minimally improved for months; without the ability to provide the required aggressive leukemia-directed chemotherapy secondary to his static encephalopathy, the patient eventually died of progressive leukemia.

Patient 2 was a 14-year-old boy diagnosed with early T-cell precursor ALL. Initiation of the best available therapy chemotherapy with dexamethasone, vincristine, and daunorubicin followed. He received a 5-day pulse of nelarabine as salvage chemotherapy. PA, he developed seizures and progressive severe encephalopathy (grade 4, definitely nelarabine-related). Beginning at 9 days PA, neuroimaging demonstrated features of PRES, which resolved spontaneously by 20 days PA. On the day 20 examination and during the subsequent 5 months (6 additional MRIs), the patient developed progressive leukoencephalopathy with increased T2-weighted signal and partially transient diffusion restriction starting in the WM of the bilateral occipital lobes. There was subsequent involvement of the WM of the pre- and postcentral gyri and posterior corpus callosum, progressing to diffuse WM involvement (Fig 4). In addition, T2 hyperintensity was seen in the inferior cerebellar peduncles and along several WM tracts (including the corticospinal tract and medial longitudinal fasciculus). On contrast-enhanced T1WI (T1+C), enhancement of cranial nerves III, V, VI, VII, VIII, IX, and XII was noted (Fig 5). Progressive diffuse cerebral volume loss was evident. In addition, during the course of 5 months, 6 spinal MRIs were performed, showing progressive development of denervation edema and enhancement of the paraspinal muscles, increasing nerve root enhancement, and gradual development of T2 hyperintensity of the dorsal column, corticospinal tract, and spinothalamic tract (Fig 6). The CSF examination was negative for leukemic involvement. The patient died secondary to end-stage recurrent leukemia that was complicated by severe chemotherapy-induced encephalopathy.

Patient 3 was a 10-year-old boy with an isolated CNS relapse of T-ALL. He received 2 doses of high-dose methotrexate,

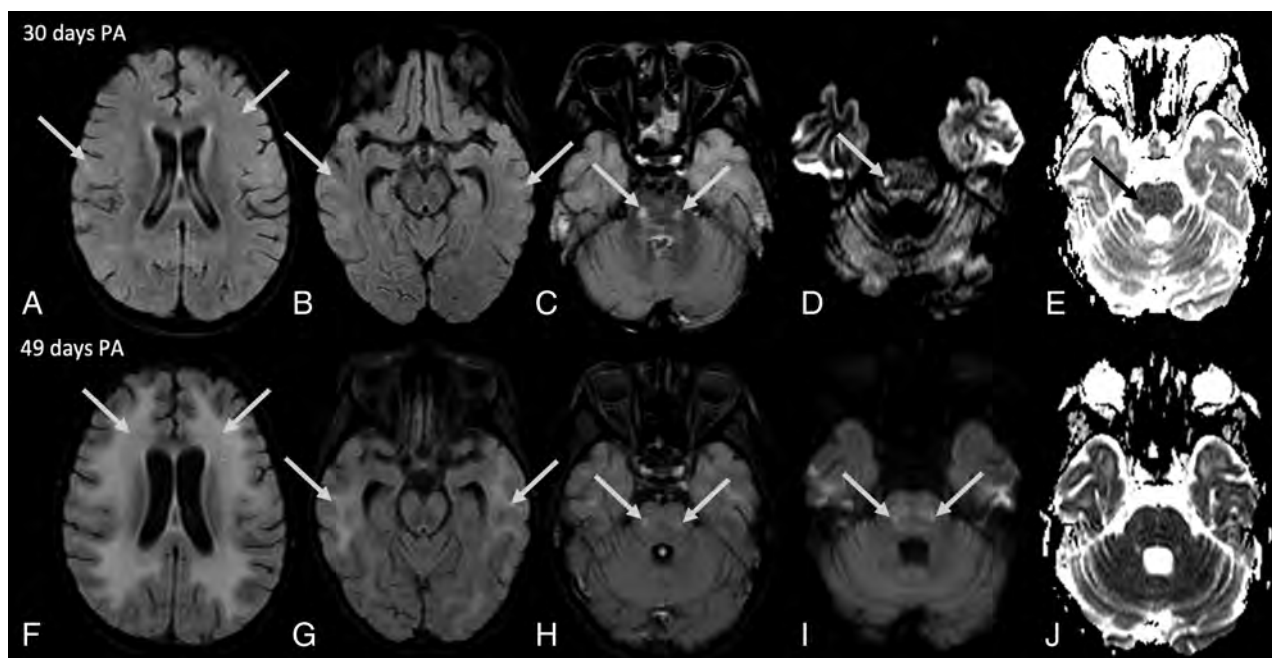


FIG 1. Brain MR images of an 8-year-old boy (patient 1) with definite nelarabine-induced toxicity. The CSF examination was negative for leukemic involvement. Axial FLAIR images with additional fat saturation (A–C and F–H), axial DWI (D and I), and corresponding ADC maps (E and J). Brain MR imaging performed 3 days PA demonstrated mild cerebral volume loss, but findings were otherwise normal (not shown). Follow-up brain MRIs 12 days PA (not shown), 30 days PA (A–E), and 49 days PA (F–J) demonstrate increasingly progressive T2-weighted/FLAIR hyperintensity, beginning as patchy areas in the cortical and subcortical regions (arrows in A and B) and expanding to confluent increased T2-weighted/FLAIR signal throughout the entire supratentorial subcortical, periventricular, and deep WM (arrows in F and G) as well as cortical regions. In addition, there was development of abnormal T2-weighted/FLAIR signal within the pons bilaterally (arrows in C and H) with transient corresponding diffusion restriction in the pons on the right side (arrows in D and E) and increased diffusion signal in the pons bilaterally (arrows in I) without definite decreased intensity on the corresponding ADC map on follow-up 49 days PA (J).

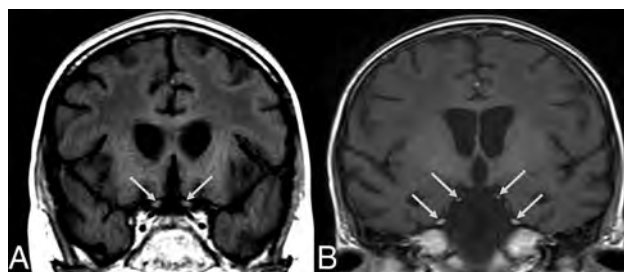


FIG 2. Brain MR images (49 days PA) of an 8-year-old boy (patient 1) with definite nelarabine-induced toxicity. The CSF examination was negative for leukemic involvement. Coronal T1+C (A and B) demonstrates slight enhancement of cranial nerve II (cisternal portion, arrows in A) and avid enhancement of cranial nerves III and V (arrows in B). In addition, the confluent leukoencephalopathy and a slight cerebral volume loss with progressing ex vacuo widening of the ventricles are evident.

followed by the nelarabine, cyclophosphamide, and etoposide regimen.²³ Twenty-one days PA, the patient presented to the emergency department with somnolence (grade 3, probably nelarabine-related), nausea, and vomiting. The only confounding chemotherapy was intrathecal triples (methotrexate, cytarabine, hydrocortisone). Brain MR imaging showed increased T2-weighted/FLAIR signal in the periventricular and deep WM (predominantly frontoparietal) and smaller areas in the left temporal subcortical WM, without corresponding diffusion restriction.

Two follow-up MRIs 139 and 154 days PA demonstrated moderate progression of periventricular and deep WM elevated signal, which was now seen in all lobes, suggestive of acute toxic leukoencephalopathy (ATL) (Fig 7). There was no corresponding diffusion restriction. Progressive cerebral volume loss was evident. At MR imaging, the CSF was negative for leukemic involvement. Nelarabine-induced toxicity fully resolved, but the patient eventually died of graft failure after undergoing a hematopoietic stem cell transplant.

Patient 4, a 10-year-old boy, was diagnosed with de novo T-ALL and CNS involvement and received an intended 5-day pulse of nelarabine followed by aBFM high-risk consolidation.⁵ On day 2 of nelarabine administration, he presented to the emergency department feeling dizzy and falling. Symptoms progressed to hypersomnia (grade 3, probably nelarabine-related), confusion, and short-term memory loss (encephalopathy grade 4, probably nelarabine-related). Brain MR imaging demonstrated subtle increased T2-weighted/FLAIR signal in the WM adjacent to the trigones of the lateral ventricles bilaterally. At MR imaging, the CSF examination was negative for leukemic involvement. The last nelarabine administration was stopped and symptoms slowly resolved and he remains in complete leukemic remission.

Patient 5 was a 10-year-old boy with de novo T-ALL and CNS involvement. He received an intended 5-day pulse of nelarabine followed by an aBFM high-risk consolidation.⁵ On day 3, the patient noted right upper and lower extremity weakness, prompting nelarabine discontinuation. On neurologic consultation, a

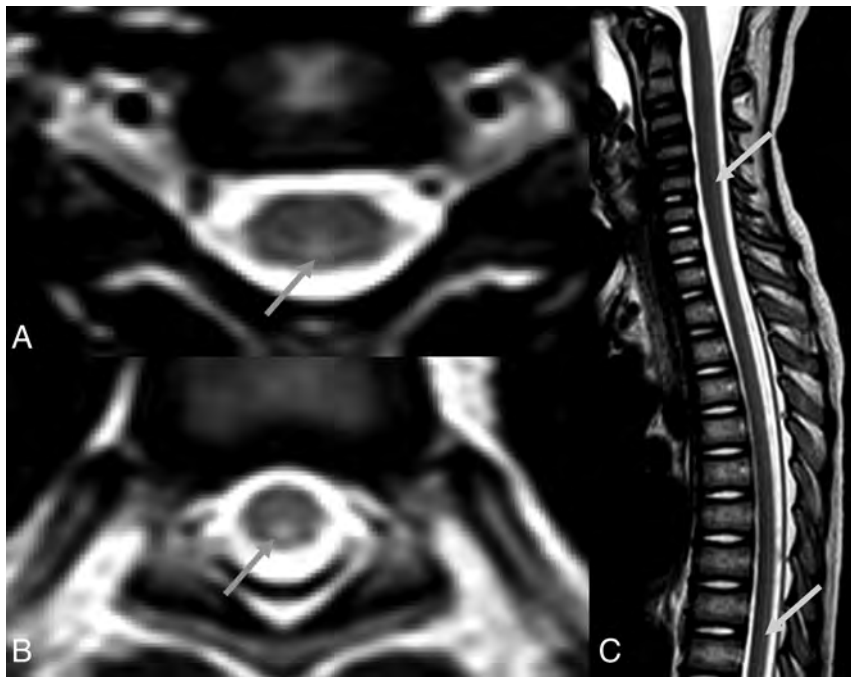


FIG 3. Spinal MR images (49 days PA) of an 8-year-old boy (patient 1) with definite nelarabine-induced toxicity. The CSF examination was negative for leukemic involvement. Axial T2-weighted images (A and B) at the level of C5 and T10, respectively, and sagittal T2-weighted image (C). Images show abnormal T2 hyperintensities throughout the spinal cord, most prominent in the dorsal aspects (arrows in A, B, and C).

distal ascending peripheral neuropathy was diagnosed (grade 3, probably nelarabine-related). Spinal MR imaging findings were unremarkable. Brain MR imaging was additionally performed and revealed subtle T2-weighted/FLAIR hyperintensities in the frontal bilateral centrum semiovale with no corresponding diffusion restriction. At the time of the MR imaging, the CSF examination was negative for leukemic involvement. The patient's nelarabine toxicity fully resolved, and he remains in complete leukemic remission.

Patient 6, a 6-year-old boy, was diagnosed with an isolated CNS relapse of T-ALL after experiencing visual disturbance, headaches, and emesis. Neurologic examination noted minimal facial movements, and an ophthalmologic examination revealed considerable disease involvement of both retinas. He received a 5-day pulse of nelarabine, followed by an aBFM high-risk consolidation.⁵ Thereafter, he received 2 additional 5-day nelarabine monotherapy courses every 28 days. Ten days PA, the patient presented to the emergency department with encephalopathy and hypersomnia (grade 3, possibly nelarabine-related). His brain MR imaging revealed increased T2-weighted signal in the periventricular and deep WM without corresponding diffusion restriction. Follow-up MR imaging 25 days PA demonstrated progression, now including T2-weighted signal abnormalities of the brainstem and central GM. In addition, the MR imaging studies demonstrated bilateral retinal leukemic involvement and presumed parenchymal, leptomeningeal, and pituitary stalk leukemic involvement. The patient's toxicity resolved, but he died shortly thereafter secondary to progressive leukemia.

DISCUSSION

In this case series, we present 6 male pediatric patients with definite (2 cases), probable (3 cases), and possible (1 case) nelarabine-induced neurotoxicity. AEs were acute (during/shortly after) or early delayed (weeks) after nelarabine treatment, and patients presented with signs and symptoms of peripheral and central neurotoxicity. Our cohort showed a mixture of neurotoxic patterns, including imaging features of ATL (seen in 6 cases), PRES (2 cases), involvement of deep GM structures (1 case) and brainstem (2 cases), cranial and spinal neuropathy (2 cases each), and myelopathy (2 cases).

Neurotoxicity can be seen in a wide variety of therapies, including immunosuppressive, chemotherapeutic, antibiotic, and anti-epileptic agents.²⁴⁻²⁷ There are known common primary medication-related neurotoxic injury patterns on MR imaging and several agents that follow these pathognomonic patterns, while other agents lead to mixed or more enigmatic patterns.^{24,25,28}

A common well-defined typical imaging pattern of neurotoxicity is ATL, and MR imaging findings typically demonstrate nonenhancing diffuse symmetric T2-weighted/FLAIR hyperintensities within the deep WM across multiple vascular beds, often associated with restricted diffusion.^{24-26,28} The ATL pattern can be seen with a wide spectrum of different agents, including, among others, methotrexate, 5-fluorouracil, and fludarabine.^{28,29} Presenting symptoms include seizures, encephalopathy, cognitive dysfunctions, and visual impairment.^{28,29} ATL is thought to be caused by microvasculature damage or an excitotoxic effect on the brain.^{28,30}

PRES is another well-known injury pattern to the pediatric brain. PRES is a clinico-radiologic syndrome, clinically presenting with headache, seizures, altered mental status, and visual impairments. On MR imaging, PRES is typically characterized by bilateral vasogenic edema seen as T2-weighted/FLAIR high signal mainly in the posterior cerebral cortex and subcortical WM, followed by involvement of the frontal and temporal lobes.^{24,25,28-30} The brainstem, basal ganglia, or cerebellum is less commonly affected.^{28,29} Atypical imaging findings include leptomeningeal, cortical, or, rarely, nodular enhancement, hemorrhage, and restricted diffusion.^{28,29} Even though PRES is usually reversible on discontinuation of the toxic agent, there are cases with irreversible brain damage.²⁸⁻³⁰ Hypertension, induction chemotherapy, and treatment with immunosuppressive agents such as cyclosporine, tacrolimus, and corticosteroids have been described as risk factors for PRES.²⁹ Normal blood pressure can be found in cases of PRES, especially in the context of chemotherapy, immunosuppressive therapy, and sepsis.²⁹ The exact pathophysiology is still not fully understood. PRES is thought to be due to a failure of

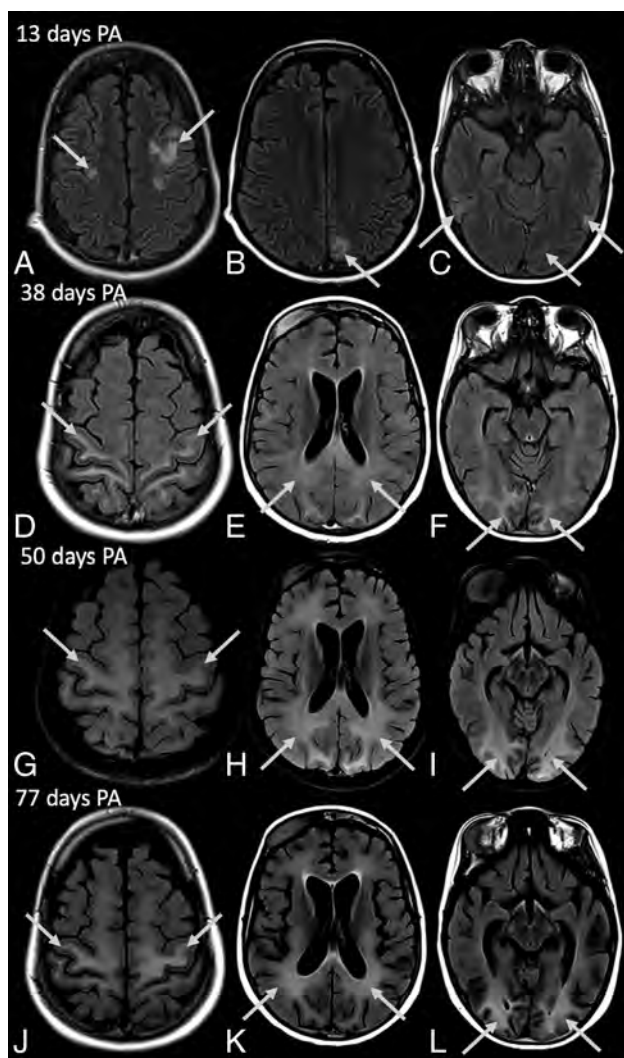


FIG 4. Brain MR images of a 14-year-old boy (patient 2) with definite nelarabine-induced toxicity. The CSF examination was negative for leukemic involvement. Axial FLAIR images (A–F and J–L) and axial FLAIR with additional fat saturation (G–I). During 5 months (exemplary MR images at 13, 38, 50, and 77 days PA are shown), the patient first demonstrated features of PRES in the occipital, parietal, frontal, and temporal lobes (arrows in A–C), followed by progressive leukoencephalopathy with increased T2-weighted/FLAIR signal starting occipitally and spreading across the pre- and postcentral gyrus and parietal and frontal WM to diffusely affect the WM (arrows in D–L). In addition, progressive global atrophy is clearly evident.

cerebrovascular autoregulation with disruption and leakage of the blood-brain barrier.^{24,25,27,28} The paucity of sympathetic innervation in the vertebrobasilar territory is postulated to be the reason for the posterior predilection.^{25,28}

Less common patterns include the involvement of the deep brain structures such as the thalami, basal ganglia, anterior commissure, dentate nuclei, brainstem, and corpus callosum and have already been described with, for example, metronidazole or vigabatrin and result in T2-weighted/FLAIR increased signal and occasionally restricted diffusion.²⁵ Myelopathy can result from different agents, including chemotherapeutics.²⁴ In the acute phase, MR imaging findings may be normal, followed by focal cord swelling with T2-weighted/FLAIR hyperintensities and,

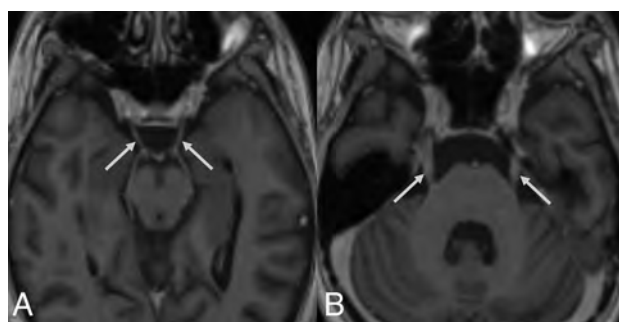


FIG 5. Brain MR images (13 days PA) of a 14-year-old boy (patient 2) with definite nelarabine-induced toxicity. The CSF examination was negative for leukemic involvement. Axial T1+C (A and B) demonstrates exemplary enhancement of the cranial nerves III (arrows in A) and V (arrows in B).

potentially, intramedullary enhancement.²⁴ Peripheral and specific cranial neuropathies are common neurologic complications of cancer treatment, and if MR imaging is performed, they may be seen as contrast enhancement of the nerve root or cranial nerves, respectively.³¹

DWI plays an important role because lesions in ATL or PRES may be more conspicuous on DWI than on conventional T2-weighted/FLAIR images. Although restricted diffusion (cytotoxic edema) is typically evident in ATL and can be an atypical imaging feature of PRES, there is mostly clinical improvement, and in contrast to ischemic-induced cytotoxic edema, a resolution of the diffusion restriction may be seen (Fig 1).^{25,28,29}

Recognizing the involvement or sparing of the subcortical U-fibers can be helpful in determining the etiology and extent of the disease process.³² Subcortical U-fibers, reflecting short association fibers, comprise thin bundles of myelinated nerve fibers that connect the cerebral cortices of adjacent gyri.³² While in the ATL pattern, seen with different agents including methotrexate, the subcortical U-fibers are mostly spared, in PRES they are frequently involved.³² In our cohort, 2 patients had a mixture of neuroimaging findings, including features of PRES and ATL, resulting in both partial sparing and partial involvement of the subcortical U-fibers (Figs 1 and 4). In 4 patients, the neuroimaging findings paralleled the ATL pattern, leading to a sparing of the U-fibers (Fig 7).

Leptomeningeal, cortical, or nodular contrast enhancement may be the result of neurotoxic-induced disruption of the blood-brain and blood-nerve barriers.^{26,31} In our cohort, we found enhancement of several cranial nerves on T1+C (patients 1 and 2), a finding seen in a wide variety of entities including neurotoxicity.³³

A systematic, larger series review of the spectrum of neuroimaging findings seen in nelarabine-induced neurotoxicity of the brain is still lacking. Hartz et al¹³ reported T2-hyperintense lesions in the superior cerebellar peduncles, cerebral peduncles, and pons and within several cranial nerves; postmortem histopathologic samples revealed further damage in the basal ganglia, thalamus, mammillary body, and occipital WM. Ewins et al¹¹ found leukoencephalopathy with T2-weighted/FLAIR signal increase in the subcortical and deep cerebral WM. Similar to Hartz et al, they further reported T2-weighted/FLAIR hyperintensities in the pons, middle cerebellar peduncles, and posterolateral aspect of the medulla oblongata.¹¹

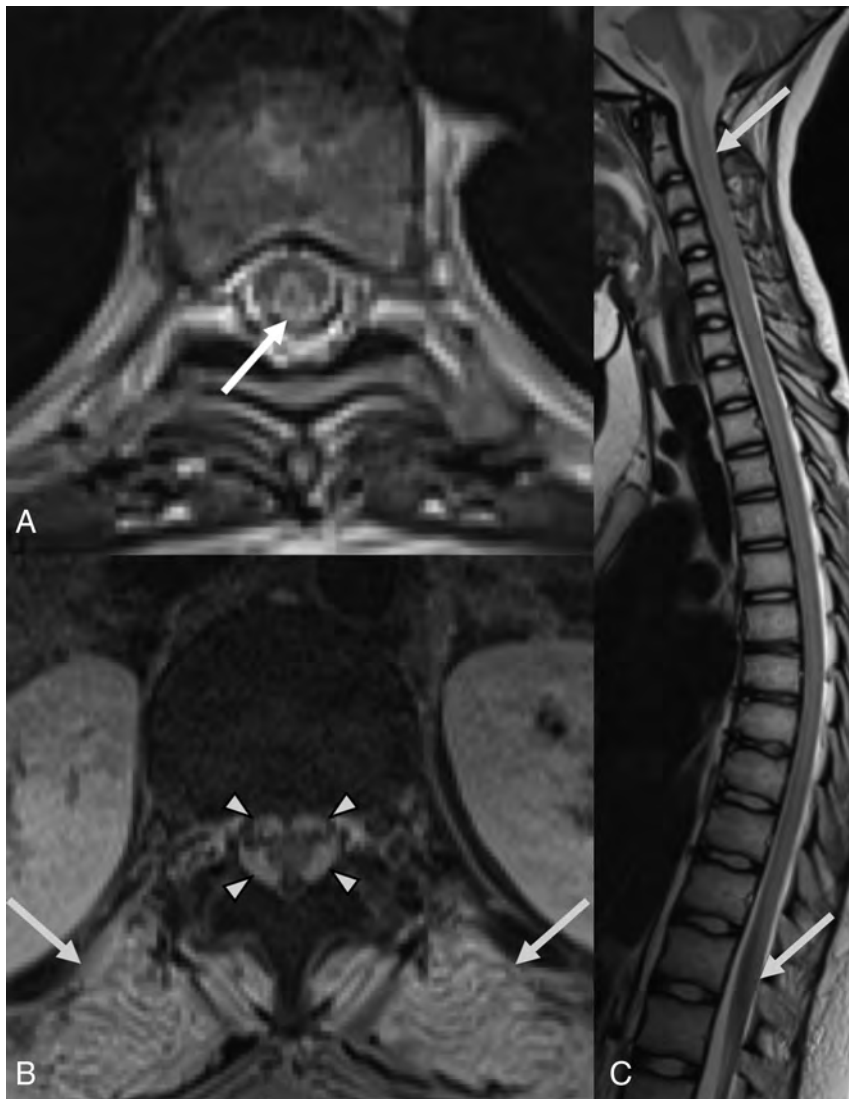


FIG 6. Spinal MR images (38 days PA) of a 14-year-old boy (patient 2) with definite nelarabine-induced toxicity. CSF examination was negative for leukemic involvement. Axial T2-weighted image (A) shows abnormal signal in the bilateral posterior columns (arrow). Axial T1+C (B) at the level of the conus medullaris demonstrates diffuse enhancement of the ventral and dorsal nerve roots of the cauda equina (arrowheads). In addition, there is diffuse enhancement of the paraspinal musculature reflecting acute denervation edema (arrows in B). Sagittal T2-weighted image (C) demonstrates longitudinally extensive dorsal column involvement extending from the cervico-medullary junction through the conus (arrows).

Neurotoxicity is, after myelosuppression, the second most dose-limiting factor of cancer treatment.^{31,34} It is thought to occur by direct damage to neurons and/or glia or indirectly by modifying the surrounding microenvironment, leading, for example, to localized vascular injury and resulting in a disruption of the blood-brain, blood-CSF, and blood-nerve barriers.^{26,31}

All patients in our case series were boys. Interestingly, we found more case reports describing neurotoxicity in males^{9,11,13-16} than in females.^{8,10,12} The significance of this finding is as yet undetermined. In general, the occurrence of nervous system toxicity is based on a broad number of different factors including drug dosage, route of administration, potential interactions with other administered agents or pre-existing structural nervous system diseases, and

the individual patient vulnerability such as, for example, polymorphisms in genes related to neurogenesis.^{9,31}

There is no strict correlation between clinical findings of neurotoxicity and imaging.³⁵ Our case series comprised 1 patient who had only symptoms of peripheral neuropathy but also demonstrated mild leukoencephalopathy on brain MR imaging.

We are aware of several limitations in our study. First, this case series is based on a retrospective study design with a very limited number of pediatric patients and with MR imaging performed on various scanners. Second, because nelarabine is administered as a part of oncologic treatment regimens, correlated imaging findings cannot be attributed to nelarabine-induced toxicity with absolute certainty. Third, due to the retrospective design, we are aware of the lack of statistical data resulting from a prospective inclusion and subsequent MR imaging of all patients treated with nelarabine during the survey period and resulting from a correlation of imaging findings with the dosage or interval of nelarabine administration as well as clinical signs/symptoms. Fourth, no postmortem histologic samples were obtainable for correlation. Finally, no long-term follow-up was available, limiting our analysis on the long-term reversibility of imaging findings as well as limiting the examination of a possible late impact on brain cognition. Subsequent future prospective studies with larger cohorts, standardized imaging protocols, and longitudinal follow-up are needed to answer these questions.

CONCLUSIONS

With this case series, we present 6 pediatric cases of possible, probable, or definite nelarabine-induced neurotoxicity. Patients presented with acute or early-delayed AE after nelarabine treatment with signs/symptoms of peripheral and central neurotoxicity. We found a wide spectrum of neuroimaging findings, including features of PRES, ATL, involvement of deep gray structures and brainstem, cranial and spinal neuropathy, and myelopathy. Even though the mentioned neuroimaging findings are completely nonspecific and cannot be attributed to nelarabine-induced toxicity with absolute certainty, the goal of this case series was to alert the pediatric neuroradiologists, radiologists, and clinicians about the possibility of nelarabine-induced neurotoxicity and its resulting broad neuroimaging spectrum. The awareness of nelarabine-induced neurotoxicity could assist the monitoring

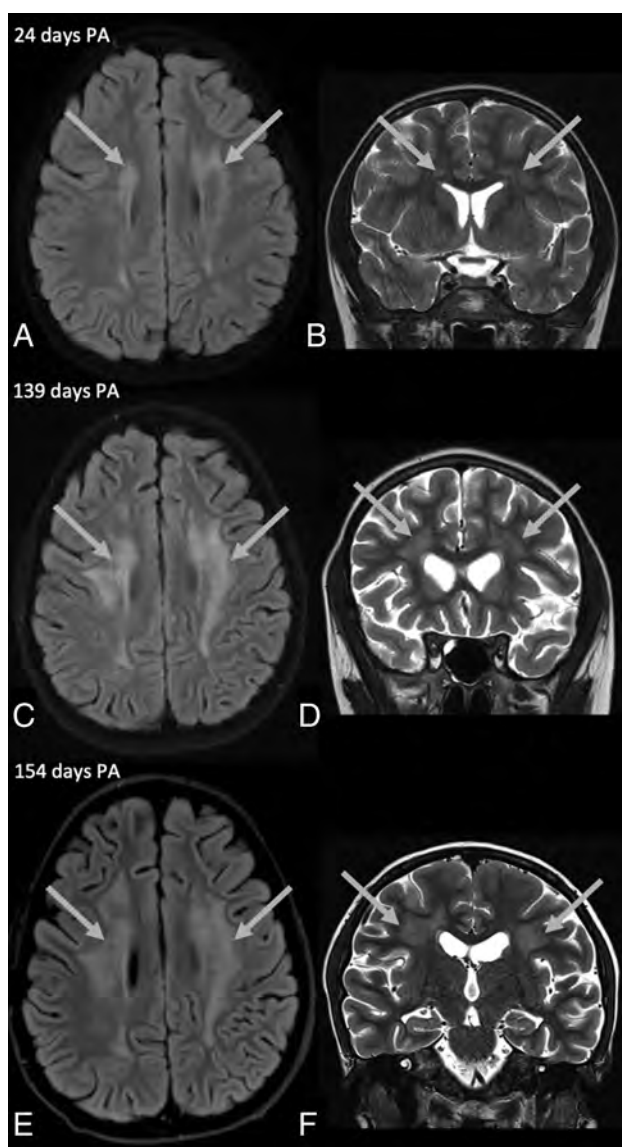


FIG 7. Brain MR imaging obtained in a 10-year-old boy (patient 3) with probable nelarabine-induced toxicity. The CSF examination was negative for leukemic involvement. Axial FLAIR with additional fat-saturation (A, C, and E) and coronal T2-weighted (B, D, and F) images obtained 24, 139, and 154 days PA. Images (A and B) show increased T2-weighted/FLAIR signal in the periventricular and deep WM, predominantly frontoparietal (arrows in A and B). Two follow-up MRIs (C and D and E and F) demonstrate progressive periventricular and deep WM elevated signal (arrows in C, D, E, and F).

of therapeutic interventions because dosage adjustment or agent discontinuation may prevent further neurologic injury.

Disclosure forms provided by the authors are available with the full text and PDF of this article at www.ajnr.org.

REFERENCES

- Gandhi V, Keating MJ, Bate G, et al. Nelarabine. *Nat Rev Drug Discov* 2006;5:17–18 CrossRef Medline
- Teachey DT, O'Connor D. How I treat newly diagnosed T-cell acute lymphoblastic leukemia and T-cell lymphoblastic lymphoma in children. *Blood* 2020;135:159–66 CrossRef Medline
- Berg SL, Blaney SM, Devidas M, et al; Children's Oncology Group. Phase II study of nelarabine (compound 506U78) in children and young adults with refractory T-cell malignancies: a report from the Children's Oncology Group. *J Clin Oncol* 2005;23:3376–82 CrossRef Medline
- DeAngelo DJ, Yu D, Johnson JL, et al. Nelarabine induces complete remissions in adults with relapsed or refractory T-lineage acute lymphoblastic leukemia or lymphoblastic lymphoma: Cancer and Leukemia Group B Study 19801. *Blood* 2007;109:5136–42 CrossRef Medline
- Dunsmore KP, Winter SS, Devidas M, et al. Children's Oncology Group AALL0434: a Phase III randomized clinical trial testing nelarabine in newly diagnosed T-cell acute lymphoblastic leukemia. *J Clin Oncol* 2020;38:3282–93 CrossRef Medline
- Kuhlen M, Bleckmann K, Moricke A, et al. Neurotoxic side effects in children with refractory or relapsed T-cell malignancies treated with nelarabine based therapy. *Br J Haematol* 2017;179:272–83 CrossRef Medline
- Schiff D, Wen PY, van den Bent MJ. Neurological adverse effects caused by cytotoxic and targeted therapies. *Nat Rev Clin Oncol* 2009;6:596–603 CrossRef Medline
- Madhavan AA, Carr CM, Alkhateeb H, et al. Nelarabine-induced myelotoxicity. *Neurology* 2021;96:175–76 CrossRef Medline
- Lalayanni C, Baldoumi E, Papayiannopoulos S, et al. Nelarabine-associated reversible Guillain-Barre-like syndrome or myelopathy in an adult patient with primary refractory T-lymphoblastic lymphoma. *Curr Probl Cancer* 2017;41:138–43 CrossRef Medline
- Kanayama T, Imamura T, Nakagawa N, et al. Pediatric T-ALL complicated by irreversible nelarabine neurotoxicity. *Pediatr Int* 2017;59:843–45 CrossRef Medline
- Ewins K, Malone A, Phelan E, et al. Nelarabine-induced peripheral and central neurotoxicity: can sequential MRI brain imaging help to define its natural history? *Br J Haematol* 2017;179:294–97 CrossRef Medline
- Dua SG, Jhaveri MD. MR imaging in nelarabine-induced myelopathy. *J Clin Neurosci* 2016;29:205–06 CrossRef Medline
- Hartz B, Lobel U, Hagel C, et al. Fatal neurological side-effects with necrosis of spinal cord following nelarabine treatment in a child with relapsed T-cell acute lymphoblastic leukemia. *Am J Hematol* 2013;88:1096–97 CrossRef Medline
- Gollard RP, Selco S. Irreversible myelopathy associated with nelarabine in T-cell acute lymphoblastic leukemia. *J Clin Oncol* 2013;31:e327–31 CrossRef Medline
- Papayannidis C, Iacobucci I, Abbenante MC, et al. Complete paraplegia after nelarabine treatment in a T-cell acute lymphoblastic leukemia adult patient. *Am J Hematol* 2010;85:608 CrossRef Medline
- Alberti P, Parma M, Pioltelli P, et al. Severe, reversible nelarabine-induced neuropathy and myelopathy. *J Peripher Nerv Syst* 2016;21:154–56 CrossRef Medline
- Dunsmore KP, Devidas M, Linda SB, et al. Pilot study of nelarabine in combination with intensive chemotherapy in high-risk T-cell acute lymphoblastic leukemia: a report from the Children's Oncology Group. *J Clin Oncol* 2012;30:2753–59 CrossRef Medline
- Eaton A, Iasonos A, Gounder MM, et al. Toxicity attribution in Phase I trials: evaluating the effect of dose on the frequency of related and unrelated toxicities. *Clin Cancer Res* 2016;22:553–59 CrossRef Medline
- National Cancer Institute. NCI Guidelines for Investigators: Adverse Event Reporting Requirements for DCTD (CTEP and CIP) and DCP INDs and IDEs. https://ctep.cancer.gov/protocoldevelopment/electronic_applications/docs/aeguidelines.pdf. Accessed June 29, 2022
- National Cancer Institute. Common Terminology Criteria for Adverse Events (CTCAE) v5.0. https://ctep.cancer.gov/protocoldevelopment/electronic_applications/ctc.htm. Accessed July 26, 2022
- Le-Rademacher J, Hillman SL, Meyers J, et al. Statistical controversies in clinical research: value of adverse events relatedness to study treatment: analyses of data from randomized double-blind placebo-controlled clinical trials. *Ann Oncol* 2017;28:1183–90 CrossRef Medline

22. Nachman J, Sather HN, Gaynon PS, et al. **Augmented Berlin-Frankfurt-Munster therapy abrogates the adverse prognostic significance of slow early response to induction chemotherapy for children and adolescents with acute lymphoblastic leukemia and unfavorable presenting features: a report from the Children's Cancer Group.** *J Clin Oncol* 1997;15:2222–30 CrossRef Medline
23. Commander LA, Seif AE, Insogna IG, et al. **Salvage therapy with nelarabine, etoposide, and cyclophosphamide in relapsed/refractory paediatric T-cell lymphoblastic leukaemia and lymphoma.** *Br J Haematol* 2010;150:345–51 CrossRef Medline
24. Arrillaga-Romany IC, Dietrich J. **Imaging findings in cancer therapy-associated neurotoxicity.** *Semin Neurol* 2012;32:476–86 CrossRef Medline
25. Iyer RS, Chaturvedi A, Pruthi S, et al. **Medication neurotoxicity in children.** *Pediatr Radiol* 2011;41:1455–64 CrossRef Medline
26. Tan AP. **CAR-T cell therapy-related neurotoxicity in pediatric acute lymphoblastic leukemia: spectrum of imaging findings.** *Pediatr Neurol* 2020;111:51–58 CrossRef Medline
27. Rossi A, Morana G, Gandolfo C, et al. **Neuroradiology of chemotherapeutic neurotoxicity in children.** *Neuroradiol J* 2010;23:183–90 CrossRef Medline
28. Kontzialis M, Huisman T. **Toxic-metabolic neurologic disorders in children: a neuroimaging review.** *J Neuroimaging* 2018;28:587–95 CrossRef Medline
29. Vazquez E, Delgado I, Sanchez-Montanez A, et al. **Side effects of oncologic therapies in the pediatric central nervous system: update on neuroimaging findings.** *Radiographics* 2011;31:1123–39 CrossRef Medline
30. Rossi Espagnet MC, Pasquini L, Napolitano A, et al. **Magnetic resonance imaging patterns of treatment-related toxicity in the pediatric brain: an update and review of the literature.** *Pediatr Radiol* 2017;47:633–48 CrossRef Medline
31. Stone JB, DeAngelis LM. **Cancer-treatment-induced neurotoxicity—focus on newer treatments.** *Nat Rev Clin Oncol* 2016;13:92–105 CrossRef Medline
32. Riley KJ, O'Neill DP, Kralik SF. **Subcortical U-fibers: signposts to the diagnosis of white matter disease.** *Neurographics* 2018;8:234–43 CrossRef
33. Saremi F, Helmy M, Farzin S, et al. **MRI of cranial nerve enhancement.** *AJR Am J Roentgenol* 2005;185:1487–97 CrossRef Medline
34. Magge RS, DeAngelis LM. **The double-edged sword: neurotoxicity of chemotherapy.** *Blood Rev* 2015;29:93–100 CrossRef Medline
35. Bhojwani D, Sabin ND, Pei D, et al. **Methotrexate-induced neurotoxicity and leukoencephalopathy in childhood acute lymphoblastic leukemia.** *J Clin Oncol* 2014;32:949–59 CrossRef Medline

Expanding the Spectrum of Early Neuroradiologic Findings in β Propeller Protein-Associated Neurodegeneration

 A. Papandreou,  A.K.S. Soo,  R. Spaul,  K. Mankad,  M.A. Kurian, and  S. Sudhakar



ABSTRACT

BACKGROUND AND PURPOSE: β propeller protein-associated neurodegeneration (BPAN) is the most common neurodegeneration with brain iron accumulation disorder. Typical radiologic findings are T2 hypointensity in the substantia nigra and globus pallidus, as well as a T1 halolike substantia nigra hyperintense signal surrounding a hypointense central area. However, these findings are often subtle or absent on initial scans, risking diagnostic delay. In this study, we sought to investigate radiologic findings that could aid in the early diagnosis of BPAN.

MATERIALS AND METHODS: A retrospective cohort study was performed in a national referral center, including all pediatric patients with confirmed pathogenic *WDR45* mutations and consistent clinical semiology. MR imaging findings were independently reported by 2 pediatric neuroradiologists.

RESULTS: Fifteen patients were included in the study, and 27 scans were available for review. The initial neuroimaging study was undertaken at a mean age of 3.2 years. Iron deposition was uncommon in patients younger than 4 years of age. Neuroradiologic features from very early on included dentate, globus pallidus, and substantia nigra swelling, as well as a thin corpus callosum and small pontine volume. Optic nerve thinning was also present in all patients.

CONCLUSIONS: Our study highlights the key early MR imaging features of BPAN. Iron deposition in the globus pallidus and substantia nigra is not common in children younger than 4 years of age; clinicians should not be deterred from suspecting BPAN in the presence of the findings described in this study and the appropriate clinical context.

ABBREVIATIONS: BPAN = β propeller protein-associated neurodegeneration; GP = globus pallidus; NBIA = neurodegeneration with brain iron accumulation; SN = substantia nigra

β propeller protein-associated neurodegeneration (BPAN) is emerging as the most common neurodegeneration with brain iron accumulation (NBIA) disorder.¹ It is caused by mutations in *WDR45*, an X-linked gene with a role in early autophagy.^{2,3} Clinically, it typically manifests in infancy with neurodevelopmental delay, epilepsy, autistic-like features, other behavioral issues, stereotypies, and sleep disturbance.

Following a relatively stable course in childhood, BPAN progresses in adolescence or early adulthood with motor regression, dementia, and parkinsonian features.¹⁻³ A core radiologic and neuropathologic hallmark is brain iron accumulation, most prominently in the substantia nigra (SN) but also in the globus pallidus (GP).^{1,3,4} The classically reported MR imaging findings are SN and GP hypointensity on T2-weighted sequences, as well as a halolike SN hyperintensity with a central hypointense band on T1-weighted images.^{3,5,6} Case reports and small cohort studies have described additional BPAN-related findings such as SN swelling, delayed myelination, corpus callosum thinning, deep cerebellar nuclei T2 hyperintensities, and cerebellar atrophy.^{5,7} However, these features are often either absent on initial scans or not specific enough to aid the diagnosis.

BPAN is a rare disease, with an estimated prevalence of 1 in 2–3 million individuals.¹ Due to this rarity and nonspecific clinical presentation at disease onset, the diagnosis is frequently not suspected and only made when nonselective genetic testing (gene

Received August 3, 2022; accepted after revision October 1.

From the Molecular Neurosciences (A.P., A.K.S.S., R.S., M.A.K.), Developmental Neurosciences Programme, Zayed Centre for Research into Rare Disease in Children, University College London Great Ormond Street Institute of Child Health, London, UK; and Departments of Neurology (A.P., A.K.S.S., R.S., M.A.K.) and Neuroradiology (K.M., S.S.), Great Ormond Street Hospital for Children National Health Service Foundation Trust, London, UK.

M.A. Kurian and S. Sudhakar contributed equally to this work.

Please address correspondence to Apostolos Papandreou, MBBS, MRCPCH, PhD, NIHR GOSH BRC Catalyst Fellow, University College London GOS Institute of Child Health, Zayed Centre for Research into Rare Disease in Children, 20c Guilford St, London WC1N 1DZ, UK; e-mail: Apostolos.papandreou@ucl.ac.uk

 Indicates article with online supplemental data.

<http://dx.doi.org/10.3174/ajnr.A7693>

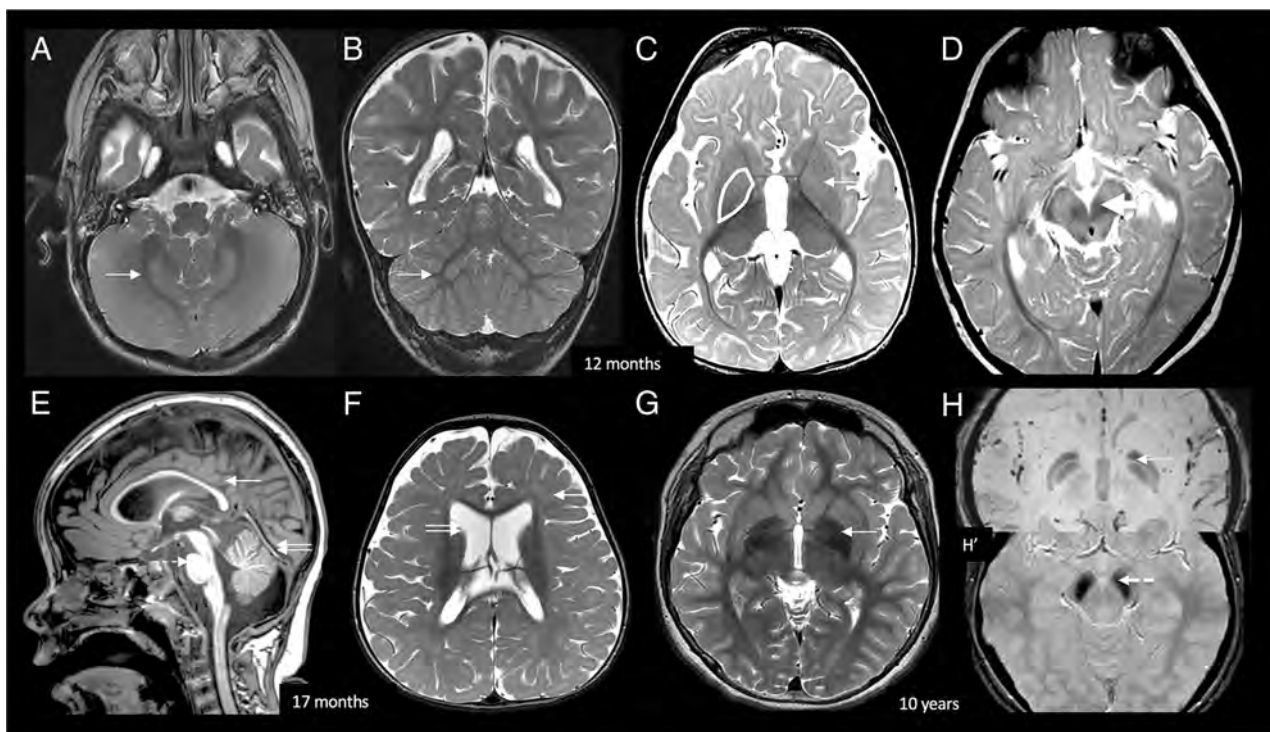


FIG 1. BPAN early radiologic signature. At 12 months of life, axial and coronal T2 (A and B) images show bilateral symmetric dentate nucleus hyperintensity and swelling (*white arrows*). Axial T2 (C) shows bilateral GP swelling and mild hyperintensity (*white arrow*). Bilateral SN swelling and T2 hyperintensity are demonstrated on D (*white arrow*). At 17 months, midsagittal T1 (E) shows diffuse callosal thinning (*white arrow*), a small pons (*dotted arrow*), and superior vermic volume loss (*double arrow*). Axial T2 (F) shows diffuse myelin reduction (*white arrow*) and prominent lateral ventricles (*double arrow*). Delayed myelination was infrequently seen in our cohort (1/15 patients). At 10 years of age, T2 axial image (G) in an older child shows GP iron deposition, which is confirmed on SWI (H). H', Increased iron deposition in the SN. The typically reported T1 halo sign was not seen in our pediatric cohort.

panel, exome, or genome sequencing) reveals a *WDR45* pathogenic variant. Prompt establishment of a BPAN diagnosis is crucial for accurate prognosis, genetic counseling, and appropriate multidisciplinary management.¹ Should disease-specific therapies emerge in the future, as has recently happened for many neuro-metabolic conditions,⁸ the need for an accurate diagnosis will become even more pertinent. However, there are currently no BPAN-specific biochemical or early radiologic markers,^{1,9} and genetic variants of unknown significance can be very difficult to interpret.

In this study, we evaluated a cohort of children with BPAN presenting to a single pediatric center and identified several neuroradiologic keys that may facilitate early diagnosis of this disease.

MATERIALS AND METHODS

The study was approved by the Great Ormond Street Hospital Research and Development Audit Department (reference: 3261). All data were anonymized by the lead care teams at the point of collection, so the study did not otherwise require ethics approval.

We undertook a single-center cohort study in patients with an established diagnosis of BPAN attending a UK pediatric neurogenetic clinic. Inclusion criteria were a disease of childhood onset (0–18 years of life), the presence of a pathogenic *WDR45* genetic variant, and clinical semiology consistent with BPAN. Characterization of the clinical phenotype was undertaken by direct clinical examination and case note review.

Brain MRIs had been performed at either Great Ormond Street Hospital or the referring local hospital and subsequently transferred for neuroradiology review. Different machine models and specifications were used for image acquisition. Brain MRIs were individually reviewed for quality and read by 2 of the authors (K.M. and S.S.), with subsequent discussion for disparate opinions to reach consensus agreement. Specifically, T2-weighted signal intensity and swelling of the dentate nuclei, GP, and SN; T1-weighted signal of the SN; SWI signal changes when available; morphology and size of the brainstem; and the rest of the brain parenchyma were assessed. Optic nerves were also assessed and measured in the prechiasmatic segments on T2- and T1-weighted axial sequences; for this assessment, 3- to 5-mm section-thickness images were used, depending on the availability, while other planes were also used for correct localization. Cerebral and cerebellar atrophy was subjectively graded as mild, moderate, and severe. Cerebellar atrophy was further qualified as vermician (including the gradient, if any), hemispheric, or both. Volumetric analysis was not performed due to insufficient number of cases with volume data. Data were analyzed with descriptive statistics.

RESULTS

Patient Cohort

Sixteen pediatric patients were identified. Some cases have previously been reported (Online Supplemental Data).¹⁰ Neuroimaging was available for 15/16 patients. Mean and median ages at last

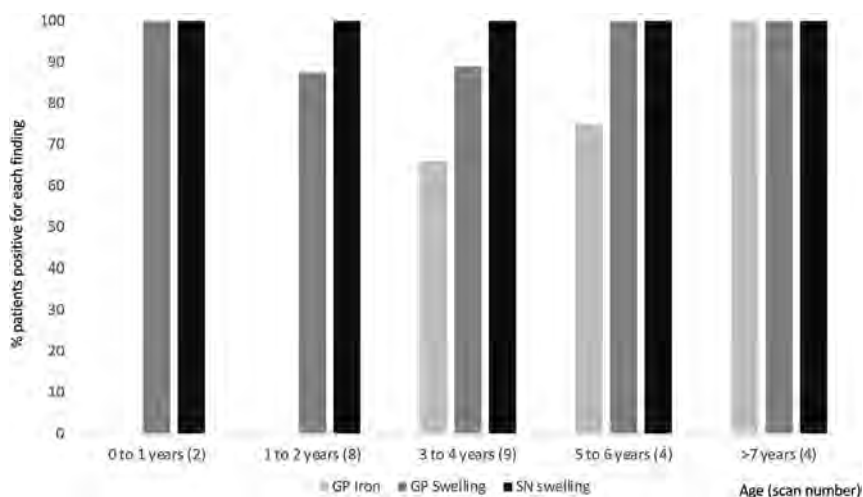


FIG 2. MR imaging findings in relation to age. GP iron deposition is not detectable early on but becomes more prominent after 4 years of age. Conversely, GP and SN swelling are findings present in young patients and persistent later on. GP swelling was absent in 1 patient (B14, 2 scans at 1.5 and 3 years of age) but was otherwise consistently present in all patients and all scans.

clinical review for patients having undergone neuroimaging were 10.5 and 9.95 years, respectively (age range, 3.9–22 years). Mean and median ages at MR imaging were 4.3 and 3 years, respectively. As expected, most (13/15) patients were female. Common clinical manifestations included early infantile-onset developmental delay (15/15), epilepsy (13/15), sleep disturbances (5/15), stereotypies (5/15), and febrile seizures (2/15). Nonstereotypy movement disorders were uncommon, as expected in this age group,¹ with parkinsonian features (1/15), tremor (1/15), dystonia (2/15), and spasticity rarely described.

A single MR imaging brain scan was available for 5/15 cases, whereas 8/15 had 2 scans, and 2/15 had 3 scans in total. Age at scanning ranged from 0.8 to 14 years (mean and median, 3.9 and 3 years, respectively). The first MR imaging was undertaken at a mean age of 3.2 years, whereas the second and third were performed at mean ages of 5.6 and 5.8 years, respectively. The time between follow-up scans ranged from 1.1 to 9.1 years.

Radiologic Findings

Twenty-seven MR imaging scans were available from 15 children (Figs 1–2 and Online Supplemental Data).

First, dentate nucleus abnormalities with T2-weighted hyperintensity and swelling or prominence were seen in 26/27 scans, all except in patient B9 who had only a single scan at 14 years of age.

Regarding the GP, swelling was seen in 26/27 scans, all except in patient B14's second scan at 3 years of age. GP signal T2-hyperintensity was observed in 11/27 scans but mostly in the younger age groups (oldest age at scan: 5 years 5 months of age). In children older than 5 years of age, the GP was either isointense or hypointense compared with the striatum and red nucleus. T1-weighted hyperintensity of the GP was appreciated on only 1 scan at 14 years of age.

Examination of the SN revealed swelling in 22/27, with T2-weighted hyperintensity in 14/27 cases and T2-weighted

hypointensity in 12/27. SN hyperintensity was more common at a younger age (ie, evident in all MR images of children younger than 2 years of age), whereas hypointensity was more prevalent in older patients (ie, in all scans of patients older than 6 years of age). On T1-weighted imaging, SN central hyperintensity was seen in 10/27, whereas peripheral hyperintensity was only present in 1/27 scans at 5 years of age. Progressive findings suggestive of SN iron accumulation, such as evolving T2-weighted hypointensity and T1-weighted central hypointensity with or without peripheral hyperintensity, were evident in 5/15 follow-up scans. The typically reported "T1 halo" sign was not seen in our cohort.

SWI sequences were available in 19/27 scans. Features consistent with iron deposition (eg, hypointensity in minimum-intensity projection algorithm images¹¹) were seen in 12/19 scans, the earliest noted in a patient (B06) at 3 years of age (range, 3–14 years; mean age, 6.8 years; median, 6 years). All cases with features consistent with GP iron deposition (12/19) also showed SN iron deposition. Moreover, iron deposition was not detectable by SWI in early childhood (only evident in 2/12 children younger than 4 years of age, and in 2/15 scans in this age group overall). Conversely, iron was seen on SWI in 6/7 patients (7/8 scans total) imaged at 5 years of age or older. When we compared the GP and SN, the SWI hypointensity was not obviously more prominent in either region. Notably, there were no demonstrable features consistent with iron deposition in the dentate nuclei.

Furthermore, cerebral volume reduction was subjectively seen in 23/27 scans; it was mild in 14/27 (mean age, 4.7 years) and moderate in 9/27 (mean age, 3.6 years) scans. Bicaudate ratio measurements were often high (97th percentile or higher for age and sex¹² in 22/27 scans), confirming the above subjective findings and indicating subcortical WM atrophy (Online Supplemental Data).¹³ Progression of cerebral volume reduction was seen in 1 child (B08, age at the first, second, and third imaging was 3, 6.5, and 7.5 years, respectively). Corpus callosum thinning was evident in all (27/27) patients; this was mainly diffuse but sometimes with body and posterior predominance. Cerebellar atrophy was subjectively seen in 24/27 scans (13/15 patients); it was mild in 15/27 scans, moderate in 9/27 scans, and progressive in 1 of the 11 children (B08) who had serial imaging. The volume reduction was restricted to the superior vermis and superior aspect of the hemispheres in all cases.

Brainstem findings included a small midbrain (less than the first percentile) in all (27/27) scans; a small pons (10th percentile or smaller) in 13/27; and relatively large medulla (75th percentile or larger) in 19/27 scans, compared with reference ranges for age and sex (Online Supplemental Data).¹² In all 27 scans, claval measurements were between 4 and 5 mm; claval prominence was evident in 6/27 scans.

Optic nerve measurements in prechiasmatic segments were lower than the mean expected for age¹⁴ in all children (0–18 months: mean 1.76 mm; 1.5–3 years: mean, 1.8 mm; older than 3 years: mean 2 mm; reference: mean values 2.92 mm, 3.08 mm, >3.2 mm, respectively).

Finally, infrequent MR imaging findings consisted of reduced myelination^{15,16} (patient B07, age 1.3 and 5.4 years at first and second scanning, respectively), large cerebellum (patient B04), and hippocampal sclerosis (patient B14) ($n = 1$ child, each). CT was available in 3 children and showed no pallidonigral calcification (data not shown).

DISCUSSION

BPAN is an X-linked progressive neurodegenerative condition characterized by brain iron accumulation across time; it initially manifests with nonspecific clinicoradiologic features, including absence of iron accumulation in the basal ganglia. Here, we sought to establish an early neuroradiologic signature that could prompt physicians to consider a diagnosis of BPAN. For this purpose, we analyzed MR imaging findings from a pediatric BPAN cohort; to our knowledge, this is the largest single-center pediatric BPAN neuroradiologic study to date.

First, we confirmed the existing literature data that radiologic features consistent with brain iron accumulation were not commonly detectable in early childhood.^{1,5–7} Features of iron deposition were evident in only 2 children younger than 4 years of age (2/15 scans performed at this age) but were seen on SWI in 6/7 patients (7/8 scans total) imaged at 5 years of age or older. Moreover, typically reported findings of T2-weighted GP/SN hypointensity and T1-weighted SN hyperintensity only evolved in a minority of children (and mostly when there were large intervals between follow-up scans). The typically associated hyperintense halo sign was not seen in our cohort.

Conversely, findings present in early disease and in almost all scans analyzed included dentate, GP, and SN T2-weighted hyperintensities and swelling; optic nerve thinning; as well as cerebral and cerebellar atrophy. Delayed myelination was only rarely evident (1/15 patients, consistent with other studies suggesting abnormal myelination in only a minority of patients [28%]).⁶ Additionally, other case reports and small case cohort studies (≤ 4 patients) have also reported GP, SN, and deep cerebellar nuclei T2 hyperintensity and swelling in BPAN, which can be transient and possibly related to pyrexia and seizures.^{5,17} In our cohort, these features tended to persist, with reversal of GP swelling in only 1/11 patients with follow-up imaging.

Although individually nonspecific, the constellation of these neuroimaging findings in the appropriate clinical background is highly suggestive of BPAN, which should be suspected. However, similar findings have recently been reported in patients with biallelic *WIPI2* mutations.¹⁸ Most interesting, *WIPI2* and *WDR45* (also known as *WIPI4*) both belong in the family of WD-repeat proteins interacting with phosphoinositides (WIPI) and have an essential role in the early stages of autophagy.¹⁹ Hence, it would be interesting to see whether similar radiologic patterns emerge in other congenital disorders of autophagy in the future. Moreover, the differential diagnosis should also include other infantile

epileptic encephalopathies, other NBIA, and mitochondrial disorders.^{20,21}

From a pathophysiologic perspective, it is unclear why GP and SN swelling and T2 hyperintensity predominate early on, with iron deposition becoming obvious at a later age. *WDR45* has a role in early autophagy, and it has been postulated that dysfunction in the autophagosome-lysosome degradation pathway might lead to chronic inflammatory changes (that might account for the swelling) and gradual iron deposition in susceptible brain areas.⁷ Overall, more research is needed to better understand the underlying mechanisms linking autophagy, iron metabolism, and neurodegeneration in BPAN.

Other radiologic findings typically associated with other NBIA disorders were also evident in our cohort. First, optic thinning was present in all patients across all scans, and optic nerve measurements were less than the mean expected for age in all cases.¹⁴ Optic nerve thinning has previously been associated with other NBIA disorders, but not specifically with BPAN.^{1,22} Moreover, optic atrophy is only rarely reported in BPAN,^{9,23} and visual electrophysiologic testing has not been systematically reviewed. It is possible that these optic nerve abnormalities might contribute to the visual impairment frequently reported in patients with BPAN in the clinic.^{1,3,9} Second, cerebellar atrophy was a prominent feature in >85% of our patients; similar findings have been reported in other studies,^{6,7,17} though at much lower frequency (eg, 23% in 1 study).⁶ Cerebellar atrophy is also a well-defined radiologic feature of other NBIA disorders such as *PLA2G6*-associated neurodegeneration and fatty acid hydroxylase-associated neurodegeneration.²² Finally, claval prominence was encountered in 4/15 cases (6/27 scans), which has not previously been reported in BPAN and is more typically associated with *PLA2G6*-associated neurodegeneration.²² Notably, the claval prominence in our cohort was milder than that seen in *PLA2G6*-associated neurodegeneration. Overall, the findings of optic nerve thinning, claval hypertrophy, and cerebellar atrophy provide interesting radiologic links with other NBIA disorders.^{1,22} More research is warranted to further characterize these links and elucidate the pathophysiologic mechanisms linking BPAN with other NBIA.

CONCLUSIONS

We describe the largest single-center pediatric neuroimaging study in BPAN. We report a distinct early radiologic signature, with dentate, GP, and SN swelling and T2 hyperintensity, a thin corpus callosum, cerebellar atrophy, optic nerve thinning, and a small pontine volume. The early disease neuroradiologic features described in this study, even in the absence of iron accumulation, should prompt clinicians to include BPAN in the differential diagnosis, especially in the appropriate clinical context. Specifically, lack of iron deposition early in the disease course does not negate the validity of a *WDR45* pathogenic variant identified through genetic testing.

Disclosure forms provided by the authors are available with the full text and PDF of this article at www.ajnr.org.

REFERENCES

1. Wilson JL, Gregory A, Kurian MA, et al; BPAN Guideline Contributing Author Group. **Consensus clinical management**

- guideline for beta-propeller protein-associated neurodegeneration. *Dev Med Child Neurol* 2021;63:1402–09 CrossRef Medline
2. Saitsu H, Nishimura T, Muramatsu K, et al. **De novo mutations in the autophagy gene WDR45 cause static encephalopathy of childhood with neurodegeneration in adulthood.** *Nat Genet* 2013;45:445–49, 449e1 CrossRef Medline
 3. Hayflick SJ, Kruer MC, Gregory A, et al. **Beta-propeller protein-associated neurodegeneration: a new X-linked dominant disorder with brain iron accumulation.** *Brain* 2013;136:1708–17 CrossRef Medline
 4. Paudel R, Li A, Wiethoff S, et al. **Neuropathology of beta-propeller protein associated neurodegeneration (BPAN): a new tauopathy.** *Acta Neuropathol Commun* 2015;3:39 CrossRef Medline
 5. Kimura Y, Sato N, Ishiyama A, et al. **Serial MRI alterations of pediatric patients with beta-propeller protein associated neurodegeneration (BPAN).** *J Neuroradiol* 2021;48:88–93 CrossRef Medline
 6. Adang LA, Pizzino A, Malhotra A, et al. **Phenotypic and imaging spectrum associated with WDR45.** *Pediatr Neurol* 2020;109:56–62 CrossRef Medline
 7. Russo C, Ardisson A, Freri E, et al. **Substantia nigra swelling and dentate nucleus T2 hyperintensity may be early magnetic resonance imaging signs of β -propeller protein-associated neurodegeneration.** *Mov Disord Clin Pract* 2019;6:51–56 CrossRef Medline
 8. Schulz A, Ajayi T, Specchio N, et al. **Study of intraventricular cerliponase alfa for CLN2 disease.** *N Engl J Med* 2018;378:1898–1907 CrossRef Medline
 9. Gregory A, Kurian MA, Haack T, et al. **Beta-propeller protein-associated neurodegeneration.** In: Adam MP, Ardinger HH, Pagon RA, et al. eds. *GeneReviews University of Washington*; 2016
 10. Willoughby J, Duff-Farrier C, Desurkar A, et al. **Functional mRNA analysis reveals aberrant splicing caused by novel intronic mutation in WDR45 in NBIA patient.** *Am J Med Genet A* 2018;176:1049–54 CrossRef Medline
 11. Halefoglu AM, Yousem DM. **Susceptibility weighted imaging: clinical applications and future directions.** *World J Radiol* 2018;10:30–45 CrossRef Medline
 12. Garbade SF, Boy N, Heringer J, et al. **Age-related changes and reference values of bicaudate ratio and sagittal brainstem diameters on MRI.** *Neuropediatrics* 2018;49:269–75 CrossRef Medline
 13. Bermel RA, Bakshi R, Tjoa C, et al. **Bicaudate ratio as a magnetic resonance imaging marker of brain atrophy in multiple sclerosis.** *Arch Neurol* 2002;59:275–80 CrossRef Medline
 14. Maresky HS, Ben Ely A, Bartischovsky T, et al. **MRI measurements of the normal pediatric optic nerve pathway.** *J Clin Neurosci* 2018;48:209–13 CrossRef Medline
 15. McErlean A, Abdalla K, Donoghue V, et al. **The dentate nucleus in children: normal development and patterns of disease.** *Pediatr Radiol* 2010;40:326–39 CrossRef Medline
 16. Barkovich AJ, Raybaud C. *Pediatric Neuroimaging*. 6th ed. Lippincott Williams & Wilkins; 2018
 17. Ishiyama A, Kimura Y, Iida A, et al. **Transient swelling in the globus pallidus and substantia nigra in childhood suggests SENDA/BPAN.** *Neurology* 2018;90:974–76 CrossRef Medline
 18. Maroofian R, Gubas A, Kaiyrzhanov R, et al. **Homozygous missense WIPI2 variants cause a congenital disorder of autophagy with neurodevelopmental impairments of variable clinical severity and disease course.** *Brain Commun* 2021;3:fcab183 CrossRef Medline
 19. Proikas-Cezanne T, Takacs Z, Donnes P, et al. **WIPI proteins: essential PtdIns3P effectors at the nascent autophagosome.** *J Cell Sci* 2015;128:207–17 CrossRef Medline
 20. Gregory A, Hayflick S. **Neurodegeneration with brain iron accumulation disorders: overview.** In: Adam MP, Everman DB, Mirzaa GM, eds. *GeneReviews University of Washington*, 1993
 21. Saneto RP, Friedman SD, Shaw DW. **Neuroimaging of mitochondrial disease.** *Mitochondrion* 2008;8:396–413 CrossRef Medline
 22. Hayflick SJ, Kurian MA, Hogarth P. **Neurodegeneration with brain iron accumulation.** *Handb Clin Neurol* 2018;147:293–305 CrossRef Medline
 23. Rathore GS, Schaaf CP, Stocco AJ. **Novel mutation of the WDR45 gene causing beta-propeller protein-associated neurodegeneration.** *Mov Disord* 2014;29:574–75 CrossRef Medline

Early Neuroimaging Markers in β Propeller Protein-Associated Neurodegeneration

Neurodegeneration with brain iron accumulation (NBIA) encompasses a heterogeneous group of rare diseases characterized by abnormal progressive iron accumulation in the basal ganglia (BG), movement disorders, and cognitive disability.¹ β propeller protein-associated neurodegeneration (BPAN) is, to date, the most common NBIA disorder.² It is caused by mutations in an X-linked gene, *WDR45*, which has an important role in autophagy.³⁻⁵ The disease is more common in females and typically presents with global developmental delay, speech impairment, abnormal gait, sleep disturbances, and epilepsy in childhood followed by severe dystonia, parkinsonism, and progressive dementia in young adulthood, though the phenotypic spectrum is broader and includes Rett syndrome, developmental and epileptic encephalopathy, and intellectual disability.⁶⁻⁸ The distinctive BPAN neuroradiologic findings are well-known in adolescence and adulthood and include the following: T2, T2*, and SWI hypointensity in the substantia nigra (SN) and GP; the “halo sign” on T1WI (ie, a symmetric hyperintense signal surrounding a thin, dark, central band in the SN and cerebral peduncles), which is pathognomonic for BPAN; a normal or thinned corpus callosum; and mild-to-moderate global cerebellar and cerebral atrophy.^{5,6,9,10} Findings of neuroimaging performed during early childhood are nearly all normal. In some cases, delayed myelination, nonspecific cerebellar and cerebral atrophy, and a thin corpus callosum have been described.^{2,11} Because the clinical features are not specific and imaging may not demonstrate the classic findings at a young age, the diagnosis is often made with gene panel or exome sequencing, which reveals a mutation in *WDR45*.⁷

The article by Papandreou et al,¹² published in the current issue of the *American Journal of Neuroradiology*, represents an important retrospective cohort study of 15 pediatric patients with a confirmed pathogenetic *WDR45* variant, focusing on early MR imaging features. The authors took into account a vast amount of neuroimaging findings and reported that early neuroradiologic features, in most cases, included dentate nuclei hyperintensity, GP and SN swelling and hyperintensity, as well as a thin corpus callosum and cerebral and cerebellar atrophy of various degrees. They also observed optic nerve thinning and an unusually small midbrain. Iron deposition was uncommon in patients younger

than 4 years of age and was never present in children younger than 3 years of age but was evident in almost all patients scanned at 5 years of age or older.

A minor criticism of the present work¹² was that the assessment of cerebral volume reduction, detected in most of the cases, was subjective and is actually unreliable due to lack of age-matched controls. Indeed, in children, subjective assessment of brain atrophy can be difficult because of craniocerebral disproportion. Furthermore, the authors report midbrain atrophy in all cases, whereas no obvious midbrain atrophy is observed in Fig 1 and, in general, in any of the other cases reported.¹³⁻¹⁶ Another critical issue concerns the assessment of optic nerve atrophy in axial sections, which we do not consider correct because in general, errors occur when measuring optic nerve diameter on axial images.

If one focuses on the GP and SN and on the iron-sensitive sequences (T2WI, T2*WI, and SWI), the most relevant evidence is that iron deposition is not present early in the course of the disease but accumulates with time. In particular, there is some sort of evolution of signal abnormalities in these structures from early childhood to early adulthood that could be considered highly specific for BPAN and that is represented by an early, enlarged GP and SN appearance, with slight T2 hyperintensity and subsequent progressive iron accumulation. SWI sequences can detect very early iron deposition. Iron accumulates in the SN, emerging as the most affected nucleus and, to a lesser extent, in the GP. On T2WI or SWI, the SN results are usually more hypointense compared with the GP, a feature that may help distinguish BPAN from other forms of NBIA.⁹ Sometimes, on the T1WI the halo sign is evident in the SN.^{2,5} This is a late sign, and its absence in the article by Papandreou et al¹² could be related to the young age of their patients (0–18 years of life).

Most interesting, it is not entirely clear why GP and SN enlargement and T2 hyperintensity predominate early. In four of our cases,¹⁵ we interpreted the swelling as a very early inflammation caused by dysfunction in the autophagy-lysosome complex. The authors¹² also noted that similar neuroimaging findings have been reported in cases with biallelic *WIP12* mutations,¹⁷ which, similar to *WDR45* (also known as *WIP14*), belong to the family of WD-repeat proteins, which have an essential role in the early

stages of autophagy. We agree that it would be interesting to ascertain whether a similar neuroimaging pattern is present in other congenital autophagy disorders. It is certain, however, that neuroinflammation evolves rapidly in neurodegeneration and progressive iron deposition,^{18,19} highlighting how the first abnormality is due to cellular damage, while the accumulation of iron is probably only a late epiphenomenon of the degenerative process.^{20,21}

Concerning other characteristic imaging signs, in all the cases reported by Papandreou et al¹² and, in general in most of the cases reported in the literature,^{13–16} transient or persistently observed T2-hyperintense signal in the dentate nuclei is a typical finding that helps suggest the diagnosis. This is a finding not seen in other NBIA disorders and, from a pathophysiologic point of view, also probably related to chronic inflammatory changes.¹² Delayed myelination is a transient, frequent finding that normalizes during the follow-up MR imaging;^{11,14} thin corpus callosum and cerebellar atrophy (present in other NBIA disorders) are prominent features frequently seen in early childhood¹¹ but are nonspecific signs.

We believe one of the major merits of the present study is stressing the important role of early MR imaging findings to reach an accurate and early BPAN diagnosis for the best multidisciplinary management of these patients. Even though normal brain MR imaging findings do not exclude BPAN in a young child, early neuroimaging markers highlighted by Papandreou et al,¹² such as GP and SN swelling, dentate nuclei T2 hyperintensity, corpus callosum thinning, and cerebral and cerebellar atrophy in the appropriate clinical context, may strongly suggest the diagnosis. In agreement with the authors, we believe that it is important to not discard a variant of *WDR45* in the absence of iron accumulation in the basal ganglia in the early stages of the disease.

REFERENCES

- Hogarth P. Neurodegeneration with brain iron accumulation: diagnosis and management. *J Mov Disord* 2015;8:1–13 CrossRef Medline
- Wilson JL, Gregory A, Kurian MA, et al; BPAN Guideline Contributing Author Group. Consensus clinical management guideline for beta-propeller protein-associated neurodegeneration. *Dev Med Child Neurol* 2021;63:1402–09 CrossRef Medline
- Saito H, Nishimura T, Muramatsu K, et al. De novo mutations in the autophagy gene *WDR45* cause static encephalopathy of childhood with neurodegeneration in adulthood. *Nat Genet* 2013;45:445–49, 449e1 CrossRef Medline
- Hong Huan Hor C, Luen Tang B. Beta-propeller protein-associated neurodegeneration (BPAN) as a genetically simple model of multifaceted neuropathology resulting from defects in autophagy. *Rev Neurosci* 2019;30:261–77 CrossRef Medline
- Hayflick SJ, Kruer MC, Gregory A, et al. Beta-propeller protein-associated neurodegeneration: a new X-linked dominant disorder with brain iron accumulation. *Brain* 2013;136:1708–17 CrossRef Medline
- Adang LA, Pizzino A, Malhotra A, et al. Phenotypic and imaging spectrum associated with *WDR45*. *Pediatr Neurol* 2020;109:56–62 CrossRef Medline
- Chen H, Qian Y, Yu S, et al. Early onset developmental delay and epilepsy in pediatric patients with *WDR45* variants. *Eur J Med Genet* 2019;62:149–60 CrossRef Medline
- Kano K, Yamanaka G, Muramatsu K, et al. Beta-propeller protein-associated neurodegeneration presenting Rett-like features: a case report and literature review. *Am J Med Genet A* 2021;185:579–83 CrossRef Medline
- Kruer MC, Boddaert N, Schneider SA, et al. Neuroimaging features of neurodegeneration with brain iron accumulation. *AJNR Am J Neuroradiol* 2012;33:407–14 CrossRef Medline
- Ichinose Y, Miwa M, Onohara A, et al. Characteristic MRI findings in beta-propeller protein-associated neurodegeneration (BPAN). *Neur Clin Pract* 2014;4:175–77 CrossRef Medline
- Rathore GS, Schaaf CP, Stocco AJ. Novel mutation of the *WDR45* gene causing beta-propeller protein-associated neurodegeneration. *Mov Disord* 2014;29:574–75 CrossRef Medline
- Papandreou A, Soo A, Spaul R, et al. Expanding the spectrum of early neuroradiological findings in β propeller protein-associated neurodegeneration. *AJNR Am J Neuroradiol* 2022;43:1810–14 CrossRef Medline
- Chard M, Appendino JP, Bello-Espinosa LE, et al. Single-center experience with beta-propeller protein-associated neurodegeneration (BPAN): expanding the phenotypic spectrum. *Mol Genet Metab Rep* 2019;20:100483 CrossRef Medline
- Kimura Y, Sato N, Ishiyama A, et al. Serial MRI alterations of pediatric patients with beta-propeller protein associated neurodegeneration (BPAN). *J Neuroradiol* 2021;48:88–93 CrossRef Medline
- Russo C, Ardisson E, Freri E, et al. Substantia nigra swelling and dentate nucleus T2 hyperintensity may be early magnetic resonance imaging signs of β -propeller protein-associated neurodegeneration. *Mov Disord Clin Pract* 2019;6:51–56 CrossRef Medline
- Christoforou S, Christodoulou K, Anastasiadou V, et al. Early-onset presentation of a new subtype of β -propeller protein-associated neurodegeneration (BPAN) caused by a de novo *WDR45* deletion in a 6-year-old female patient. *Eur J Med Genet* 2020;63:103765 CrossRef Medline
- Maroofian R, Gubas A, Kaiyryzhano V, et al. Homozygous missense *WIPI2* variants cause a congenital disorder of autophagy with neurodevelopmental impairments of variable clinical severity and disease course. *Brain Commun* 2021;3:fcab183 CrossRef Medline
- Liu Z, Shen H, Lian T, et al. Iron deposition in substantia nigra: abnormal iron metabolism, neuroinflammatory mechanism and clinical relevance. *Sci Rep* 2017;7:1–7 CrossRef
- Thomsen MS, Andersen MV, Christoffersen PR, et al. Neurodegeneration with inflammation is accompanied by accumulation of iron and ferritin in microglia and neurons. *Neurobiol Dis* 2015;81:108–18 CrossRef Medline
- Bodea L, Wang Y, Linnartz-Gerlach B, et al. Neurodegeneration by activation of the microglial complement: phagosome pathway. *J Neurosci* 2014;34:8546–56 CrossRef Medline
- Ward RJ, Zucca FA, Duyen JH, et al. The role of iron in brain ageing and neurodegenerative disorders. *Lancet Neurol* 2014;13:1045–60 CrossRef Medline

© L. Chiapparini

Neuroradiology Unit

Fondazione Institute for

Hospitalization and Healthcare Policlinico San Matteo

Pavia, Italy

Neuroradiology Unit

Fondazione Institute for

Hospitalization and Healthcare Istituto Neurologico Carlo Besta

Milan, Italy

© G. Zorzi

Department of Paediatric Neuroscience

Fondazione Institute for Hospitalization and
















Healthcare Istituto

Neurologico Carlo Besta

Milan, Italy

<http://dx.doi.org/10.3174/ajnr.A7723>

Synthetic MR Imaging–Based WM Signal Suppression Identifies Neonatal Brainstem Pathways in Vivo

 V.U. Schmidbauer,  M.S. Yildirim,  G.O. Dovjak,  M. Weber,  M.C. Diogo,  R.-I. Milos,  V. Giordano,  F. Prayer,  M. Stuempflen,  K. Goeral,  J. Buchmayer,  K. Klebermass-Schrehof,  A. Berger,  D. Prayer, and  G. Kasprian



ABSTRACT

BACKGROUND AND PURPOSE: Multidynamic multiecho sequence–based imaging enables investigators to reconstruct multiple MR imaging contrasts on the basis of a single scan. This study investigated the feasibility of synthetic MRI-based WM signal suppression (syWMSS), a synthetic inversion recovery approach in which a short T1 suppresses myelin-related signals, for the identification of early myelinating brainstem pathways.

MATERIALS AND METHODS: Thirty-one cases of neonatal MR imaging, which included multidynamic multiecho data and conventionally acquired T1- and T2-weighted sequences, were analyzed. The multidynamic multiecho postprocessing software SyMRI was used to generate syWMSS data (TR/TE/TI = 3000/5/410 ms). Two raters discriminated early myelinating brainstem pathways (decussation of the superior cerebellar peduncle, medial lemniscus, central tegmental tract, and medial longitudinal fascicle [the latter 3 assessed at the level of the pons]) on syWMSS data and reference standard contrasts.

RESULTS: On the basis of syWMSS data, the decussation of the superior cerebellar peduncle (31/31); left/right medial lemniscus (31/31; 30/31); left/right central tegmental tract (19/31; 20/31); and left/right medial longitudinal fascicle (30/31) were reliably identified by both raters. On the basis of T1-weighted contrasts, the decussation of the superior cerebellar peduncle (14/31); left/right medial lemniscus (22/31; 16/31); left/right central tegmental tract (1/31); and left/right medial longitudinal fascicle (9/31; 8/31) were reliably identified by both raters. On the basis of T2-weighted contrasts, the decussation of the superior cerebellar peduncle (28/31); left/right medial lemniscus (16/31; 12/31); left/right central tegmental tract (23/31; 18/31); and left/right medial longitudinal fascicle (15/31; 14/31) were reliably identified by both raters.

CONCLUSIONS: syWMSS data provide a feasible imaging technique with which to study early myelinating brainstem pathways. MR imaging approaches that use myelin signal suppression contribute to a more sensitive assessment of myelination patterns at early stages of cerebral development.

ABBREVIATIONS: CTT = central tegmental tract; DSCP = decussation of superior cerebellar peduncle; FGATIR = fast gray matter acquisition T1 inversion recovery; GA = gestational age; ICC = intraclass correlation coefficient; MDME = multidynamic multiecho; ML = medial lemniscus; MLF = medial longitudinal fascicle; syWMSS = synthetic MRI-based WM signal suppression

At early stages of brain maturation, myelination proceeds in a stepwise manner.¹ In the fetal period, myelin is first detectable in the spinal cord at about 16 weeks of gestation, followed by


its developmental course cephalad along the projection tracts.¹ Thus, postnatally, the brainstem has the most myelinated tissue, while brain myelination is relatively scarce supratentorially.^{1,2}

Prematurity is considered a matter of increasing interest in the medical field.³ Because preterm birth interferes with the normal brain maturation processes, imaging modalities that enable a reliable assessment of the structural and biochemical aspects of cerebral development are greatly needed.^{4–8} Currently, MR imaging is considered the diagnostic mainstay for the assessment of human brain myelination in vivo.^{9,10} However, the subtle effects of small myelin quantities on conventional T1- and T2-weighted MR imaging contrasts currently limit qualitative evaluations and, therefore, impede insight into certain pathologic conditions linked to myelin delays in the neonatal period.¹

Received July 27, 2022; accepted after revision October 14.

From the Department of Biomedical Imaging and Image-Guided Therapy (V.U.S., M.S.Y., G.O.D., M.W., R.-I.M., F.P., M.S., D.P., G.K.) and Comprehensive Center for Pediatrics (V.G., K.G., J.B., K.K.-S., A.B.), Department of Pediatrics and Adolescent Medicine, Division of Neonatology, Pediatric Intensive Care and Neuropediatrics, Medical University of Vienna, Vienna, Austria; and Department of Neuroradiology (M.C.D.), Hospital Garcia de Orta, Almada, Portugal.

Please address correspondence to Gregor Kasprian, MD, Department of Biomedical Imaging and Image-Guided Therapy, Medical University of Vienna, Waehringer Guertel 18-20, 1090 Vienna, Austria; e-mail: gregor.kasprian@medu.niwi.ac.at

 Indicates article with online supplemental data.

<http://dx.doi.org/10.3174/ajnr.A7710>

Table 1: Study sample

Neonates	n = 31
GA	
Born <28 + 0 ^a	n = 23
Born 28 + 0–36 + 6 ^a	n = 3
Born ≥37 + 0 ^a	n = 5
Characteristics	
Female/male	13:18
GA at birth ^b	27 + 0 (23 + 4–41 + 6)
PMA at MR imaging ^b	37 + 3 (34 + 5–47 + 2)

Note:—PMA indicates postmenstrual age (ie, GA plus chronologic age³⁷).

^a Data (weeks + days) presented as total number.

^b Data (weeks + days) presented as median and range (in parentheses).

Recent advances in synthetic imaging provide multiple contrasts (ie, TR, TE, and TI are synthetically defined in retrospect) based on the tissue-specific properties (ie, relaxation time and spin density) determined via a single multidynamic multiecho (MDME) sequence.^{8,11–16} Novel inversion recovery acquisition strategies (ie, fast gray matter acquisition T1 inversion recovery [FGATIR]) use a short TI to suppress the myelin signal, therefore improving discrimination of brainstem pathways and identification of myelinated tissue.¹⁷ While this approach has proved beneficial primarily in a neurosurgical imaging setting, there is a lack of information on the applicability of such contrasts for the assessment of neonatal brain myelination.^{17–19}

This study aimed to investigate the feasibility of synthetic MRI-based WM signal suppression (syWMSS) for the qualitative evaluation of neonatal brainstem anatomy and brain myelination in vivo. Thus, 2 raters independently analyzed brainstem pathways on syWMSS data and conventionally acquired, standard-of-reference, T1- and T2-weighted MR imaging contrasts. In addition, brain myelination was assessed semiquantitatively on both imaging modalities (MDME-based versus conventionally acquired MR imaging contrasts). The results based on syWMSS data and conventionally acquired MR imaging contrasts were compared.

MATERIALS AND METHODS

Ethics Approval

The local ethics commission approved the protocol of this retrospective study. All guardians provided written, informed consent for neonatal brain MR imaging before scanning and agreed to the scientific use of the acquired imaging data.

Study Cohort

Between January 2018 and September 2020, forty-three cases of neonatal MR imaging (without detectable intracranial pathology), which included MDME data and conventionally acquired T1- and T2-weighted MR images, were collected. Neuroimaging was performed at the Department of Neuroradiology of Vienna General Hospital, Medical University of Vienna. All neonates were referred for brain MR imaging by the Department of Pediatrics and Adolescent Medicine of the same tertiary care center. Indications for MR imaging included routine imaging in former preterm infants at approximately term-equivalent ages and clinical suspicion of cerebral injury. However, only neonates in whom MR imaging ruled out pathologic abnormalities were included in this research. Studied patients (Table 1) have been reported previously. However, these studies focused on different research objectives.^{8,11,15,16}

Neonatal MR Imaging, MDME Sequence, and MR Imaging Data Postprocessing

MR imaging was performed according to the institutional feed-and-wrap protocol, and infants were bedded on a vacuum mattress to reduce motion-related artifacts. All infants were imaged using a standardized neonatal MR imaging protocol (Online Supplemental Data) on an Ingenia (Philips Healthcare) 1.5T MR imaging system. The MDME sequence (axial plane, acquisition time = 5 minutes 24 seconds, TR = 3309 ms, TE = 13/100 ms, voxel = 0.9 × 1 × 4 mm, FOV = 200 × 165 × 109 mm; section number = 22, gap = 1 mm, echo-train = 10, pixel/Hz = 1.366/159.0; sense factor = 2) uses 2 repeat acquisition phases to derive information about tissue-specific relaxation time properties and proton density (phase a: application of a section-selective saturation pulse [flip angle = 120°] to saturate 1 section; and phase b: application of section-selective refocusing pulses [flip angle = 80°] and section-selective excitation pulses [flip angle = 90°] to generate a series of spin-echoes for another section).^{14,20,21} The MDME data postprocessing software SyMRI (Version 11.2; SyntheticMR) was used to generate syWMSS data. Although the acquisition procedures for the original FGATIR sequences and MDME data differ, the contrast parameters to suppress myelin-related signals synthetically were applied according to the descriptions by Sudhyadhom et al²² and Shepherd et al¹⁷ (TR/TE/TI = 3000/5/410 ms).

Assessment of Brainstem Pathway Anatomy and Semiquantitative Evaluation of Myelination

Before evaluating MR imaging data, a critical visual review was performed by 1 neonatal imaging expert with 15 years of experience. Imaging data of inferior quality (ie, motion-degraded MR imaging acquisitions) were excluded from this investigation. In case multiple sequences were available (eg, multiple T1-weighted contrasts and so forth), those that provided the best image quality were used for further analysis. Two readers (observer 1 with 4 years of experience and observer 2 with 2 years of experience with neonatal MR imaging) independently discriminated early myelinating brainstem pathways at a given level on the basis of syWMSS data and conventionally acquired T1- and T2-weighted contrasts. Before the analysis, an evaluation was performed regarding the identifiability/ability to discriminate various brainstem tracts in terms of spatial resolution. Accordingly, the following anatomic tracts were defined for qualitative assessment: decussation of superior cerebellar peduncle (DSCP); left/right medial lemniscus (ML) (for the readers to identify separately at the level of the medulla oblongata [decussation of the ML], pons, and midbrain); left/right central tegmental tract (CTT) (for the readers to identify at the level of the pons); and left/right medial longitudinal fascicle (MLF) (for the readers to identify at the level of the pons).

Furthermore, both readers assessed myelination of the brainstem (ie, medulla oblongata, pons, and midbrain) and the posterior limb of the internal capsule semiquantitatively on syWMSS data and conventionally acquired T1- and T2-weighted contrasts using a previously described scoring system (Online Supplemental Data).⁸ The allocated points for each region were totaled, resulting in a myelin total score.⁸

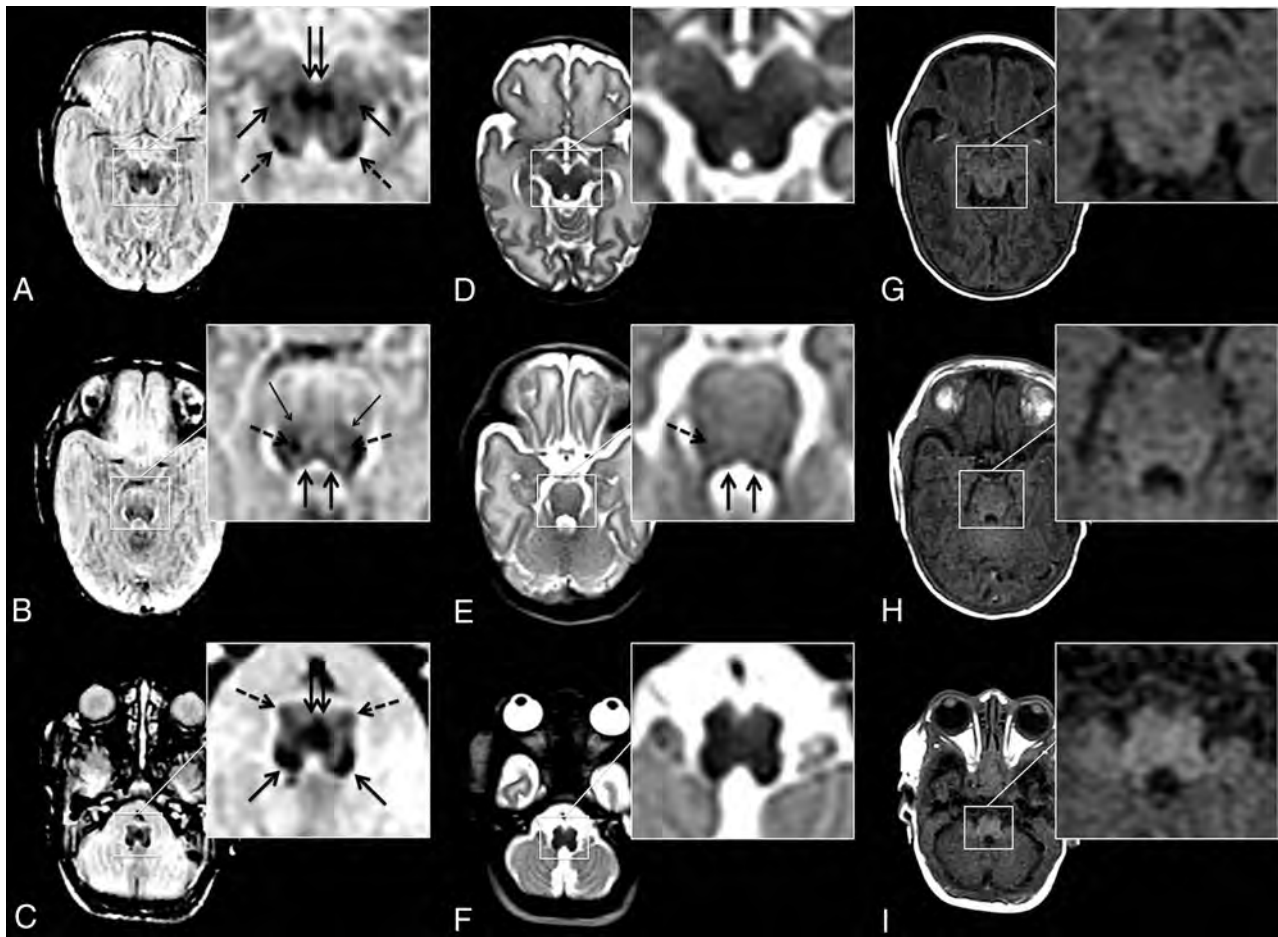


FIG 1. Neonatal brainstem anatomy is shown in an infant born at 24 + 3 weeks' GA (MR imaging at 38 + 0 weeks postmenstrual age) at the level of the midbrain (A, D, and G), pons (B, E, and H), and the medulla oblongata (C, F, and I) on syWMSS data (A, B, and C), conventional T2-weighted contrasts (D, E, and F), and conventional T1-weighted contrasts (G, H, and I). syWMSS data (A, B, and C) depict early myelinating structures: DSCP (double arrow in A); ML (arrows in A; thin arrows in B) and its decussation (double arrow in C); inferior colliculus (dotted arrows in A); CTT (dotted arrows in B); MLF (arrows in B); amiculum of the inferior olivary nucleus (dotted arrows in C); and inferior cerebellar peduncle (arrows in C). Pontine bundles are depicted sufficiently on T2-weighted imaging data (D, E, and F) (CTT [dotted arrow in E] and MLF [arrows in E]). On the basis of T1-weighted contrasts, a reliable delineation of brainstem pathways is limited (G, H, and I). Center/width at the reader's discretion.

A window center/width default setting was defined at 26.0/26.0 for syWMSS data. For the discrimination of brainstem pathway anatomy, the readers had the opportunity to adjust the windowing at their discretion. Semiquantitative assessment of myelination was performed at a baseline setting with a narrowed center/width range to keep myelin-related signal intensity differences perceivable and objective across the cohort.

Statistical Analysis

SPSS Statistics for Macintosh (IBM; Version 25.0) was used for statistical analyses at a significance level of $\alpha = 5\%$ ($P < .05$). All analyses were performed as proposed by 1 expert in biomedical statistics with 30 years of experience in the field. For the analysis of brainstem pathway anatomy, the percentage of interrater agreement (ie, total percentage agreement regardless of whether tracts had been correctly or not correctly identified) and the total number of tracts reliably identified by both observers (ie, only the number of tracts that had been correctly identified by both raters) were reported. To summarize overall agreement for the semiquantitative scoring

(myelin total score) of neonatal brain myelination, we calculated an intraclass correlation coefficient (ICC). ICC values were interpreted as proposed by Koo and Li²³ (<0.5 , poor; 0.5–0.75, moderate; 0.75–0.9, good; and >0.9 , excellent). In addition, a Pearson correlation analysis was performed to detect relationships between semiquantitative myelin assessment (myelin total score) and gestational age (GA) at birth.

RESULTS

Non-motion-degraded syWMSS data were provided in 31/43 (72.09%) cases (Table 1). In 12/43 (27.91%) neonatal MDME sequence acquisitions, image quality was not sufficient for further analysis due to severe movement-related artifacts.

Assessment of Brainstem Pathway Anatomy

On the basis of syWMSS data, the percentage agreement between both raters for the discrimination of brainstem pathway anatomy ranged between 74.19% and 100% (number of tracts correctly identified by both readers; range, 18–31).

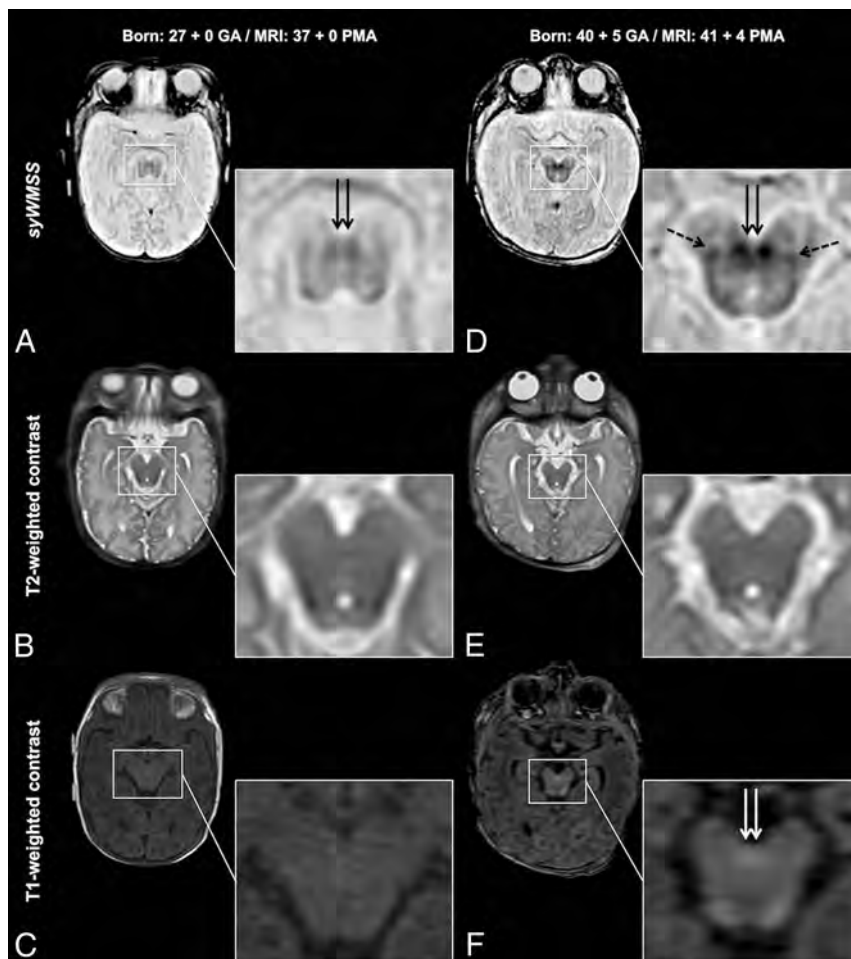


FIG 2. Myelin-related signal intensity differences between preterm-born neonates and term-born infants are demonstrated. The midbrain is shown in a neonate born at 27 + 0 weeks' GA (MR imaging at 37 + 0 weeks postmenstrual age) (A, B, and C) and an infant born at 40 + 5 weeks' GA (MR imaging at 41 + 4 weeks postmenstrual age) (D, E, and F) on syWMSS data (A and D), conventional T2-weighted contrasts (B and E), and conventional T1-weighted contrasts (C and F). While proceeding myelination is perceivable on conventional T1-weighted MR contrasts (DSCP, double arrows in F), the information provided by conventional T2-weighted MR imaging contrasts regarding myelin-related signal alterations is limited. In contrast to standard-of-reference MR imaging acquisitions, WM signal suppression enables a reliable identification and assessment of progressively myelinating structures in the course of brain development (DSCP, double arrows in A and D and ML, dotted arrows in D). Center/width at the default setting.

On the basis of conventionally acquired T1-weighted contrasts, the percentage agreement between both raters for the discrimination of brainstem pathway anatomy ranged between 48.39% and 80.65% (number of tracts correctly identified by both readers; range, 0–22).

On the basis of conventionally acquired T2-weighted contrasts, the percentage agreement between both raters for the discrimination of brainstem pathway anatomy ranged between 45.16% and 93.55% (number of tracts correctly identified by both readers; range, 3–28) (Fig 1 and Online Supplemental Data).

Semiquantitative Evaluation of Myelination

Significant correlations were observed between semiquantitative myelin scorings based on syWMSS data and GA at birth: $r = 0.887$ ($P < .001$) (rater 1); $r = 0.737$ ($P < .001$) (rater 2).

Significant correlations were observed between semiquantitative myelin scorings based on conventionally acquired T1-weighted contrasts and GA at birth: $r = 0.546$ ($P = .002$) (rater 1); $r = 0.495$ ($P = .005$) (rater 2).

Insignificant correlations were observed between semiquantitative myelin scorings based on conventionally acquired T2-weighted contrasts and GA at birth: $r = 0.117$ ($P = .530$) (rater 1); $r = 0.039$ ($P = .837$) (rater 2) (Figs 2 and 3).

The ICC analysis for semiquantitative myelin scoring is shown in Table 2.

DISCUSSION

In this investigation, the neonatal brainstem anatomy of early myelinating pathways was studied using synthetically generated MR imaging contrasts in which a short TI suppresses the signal of myelinated tissue.¹⁷ Furthermore, semiquantitative assessment of myelination was performed. This study demonstrates the feasibility of syWMSS data for the identification of infratentorial WM tracts and the assessment of myelination at early developmental stages. While this novel imaging approach depicts neonatal brainstem bundles and myelinated tissue in excellent detail, conventionally acquired, standard-of-reference, T1- and T2-weighted MR imaging contrasts did not approach a similar performance.

In the second trimester, myelin becomes histologically detectable in numerous brainstem tracts.¹ While several rules govern the patterns of myelin development, the fact that tract myelination initiates according to its functionality is of note.¹ Thus, myelin deposition in neonatal brainstem pathways

corresponds to essential functional circuits that ensure sensory processing and general movement at early developmental stages.^{1,2} Even in the absence of gross brain damage, prematurity interferes with the regular brain-maturation processes.²⁴ In patients with a preterm birth history, the GA at birth correlates with the neurologic outcome, characterized by more severely impaired development in subjects born extremely prematurely (ie, <28 weeks of gestation).^{6,7} Therefore, delayed myelination of brainstem pathways and disturbances in neuronal circuit integrity are associated with future neurologic deficits.^{6,7,25–29} Moreover, certain pathologic conditions in the neonatal period appear directly linked to maturational delays of brainstem structures.^{30–32} Evidence suggests myelination deficits and maturational delay as the potential risk factors for sudden infant death syndrome in preterm neonates.^{32,33} Thus, the detection of myelin delay and the

identification of damage to these early myelinating brainstem tracts are of clinical relevance.

In this study, early myelinating brainstem pathways were more reliably identified on the basis of syWMSS data compared with the current standard-of-reference. Furthermore, assessment of brain myelination on the basis of syWMSS data revealed higher interrater agreement and stronger correlation with GA at

birth than conventional MR imaging contrasts, suggesting a more reliable evaluation of cerebral development. While the potential of this sophisticated inversion recovery approach has not yet been fully investigated in pediatric cohorts, studies in the adult human brain have already revealed remarkable results. As demonstrated by Shepherd et al,¹⁷ the suppression of myelin-related signals improves the identifiability of brainstem pathway anatomy and highly myelinated structures. Therefore, such contrasts have proved beneficial before neurosurgical interventions (eg, deep brain stimulation) because these data allow a more reliable targeting of anatomic structures.^{18,19,22} The data presented here suggest that myelin signal suppression represents a feasible imaging approach for the in vivo tracking of WM pathway maturation, which is key to obtaining knowledge about normal and aberrant myelination processes throughout development.

Premature delivery accounts for approximately 7% of all births.³⁴ Neonatal brain MR imaging can provide biomarkers for future development.³⁵ However, conventional, MR imaging-based neuroimaging currently lacks sensitivity for the evaluation of delayed brain myelination.⁸ The investigated imaging approach provides the opportunity to reliably characterize myelin development in vivo and may help to identify patients in need of special postnatal effort to prevent adverse future outcomes. However, this prospect was outside the scope of the present study and needs to be elucidated in future investigations.

This study has several limitations. Due to the retrospective design, the included sample size was small. In addition, most included infants were born extremely prematurely, limiting selective investigations of this imaging approach in infants born at different gestational stages. Furthermore, there was no possibility of performing a blinded data analysis. While myelin signal suppression was applied using a synthetic MR imaging-based approach, no original sequences were used to acquire imaging data in which WM-related signals are suppressed (ie, FGATIR).^{17,22} Thus, the comparison of conventional and synthetic WM signal suppression was not possible. Nonetheless, as demonstrated previously, SyMRI-based imaging data provide a diagnostic accuracy comparable with that of conventionally acquired sequences.¹¹ However, the technical features (eg, resolution, section thickness, acquisition time, and so forth) of conventional T1- and T2-weighted imaging data and MDME sequence acquisitions differed (synthetic MR imaging-based data versus conventionally acquired sequences). Thus, partial volume effects may have increased the identifiability of certain brainstem pathways in various areas of interest, while several fibers could not be reliably identified (eg, limited identifiability of the MLF at the level of the midbrain), most likely due to resolutional issues.

Furthermore, although only MR imaging acquisitions of superior quality were included, small movement-related artifacts were still present in most of the cases. However, subject motion is still a pervasive and difficult-to-manage issue in neonatal neuroimaging.

Nonetheless, overall, these limitations did not affect the primary outcome of this investigation. Finally, this study did not elaborate on the correlations between diffusion tensor-based assessments of brainstem pathway anatomy and the presented imaging approach.



FIG 3. Pearson correlations between GA at birth (x-axis) and myelin scorings (performed by rater 1) (y-axis) based on syWMSS data ($r = 0.887$, $P < .001$) (A), conventionally acquired T1WI contrasts ($r = 0.546$, $P = .002$) (B), and conventionally acquired T2WI contrasts ($r = 0.117$, $P = .530$) (C).

Table 2: ICC for semiquantitative myelin scoring^a

	ICC
syWMSS	Moderate agreement: 0.535 (0.032–0.788)
Conventional T1-weighted	Poor agreement: 0.404 (–0.034–0.694)
Conventional T2-weighted	Poor agreement: –0.050 (–0.315–0.259)

^a Numbers in parentheses are 95% confidence intervals.

However, currently, the applicability of neonatal brainstem tractography is limited, foremost due to motion-related issues.³⁶ Nonetheless, the relationship between advanced diffusion MR imaging fiber-tracking and MDME-based mapping is of highest interest and need to be assessed in future works.

CONCLUSIONS

Synthetically generated MR imaging contrasts with suppressed myelin-related signals provide a feasible imaging technique for the in vivo study of neonatal brainstem pathway anatomy. Furthermore, the presented MR imaging approach enables a more reliable evaluation of postnatal brain maturation compared with conventionally used, standard-of-reference, sequence-derived T1- and T2-weighted contrasts. WM signal suppression contributes to a more sensitive neuroradiologic assessment of myelination at a very early stage of cerebral development.

Disclosure forms provided by the authors are available with the full text and PDF of this article at www.ajnr.org.

REFERENCES

- van der Knaap MS, Valk J. *Magnetic Resonance of Myelination and Myelin Disorders*. 3rd ed. Springer-Verlag; 2005
- Yakovlev P, Lecours A. The myelogenetic cycles of regional maturation of the brain. In: Minkowski A, ed. *Regional Development of the Brain in Early Life*. Blackwell Scientific; 1967:3–70
- Taylor GL, O'Shea TM. **Extreme prematurity: risk and resiliency**. *Curr Probl Pediatr Adolesc Health Care* 2022;52:101132 CrossRef Medline
- Ibrahim J, Mir I, Chalak L. **Brain imaging in preterm infants <32 weeks gestation: a clinical review and algorithm for the use of cranial ultrasound and qualitative brain MRI**. *Pediatr Res* 2018;84:799–806 CrossRef Medline
- Parikh NA. **Advanced neuroimaging and its role in predicting neurodevelopmental outcomes in very preterm infants**. *Semin Perinatol* 2016;40:530–41 CrossRef Medline
- Glass HC, Costantino AT, Stayer SA, et al. **Outcomes for extremely premature infants**. *Anesth Analg* 2015;120:1337–51 CrossRef Medline
- Marlow N, Wolke D, Bracewell MA, et al; EPICure Study Group. **Neurologic and developmental disability at six years of age after extremely preterm birth**. *N Engl J Med* 2005;352:9–19 CrossRef Medline
- Schmidbauer V, Geisl G, Diogo M, et al. **SyMRI detects delayed myelination in preterm neonates**. *Eur Radiol* 2019;29:7063–72 CrossRef Medline
- van der Knaap MS, Valk J. **MR imaging of the various stages of normal myelination during the first year of life**. *Neuroradiology* 1990;31:459–70 CrossRef Medline
- Barkovich AJ, Kjos BO, Jackson DE, et al. **Normal maturation of the neonatal and infant brain: MR imaging at 1.5 T**. *Radiology* 1988;166:173–80 CrossRef Medline
- Schmidbauer V, Geisl G, Cardoso Diogo M, et al. **Validity of SyMRI for assessment of the neonatal brain**. *Clin Neuroradiol* 2021;31:315–23 CrossRef Medline
- McAllister A, Leach J, West H, et al. **Quantitative synthetic MRI in children: normative intracranial tissue segmentation values during development**. *AJNR Am J Neuroradiol* 2017;38:2364–72 CrossRef Medline
- Tanenbaum LN, Tsiouris AJ, Johnson AN, et al. **Synthetic MRI for clinical neuroimaging: results of the magnetic resonance image compilation (MAGiC) prospective, multicenter, multireader trial**. *AJNR Am J Neuroradiol* 2017;38:1103–10 CrossRef Medline
- Warntjes JB, Leinhard OD, West J, et al. **Rapid magnetic resonance quantification on the brain: optimization for clinical usage**. *Magn Reson Med* 2008;60:320–29 CrossRef Medline
- Schmidbauer V, Dovjak G, Geisl G, et al. **Impact of prematurity on the tissue properties of the neonatal brainstem: a quantitative MR approach**. *AJNR Am J Neuroradiol* 2021;42:581–89 CrossRef Medline
- Schmidbauer VU, Yildirim MS, Dovjak GO, et al. **Different from the beginning: WM maturity of female and male extremely preterm neonates: a quantitative MRI study**. *AJNR Am J Neuroradiol* 2022;43:611–19 CrossRef Medline
- Shepherd TM, Ades-Aron B, Bruno M, et al. **Direct in vivo MRI discrimination of brainstem nuclei and pathways**. *AJNR Am J Neuroradiol* 2020;41:777–84 CrossRef Medline
- Grewal SS, Middlebrooks EH, Kaufmann TJ, et al. **Fast gray matter acquisition T1 inversion recovery MRI to delineate the mammillothalamic tract for preoperative direct targeting of the anterior nucleus of the thalamus for deep brain stimulation in epilepsy**. *Neurosurg Focus* 2018;45:E6 CrossRef Medline
- Bot M, Pauwels R, van den Munkhof P, et al. **The fast gray matter acquisition T1 inversion recovery sequence in deep brain stimulation: introducing the rubral wing for dentato-rubro-thalamic tract depiction and tremor control**. *Neuromodulation* 2022 Jan 15. [Epub ahead of print] CrossRef Medline
- Hagiwara A, Warntjes M, Hori M, et al. **SyMRI of the brain: rapid quantification of relaxation rates and proton density, with synthetic MRI, automatic brain segmentation, and myelin measurement**. *Invest Radiology* 2017;52:647–57 CrossRef Medline
- Kang KM, Choi SH, Kim H, et al. **The effect of varying slice thickness and interslice gap on T1 and T2 measured with the multidynamic multiecho sequence**. *Magn Reson Med* 2019;81:126–33 CrossRef Medline
- Sudhyadhom A, Haq IU, Foote KD, et al. **A high resolution and high contrast MRI for differentiation of subcortical structures for DBS targeting: the fast gray matter acquisition T1 inversion recovery (FGATIR)**. *Neuroimage* 2009;47:T44–52 CrossRef Medline
- Koo TK, Li MY. **A guideline of selecting and reporting intraclass correlation coefficients for reliability research**. *J Chiropr Med* 2016;15:155–63 CrossRef Medline
- Provenzi L, Scotto di Minico G, Giorda R, et al. **Telomere length in preterm infants: a promising biomarker of early adversity and care in the neonatal intensive care unit?** *Front Endocrinol (Lausanne)* 2017;8:295 CrossRef
- Dieterich M, Brandt T. **The bilateral central vestibular system: its pathways, functions, and disorders**. *Ann N Y Acad Sci* 2015;1343:10–26 CrossRef Medline
- Eshaghi Z, Jafari Z, Jalaie S. **Static balance function in children with a history of preterm birth**. *Med J Islam Repub Iran* 2015;29:310 Medline
- Kuczynski AM, Carlson HL, Lebel C, et al. **Sensory tractography and robot-quantified proprioception in hemiparetic children with perinatal stroke: sensory tractography in perinatal stroke**. *Hum Brain Mapp* 2017;38:2424–40 CrossRef Medline
- Günal A, Pekçetin S, Öksüz Ç. **Sensory processing patterns of young adults with preterm birth history**. *Somatosens Mot Res* 2020;37:288–92 CrossRef Medline
- Kwong AK, Doyle LW, Olsen JE, et al. **Early motor repertoire and neurodevelopment at 2 years in infants born extremely preterm or extremely-low-birthweight**. *Dev Med Child Neurol* 2022;64:855–62 CrossRef Medline
- Jost K, Pramana I, Delgado-Eckert E, et al. **Dynamics and complexity of body temperature in preterm infants nursed in incubators**. *PLoS One* 2017;12:e0176670 CrossRef Medline
- Knobel RB, Levy J, Katz L, et al. **A pilot study to examine maturation of body temperature control in preterm infants**. *J Obstet Gynecol Neonatal Nurs* 2013;42:562–74 CrossRef Medline
- Sarnat HB, Flores-Sarnat L, Auer RN. **Sequence of synaptogenesis in the fetal and neonatal cerebellar system, Part 1: Guillain-Mollaret triangle (dentato-rubro-olivo-cerebellar circuit)**. *Dev Neurosci* 2013;35:69–81 CrossRef Medline
- Kinney HC, Brody BA, Finkelstein DM, et al. **Delayed central nervous system myelination in the sudden infant death syndrome**. *J Neuropathol Exp Neurol* 1991;50:29–48 CrossRef Medline

34. Kramarz S. **Preterm birth rate in Germany: no numbers exist for this.** *Dtsch Arztebl Int* 2020;117:509 CrossRef Medline
35. Goeral K, Kasprian G, Hüning BM, et al. **A novel magnetic resonance imaging-based scoring system to predict outcome in neonates born preterm with intraventricular haemorrhage.** *Dev Med Child Neurol* 2022;64:608–77 CrossRef Medline
36. Dubois J, Alison M, Counsell SJ, et al. **MRI of the neonatal brain: a review of methodological challenges and neuroscientific advances.** *J Magn Reson Imaging* 2021;53:1318–43 CrossRef Medline
37. Engle WA, American Academy of Pediatrics Committee on Fetus and Newborn. **Age terminology during the perinatal period.** *Pediatrics* 2004;114:1362–64 CrossRef Medline

Sacral CSF-Venous Fistulas and Potential Imaging Techniques

I.T. Mark, P.P. Morris, W. Brinjikji, A.A. Madhavan, J.K. Cutsforth-Gregory, and J.T. Verdoorn

ABSTRACT

SUMMARY: This is the first study to describe CSF-venous fistulas involving the sacrum, a location that may be underrecognized on the basis of current imaging techniques. We describe a delayed decubitus flat CT myelogram technique that may be useful to identify sacral CSF-venous fistulas.

ABBREVIATIONS: CTM = CT myelography; CVF = CSF-venous fistula; DAVF = dural arteriovenous fistula; DECT = dual-energy CT; DSM = digital subtraction myelography

Spontaneous intracranial hypotension can cause debilitating headaches and other symptoms. One cause, which likely represents at least 25% of cases of spontaneous intracranial hypotension, is a CSF-venous fistula (CVF).¹ CVFs are occult on conventional MR imaging and CT. Diagnosis thus depends on myelography, most commonly with lateral decubitus digital subtraction myelography (DSM) and dynamic CT myelography (CTM).^{2,3}

CVFs are usually found in the thoracic spine, less often in the lower cervical or upper lumbar spine,⁴ but not previously reported in the sacrum. We present 2 patients with sacral CVFs. Our aim was to promote awareness of sacral CVFs and present a potential myelographic technique to aid in their discovery.

Cases

Two cases of sacral CVF and the myelographic techniques used to find them are described below.

Patient 1

A 56-year-old woman presented with 2 years of orthostatic headaches, brain fog, and nausea. Brain MR imaging demonstrated effacement of the suprasellar cistern and narrowing of the

mamillopontine distance (Bern score = 3/9).⁵ Spine MR imaging did not demonstrate extradural fluid. Lateral decubitus DSM showed a possible left T5 CVF, and she underwent a left T5 transvenous catheter embolization, after which symptoms improved but did not resolve.

Six months after her initial DSM, repeat left lateral decubitus DSM was performed. The thecal sac was accessed at L2–L3, and 11 mL of Omnipaque 300 (GE Healthcare) was injected with the patient in the Trendelenburg position. The DSM inferior FOV extended to the needle-access site. Following the DSM, per our standard technique, the patient was kept in the left lateral decubitus position and imaged with dual-energy CT (DECT) approximately 30 minutes after the DSM. The CT included nearly the entire sacrum in the FOV (below the S3 neural foramen). DECT images revealed a CVF originating from a left S2 diverticulum that extended to the left internal iliac vein (Fig 1), outside the DSM FOV. She was treated with a transvenous catheter embolization. One month later the patient had modest improvement in headache and brain fog, and resolution of the nausea.

Patient 2

A 48-year-old man presented with 2 years of nonorthostatic headaches, which were exacerbated by straining. Brain MR imaging was highly suggestive of a CSF leak (Bern score = 8/9). Spine MR imaging did not show extradural fluid. A nuclear medicine cisternogram showed radiotracer accumulation in the kidneys and bladder at 1 hour and failure of radiotracer ascent at 6 hours, suggestive of a CSF leak.

Conventional CTM was performed and read as having negative findings. Further work-up continued with a right-side-down DSM, with imaging down to the lumbar puncture level at L3–L4. A right lateral decubitus DECT extending to the sacrum was

Received September 8, 2022; accepted after revision October 5.

From the Departments of Radiology (I.T.M., P.P.M., W.B., A.A.M., J.T.V.) and Neurology (J.K.C.-G.), Mayo Clinic, Rochester, Minnesota.

Each of the authors (I.T.M., P.P.M., W.B., A.A.M., J.K.C.-G., J.T.V.) contributed to all categories established by the International Committee of Medical Journal Editors including the following: conception and design, or acquisition of data, or analysis and interpretation of data; drafting the article or revising it critically for important intellectual content; final approval of the version to be published; and agreement to be accountable for all aspects of the work in ensuring that questions related to the accuracy or integrity of any part of the work are appropriately investigated and resolved.

Please address correspondence to Ian Mark, MD, Department of Radiology, Mayo Building, 3-72W, Rochester, MN 55905; e-mail: Mark.Ian@mayo.edu; @iantmark
<http://dx.doi.org/10.3174/ajnr.A7699>

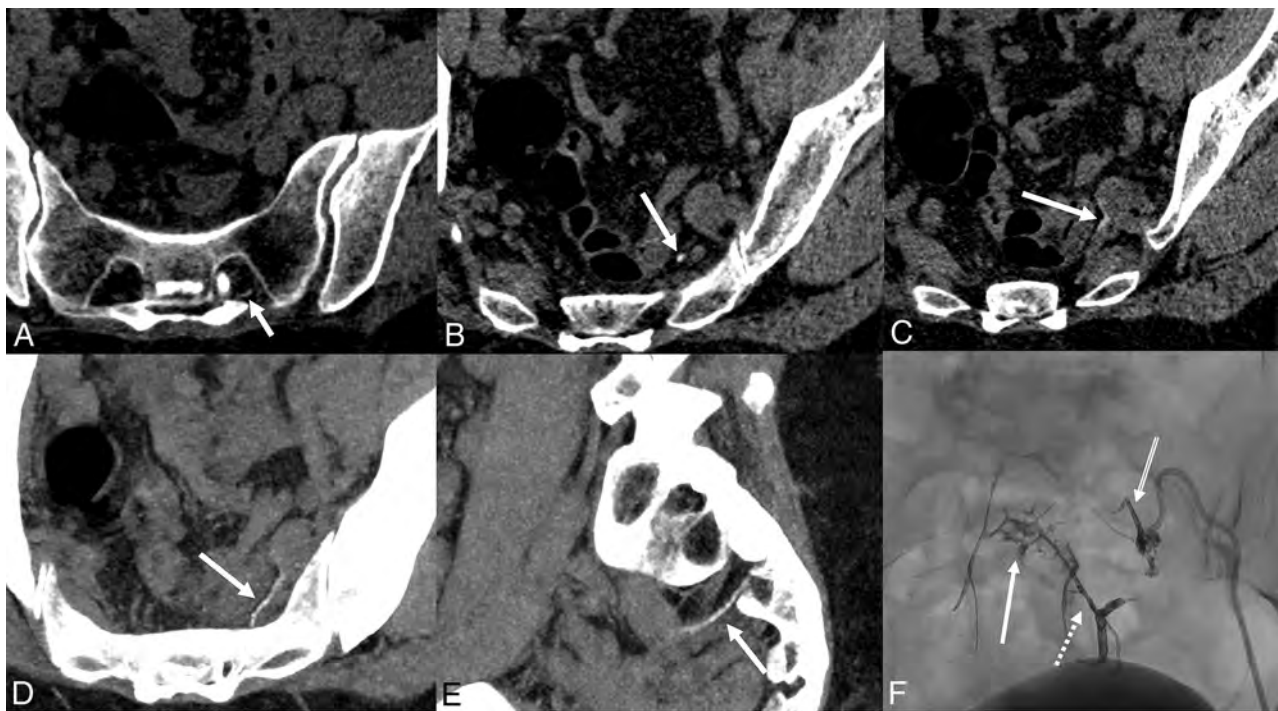


FIG 1. Left S2 CVF in patient 1. A–C, Axial images from a flat left-side-down CTM after DSM show a CVF (arrows) that arises from a left S2 nerve sheath diverticulum that empties into the left internal iliac vein. These images were reconstructed into 0.625-mm-thick slices from the 50-keV monoenergetic reconstructions from DECT. D and E, Multiplanar reformatted images from the CTM highlight the CVF (arrows). F, Postprocedural frontal projection image from transvenous catheter Onyx (Covidien) embolization of the CVF. The left S2 vein (double-line arrow), left S3 vein (broken arrow), and the pelvic epidural venous plexus (solid arrow) are opacified.

performed approximately 20 minutes after the DSM. On the inferior-most images, a CVF arising from a right S3 diverticulum was partially visualized, which, in retrospect, could be seen on the conventional CTM. A repeat DSM was performed several days later, this time with the patient in the reverse Trendelenburg position to opacify the CVF (Fig 2). Immediate post-DSM DECT in a flat right lateral decubitus position depicted the CVF as it arose from a complex multilobulated right S3 diverticulum and connected to the ipsilateral internal iliac vein. The patient encounter occurred before the advent of transvenous embolization, and the patient underwent a CT-guided epidural blood patch with fibrin glue. The patient had symptom relief for 1.5 years and is currently undergoing evaluation for a recurrent CSF leak.

DISCUSSION

We present our technique to identify sacral CVFs in 2 patients involving reverse Trendelenburg positioning during DSM and delayed decubitus CTM including the sacrum. To our knowledge, these are the first reported cases of sacral CVF. This report is important because the sacrum has not previously been described as a location for CVF and is not well-evaluated by current dynamic myelographic techniques, which typically involve a lumbar puncture with imaging superiorly from that site as contrast flows superiorly with the patient in the Trendelenburg position.

Prior work, including a systematic review, described most CVFs in the thoracic spine, with rare occurrence in the cervical or upper lumbar spine, without prior description of a sacral CVF.^{4,6–8}

To perform decubitus myelography, either DSM or CTM, contrast is injected via lumbar puncture and the patient must be in the Trendelenburg position for cranial flow of contrast. Therefore, this technique draws contrast away from the sacrum and negates the possibility of detecting a sacral CVF. Our technique involves a post-DSM CT in the flat (non-Trendelenburg) lateral decubitus position, allowing contrast to redistribute caudally and thereby opacify the sacral CSF, and could be performed after DSM or dynamic CTM.

While dynamic myelography is the preferred work-up for a CVF, CVF can occasionally be detected on conventional (nondynamic) myelograms.⁹ In retrospect, the sacral CVF was present on the conventional myelogram of patient 2. Important features of imaging for sacral CVF include patient positioning that allows contrast to distribute caudally to the sacrum and imaging through the inferior aspect of the sacrum. An additional option to interrogate the sacrum includes injecting contrast with the patient in the reverse Trendelenburg position during lateral decubitus DSM, as in patient 2.

Despite a clear thoracic predominance of CVF, the sacrum may be an underrecognized site of CVF, like what has been suggested with a dural arteriovenous fistula (DAVF). The sacrum has traditionally been thought to account for only 5%–10% of DAVFs, but Gioppo et al¹⁰ reported a sacral DAVF in 14% of cases. Lack of awareness may similarly cause sacral CVFs to be underrecognized.

Our standard practice includes lateral decubitus DSM from the cervicothoracic junction to the needle-insertion site in the lumbar

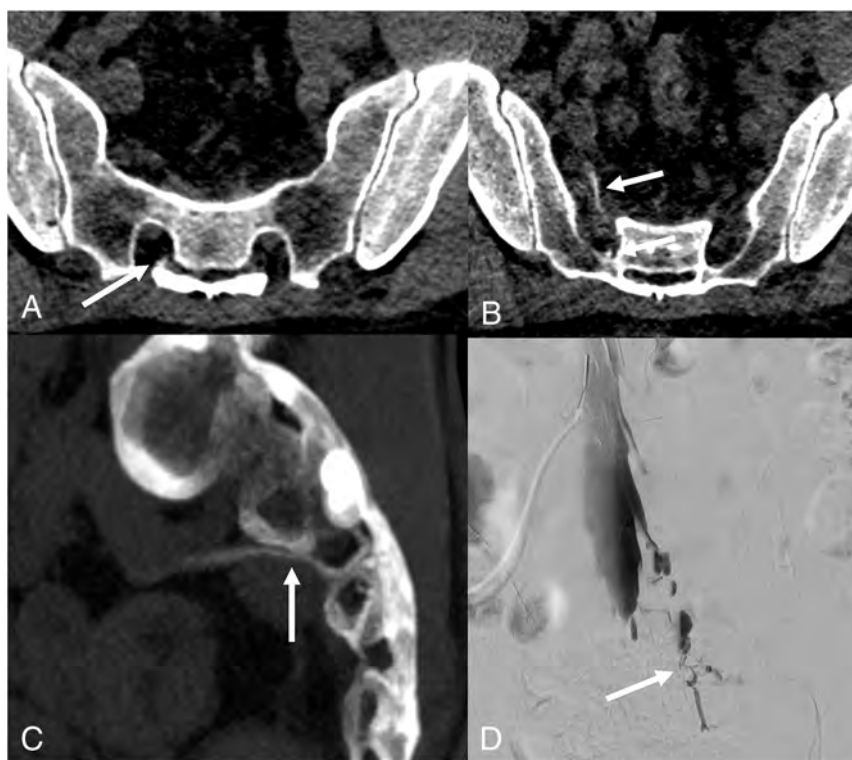


FIG 2. Right S3 CVF in patient 2. A and B, Axial images from a flat right-side-down CTM after DSM follow a CVF (arrows) that arises from a right S3 nerve sheath diverticulum and empties into the right internal iliac vein. These images were reconstructed into 0.625-mm-thick slices from the monoenergetic reconstructions from DECT. C, Reformatted image from the same examination better demonstrates the entire CVF (arrow). D, Right-side-down DSM frontal image with the patient in reverse Trendelenburg position shows the CVF (arrow).

spine. We then perform a post-DSM lateral decubitus DECT of the entire spine, including the inferior aspect of the sacrum. This series is performed during 2 days, with the right side on day 1 and the left side on day 2. A nuclear medicine cisternogram is performed in cases of “low probability” Bern scores⁵ on brain MR imaging.

This study is limited by its small size. Nonetheless, these 2 cases highlight the sacrum as a potential location of a CVF that is typically not investigated during a CVF work-up. A sacral CVF may account for an undiagnosed source of CSF leak in some patients who have undergone extensive work-up, and various technical modifications that we have described may be needed for its identification.

CONCLUSIONS

We describe 2 modifications to dynamic myelography that may aid in the detection of sacral CVFs, namely a delayed flat lateral decubitus DECT imaging inferiorly through the sacrum and

reverse Trendelenburg positioning during DSM while imaging the sacrum. These were instrumental in identifying sacral CVFs.

Disclosure forms provided by the authors are available with the full text and PDF of this article at www.ajnr.org.

REFERENCES

1. Schievink WI, Moser FG, Maya MM. CSF-venous fistula in spontaneous intracranial hypotension. *Neurology* 2014;83:472–73 CrossRef Medline
2. Kim DK, Brinjikji W, Morris PP, et al. Lateral decubitus digital subtraction myelography: tips, tricks, and pitfalls. *AJNR Am J Neuroradiol* 2020;41:21–28 CrossRef Medline
3. Kranz PG, Amrhein TJ, Gray L. CSF venous fistulas in spontaneous intracranial hypotension: imaging characteristics on dynamic and CT myelography. *AJR Am J Roentgenol* 2017;209:1360–66 CrossRef Medline
4. Shlobin NA, Shah VN, Chin CT, et al. Cerebrospinal fluid-venous fistulas: a systematic review and examination of individual patient data. *Neurosurgery* 2021;88:931–41 CrossRef Medline
5. Dobrocky T, Grunder L, Breiding PS, et al. Assessing spinal cerebrospinal fluid leaks in spontaneous intracranial hypotension with a scoring system based on brain magnetic resonance imaging findings. *JAMA Neurol* 2019;76:580–87 CrossRef Medline
6. Kim DK, Carr CM, Benson JC, et al. Diagnostic yield of lateral decubitus digital subtraction myelogram stratified by brain MRI findings. *Neurology* 2021;96:e1312–18 CrossRef Medline
7. Mamlouk MD, Ochi RP, Jun P, et al. Decubitus CT myelography for CSF-venous fistulas: a procedural approach. *AJNR Am J Neuroradiol* 2021;42:32–36 CrossRef Medline
8. Schievink WI, Moser FG, Maya MM, et al. Digital subtraction myelography for the identification of spontaneous spinal CSF-venous fistulas. *J Neurosurg Spine* 2016;24:960–64 CrossRef Medline
9. Clark MS, Diehn FE, Verdoorn JT, et al. Prevalence of hyperdense paraspinal vein sign in patients with spontaneous intracranial hypotension without dural CSF leak on standard CT myelography. *Diagn Interv Radiol* 2018;24:54–59 CrossRef Medline
10. Gioppo A, Faragò G, Giannitto C, et al. Sacral dural arteriovenous fistulas: a diagnostic and therapeutic challenge: single-centre experience of 13 cases and review of the literature. *J Neurointerv Surg* 2018;10:415–21 CrossRef Medline

How Are We Handling Fluoroscopy-Guided Lumbar Puncture Requests? A Nationwide Survey of Practice Trends

T.J. Richards, J.C. Durieux, and A.P. Nayate



ABSTRACT

BACKGROUND AND PURPOSE: Referrals to perform fluoroscopy-guided lumbar punctures by neuroradiologists have increased. The purpose of our study was to determine the management of fluoroscopy-guided lumbar puncture referrals in different practice settings.

MATERIALS AND METHODS: We sent an online questionnaire to neuroradiologists and radiology trainees between May and June 2020 to survey their handling of fluoroscopy-guided lumbar puncture requests, preprocedural work-up, and the use of physician extenders/trainees to perform fluoroscopy-guided lumbar punctures, among other questions. Categories were compared using ORs.

RESULTS: Of the 123 US respondents, 81.3% were in combined academic and 18.7% in combined private practice groups. Regarding fluoroscopy-guided lumbar puncture referrals, 27.6% of respondents did not require a bedside lumbar puncture attempt before a fluoroscopy-guided lumbar puncture. Of private practice, 95.7%, and of academic respondents, 85.0%, were often asked to perform fluoroscopy-guided lumbar punctures by clinicians because of the clinician's lack of procedural competence. Of those, 74.8% stated that they always or sometimes agreed to the request. 41.5% of respondents stated that they would always comply with patients' requests for a fluoroscopy-guided lumbar puncture without a bedside lumbar puncture attempt, a 5.26 times higher likelihood (95% CI, 2.04–14.29) for private practice respondents. To perform fluoroscopy-guided lumbar punctures, 32.0% of academic respondents and 47.8% of private practice respondents use physician extenders. 75.0% of academic respondents reported that trainees perform >50% of their fluoroscopy-guided lumbar punctures.

CONCLUSIONS: This survey demonstrates that many academic and private practice neuroradiologists engage in practices that may promote an increase in fluoroscopy-guided lumbar puncture referrals including not requiring a non-image-guided lumbar puncture attempt, complying with clinicians' requests for a fluoroscopy-guided lumbar puncture due to lack of competence in performing lumbar punctures, and fulfilling patient requests for fluoroscopy-guided lumbar punctures.

ABBREVIATIONS: FGLP = fluoroscopy-guided lumbar puncture; LP = lumbar puncture

During the past few decades, there has been a large shift in the lumbar puncture (LP) volume to radiologists, and now radiologists are the primary performers of LPs in both Medicare inpatients and outpatients.¹ Performing LP under image guidance, usually using fluoroscopy, allows the radiologist to directly visualize the needle, which is especially useful in challenging

cases, including patients with extensive spinal hardware, scoliosis, or morbid obesity, among others. These advantages likely play a large role in the increased rates of referrals to radiology for fluoroscopy-guided lumbar punctures (FGLPs), but we believe other factors also contribute, including the time required of the patient's primary clinical provider, poor monetary reimbursement, incomplete mastery of the LP technique by the provider, and disruption of the provider's workflow.^{2,3} Performing FGLPs also creates difficulty for radiologists, including disrupting the flow of the normal workday, which is of growing concern especially because the diagnostic imaging workload continues to increase.⁴ In addition, performing emergent after-hours FGLPs is often medically necessary and can further challenge radiology departments because after-hours radiology technologists and FGLP operators are required. Many academic radiology departments rely

Received June 3, 2022; accepted after revision September 26.

From the Department of Radiology and Imaging Sciences (T.J.R.), University of Utah School of Medicine, Salt Lake City, Utah; and Department of Radiology (J.C.D., A.P.N.), University Hospitals Cleveland Medical Center, University Hospitals, Cleveland, Ohio.

Please address correspondence to Ameya Nayate, MD, Department of Radiology, UH, 11100 Euclid Ave, BSH 5056, Cleveland, OH 44106; e-mail: Ameya.Nayate@UHospitals.org; @UHNuroads



Indicates article with online supplemental data.

<http://dx.doi.org/10.3174/ajnr.A7684>

on trainees (residents/fellows) to perform FGLPs, while other practices, both academic and private, rely on assistance from physician extenders (such as physician assistants and nurse practitioners). To our knowledge, there is not much information available on the use of trainees or physician extenders in academic or nonacademic groups.

LPs are considered a moderate-risk procedure due to the low incidence of complications, and there are societal recommendations for preprocedural work-up before performing LPs.^{5,6} However, in our experience, there is institutional variability on obtaining pre-LP head imaging and laboratory values.

The purpose of this investigation was to survey US and international neuroradiologist FGLP practices, including handling requests from providers, preprocedural work-up, and use of physician extenders and trainees to perform FGLPs.

MATERIALS AND METHODS

The study was approved by the University Hospitals Cleveland Medical Center institutional review board. The link to participate in a voluntary online survey was included in a monthly newsletter (May 2020) for members of the American Society of Neuroradiology. Due to an initial low response rate, a brief description of our aims (Online Supplemental Data) and the link to the survey were also e-mailed to a LISTSERV for neuroradiology section chiefs and neuroradiology fellowship directors of academic practices in the United States. Also, given the initial low response rate of private practice radiologists and to obtain a comparison nonacademic group, the survey invitation was also e-mailed to neuroradiology fellowship alumni (practicing in the United States and internationally in varying types of practices) of both the first and last authors. The survey was launched on May 7, 2020, and was closed on June 30, 2020. The survey included responses from both practicing board-certified radiologists and current radiology trainees (distinction between neuroradiology fellow or radiology resident was not made) both within the United States and internationally. Except for the initial e-mail, no further contact occurred between the authors and the survey respondents. There was no reward for completing the survey and no provided incentive to answer questions in a particular manner.

The survey (Online Supplemental Data) included 13 questions, and responses were collected electronically using an online survey tool that allows viewing of the responses by the owner of the survey (first author). Other than respondents' answers to the type of practice setting in which they worked and their geographic location, no identifiable data about the respondents, including the respondent's name, e-mail, or practice/hospital name, were obtained. Data were exported from the online survey manager for advanced statistical analysis.

Subgroup analysis was performed evaluating responses on the basis of practice type, practice location, and the use of physician extenders and trainees for performing FGLPs. To simplify analysis by practice type, we grouped together respondents that identified as "academic" and "hybrid academic and private practice," single respondents that identified as "other: hospital-based and academic," and 3 trainee respondents grouped together under "combined academic." Respondents who identified as "private practice" or "hospital-based radiology practice" were grouped together under "combined private practice." "Hospital-

based radiology practice" was grouped with the combined private practice group on the basis of our experience that many of these practices essentially function as a private practice (ie, limited academic and teaching responsibilities) and that only 2 of 7 respondents within this group stated that trainees perform FGLPs in their practice. Unadjusted ORs and 95% confidence intervals were calculated to quantify responses by practice type. *P* values < .05 were considered statistically significant.

RESULTS

Respondents

The survey was distributed to 7028 American Society of Neuroradiology members as a part of their May 2020 e-newsletter, and 2734 individuals opened the e-mails. An invitation to take the survey was also sent to 44 neuroradiology fellowship directors, 82 neuroradiology section chiefs, and 78 neuroradiology fellowship alumni of the first and last authors for a total of 7232 invited individuals. There were a total of 131 responses for a response rate of 1.8%.

Of the respondents, 6.1% ($n = 8$) were from outside the United States. Given that the low number of responses was unlikely to accurately reflect FGLP practices outside the United States, these responses were excluded from analysis but were included in the Online Supplemental Data. Of the remaining 123 responses limited to the United States, 81.3% ($n = 100$) were in the combined academic group, which included 89 respondents (72.4% of total) identifying as an academic practice; 10 respondents, as "hybrid academic/private" practice (8.1%); and 1 respondent, as "trainee" (0.8%). Of respondents, 18.7% ($n = 23$) were in the combined private practice group, including 16 as "private" practice (13.0%) and 7 as "hospital-based private" practice (5.7%). Of respondents, 84.6% ($n = 104$) interpreted only neuroradiology studies in adults and/or pediatric patients, 11.4% ($n = 14$) interpreted a mixture of neuroradiology and non-neuroradiology studies, and only 1.6% ($n = 2$) of respondents interpreted mostly non-neuroradiology studies. Of those that chose academic for practice, 3 respondents (2.4%) chose trainee for the type of studies read.

The highest number of respondents were from the Northeast at 36 (29.3%), and lowest, from the Southwest at 12 (9.8%) (Fig 1 shows depiction of geographic locations and the geographic distribution of US respondents). Of the combined private practice respondents, 52.2% ($n = 12$) were from the West. Respondents in the United States were from 31 of the 50 states, and 4 respondents were from the District of Columbia.

FGLP Operators

Trainees. The subgroup of the combined academic group that described their practice as academic had the highest overall proportion of FGLPs performed by trainees, with 80.9% indicating that trainees performed at least half of the FGLPs. For those who identified with practicing in an academic private practice hybrid, only 20.0% ($n = 2$) responded that trainees perform at least half of their FGLPs, but 80.0% stated that trainees do perform FGLPs at their institution. In the combined private practice group, 8.7% ($n = 2$) stated that trainees perform FGLPs at their practice; both of these respondents were in the hospital-based practice group. Figure 2 shows a comparison of FGLPs

performed by trainees and physician extenders in the combined-academic-versus-combined-private practice groups.

Physician Extenders. The combined private practice group had more respondents state that physician extenders perform any FGLPs at their institution compared to the academic group (47.8% compared with 32.0%, respectively). Private practice radiologists are 4.54 times (95% CI, 1.20–16.67) more likely to have

all or nearly all (75%–100%) FGLPs performed by physician extenders compared with academic practice radiologists.

Regional Variation. By region, the Northeast had the lowest use of physician extenders performing FGLPs, with only 33.3% stating that physician extenders performed any FGLPs, while the Midwest had the highest at 42.9%. The West had the highest percentage of respondents stating that physician extenders performed at least half of the FGLPs (27.6%).

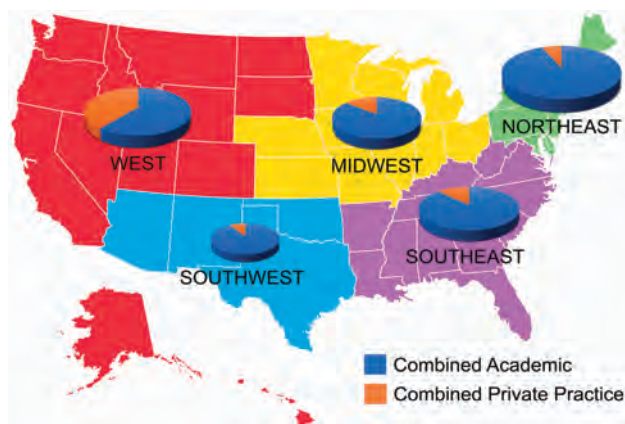


FIG 1. US map demonstrating the regional divisions for subgroup analysis. This pie chart demonstrates the proportion of respondents in the combined academic group (blue) compared with the combined private practice group (orange). The size of the pie chart is scaled according to the proportion of the total respondents from each region.

Bedside Lumbar Puncture Attempt Requirements. Compared with private practice, respondents from an academic type of practice were 5.99 times (95% CI, 2.35–16.01 times) more likely to require a bedside LP attempt before an FGLP. In practices in which neither physician extenders nor trainees performed FGLPs, only 25% required a bedside attempt. When asked about possible reasons that a patient could skip undergoing a bedside LP and go directly to FGLP, the 2 most common reasons were morbid obesity in which the bony landmarks (81.3%) cannot be palpated and surgical wound or infection limiting access (75.6%). Figure 3 shows additional responses.

Clinician Requests Due to Lack of LP Competency

Of combined private practices, 95.7% and 85.0% of combined academic respondents were often asked to perform FGLPs by clinicians because the clinician did not feel competent performing LPs. Of those, combined private practice respondents more commonly stated that they would either “always” or “sometimes” oblige this request compared with combined academic respondents (86.3%)

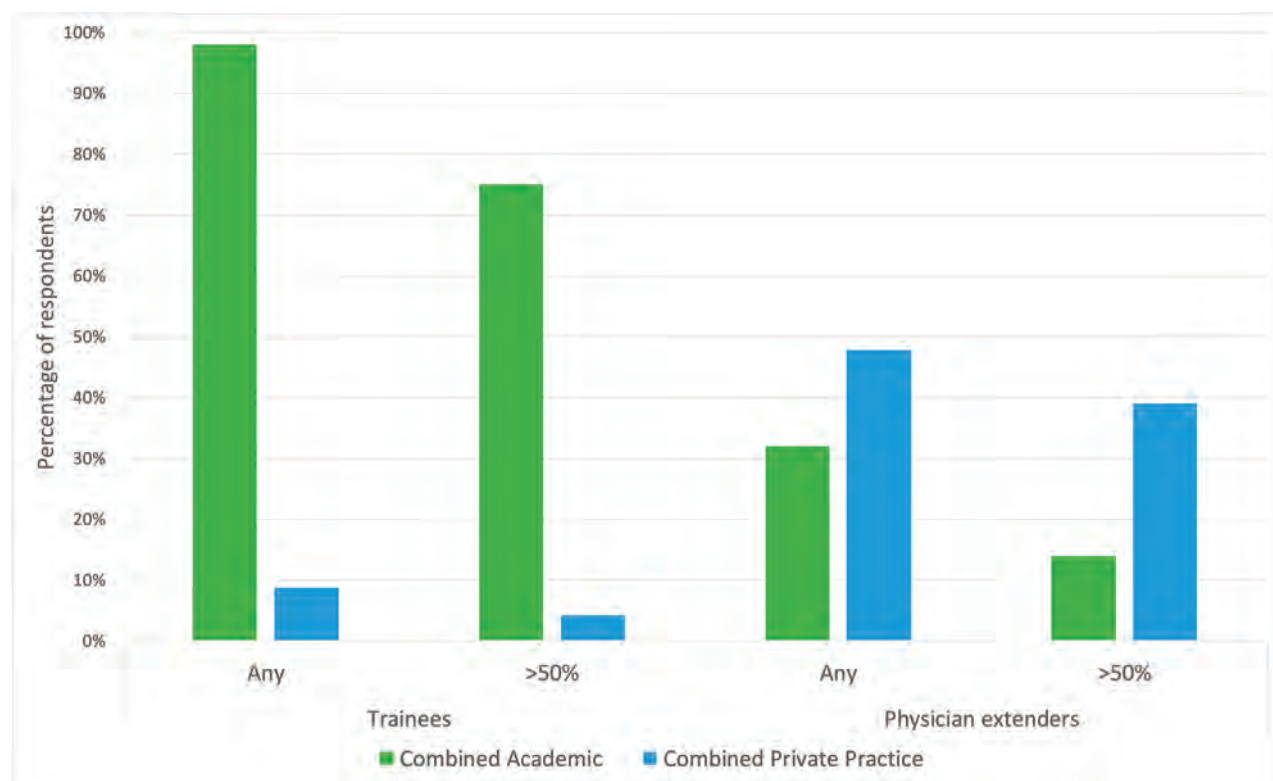


FIG 2. Column graph demonstrating the percentage of FGLPs performed by trainees and physician extenders according to the survey respondents in the combined academic compared with private practice groups.

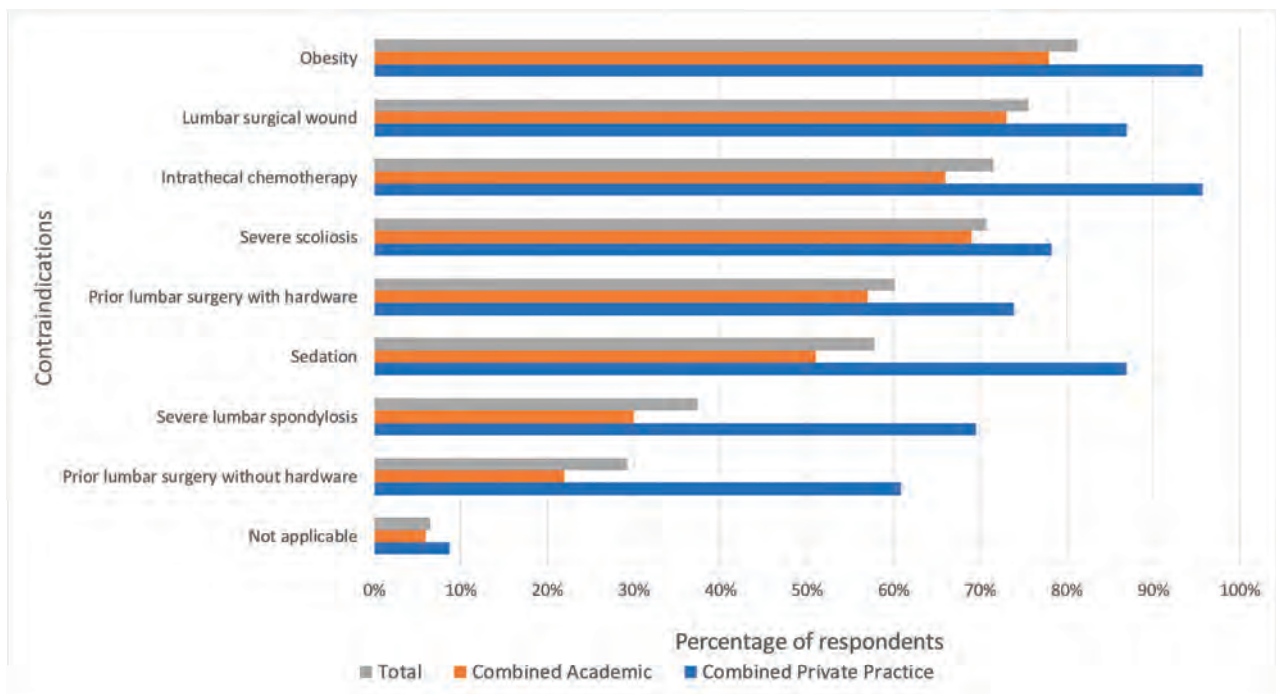


FIG 3. Bar graph demonstrating the percentage of respondents that chose each possible contraindication to a bedside LP and having the patient go directly to a FGLP according to all respondents, combined academic, and combined private practice groups.

compared with 71.8%, respectively). The Online Supplemental Data give additional FGLP practice requirements.

Patient FGLP Requests. Overall, 41.5% ($n = 51$) of respondents stated that they would always accommodate a patient request for FGLP before a bedside attempt. Compared with respondents from an academic-type practice, private practice radiologists were 5.26 times (95% CI, 2.04–14.29 times) more likely to accommodate a patient's request for FGLP. The subgroup in which physician extenders performed at least half of the FGLPs had the highest percentage of refusing this patient request, at 13.0%.

Outpatient FGLP Requests. When an outpatient is referred for an FGLP, none of the combined private practice groups stated that they always required a bedside LP attempt compared with 13.0% of the combined academic group.

Laboratory and Imaging Requirements. Pre-FGLP coagulation test requirements were very similar between the combined private practice and academic groups, with 39.0% and 39.1% (respectively) always checking preprocedural coagulation test results and platelet counts. Of the respondents that did not require all patients to get coagulation tests before an FGLP, most checked these labs in patients with an increased risk of coagulopathy (92.0%). Figure 4 shows additional details.

Of all respondents, most (82.9%) stated that patients are required to get a CT of the head before an FGLP only if there is high suspicion of increased intracranial pressure and CSF is being removed. More respondents in the combined private practice group always required head imaging compared with the combined

academic group (17.4% compared with 8.0%, respectively). Figure 5 shows response data for additional head imaging requirements.

After-Hours Emergent FGLPs. Overall, 83.7% of respondents (78.3% of the combined private practice group and 85.0% of the combined academic group) stated that they performed emergency FGLPs after regular work hours. The subgroup with the lowest proportion that performed emergent after-hours FGLPs was respondents (both academic and private practice) where neither physician extenders nor trainees performed any FGLPs. In this subgroup, only 66.7% performed emergent FGLPs.

DISCUSSION

This article presents the only published survey on FGLP practice trends among neuroradiologists across the United States. The survey evaluated expectations for bedside LP attempts before FGLP as well as exceptions to this expectation, including patient and referring clinician requests and complicating patient factors including surgical hardware or variant anatomy. The survey also investigated the primary operators of FGLPs, preoperative imaging and laboratory requirements, and the availability of FGLPs performed as an emergent after-hours procedure.

Bedside LP Attempt Requirements

Most respondents (72.4%) stated that they required a bedside LP attempt by a clinician for inpatients before referral for an FGLP. Respondents who stated that this was their standard practice were approximately 6 times more likely to come from an academic-type practice compared with a private-type practice. When clinicians requested a radiologist to perform an FGLP without a bedside LP attempt due to lack of competence in performing bedside LPs, only

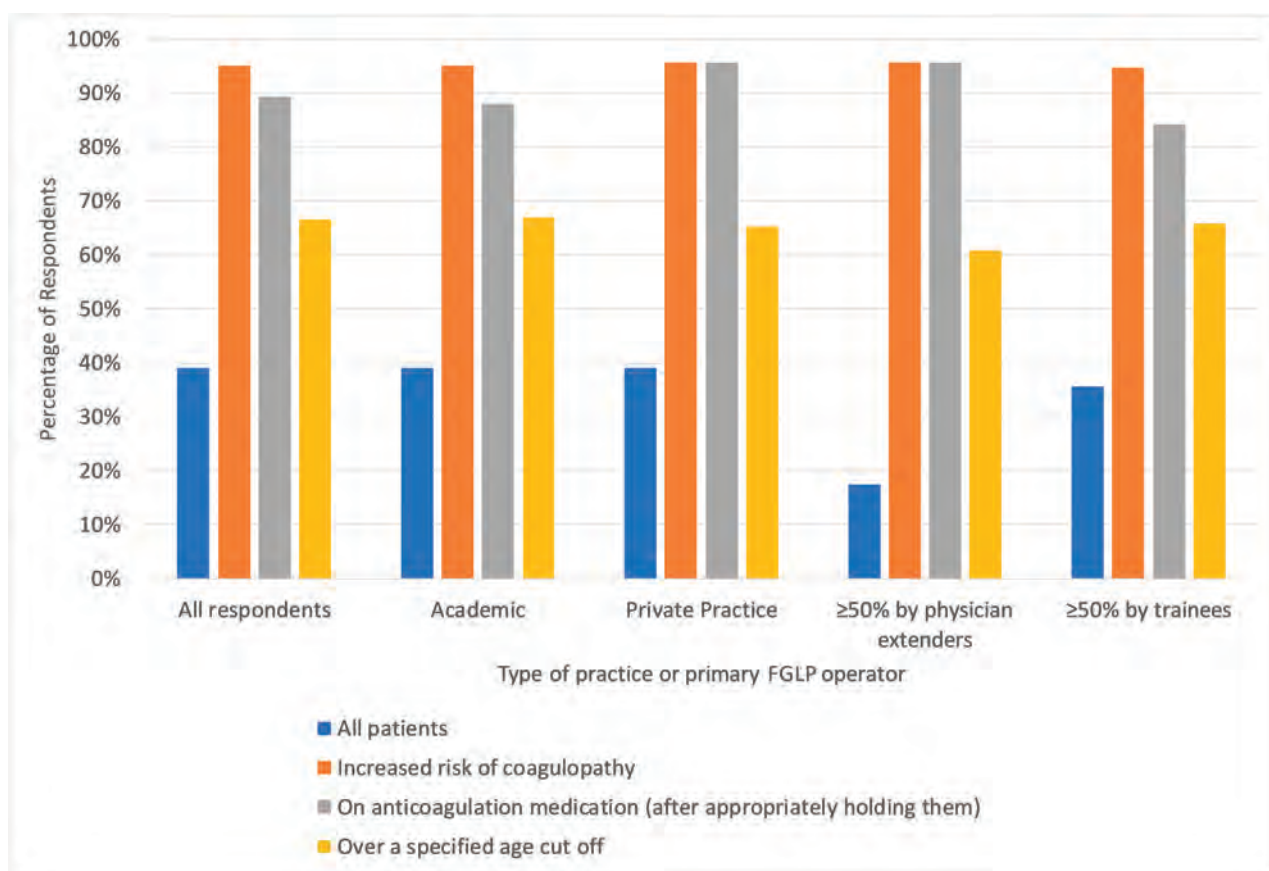


FIG 4. Column graph demonstrating the percentage of all respondents and each major subgroup of respondents that checked coagulation test results and platelet counts in each patient situation. Of note, the respondents that checked laboratory values in all patients were added to each of the other responses, given that if a respondent checked laboratory values in all patients, they would also check them in each of the additional situations.

25.2% of respondents typically refused. Furthermore, when patients requested going directly to FGLP, private practice respondents were approximately 5.3 times more likely to always accommodate the request compared with academic respondents. We believe the dramatic differences between the responses by private practice–versus-academic radiologists are at least partially related to the different practice models. Overall, the high proportion of survey respondents who appease patients and hospitalists with these requests demonstrates the shift in both radiology and medicine as a whole toward a service industry targeted toward patient satisfaction. Despite this shift, it is important to balance the desire to please the patient and referring clinician with doing what is best for the patient and using costs and resources responsibly. FGLPs potentially add unnecessary ionizing radiation and have added cost compared with bedside LPs. Furthermore, FGLPs can be disruptive to both trainees in academic practices and radiologists.^{7,8}

Performing FGLPs on outpatients without a bedside attempt also appears to be common practice, with only 10.6% of respondent indicating that they always require a bedside attempt before performing an FGLP on outpatients. FGLPs have a high success rate, and we suspect that FGLPs are requested by outpatient clinicians to potentially decrease the inconvenience of a longer procedure and possibly requiring a return for a second attempt if the bedside LP is unsuccessful.

Procedural hesitancy is especially of concern because many clinicians do not feel competent in performing LPs.^{3,9} For the internal medicine physician, this problem is, in part, related to their performing fewer bedside LPs¹⁰ and bedside LP procedural skills are no longer considered necessary for certification by the Board of Internal Medicine.¹¹ While it is important to appease the referring clinicians and patients, it is also important for radiologists to be good stewards of medical resources and limit unnecessary exposure of patients to ionizing radiation.

Use of Trainees and Physician Extenders to Perform FGLPs

Our survey demonstrates that trainees perform most FGLPs in academic practices. Only 32.0% of the combined academic group use physician extenders to perform FGLPs, and 14.0% stated that physician extenders perform greater than half of the FGLPs. While radiology trainees need to learn to perform FGLPs as part of their clinical training and they provide no added cost to the radiology department for performing this service, it is important to not overburden trainees with performing a superfluous number of FGLPs to avoid impacting their diagnostic neuroradiology training. Richards et al⁸ reported that for each FGLP performed by a radiology resident, there was a predictable and significant decrease in the number of diagnostic cross-sectional neuroradiology studies that they read in a day. Increased use of physician

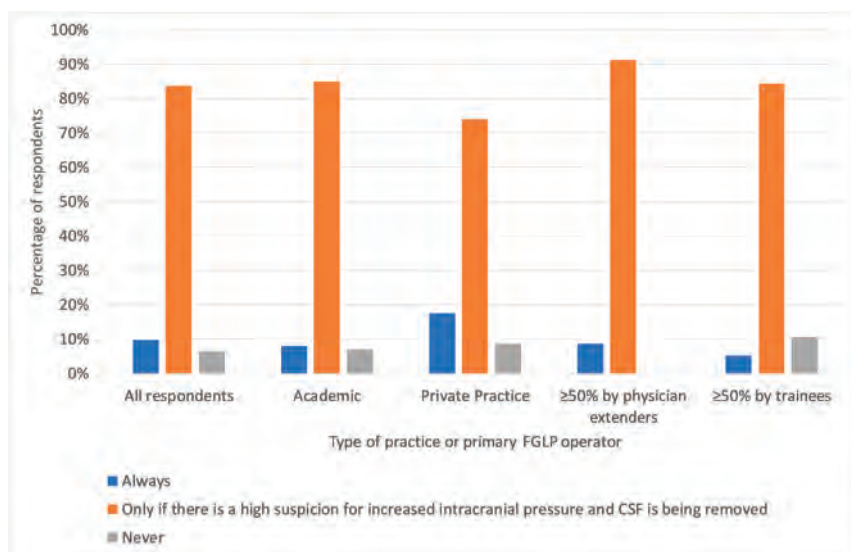


FIG 5. Column graph demonstrating the percentage of all respondents and each major subgroup of respondents that required head imaging in each patient situation.

extenders in academic centers may help relieve some of the burden on trainees of performing increasing number of FGLPs.

Coagulation Test and Head Imaging

Guidelines for when coagulation tests and platelet counts should be checked are controversial and, in our experience, often variable among neuroradiologists, even within the same practice. The updated Society of Interventional Radiology guidelines for periprocedural bleeding risk in 2012 recommended checking platelet counts and international normalized ratios in all patients before procedures with a moderate bleeding risk such as FGLPs, but ultimately the decision was left to the clinician's judgment.⁵ Despite this recommendation, only 39.0% of respondents stated that they check these tests on all patients before FGLP, but most respondents checked them in patients with a high risk of bleeding or those on anticoagulation medications.

In contrast to laboratory requirements, there is a high level of consensus among our survey respondents regarding preprocedural head imaging, with most stating that patients should get a CT of the head before an FGLP only if there is high suspicion for increased intracranial pressure and CSF is being removed, with a minority requiring CT head studies on all patients before performing FGLPs. Most interesting, despite essentially all available society guidelines^{12,13} recommending head CT before diagnostic LP under certain clinical criteria, 6.6% stated that they never require a preprocedural head CT.

Emergent After-Hours FGLPs

There are several indications for which lumbar punctures may be considered emergent or very urgent as part of the patient's essential medical care.^{14,15} Of the survey respondents, 83.7% stated that they perform emergent FGLPs after hours. The subgroup that performed the lowest proportion of emergent FGLPs was the group in which neither physician extenders nor trainees performed any of

their FGLPs. Although the reasons are probably multifactorial, this finding is logical from a financial perspective, given that compensating attending radiologists to cover FGLPs overnight is an expensive means of covering this service and in many cases may not be affordable.

Indications for FGLP without Bedside Attempt

Morbid obesity, severe scoliosis or congenitally altered anatomy, and prior lumbar surgery with hardware were some of the most frequent reasons that respondents did not require a bedside LP attempt before referral for FGLP. These findings are logical and pertain to the inability or high likelihood of the clinician not being certain of the lumbar level or exact location at which the needle is entering the spinal canal due to anatomic issues related to increased

flank adiposity from obesity, altered anatomic landmarks due to spinal curvature, congenital issues, or prior lumbar surgery with hardware. Knowledge of the lumbar level where the spinal needle is entering the thecal sac is important because entering the spinal canal at or above the level of the conus medullaris increases the risk of spinal cord injury. Most interesting, most respondents stated that performing LPs for intrathecal chemotherapy administration and patients requiring sedation or general anesthesia were reasons for which a prior bedside LP was not required. We believe these responses are congruent with the mission of many radiology departments, which is to provide aid to our referring clinicians in the diagnosis and treatment of patients.

Our study has multiple limitations that should be considered when interpreting our results. First, with survey research, there is a chance of self-reporting and recall bias. Second, our findings are based on a relatively small sample size compared with the larger population of neuroradiologists across the country, and more of our respondents practiced in an academic group than in a private practice group. However, we had respondents from all the major geographic sections of the country and statistical power to demonstrate differences between private and academic groups. Also, while sending the e-mail to the neuroradiology fellowship alumni of 2 of the authors could introduce regional bias, the alumni were from different parts of the country and from different types of practices. Third, there is a possibility that multiple respondents from the same institution participated in our survey. There were 7/131 (5%) completed surveys in which the answers were exactly the same as in another survey from the same state. It is possible that either the same person filled out the survey more than once or the respondents were from the same practice and handled FGLPs referrals in the same manner. If the potentially duplicated entries were deleted, we still had very similar results (not presented). Furthermore, recall bias may have also increased the rate of duplicate entries and, therefore, present bias toward

larger institutions and practices and to respondents with more of a vested interest in the results. Finally, the survey was limited to neuroradiologists; however, in some practices, FGLPs are considered a general procedure and performed by many non-neuroradiologists. FGLP practices by other radiologists may vary and would not be captured by this survey.

CONCLUSIONS

This survey demonstrates that many academic and private practice neuroradiologists in the United States engage in practices that may promote an increase in FGLP referrals, including not requiring a non-image-guided LP attempt, complying with requests by clinicians to perform an FGLP due to lack of competence in performing LPs, and fulfilling requests by patients to perform an FGLP without a prior bedside attempt. In general, private practice groups were more lenient in requiring a non-image-guided LP compared with academic groups. Some of our findings are consistent with a known national trend toward reliance on radiology to perform LPs, including most radiologists stating that they were asked by clinicians to perform FGLPs without a prior bedside attempt because the clinician did not feel competent performing LPs. However, radiologists also play a role in this trend because most radiologists stated that they would oblige clinicians' requests to perform a FGLP if the clinician did not feel competent performing a bedside LP and would often perform FGLPs without a prior bedside LP attempt if the patient requested it. The survey also demonstrated a lack of consensus on preprocedural laboratory requirements and reasons to forgo a bedside LP attempt before FGLP referral among radiology practices. We hope that this information can help promote further studies on developing evidence-based guidelines for best FGLP practices.

ACKNOWLEDGMENTS

The authors would like to thank Dr Lubdha Shah, MD, for her feedback on the survey.

Disclosure forms provided by the authors are available with the full text and PDF of this article at www.ajnr.org.

REFERENCES

1. Johnson DR, Waid MD, Rula EY, et al. **Comparison of radiologists and other specialists in the performance of lumbar puncture procedures over time.** *AJNR Am J Neuroradiol* 2021;42:1174–81 CrossRef Medline
2. Allard M, Jelovac I, Léger PT. **Treatment and referral decisions under different physician payment mechanisms.** *J Health Econ* 2011;30:880–93 CrossRef Medline
3. Vaisman A, Cram P. **Procedural competence among faculty in academic health centers: challenges and future directions.** *Acad Med J Med* 2017;92:31–34 CrossRef Medline
4. Smith-Bindman R, Kwan ML, Marlow EC, et al. **Trends in use of medical imaging in US health care systems and in Ontario, Canada, 2000–2016.** *JAMA* 2019;322:843–56 CrossRef Medline
5. Patel JJ, Davidson JC, Nikolic B, et al; Standards of Practice Committee, with Cardiovascular and Interventional Radiological Society of Europe (CIRSE) Endorsement. **Consensus guidelines for periprocedural management of coagulation status and hemostasis risk in percutaneous image-guided interventions.** *J Vasc Interv Radiol* 2012;23:727–36 CrossRef Medline
6. Malloy PC, Grassi CJ, Kundu S, et al; Standards of Practice Committee with Cardiovascular and Interventional Radiological Society of Europe (CIRSE) Endorsement. **Consensus guidelines for periprocedural management of coagulation status and hemostasis risk in percutaneous image-guided interventions.** *J Vasc Interv Radiol* 2009;20:S240–49 CrossRef Medline
7. Schemmel A, Lee M, Hanley T, et al. **Radiology workflow disruptors: a detailed analysis.** *J Am Coll Radiol* 2016;13:1210–14 CrossRef Medline
8. Richards TJ, Schmitt JE, Wolansky LJ, et al. **Radiology performed fluoroscopy-guided lumbar punctures decrease volume of diagnostic study interpretation: impact on resident training and potential solutions.** *J Clin Imaging Sci* 2021;11:39 CrossRef Medline
9. Mourad M, Kohlwes J, Maselli J, et al; MERN Group. **Supervising the supervisor: procedural training and supervision in internal medicine residency.** *J Gen Intern Med* 2010;25:351–56 CrossRef Medline
10. Wigton RS, Alguire P; American College of Physicians. **The declining number and variety of procedures done by general internists: a resurvey of members of the American College of Physicians.** *Ann Intern Med* 2007;146:355–60 CrossRef Medline
11. Duffy FD, Holmboe ES. **What procedures should internists do?** *Ann Intern Med* 2007;146:392–93 CrossRef Medline
12. Dodd KC, Emsley HCA, Desborough MJR, et al. **Periprocedural antithrombotic management for lumbar puncture: Association of British Neurologists clinical guideline.** *Pract Neurol* 2018;18:436–46 CrossRef Medline
13. The American College of Radiology. **ACR-ASNR-SPR practice parameter for the performance of myelography and cisternography.** 2019. <https://www.acr.org/-/media/ACR/Files/Practice-Parameters/Myelog-Cisternog.pdf>. Accessed March 1, 2022
14. Glimåker M, Johansson B, Grindborg Ö, et al. **Adult bacterial meningitis: earlier treatment and improved outcome following guideline revision promoting prompt lumbar puncture.** *Clin Infect Dis* 2015;60:1162–69 CrossRef Medline
15. Evans RW, Friedman DI. **Expert opinion: the management of pseudotumor cerebri during pregnancy.** *Headache* 2000;40:495–97 CrossRef Medline

ACR White Paper on Magnetoencephalography and Magnetic Source Imaging: A Report from the ACR Commission on Neuroradiology

J.A. Maldjian, R. Lee, J. Jordan, E.M. Davenport, A.L. Proskovec, M. Wintermark, S. Stufflebeam, J. Anderson, P. Mukherjee, S.S. Nagarajan, P. Ferrari, W. Gaetz, E. Schwartz, and T.P.L. Roberts



ABSTRACT

SUMMARY: Magnetoencephalography, the extracranial detection of tiny magnetic fields emanating from intracranial electrical activity of neurons, and its source modeling relation, magnetic source imaging, represent a powerful functional neuroimaging technique, able to detect and localize both spontaneous and evoked activity of the brain in health and disease. Recent years have seen an increased utilization of this technique for both clinical practice and research, in the United States and worldwide. This report summarizes current thinking, presents recommendations for clinical implementation, and offers an outlook for emerging new clinical indications.

ABBREVIATIONS: ACR = American College of Radiology; AD = Alzheimer disease; ASD = autism spectrum disorder; CMS = Centers for Medicare and Medicaid Services; CPT = Current Procedural Terminology; ECD = equivalent current dipole; iEEG = intracranial electroencephalography; MEG = magnetoencephalography; MSI = magnetic source imaging

Magnetoencephalography (MEG) is a noninvasive method of detecting neural activity in the brain with millisecond time resolution. The current clinically approved indications for MEG are localization of epileptic foci and localization of eloquent cortices for presurgical planning. The goal of the MEG community at large is to advance current clinical practices and to develop new clinical indications for MEG. Multiple groups have researched the use of MEG in a variety of clinical disorders including concussion, Alzheimer's disease, autism, and others. Additionally, MEG can be used as an adjunct to other therapies, such as neuromodulation. Multispecialty collaboration

is necessary for the successful development of a comprehensive clinical MEG program. The team includes clinicians, MEG scientists, and technologists, often with complementary and/or overlapping skill sets. MEG centers across the United States operate in various clinical departments. Close collaboration with Radiology, Neurology, and Neurosurgery has been instrumental in advancing MEG for clinical use. While there are several publications outlining good clinical practice for acquiring and analyzing clinical MEG data, at the current time, implementation varies across sites. In this report, we describe the current clinical landscape for MEG and emerging applications, as well as provide recommendations for the composition and training of multidisciplinary teams involved in the performance and interpretation of clinical MEG studies, including the roles of the physician, MEG scientist, and MEG technologist in performance of current and future clinically approved MEG studies. We advocate that clinical reporting should be performed after consultation with the entire team, including technologists, MEG scientists, and physicians.

Prior American College of Radiology Involvement in MEG

In 2001, with the joint support of the American College of Radiology (ACR), American Society of Neuroradiology, and American Academy of Neurology, 2 neuroradiologists (Roland Lee, Steven Stufflebeam) and 1 neurologist (Michael Funke) testified at the Centers for Medicare and Medicaid Services (CMS) in support of 3 new Current Procedural Terminology (CPT) codes for MEG:

95965 (MEG recording and analysis of spontaneous brain activity)

Received September 30, 2022; accepted after revision October 4.

From the Advanced Neuroscience Imaging Research Laboratory (J.A.M., E.M.D., A.L.P.), MEG Center of Excellence (J.A.M., E.M.D., A.L.P.), and Department of Radiology (J.A.M., E.M.D., A.L.P.), University of Texas Southwestern Medical Center, Dallas, Texas; Department of Neuroradiology (R.L.), University of California San Diego, San Diego, California; ACR Commission on Neuroradiology (J.J.), American College of Radiology, Reston, Virginia; Stanford University School of Medicine (J.J.), Stanford, California; Department of Neuroradiology (M.W.), University of Texas MD Anderson Center, Houston, Texas; Athinoula A. Martinos Center for Biomedical Imaging (S.S.), Department of Radiology, Massachusetts General Hospital, Charlestown, Massachusetts; Department of Radiology and Imaging Sciences (J.A.), University of Utah School of Medicine, Salt Lake City, Utah; Department of Radiology and Biomedical Imaging (P.M., S.S.N.), University of California, San Francisco, San Francisco, California; Pediatric Neurosciences (P.F.), Helen DeVos Children's Hospital, Grand Rapids, Michigan; Department of Pediatrics and Human Development (P.F.), College of Human Medicine, Michigan State University, Grand Rapids, Michigan; and Department of Radiology (W.G., E.S., T.P.L.R.), Children's Hospital of Philadelphia, Perelman School of Medicine at the University of Pennsylvania, Philadelphia, Pennsylvania.

Please address correspondence to Joseph Maldjian, MD, University of Texas Southwestern Department of Clinical Sciences, Radiology, 5323 Harry Hines Blvd, Dallas, TX 75390-9178; e-mail: joseph.maldjian@utsouthwestern.edu; @EMDavenport_PhD

Indicates open access to non-subscribers at [www.ajnr.org](http://dx.doi.org/10.3174/ajnr.A7714)
<http://dx.doi.org/10.3174/ajnr.A7714>

95966 (MEG recording and analysis of evoked magnetic fields, single technique)

95967 (MEG recording and analysis of evoked magnetic fields, each additional technique, after invoking 95966 once).

The Relative Value Scale Update Committee reviewed these codes at the April 2001 meeting, and CMS implemented the codes and payment rates in 2002, with subsequent scheduled reviews and revisions of the payment rates.

fMRI versus MEG

fMRI has been in clinical use for over 2 decades, slightly predating the clinical adoption of MEG. Clinical indications for fMRI involve presurgical mapping of eloquent cortex. While fMRI provides complementary information to MEG, the underlying neurophysiologic basis of the signal is quite different. Functional MR imaging relies on changes in blood flow associated with neuronal activity, making it an indirect measure of brain function, whereas MEG provides a more direct measure. Both modalities can provide accurate delineation of eloquent cortex. However, MEG is uniquely suited to identification of epileptogenic activity. Mapping of eloquent cortices can be performed at the same time as the epilepsy study with MEG. Clinical MR imaging scans are obtained separately from fMRI and MEG studies, with distinct CPT codes, and provide anatomic reference for functional maps. For both fMRI and MEG, robust paradigms exist for motor, sensory, and language mapping. For both modalities, areas of activation are mapped onto a structural MR imaging study as part of the presurgical evaluation.

Current Indications for MEG and Magnetic Source Imaging

Presurgical Mapping of Epileptogenic Zones. MEG is clinically approved for preoperative planning in patients with intractable, or drug-resistant, epilepsy. The millisecond time resolution of MEG is ideally suited to capture bursts of abnormal neuroelectric activity, as seen in epilepsy, and the spatial precision of magnetic source imaging (MSI) allows the accurate localization of the epileptogenic zone(s) (ie, seizure-generating tissue).¹ The onset of each interictal epileptiform discharge is projected to source space (ie, brain space) as an equivalent current dipole (ECD) to visualize the location of potential seizure onset zone(s). In this way, MEG and MSI can provide unique information for presurgical planning in intractable epilepsy. MEG is optimally beneficial during presurgical planning for cases in which common noninvasive modalities result in an inconclusive hypothesis regarding epileptogenic zone location, MR imaging-negative (ie, nonlesional) cases, cases in which MR imaging identifies multiple lesions (eg, tuberous sclerosis), and patients with large lesions, anatomical malformations, and/or prior resection.¹⁻³

Empirical investigations have found that MEG and MSI contribute added clinical value during presurgical planning in patients with intractable epilepsy, as surgical resection of the epileptogenic zone(s) can eliminate or reduce seizures.⁴⁻⁶ Presurgical planning often involves the acquisition of multiple neuroimaging modalities (eg, MR imaging, FDG-PET, ictal-SPECT, single-photon emission CT). These data are used to plan intracranial electroencephalography (iEEG), in which a grid of subdural electrodes and/or depth electrodes is implanted directly into the brain to confirm

epileptogenic zone localization. Recent studies have revealed good concordance between MEG and iEEG in localizing epileptogenic activity, bolstering MEG's potential as an alternative, noninvasive tool for preoperative planning.⁷

Inclusion of MEG in the presurgical neuroimaging battery bestows better clinical outcomes and correlates with postoperative seizure freedom.^{8,9} Specifically, resection patients in whom the MEG dipole cluster was completely sampled by iEEG had a strikingly higher chance of seizure freedom relative to patients with incomplete/no iEEG sampling. A similar finding was observed for patients in whom the MEG dipole cluster was completely resected relative to those with partial/no resection of the MEG cluster.⁹ Finally, patients with a single tight dipole cluster, those with a cluster that had stable orientation perpendicular to the closest major sulcus, and those with agreement between MEG and iEEG localization were more likely to be seizure-free postresection.

Presurgical Mapping of Eloquent Cortices. MEG is used to non-invasively map the eloquent cortex in patients before they undergo epilepsy or brain tumor surgery. The goals are to minimize deleterious postoperative functional outcomes and/or identify whether functional reorganization has occurred. Specifically, localization of somatosensory, motor, auditory, and/or visual cortices, as well as localization and lateralization of language cortices may be performed to predict postsurgical outcomes and optimize the preservation of these functions postoperatively.¹⁰

Eloquent cortex mapping requires the application of specific tasks during MEG recording that are designed to elicit the functions of interest. These tasks generate magnetic evoked fields, and MSI is employed to localize stereotyped deflections in, or components of, the evoked magnetic field. The ability to capture different neurophysiological responses within 1 recording is a distinct advantage of MEG relative to fMRI, and MEG may be superior for functional mapping in patients who have cerebrovascular malformations or tumors near the functional cortex. However, MEG and fMRI often serve complementary roles in eloquent cortex mapping, and their amalgamation can enhance the reliability of functional localization.^{11,12}

With respect to each function, somatosensory responses reliably map to the posterior bank of the central sulcus contralateral to the side of stimulation in a manner that follows expected somatotopic organization. In a similar fashion, motor responses localize to the primary motor cortex contralateral to the side of movement. Both contralateral and ipsilateral auditory responses may be localized and map to Heschl's gyri. Visual responses localize to the primary visual cortex contralateral to the stimulated visual hemifield near the calcarine fissure.^{13,14} Importantly, prior research has found that such MEG-based localizations have high concordance with intraoperative cortical mapping. Finally, a distributed network of bilateral cortical regions often underlies language processing. Receptive language responses often localize to the posterior superior temporal gyrus (ie, Wernicke's area), supramarginal gyrus, and angular gyrus, while expressive language responses often map to the pars triangularis and pars opercularis in the inferior frontal cortex (ie, Broca's area). A laterality index is computed to determine hemispheric dominance of

language function. Multiple studies have demonstrated high concordance between MEG-based language mapping and invasive procedures (eg, intracarotid amobarbital procedure or Wada), favoring MEG as a noninvasive option for language mapping and lateralization.^{10,15-18}

A key transformative step is the integration of source-modeled MEG data with MR imaging to yield MSI, either by the overlay of single equivalent dipole sources or by statistical mapping of either spontaneous or event-related changes.^{19,20} This renders MEG data directly interpretable by the neuroradiologist in a fashion very analogous to fMRI, but combining both mapping of functional, eloquent cortex, as well as the sources of interictal spontaneous discharges (dysfunctional MR imaging).

CLINICAL MEG RECOMMENDATIONS

Roles, Training, and Certification/Accreditation

Qualifications of Physicians Interpreting Clinical MEG Studies. Physicians interpreting and reporting clinical MEG studies should have appropriate medical licensure and proper training for the clinical application. For radiologists, this may include specialized clinical knowledge of neurophysiology, neuroanatomy, brain mapping, neuropsychology, and image acquisition and interpretation such as required through the American Board of Radiology Subspecialty Certification in Neuroradiology. In addition, MEG-specific training is recommended to include supervised learning or clinical practice of at least 50 MEG studies for the specific indication being reported. Alternatively, a minimum of 2 years of experience interpreting clinical fMRI or MEG brain mapping studies is recommended.

Qualifications of MEG Scientists Involved in Clinical MEG Studies. MEG scientists involved in clinical MEG studies should be well-versed in signal processing, source analysis, neurophysiology, cognitive neuroscience, image processing, physics, and other scientific aspects of MEG and its application to patient care. In addition, MEG-specific training is recommended to include supervised learning or clinical practice of at least 50 MEG studies for the specific indication being reported, which can also be fulfilled through a minimum of 2 years of experience in the source modeling of MEG studies by a postdoctoral fellowship with a clinical MEG component, or through rotations at clinical MEG facilities.

Qualifications of MEG Technologists. The MEG technologist should have a background in either EEG or imaging (eg, MR imaging) or related disciplines. Supervised learning or clinical practice of at least 50 MEG studies, including a review of the principles of MEG technology, technical aspects of the MEG systems, patient preparation, data acquisition, operational routines, tuning procedures, testing procedures, troubleshooting, artifact identification, prevention, and elimination, data storage, and basic source localization procedures. Alternatively, a minimum of 6 months of supervised clinical experience in an active MEG center is recommended.

Procedure/Workflow of Clinical MEG Examination, Analysis, and Reporting

MEG-guided localization of epileptogenic zones involves several key steps. Before recording, surface EEG electrodes and head

position indicator coils are affixed to manufacturer-specified locations on the patient's head. These coils generate a specific frequency during MEG recording to allow for head localization. The patient's head shape and location of head position indicator coils is digitized for subsequent co-registration of MEG and structural MR imaging data. Simultaneous MEG and scalp EEG data are recorded. Typically, 40–120 minutes of spontaneous (ie, resting-state) data are collected. Due to the limited duration of recordings and the movement-related artifact introduced by seizures, ictal discharges are rarely captured. Rather, MEG recordings primarily capture interictal epileptiform discharges.⁸ To increase the yield of interictal epileptiform discharges during the scan, patients are asked to come sleep-deprived and sleep in the scanner.²¹ These data are preprocessed to remove noise and co-register the MEG data with a structural MR imaging (typically a 3D T1). Preprocessing algorithms and steps vary depending on the manufacturer. A professional with specialized training (eg, epileptologist, neurophysiologist, etc) reads the time-series EEG and MEG data and identifies epileptic discharges. The identified discharges are localized to source space via the ECD model, referred to as modeling in this article.²² Modeling can be completed by anyone with specialized training in the neuroscience, physics, and mathematical concepts behind the dipole model (eg, scientist, physician, technologist). Dipoles that meet statistical cutoff criteria (eg, goodness of fit, volume of confidence) are displayed on a structural MR imaging scan, which can be exported to PACS.

Dipoles may form clusters within a specific region. The clustering of 5 or more dipoles within a region is considered a reliable indicator of an epileptogenic zone.²³ Both the tightness and orientation of the dipoles within a cluster have clinical relevance.^{1,9} The location of these dipoles and characteristics of any clusters formed are reported by a physician. A suggested template for reporting is located in the Appendix.

In contrast to presurgical mapping of epileptogenic zones, which relies on resting-state recordings, eloquent cortex mapping relies on task-based recordings. The patient should be awake and alert. During a task, identical or similar stimuli are repetitively delivered to the patient, and a corresponding trigger (eg, number) is time-stamped into the data. Offline, the data are epoched into meaningful windows of time surrounding each stimulus, baseline-normalized, and averaged together to enhance the signal-to-noise ratio. This distinguishes the magnetic evoked field generated by the stimuli, and components of the field are modeled to localize the functional cortex. The time and location of each component modeled are reported by a physician.

Somatosensory cortex mapping most often employs brief electrical stimulations to the median nerve. However, stimulation of the posterior tibial nerve and/or mechanical stimulation of the hand, foot, or other body regions may also be performed. To map the motor cortex, the patient is asked to perform a simple movement such as pressing a button, tapping a finger, or moving a foot at either a self-paced or visually- or auditorily-cued time interval. For auditory cortex mapping, often 1000-Hz tones are briefly presented through inserted ear tubes at 60 dB above the patient's hearing threshold, either monaurally or binaurally.^{10,13} To map the visual cortex, stimuli, often checkerboards, are presented on a projector screen to the full visual field, each hemifield,

or each quadrant. Language cortex mapping may utilize auditory and/or visual stimuli and can be grouped into 2 categories: receptive or expressive. Receptive language tasks include passively listening to words or silently reading words presented on the projector screen. Expressive language tasks include covert verb generation and picture naming.^{10,14,24}

Many of the patients undergoing MEG have epilepsy that is poorly controlled by medications. It is important that safeguards be put in place for responding to medical emergencies. This includes the availability of emergency personnel and supplies depending on the setting.

Billing and Reimbursement

As noted in the Background, since 2002, the CMS has authorized and implemented 3 CPT codes and their payment rates for MEG: 95965, 95966, 95967. Using these 3 codes, clinical MEG is a well-established reimbursable procedure and is accepted as the standard of care in evaluation of patients with epilepsy and in the presurgical mapping of eloquent cortices.

Quality Improvement and Quality Control

A critical component of establishing and maintaining a high-quality clinical MEG program is to invest in the training and education of all team members. Most manufacturers offer training programs for new sites. The American Board of Registration of Electroencephalographic and Evoked Potential Technologists offers a MEG technologist certification program. Both the American Clinical MEG Society and the American Society for Functional Neuroradiology offer clinical guidelines, continuing education at annual meetings, and clinical MEG fellowship training programs for neurologists and neuroradiologists, respectively. Other relevant conferences include the biannual meeting of the International Society for the Advancement of Clinical MEG and the biannual International Conference on Biomagnetism. A number of excellent publications are available, including the *MEG-EEG Primer* textbook, *Clinical Magnetoencephalography and Magnetic Source Imaging* textbook, the November 2020 issue of the *Journal of Clinical Neurophysiology*, and clinical MEG guideline articles published by the International Federation of Clinical Neurophysiology and American Clinical MEG Society.^{13,24,25}

A clear protocol for assessing the technical quality of the data is vital. Noise measurements and empty room recordings are often collected daily or before recording each patient to monitor changes in the environment and identify issues with equipment. During data acquisition, the position of the patient's head within the MEG helmet is monitored for proper placement, observations of artifact and noise are documented, and averages of events during evoked testing may be computed online to visually inspect for the presence of the expected magnetic evoked fields. Routine (eg, monthly) quality-assurance testing of the digitization equipment, MEG system, and software is often conducted by utilizing a phantom for recordings. Collaborative interdepartmental conferences should also be held regularly to compare MEG results with clinical outcomes (eg, stereoelectroencephalography data).

EMERGING INDICATIONS

Concussion

Many articles in the peer-reviewed literature show that MEG can objectively diagnose concussions (mild traumatic brain injury) with significantly more sensitivity (about 85% sensitivity) than the relatively insensitive standard neuroimaging techniques such as CT or MR imaging.^{26–33} EEG has long demonstrated that low-frequency activity in the delta-band (1–4 Hz) is abnormal in awake, alert adults. Studies in animal models confirm that deafferentation of neurons due to traumatic injury to axons or blockage of cholinergic transmission will generate these slow/delta-waves.^{31,34} Resting-state MEG more sensitively detects delta waves than EEG, with about 85% sensitivity in diagnosing concussions compared with normal controls, even in single subjects when using an automated voxelwise algorithm, which also localizes the areas of abnormal slow-waves.²⁶

Another MEG finding in patients with concussion is excessive synchronous resting-state high-frequency gamma-band activity (30–80 Hz) in certain frontal and other brain regions, which may be due to selective vulnerability of inhibitory GABAergic interneurons due to head trauma.²⁹

Resting-state functional connectivity studies with MEG reveal various patterns of aberrant functional connectivity in patients with mild traumatic brain injury, likely reflecting differing mechanisms of injury, including disruption of networks, and injury to inhibitory GABAergic interneurons.^{32,33}

Post-Traumatic Stress Disorder

Post-traumatic stress disorder affects about 7% of American adults during their lifetime and is especially prevalent in combat veterans. Compared with normal controls, MEG in patients with post-traumatic stress disorder shows differences in resting-state neurocircuitry, including hyperactivity in the amygdala, hippocampus, posterolateral orbitofrontal cortex, dorsomedial prefrontal cortex, and insular cortex in high-frequency (beta and gamma) bands; hypoactivity from the ventromedial prefrontal cortex, frontal pole, dorsolateral prefrontal cortex in high-frequency bands; and hypoactivity in the precuneus, dorsolateral prefrontal cortex, temporal and frontal poles, and sensorimotor cortex in alpha and low-frequency bands.³⁵

Autism Spectrum Disorder

The physical properties of MEG offer sensitivity not only to spatial localization of detected signals but also characterization in terms of the time course and spectral content of such brain activity. As such, it may allow description of not just functional centers but also “when” the brain activity is occurring and, indeed, “what” is the nature of such activity. This opens up considerable promise for application to psychiatric disorders, commonly with no MR imaging–visible structural anomaly. One promising target disorder is autism spectrum disorder (ASD), a highly prevalent (~2%) neurodevelopmental disorder. Although there is indeed an ultimate possibility (and current exploration) of identifying early electrophysiologic predictors of ASD in infants and young children, an alternative promising role for MEG lies in the stratification, or subtyping, of the remarkably heterogeneous ASD population. Such stratification may have value in terms of

potential enrichment of clinical trials for behavioral/pharmaceutical therapies as well as potentially providing early “brain-level” indices of drug “target-engagement” as a predictor of ultimate efficacy. Considerable promise is shown in the *latency* of simple sensory evoked responses (eg, the auditory cortex 50-ms [M50] and 100-ms [M100] components, which tend to be delayed in children with ASD, perhaps triggering a cascade of delayed neural communication, with ultimate behavioral sequelae).^{36–38}

Dementia

Dementia is a neurodegenerative condition that usually affects people aged older than 65 years that causes major cognitive dysfunction, loss of independence, and reduced quality of life. The ever-increasing proportion of aged people in modern societies is leading to a substantial increase in the number of people affected by dementia and Alzheimer’s disease (AD) in particular, which is the most common cause for dementia. Several resting-state MEG studies have shown frequency-specific alterations in local and long-range neural synchrony in various dementias, even at the earliest prodromal stages of AD manifestation.³⁹ Increased synchrony delta-theta bands and decreased alpha or beta bands are consistently reported not only in patients with the AD neuropathological spectrum including those who are asymptomatic but carry higher risk of AD, as well as in clinically symptomatic individuals with positive AD biomarkers,^{40–46} but also in patients with variants of primary progressive aphasia, a form of dementia that impacts language function.⁴⁷ Disruption of information flow quantified by MEG source imaging may also underlie clinical symptoms in AD.⁴⁸ Studies have also reported task-induced MEG activity changes in AD with mismatch paradigms that highlight the translational potential for neurophysiological “signatures” of dementia, to understand disease mechanisms in humans and facilitate experimental medicine studies.⁴⁹

CONCLUSIONS

MEG and MSI provide a powerful tool for characterizing brain activity in health and disease. Clinical applications as of this date are in the localization of spontaneous epileptiform activity as part of surgical work-up of patients with seizure disorders as well as presurgical mapping of eloquent cortex for patients undergoing resective surgery of tumors, AVMs, etc. However, there are many emerging applications being researched currently.

A neuroradiologist can be a key member of the team conducting and interpreting MEG studies. Promising future areas of MEG/MSI application will also likely capitalize on the neuroradiologist’s ability to work in a multidisciplinary team, integrating anatomic, physiologic, functional, and clinical information.

Disclosure forms provided by the authors are available with the full text and PDF of this article at www.ajnr.org.

REFERENCES

- Burgess RC. MEG for greater sensitivity and more precise localization in epilepsy. *Neuroimaging Clin N Am* 2020;30:145–58 CrossRef Medline
- Bagić AI, Burgess RC. Utilization of MEG among the US epilepsy centers: a survey-based appraisal. *J Clin Neurophysiol* 2020;37:599–605 CrossRef Medline
- Jung J, Bouet R, Delpuech C, et al. The value of magnetoencephalography for seizure-onset zone localization in magnetic resonance imaging-negative partial epilepsy. *Brain* 2013;136:3176–86 CrossRef Medline
- De Tiège X, Carrette E, Legros B, et al. Clinical added value of magnetic source imaging in the presurgical evaluation of refractory focal epilepsy. *J Neurol Neurosurg Psychiatry* 2012;83:417–23 CrossRef Medline
- Mohamed IS, Toffa DH, Robert M, et al. Utility of magnetic source imaging in nonlesional focal epilepsy: a prospective study. *Neurosurg Focus* 2020;48:E16 CrossRef Medline
- Englot DJ, Nagarajan SS, Imber BS, et al. Epileptogenic zone localization using magnetoencephalography predicts seizure freedom in epilepsy surgery. *Epilepsia* 2015;56:949–58 CrossRef Medline
- Knowlton RC. The role of FDG-PET, ictal SPECT, and MEG in the epilepsy surgery evaluation. *Epilepsy Behav* 2006;8:91–101 CrossRef Medline
- Supek S, Aine CJ. *Magnetoencephalography: From Signals to Dynamic Cortical Networks*. Springer; 2019
- Murakami H, Wang ZI, Marashly A, et al. Correlating magnetoencephalography to stereo-electroencephalography in patients undergoing epilepsy surgery. *Brain* 2016;139:2935–47 CrossRef Medline
- Bowyer SM, Pang EW, Huang M, et al. Presurgical functional mapping with magnetoencephalography. *Neuroimaging Clin N Am* 2020;30:159–74 CrossRef Medline
- Stufflebeam SM. Clinical magnetoencephalography for neurosurgery. *Neurosurg Clin N Am* 2011;22:153–67 CrossRef Medline
- Grummich P, Nimsky C, Pauli E, et al. Combining fMRI and MEG increases the reliability of presurgical language localization: a clinical study on the difference between and congruence of both modalities. *Neuroimage* 2006;32:1793–1803 CrossRef Medline
- Hari R, Baillet S, Barnes G, et al. IFCN-endorsed practical guidelines for clinical magnetoencephalography (MEG). *Clin Neurophysiol* 2018;129:1720–47 CrossRef Medline
- Zillgitt A, Barkley GL, Bowyer SM. Visual mapping with magnetoencephalography: an update on the current state of clinical research and practice with considerations for clinical practice guidelines. *J Clin Neurophysiol* 2020;37:585–91 CrossRef Medline
- Kreidenhuber R, De Tiège X, Rampp S. Presurgical functional cortical mapping using electromagnetic source imaging. *Front Neurol* 2019;10:628 CrossRef Medline
- Hirata M, Kato A, Taniguchi M, et al. Determination of language dominance with synthetic aperture magnetometry: comparison with the Wada test. *Neuroimage* 2004;23:46–53 CrossRef Medline
- Hirata M, Goto T, Barnes G, et al. Language dominance and mapping based on neuromagnetic oscillatory changes: comparison with invasive procedures. *J Neurosurg* 2010;112:528–38 CrossRef Medline
- Findlay AM, Ambrose JB, Cahn-Weiner DA, et al. Dynamics of hemispheric dominance for language assessed by magnetoencephalographic imaging. *Ann Neurol* 2012;71:668–86 CrossRef Medline
- Gofshteyn JS, Le T, Kessler S, et al. Synthetic aperture magnetometry and excess kurtosis mapping of magnetoencephalography (MEG) is predictive of epilepsy surgical outcome in a large pediatric cohort. *Epilepsy Res* 2019;155:106151 CrossRef Medline
- Hillebrand A, Barnes GR. Beamformer analysis of MEG data. *Int Rev Neurobiol* 2005;68:149–71 CrossRef Medline
- King MA, Newton MR, Jackson GD, et al. Epileptology of the first-seizure presentation: a clinical, electroencephalographic, and magnetic resonance imaging study of 300 consecutive patients. *Lancet* 1998;352:1007–11 CrossRef Medline
- Sarvas J. Basic mathematical and electromagnetic concepts of the biomagnetic inverse problem. *Phys Med Biol* 1987;32:11–22 CrossRef Medline
- Burgess RC. In: Levin KH, Chauvel KH, eds. *Handbook of Clinical Neurology; Clinical Neurophysiology: Basis and Technical Aspects*. Vol 160, Chapter 13. Elsevier; 2019:203–14
- Burgess RC, Funke ME, Bowyer SM, et al; ACMEGS Clinical Practice Guideline (CPG) Committee. American Clinical Magnetoencephalography Society Clinical Practice Guideline 2: presurgical

- functional brain mapping using magnetic evoked fields. *J Clin Neurophysiol* 2011;28:355–56 CrossRef Medline
25. Bagic AI, Knowlton RC, Rose DF, et al; ACMEGS Clinical Practice Guideline (CPG) Committee. **American Clinical Magnetoencephalography Society clinical practice guideline 1: recording and analysis of spontaneous cerebral activity.** *J Clin Neurophysiol* 2011;28:348–54 CrossRef Medline
 26. Huang MX, Nichols S, Baker DG, et al. **Single-subject-based whole-brain MEG slow-wave imaging approach for detecting abnormality in patients with mild traumatic brain injury.** *Neuroimage Clin* 2014;5:109–19 CrossRef Medline
 27. Huang MX, Nichols S, Robb A, et al. **An automatic MEG low-frequency source imaging approach for detecting injuries in mild and moderate TBI patients with blast and non-blast causes.** *Neuroimage* 2012;61:1067–82 CrossRef Medline
 28. Huang MX, Theilmann RJ, Robb A, et al. **Integrated imaging approach with MEG and DTI to detect mild traumatic brain injury in military and civilian patients.** *J Neurotrauma* 2009;26:1213–26 CrossRef Medline
 29. Huang MX, Huang CW, Harrington DL, et al. **Marked increases in resting-state MEG gamma-band activity in combat-related mild traumatic brain injury.** *Cereb Cortex* 2020;30:283–95 CrossRef Medline
 30. Lewine JD, Davis JT, Bigler ED, et al. **Objective documentation of traumatic brain injury subsequent to mild head trauma: multimodal brain imaging with MEG, SPECT, and MRI.** *J Head Trauma Rehabil* 2007;22:141–55 CrossRef Medline
 31. Gloor P, Ball G, Schaul N. **Brain lesions that produce delta waves in the EEG.** *Neurology* 1977;27:326–33 CrossRef Medline
 32. Huang MX, Harrington DL, Robb Swan A, et al. **Resting-state magnetoencephalography reveals different patterns of aberrant functional connectivity in combat-related mild traumatic brain injury.** *J Neurotrauma* 2017;34:1412–26 CrossRef Medline
 33. Tarapore PE, Findlay AM, Lahue SC, et al. **Resting state magnetoencephalography functional connectivity in traumatic brain injury.** *J Neurosurg* 2013;118:1306–16 CrossRef Medline
 34. Ball GJ, Gloor P, Schaul N. **The cortical electromicrophysiology of pathological delta waves in the electroencephalogram of cats.** *Electroencephalogr Clin Neurophysiol* 1977;43:346–61 CrossRef Medline
 35. Huang M, Risling M, Baker DG. **The role of biomarkers and MEG-based imaging markers in the diagnosis of post-traumatic stress disorder and blast-induced mild traumatic brain injury.** *Psychoneuroendocrinology* 2016;63:398–409 CrossRef Medline
 36. Roberts TPL, Khan SY, Rey M, et al. **MEG detection of delayed auditory evoked responses in autism spectrum disorders: towards an imaging biomarker for autism.** *Autism Res* 2010;3:8–18 CrossRef Medline
 37. Roberts TP, Cannon KM, Tavabi K, et al. **Auditory magnetic mismatch field latency: a biomarker for language impairment in autism.** *Biol Psychiatry* 2011;70:263–69 CrossRef Medline
 38. Matsuzaki J, Kuschner ES, Blaskey L, et al. **Abnormal auditory mismatch fields are associated with communication impairment in both verbal and minimally verbal/nonverbal children who have autism spectrum disorder.** *Autism Res* 2019;12:1225–35 CrossRef Medline
 39. López-Sanz D, Serrano N, Maestú F. **The role of magnetoencephalography in the early stages of Alzheimer's disease.** *Front Neurosci* 2018;12:572 CrossRef Medline
 40. Nakamura A, Cuesta P, Fernández A, et al. **Electromagnetic signatures of the preclinical and prodromal stages of Alzheimer's disease.** *Brain* 2018;141:1470–85 CrossRef Medline
 41. Pusil S, López ME, Cuesta P, et al. **Hypersynchronization in mild cognitive impairment: the 'X' model.** *Brain* 2019;142:3936–50 CrossRef Medline
 42. Canuet L, Pusil S, López ME, et al. **Network disruption and cerebrospinal fluid amyloid-beta and phospho-tau levels in mild cognitive impairment.** *J Neurosci* 2015;35:10325–30 CrossRef Medline
 43. Ranasinghe KG, Cha J, Iaccarino L, et al. **Neurophysiological signatures in Alzheimer's disease are distinctly associated with TAU, amyloid-beta accumulation, and cognitive decline.** *Sci Transl Med* 2020;12:eaa4069 CrossRef Medline
 44. Ranasinghe KG, Hinkley LB, Beagle AJ, et al. **Regional functional connectivity predicts distinct cognitive impairments in Alzheimer's disease spectrum.** *Neuroimage Clin* 2014;5:385–95 CrossRef Medline
 45. Sami S, Williams N, Hughes LE, et al. **Neurophysiological signatures of Alzheimer's disease and frontotemporal lobar degeneration: pathology versus phenotype.** *Brain* 2018;141:2500–10 CrossRef Medline
 46. Cuesta P, Barabash A, Aurtinetxe S, et al. **Source analysis of spontaneous magnetoencephalographic activity in healthy aging and mild cognitive impairment: influence of apolipoprotein E polymorphism.** *J Alzheimers Dis* 2015;43:259–73 CrossRef Medline
 47. Ranasinghe KG, Hinkley LB, Beagle AJ, et al. **Distinct spatiotemporal patterns of neuronal functional connectivity in primary progressive aphasia variants.** *Brain* 2017;140:2737–51 CrossRef Medline
 48. Engels MM, Yu M, Stam CJ, et al. **Directional information flow in patients with Alzheimer's disease: a source-space resting-state MEG study.** *Neuroimage Clin* 2017;15:673–81 CrossRef Medline
 49. Kocagoncu E, Quinn A, Firouzian A, et al; Deep and Frequent Phenotyping Study Team. **Tau pathology in early Alzheimer's disease is linked to selective disruptions in neurophysiological network dynamics.** *Neurobiol Aging* 2020;92:141–52 CrossRef Medline

APPENDIX

Sample MEG Report

Patient:

Date of Birth:

MRN:

Acc#:

EXAM: MAGNETOENCEPHALOGRAPHY (MEG)

DATE OF EXAM:

History and reason for Study:

Copy from Tech report

MEG is performed as part of presurgical planning.

Technique:

The Magnetoencephalography (MEG) scan was performed at **. There were [] minutes of spontaneous magnetoencephalography (MEG) with electroencephalograph (EEG) data acquired with a ** MEG system and individual/cap EEG electrodes. The patient was asked to be sleep-deprived before the appointment.

Somatosensory: Somatosensory functioning was assessed by using electrical stimulation of the right and left median nerves, each median nerve was tested twice for waveform reproduction. 200 stimuli were delivered at 800- to 1100-ms intervals. 200 trials of 300 ms were averaged with a prestimulus baseline of 100 ms and a 200-ms poststimulus time.

Language: Receptive language fields were obtained by binaural presentation of 180 audio words. The subject was tested twice, once in a passive listening mode, and again with the task to overtly repeat 5 target words, when presented. At least 120 trials were averaged for each test with a 500 seconds prestimulus baseline and 1000 ms poststimulus time.

Motor: The patient was instructed to press a button pad with index finger of their right and left hand. There were 2 trials run for waveform reproduction. The rate of tapping was deliberately varied but averaged about one tap every 2–3 seconds. Each epoch was 2 seconds capturing 100 button press stimuli.

Auditory: 1000 Hz tones were generated and delivered monaurally without masking at 60-dB hearing loss to ear inserts. The tone burst consisted of a 250-ms duration tone with a 15-ms rise/fall time. The tone burst was repeated 100 times, delivered once every 2 seconds. One hundred trials were averaged with a 200-ms prestimulus baseline and 1800 ms poststimulus time.

Visual: Pattern reversal stimuli were projected into the shielded room, reflected via one mirror onto an opaque white screen, and then reflected directly into the patient's eyes. The patient [did/did not] require vision correction glasses [rx L/rx R]. The checkerboard had a 50° radius and size of the projected checkerboard squares were approximately 5°, which were alternated with a refresh rate of 0.4 Hz. Six hundred epochs of hemifield stimulation were recorded for each hemifield with a 100-ms prestimulus baseline and 3000-ms poststimulus time following each pattern shift. The patient was asked to fixate on a single spot located just to the left or right of the pattern checkerboard image for hemifield studies.

All recorded data were analyzed utilizing ** software. MEG activity was superimposed on the patient's 3D-volumetric brain images obtained on the MR imaging performed on [].

Artifacts:

delete if none

Comparisons:

* include MR imaging, fMRI, PET, SPECT *

FINDINGS:

Interictal Findings:

The patient was awake, drowsy, and sleeping during the recording. Epileptiform discharges [were/were not] observed during spontaneous MEG recordings. [] selected epileptiform discharges in the MEG were mapped by using a single equivalent current dipole (ECD) model. A single dipole was selected to represent each epileptiform discharge. The dipole selection criteria included a goodness of fit of 80% or better, and a confidence volume less than 1 cm³. Dipole locations were calculated and projected onto the patient's MR imaging where they appear as yellow triangles for interictal spikes.

Interictal Epileptiform Discharge Source Modeling Showed Dipoles From:

Tight/Loose/Scattered cluster in the left/right *** with stable/variable perpendicular/oblique/parallel orientation.

Ictal Findings:

No seizures were captured.

Somatosensory Findings:

All runs produced robust responses with consistent mapping of corresponding peaks for each run.

For stimulation of the left thumb, the latency of N20m response was *** msec.

For stimulation of the left thumb, the latency of N30m response was *** msec.

For stimulation of the right thumb, the latency of N20m response was *** msec.

For stimulation of the right thumb, the latency of N30m response was *** msec.

Somatosensory Response Source Modeling:

Localized to expected locations.

Language Findings:

ECD models were calculated every millisecond from 250- to 750-ms poststimulus onset independently for each sensor's hemisphere corresponding to left and right evoked fields. All ECD estimates meeting the statistical thresholds and localizing to temporal cortical areas were entered into laterality quantification.

Language Response Source Modeling:

Receptive language with active word recall task localized to the left/right temporal lobe with a laterality index of +/- X.XX, concentrated in the Wernicke area.

Receptive language with passive listening localized.

Motor Findings:

Movement of the left second digit generated a good response. The motor response was seen with a latency of *** ms following the activation of the button.

Movement of the right second digit generated a good response. The motor response was seen with a latency of *** ms following the activation of the button.

Motor Response Source Modeling:

Localized to expected locations.

Auditory Findings:

Trials for each ear were performed. The N100m response was a sustained response. The best fields picked to represent the contralateral responses had a latency of *** ms for the left ear stimulation and *** ms for the right ear stimulation. The best fields picked to represent the ipsilateral responses had latency of *** ms for the left ear stimulation and *** ms for the right ear stimulation.

Auditory Response Source Modeling:

Localized to expected locations in the primary auditory cortex.

Visual Findings:

All runs produced robust responses with consistent mapping of corresponding peaks for each run.

For right visual hemifield mapping, the N75m, P100m, and N145m responses were easily identified and had typical latencies, waveform morphology, topographic field maps, and dipole moments.

For left visual hemifield mapping, the N75m, P100m, and N145m had typical latencies, waveform morphology, topographic field maps, and dipole moments.

Visual Response Source Modeling:

Localized appropriately to the primary visual cortex (V1).

IMPRESSION:

-attending, MD.

A Brief History of Neuroradiology and the 60th Anniversary of the ASNR: “Through the Decades with ASNR”

On Friday November 8, 1895, Wilhelm Conrad Roentgen revolutionized the field of medicine with the discovery of x-rays, by creating a photographic image of the bones of his wife Bertha's hand wearing her wedding ring. Within weeks, Roentgen reported his preliminary findings, “On a New Kind of Rays,” in the *Proceedings of the Würzburg Physico-Medical Society*, which was subsequently published in the journal *Science*.¹ Just a few months later in February 1896, the first clinical x-ray was performed at Dartmouth College in Hanover, New Hampshire, which diagnosed a Colles fracture; early efforts at angiography soon followed. For his pioneering work, Roentgen was awarded the first Nobel Prize in Physics in 1901.

Applications of Roentgen's discovery to imaging of the skull and nervous system quickly followed, and by the early 1900s, the term “Neuro-Röntgenologie” was coined by an Austrian doctor at Vienna University, Arthur Schüller (December 28, 1874, to October 13, 1957, of Hand-Schüller-Christian disease fame).^{2,3} Schüller published *Die Schädelbasis im Röntgenbilde (The Skull Base on the Radiogram)*, the first systematic survey of head x-rays, in 1905. Although his 1912 book *Röntgendiagnostik der Erkrankungen des Kopfes (X-ray Diagnosis of Diseases of the Head)* became the then standard text on neuroimaging, Schüller, owing to his Jewish origins, was expelled from Austria in 1938 after it was annexed by the Nazis, ultimately relocating to Melbourne, Australia (his sons Franz and Hans were killed in concentration camps in 1943 and 1944). In 1949, Schüller was elected as honorary president (in absentia) of the second Symposium Neuroradiologicum.

As early as 1902, Antoine Bécclère studied acromegaly on skull x-rays and was an early leader in the development of radiation therapy.⁴ In 1908, G.E. Pfahler, who studied the use of x-rays in oral surgery, made several technical advances in x-ray tube technology, such as focal spot optimization.⁵ Head and neck radiology, as an early subspecialty within neuroradiology, further expanded with the description of the Waters view of the paranasal sinuses in 1914 (Fig 1).

The next set of innovations that moved the field of neuroimaging forward related to the use of contrast media. Before the advent of cross-sectional imaging, x-ray projections could only reliably distinguish the density differences among bone, air, fat, and soft-tissue water, markedly limiting assessment of gray matter, white matter, and supporting vascular and neural parenchymal tissues. The first big advance in this regard was the seminal development of air contrast ventriculography and pneumoencephalography in 1918 by Dr Walter Edward Dandy (April 6, 1886, to April 19, 1946, of Dandy-Walker syndrome fame), an American neurosurgeon and scientist, considered one of the founding fathers of neurosurgery.^{6,7} In 1921, Julius Sicard published the first use of iodized oil as an intrathecal myelography contrast material.⁸ Further refinement of the myelo-

graphic technique continued during the next several decades, including with the development of safer, more effective water-soluble nonionic contrast agents. Soon after the widespread adoption of CT scanning in the mid-1970s, this technique evolved into CT myelography, first published in 1976 by Di Chiro and Schellinger.⁹ Indeed, today myelography remains an essential tool in our diagnostic armamentarium for selected patients, even in this current age of MR imaging as a cornerstone of neurodiagnosis.¹⁰

The adoption of cerebral angiography in advancing both neurodiagnosis and neurotherapeutics cannot be overstated. In 1927, António Caetano de Abreu Freire Egas Moniz (November 29, 1874, to December 13, 1955), a Portuguese neurologist and creator of cerebral angiography, presented his findings at the Neurological Society in Paris and the French Academy of Medicine.¹¹ He was the first person to successfully visualize the brain vasculature by using radiopaque substances, which, together with contrast-enhanced myelography and pneumoencephalography, formed the basis of all advanced neurodiagnosis until the advent of CT (and later MR) cross-sectional imaging. Additional refinements included those by Dr Bernard George Ziedses des Plantes, who was first to publish the methodology for both plain film tomography (1931) and DSA (1934).¹²

Indeed, the origin of the North American subspecialization in radiology in general and of neuroradiology in particular can largely be traced to the efforts of Dr Juan Taveras and Dr Ernest Wood at the Neurologic Institute of New York City's Columbia Presbyterian Medical Center, beginning in the early 1950s. Taveras was successful in creating the first National Institutes of Health-funded neuroradiology fellowship in North America (Fig 2),¹³ as well as establishing radiologist expertise for both performance and interpretation of arteriograms, pneumoencephalograms, and myelograms, a practice already well-established in Europe.

Moreover, and perhaps more important, Taveras and Wood collated, codified, and disseminated their decades of collective experience with neuroangiography, pneumoencephalography, and myelography diagnostic techniques to write their magnum opus, state-of-the-art, 2-volume, almost 2000-page textbook, titled *Diagnostic Neuroradiology* (Fig 3). This work was recognized as “monumental” in a 1964 *Archives of Neurology* book review, which also acknowledged “the heritage of Dr. Cornelius Dyke” (for whom a major American Society of Neuroradiology [ASNR] research award is named) regarding the depth and breadth of material covered.¹⁴

“It is, indeed, a rare privilege to review the volume on ‘Diagnostic Neuroradiology’ by Drs. Taveras and Wood, as one at once recognizes the monumental character of this work. With great humility the authors, both leaders in this relatively new field of radiology, present this book as a text for students, a handbook for graduates in the field, and a record of working principles found useful in their cumulative experience. The book, not only achieves these objectives, but, based on almost 20 years of consecutive service, first by Dr. Wood and then by Dr. Taveras as Directors of Radiology at the Neurological Institute of New York, it reflects the heritage of Dr. Cornelius Dyke and the author's

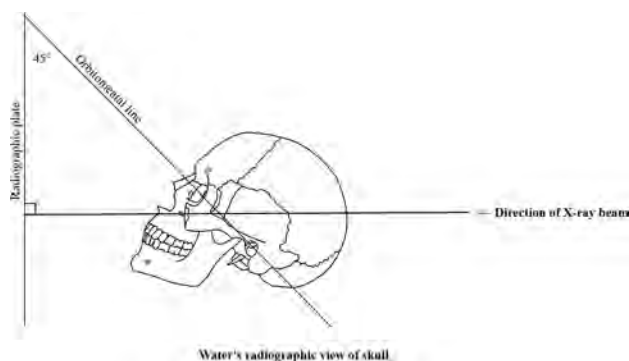


FIG 1. Waters projection of the paranasal sinuses. Image created by Saurabh Patil, 2012 and reproduced under Creative Commons Attribution-SA license.

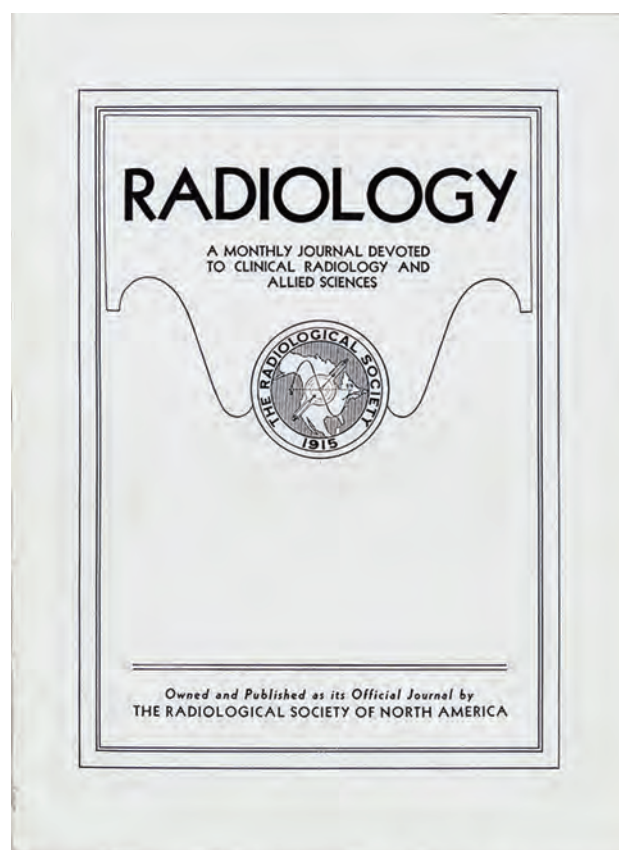
wealth of clinical exposure in the depth and richness of the material presented.

"The work is divided into 4 major areas: (1) The Skull, (2) Intracranial Pneumography, (3) Angiography, and (4) Diseases of the Spinal Cord"

Dr. Taveras established one of the first annual postgraduate courses in neuroradiology in 1956, and in 1961, New York City was selected to host the VII Symposium Neuroradiologicum, to be held in 1964 (Fig 4). History was made, however, on April 19, 1962, at a dinner organized by Dr Taveras at Keen's English Chop House in New York City, during which the ASNR was founded.¹⁵ Per Dr Gordon Potts, Dr Taveras' motivation for forming a society was 2-fold:

"First, he [Juan] felt that there should be a society that would bring together all neuroradiologists in North America to exchange ideas and to have some unity of purpose as we planned the future of the specialty. Second, he wanted those neuroradiologists to participate in the planning of the symposium, which he felt had the potential to enhance the international recognition of neuroradiology in North America."

Invitations were extended to radiologists from strong programs, with broad geographic diversity, who were full-time dedicated neuroimagers; participants included Ernest Wood (Dr. Taveras' predecessor and successor at the Neurologic Institute), Norman Chase and Gordon Potts (also Neurologic Institute staff), Norman Leeds (first National Institutes of Health-funded neuroradiology fellow in North America), Mannie Schecter (St. Vincent's Hospital, trained at Queen Square London), Giovanni di Chiro (Director of National Institutes of Health Neuroradiology), Eugene Leslie (University of Buffalo and first National Institutes of Health-funded neuroradiology fellowship for training outside the US), Donald McRae (from the Montreal Neurological Institute, the only Canadian, and considered the "father of Canadian neuroradiology"), Fred Hodges III (Mallinckrodt Institute of Radiology in St. Louis), Harold O. Peterson and Colin B. Holman (University of Minnesota and organizer of the first neuroradiology postgraduate course in 1939, and Mayo Clinic Minnesota, respectively),¹⁶⁻¹⁸ and



FELLOWSHIP IN NEURORADIOLOGY COLUMBIA UNIVERSITY, NEW YORK

The Department of Radiology at Columbia University-Presbyterian Medical Center, in co-operation with the National Institute of Neurological Diseases and Blindness, offers a two-year Fellowship in Neuroradiology at the Neurological Institute. The candidates must be radiologists who have completed their three-year residency training. The stipend is to be determined by the individual needs of the applicant.

Further information may be obtained from Juan M. Taveras, M.D., Columbia-Presbyterian Medical Center, New York 32, N. Y.

FIG 2. Advertisement for first neuroradiology fellowship program in North America, funded by the National Institute of Neurological Diseases and Blindness around March, 1960. The "stipend" was negotiable on the basis of the "individual needs of the applicant." Reproduced with permission of the Radiological Society of North America from: Fellowship in Neuroradiology Columbia University, New York. *Radiology* 1960 74:3, 491.

finally, Hans Newton and William Hanafée (both west coast angiographers at University of California, San Francisco, and University of California, Los Angeles, respectively, the latter of Bentson-Hanafée catheter fame). Most interesting, Keen's English Chop House, founded in 1885 as a "gentlemen's only" restaurant until it was "invaded" in 1901 by "infamous" British actress Lilly Langtry, is still in operation, just northeast of Macy's Herald Square on 36th Street in New York City; its Web presence continues to highlight

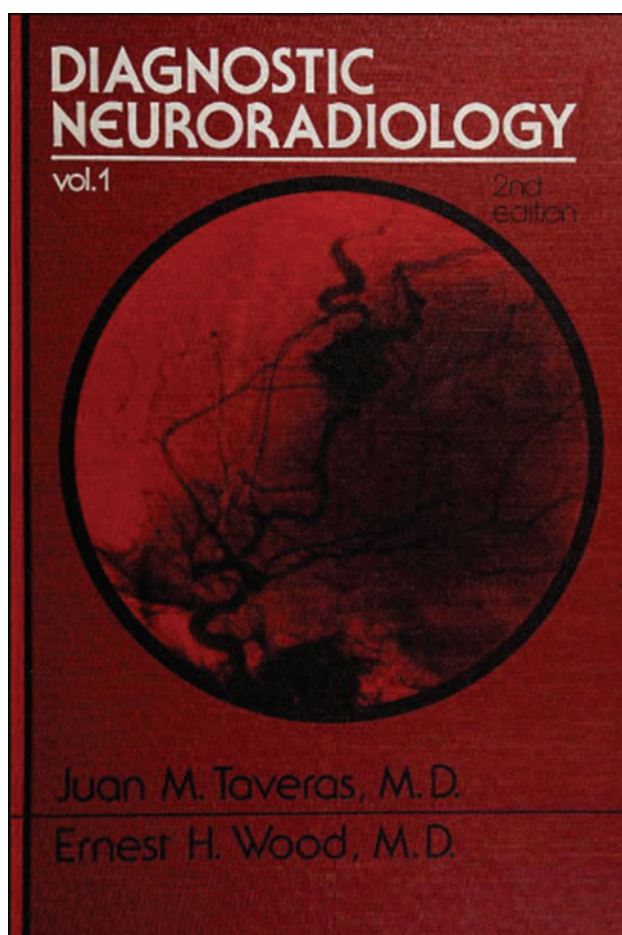


FIG 3. Cover of volume 1, *Diagnostic Neuroradiology*, by Taveras and Wood (Courtesy of Eric Russell, MD). Reproduced with permission of Wolters Kluwer (Williams and Wilkins) from JM Taveras and EH Wood: *Diagnostic Radiology 2 Volume Set*, 1976.

“enormous steaks and signature mutton chops served in a maze of clubby, wood-paneled rooms.”

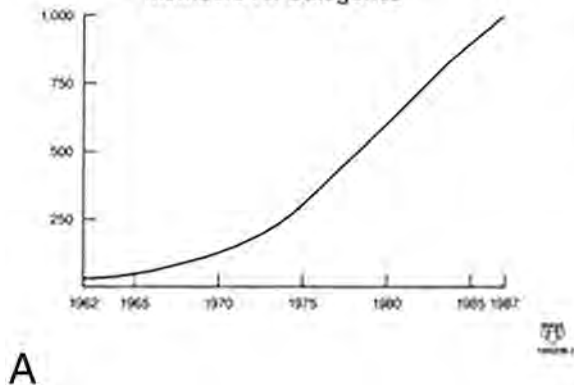
From this small group of 14 all-male neuroradiologists, sitting at a single long table eating a meal of beef in a wood-paneled room, the ASNR grew rapidly, maturing to its current diverse and inclusive membership of more than 6000 neuroimagers and neurointerventionalists in 2022. Its first annual meeting, less than 6 months later, on October 7, 1963, was held in Montreal, Canada at the Queen Elizabeth Hotel. A little more than 1 year later in February 1, 1965, the ASNR was incorporated in the state of New York, and during the next decade, it continued to grow at an accelerating pace (Fig 5). Moreover, although its name states “American,” the ASNR has had an increasingly international membership and presence, with its 10th annual meeting held in Mexico City at the Maria-Isabel Sheraton Hotel. Indeed, 54 years after the “dinner at Keen’s,” the ASNR International Imaging Series was founded, providing speakers for global programs, with the first meeting held in Bangkok in May 2016. The next year, 2017, saw the launch of the Anne G. Osborn ASNR International Outreach Professor Program.

Through the *American Journal of Neuroradiology* (*AJNR*), the ASNR has maintained a leadership role in the advancement and dissemination of research, reviews, guidelines, and expert opinion related to neuroimaging and neurointervention. On July 27, 1978, Norman Leeds formed a committee to consider publication of an ASNR journal, culminating in the first issue of the *AJNR* appearing on January 1, 1980; an editorial by Dr Taveras appeared on page 1, volume 1 of that inaugural issue (Fig 6). Although initially the *AJNR* was published as a bimonthly joint venture between the American Roentgen Ray Society and the ASNR, with Juan Taveras as the Editor-in-Chief,^{16,19} in 1986, ownership of the *AJNR* officially passed solely to the ASNR; the only changes at that time were to the front cover, including both a minor change in color shading and



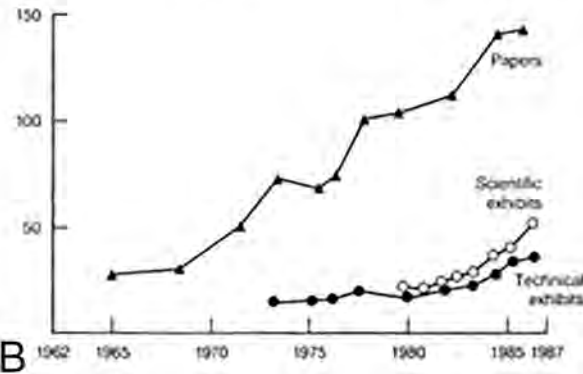
FIG 4. Photo of a medallion from the VIII Symposium Neuroradiologicum, which took place in Paris in 1967. This front side shows individuals considered to be pivotal in the development of neuroradiology; the opposite side lists the locations and dates of previous meetings, including the VII Symposium in New York City (courtesy of Jonathan D. Clem, MD).

AMERICAN SOCIETY OF NEURORADIOLOGY Members All Categories



A

ASNR PRESENTATIONS



B

FIG 5. Growth of ASNR membership and scientific presentations during its first 25 years.

Editorial

The Development of Neuroradiology in the United States

The concept of subspecialization within radiology began to take shape more than 30 years after the discovery of the roentgen rays. Probably the ideal of specializing in the radiology of the nervous system was the earliest one to occur. Contributing factors were the first "special procedures" in diagnostic radiology (pneumoencephalography, cerebral angiography, myelography) and the spectacular development (and accompanying glamour) of neurological surgery under the impetus of Harvey Cushing and others in the second to the fourth decades of this century. Dr. Cornelius Dyke was the first full-time neuroradiologist in the United States. He joined the Department of Radiology at the Neurological Institute of New York in 1929, after having trained at the Peter Bent Brigham Hospital where he was stimulated by what he saw there in radiology of the nervous system in Harvey Cushing's service. His untimely death in 1943 at the young age of 42 cut short what promised to be a brilliant career. Undoubtedly, Dyke would have trained

Much had been done before the 50s to demonstrate the importance of radiologic diagnosis in the management of the neurological patient, a fact well recognized by the neurologists and particularly by the neurosurgeons. In this country, Leo M. Dineffort, a neurosurgeon, had written extensively in this field, and had given his support and was responsible for awakening an interest in neurological radiology among the general radiologists in the hospitals with whom he was associated. But in the absence of any formal training, for a long time it remained just that—general radiologists with some interest in neuroradiology—without any possibility of developing real specialists in the field.

This lack of training opportunity was recognized by the National Institute of Neurological Diseases and Blindness (NINDS). A decision was made by the National Advisory Council of that Institute to support training in neuroradiology which was to combine clinical and research training, similar to established training programs in neurology and neurology.

FIG 6. *AJNR*, page 1/volume 1, January/February 1980; editorial by Juan Taveras, Editor-in-Chief.



FIG 8. Part of the brochure for the ASNR 50th "Golden Anniversary" Annual Meeting and Foundation of the ASNR Symposium in New York, the city in which the ASNR was founded.



FIG 7. Cover design and shading changes have continued periodically for the *AJNR* (Courtesy of Eric Russell, MD).

insertion of the words, "Official Journal, American Society of Neuroradiology."²⁰ Periodic changes in cover design and shading have continued during the next several decades (Fig 7).

The 20th, 25th, and 30th annual meetings were held at the Washington, DC Hilton (1982), New York City Hilton (1987), and St. Louis Adam's Mark Hotel (1992), respectively.²¹⁻²³ Another major milestone in 1992 was the adoption of a neuroradiology "Certificate of Added Qualification" (CAQ) examination by the American Board of Radiology; Dr Taveras participated in that first neuro-CAQ oral board examination, held in Louisville, Kentucky. The Foundation of the ASNR, the philanthropic arm of the American Society of Neuroradiology, a 501 (c) (6) professional society for neuroradiologists, was founded in 1995. The first ASNR website went live on December 20, 1996; it contained only two pages of information. ASNR joined Twitter in 2010. The 40th annual meeting was held in 2002 at the Vancouver, Canada Convention & Exhibition Center, and the 50th annual meeting again was held at the New York City Hilton on 6th Avenue (Fig 8). Golden anniversary celebration events included a dinner at Keen's for the ASNR leadership.

ASNR Past Presidents

2022-23 Erin Simon Schwartz, MD, FACP
 2021-22 Tina Young Poussaint, MD, FACP
 2020-21 Joshua A. Hirsch, MD, FACP, FSIR, FSNIS
 2019-20 Robert M. Barr, MD, FACP
 2018-19 Pina C. Sanelli, MD, MPH, FACP
 2017-18 Jacqueline A. Bello, MD, FACP
 2016-17 Howard A. Rowley, MD
 2015-16 Laurie A. Loevner, MD
 2014-15 Gordon K. Sze, MD, FACP
 2013-14 Mauricio Castillo, MD, FACP
 2012-13 Pamela W. Schaefer, MD
 2011-12 David B. Hackney, MD, FACP
 2010-11 Carolyn Cidis Meltzer, MD, FACP
 2009-10 John R. Hesselink, MD, FACP
 2008-09 Robert D. Zimmerman, MD, FACP
 2007-08 David M. Yousef, MD, MBA
 2006-07 Robert I. Grossman, MD
 2005-06 Patricia A. Hudgins, MD
 2004-05 Victor M. Haughton, MD
 2003-04 Charles M. Strother, MD
 2002-03 Patrick A. Turski, MD, FACP
 2001-02 William P. Dillon, MD
 2000-01 William S. Ball, Jr., MD
 1999-00 Eric J. Russell, MD, FACP
 1998-99 A. James Barkovich, MD
 1997-98 Richard E. Latchaw, MD
 1996-97 Burton P. Drayer, MD
 1995-96 Robert R. Lukin, MD
 1994-95 Robert M. Quencer, MD
 1993-94 Glenn S. Forbes, MD, FACP
 1992-93 David Norman, MD
 1991-92 R. Nick Bryan, MD, PhD
 1990-91 Anton N. Hasso, MD, FACP
 1989-90 Joseph F. Sackett, MD
 1988-89 Anne G. Osborn, MD
 1987-88 Michael S. Huckman, MD
 1986-87 Derek C. Hanwood-Nash, MD
 1985-86 R. Thomas Bergeron, MD
 1984-85 Samuel M. Wolpert, MD

1983-84 O. Wayne Houser, MD
 1982-83 Arthur E. Rosenbaum, MD
 1981-82 Gabriel H. Wilson, MD
 1980-81 George Wortzman, MD
 1979-80 David O. Davis, MD
 1978-79 Stephen A. Kieffer, MD
 1977-78 Sadek K. Hilal, MD
 1976-77 Norman E. Leeds, MD
 1975-76 Irvin I. Kricheff, MD
 1974-75 Hillier L. Baker, Jr., MD
 1973-74 T. Hans Newton, MD
 1972-73 Fred J. Hodges, III, MD
 1971-72 Norman E. Chase, MD
 1970-71 D. Gordon Potts, MD
 1969-70 Giovanni Di Chiro, MD
 1968-69 Colin B. Holman, MD
 1967-68 Harold O. Peterson, MD
 1966-67 Ernest H. Wood, MD
 1965-66 Donald L. McRae, MD
 1964-65 Mannie M. Schechter, MD
 1962-64 Juan M. Taveras, MD

Founders

Norman E. Chase, MD
 Giovanni Di Chiro, MD
 William N. Hanafec, MD
 Fred J. Hodges, III, MD
 Colin B. Holman, MD
 Norman E. Leeds, MD
 Eugene V. Leslie, MD
 Donald L. McRae, MD
 Thomas H. Newton, MD
 Harold O. Peterson, MD
 D. Gordon Potts, MD
 Mannie M. Schechter, MD
 Juan M. Taveras, MD
 Ernest H. Wood, MD

* Deceased

FIG 9. Sixtieth anniversary roster of ASNR presidents, 1962–2022.

PAST OFFICERS	
1962–64	
President	Juan M. Taveras
Vice-President	Mannie M. Schechter
Secretary-Treasurer	Norman E. Chase
1964–65	
President	Mannie M. Schechter
Vice-President	Donald L. McRae
Secretary-Treasurer	Norman E. Chase
1965–66	
President	Donald L. McRae
Vice-President	Ernest H. Wood
Secretary-Treasurer	Alan E. Zimmer
1966–67	
President	Ernest H. Wood
Vice-President	Harold O. Peterson
Secretary-Treasurer	Alan E. Zimmer
1967–68	
President	Harold O. Peterson
Vice-President	Colin B. Holman
Secretary-Treasurer	Alan E. Zimmer
1968–69	
President	Colin B. Holman
Vice-President	D. Gordon Potts
Secretary-Treasurer	Alan E. Zimmer
1969–70	
President	Giovanni DiChiro
Vice-President	Norman E. Chase
Secretary	Eugene V. Leslie
Treasurer	Thomas H. Newton

FIG 10. Slate of officers from the early, founding years of the ASNR, 1962–1970.

The ASNR Past Presidents Association was established in 2019; a roster of all ASNR presidents since the society's founding 60 years ago (Fig 9) as well as a listing of the officers during the initial, early years of the society (Fig 10) are presented in Figures 9 and 10. Across the years, several of the pioneering founding and early leaders of the society have been memorialized in the pages of the *AJNR*.^{24–28} An oral history of the ASNR is currently in preparation, which will include numerous personal recollections, along with amusing anecdotes. One example, recounted by Ralph Heinz, one of Dr Taveras' first trainees, to his friend Dr Jim Provenzale concerns Mannie Schechter, first Vice President and second President of the ASNR (Fig 10). Mannie, who in original photos is often seen sporting an impish grin, was asked by Dr Taveras to describe a skull radiograph during teaching rounds. Schechter replied, "I see abnormal calcification near the vertex; the patient has a vertex meningioma." Being his playful self, Juan replied, "Well, what if I told you that this patient had just been walking under a construction site and a brick fell on the top of his head? What would you say then?" Without missing a beat, Schechter replied, "I'd say 'God damn', it fell right on that meningioma!"

The ASNR's first fully virtual meeting was held remotely from May 30 to June 4, 2020, during the first year of coronavirus disease (COVID) social distancing. A virtual meeting was again held in 2021, with "social events" that ranged from online

wine-tasting (led by ASNR senior member and Master Sommelier Alisa Gean) to "wellness" yoga and "relaxation response" sessions. Our 2022, Sixtieth Anniversary ASNR meeting was again held at the New York City Hilton as our first hybrid live/remote annual meeting, 3 years into COVID; this was a joint meeting with the Symposium Neuroradiologicum XXII.

CONCLUSIONS

An update of the 20-year-old numbers cited in the final paragraph of Michael Huckman's 2001 *AJNR* historical retrospective, *Dinner at Keen's: The Founding of the American Society of Neuroradiology*¹⁵ is the following:

"From an intimate meeting of 14 radiologists seated at a single table (in 1962), the ASNR (in 2022) has grown to a membership of nearly 6000, publishes a journal with worldwide circulation of 7102, holds an annual meeting with attendance of approximately 1800, oversees a well-funded foundation to support the research efforts of

young investigators, and has among its membership numerous department chairs and major officeholders in prestigious national and international medical organizations. It was the first organized subspecialty society in radiology and, during its 60-year existence, has set an example of establishing training standards and educational programs that have been emulated many times by younger radiologic subspecialty societies.”

In 2022, the year of our 60th “Diamond” Anniversary, the ASNR has matured into a global society that manages 6 regional and specialty societies, including the American Society of Functional Neuroradiology, American Society of Head and Neck Radiology, American Society of Spine Radiology, Eastern Neuroradiological Society, and Western Neuroradiological Society, plus the World Federation of Neuroradiological Societies, and is run by 18 full-time staff members. The society remains true to its founding mission statement of April 19, 1962:

- 1) To develop and support standards for the training in the practice of neuroradiology
- 2) To foster independent research in neuroradiology
- 3) To promote a closer fellowship and exchange of ideas among neuroradiologists.

The ASNR has been leading the cutting edge in the development, clinical translation, and dissemination of novel, game-changing imaging technologies since its earliest days, including—but-not-limited-to CT scanning in the early/mid-1970s and MR imaging in the late 1970s/early 1980s, both Nobel Prize-winning, and details of which are well-described throughout the literature.^{29–33} We look forward to continued growth, as well as to the exciting new innovations certain to occur in the next 60 years, confident that the future holds promise.^{34,35}

REFERENCES

1. Röntgen WC. **On a new kind of rays.** *Science* 1896;3:227–31 CrossRef Medline
2. Leeds NE, Kieffer SA. **Evolution of diagnostic neuroradiology from 1904 to 1999.** *Radiology* 2000;217:309–18 CrossRef Medline
3. Taveras JM. **Neuroradiology: past, present, future.** *Radiology* 1990;175:593–602 CrossRef Medline
4. Bécélère A. **The radio-therapeutic treatment of tumours of the hypophysis, gigantism and acromegaly.** *Archives of The Roentgen Ray* 1909;14:147–50 CrossRef
5. Pfahler GE. **Roentgen rays in oral surgery.** *JAMA* 1908;L:432 CrossRef
6. Dandy WE. **Ventriculography following the injection of air into the cerebral ventricles.** *Ann Surg* 1918;68:5–11 CrossRef Medline
7. Dandy WE. **Roentgenography of the brain after injection of air into the spinal canal.** *Ann Surg* 1919;70:397–403 CrossRef Medline
8. Sicard JA, Forestier J. **Méthode radiologique d'exploration de la cavité épidurale par le lipiodol.** *Revista de Neurologia* 1921;47:1264–66
9. Di Chiro G, Schellinger D. **Computed tomography of spinal cord after lumbar intrathecal introduction of metrizamide (computer assisted myelography).** *Radiology* 1976;120:101–04 CrossRef Medline
10. Ozdoba C, Gralla J, Rieke A, et al. **Myelography in the age of MRI: why we do it, and how we do it.** *Radiol Res Pract* 2011;2011:329017 CrossRef Medline
11. Moniz E. **Radiografia das artérias cerebrais.** *Jornal da Sociedade das ciências Médicas de Lisboa* 1927;XCI
12. van der Stelt PF. **From pixel to image analysis.** *Dentomaxillofac Radiology* 2021;50:20200305. CrossRef Medline
13. Taveras JM. **Development of the first fellowship training program in neuroradiology in North America.** *AJNR Am J Neuroradiol* 1991;12:587–90 Medline
14. Ransohoff J. **Diagnostic neuroradiology.** *Arch Neurol* 1964;11:682 CrossRef
15. Huckman MS. **Dinner at Keen's: the founding of the American Society of Neuroradiology.** *AJNR Am J Neuroradiol* 2001;22:1803–05 Medline
16. Taveras JM. **The development of neuroradiology in the United States (editorial).** *AJNR Am J Neuroradiol* 1980;1:1–2 CrossRef
17. Peterson HO. **The early history of neuroradiology at the Medical School of the University of Minnesota, 1937–1939.** *AJNR Am J Neuroradiol* 1992;13:873–87 Medline
18. Kieffer SA, Harold O. **Peterson, MD: a life in neuroradiology.** *AJNR Am J Neuroradiol* 1993;14:1427–35 Medline
19. Figley MM, Taveras JM. **The American Journal of Neuroradiology (editorial).** *AJNR Am J Neuroradiol* 1980;1:103
20. Taveras JM. **Editor's comments on the 10th anniversary of AJNR (editorial).** *AJNR Am J Neuroradiol* 1989;10:1–2
21. Taveras JM. **ASNR: the silver anniversary—Neuroradiology: the next 25 years.** *AJNR Am J Neuroradiol* 1987;8:393–95 Medline
22. Huckman MS, Davis PC, Davis WL, et al. **Highlights of the 30th annual meeting of the American Society of Neuroradiology.** *AJNR Am J Neuroradiol* 1992;13:1642–51 Medline
23. Huckman MS. **ASNR Presidential Address, 1988.** *AJNR Am J Neuroradiol* 1988;9:995–97 Medline
24. Huckman MS. **Paul F.J. New, MD, FACR.** *AJNR Am J Neuroradiol* 2003;24:1264–65 Medline
25. Huckman MS. **Juan Manuel Taveras, 1919–2002.** *AJNR Am J Neuroradiol* 2002;23:1065–68 Medline
26. Huckman MS. **Giovanni Di Chiro (1926–1997).** *AJNR Am J Neuroradiol* 1998;19:1007–10 Medline
27. Huckman MS. **Derek FC, Harwood Nash, MB, ChB, DSc, FRCPC, FACR, FC RAD (SA).** *AJNR Am J Neuroradiol* 1997;18:1803–12 Medline
28. Zimmerman RD. **Norman Leeds, MD.** *AJNR Am J Neuroradiol* 2020;41:1323–24 CrossRef
29. Ambrose J. **Computerized transverse axial scanning (tomography), 2: clinical application.** *Br J Radiol* 1973;46:1023–47 CrossRef Medline
30. New PF, Scott WR, Schnur JA, et al. **Computerized axial tomography with the EMI scanner.** *Radiology* 1974;110:109–23 CrossRef Medline
31. Huckman MS. **Neuroradiology without benefit of computers: a memoir.** *AJNR Am J Neuroradiol* 2010;31:784–86 CrossRef Medline
32. Lauterbur PC. **Image formation by induced local interactions: examples employing nuclear magnetic resonance.** 1973. *Clin Orthop Relat Res* 1989;(244):3–6 Medline
33. Wedeen VJ, Meuli RA, Edelman RR, et al. **Projective imaging of pulsatile flow with magnetic resonance.** *Science* 1985;230:946–48 CrossRef Medline
34. Huckman MS. **The lessons of history.** *AJNR Am J Neuroradiol* 1993;14:1–2 Medline
35. Ackerman RH. **Neuroimaging looks to the future.** *J Neurol Sci* 1995;128:117–21 CrossRef

✉ M.H. Lev

Department of Radiology
Massachusetts General Hospital/Harvard Medical School
Boston, Massachusetts

✉ J.A. Gadde

Ann & Robert H. Lurie Children's Hospital of Chicago
Chicago, Illinois

✉ R.H. Wiggins

University of Utah
Health Science Center
Salt Lake City, Utah

<http://dx.doi.org/10.3174/ajnr.A7712>

Regarding “Altered Blood Flow in the Ophthalmic and Internal Carotid Arteries in Patients with Age-Related Macular Degeneration Measured Using Noncontrast MR Angiography at 7T”

We read with great interest the article by Hibert et al,¹ “Altered Blood Flow in the Ophthalmic and Internal Carotid Arteries in Patients with Age-Related Macular Degeneration Measured Using Noncontrast MR Angiography at 7T.” On the basis of MR imaging of the ophthalmic arteries (OAs) and the internal carotid artery and the study of the difference between patients with age-related macular degeneration (AMD) and healthy controls in terms of flow velocities and volume flows, they suggested that OA volume flow is reduced and flow velocity is increased in patients with AMD, particularly in the late-stage disease.

We have some methodologic concerns, and we would be grateful if the authors could clarify the following important points, which may have led to important misinterpretation.

First, it seems that there was no strict age-matching protocol, as the two cohorts were shown to have a mean difference of 8.5 years of age. Moreover, statistical tests for the difference of means were not reported for this variable. We would therefore, be grateful if the authors could provide significance values for the age comparison between the two groups. We believe that such a difference can be partly to blame for the difference found in volume flows and OA diameter; in fact, it has been shown that flow velocity in this vessel increases with age.² Furthermore, whether these patients underwent cardiovascular evaluation was not reported. This omission could mean that controls not only had no AMD but may have also had a lower cardiovascular risk and a lower atherosclerotic burden and, therefore, higher OA diameters and volume flows, leading to a better choroidal perfusion.³

In addition, the authors reported that when MR imaging was repeated for a patient, it yielded a difference of 10% with regard to volume flow. Although differences between controls and patients with AMD were higher, up to 46% when patients with late AMD and controls were taken into consideration, a

single measurement cannot conclude that the maximum variability is indeed 10%. This issue is especially true if we consider that flow measurement with phase-contrast MR imaging was shown to have a certain level of intermeasurement variability, increasing with higher-degree stenosis.⁴ We believe that further assessment was necessary to conclude that variability in the measurements did not exceed or invalidate the findings of this study.

Furthermore, the authors mentioned a specific analysis of patients who had AMD at different stages between the 2 eyes; however, they also reported 2 patients who had only 1 eye affected by AMD. It would have been interesting to know whether the OA volume flow reduction trend was also observed in the nonaffected eye of such patients with AMD. This evidence, though without statistical significance, would have helped to understand whether vascular changes occur before or after the development of AMD. Moreover, differences in terms of OA volume flow between 2 eyes of the same patient, one affected by AMD and the other one healthy, may suggest the feasibility of OA angioplasty.⁵

Finally, apart from the small number of patients enrolled in this study, which did not jeopardize the significance of the results, the proportion of excluded patients and relative data was remarkable. Most such measurements were discarded due to motion artifacts, making a reliable analysis of flow rates impossible. This issue could have been overcome by repeating the scan in these patients, and it would have also increased the sample size, thus strengthening the findings of the study.

We would be grateful if the authors responded to our letter and addressed our concerns. We believe that the aforementioned points should be further investigated to help shed light on the role of OA flow alterations in AMD pathogenesis.

<http://dx.doi.org/10.3174/ajnr.A7479>

REFERENCES

1. Hibert ML, Chen YI, Ohringer N, et al. **Altered blood flow in the ophthalmic and internal carotid arteries in patients with age-related macular degeneration measured using noncontrast MR angiography at 7T.** *AJNR Am J Neuroradiol* 2021;42:1653–60 CrossRef Medline
2. Yang XY, Xu LF, Luo Y, et al. **Effects of age on the peak ratio of ophthalmic artery Doppler.** *Medicine (Baltimore)* 2020;99:e23694 CrossRef Medline
3. Mitu O, Crisan A, Redwood S, et al. **The relationship between cardiovascular risk scores and several markers of subclinical atherosclerosis in an asymptomatic population.** *J Clin Med* 2021;10:955–12 CrossRef Medline
4. Khodarahmi I, Shakeri M, Kotys-Traughber M, et al. **Accuracy of flow measurement with phase contrast MRI in a stenotic phantom: where should flow be measured?** *J Cardiovasc Magn Reson* 2012;14: P219 CrossRef
5. Lylyk I, Bleise C, Lylyk PN, et al. **Ophthalmic artery angioplasty for age-related macular degeneration.** *J Neurointerv Surg* 2022 Jan 5. [Epub ahead of print] CrossRef Medline

 **N. Ribarich**

School of Medicine
Vita-Salute San Raffaele University
Milan, Italy

 **R. Sacconi**

School of Medicine
Vita-Salute San Raffaele University
Milan, Italy
Department of Ophthalmology
Ospedale San Raffaele
Milan, Italy

 **A. Servillo**

School of Medicine
Vita-Salute San Raffaele University
Milan, Italy

 **G. Querques**

School of Medicine
Vita-Salute San Raffaele University
Milan, Italy
Department of Ophthalmology
Ospedale San Raffaele
Milan, Italy

REPLY:

We thank Ribarich et al for their interest in our work and thank the editors of *AJNR* for giving us the opportunity to respond to this letter. Dialogues such as this are an important part of healthy scientific discourse and progress, and we hope that our responses can help clarify several points of our article and thereby help strengthen our study.

Ribarich et al noted that our patients with age-related macular degeneration (AMD) and control groups were not perfectly age-matched, but this was addressed in our description of the statistical analysis performed. We used a generalized estimating equations (GEE) method and explained that age was included as a variable in our model as well as in the calculation of post hoc comparisons if it was statistically significant. Table 1 identifies the comparisons for which age was statistically significant and was, therefore, included in the GEE model.

Ribarich et al also noted that our article did not report cardiovascular disease burden in the study population. This is true, though it was not the focus of the article because cardiovascular risk is known to be associated with AMD;¹⁻⁴ our focus remained on the potential effects of that association by examining the vascular condition as it related to disease progression. The differences between the population with AMD and the similarly matched controls are interesting and need to be explored further.

Nevertheless, as part of this discussion, it is important to maintain the distinction between linear flow and volumetric flow. It is understood that linear flow (velocity) in the ophthalmic artery (OA) increases with age, as Ribarich et al state. An increase in linear flow is thought to be the result of decreased volume. The volume is decreased due to atherosclerotic changes, and the linear flow (velocity) increases from an otherwise unchanged pressure system. Because the patient group with AMD is, on average, slightly older than the control group, the age difference could be expected to yield a small linear flow increase in patients with AMD; however, it is not thought to account for the statistically significant differences reported. The more interesting takeaway is the trend test plot (presented in Figure 4 of our published article) demonstrating that the association between the rate of decline in OA volumetric flow with AMD disease progression is statistically significant. This finding demonstrates the potential for decreased ocular perfusion to affect the AMD process, perhaps in those patients who are genetically predisposed.

Regarding the question of our reported measurement variability, we acknowledged the limitation of estimating variability in 1 subject, and we agree that additional measurements would be valuable to improve this estimate. As Ribarich et al note, the within-subject variability that we estimated was still substantially lower than the difference between groups. We note here that as indicated in the discussion section of our article, our phase-contrast MRA measurements were remarkably similar to those reported in the prior study of Ambarki et al,⁵ who reported a resistance index of 0.68 (SD, 0.08) in the OA compared with our value of 0.70 (SD, 0.10) in similarly aged control subjects. These findings

provided us with additional confidence in the quantitative validity of our measurements.

Ribarich et al noted that 2 patients with AMD had only 1 eye affected by AMD and suggested a new analysis of our data that may be helpful to understand whether vascular changes occur before or after the development of AMD. This observation does not appear to be a criticism per se, and we agree that this suggested analysis based on $n = 2$ subjects should not be overinterpreted. In reviewing our data for this response letter, we realized that 1 of the eyes that we reported was excluded from analysis due to motion and not due to diagnosis, and we apologize for the misstatement in our article. Thus only 1 patient in our group was diagnosed with AMD in a single eye. We reviewed our data from this 1 patient, and we can confirm that the trend that we reported is also seen in this patient: The OA of the healthy eye has a volumetric flow rate of 13.3 mL/min and a resistance index of 0.77, while the OA of the AMD eye has a volumetric flow rate of 2.9 mL/min and a resistance index of 0.86. Again, we should not overinterpret this $n = 1$ analysis, but it is reassuring.

Finally, Ribarich et al noted that the proportion of excluded patients was remarkable, and that a “majority” of measurements were discarded due to motion; however, this statement is incorrect and may be a misunderstanding. We apologize if this was unclear in our article. Data were included from 21 of 24 patients with AMD, and from 12 of 13 controls. We excluded approximately 30% of OAs from patients with AMD and 25% from controls, and far fewer ICAs were excluded in both groups. We agree that there was an unfortunately large number data sets that could not be analyzed due to motion artifacts, but fortunately, the number of data sets included in our analysis was still sufficiently high due to the large overall number of volunteers. We note again that all volunteers were cooperative; however, these were all older individuals, and our 7T MR imaging scanner is somewhat less comfortable than clinical MR imaging scanners due to the long bore size and the tight-fitting radiofrequency head coil, which contribute to a less pleasant patient experience, increasing the potential for motion.

Again, we are glad to have the opportunity to clarify these points, which we hope will help further strengthen our article. We hope that Ribarich et al agree that all points that they have raised have been fully addressed, and there is no evidence of “significant misinterpretation” of the data reported in our article. We agree with Ribarich et al that this is an important topic that warrants further investigation that will build on our findings to better understand the role of abnormal OA flow in AMD.

REFERENCES

1. Pennington KL, DeAngelis MM. **Epidemiology of age-related macular degeneration (AMD): associations with cardiovascular disease phenotypes and lipid factors.** *Eye Vis (Lond)* 2016;3:34 CrossRef Medline
2. Hyman L, Schachat AP, He Q, et al. **Hypertension, cardiovascular disease, and age-related macular degeneration.** *Arch Ophthalmol* 2000;118:351–58 CrossRef Medline
3. Klein R, Klein BEK, Tomany SC, et al. **The association of cardiovascular disease with the long-term incidence of age-related maculopathy: the Beaver Dam eye study.** *Ophthalmology* 2003;110:636–43 CrossRef

<http://dx.doi.org/10.3174/ajnr.A7717>

4. Thomson RJ, Chazaro J, Otero-Marquez O, et al. **Subretinal drusenoid deposits and soft drusen: are they markers for distinct retinal diseases?** *Retina* 2022;42:1311–18 CrossRef Medline
5. Ambarki K, Hallberg P, Jóhannesson G, et al. **Blood flow of ophthalmic artery in healthy individuals determined by phase-contrast magnetic resonance imaging.** *Invest Ophthalmol Vis Sci* 2013;54:2738–45 CrossRef Medline

 **M.L. Hibert**

Athinoula A. Martinos Center for Biomedical Imaging
Massachusetts General Hospital
Charlestown, Massachusetts

 **Y.I. Chen**

Athinoula A. Martinos Center for Biomedical Imaging
Massachusetts General Hospital
Charlestown, Massachusetts
Department of Radiology
Harvard Medical School
Boston, Massachusetts

 **N. Ohringer**

Athinoula A. Martinos Center for Biomedical Imaging
Massachusetts General Hospital
Charlestown, Massachusetts

L.R. Wilbur

OcuDyne, Inc
Roseville, Minnesota

 **N.K. Waheed**

New England Eye Center
Tufts Medical Center
Boston, Massachusetts

 **J.S. Heier**

Ophthalmic Consultants of Boston
Boston, Massachusetts

 **M.W. Calhoun**

OcuDyne, Inc
Roseville, Minnesota

 **P.J. Rosenfeld**

Department of Ophthalmology, Bascom Palmer Eye Institute
University of Miami Miller School of Medicine
Miami, Florida

 **J.R. Polimeni**

Athinoula A. Martinos Center for Biomedical Imaging
Massachusetts General Hospital
Charlestown, Massachusetts
Department of Radiology
Harvard Medical School
Boston, Massachusetts
Harvard-MIT Division of Health Sciences and Technology
Massachusetts Institute of Technology
Cambridge, Massachusetts

Fair Performance of CT in Diagnosing Unilateral Vocal Fold Paralysis

Bashir et al¹ reported the diagnostic performance of CT signs of unilateral vocal fold paralysis as evaluated by blinded radiologists. They highlighted the 2 best signs combined, medialization of the posterior vocal fold margin and laryngeal ventricle dilation, as having a positive predictive value of 87%, specificity of 74%, and interrater reliability of $\kappa = 0.50$ – 0.54 . The authors concluded that these CT signs should raise concern for ipsilateral vocal fold paralysis. However, important limitations apply.

The first limitation pertains to the study design. In this retrospective, case-control study, only patients who underwent laryngoscopy by an otolaryngologist were included, while patients were excluded if they had a history of cancer, trauma, radiation, or surgery involving the larynx or pharynx. Spectrum bias arises when the study sample differs in case mix from that encountered in the clinical setting where these signs are intended to be used.² Patients who undergo laryngoscopy may have more advanced disease, such as obvious dysphonia, resulting in overestimation of sensitivity. Excluding controls likely to have anatomic distortions for other reasons results in overestimation of specificity. This study may not generalize to many common scenarios for neck CT, such as surveillance for head and neck cancer or trauma.

The second limitation pertains to the results interpretation. Predictive values depend on the underlying disease prevalence (Figure), especially when the inherent test characteristics are overall fair as in this case (sensitivity 62%, specificity 74%). Case-control studies typically do not reflect the prevalence of disease in the relevant clinical population, rendering predictive values misleading.^{2,3} The positive predictive values in this study are inflated from those expected in real clinical practice because the prevalence of unilateral vocal fold paralysis was 73%. If the prevalence is 10%, which is still likely an overestimate on typical neck CTs in my opinion, the positive predictive value of these CT signs would only be 21%.

I agree with the authors' conclusion that "care must be taken to translate suspicious findings appropriately." Clinicians should consider the patient's risk factors and pretest probability of vocal fold paralysis, as well as the fair diagnostic performance and reliability of these CT signs, demonstrated in this study within the limitations of its design.

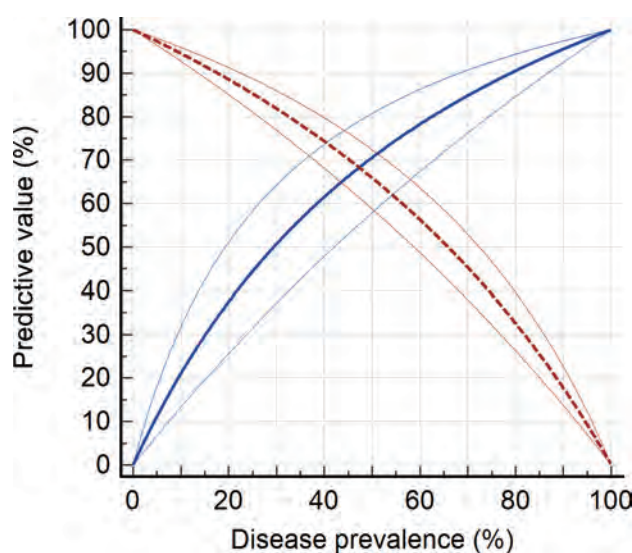


FIGURE. Conditional probability for the diagnosis of unilateral vocal fold paralysis based on CT. Predictive values (blue/solid lines, positive predictive value; red/dashed lines, negative predictive value) with 95% confidence intervals (thin lines) were calculated from the sample sizes and estimated sensitivity and specificity of the 2-sign model in Bashir et al,¹ using a standard logit method (MedCalc, Version 20.109; MedCalc Software).

Disclosure forms provided by the authors are available with the full text and PDF of this article at www.ajnr.org.

REFERENCES

1. Bashir MH, Joyce C, Bolduan A, et al. Revisiting CT signs of unilateral vocal fold paralysis: a single, blinded study. *AJNR Am J Neuroradiol* 2022;43:592–96 CrossRef Medline
2. Pavlou A, Kurtz RM, Song JW. Diagnostic accuracy studies in radiology: how to recognize and address potential sources of bias. *Radiol Res Pract* 2021;2021:e5801662 CrossRef Medline
3. Deng F. Reporting predictive values for diagnostic tests. *AJR Am J Roentgenol* 2018;211:W278 CrossRef Medline

F. Deng

The Russell H. Morgan Department of Radiology and Radiological Science
Johns Hopkins University School of Medicine
Baltimore, Maryland